Poster Proceedings

ICCE

2008

31st International Conference on Coastal Engineering
31st August to 5th September 2008
Hamburg, Germany

editors
Rainer Lehfeldt
Holger Schüttrumpf

Poster Proceedings

ICCE

2008

31st International Conference on Coastal Engineering
31st August to 5th September 2008
Hamburg, Germany

editors
Rainer Lehfeldt
Holger Schüttrumpf

Organized by:

Kuratorium für Forschung und Küsteningenieurwesen (KFKI)
der Bundesanstalt für Wasserbau

Hafentechnische Gesellschaft e.V. (HTG)

Coasts, Oceans, Ports ans Rivers Institute (COPRI) of the
American Society of Civil Engineering

Editors:

Dr.-Ing. Rainer Lehfeldt
Kuratorium für Forschung und Küsteningenieurwesen, BAW

Prof. Dr.-Ing. Holger Schüttrumpf
Institut für Wasserbau und Wasserwirtschaft, RWTH Aachen

1. Auflage Aachen:

Verlag R. Zillekens, 2009
ISBN: 978-3-941277-05-2

Gesamtherstellung:
Druckservice Zillekens
Am Bachpütz 4; 52224 Stolberg
Telefon 02408. 958216; Telefax 02408. 958217
www.druckservice-zillekens.de; E-Mail: info@druckservice-zillekens.de

Bibliografische Information der deutschen Bibliothek

Die deutsche Bibliothek verzeichnet diese Publikation in der Deutschen Nationalbibliografie.
Detaillierte bibliografische Daten sind im Internet unter http://dnb.ddb.de abrufbar.

Foreword

The 31st International Conference on Coastal Engineering (ICCE 2008) was held in Hamburg, Germany, 31 August to 5 September 2008 under the auspices of the Coastal Engineering Research Council (CERC).

It was a long way from the application to host this conference in Cardiff / Wales in 2002, and many colleagues contributed significantly to the success of the conference. Herewith, we would like to acknowledge all involved colleagues, delegates, CERC and LOC members as well as the supporting institutions and exhibitors for making this conference a successful and memorable event. Namely, we would like to thank the Coastal Engineering Research Council, especially Prof. Robert A. Dalrymple, CERC chairman, and Jane Smith, CERC secretary, for their guidance and encouragement as well as for their help and continuous motivation. It was a pleasant experience to organise this conference together with our US-colleagues. On the other hand, we would like to thank all members of the Local Organising Committee, chaired by Prof. Hans Dücker, representing coastal and harbour authorities, ministries, universities and consultant companies in Germany. Mainly the permanent support of the Local Organising Committee made this conference successful. Many institutions supported this 31st International Conference on Coastal Engineering as a sponsor or as an exhibitor, which was a prerequisite to organise an unforgettable conference. Finally, we would like to acknowledge all the contributions of the delegates, who presented and discussed state of the art papers for a wide range of coastal topics.

The present poster proceedings are edited to acknowledge all the excellent posters which were presented and discussed during the conference. It is the intention of the editors to make these posters available for many colleagues world wide. Therefore, the poster proceedings are also uploaded to the conference website (http://icce2008.hamburg.baw.de) which will remain active during the coming years.

Dr.-Ing. Rainer Lehfeldt
German Coastal Engineering Research Council
Hamburg
rainer.lehfeldt@baw.de

Prof. Dr.-Ing. Holger Schüttrumpf
RWTH Aachen University
Aachen
schuettrumpf@iww.rwth-aachen.de

CONTENTS

CONTENTS

CONTENTS

CONTENTS

THE DEVELOPMENT OF THE FLOW VELOCTIES SINCE THE ELBE FAIRWAY DEEPENING IN 1999

Maja Fickert[1] and Thomas Strotmann[2]

For the Elbe fairway deepening of 1999 changes of the flow velocities in the Elbe estuary of up to 5 cm/s were predicted by a numerical model of the Federal Waterways Engineering and Research Institute. In this work, the existing data were processed and analyzed with statistical methods regarding the permanent changes. Complex statistical analyzes were developed and performed relying on the linear wave theory and the channel hydraulics. The analyzes brought success insofar that it is now possible to create the full hydrograph of the tidal currents in good approximation by taking into account the gradient of the water level curve.

Introduction

To keep up the competitiveness of the port of Hamburg time and again it is necessary to adapt its seawards access to the shipbuilding developments. The last deepening of the fairway of the lower and outer Elbe to the requirements of the container ship navigation was carried out in 1999/ 2000. The adaptation of the port access always causes an interference with nature, not only changing the flora and fauna but also the dynamics of the tidal wave in the estuary. The modified fairway depths and cross-sections can influence the tidal water levels, and thus the tidal amplitude, the duration of the flood tide and the ebb tide as well as the flood and ebb flow velocities. To analyse these changes the evidence report of the last fairway deepening established an extensive monitoring program in which the flow velocities of the lower and outer Elbe have been measured permanently at 13 stations since 1997/ 1998.

[1] Hydrology, Hamburg Port Authority, Neuer Wandrahm 4, Hamburg, 20457, Germany

Figure 1. Tidal River Elbe with flow velocity measuring stations

The environmental impact analysis of the fairway deepening assumed an increase of the current velocities by 0 to 3 cm/s or even up to 5 cm/s at some sights. While for the fairway channel itself a velocity increase was predicted, an unquantifiable decrease for the shallow water areas was expected.

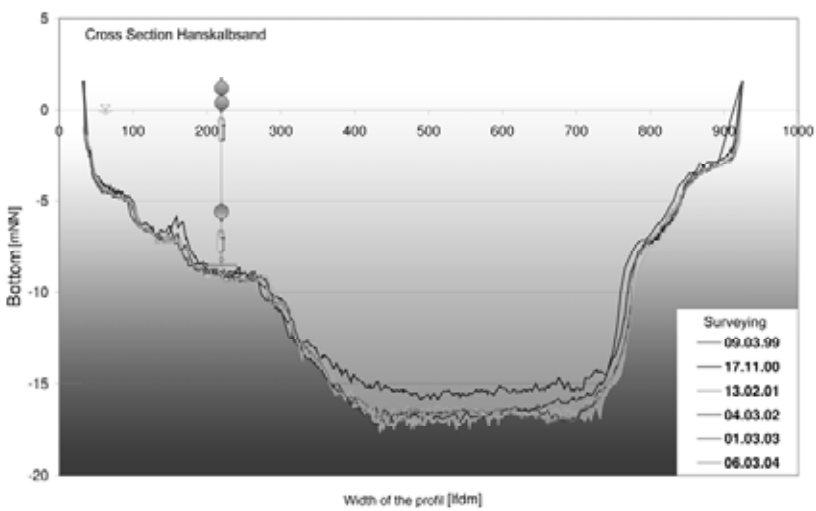

Figure 2. Cross section at Hanskalbsand with measuring instrument

The aim of this work is to process the existing data of the flow velocities and to analyse them with statistical methods regarding to permanent changes. Thereby changing boundary conditions (freshwater discharge and tidal

influence) must be considered, so that different hydrological situations before and after the fairway deepening can be compared.

Figure 3. RCM 9 Measuring instrument

The station which data is analyzed is D1 Hanskalbsand, close to the Hamburg Port. The station is equipped with an instrument Anderaa RCM 9 working on acoustic bases. It was chosen because the station lies upstream of the turbidity zone and therewith beyond the unknown density currents.

The accuracy of the RCM 9 which measures the current velocity depends on the calibration of the instruments and the resulting infeed of data, the material that is carried along in the water column and the deviation of the instrument chain. Therefore, the identification of the minor predicted changes due to the fairway deepening is within the range of the measuring and analytical accuracy.

The current conditions create an always-changing image and its depiction must be reduced to a few key characteristics. Complex statistical analyses were developed and performed relying on the linear wave theory and the channel hydraulics. Nevertheless a direct empirical correlation between tidal parameters, freshwater discharge and the flow velocities could not be established sufficiently.

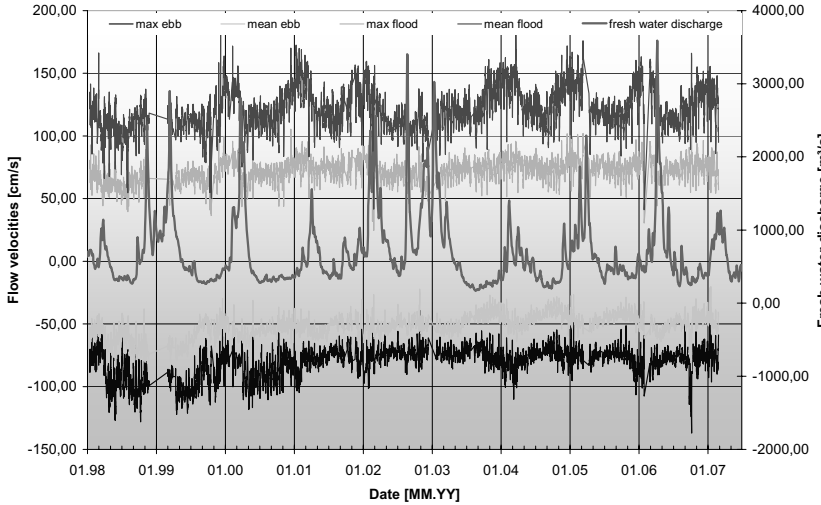

Figure 4. Flow velocities with freshwater discharge

However it succeeded to recreate the full hydrograph of the tidal currents in good approximation by taking into account the preceded "history" of the water level gradient. Due to the inertia of the oscillating water body and reflection components there is a lag between the local change in the water level gradient and the reaction of the tidal currents at the same cross-section. This can be judged as a success because now it was possible to fill up data gaps and create velocity hydrographs for time periods when the flow velocity has not been measured.

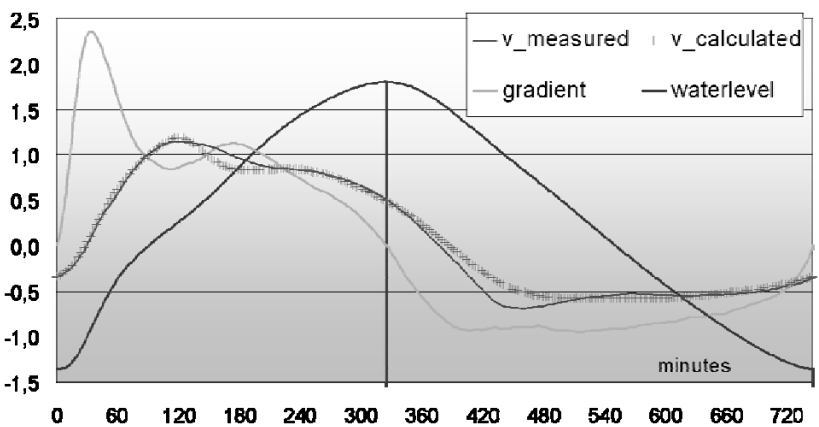

Figure 5. Measured and "constructed" graph of the flow velocities with the gradient and water level

These continuous time series of tidal currents and water levels in different cross-sections enables the calculation of accumulated volume flow rates and makes it possible to balance the sediment transport capacity during the changeable hydrological season.

This is very interesting, especially with respect to the different questions that come up with the matter of the upstream transport of sediments in consequence of the tidal pumping. Due to the increasing amounts of dredged material in the Port of Hamburg a better understanding of the complex interrelations in the Elbe estuary is needed to reverse this phenomenon.

REFERNCES

Wasser- und Schifffahrtsamt Hamburg, Hamburg Port Authority. 2006. *Bericht zur Beweissicherung 2005*.

ANALYSES OF TIME SERIES & MODEL HINDCAST OF WATER LEVELS AFTER THE LAST DEEPENING OF THE ELBE ESTUARY - A COMPARISON

Marko Kastens[1]

In 1998/99 the maintained fairway depth of the river Elbe was lowered from 13,5 m to 14,4 m - an amount of about 20 mio tons of sediment was dredged and dumped. The predicted change of water level due to the deepening was a decrease in mean low water of 10 cm and an increase in mean high water of 5 cm e.g. at the tide gauge St.Pauli. The following investigation based on measurement data, model hindcast and scenarios shows the changes of water levels due to the last deepening.

Overview and Introduction

For a brief overview Figure 1 shows a small map with the model area, the tide gauges and the dimensions of the investigation area.

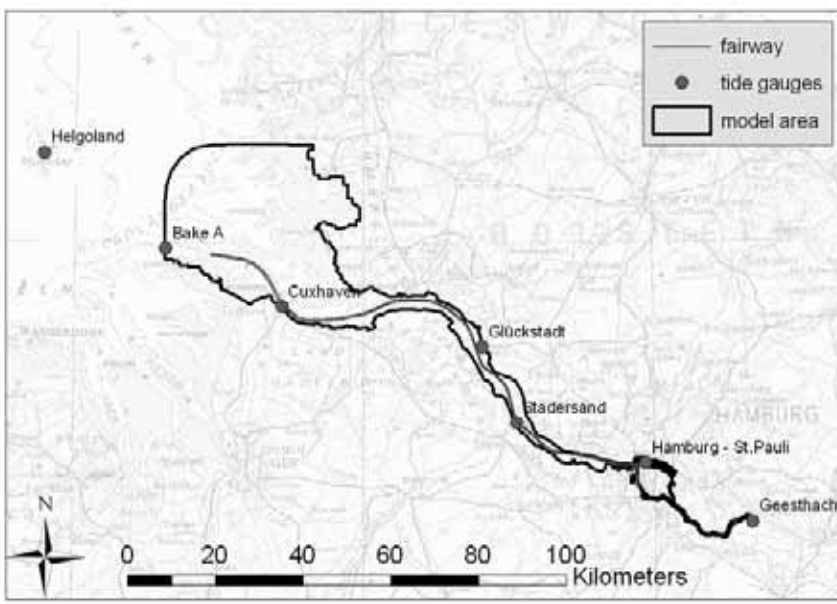

Figure 1. Map with tide gauges and the model area

The major aim in this work was, to find out, how the water levels changed due to the last deepening of the Elbe estuary.

[1] Federal Waterways Engineering and Research Institute, Coastal Department, Wedeler Landstraße 157, 22559 Hamburg, Germany

Interpreting water level measurements at the tide gauges is not a trivial *job* because all the different processes such as changes in the North Sea, meteorological effects, changes in fresh water discharge and anthropogenic impacts are superimposed.

In the first part of this paper a method is introduced that filters out water level dependencies in tide gauges in the Elbe estuary from tide gauges in the North Sea and dependencies from the fresh water discharge. By removing these dependencies the remaining changes in the water level signal are majorly based on local developments. The presented method is based on measured water levels. A detailed description of the method with background information and literature review can be found in [1].

In the second part a hydrodynamic model is used to determine the water level changes due to the deepening and, in different scenarios, due to natural morphologic changes. Finally the results are compared and discussed.

Analyses of Time Series of Water Levels

Separation of the mean water

The water level is a superposition of a stochastic meteorological triggered signal and the tides, a harmonic signal. The mean water represents mostly the stochastic part of the water level. Separating the mean water from the measured water levels can give more insights to the correlation of the mean water to the tidal range, the high and the low water.

For the following analyses the mean water is obtained by a low pass Butterworth filter in Fourier space. The cut-off frequency of the Butterworth filter is 13 degrees/hour – close to the first mentionable partial tide in a one year amplitude spectrum (s. Figure 2). Subtracting the mean water from the measured signal gives some kind of a *pure* tidal signal. From this pure tidal signal the high and low waters, as well as tidal ranges, are determined.

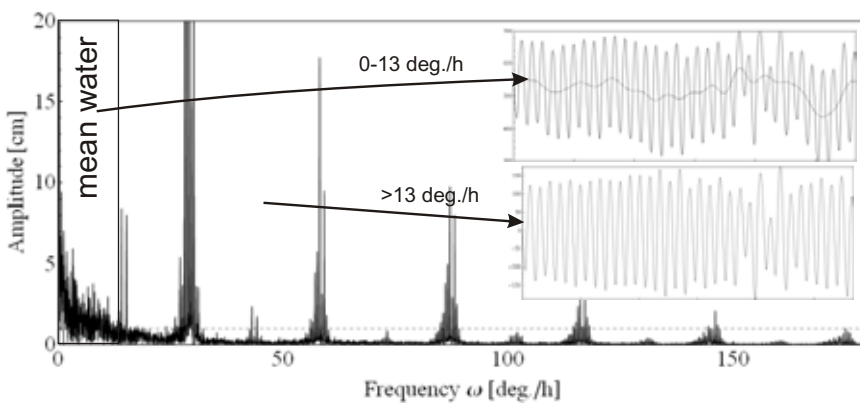

Figure 2 Measured water levels in the frequency and in the corresponding time domain (small pictures). The mean water is defined as the signal from 0 - 13 deg./h in the frequency domain.

Setting up a model function

Scatter plots of different parameters (tidal range, discharge and mean water) and locations show the noisy dependencies of the parameters to each other (s. Figure 3). At the position St.Pauli it can be clearly seen, that the tidal range depends linear on the tidal range in Helgoland.

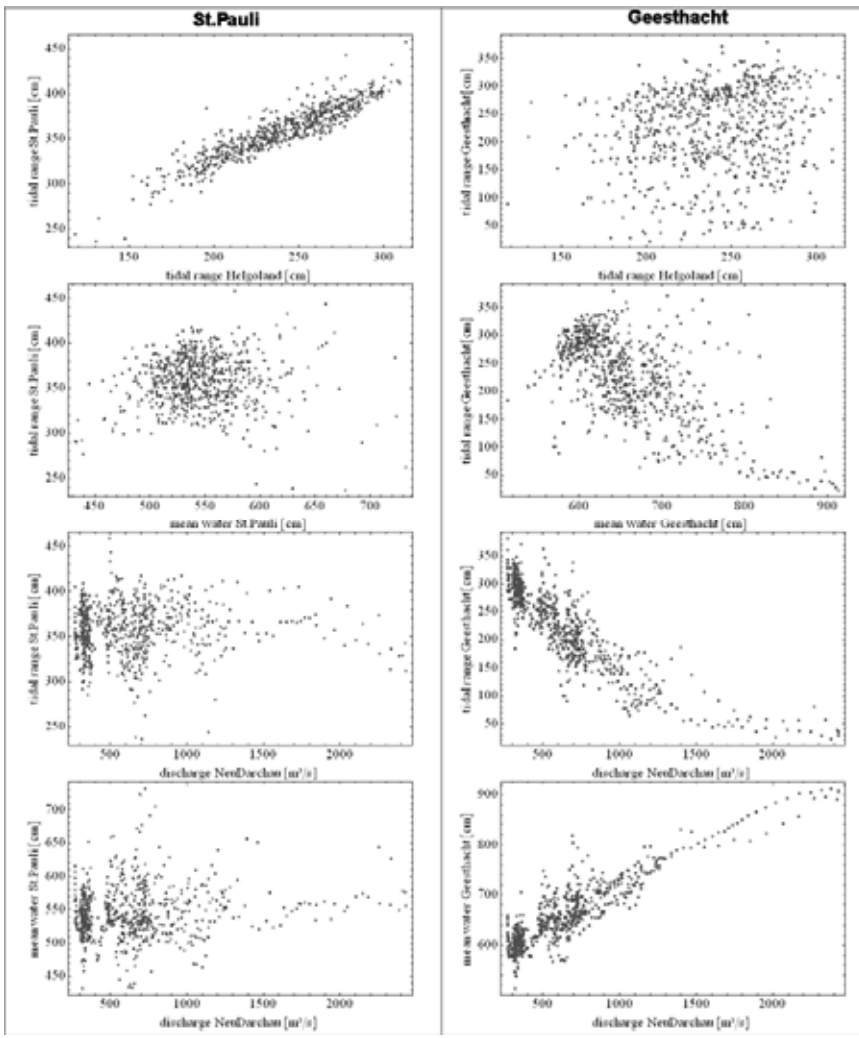

Figure 3. Scatterplots of the parameters tidal range, mean water and discharge at different locations. Note: The discharge location NeuDarchau lies approximately 50 km upstream of the tide gauge Geesthacht.

However, a linear correlation cannot be seen at the location Geesthacht, because two other – more important - impacts are visible at this location: the tidal range is influenced by the mean water and by the fresh water discharge. Furthermore the mean water itself depends on the fresh water discharge.

These parameter dependencies are shown schematically in the diagram below (s. Figure 4).

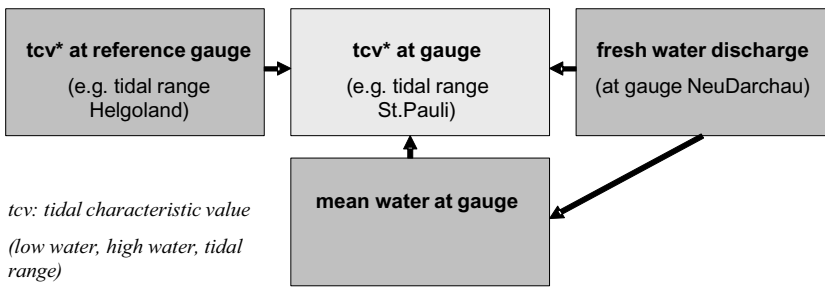

Figure 4. Parameter dependencies: E.g. the tidal range at St.Pauli is influenced by the tidal range at Helgoland, the fresh water discharge and the mean water at St.Pauli.

A simple model function can be set up which reflects the observed phenomena. Because the influence of the fresh water seems to be nonlinear a power n is inserted to the fresh water term. The tidal characteristic value can be expressed:

$$tcv_{Gauge} = a \cdot tcv_{Helgoland} + b \cdot freshwater_{NeuDarchau}^{\ n} + c \cdot meanwater_{Gauge} + z \quad (1)$$

Four of these model functions can be set up for each tide gauge in the same way substituting tcv with the parameters tidal range, high water, low water and mean water respectively. For the parameter mean water the term $c \cdot meanwater_{Gauge}$ is not needed. The coefficients a, b, c, z, n in the equations can be fitted with nonlinear regression. The regression period is a one year period before the deepening. This means that more than 700 points (= tides) are available for the regression, which makes the regression pretty stable. **Figure 5** shows an example of a best fit of a model function with a scatterplot of the measurements.

With the fitted model functions the tidal range, the high and low waters and the mean water can be calculated for each tide gauge in the Elbe estuary. Afterwards the difference to the measured values is calculated and aggregated to yearly means. These yearly mean differences show the local development of the parameters without the influence of the North Sea and the fresh water discharge.

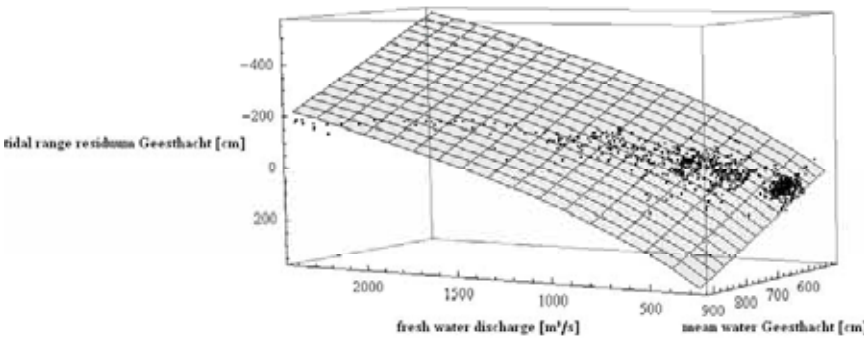

Figure 5. Best fit of a model function (Eq.1) with dotted points as the measurements. Note: Eq.1 is four dimensional – to make the function visible in perspective three dimensions, one dimension is removed: the influence of the tidal range from Helgoland is filtered out with the first term of Eq. 1. The rest is called the tidal range residuum Geesthacht.

Results

As one result Figure 6 shows the development of all four parameters at the tide gauge St.Pauli. The filtered signal is obtained with the presented method. The decline of the mean water after the dredging and the parameter variations in time is remarkable. The latter effect is due to the ongoing morphodynamic behaviour of the Elbe River and due to other anthropogenic impacts.

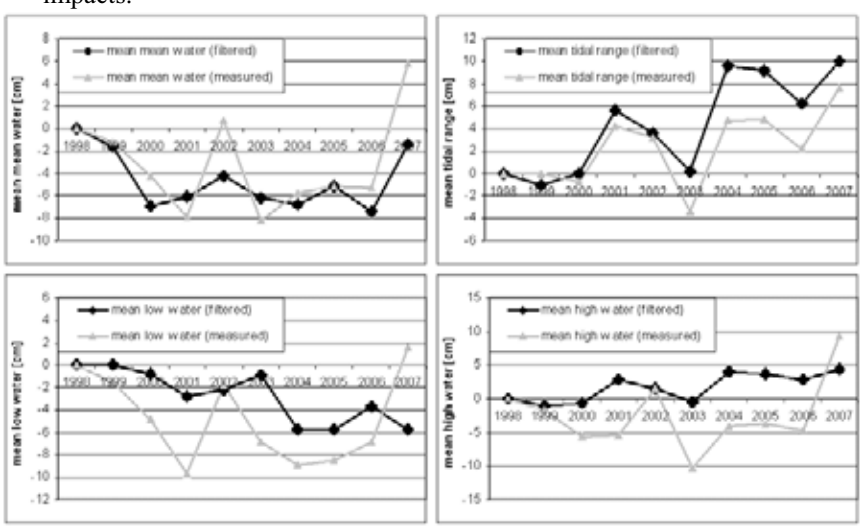

Figure 6. Development of different parameters at the tide gauge St.Pauli since 1998 – pure and filtered measurements

Model Hindcast & Scenarios

Another way to determine the impacts on water levels due to the deepening can be done with hydrodynamic-numerical models. These models are used at Federal Waterways Engineering and Research Institute (BAW), Coastal Department. In this study, a model based on UnTRIM [2], is calibrated, validated and used for a hindcast of the year 2000. Figure 1 shows the model domain.

The results are compared with a second model using the same grid but a digital terrain model from 1997, which was before the last deepening. Other model parameters and steering remain the same.

The main differences between the two bathymetries (1997 and 2000) can be found at the mouth of the estuary (s. Figure 7).

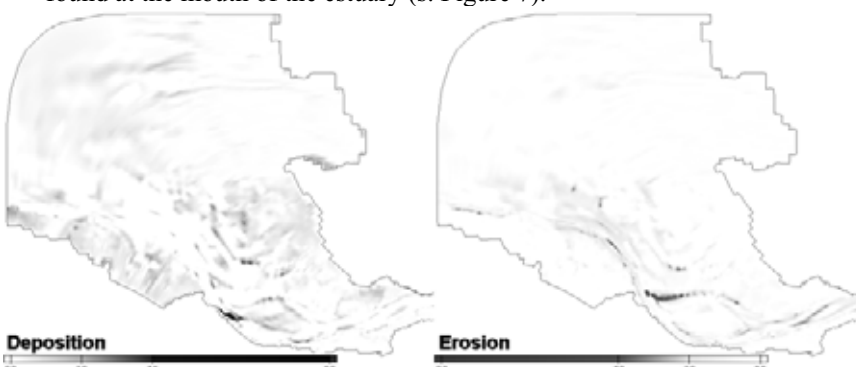

Figure 7. The differences between the bathymetries 1997 and 2000 at the mouth of the Elbe River.

It can be easily seen, that the deepening of the fairway is not the only morphologic change from 1997 to 2000. An ebb branch of the Elbe River (see the dark spots in Figure 7, Erosion) is migrating to the north. This sensitive area plays a major role in the development of the water levels in the river Elbe. To get an idea what kind of morphologic change cause what kind of change in water level, three model scenarios in addition to the hindcast were built up and calculated:

- Scenario A: What would have happened to the water levels if the Elbe River was not dredged? This Scenario includes all the morphological changes from 1997 to 2000 but with a fairway-depth of 1997 from Hamburg to close to Cuxhaven (without the last deepening) and implies, that all the morphological changes have happened as well as there was no deepening.
- Scenario B: The same as A, but with a fairway-depth of 1997 from Hamburg to Bake A. This scenario takes account to the fact that the

changes from Cuxhaven to Bake A are uncertain to assign to nature or to the deepening.

- Scenario C: What would have happened to the water levels if there was no morphologic change by nature and the only change was made by the deepening? In this scenario the digital terrain models of 1997 and 2000 are nearly the same. Only the fairway was lowered to the depth of the year 2000.

All the results regarding the mean tidal range can be seen in the following figure (Figure 8).

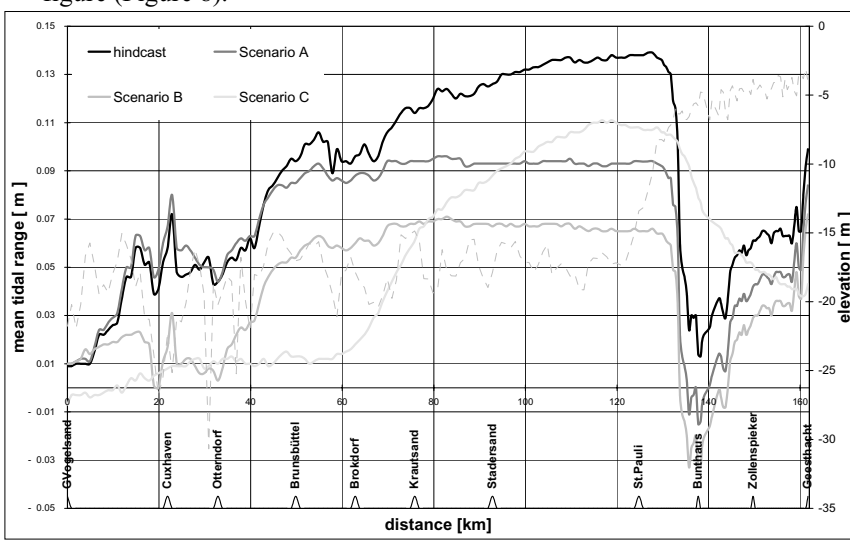

Figure 8. Change of the mean tidal range for different scenarios (see text).

Model results

The deepening is superimposed by natural morphodynamics, therefore the hindcast model is not suitable to determine changes in water levels only to the deepening. Both processes together have an impact of about 14 cm on the tidal range at the tide gauge St.Pauli.

The two scenarios A and B neglect the deepening and assume all changes in morphology to be natural. Both scenario results differ slightly from each other. The difference between them is the assumption of morphologic change in the mouth of the Elbe River. The influence regarding the tidal range for the tide gauge St.Pauli is from 7 to 9 cm.

The last scenario C neglects natural morphologic changes. The only change is the deeper fairway. This assumption is as imperfect as the hindcast,

because the deepening will trigger other changes that might look natural at first. The change in tidal range for the tide gauge St.Pauli is about 11 cm.

Results and Comparison

Model and analyses results

Analyses results should be compared with hindcast results because the analyses cannot distinguish between natural and anthropogenic changes in morphology. It can filter out dependencies due to developments outside the system and implies that the coefficients of the model function do not change in time. The main difference to the model results is the decline of the mean water of about 10 cm. If the mean water is neglected (analyses without mw, s. Figure 9), the results of the analyses point in the same direction but they have smaller values than the model results.

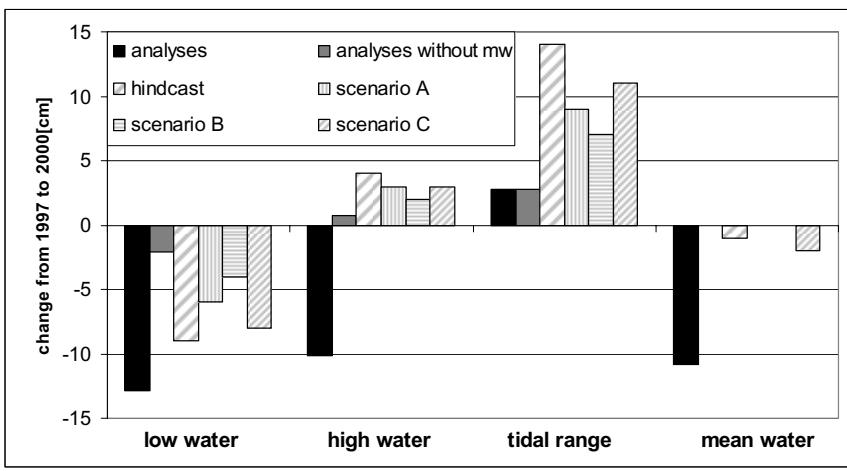

Figure 9. Changes for the tide gauge St.Pauli

Conclusions

Both methods - which are equal in relevance - show different results. These different results give an idea of the range of uncertainty and trustworthiness in the used methods.

Assessing the results requires keeping in mind the strength and the weakness of both methods:

Analyses:

- cannot distinguish between natural and anthropogenic changes
+ can filter out dependency of developments outside the system
+ based on measured data
+ Little computational effort

Computer models:

- cost a lot of computer time and human resources
+ gives the opportunity to calculate scenarios (essential in understanding a system)

REFERENCES

[1] Kastens, M. 2008. Tidewasserstandsanalysen in Ästuaren am Beispiel der Elbe, Die Küste, Heft 72 (2007), Hamburg, 145-169

[2] Federal Waterways Engineering and Research Institute (BAW), Coastal Department (2005): The Mathematical Model UnTRIM; Online in Internet: URL: http://www.baw.de/vip/en/departments/department_k/methods/hnm/untrim/hnm_untrim-en.html (last request: 04.11.2008)

PROPERTIES OF LONG-PERIOD WAVES AND VELOCITY FLUCTUATIONS NEAR RIVER MOUTH AND NARROW INLET

Takumi OKABE[1], Shin-ichi AOKI[2] and Shigeru KATO[3]

To estimate sediment exchange between an estuary and the open sea through a narrow inlet, it may be important to investigate the behavior of the long-period waves with periods of several minutes generated by wave groups in the sea. In this study, characteristics of the long-period waves and associated flows outside and inside the inlet of Hamana Lake and off Tenryu River mouth are discussed based on field data. The results show that long-period waves are developed almost linearly to the products of significant wave heights and periods outside the inlet, but they are reduced by about half in the inlet. The long-period fluctuations in the flow seem to consist of two components; one is associated with the long-period waves and the other is induced by tidal currents.

INTRODUCTION

In the vicinity of an inlet, tidal and wave actions yield complex currents. At a river mouth, complicated wave and flow fields arise from interactions between waves and outflow. Relatively little is known about the sediment transport and associated topographic change around an inlet and river mouth. For example, sediment exchange between an estuary and the sea, and influence of river discharge or tidal currents on longshore sediment transport, are difficult to estimate. External forces that induce sediment transport around the inlet and river mouth have wide range of periods from those of wind waves (seconds) to tides (hours). However, predominant factors or relative importance between the forces with different time scale have not been well investigated. In this paper, we focus on long-period components of several minutes and investigate their characteristics based on field data.

Although previous researches (e.g., Bowen 1980; Sato 2002) have shown that long-period waves with periods of several minutes can influence sediment transport, studies on long-period waves and associated flows near an inlet and a river mouth are very limited. It remains unclear either qualitatively or quantitatively how long-period waves influence sediment transport near the inlet and the river mouth. Detailed investigations of behavior of the long-period waves generated by wave groups in the sea may be necessary in order to estimate influences of the long-period waves on sediment transport near the inlet and river mouth.

[1] Department of Architecture and Civil Engineering, Toyohashi University of Technology, Tempaku-cho, Toyohashi, Aichi 441-8580, JAPAN
[2] Department of Architecture and Civil Engineering, Toyohashi University of Technology, Tempaku-cho, Toyohashi, Aichi 441-8580, JAPAN
[3] International Cooperation Center for Engineering Education Development, Toyohashi University of Technology, Tempaku-cho, Toyohashi, Aichi 441-8580, JAPAN

In this study, characteristics of the long-period waves and associated flows inside and outside the inlet channel and off the river mouth are discussed based on field data at two different sites. We focus on wave components with periods larger than 30 s. We discuss the relations between long-period waves and significant wave heights and periods, and propagation properties of the long-period waves. Generations of long-period fluctuations in the currents induced by tidal action are also shown in the paper.

FIELD OBSERVATIONS

Field measurements were conducted at the inlet of Hamana Lake and off Tenryu River mouth, Japan, for about two months from August to November 2006. Figure 1 and Photo 1 show the locations of the inlet and the river mouth, and the observation stations. In the figure, Stn-in denotes the station inside the inlet, where two-dimensional horizontal flow velocities and water pressure were collected at the bottom. At the station Stn-out located outside the inlet, two-dimensional bottom velocities, water pressure and water surface elevation were measured. The station Stn-R was located at the bottom off Tenryu River mouth, where similar measurements to Stn-out were conducted.

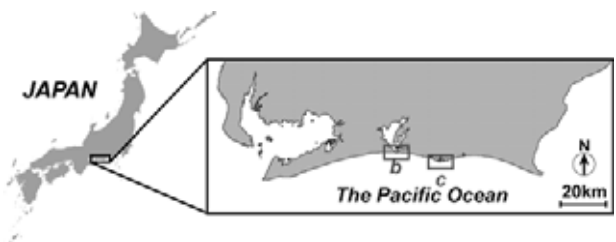

(a) Location of Hamana Lake and Tenryu River in Japan

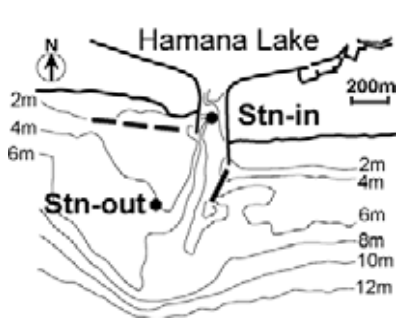

(b) Inlet of Hamana Lake

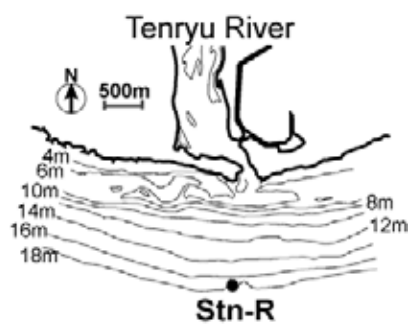

(c) Tenryu River mouth

Figure 1. Location of observation stations

All the data were recorded at sampling rate of 0.5 s continuously except for data loss that occurred in the period of maintenance of the equipment. The water surface elevations were obtained using ultrasonic wave gauges, and an electromagnetic current meter was used in the measurements of 2-D horizontal velocity components. All sensors were synchronized at the start of each field study. Mean water depths during the measurements were 5.6 m at Stn-in, 4.8 m at Stn-out and 18.2 m at Stn-R, respectively. As Stn-out was sometimes in the surf zone due to high waves, water surface elevation measured by the ultrasonic wave gauge could not be used because of noisy signals under storm conditions. So we used wave data calculated from water pressure data for analysis. The details of the field measurements are shown in Table 1.

(a) Inlet of Hamana Lake

(b) Tenryu River mouth

Photo 1. Aerial photographs of the fields

Table 1. Summary of field investigations			
Station name	Stn-in	Stn-out	Stin-R
Location	Inside Hamana Lake inlet	Offshore Hamana Lake inlet	Offshore Tenryu River mouth
Average water depth	5.6 m	4.8 m	18.2 m
Equipment type	WaveHunter-04	WaveHunter-04 Sigma	WaveHunter-04 Sigma
Sampling frequency	2 Hz	2 Hz	2 Hz
Measurements	Water pressure, 2-D flow velocity	Water surface elevation, Water pressure, 2-D flow velocity	Water surface elevation, Water pressure, 2-D flow velocity
Height of sensors above sea bottom	0.7 to 0.9 m	0.7 to 0.9 m	0.7 to 0.9 m

CHARACTERISTICS OF LONG-PERIOD WAVES

In this study, long-period waves were classified into two categories that have different nature in generation mechanism: wave-group-induced long-period waves and meteorologically-generated long-period waves. Judging from the power spectra under high wave conditions, we defined the period range of wave-group-induced waves as 30 s to 300 s. Wave components that had periods larger than 300 s were classified as meteorologically-generated long-period waves. These long-period wave components were extracted from the raw data by the numerical filtering using FFT.

Development of long-period waves

Figure 2 shows time series of significant wave height $H_{1/3}$, significant wave period $T_{1/3}$, and root mean square (RMS) value of long-period components in water surface variation $\eta^{L}{}_{RMS}$ at Stn-out and Stn-R. In the period of measurement, some low-pressures passed near the coast and high waves were observed. From the comparison between the figures, the wave-group-induced long-period waves (30 s to 300 s) clearly developed under high wave conditions. Although similar trend can be seen for the meteorologically-generated long-period waves with periods over 300 s, the increase in the amplitude was smaller than the wave-group-induced long-period waves.

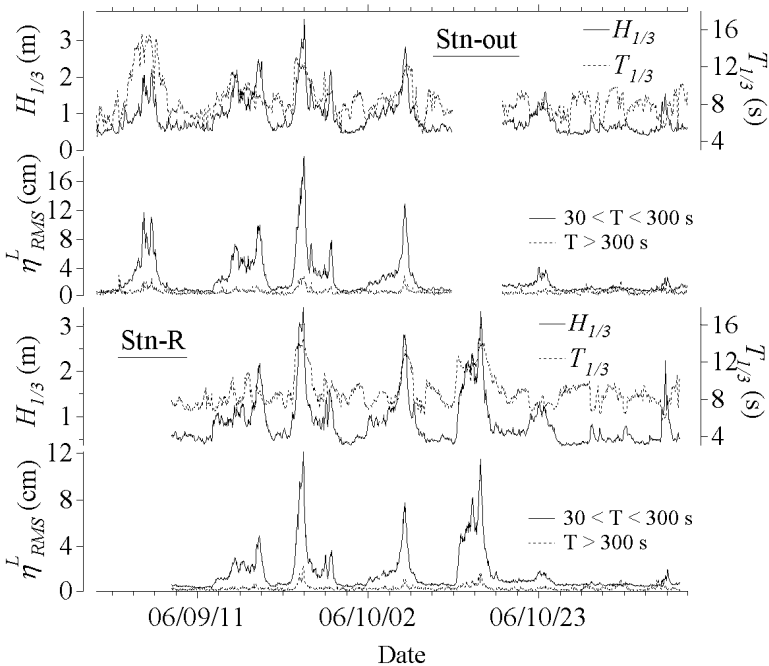

Figure 2. Time series of significant wave height, significant wave period and the RMS values of long-period wave elevations at both offshore sites, Stn-out and Stn-R

Figure 3 plots the RMS values of the long-period wave elevations as functions of the product of the significant wave heights and periods observed at Stn-out and Stn-R. The RMS values of the wave-group-induced long-period wave properties increase almost linearly to the product $H_{1/3}\ T_{1/3}$ except for large values at Stn-out. On the other hand, those of the meteorologically-generated long-period wave properties seem to have little relation with wave heights and wave periods of short waves. Aoki (2002) showed that the linear relationship tends to be seen in the wave data obtained on the mild-slope coast with wide surf zone.

Propagation of long-period waves into an inlet

Figure 4 shows relationship between the RMS values of long-period wave elevations observed inside and outside the inlet, Stn-in and Stn-out, in which the broken lines indicate that the same values were observed at both stations. For the wave-group-induced long-period waves in Fig. 4(a), the RMS values of long-period wave elevations in the inlet are almost half of those measured outside. On the other hand, the meteorologically-generated long-period waves did not decay in the inlet and even amplified for some data.

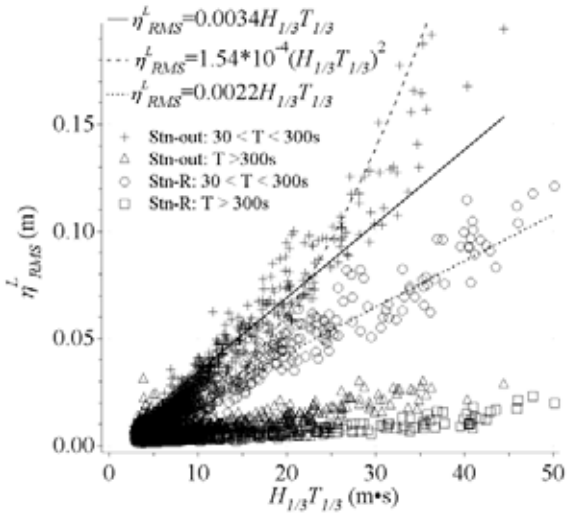

Figure 3. Relationship between the RMS values of long-period wave elevations and the product of significant wave height times wave period at Stn-out and Stn-R

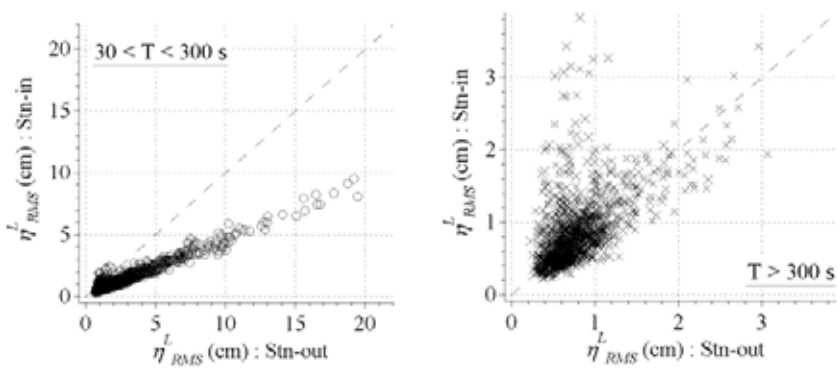

(a) Wave-group-induced long waves

(b) Meteorologically-generated long waves

Figure 4. Relationship between long-period wave elevations inside and outside Hamana Lake inlet

The transmission of waves in an infinitely-long narrow channel with no reflection is theoretically given by Mei (1989) as

$$B = \frac{-2A}{[1 + ka + (2ika/\pi)\ln(2\gamma ka/\pi e)]} \tag{1}$$

where A is complex amplitude of the incident waves from ocean, B is complex amplitude of waves in the narrow channel, k is wave number, γ is the Euler's constant (approximate value is 0.5772) and $2a$ is width of the channel. The inlet of Hamana Lake can be assumed to be narrow but there should be some wave reflection from the lake. The transmission coefficient is given as $|B/A|$. Figure 5 shows transmission coefficients as functions of ka.

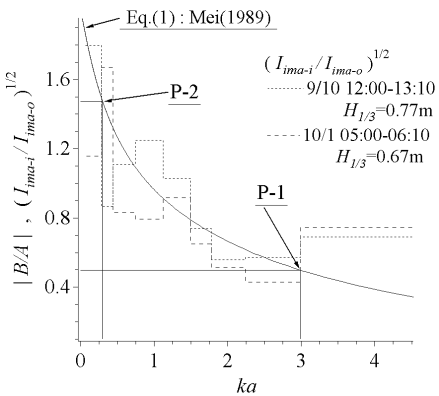

(a) At calm wave conditions

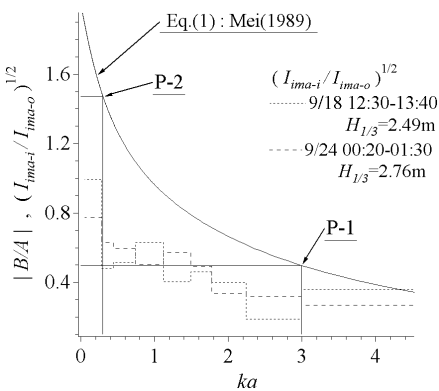

(b) At high wave conditions

Figure 5. Transmission coefficient in the inlet for calm and high wave conditions – comparison with the theory

In the case of 5 m water depth (h = 5 m) and 200 m channel width (a = 100 m), Eq. (1) gives the transmission coefficient 0.498 for the wave with period of 30 s, which corresponds to the point P-1 in Fig. 5. For the wave with period of 300 s, the transmission coefficient yields 1.472 as indicated by P-2 in the figure. The bar charts in the figure show the results estimated from the field data, which are calculated from the ratio of the energy spectra for calm and high wave conditions, figures (a) and (b) respectively. Under the calm wave conditions, the transmission coefficient show closer values to the theoretical ones, while the factors show smaller values under high wave conditions. One of the reasons why the transmission becomes small may be that the long-period free waves generated near the surf zone tend to be reflected offshore in storm conditions.

LONG-PERIOD VELOCITY FLUCTUATIONS

Figure 6 shows the power spectra of the longshore (West-East) horizontal velocities measured at Stn-out for different wave conditions. Under high wave conditions, both the energy in the frequency range of wind waves (less than 30 s in wave period), and that in the low-frequency range, especially with periods between 30 s and 300 s, increased.

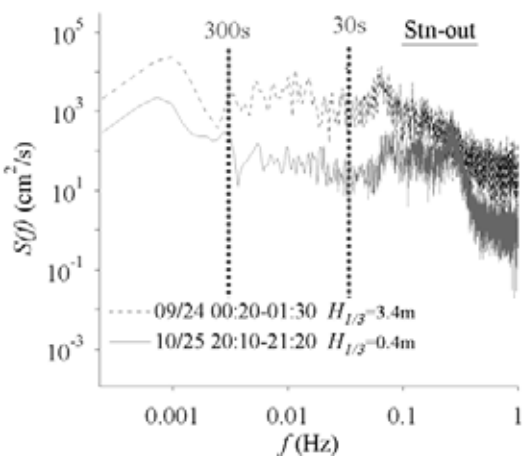

Figure 6. Power spectra of longshore (East-West) horizontal bottom velocities for calm and high wave conditions

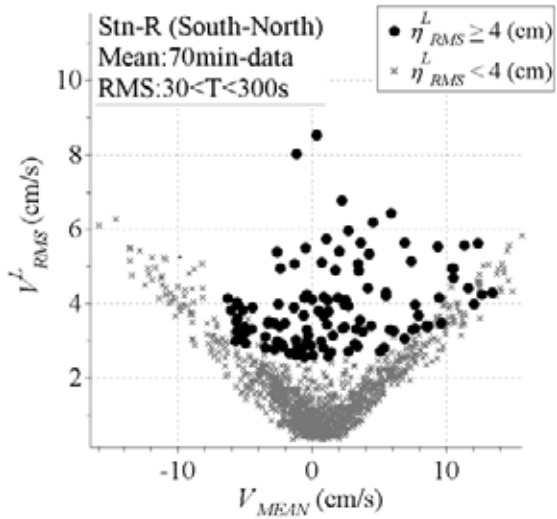

(a) Velocity components in the range between 30 s to 300 s

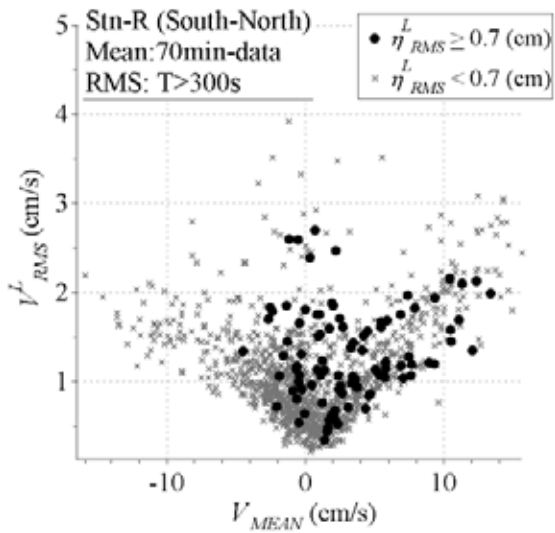

(b) Velocity components in the range between 300 s to 2100 s

Figure 7. Relationship between mean cross-shore (South-North) velocities and the RMS values of long-period cross-shore (South-North) velocities at Stn-R (Tenryu River mouth, offshore) – V_{MEAN} positive towards North

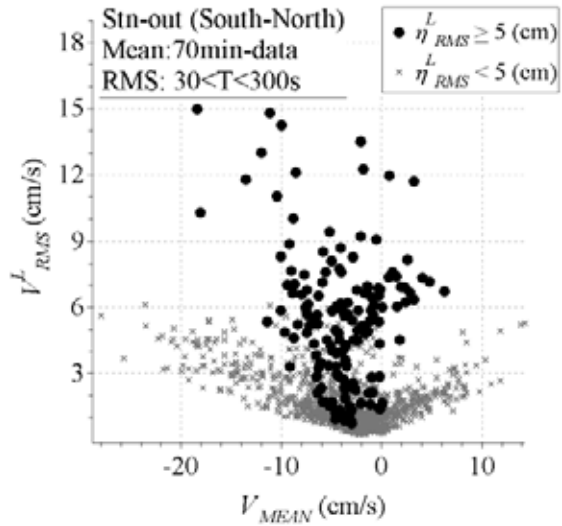

(a) Velocity components in the range between 30 s to 300 s

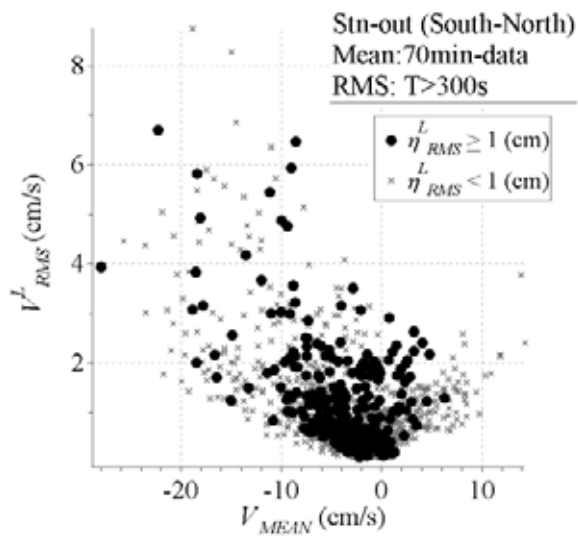

(b) Velocity components in the range between 300 s to 2100 s

Figure 8. Relationship between mean cross-shore (South-North) velocities and the RMS values of long-period cross-shore (South-North) velocities at Stn-out (Hamana Lake inlet, offshore) – V_{MEAN} positive towards North

In Figs. 7 and 8, the RMS values of the long-period cross-shore (South-North) velocities V^L_{RMS} observed at Stn-R and Stn-out are plotted as functions of mean current cross-shore (South-North) velocities V_{MEAN} obtained by averaging the velocity data over 70 minutes. Herein V_{MEAN} is positive towards the North. In the figures, the plotted velocity data are classified into two groups according to η^L_{RMS} values of corresponding wave data. The groups are distinguished at 1/3 of the maximum η^L_{RMS}. Figures 7(a) and 8(a) respectively show long-period velocity fluctuations of the same periods as those of the wave-group-induced long-period waves at Stn-R and Stn-out. The figures show that there are components (indicated by crosses) that are highly correlated with steady flow like tidal currents and components (indicated by circles) that have no correlation with steady flow but are believed to be caused by wave-group-induced long-period waves. On the other hand, the velocity components of 300 s to 1 hr periods, shown in Figs. 7(b) and 8(b), do not show clear grouping nor correlation between steady flow and long-period velocity fluctuations as observed in Figs. 7(a) and 8(a).

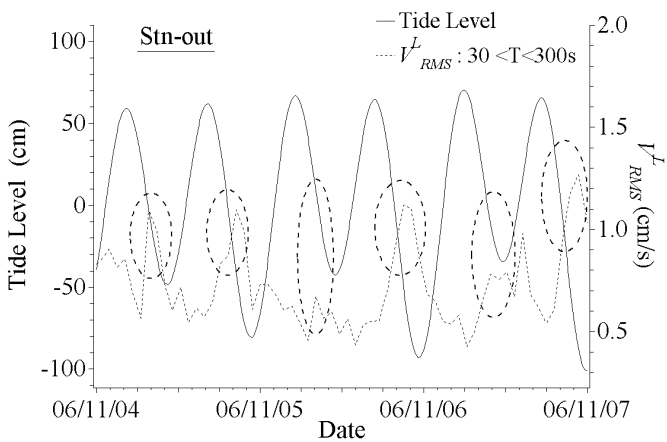

Figure 9. Time series of tide level and the RMS value of long-period cross-shore (South-North) velocity at Stn-out (Hamana Lake inlet, offshore)

Figure 9 shows an example of time series of the RMS value of the long-period cross-shore (South-North) velocity compared with tidal fluctuation of water surface at Stn-out. Some increase in the long-period velocity appears at the phase of ebb tide highlighted by ellipses in the figure. The trend implies that

the strong tidal current has some influence on the generation of long-period velocities under calm wave conditions. Figures 7 and 8 show that there seem to be two different sources for the generation of long-period velocity fluctuations around an inlet with strong tidal current.

Conclusion

The conclusions obtained in the study are summarized as follows:

1. Outside the inlet and off the river mouth, the RMS values of the wave-group-induced long-period wave properties are increased proportionally to the products of the significant wave heights and periods.
2. The RMS values of wave-group-induced long-period wave properties are reduced by half in the inlet. The transmission coefficients of the long-period waves into the inlet show a good agreement with the theory under calm wave condition, while they show smaller values under high wave conditions.
3. Some of the 30 s to 300 s long-period velocity components increase with waves of the same periods while others are induced from steady flow like tidal currents. At Hamana Lake inlet offshore, the long-period flow tends to increase during ebb tide.

ACKNOWLEDGMENTS

This study was carried out as a part of research project “Dynamic sediment management and coastal disaster prevention by advanced technologies” supported by the Special Coordination Funds for promoting Science and Technology of Ministry of Education, Culture, Sports, Science and Technology. The authors are grateful to the financial support and collaborations related to the project.

REFERENCES

Aoki, S. 2002. Generation and Propagation of Coastal Long Waves. *Proceedings of Civil Engineering in the Ocean* Vol.18, pp.155-160. (in Japanese)

Bowen, A. J. 1980. Simple models of nearshore sedimentation; beach profiles and longshore bars, *The Coastline of Canada*, edited by McCann, S. B., Geological Survey of Canada, pp.1-11

Mei, C. C. 1989. *The Applied Dynamics of Ocean Surface Waves*, World Scientific Publishing, pp. 199-202.

Sato, S. 2002. Interaction between Infragravity Waves and Coastal Sedimentary Processes, *Proceedings of Civil Engineering in the Ocean*, Vol.18, pp.161-166. (in Japanese)

DEVELOPMENT OF A STORM TIDE DECISION SUPPORT SYSTEM

Hamid Mirfenderesk[1], Steve Davies[2] Rodger Tomlinson[3]

In recent years there has been a growing concern worldwide about climate change impacts including increased frequency and severity of cyclonic storms. Implications resulting from these changes include increase in the risk of flooding. Therefore, future floods are more likely to overwhelm existing protection measures, exposing us to more residual flood risks. Addressing the issue of an increase in residual flood risk in coastal zones, this study introduces a storm tide flood emergency management decision support system. This system integrates a suite of hydrodynamic-spectral wave models, properties, infrastructure and population data into a single easy-to-use package. Using this system, emergency managers are able to have access to valuable forecasted storm tide flood information. The system is capable of undertaking what if scenarios with respect to alternative possible weather forecasts.

INTRODUCTION

Background

Most of Queensland communities have been developed in close proximity to beach front, estuaries and tidal entrances, or within a coastal floodplain. These communities have been historically susceptible to flooding as a result of passing tropical cyclones or east coast lows. The Gold Coast, in south east Queensland, has experienced more than 45 floods since 1925. Passing cyclones have triggered many of the floods. Historical records indicate that more than 40 cyclones have passed the Gold Coast region over the past 120 years. The last major flood (1974) was triggered by Cyclone Wanda. This led to the evacuation of 1500 people and in many places homes were swamped with 1.2m to 1.5m of water. A more recent flooding events in 2005 resulted in loss of 2 lives on the Gold Coast.

Current planning and management strategies in many of the coastal communities in Queensland have not embraced the full extent of known climate variability, nor predicted greenhouse induced climate change. Many people in these communities assume that the physical nature of their environment will remain unchanged. However, most of these communities are susceptible to an increase in the intensity and frequency of extreme weather events. In cairns, in northern part of Queensland coast line, an increase of just 1-2 degrees in temperature would be sufficient to lift the 100 year storm surge height to double the area flooded. If the projections in the variability in the frequency and

[1] Gold Coast City Council, PO BOX 10242, Southport BC, QLD, 4215, Australia
[2] DHI, Water and Environment, PO BOX 3596, Australia Fair, QLD 4215, Australia
[3] Griffith University, Griffith Centre for Coastal Management, PMB 50 Gold Coast MC 9726, Australia

intensity of storms are correct, then future coastal inundation will be outside the extent of historical experience.

On this basis both existing and future (climate change-induced) flood risks are regarded as a key sustainability issue for many of the coastal communities in Queensland. Flood risk management has been traditionally dealt with by dissecting flood risk in its three main components hazard, exposure and vulnerability.

$$Flood \quad Risk = Hazard \times Exposure \times VuLnerability \tag{1}$$

Exposure to hazard means presence of people/properties in flood risk areas and vulnerability means lack of resistance/preparedness of the community. In this context management of flood risk is achieved through taking measures to reduce the hazard a community is subject to, the degree of the exposure of the community to the hazard and the community vulnerability. Historical evidence has shown that the actual consequence of flooding depends highly on how vulnerable people are to the danger and damage resulting from flooding. Vulnerability, and as a result flood risk, can be reduced, for instance, if people are prepared in advance of flooding, if they have knowledge on how to protect themselves during a flood and if they receive flood warnings in time.

The aim of this study is to introduce a methodology and tool to reduce the element of vulnerability in equation (1) through the development of a reliable and comprehensive forecasting and flood emergency decision support system. Such a system is essential for increasing coastal communities' resilience against tropical cyclones. The purpose of flood warning is to inform people and enable them to take action to increase their safety and reduce the costs of flooding. This study introduces a storm tide decision support system (STDSS) as a concept and a tool that can be used to warn people of the impending flood risk.

Tangible benefits of a flood emergency decision support system

Mirfenderesk et al (2008b) showed the tangible benefit of a flood emergency decision support system for an average-size catchment in South East Queensland in Australia. The study area is the Nerang River catchment with an area of 493 km^2. A flood damage estimate for this Catchment is approximately $217,000,000. This includes the inundation of more than 5000 properties. It is important to note that these figures are sensitive to some of the basic assumptions and only represent an approximation of real damage and real number of properties, which will be affected.

The above-mentioned figure refers to potential damage. By adopting proper measures such as development of a Decision Support System, the actual damage can be substantially smaller than the potential damage. This is mainly due to the fact that a decision support system will allow authorities to warn and guide the general public to take appropriate measures and reduce the level of damage to

their properties and belongings. Water Studies (1997) estimates that for a community with a low level of flood awareness and a warning time of 12 hours, the damage reduction factor for internal damages is 0.7. If the warning time is 24 hours, the damage reduction factor is 0.4, i.e. householders should be able to limit damage to the contents of dwellings between 40% and 70% of the potential value through lifting items onto tables and benches, by evacuating items, etc. the same study recommended a reduction factor of 0.35 for external damages".

Based on a study undertaken by WRM Water & Environment (2006) for the Gold Coast City Council, structural, internal and external damage contributes roughly 30%, 50% and 20% to the total damage. On this basis the potential damage resulting from structural, internal and external damage are approximately, $65,000,000 $109,000,000 and $43,000,000. Using the above-mentioned reduction factors the difference between potential and actual damage for structural, internal and external damages are, $0 (indicating no reduction in structural damage), $32,000,000 and $28,000,000, i.e. the total difference between potential and actual damage can equal to $60,000,000.

The $60,000,000 reduction in potential damage can only be materialized if the community is warned before the flood and adequately trained to protect itself during a flood emergency situation. It is important to note that damage is not just financial and tangible. Intangible losses represent those where market evaluation values are generally not commonly agreed. Some elements of intangible damage can be alleviated by preparedness that can be achieved because of having a proper flood emergency decision support system in place. Some of the important intangible damages that can be easily alleviated with the help of such a system includes: loss of memorabilia, death, injury and loss of health.

STORM TIDE DECISION SUPPORT SYSTEM (STDSS)

General

Figure 1 shows a schematic of the STDSS. The system uses five forecasted hydrological parameters, maximum wind velocity, bearing of the cyclone, tidal condition, cyclone landfall and speed of movement as inputs. STDSS interpolates flood surfaces, using an electronic library of flood maps, based on the input parameters. The interpolated map is fed to the GIS modeling tool. GIS tool can be interrogated to identify those who are at risk and to determine the best way to provide help to those who are in need.

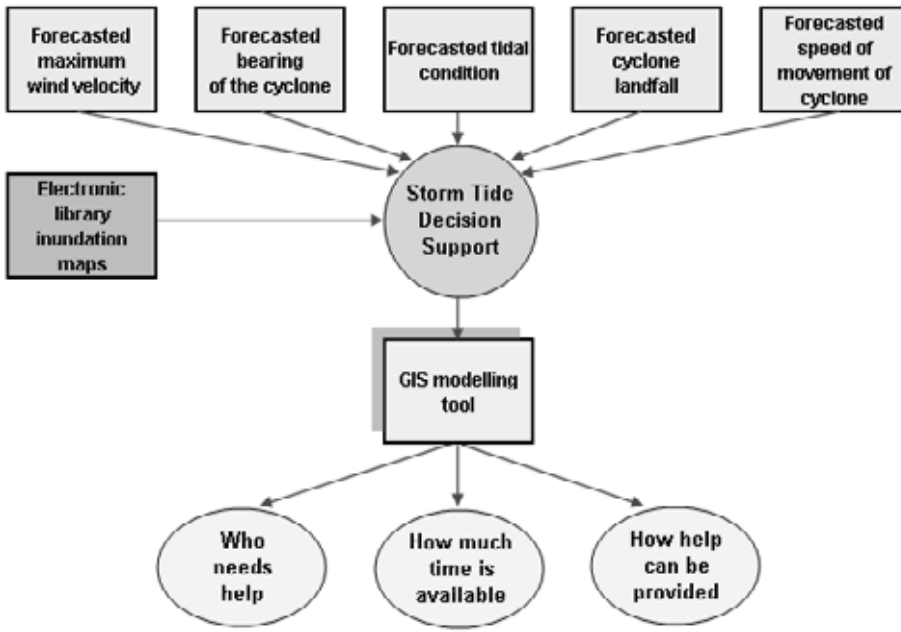

Figure 1. Layout of the Storm Tide Decision Support System.

The electronic library that is used in STDSS is a collection of flood maps resulting from the likely storm conditions on the Gold Coast. A storm tide condition is defined as a cyclone with a given maximum wind speed, bearing, tidal condition, landfall and speed of movement. Table 1 provides the range of values that are adopted for the Gold Coast STDSS. A combination of all the values in Table 1 constitutes 108 possible storm tide conditions. The resulting flood maps are archived in the electronic library.

Table 1- Selected input parameters for cyclone surge model

Maximum Wind Speed (knots)	25	37.5	50
Bearing	N	NE	E
Tide level	Mean Water	High Water	
Landfall*	North	Centre	South
Speed of movement (km/h)	8	14	

* Landfall could be north (north of Brisbane) or centre (between Brisbane or southern end of Gold Coast) or south (south of Gold Coast).

Development of electronic library of inundation maps

To create the electronic library of inundation maps, a suite of hydrodynamic and spectral wave model at local and regional scales are used. Except the local hydrodynamic model that was developed as part of a separate project (Mirfenderesk et al, 2005, 2007, 2008a) and (Davis et al, 2009), other models were developed as part of this study. The hydrodynamic and wave model simulations are based on DHI's two-dimensional flexible mesh code, MIKE21 FM. The code is based on the numerical solution of the two dimensional incompressible Reynolds averaged Navier-Stokes equations invoking the assumptions of Boussinesq and of hydrostatic pressure. The model solves the momentum and depth average continuity equations. The spatial discretization of the governing equations is performed using a cell-centered finite volume method. The spatial domain is discretized by subdivision of the modeled area into non-overlapping triangular and quadrilateral elements. The flexi mesh enables a fair description of the details and channels throughout the study area.

Initially a combined Hydrodynamic (HD), Spectral Wave (SW) model that covers area "B" (Figure 2) is developed. The boundary condition at the three open boundaries of this model is a constant water level as tidal changes along the model do not affect the wind induced surge or wave parameters due to the overall depth along the boundaries. The regional HD and SW model is run with a wind forcing made up of two horizontal components of the wind vector and atmospheric pressure. The aim of the regional HD and SW models is to generate wind induced surge boundaries for the local HD model and wave spectrum boundaries for the local SW model (shown as area "A" in Figure 2 or 3). Once the boundary conditions for local models are determined, these models are run to rout the surge throughout the Gold Coast Waterways. The local SW model has three open ocean boundaries that are forced by the wave energy spectrum data extracted from the regional SW model. The local SW model uses a constant water level at its boundaries. A constant water level has been used to reduce run times and has been shown to produce similar results to using a varying water level. The local SW model also has a wind field applied so local wind waves are also taken into account. The local SW model is run to produce detailed radiation stresses in the coastal breaking zone so wave set-up can be taken into account when running the local HD model.

The local HD model has three boundaries that are forced by a combination of tide and wind induced surge extracted from the regional HD model. The tide and wind induced surge are added together to create the ocean boundaries; this can be seen in Figure 4. This water level boundary is amplified as it moves into the shallower water along the coast. The HD model also takes into account wave set-up by using the wave radiation stress map produced by the local SW model. Model simulation shows that applying the wave radiation stresses increases the surface elevation within the Broadwater (at the Gold Coast) by approximately 0.5 meter due to wave set-up. Wind is also applied to the local HD model to produce local surge.

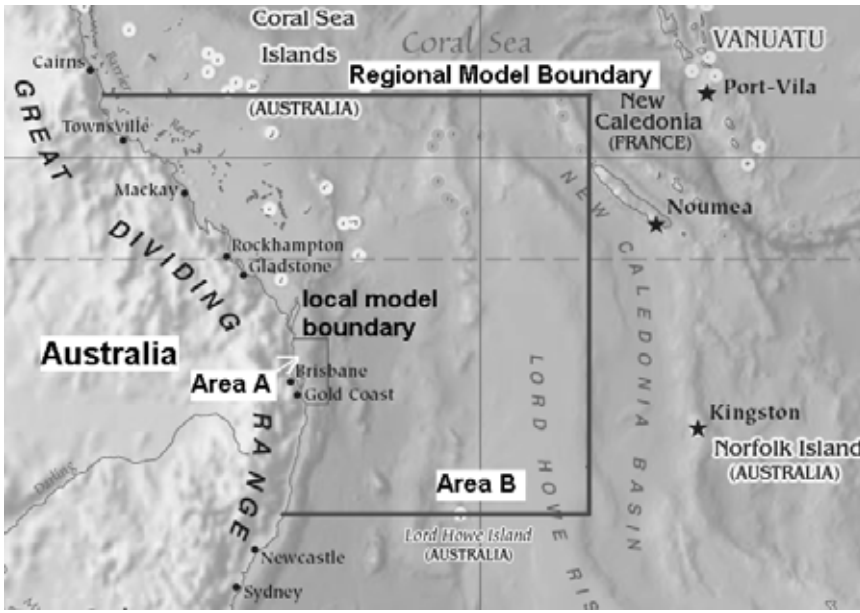

Figure 2. Study area (Regional and local models extent).

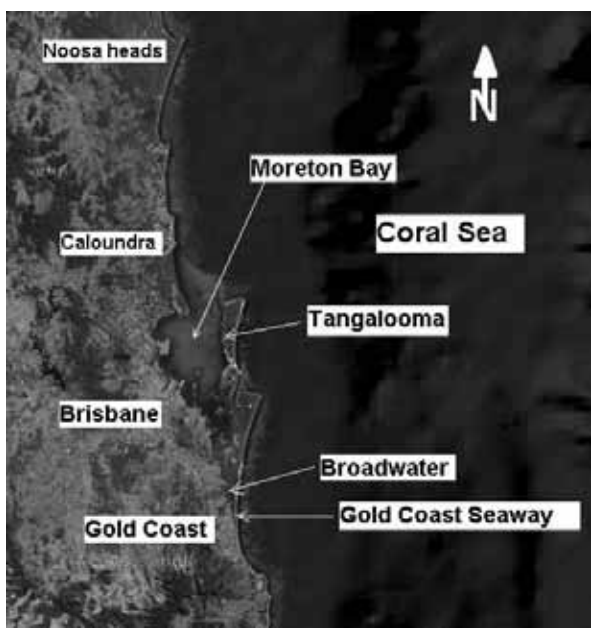

Figure 3. Study area (Local model extent – Area A).

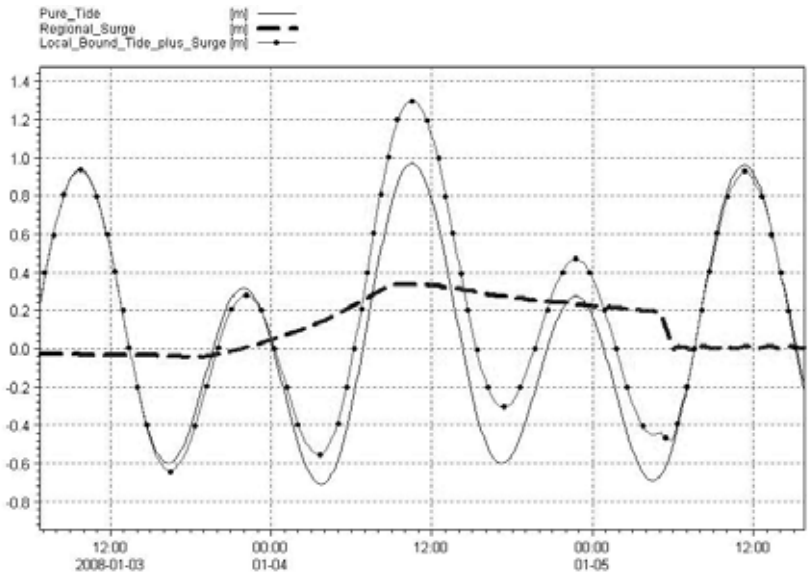

Figure 4. Local HD boundary.

Model verification

The suite of HD and SW models was verified against a large East Coast Low that affected the south east Queensland over the Christmas period of 2007-2008. Water level data along with wave and wind data were used to verify the model. Water level data was compared at five locations along the coast from Noosa to Tweed Heads and in Moreton Bay. Wave Buoy data was also used from 5 locations within the same area. Modeled wind was also compared to five permanent land wind stations along the coastal area. There was a small underestimation of around 20% for wave heights and modeled winds. This probably reflects the fact that the coastal wind stations may be influenced by local topography and therefore may show lower wind speeds than a general hindcast model which may not include the local topography or only include it in a very coarse manner. Whether the underestimation is wholly or only partly caused by the local topography is outside the scope of this study. But assuming that the underestimation is only partly caused by the local topography, and that the winds thus in general still are a little on the low side, this will result in the waves also being a little too low. This corresponds to what is seen for the wave comparisons. Thus, based on this assumption the wave model is considered to be calibrated to the extent possible with the available data. Figures 5, 6 and 7 show verification of the model simulation to the measured data.

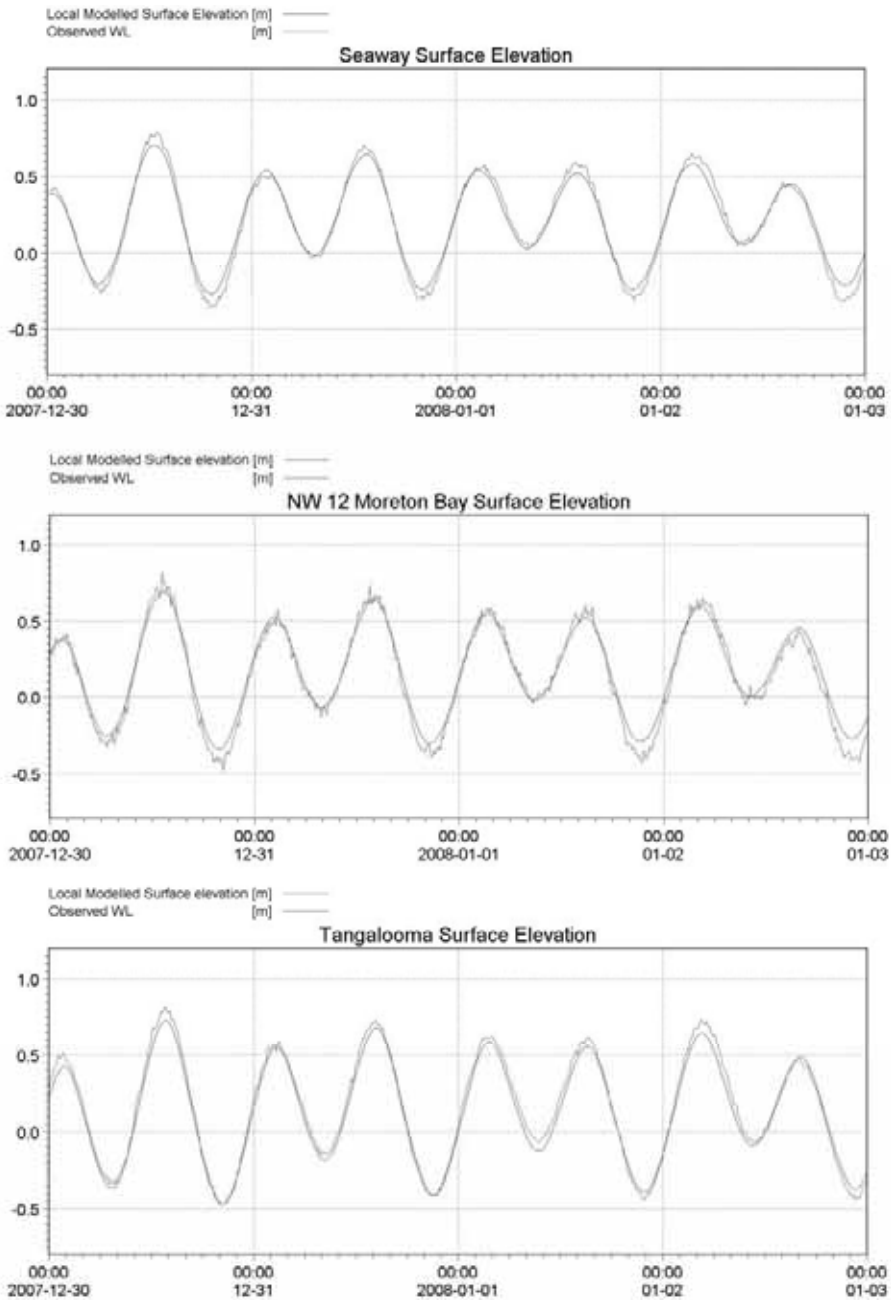

Figure 5. Surface elevation verification.

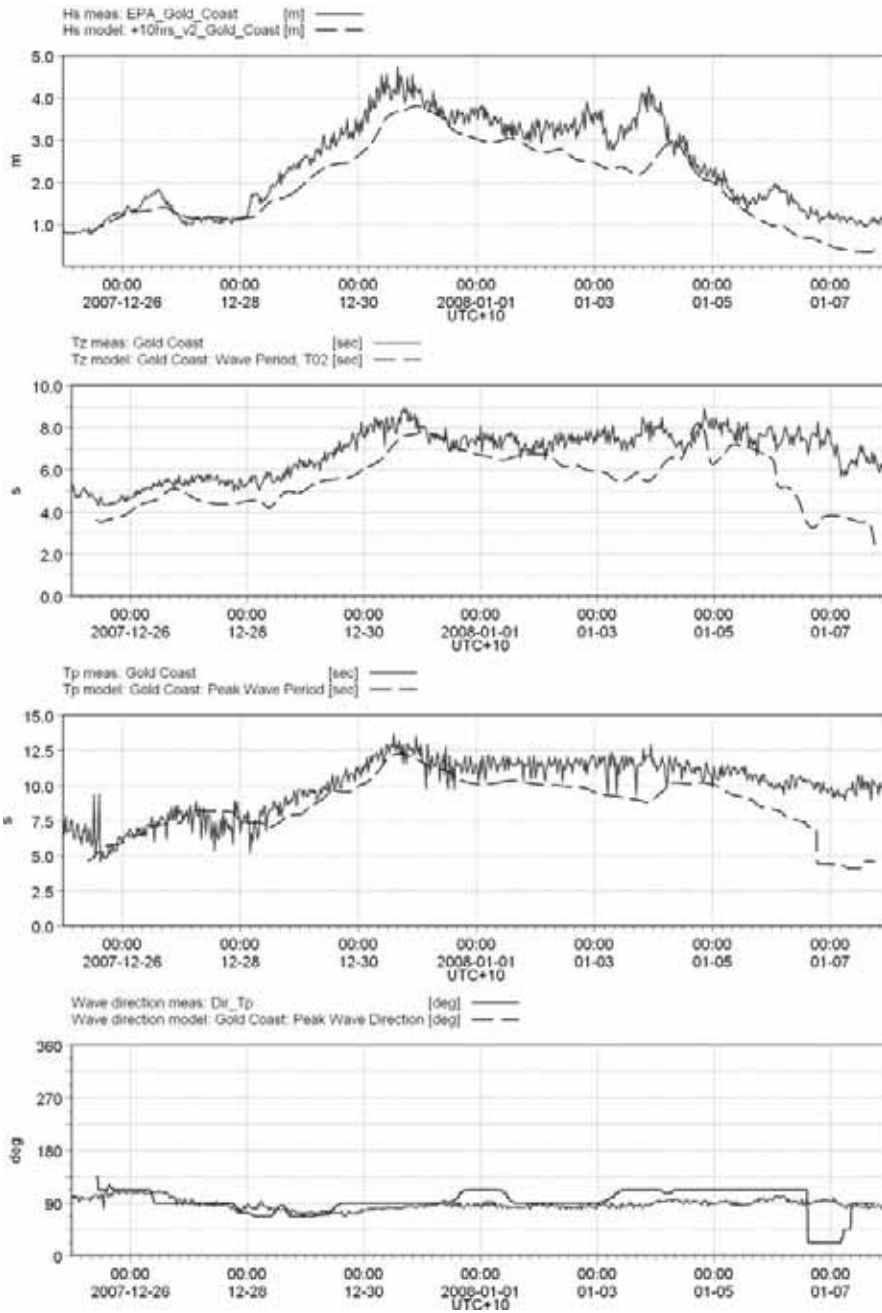

Figure 6. Wave verification

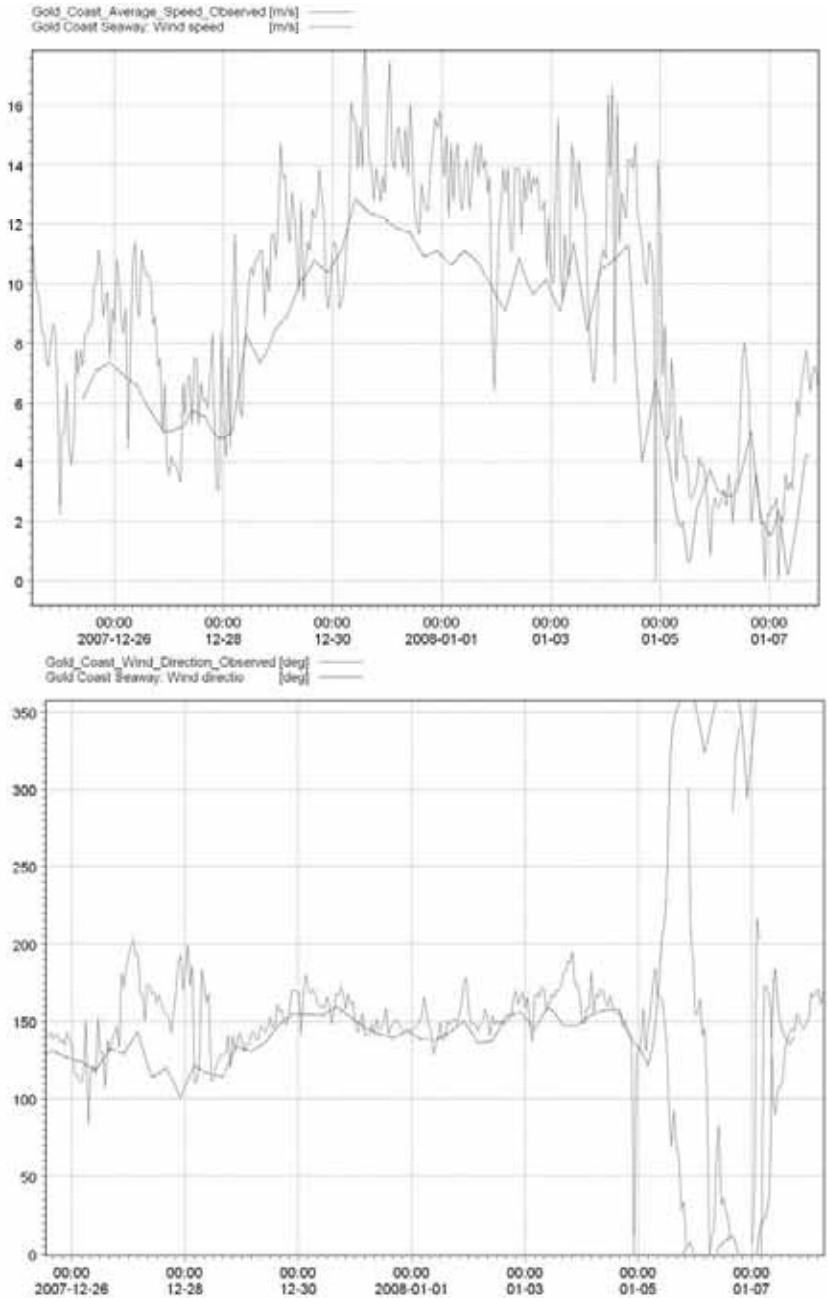

Figure 7. Wind verification at the Gold Coast Seaway

GIS Element

Central to the decision support system is a GIS user interface based on WaterRide software platform, developed by the Pattersons Britton & Partners Pty Ltd. The outputs of the GIS tool are answers to the flood emergency managers' questions, such as who needs help; or what is the best way to access people in need or what is the best evacuation route; or how much time is available for certain actions; etc. To enable these types of questions to be answered, the GIS tool uses Council's data base, simulates flood levels and generates the following information (in the form of map, graph or table) for the forecasted period.

- Flood level map,
- Flood inundation map,
- Evacuation routes map
- House-specific flood inundation information (for properties that have been surveyed).
- Evacuation route maps
- A report containing a list of inundated houses and vulnerable elements (such as age care centers, schools, child care centre's, etc).

The GIS element provides a Graphic User Interface that allows predicted parameters of cyclone such as bearing, landfall, maximum wind speed, speed of movement, radius of gale and tidal condition fed into the system. The GIS element then produces a number of maps of forecasted risk, hazard and vulnerability in digital forms such as the one shown in Figure 8. This map shows the forecasted flood level map for a hypotetical cyclonic event in the study area. The user can see the predicted flood level at any time by clicking a button on the menu bar. Moving the mouse cursor anywhere over the flood surface will indicate the water level of that point at the bottom of the screen. The user can click anywhere over the flood surface to get information about the topography, water level and depth at the selected point.

The GIS element has a number of additional features. It identifies houses that are at risk and allows the user, by clicking on a button on the menu bar, to get this information at any time during the forecasted period. The user can click over any flooded property and have a window popping up that shows the property details including the over floor flooding depth, property floor level, road level, etc. The user can move the mouse over the flooded property to have the depth of over floor flooding. The user can click anywhere over the flood surface to obtain information about topography, water Level and water depth at the selected point in particular along the road network. The system can also provide forecasted situation for vulnerable places such as child care centers, nursing homes and schools. The user can move the mouse over any vulnerable elements (such as a Child Care Centre) to have the depth of over floor flooding of the facility.

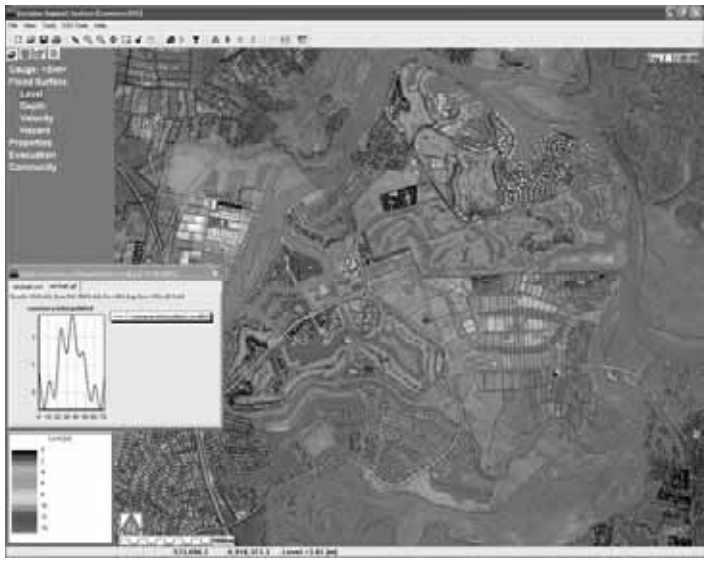

Figure 8 – This figure shows the forecasted flood level map.

CONCLUSION

This study describes a simple concept for the development of a Storm Tide Decision Support System that can provide emergency managers with vitally important information in relation to impending flood risk in coastal zones. The study demonstrates how this concept can be turned into a reliable system based on computer simulation of alternative possible cyclonic storms. Any real time modeling for forecasting the impact of a cyclone during an event is simply out of question due to time that a typical suitable model will take to simulate a forecasted event. Therefore, the proposed system works based on a library of pre-cooked inundation maps. The significance of this system comes from the fact that it takes only a short period of time to produce important forecasts in relation to a cyclonic event. The system is capable of undertaking what if scenarios and is extremely easy to operate.

ACKNOWLEDGEMENT

The project was funded jointly by the Department of Emergency Services Queensland, Commonwealth Department of Transport and Regional Services and Gold Coast City Council under the Natural Disaster Mitigation Program 2007-2008 Funding Year. The authors would like to acknowledge the support from the Queensland Department of Tourism, Regional Development and Industry for this project that was provided through the Future Coastline Project.

REFERENCES

Davis, S., H. Mirfenderesk, R. Tomlinson and S. Szylkarski. 2009. Numerical Modelling of Estuarine and Coastal Waters on the Gold Coast, Australia, 10th International Coastal Symposium, Lisbon, Portugal. In process.

Mirfenderesk, H. and R. Tomlinson. 2008a. Observation and Analysis of Hydrodynamic Parameters in Tidal Inlets in a Predominantly Semidiurnal Regime, *Journal of Coastal Research*, V24-5, pp 1229-1239, ISSN 0749.0208.

Mirfenderesk, H., G. Cox, and S. Szylkarski. 2008b. A New Generation Decision Support System for Flood Prediction and Emergency Management on the Gold Coast, *31st Hydrology and Water Resources Symposium and 4th International Conference on Water Resources and Environment Research*, Adelaide, Australia, pp 671-681, ISBN 0 858 25735 1.,

Mirfenderesk, H. and R. Tomlinson. 2007. Numerical Modeling of Tidal Dynamic and Water Circulation at the Gold Coast Broadwater, Australia, *Journal of Coastal Research*, SI50, p277-281. ISSN 0749.0208.

Mirfenderesk H., R. Tomlinson and L. Hughes. 2005. Field Data Collection and analysis at the Broadwater, Gold Coast, *Proceedings of 17th Australasian Conference on Coastal and Ocean Engineering*, Adelaide, Australia. P477-482.

Markar, S. 2006. Flood Stage-Damage Curves for Floodplains in Gold Coast. WRM, Water& Environment Pty Ltd. A report prepared for the Gold Coast City Council.

Water Studies Pty Ltd. 1997. Assessment of Flood Damage across the Nerang River Floodplains, Gold Coast. A report prepared for the Gold City Council.

HIGHLY-RESOLVED NUMERICAL MODELING OF TSUNAMI RUN-UP AND INUNDATION SCENARIO IN THE CITY OF PADANG, WEST SUMATRA

Nils Goseberg[1], Arne Stahlmann[2], Stefan Schimmels[3] and Torsten Schlurmann[4]

In-depth studies of inundation dynamics extracted from tsunami simulations could contribute widely where detailed information about velocity fields and flow depth is needed for evacuation simulation in coastal urban areas. Therefore we have taken the city of Padang, West Sumatra, Indonesia, into closer consideration for detailed analysis of tsunami inundation risks. In this context, the paper presents a 2D numerical study that is used to evaluate relevant factors influencing the quality and reliability of the simulation results. We found basic factors such as the accuracy and resolution of the underlying digital elevation model as well as the influence of macro-roughness elements like buildings and other infrastructure significantly affecting flow fields and water depths on microscopic level. The results clearly show that attention must be drawn to the fact that it is highly important to collect and analyze highly-resolved spatial data in shallow water and near shore (on land) in order to deduce credible tsunami inundation scenarios as a basis for adequate coping and evacuation strategies for imperiled coastal regions.

INTRODUCTION

The disastrous Indian-Ocean tsunami has strongly emphasized the need for an assessment of scientific methodologies and engineering approaches to intensify basic as well as applied research leading to a greater insight into tsunami run-up and inundation mechanisms (Schiermeyer 2005 and Oumeraci 2007). The vastly exposed urban coastal agglomeration of Padang, West Sumatra, Indonesia, has recently been taken into consideration for further evaluation and risk assessment to the potential threat of tsunamis due to the amplified risk of future earthquakes in this region (McCaffrey 2007). It is well documented that Sumatra's third largest urban (Fig. 1.) area counting more than one million inhabitants is one of the most imperiled cities in the Indian Ocean rim due to potential tsunami hazards originating off the coasts of Padang. The city is located directly on the coast, partially sited beneath the sea level and drained by numerous artificial waterways and rivers. Thus, the city of Padang is located in a zone of extreme risk due to severe earthquakes and tentatively triggered tsunamis (Birkmann and Schlurmann 2007).

[1-4] Franzius-Institute for Hydraulic, Waterways and Coastal Engineering, Leibniz Universität Hannover, Nienburger Straße 4, Hannover, 30167, Germany
[1] Corresponding author: goseberg@fi.uni-hannover.de

The present paper as a work package of a large transdisciplinary research project 'Last-Mile – Evacuation' shows the results of hydrodynamic simulations of the inundation dynamics for possible tsunami series in the urban coastal hinterland of Western Sumatra. A first substantial inundation study for Padang gives a good overview of the general extent of inundation for several scenarios including historical and hypothetical earthquakes (Borrero et al. 2006) on a very coarse grid. More detailed studies so far lacked highly-resolved spatial datasets for that specific region in order to analyze the flow pattern in detail and to extract confidential recommendations on the evacuation procedure and general coping strategies to deal with tsunami risk on microscopic scale. The overall aim of the research project is to combine and interchange detailed information about processes of on-land flow pattern with socio-economic and physical vulnerability analysis as well as evacuation simulations for pedestrians. First outcomes already help to detect infrastructural bottlenecks and hot spots of vulnerability in the sequence of tentative evacuation procedures. Hence, the model requires a highly-resolved spatial database to determine detailed features of the major city. These could be achieved by extensive multi-beam echo sounder surveys in the shallow waters near shore and by airborne topographical field data surveys in the hinterland. To obtain a final digital elevation model (DEM) as a basis for the simulations, these data were merged and cross-checked with DGPS data of relevant boundaries and cross sectional data of flood water channels and rivers.

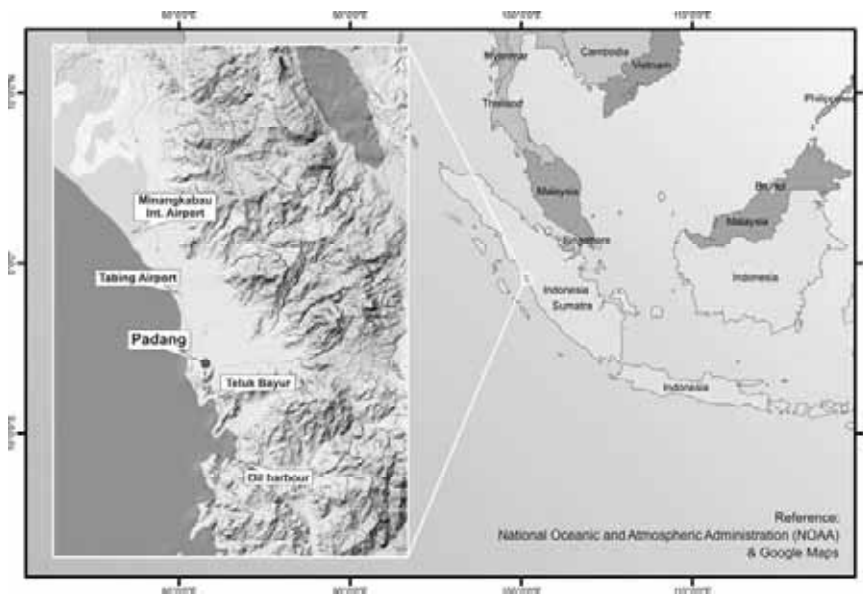

Figure 1. Indonesian archipelago with main island Sumatra, location of interest for the numerical simulations, geography of Padang region

DESCRIPTION OF SPATIAL DATASET

The spatial data we found at the beginning of our work lacked accuracy and resolution in order to conduct simulations of the detailed flow pattern. Nevertheless, these datasets allowed us to start investigations with a first geometrical representation of the city of Padang. After having conducted a number of simulations with this first digital elevation model (DEM), we additionally prepared a second, more refined DEM consisting of newly surveyed and assimilated datasets to upgrade the prior coarse DEM. In the following, a description and characterization of both applied DEMs is provided. As this paper presents work in progress, a third generation DEM will be available in the near future, based on a high-resolution geodetic dataset with high accuracy. It will allow for a deduction of most relevant tsunami inundation patterns to acquire adequate coping and evacuation strategies for the city of Padang.

Coarse digital elevation model

The first geometrical representation of the area to be modeled consists of different datasets. Topography data were derived from 1 arcs SRTM data. We carried out additional GPS measurements at distinctive locations in Padang to validate and adjust ground level elevations. Artificial height differences in the topography were corrected by applying a low-pass filter. For the consideration of waterways and channels, digitized construction plans were used, as well as locally available single echo beam soundings, allowing for a proper representation of potential flow paths. Bathymetric data originate from digitized nautical charts and from echo soundings distributed by local agencies. Topography and bathymetry were merged to a final DEM, represented by a uniformly spaced grid dataset that was then used for further investigations.

Highly-resolved digital elevation model

Requirements regarding accuracy and resolution of DEMs to adequately assess evacuation procedures on urban environments are generally high. Infrastructural features and buildings need to be resolved properly. Therefore, two autonomous surveys were conducted to map topographical and bathymetrical features for the area of interest. A hydrographic survey was planned and carried out in September and November 2007. Approximately 42 km² have been mapped by means of multibeam echo sounder with ship motion sensor correction and DGPS assistance. The acquired data were finally merged in post-processing to a uniformly spaced grid with a resolution of 3 m. In addition, an airborne flight campaign was initiated within the framework of the 'Last-mile - Evacuation' project and took place in August 2007. Major parts of the city of Padang could be mapped. The post-processing of the dataset comprises correction routines for vegetation influences, height correction and filtering of outliers. It is still in progress due to the enormous amounts of acquired data (few TBytes). Yet, a small test region has been made available in advance, principally for the purpose of validation with existing DEMs. Based on the datasets described above, we presently merge topography, bathymetry and

data of waterways and channels to a preliminary DEM which will be assessed and compared in the next paragraph.

Assessment of digital elevation models

Visual inspection and assessment of the data quality were the starting point for the comparison of the two models. Fig. 2 reveals the numerous, obviously important infrastructural features that form the flow paths across streets and in between buildings and which apparently cannot be represented in the coarse DEM. However, the coast line (on the left), the mouth of the flood control channel (top) and the overall gradient of the terrain are already represented. In contrast, considering the highly-resolved DEM, we found all major structural features of the city to be resolved extraordinarily well. Footprints of the buildings are generally captured satisfactorily for these purposes.

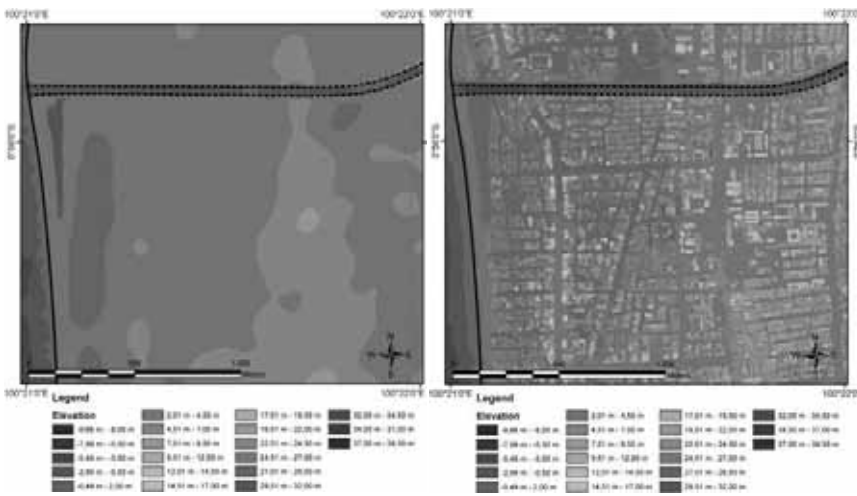

Figure 2. Sections of the digital elevation models used for hydrodynamic simulations in coarse (left) and highly-resolved (right) accuracy and resolution, height values in m above MSL. Coastline indicated by solid black line, flood relief channel (FRC) Padang indicated by dashed black line

Furthermore terrain elevation heights along a cross section are shown in Fig. 3. The analysis differentiates between bathymetrical and topographical data. The position of the cross section and some gauges are shown in the upper region of the figure. Elevations of both DEMs are plotted over the length of the cross section A-A. Absolute differences between both geometries are indicated in blue. It can generally be noted that significant differences exist in the important near shore region and reach almost 50 percent of the water depth measured during the multibeam survey. Thus, the physical effect of shoaling of these two chosen geometries varies considerably. Besides this feature, height differences on land are likewise noteworthy. The considered cross section shows lower elevation data for the highly-resolved DEM, especially in the important 1000 m

wide stretch from the coast, whereas the area behind that line is generally located higher than the one of the coarse DEM. Nevertheless, the fact that buildings are represented in the model is even more important than small differences in the ground level. Based on the knowledge about the considered DEMs, the numerical scheme that was applied to analyze the inundation pattern for tsunami scenarios in the vicinity of Padang is described in the following paragraph.

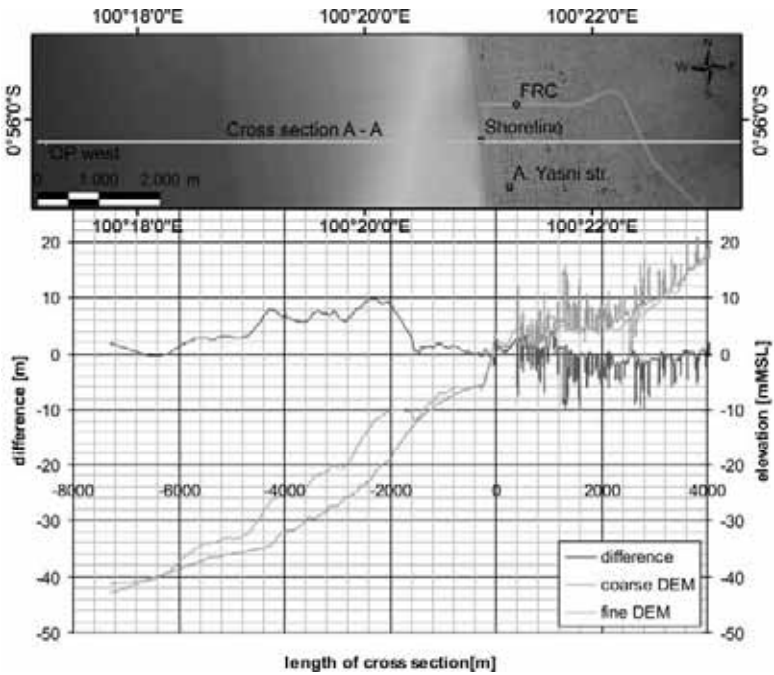

Figure 3. Overview of the highly-resolved DEM (only the shown region is available at present), position of the cross section and the analyzed gauges, elevation and difference between height values along the cross section

METHODOLOGY

We have chosen a hybrid approach coupling two numerical models in subsequent steps. At a first step the ocean-wide Tsunami propagation was modeled using TsunAWI (Harig et al. 2007). The simulation results were saved at several spatially varying locations on the TsunAWI mesh and were then taken as boundary conditions for the second numerical model. Tsunami generation and wave propagation in the TsunAWI code is modeled by employing the non-linear shallow water wave equations as a basic set of equations. The discretization for the model is achieved by using a finite-element approach on an unstructured mesh that is thoroughly built under several constraints due to the underlying explicit numerical scheme (Behrens 2008).

The hydrodynamic inundation modeling tool used for the detailed run-up and inundation simulations is developed and constantly improved by the Australian National University and Geoscience Australia (software called ANUGA). A finite-volume approach is used to solve the nonlinear shallow water wave equations in conservative form and a triangular mesh with spatially varying resolution is used to discretize the considered area of interest. The conserved quantities are water depth and horizontal momentum in x and y direction (Nielsen et al. 2005). The friction term is modeled using Manning's resistance law. A robust algorithm is obtained by employing a piece-wise linear vector function of x and y for the conserved quantities which allows discontinuities across the edges of a cell while slope limiting functions assure numerical stability. A detailed description of the applied numerical scheme can be found in (Zoppou and Roberts 1999).

NUMERICAL RESULTS

By means of the hydronumerical scheme several tsunami scenarios were calculated for simulations with both applied DEMs and the results were compared. Comparison was drawn on the basis of inundation maps and distinct time series of current flow depths and velocities at two locations in the city of Padang. The achieved results are presented and discussed below.

Tsunami inundation maps

Fig. 4 demonstrates two snapshots of tsunami inundation areas in the urban area of Padang for a simulation time of t=2040 sec. Inundations relying on both used DEMs at this chosen instant deviate significantly. The coarse DEM shows a more distinct non-uniform run-up and flow pattern than the highly-resolved DEM. Especially the area along the flood relief channel faces larger flow depths than the ones calculated with the highly-resolved DEM. This examination implies that the usage of highly-resolved DEMs including a representation of buildings and other infrastructures channels the tsunami-induced kinetic energy to locations where flow paths are less obstructed.

An even more striking result is the fact that major streets considered in the highly-resolved model mimic a sort of tsunami floodways indicating channelized flows with significantly stronger currents. However, not only flow velocities are amplified when a more sophisticated DEM is used. Flow depths and water levels directly at the shoreline are increased as well. Even though our model can not deal adequately with flow-induced damages to structures at present, it can easily be deduced that tsunami-induced hydrodynamic loads on structures are likewise higher in the latter case. This has an effect on evacuation routines due to an enlarged risk of collapse and structure failures. In contrast, when considering higher DEM resolutions tsunami inundations on land are retarded due to higher macro-frictional losses resulting from structures. We could state that differences in run-up between the DEMs that where compared at the chosen simulation time of t=2040 sec. vary from 50m to 200m. Fig. 5 illustrates maximum inundation for the simulated scenario for both geometries.

Here differences in run-up height are even more distinct ranging from 100m to 670m.

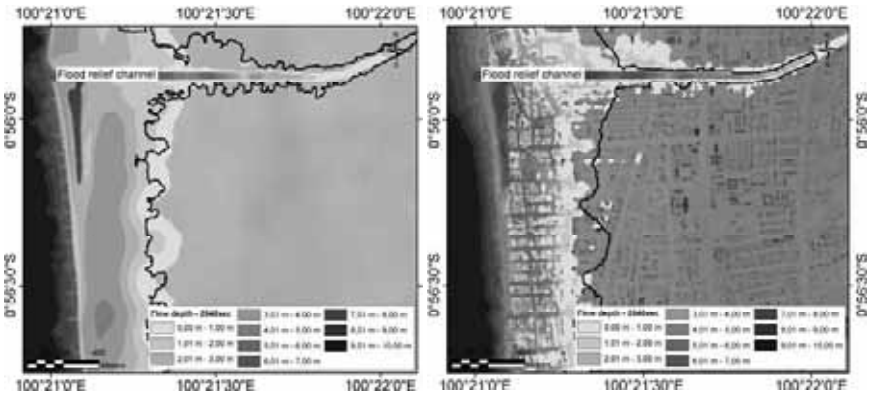

Figure 4. Inundation for the coarse DEM (left) and the highly-resolved DEM (right) at t=2040 sec., black lines indicate the inundation limit of the coarse and the highly-resolved DEM respectively at the same time step

Furthermore, noteworthy time shifts of a few hundred seconds for the wave arriving at distinct points are deduced and might indicate crucial additional time frames regarding evacuation routines and strategies. This physical fact stems from higher roughness of the surface domain exposed to the flow and is generated by the presence of buildings and infrastructure in the simulation model. It should be noticed that a fine-tuning of a state-of-the-art roughness law such as the Manning approach failed to represent the effects mentioned above. Hence this sort of macro-roughness should be addressed in upcoming studies and signifies the work in progress.

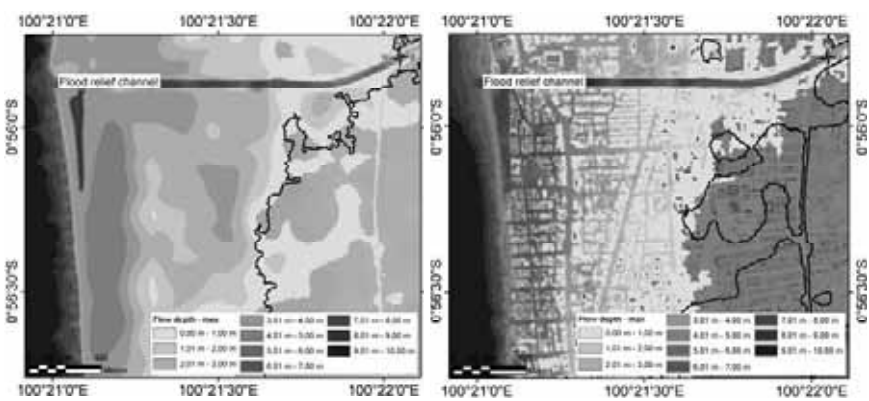

Figure 5. Maximum inundation for the coarse DEM (left), reached after t=2520 sec. and the highly-resolved DEM (right), reached after t=3030 sec. Black lines indicate the inundation limit of the coarse and the highly-resolved DEM respectively

Time series at gauges

We additionally compared time series at two locations as indicated in Fig. 3. Here, flow depths and velocities were analyzed and evaluated. The two locations were chosen to highlight different aspects of the flow characteristics when DEMs with different accuracies and resolutions are taken into consideration. The 'flood relief channel' (FRC) in Padang is represented with identical geometry in both DEMs, buildings and infrastructure are represented solely in the highly-resolved DEM. In the latter case, they have a strong influence on the flow regime and the flow path pattern at densely built areas.

Time series from the 'A. Yasni street' gauge show higher magnitudes for velocities as well as for flow depths (Fig. 6) when running the numerical model with the highly-resolved DEM. In this case, flow depths increase by a factor of 1.5 compared to simulations using the coarse DEM. Velocities at that particular location are even more pronounced and impressively illustrate that pedestrian evacuation may no longer be feasible when inundation starts taking place in the urban network of Padang. The obvious short-term drop in the time series at the A. Yasni street location for the coarse DEM may arise from partial reflections at the seawall but is still not completely understood. At the second examined gauge location, the FCR, differences in flow velocities and water depths are still present, but smaller when comparing both DEMs. The trends show similar tendencies. Higher flow depths at the FCR result from buildings at both sides of the channel when these are represented in the model.

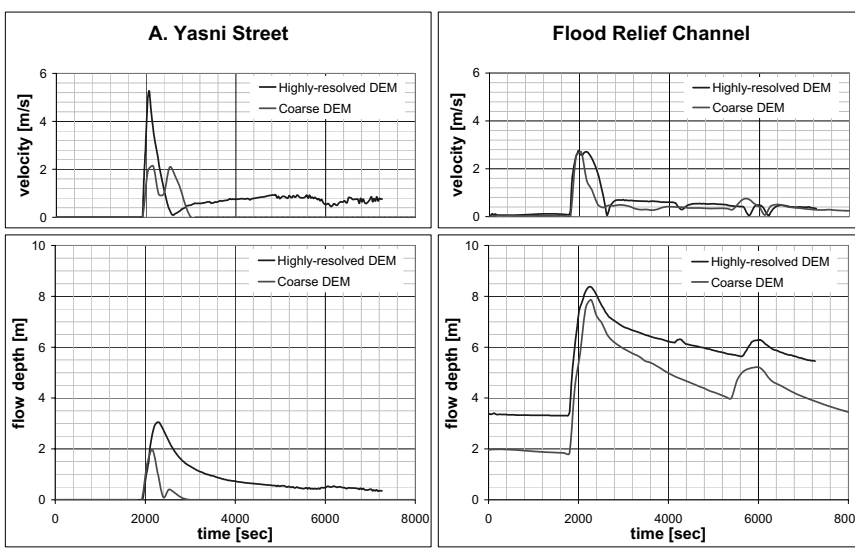

Figure 6. Time series for velocity and flow depth of analyzed gauges 'A. Yasni Street' and 'Flood Relief Channel' (blue line: highly-resolved DEM, red line: coarse DEM)

In conclusion, the major implications and differences due to varied geometries are mainly caused by friction and energy dissipation induced by infrastructure that is represented in the highly-resolved DEM. This furthermore leads to higher water stages near the coast and significantly higher velocities in flooded streets. By contrast, this effect is absent in the flood relief channel, where the quantities of velocity and flow depth are similar for both models. This might help supporting the argument of accuracy and quality of the optimized DEM and the subsequently conducted simulations.

CONCLUSION AND DISCUSSION

Accuracy and resolution of digital elevation models (DEM) used for small-scale hydrodynamics are crucial requirements when detailed information about tsunami inundation dynamics as well as evacuation routes and strategies are demanded. Hence, there is an urgent demand for acquiring highly-resolved data not only for the highly endangered region along the Sunda trench, but for any other coastal region worldwide, where disaster strategies and evacuation routines for urban agglomerations must be improved. It must be ensured that at least basic building patterns as well as infrastructural features are reproduced in the DEM. Beside a highly-resolved and accurate database, macro-roughness elements are the most important factors for meaningful and significant small scale simulations of tsunami inundation processes. Since this paper presents work in progress at this stage and a third generation DEM will be available in the near future, we will be able to utilize a database with an even higher resolution and accuracy in order to deduce most relevant tsunami inundation patterns on an individual building level to acquire the most adequate coping and evacuation strategies for the investigated city of Padang.

ACKNOWLEDGMENTS

The authors gratefully acknowledge the support of the Federal Ministry of Education and Research, Germany (BMBF) within the funded project "Numerical Last-mile Tsunami Early Warning and Evacuation Information System (BMBF code 03G0666A-H)" in the framework of the special DFG/BMBF program Geotechnology – Early Warning Systems in Earth Management. We also acknowledge the assistance of the State Ministry of Research and Technology, Indonesia (RISTEK) in connection with any administrative backing given in order to successfully complete the hydrographical survey off the coast of Padang conducted in 2007 by Franzius-Institute for Hydraulic, Waterways and Coastal Engineering.

REFERENCES

Birkmann, J. and T. Schlurmann (2007). Numerical Last-Mile Tsunami Early Warning and Evacuation Information System. *GEOTECHNOLOGIEN Science Report* No. 10, pp. 62-74

Borrero, J. C., Sieh, K., Chlieh, M. and Synolakis, C. E. (2006): "Tsunami inundation modeling for Western Sumatra", *PNAS*, Vol. 103, pp. 19673–19677

Harig, S., Chaeroni, C., Behrens, J., Schroeter, J. (2007): "Tsunami Simulations with unstructured grids (TsunAWI) and a comparison to simulations with nested grids (Tsunami-N3)", *6th Int. Workshop on Unstructured Mesh Numerical Modelling of Coastal, Shelf and Ocean Flows*, London

McCaffrey, R. (2007): "The next Great Earthquake", *Science*, Vol. 315, pp. 1675-1676

Nielsen, O., Roberts, S., Gray, D., McPherson, A. and Hitchman, A. (2005): "Hydrodynamic modelling of coastal Inundation". In: Zerger, A. (Hrsg.): *MODSIM 2005 Int. Congress on Modelling and Simulation*, pp. 518-523, Modelling and Simulation Society of Australia and New Zealand

Oumeraci, H. (2007): Motivation, Primary Objectives and Prospective Outcomes of future tsunami research, *Note from the DFG round table meeting*, Hannover, Germany

Stahlmann, A. (2007): "*Ausbreitung und Wellenauflauf langperiodischer Wellen (Tsunami) im küstennahen Bereich vor West-Sumatra*", Franzius-Institute for Hydraulic, Waterways and Coastal Engineering, Leibniz Universität Hannover, diploma thesis

ASSESSING METHODS FOR INTERACTION BETWEEN SWELL AND WIND WAVES

Melissa M-J. Yu[1], John R-C. Hsu[1], F-C. Lee[1],C-S. Chang[2] and N-J. Wu[2]

This paper discusses the reliability of two different methods of combining swell and wind waves to obtain the significant wave height, one is empirical method and the other is analytical method. The wave data are visual wave data from the International Comprehensive Ocean-Atmosphere Data Set (ICOADS) in the open sea area of Taiwan. For practical application, the wave data are calibrated with satellite measurement. The results are then used for establishing a preprocess module (Odin) in the Spanish Coastal Modeling System (SMC) to be promoted in Taiwan for coastal planning and design of recreational beaches.

INTRODUCTION

Different sources of long-term wind and wave data are available in the open sea almost worldwide, from visual observations, buoys, satellites and numerical methods (Cavaleri and Sclavo, 2006). Within these sources, abundant evidence can be found of wave interactions between swell and local wind waves in an open sea and nearshore where most engineering activities have taken place. Therefore, appropriate methods capable of achieving the reliable resultant wave conditions are vital for the success or failure of any subsequent engineering design and operations.

Taiwan is a small island state with unique marine geographic features on the west of the Pacific Rims and in the southeast of Chinese mainland which separates from Taiwan by a shallow continental shelf, the Taiwan Strait. While embarking on a research project to establish a nationwide coastal modeling system similar to the Coastal Modeling System (SMC, Gonzalez and Medina, 2007) commonly adopted in Spain, we have faced a technical problem of assessing the methods available for combining swell and local wind waves in the open sea covering from 118°E to 123°E and 21°N to 26°N (Figure 1). Given the variations in local wave climate, the sea area surrounding Taiwan is tentatively divided into four sub-regions (also in Figure 1). Representative wave heights and periods are sought after for each part.

In this article, two sources of wave data are first calibrated for establishing the long-term wave climate in the open sea surrounding Taiwan. One is the visual observation records from International Comprehensive Ocean-Atmosphere Data Set (ICOADS), and the other is the satellite data taken by

[1] Dept. of Marine Environment and Eng., National Sun Yat-sen University, Kaohsiung 804, Taiwan (ROC)
[2] Coastal and Harbor Department, CECI Engineering Consultants, Inc., Taipei 106, Taiwan (ROC)

TOPEX/Poseidom. Despite there may be some concern about the accuracy of these visual observation records; it has been for a long time the only source of information for wind and wave data in the open sea, hence long-term wave statistics.

For practical applications, the design significant wave height (SWH) is derived following empirical method, i.e. combining the wave height of swell and wind waves using superposition of wave energy, when relative wave obliquity between them is less then 30 degree, otherwise the larger wave height is used. Nowadays, this principle has been widely used by marine and coastal engineers in many countries.

The empirical method (i.e., Eq. 1), though very popular, does not consider the interactions between swell and the seas with different wave periods. For this, a better alternative can be found in Hsu and Chen (1992) in which a third order analytical method was proposed to calculate the resultant wave heights and periods for two waves in different heights and periods intersecting obliquely in deepwater. A series of comparisons on the results obtained from these two methods will be discussed in details in this paper.

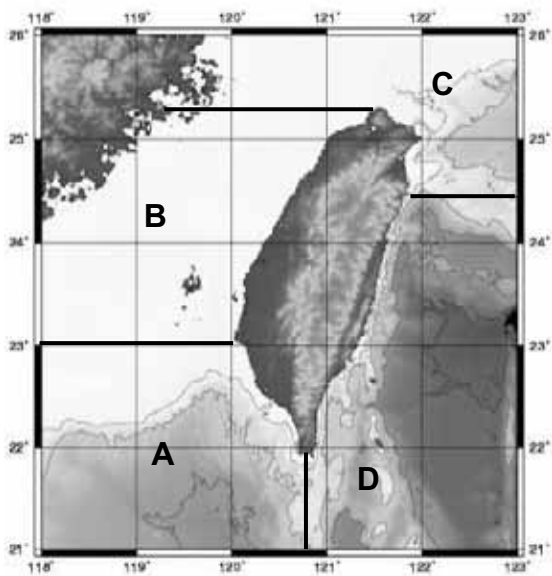

Figure 1. wave climate subregions around Taiwan.

WAVE DATA

Two sources of wave data are calibrated for establishing the long-term wave climate in the open sea surrounding Taiwan. One is the visual observation records from International Comprehensive Ocean-Atmosphere Data Set (ICOADS), and the other is the satellite data taken by TOPEX/Poseidom.

Despite there may be some concern about the accuracy of these visual observation records; it has been for a long time the only source of information for wind and wave data in the open sea, hence long-term wave statistics.

Prior to wave calibration, error noise and abnormal wave records are filtered out. The wave variables extracted from these sources are wind direction, wave height and period, and direction of wind waves (i.e., the seas) and swell.

Visual observation

Worldwide visual wave data reported by marine officers on the Voluntary Observation Ship (VOS) have covered a period of many decades since 1856 (Worley et al., 2005; Gulev et al., 2003; Gulev and Grigorieva, 2004). In comparison with the other data sources, these data have the longest records and provide independent estimates of local wind waves and swell. In this paper, the wave data analyzed is based on the newly updated ICOADS releases 2.3, which covers global ocean meteorology in the period of 1784-2005. However, only the wave data during 1950-2005 in the open sea covering from 118°E to 123°E and 21°N to 26°N are used for establishing the long-term wave climate around Taiwan.

Despite there may be some concern about the accuracy of these visual observation records; it has been for a long time the only source of information for wind and wave data in the open sea, hence long-term wave statistics.

Satellite measurement

Satellite wave data is one of the most popular wave resources worldwide in recent years. From a vantage point of 1336 kilometers (830 miles) high above the surface of the Earth, TOPEX/Poseidon can measure the height of the ocean surface directly underneath the satellite with an accuracy of 4-5 centimeters (see Fu et al., 1994 or the official website). Traveling in excess of 7 kilometers every second as it traces out its orbit; TOPEX/Poseidon covers the global oceans every 10 days. The specific merit of satellite wave data is in high accuracy and in a good quality. Moreover, the measurement will not be limited due to bathymetry. Despite there's no time-continuous records for a specific point. However, nearly the plan wave data, including wave elevation, wave height, wave period, wind speed etc can be obtained from TOPEX/Poseidom. That's very useful for validation. Satellite measurements in the period of 1997-2003 around Taiwan coast are used in this article.

EMPIRICAL METHOD FOR COMBINING WIND WAVE AND SWELL

For practical applications, the design significant wave height (SWH) is derived by combining the wave height of swell and wind waves using superposition of wave energy, when relative wave obliquity between them is less then 30°, otherwise the larger wave height is used. Nowadays, this principle has been widely used by marine and coastal engineers in many countries. For example, Gulev et al. (2003) has outlined this principle as:

$$SWH = \begin{cases} (h_w^2 + h_s^2)^{1/2}, [dir_{sea}, dir_{swell}] \in 30^\circ \sec tor \\ \max[h_w, h_s], [dir_{sea}, dir_{swell}] \notin 30^\circ \sec tor \end{cases} \quad (1)$$

The above method (i.e., Eq. 1), though very popular, does not consider the interactions between swell and the seas with different wave periods.

ANALYTICAL SOLUTION FOR WAVE-WAVE INTERACTION

The theoretical methodology for wave and wave interaction can be found in Hsu and Chen (1992), a third order analytical method was proposed to calculate the resultant wave heights and periods for two waves in different heights and periods intersecting obliquely in deepwater (Figure 2).

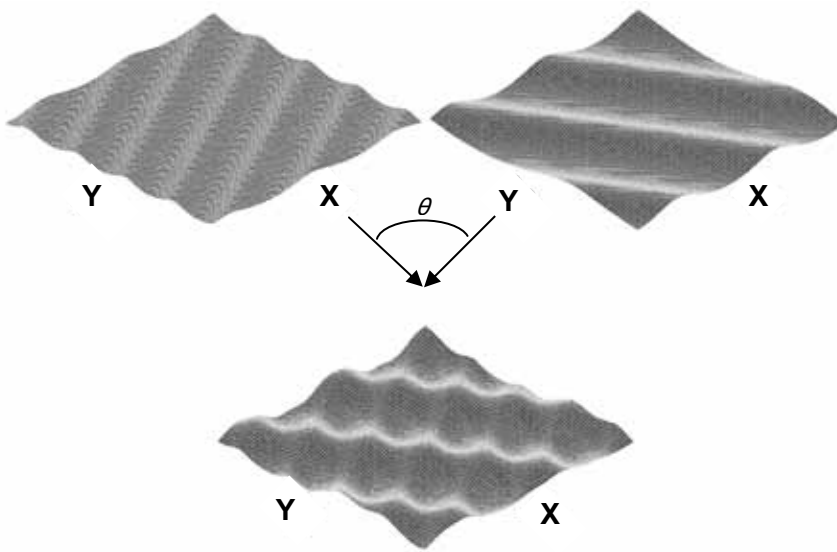

Figure 2. Perspective drawing of water surface fluctuations for two intersecting waves in different heights and periods, and their resultant wave form .

RELIABILITY CONSIDERATION

The empirical method as mentioned above is now widely accepted and used for combining wind sea and swell, however, it is not supported by a strong theoretical background. To discuss the reliability of significant wave height (SWH) obtained from these two methods, several wave records form ICOADS are selected. The difference in wave angle between wind wave and swell are listed in Table1. The first column of SWH is derived following the empirical method proposed by Gulve et al in 1992, while the second column of SWH is

calculated through analytical solution (Hsu and Chen, 1992). Because the theoretical methodology for wave and wave interaction is phase solution, therefore we can obtain the highest and lowest elevation individually. As shown in Table 1, the SWH from empirical method falls within the range of analytical solution, hence it can be used with reasonable confidence.

Table 1. Comparison of SWH between empirical and theoretical methods

Date (yyyymmddh h)	Lat	Lon	Wind wave			Swell			Δ θ	SWH (Gulev et al)	SWH (Hsu & Chen)
			θ *s*	*Hs*	*Ts*	θ *w*	*Hw*	*Tw*			
2004113021	23.6	122.0	50	5	5	50	7	6	0	8.6	9.5
2004072306	24.5	121.9	150	1	2	140	2	5	10	2.2	4.2
2004122412	21.9	120.1	50	3	3	70	4	4	20	5.0	6.9
2005100509	23.7	122.1	30	3	4	60	4	5	30	5.0	5.5
2003041400	24.0	121.9	330	1	2	90	1	3	60	1.0	1.5
2004092801	21.9	119.9	80	1	2	350	2	5	70	2.0	3.0
2004090100	21.9	120.6	10	1	2	230	2	4	120	2.0	2.6
2004060900	22.5	120.2	360	3	3	180	4	5	180	4.0	5.8

APPLICATION

Following the empirical method, SWH can be obtained for the visual wave records extracting from ICOADS distributed in the sea area surrounding Taiwan. After calibrating with satellite measurements of TOPEX/Poseidom, these results are included into a pre-process module of SMC. Therefore, the long-term wave climate for a specific investigation site, including wave rose diagram, cumulative probability distribution of Hs and Tp etc. can be generated immediately through the user-friendly module in SMC (Figure 3).

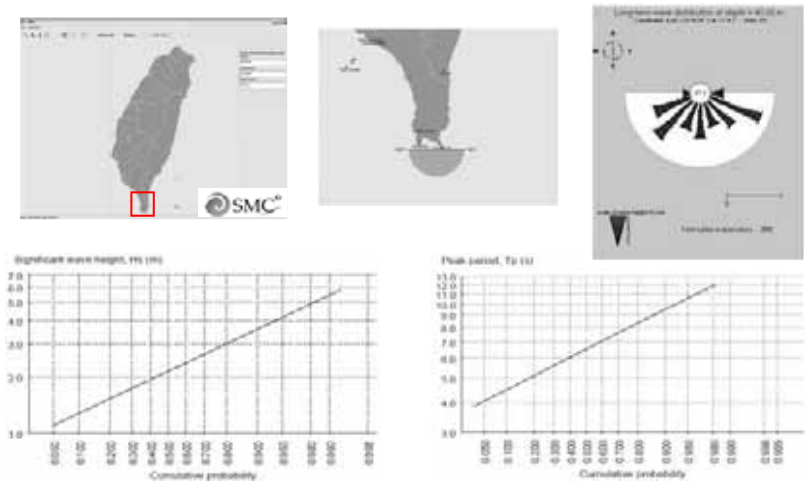

Figure 3. Long-term wave climate for O-luan-pi coast in the southern Taiwan .

REFERNCES

Cavaleri, L. and M. Sclavo. 2006. The calibration of wind and wave model data in the Mediterranean Sea, *Coastal Engineering*, 53, 613-627.

González, M., R. Medina, J. Gonzalez-Ondina, A. Osorio, F.J. Méndez and E. García. 2007. An integrated coastal modeling system for analyzing beach processes and beach restoration projects, SMC, *Computers & Geosciences*, 33(7),916-931.

Gulev S. K., V. Grigorieva, A. Sterl, and D. Woolf. 2003. Assessment of the reliability of wave observations from voluntary observing ships: Insights from the validation of a global wind wave climatology based on voluntary observing ship data, *Journal of Geophysical Research*, 108, no. c7, 3236.

Hsu, J.R.C. and Y.Y. Chen. 1992. Frequency modulation between two intersecting waves in deep water. In (ed., L. Debnath) *Nonlinear Dispersive Wave Systems*, World Scientific, Singapore, 299-328 pp.

SEDIMENT TRANSPORT STUDY ON THE TENRYU RIVER AND THE ENSHU COAST BASED ON ANALYSES OF SURFACE SEDIMENTS

Takuya Yoshii[1], Hirokazu Fujiwara[2], Shinji Sato[1], Guangwei Huang[3], Masaaki Shirai[4] and Yoshimitsu Tajima[1]

We investigated the present condition of regional sediment transport and its temporal change in Tenryu River and Enshu Coast in Japan. We focused on the distribution of geology in Tenryu River basin. By analyzing color and kinds of sediments, we tried to identify the origin of sediments and the impact of each tributary, dams and river vegetation on sediment transport. To obtain the sediment in old time (before dam construction) for comparison, we also performed trench study on the old track of the Tenryu River. We also investigated grain size distribution of sediments in the river vegetation. Through those studies above, we recognized that fine sediments do not accumulate on riverbed in lower Tenryu River except in the river vegetation but go straightly to the river mouth. It is why the effect of dams in midstream of the Tenryu River is not clear in riverbed in lower Tenryu River, but clear on coast around the river mouth.

1. INTRODUCTION AND RESEARCH AREA

Enshu coast, located in the central district of Japan, has been eroded significantly because of decrease in sediment supply from the Tenryu River, which has largest amount of sediment discharge in Japanese Rivers. It is mainly caused by the sediment retention in dam reservoirs in the midstream of the Tenryu River and sand mining for construction works. Among the dams, the largest one is the Sakuma Dam, which was completed in 1957 and has accumulated over 100 millions m3 of sediments up to now. Still now, the sediment transport is completely blocked by the Sakuma Dam. Therefore, comprehensive sediment management to the whole fluvial system is needed to solve this problem. First of all, to understand the present condition of sediment transport is important.

In terms of the attempt to investigate the sediment transport in the Enshu-Tenryu sediment system, Torii et al. (2004) performed numerical simulation of riverbed and shoreline change, which also predicted the change in grain size component. However, no studies of the regional sediment transport based on analyses of surface sediment itself have been carried out so far.

---

[1] Department of Civil Engineering, The University of Tokyo, 7-3-1 Hongo Bunkyo-ku, Tokyo, 113-8656, Japan
[2] SHIMIZU Corporation, 1-2-3 Shibaura, Minato-ku, Tokyo, 105-8007, Japan
[3] Department of Socio-Cultural Enviromental Studies, The University of Tokyo
[4] Ocean Research Institute, The University of Tokyo

In this study, we tried to understand the present condition of sediment transport process in the whole Enshu-Tenryu system by analyzing surface sediments. With regard to geology, Tenryu River has the Median Tectonic Line (MTL) in the middle of its basin. This tectonic line separates the geology extensively. On the north-western side of MTL, granite and its metamorphic rocks are dominant, therefore, whitish sand are dominant on the riverbed. On the other hand, on the south-eastern side, sedimentary rocks of Mesozoic or Paleozoic era, schist, and blackish sand are dominant. Because of such distribution of geology, every branch of Tenryu River has its characteristic in its sediments. And the largest dam, the Sakuma Dam is located nearly on MTL. Therefore, we tried to obtain the information of the geological component of the sediments at each place in Tenryu River and Enshu Coast, which tells us the origin of sediments and contribution of each branch and dams on sediment transport.

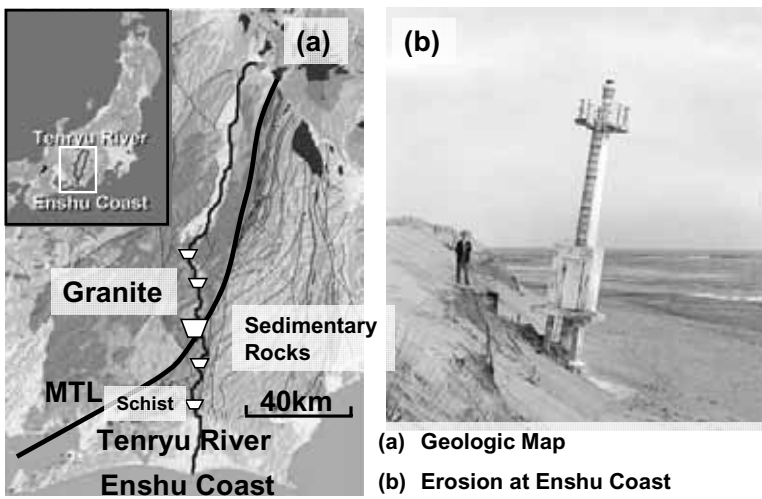

Figure 1: (a) Geologic Map of Tenryu River Basin (b) Lighthouse whose foot was scoured

Table 1: Dams in Tenryu River and Their Status (data from Okano, et al (2004))

Dam Name	Distance From the River Mouth	Capacity (1000m³)	Comp-letion	Status of Sedimentation	Sand/ Capacity
Yasuoka	130km	10761	1935	almost full	81.6%
Hiraoka	110km	42425	1952	almost full	84.5%
Sakuma	71km	326848	1956	not full/ accumulating	34.6%
Akiha	47km	34703	1958	not full/ decreasing	36.6%
Hunagira	30km	10900	1977	not full	8.3%

2. METHODOLOGY

2-1 Sampling of Surface Sediments and Analyses with Magnet

On May 12th and 13th in 2006, we collected surface sand in Enshu Coast at each place indicated in **Fig.2**. Sampling points were arranged to be nearly on the shoreline at high tide on that day. We collected samples which were located upper than the depth of 10cm from the surface.

Also, to obtain the sediments of riverbed in Tenryu River, on June 16th and 17th in 2006, we collected surface sand and gravels of riverbed at each place in **Fig.2**. We collected samples which located near the waterway, and upper than the depth of 10cm from the surface.

Fig.2 also shows the scanned image of sample sand which was pasted on two sided tape glued on white paper.

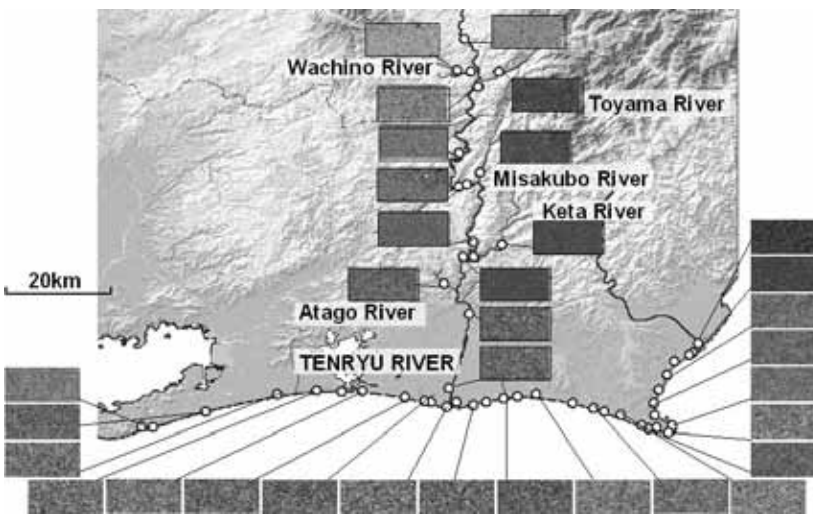

Figure 2: Scanned Image of Sand Samples

As we discussed in the above, sediments from the Tenryu River contain many kinds of minerals and rock fragments, and it indicates the origin of the sediments. Therefore, we classified the samples according to their geology.

To classify the sand samples effectively, we utilized its magnetism. By using magnets, we separated sand into magnet and non-magnet, which correspond to blackish sand and whitish sand. First, to remove an effect of grain size, we sieved the sand into same grain size class of 0.075-0.425mm. Next, we laid the sand in monolayer on a plate. As shown in **Fig.3**, we picked up sand grains which were attracted by Ferrite magnet (normal magnet) and Neodymium magnet (strong magnet) in this sequence. Sand which is attracted by Ferrite magnet is Ferro magnet. On the other hand, sand attracted only by

Neodymium magnet is Parra magnet. By using magnet, we succeeded in quantifying the fraction of whitish sand and blackish sand.

We classified gravels according to their kinds of rocks (sedimentary rocks, granite, metamorphic rocks and others) by visual observation. Before the observation, we sieved the rocks into grain size 4-16mm.

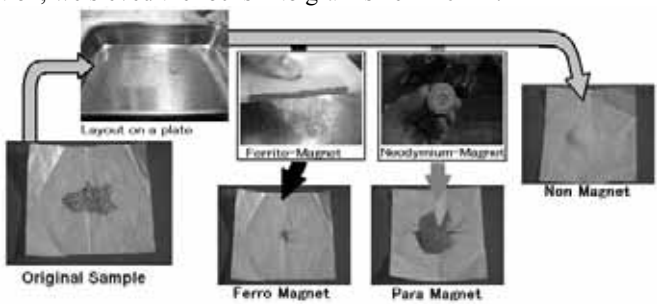

Figure 3: Procedure to Classification with Magnet

2-2 Trench Study and Optical Dating with OSL

Sediments on riverbed or coast are considered to be affected by dams or any other artificial structures or human activities. To compare the collected sediment with the sediments deposited before the dam construction, we performed trench survey on the old track of the Tenryu River shown in **Fig.4**, which was buried before the completion of the Sakuma Dam. Now, the place is utilized as a park. We selected investigation point in that park, which is indicated in **Fig.4**.

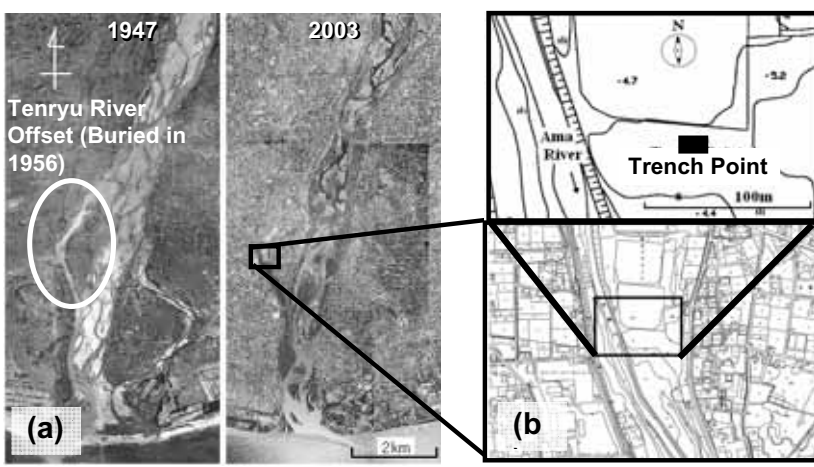

Figure 4: (a) Comparison of Aerial Photograph Around Tenryu River mouth
(b) Location of the Trench

First, we performed a preliminary survey by digging the ground about 1m. At the bottom of that small trench, we found the "old" riverbed below the surface soil. Then, we dug the trench of 4m length, 1m width and 2m depth. **Fig.5** shows the sediment structures of the old riverbed observed at the trench wall. We collected sediment samples at every 10cm depth in the trench below the surface soil. We also investigated these sediments (sand and gravels) in the same methods with sediments sampled from coast and riverbed.

In addition, to confirm the difference of sediment from the trench and one from the present riverbed, we employed the dating technique using Optically Stimulated Luminescence (OSL). As introduced by Aitken (1998) and others, OSL is generated when quartz or feldspar is exposed to light. OSL intensity increases as the mineral grain absorbs dose, and the OSL signal is reset with enough exposure to sunlight. This resetting process is called "bleaching". OSL is usually used to estimate the burial age of the sediments in the last hundred thousand years. Shirai, et al. (2006) showed that by investigating the ratio of bleached grains, which implies sunlight exposure condition of the grains in recent years, information on the sediment transport process was extracted. We compared sample's OSL intensity between original condition (natural) and after sunlight bleaching to get the percentage of the bleached sediment grains.

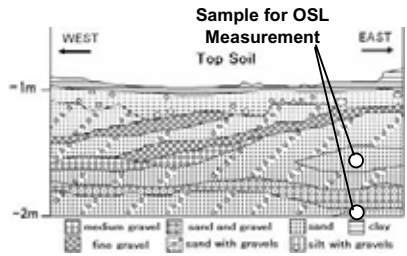

Figure5: Sketch of Trench Wall

To investigate the difference of condition of exposure to sunlight between sediments on old riverbed and present riverbed, we compared the bleaching percentage among the 2 samples from the trench and 1 sample from the present riverbed of the Tenryu River. Sampling points of the 2 samples of the trench are located at the depth of 160cm and 200cm from the ground respectively (see **Fig.5**). Sampling point of the riverbed is about 4km upstream from the Tenryu River mouth. Because the OSL intensity is easily canceled by the sunlight, we conducted sampling carefully to avoid the sample from being exposed to sunlight. We obtained samples by setting in opaque chlorinated polyvinyl chloride pipes capped with aluminum foil.

We followed Shirai, et al. (2008) in the process of the measurement except in the grain size of the specimens. We chose feldspar as specimen for OSL intensity investigation. All the processes were carried out in dark room with subdued orange light. Procedures of preparation of the specimen are as follows.

First, we sieved washed samples to collect particles whose grain size is 0.3-0.5mm. Next, we removed organic material and carbonate from specimens with peroxide (10%) and hydrochloric acid (10%), respectively. After heavy liquid

separation using LST heavy liquid, we extracted feldspar by microscopic handpicking.

After this preparation, we laid the individual feldspar grain on the measurement disc with 1 cm diameter. Then, we start the measurement by an OSL-TL reader (Risø). The process of measurement is as follows.

After removing unstable OSL signals by pre-heating (250℃, 60s), we measured natural OSL intensity (OSL intensity of original condition of the particles) by irradiating infra-red (870nm). Next, we measured its sensitivity of the specimen to the artificial radiation for normalization. After irradiating β-ray (ca. 2 Gy), we performed cut-heating (250℃, 60s) to remove unstable signals and then measured OSL intensity again with infra-red.

With the procedures above, we estimated the normalized OSL intensity of every specimen. To obtain the OSL intensity of bleached samples, after exposing the measured samples to sunlight enough (over 7 hours), we measured OSL intensity again by the same procedure.

2-3 Investigation in River Vegetation

In recent years, river vegetation has developed significantly in the lower part of the Tenryu River. It is mainly caused by degradation of the low water channel compared to the high water channel because of the decrease in sediment supply from upstream and the reduction of floods by dam operations. We considered that the sedimentation process in such vegetation area is different from that in non-vegetated riverbed.

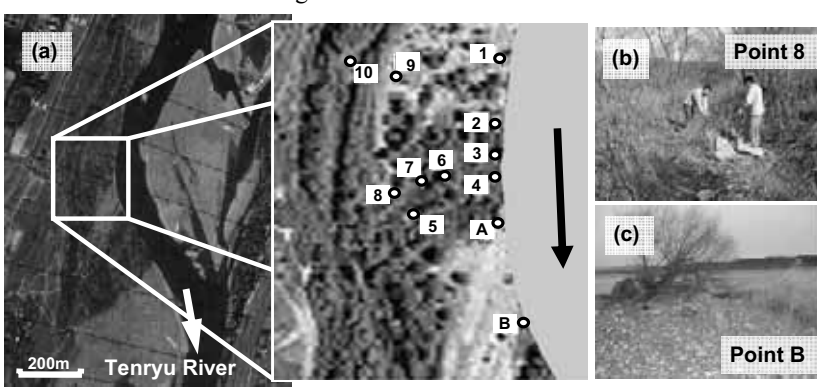

Figure 6: (a) Location of Investigation Point (b), (c) Condition of Point 8 and B

To investigate the sedimentation process in river vegetation, we performed grain size investigation on Jan. 14th and 15th in 2007. **Fig.6-(a)** shows the target area of this survey. It is located about 14km upstream from Tenryu river mouth. Points 1 to 10 were located inside the vegetation area (see **Fig.6-(b)**). To

investigate the relationship between condition of vegetation and the grain size, we recorded the condition of vegetation (number of trees around the point, height and density of the grass) at every investigation point. Point A and B were selected as a point in non-vegetated riverbed for comparison. Point A was located at the middle of riverbed, without any shields against river flow. On the other hand, Point B was just downstream of drift wood whose height was about 3 to 4m (see **Fig.6-(c)**).

We investigated grain size distribution of the surface sediments at every investigation point. Because it is difficult to sieve wet samples, we sieved only sediments larger than 8mm on site, and the remainings were sieved after drying at laboratory.

To compare the magnetic component of sand in vegetation with that of other samples, we collected sand in river vegetation on Aug. 9th in 2007. In this time, because the river vegetation investigated above has been removed artificially, we chose another vegetation area near the river mouth (see **Fig.7**).

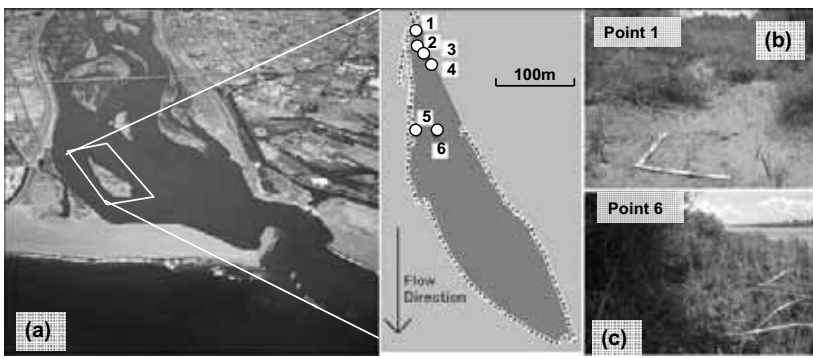

Figure 7: (a) Location of Investigation Points (b), (c) Condition of Point 1 and 6

3. RESULTS AND DISCUSSIONS

3-1 Results of Classification of Sediment Samples

Fig.8 shows the results of analyses on sand samples of coast with magnet. When we see the results from east to west, samples near the Ooi River mouth contains largest fraction of magnet, which means they are blackish. It is caused by the geology of the Ooi River basin, which is mainly composed of sedimentary rocks of the Mesozoic era and the Tertiary period. As it become far away from the Ooi River mouth, fraction of black sand in samples decreases because of the effect of the Tenryu River which has granite belt in upstream. However, at the points around Tenryu River mouth, fraction of black sand becomes larger to some extent. And as it becomes far from Tenryu River mouth westward, fraction of black sand decreases again. As a whole, except the area strongly affected by the Ooi River, only the points around Tenryu River mouth have blackish sand.

Recently, sediments from upstream of the Sakuma Dam do not reach downstream because the Sakuma Dam continues to trap sediments. Therefore, sediments discharged from the Tenryu River mouth should be affected such tributaries as the Misakubo River and the Keta River, whose sediments are blackish. Result of analyses on coastal sand suggests that because of the effect of the Sakuma Dam, sand discharged from Tenryu River mouth has become blackish in recent years, and its effect is now spreading to the coast around the Tenryu River mouth.

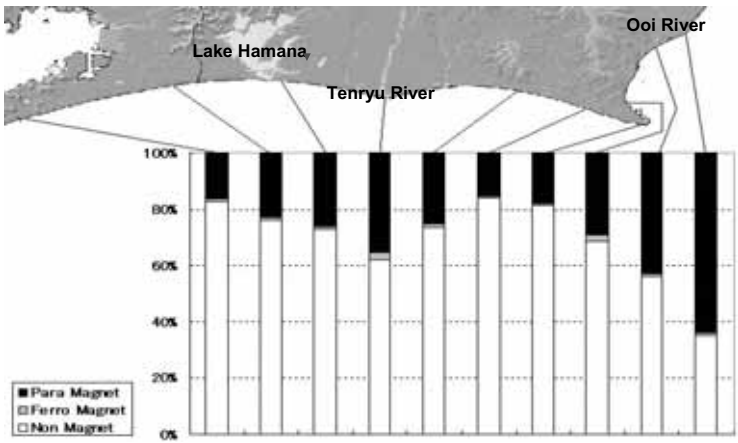

Figure 8: Result of Classification of Coastal Sand with Magnet

Fig.9 shows the results of analyses by magnet on samples from Tenryu riverbed, the trench (the depth of the sampling point was 190-200cm from the ground) and the river vegetation. When we see samples from riverbed, first, it appears that component of samples is strongly affected by geology of each tributary. The Wachino River is located in the granite belt, therefore, most part is white sand. The Tooyama River, the Misakubo River and the Keta River are located in the sedimentary rock area, therefore, it contains large amount of black sand. In the upstream of Tenryu mainstream, most part is white sand because of such rivers as the Wachino River, which comes from granite area. As it comes downstream, mainstream meets several tributaries from sedimentary rock area, such as the Tooyama River and the Keta River. Because of the effect of such tributaries, fraction of black sand becomes larger as it comes downstream. However, samples downstream of the Funagira Dam show smaller content of black sand (see the sample of **22km** and **4km**). The fraction of black sand in the sample from lowest part of the Tenryu River is smaller than that in the sample of coastal sand near the river mouth.

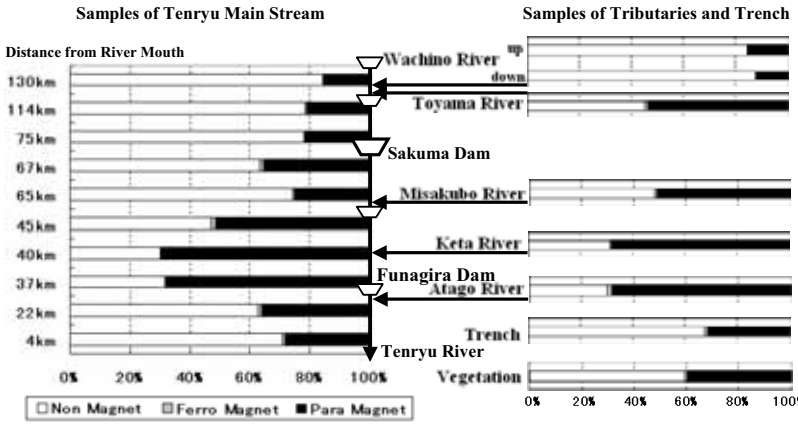

Figure 9: Result of Classification of Sand of Riverbed with Magnet (Grain Size: 0.075-0.425mm)

With respect to the effect of the Sakuma Dam, it is expected that in the downstream of the Sakuma Dam, sediments of the riverbed are strongly affected by such tributaries as the Misakubo River and the Keta River, whose main contents is black sand. Then, sand is expected to be blackish at every place lower than the Sakuma Dam. However, result of the analyses of sand was inconsistent with this prospect only in the downstream of the Funagira Dam.

As we explained in Section **2-3**, we also investigated the component of white and black sand of the samples in river vegetation. When we compare those results with those of non-vegetated riverbed (the sample of **4km** of mainstream), there are significant difference between them. Fraction of black sand in the sample from vegetation is larger than that of samples not only from riverbed but also from coast near the river mouth.

This result means not only that sand in the river vegetation are affected by such rivers as the Keta River and the Misakubo River which discharge black sand, but also that in the lower part of the Tenryu River, sand from upstream deposits only in vegetation, and on coast. The prominence of white sand in the sample of riverbed in lowest part of Tenryu River shows that riverbed is still being eroded and the no fresh sediments are deposited on the present riverbed. This is considered to be due to the Funagira Dam (see **Fig.9**) equipped with sediment discharge gates. Since the Funagira Dam flushes sediments in its reservoir only during heavy floods, fine sediments, originated from the Misakubo River and the Keta River, will be transported as washload and therefore will not be deposited on the riverbed except for vegetation zones. This scenario also accounts for the prominence of black sand on the coast around the river mouth. In addition, there were no significant differences in the ratio of black sand between sample from the trench and the present riverbed (**4km**).

This result means sample from the present riverbed is 'old' and the riverbed is eroded now, which also supports our scenario.

Fig.10 shows the result of classification of gravels whose grain size is 4-16mm. In the most part, it shows the same tendency with the result of analyses of sand. Because of the difference of structural durability between granite and sedimentary rocks, the fraction of granite in these samples is smaller than that of white sand in sand samples. Although the effect of the Funagira Dam is not so clear in this result, it is consistent with the scenario explained in the above, because there is no significant difference between the components of riverbed sample (**4km**) and trench sample.

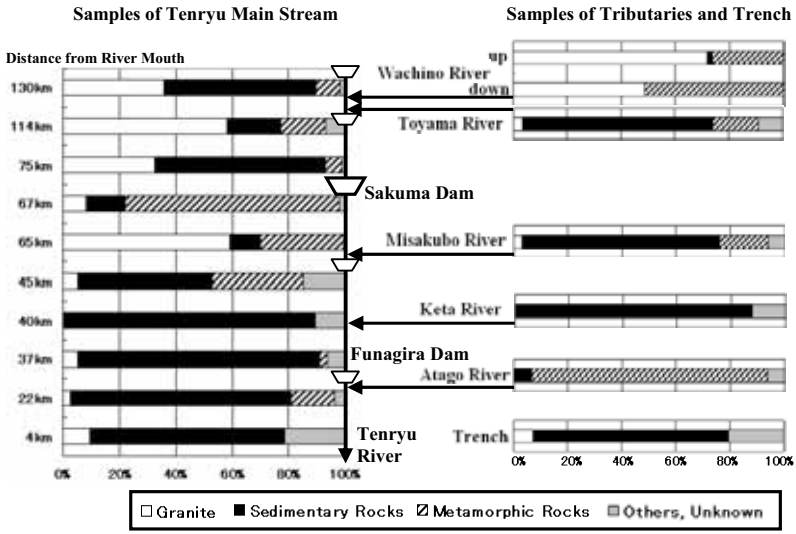

Figure 10: Result of Classification of Gravels from Riverbed by Visual Observation (Grain Size: 4-16mm)

3-2 Results of OSL Measurements

Fig.11-(a) shows the OSL intensity of samples from the trench, which was located at 160cm below the ground. Natural OSL intensity is higher than that of bleached sample in every specimen, which means no particle has been exposed to sunlight in recent years, which supported that we correctly found sediments of old riverbed. The result of sample from 200cm depth showed almost same result.

Fig 11-(b) shows the result of sample from present Tenryu riverbed which is located about 4km upstream from the river mouth. Most of the particles show no sign of exposure to sunlight in recent years. This result supports our scenario that the riverbed of lower Tenryu River is still being eroded and sediments on the riverbed is 'old', which are free from effect of Dams.

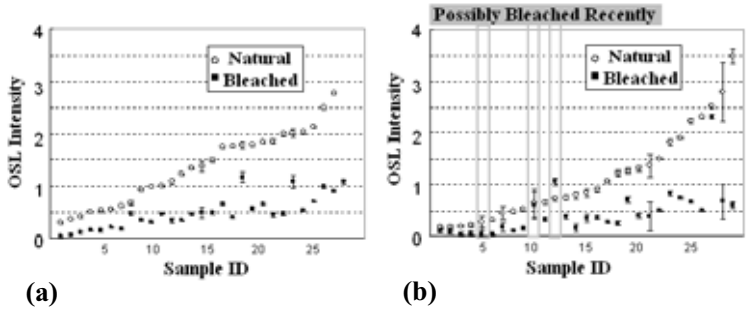

Figure 11: Comparison of OSL Intensity of Samples from Trench and Riverbed (a) Trench Sample (b) Riverbed Sample

3-3 Grain Size Distribution of Sediments in River Vegetation

Fig.12 shows the result of grain size investigation at the river vegetation 14km upstream from the river mouth. The pie chart indicates the weight ratio of each grain size range. Compared with the result of point A and B which were located on the non-vegetated riverbed, grain size of the sediments inside the vegetation area is significantly finer. As shown in **Fig.12-(b) and (c)**, as it becomes far from the water channel or it is surrounded by more trees, the sediments would also become finer. Especially, the points far from water channel such as point 7-10 contain considerable amount of silt (finer sediments than 0.075mm).

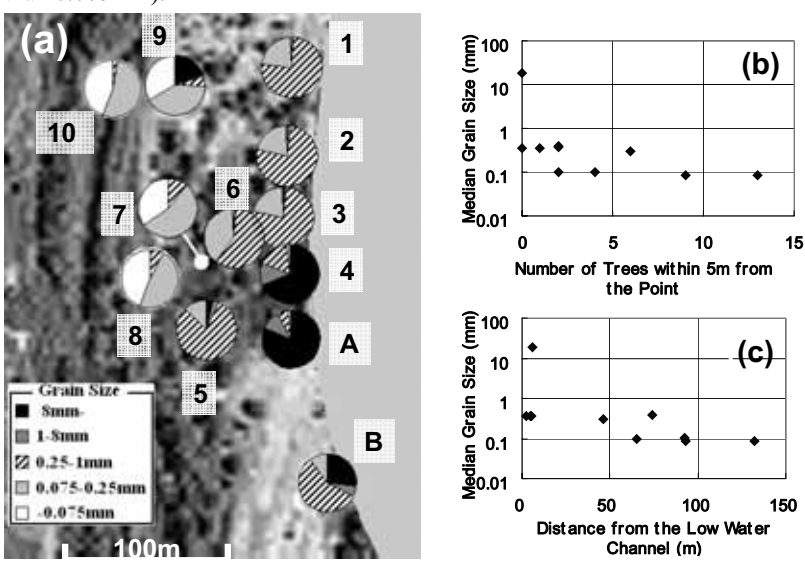

Figure 12: (a) Grain Size Distribution of Sediments in River Vegetation (b) Relation between Number of Trees around the Point and Grain Size (c) Relation between Distance from Water Channel and Grain Size

Fig.13 shows the spatial distribution of thickness of surface sediments layer and ratio of beach sand trapped by the vegetation more than non vegetated riverbed (point **A**). By counting the area of each category multiplied by the depth of surface layer, we calculated the amount of trapped beach sand in this vegetation area. It was estimated as 25,000m^3. Through the analyses of aerial photographs in time series, we estimated the period of deposit of fine sediments in this vegetation to be within 15years. Also, this kind of river vegetation has developed in whole area in the lower Tenryu River, which is defined as the section between the river mouth and 25km point. Taking those conditions into account, the amount of annual deposit of beach sand in the vegetation zone in the whole lower Tenryu River was estimated as 4.2x10^{4}m^3. Torii et al. (2004) estimated annual discharge of sediments whose grain size is between 0.106mm and 0.85mm is 10.8x10^{4}m^3. Compared to this amount, deposition of beach sand to the vegetation zone is significant.

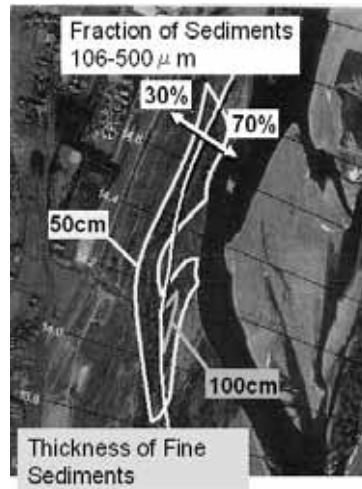

Figure 13: Estimation of Volume of Deposition of Fine Sediments in the River Vegetation

4. CONCLUSIONS

Analyses of surface sediments focused on their color and grain size were carried out to understand the present condition of sediment transport process of the Tenryu River-Enshu Coast system. We employed analyses technique using magnet to quantify the ratio of color of sample sand, and OSL intensity to confirm whether the sediment has been buried for a long time. We also investigated grain size distribution of sediments in river vegetation area to estimate its effect to entrap fine sediments. Main conclusion is as follows.

1. Effect of dams in the Tenryu River, which is observed as the prominence of blackish sand, is expanding on the coast around the Tenryu River mouth.
2. In the lower Tenryu River, fine sediments which compose beach sand will not deposit on the riverbed except in the river vegetation, but go straightly to the river mouth.
3. Measurements of OSL intensity support our scenario that the riverbed of the lower Tenryu River is still being eroded, and the present riverbed surface is covered with ‘old’ sediments.
4. The amount of deposition of beach sand in the river vegetation was estimated as 4.2x10^{4}m^3/year in the whole lower Tenryu River, which is

significant compared with the amount of sediment discharged from the Tenryu River mouth which amounts to $10.8 \times 10^4 m^3$/year.

ACKNOWLEDGMENTS

This study is a part of Tenryu-Enshunada Project financially supported by the Japan Science and Technology Agency (JST).

REFERNCES

Torii, K., Sato, S., Uda, T., and Okayasu, T., 2004. Regional Sediment Management Based on Sediment Budget for Graded Sediments – A Case Study of Tenryu Watershed and Enshu-Nada Coast. International Conference on Coastal Engineering 2004, p3110-3122

Okano, M., Yasuda, Y, Mori, K., 2004. Study on the influence of the dam reservoirs in Tenryu middle stream on the whole sediment-flow system in the basin. Annual report of the Water Resources Environment Technology Center, 2003, I-2-1 (in Japanese)

Aitken, MJ., 1998. An Introduction to Optical Dating:The Dating of Quaternary Sediments by the Use of Photon-Stimulated Luminescence. London:Oxford Science Publications.

Shirai, M., Tsukamoto, S., and Omura A., 2006. An attempt estimating incorporation ratio of old grains into turbidity current using an optically stimulated luminescence technique. Abstructs of 17th International Sedimentological Congress 2006, Fukuoka (A), p319

Shirai, M., Tsukamoto, S. and Kondo, R., 2008. Transport-depositional processes of present fluvial deposits estimated from OSL intensity of sand-sized grains. The Quaternary Research, 47 (6), 377-386 (in Japanese with English abstract, in press)

MODELLING THE MORPHODYNAMIC EVOLUTION OF THE DIFFRACTION CROSSHORE PROFILE

Jose M. Medina-Villaverde[1,2], Agustin Sánchez-Arcilla[3], Juan M. Prada[4], José S. López[1,5] and Alex Palmeiro[1]

At the present day, conventional models on morphodynamic evolution of the beach crosshore profile are limited to the analysis of cylindrical beaches. This is due to the simplification of the governing equation (flux energy conservation) assuming that the beach is constant alongshore. This assumption has some inconvenient; one of the most limiting consists of these models can't be applied to beaches with groins, or close to tidal inlets, river mouths, etc.

This paper aims to present a very easy and cheap approach to analyze cross-shore profile on non-cylindrical beaches, simply by using a 2DH wave propagation model and a conventional 2DV cross-shore profile model. Respecting the wave propagation model, one should use a tool which could be able to account for wave refraction (all the models do), wave diffraction (not all the models do) and wave reflection (only a few models do). Wave reflection can be important, since the main reason of a beach to be non-cylindrical generally consists of the existence of a groin or a natural salient, which usually is responsible of reflections on incident waves. Due to that, an elliptical model based on the integration of the mild slope equations is used: MIKE 21 EMS. The crosshore profile evolution model to be employed will be LITPROF, from the LITPACK modeling system. A Boussinesq model provided with swash effects could be a good choice as well, but the process would be more complicated. The process is being checked against physical model results.

INTRODUCTION

Motivation

Frequently, morphodynamic evolution of the crosshore profile must be assessed. That is the case of projects on artificial nourishment of beaches, study of the seasonal changing profile, etc., where profiles are supposed to be constant alongshore.

The main equation governing the wave propagation model states the conservation of energy flux:

---

[1] DHI Water & Environment. Isabel de Valois, 20; 28660 Boadilla del Monte, Spain. jmv@dhigroup.com

[2] European University of Madrid (UEM). Ana de Austria, 4; 28660 Boadilla del Monte, Spain. jmedvil@ciccp.es

[3] Catalonia University of Technology (UPC). Head of the Laboratory of Maritime Engineering. Barcelona, Spain. agustin.arcilla@upc.edu

[4] CEDEX, Harbor and Coasts Research Center. Antonio López, 81. Madrid, Spain. Juan.M.Prada@cedex.es

[5] Madrid University of Technology. School of Civil Engineering. Ciudad Universitaria, s/n. Madrid, Spain. jslopez@caminos.upm.es

$$\nabla\left(\overrightarrow{E \cdot C_g}\right) + \frac{D}{\sigma} = 0 \qquad [1]$$

The integration of Eq. [1] is done assuming the spatial coordinates x and y are respectively the crosshore and alongshore directions. So, Eq. [1] becomes:

$$\frac{\partial}{\partial x}(E \cdot C_g) + \frac{\partial}{\partial y}(E \cdot C_g) + \frac{D}{\sigma} = 0 \qquad [2]$$

Usually, beaches are assumed to be uniform in the longshore direction. This implies that no change appears alongshore in any parameter involved in wave propagation, i.e.:

$$\frac{\partial K}{\partial y} = 0 \qquad \forall K \qquad [3]$$

As a conclusion of that assumption, Eq. [2] becomes:

$$\frac{\partial}{\partial x}(E \cdot C_g) + \frac{D}{\sigma} = 0 \qquad [4]$$

which is the governing equation for wave transformation. Equation [4] implies that such a type of models can only be used on cylindrical beaches. In other words: most of the common beaches do not really admit the use of a standard model on morphodynamic evolution of the crosshore profile.

That means that beaches as Zurriola (figure 1, left) can't be assessed with conventional models. They can be applied only to cylindrical beaches, as Castilla beach (figure 1, right)

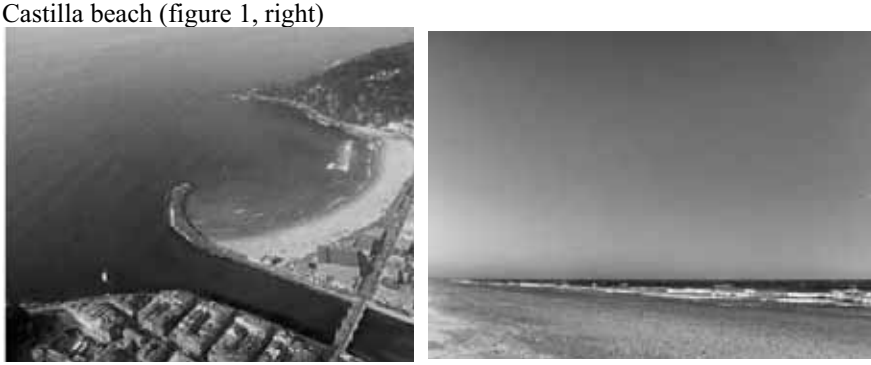

figure 1.Zurriola beach (north Spain, Cantabric coast) and Castilla beach (south Spain, Atlantic coast)

The problem arises when the coastal engineer is forced to give an assessment of the morphodynamic evolution of a diffracting profile, i.e., when he is involved on a civil prosecution as an assistant to a judge. Frequently, there is neither time enough nor budget to provide a solution from a physical model of movable bed, and in addition, those models are also affected by scale effects,

and other uncertainties derived from the similarity criteria which have been chosen, commonly Froude criterion.

Quasy 3D models are becoming more and more popular, but they are limited in several ways to asses morphodynamic evolution of crosshore profiles: in one hand, they use to be depth integrated, what invalidates most of the physical hydrodynamic processes appearing in the profile (such as undertow, for instance), and frequently they accounts only for longshore transport, what implies that they are not valid in the short term.

There are other limitations, perhaps more mundane: Engineering Consultancy firms usually need “cheap” models as accurate as possible; in this case, “cheap” means quick, accurate, user friendly and having a feasible cost to implement it in the company.

Due to that, a new approach has been started not only as a r&d exercise, but also to assess the evolution of a diffracting crosshore profile on the Spanish Mediterranean coast at Catalonia (figure 2), as result of evaluating damages produced by a severe wave storm.

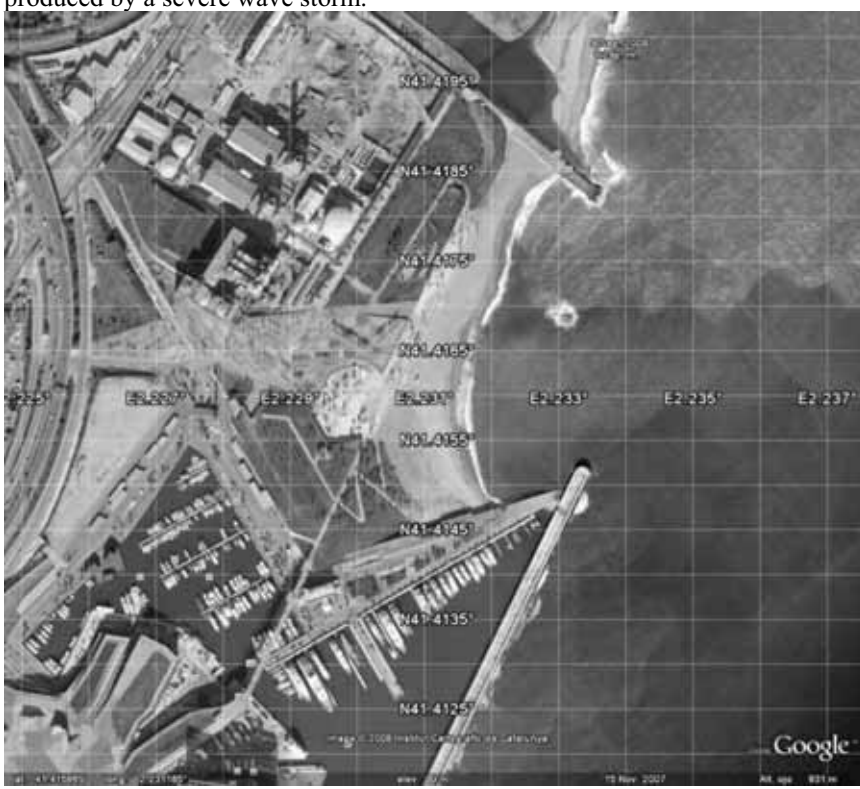

figure 2.Forum 2.004 beaches. Barcelona, Spain

APPROACH

Background

There are several ways to solve the problem:

1. Avoiding longshore uniformity.
2. Using a 3D model.
3. Using conventional models with empirical corrections.

Let us do a short review of the three exposed ways.

Avoiding longshore uniformity

This implies to build a new model, what is the best solution, but perhaps not the cheapest and quickest way to solve the problem. Of course, this should be the target to achieve in the medium – large term, trying to assess the beach evolution as a unity, depending on the different points of view, both in the time and special scale.

Using a 3D model

As a matter of fact, this is the conclusion of avoiding longshore uniformity and implementing longshore processes in the model. At the present day, quasi 3D models have some limitations, as shown in the introduction, derived from the facts of:

- They are depth integrated.
- They pay attention mainly to longshore processes, what invalidates the motion of the crosshore profile, which has a minor time scale.

Using conventional models with empirical corrections

This solution presents some advantages:

- it is one of the cheapest ways of working, since most of coastal engineers have conventional models on morphodynamic evolution of the crosshore profile,
- it is the fastest, since it does not implies complicated calculations, and
- depending on the approach, ongoing research shows that it can be able to effectively avoid the longshore uniformity hypothesis

For this reasons, these is the way in which the approach has been developed.

General description

This paragraph describes the approach under research. Validation against data from movable bed physical modelling is shown in the next paragraph.

The approach relies in the assumption of a diffracting profile shows a morphodynamic evolution different to a, let us say, uniform profile derived from a different wave propagation patterns; figure 3 shows different physical processes appearing in the diffracting profile, due mainly to:

- breakwater on the left hand side of the profile
- different propagation angle due to profile orientation

- existence on a cliffy coast in the neighborhood

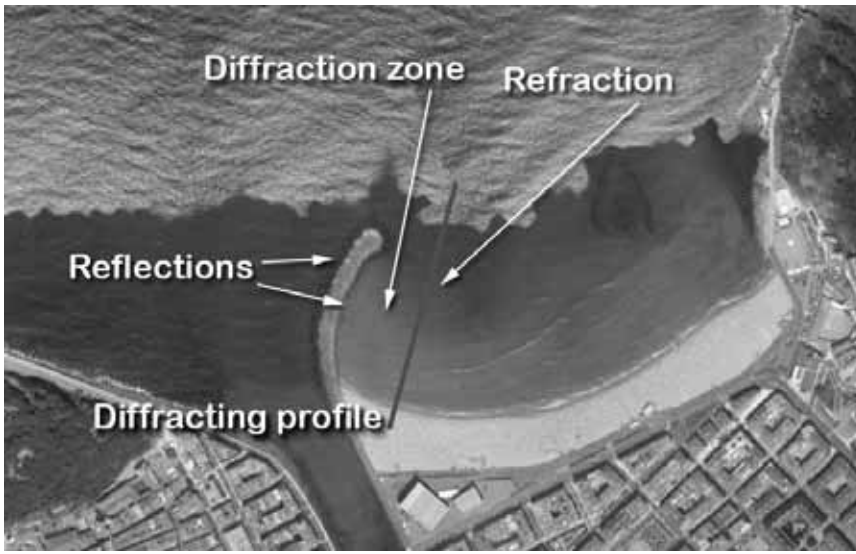

figure 3. Zurriola beach, showing different wave processes affecting the diffracting profile

One of the first approaches to solid transport has been given by the CERC formula (U.S. Army Corps of Engineers, Coastal Engineering Research Center, 1.984) which, based on the assumption that the total longshore sediment transport rate is proportional to longshore energy flux, can be written as:

$$Q = \frac{K}{16\sqrt{\gamma_b}} \rho g^{\frac{3}{2}} H_{sb}^{\frac{5}{2}} \sin(2\theta_b) \qquad [5]$$

From eq. [5] it can be seen that the main variables from transport caused by waves are the significant wave height (H_s) and the angle of propagation (θ). So, in our approach, a factor K_m will be defined as

$$K_m = H_s^{\frac{5}{2}} \sin(2\theta) \qquad [6]$$

This factor will be used on two different, but correspondent, beaches: the first one, which will be called *real* beach and the variables referred to it will be designed with the sub index "R"; the second one will be called *uniform*, and its variables will be designed with sub index "U".

The *uniform* beach will be constructed as a cylindrical one with the diffracting profile to be analyzed. An example, used for validation (see next paragraph) is shown at figure 4.

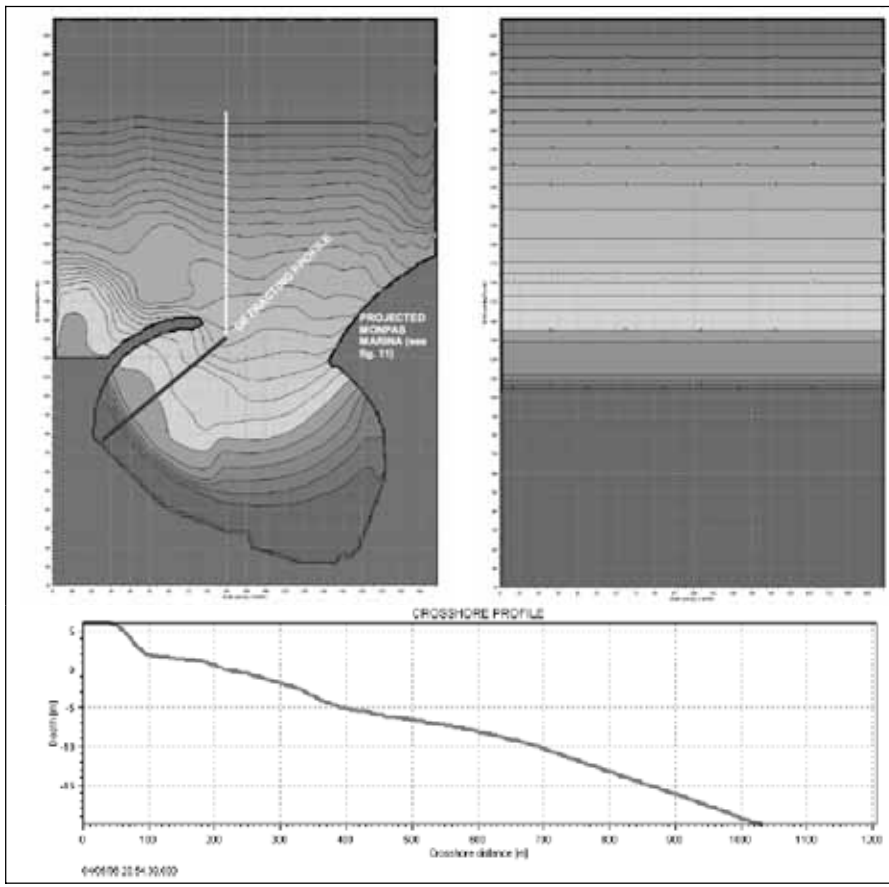

figure 4. Real beach (upper left) showing the diffracting profile (lower center), uniform beach (upper right).

From the two beaches a new coefficient Kmu(x) appears, dependant of the x-coordinate as:

$$K_{mu,A}(x) = \frac{\left(H_s^{5/2}\sin(2\theta)\right)_R}{\left(H_s^{5/2}\sin(2\theta)\right)_U(x)} \qquad [7]$$

On this coefficient the group celerity (as the parameter which relates Km with energy flux) does not appear, since can be assumed that $(C_g)_R \approx (C_g)_U$. In effect, if linear theory is accepted, then in shallow water, the group celerity is

$$C_g = C = \sqrt{gd} \qquad [8]$$

From eq. [8], since $[d(x)]_R = [d(x)]_U \ \forall x$ it results that C_g is exactly equal in both profiles and consequently, can be voided in eq. [7].

If we assume that wave height is similar out of the beach in both profiles (wave reflection in breakwaters or groins can affect slightly), then out of the beach should be $K_{mu,A} = 1$. This leads to a new definitive parameter, Kmu, got normalizing $K_{mu,A}$:

$$K_{mu}(x) = \frac{K_{mu,A}(x)}{[K_{mu,A}(x)]_{max}} \quad [9]$$

And finally, if a wave rose is acting on the profile, the final K_{mu} (x) will be got as a composition of the individual K_{mu}, as

$$K_{mu}(x) = \sum_{\theta} f_{\theta}[K_{mu,\theta}(x)] \quad [10]$$

To get the evolution of the diffracting profile, each point's depth will be got from the results on the uniform beach, correcting it with K_{mu} (x) as

$$\Delta z_R(x) = \Delta z_U(x) \cdot K_{mu}(x) \quad [11]$$

Validation

Physical model data

The most convenient data (field data) are difficult to collect, since simultaneous data on waves, currents, bathymetry and sea level are needed. Due to that, data from a physical model with movable bed was used (Medina Villaverde J. M., 1.997).

The model (see figure 5) was carried out at the Harbor and Coasts Research Center of CEDEX to check the incidence of a marina projected on the Zurriola bay, at San Sebastian (Northern Spain).

figure 5.Physical model at CEDEX

Comparisons

The whole wave set used on the physical model is shown in table 1.

table 1.Sea parameters used in the physical model				
	Hs [m]	Tp [s]	θ [º]	Duration [h]
S – 1	3.14	12.00	0.00	9.00
S – 2	5.90	16.00	0.00	2.00
S – 3	3.14	12.00	0.00	9.00
Tide	Semidiurnal, range = 4.00 m			

Stationary waves are shown in figure 6. Next paragraph will refer to the mathematical models used on this approach.

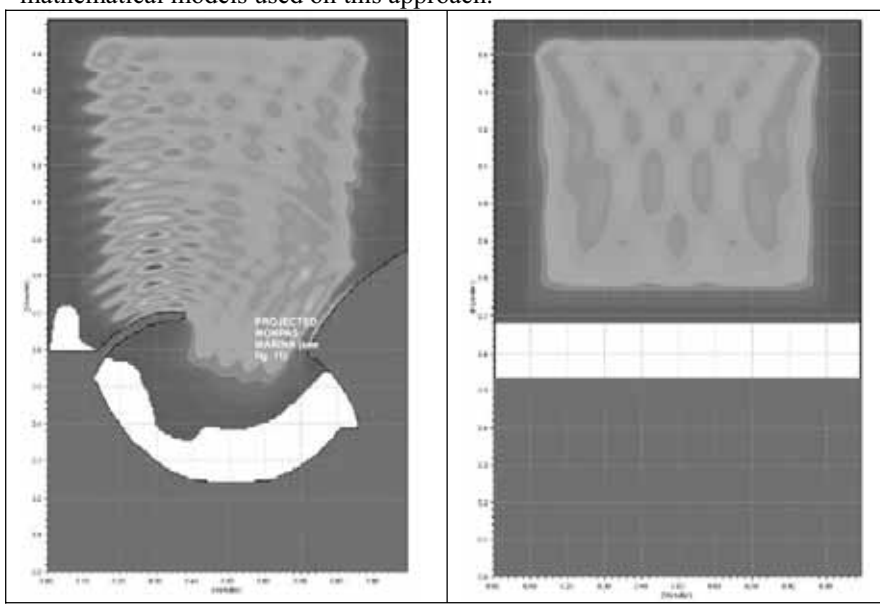

figure 6. Stationary waves on the real beach (left) and on the uniform beach (right)

Next figure shows a comparison between the wave height in the two profiles. The square indicates the zone of interest. Real profile shows the effects of reflection on the breakwater and diffraction beyond it.

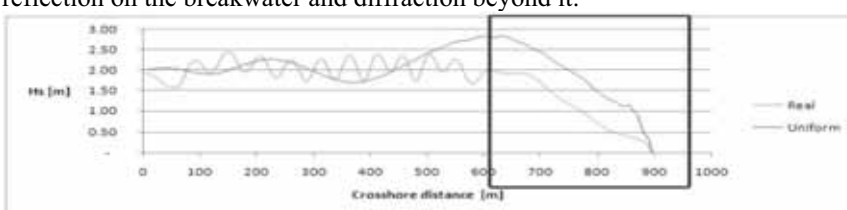

figure 7.Significant wave height over both profiles

From these results, the normalized $K_{mu}(x)$ can be got. It is shown in figure 8.

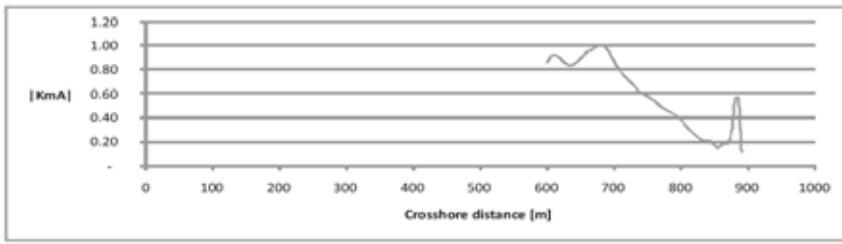

figure 8. Normalized K_{mu}

And finally, using eq. [11] on the uniform profile, the first result is obtained and depicted in figure 9.

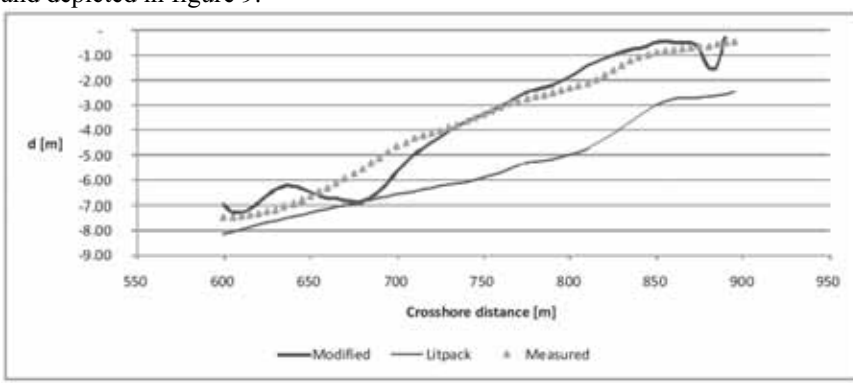

figure 9. Plotting of the result

Mathematical models used on this research

Mathematical models needed for computing this approach are well known:

- On wave propagation, since the approach lies in the existence of a diffracting profile, this implies a breakwater, a groin, etc., what means that reflection and diffraction phenomena are present; due to that, an elliptical mild slope model is the most feasible. Here, Mike 21 EMS has been used.
- To account for morphodynamic evolution of the profile in the uniform beach, a conventional model of profile evolution can be used. Here, LITPROF was employed.

Ongoing research

Research on this subject is now being oriented to manage field data enough to check the preliminary results and update eq. [7], which is the heart of this approach.

Getting field data is difficult, since several and very different data sources have to be collected *simultaneously* (wave data, currents data, bathymetry, sediment data, wind data, …). At present day, a proposal of monitoring is being

prepared at the Spanish Atlantic coast jointly with Andalusia Ports Authority and the University of Huelva, which should start in the short term.

CONCLUSIONS

- A new approach to assess morphodynamic evolution of diffracting profiles is being carried out by the Marine Dpt. of DHI Spain.
- The approach relies in conventional models of wave propagation (elliptical) and morphodynamic evolution of crosshore profile.
- First results have been validated with data from physical model of movable bed and are reasonably good.
- Further research is being carried out supported by field data

ACKNOWLEDGMENTS

First author acknowledges the Spanish Institution of Civil Engineers (*Colegio de Ingenieros de Caminos, Canales y Puertos*) for partially funding its Ph.D. Thesis, from which this work was extracted.

APPENDIX

Variables

A list of variables which have been used in the article is shown beneath:

C	: Wave celerity	[m·s^{-1}]
C_g	: Group celerity	[m·s^{-1}]
D	: Energy dissipation	[m²]
d	: Depth	[m]
E	: Wave Energy	[m²]
g	: Acceleration of gravity	[m/s²]
H_{sb}	: Significant wave height at breaking	[m]
K	: Empirical coefficient (~ 0.39 [6])	Adim.
Km Kmu,A Kmu	: Empirical factors representative of wave energy	Adim.
Q	: Submerged total longshore transport rate	[m^3/yr]
R	: Sub index indicating a relation with real beach	Adim.
U	: Sub index indicating a relation with uniform beach	Adim.
x	: Crosshore coordinate	[m]
y	: Alongshore coordinate	[m]
γ_b	: Wave breaking index	Adim.
ρ	: Density of water	[ton/m^3]
θ_b	: Wave angle at breaking	[º]

[6] Cfr. (Komar & Inman, 1.970)

REFERENCES

Battjes, J. A., & Janssen, J. F. (1.978). Energy loss and setup due to breaking of random waves. *Proceedings of the 14th International Conference on Coastal Engineering* (págs. 466-480). ASCE.

Dean, R. (1.985). *Physical modeling of littoral processes.* Totterdam: Balkema.

Hallermeier, R. (1.984). Added evidence on new scale law for coastal models. *Proceedings of the International Conference on Coastal Engineering.*

Kamphuis, J. (1.975). Coastal Mobile Bel Model - Doest it work? *Modeling Techniques* .

Kamphuis, J. (1.974). Practical scaling of coastal models. *Proceedinmgs of the International Conference on Coastal Engineering.*

Komar, P. D., & Inman, D. L. (1.970). Longshore sand transport on beaches. *Journal of Geophysical Research, 75(30)* , 5514-5527.

Kriebel, D. D. (1.986). Undistorted Froude Model for Surf Zone Sediment Transport. *Proceedings of the International Conference on Coastal Engineering.*

Leont'yev, I. O. (1.999). Modelling of morphological changes due to coastal structures. *Coastal Engineering 38* , 143–166.

Leont'yev, I. O. (1.996). Numerical modelling of beach erosion during storm event. *Coastal Engineering 29* , 187-200.

Leont'yev, I. O. (1.997). Short-term shoreline changes due to cross-shore structures: a one-line numerical model. *Coastal Engineering 31* , 59-75.

Lippmann, T. C., Brookins, A. H., & Thornton, E. (1.996). Wave energy transformation on natural profiles. *Coastal Engineering 27* , 1-20.

Medina Villaverde, J. M. (1.997). *Technical Assistance consisting of evaluation of the incidence of the construction of Monpas Marina on Gros Beach, in longshore stability and profile stability. (In Spanish).* Madrid: CEDEX.

Medina Villaverde, J. (2.007). *Modeling the dynamics of the crosshore profile. Ph.D. Thesis (in Spanish).* Barcelona: Catalonia University of Technology - University of Barcelona - Superior Council of Scientific Research.

Noda, H. (1.978). Scale relations for equilibrium beach profiles. *Proceedings of the International Conference on Coastal Engineering.*

Roelvink, J., & Broker, I. (1.993). Cross-shore Profile Models. *Coastal Engineering, 21* , 163-191.

Srinivas, R., & Dean, R. G. (1.996). Cross-shore hydrodynamics and profile response modeling. *Coastal Engineering 27* , 195-221.

U.S. Army Corps of Engineers, Coastal Engineering Research Center. (1.984). *Shore Protection Manual.* Washington, D.C.: U.S. Government Printing Office.

A VIDEO BASED INVESTIGATION INTO THE MORPHOLOGICAL IMPACTS OF STORMS BEHIND A SERIES OF DETACHED BREAKWATERS

Fairley, I.,[1] Davidson, M.[1] and Kingston, K.[1]

A coastal imaging system was used to investigate storm scale changes to beach morphology at a meso-tidal, high energy site where two different designs of detached rubble mound breakwater are present. Intertidal bathymetries were mapped from images pre- and post-storm and thus the protected beaches storm response was measured. Beach responses to the different types of breakwaters were compared. Oblique waves moved the salients/tombolos in a down drift direction; larger breakwaters constrained this response to a greater extent. Beach gradients were largely unchanged over individual storms except for storms combined with large surge events where beach flattening was observed. Greater flattening of beach gradients were observed on the beach protected by the larger breakwaters. It is believed that this is related to sediment abundance as much as breakwater design. General accretion was observed in the intertidal region over storms for both breakwater geometries.

INTRODUCTION

Detached shore parallel breakwaters are a common method of shoreline protection, aiming to increase beach widths via the production of accretionary features in the sheltered lee of the structures. A significant body of work exists as to the hydrodynamic function of such structures (Archetti, 2006; Fairley, 2007; Loveless, 1998; Van Der Meer, 2004) and several design guidelines (Ahrens, 1990; McCormick, 1993; Pope. J., 1986) produced that aim to predict the shape of the resultant morphology. Such work largely assumes the development of equilibrium morphology and produces one line predictions for the response of such structures. A far lesser body of work considers the morphological responses of these protected beaches in detail and in non equilibrium conditions. The responses of detached breakwaters in tidal environments is also poorly understood (Pilarczyk, 1996), with design guidelines commonly failing to predict shoreline response in tidal conditions (Thomella, 2004). The EPSRC funded LeaCoast2 project aims to build upon previous work (LeaCoast) and investigate detached breakwaters in a meso-tidal setting. The site investigated in this work contains two different phases of breakwater design allowing comparison of beach response to two different breakwater geometries undergoing near identical forcing.

Beach responses to storms are of paramount importance in evaluating the success of a coastal protection scheme, as catastrophic erosion is usually

[1] School of Earth, Ocean and Environmental Sciences, University of Plymouth, Drake Circus, Plymouth, Devon, PL4 8AA, UK

synonymous with storm conditions. In addition, previous work on longer term mean water level shoreline response at the system studied here has highlighted the importance of storm scale changes on the longer term shoreline responses of this scheme (Fairley, in Prep.).

Six argus cameras (Holman and Stanley, 2007) have been deployed at this site giving coverage of both phases. Argus systems are superior to traditional survey techniques in the investigation of storm scale responses because they allow the extraction of intertidal bathymetries directly pre and post storm resulting in better isolation of storm scale responses. Standard survey regimes have frequencies between monthly and annual meaning the response to individual storms is not easily distinguishable from other events. Whilst intertidal bathymetries extracted from images suffer some reduction of accuracy compared to DGPS surveys the large magnitude of storm response means the signal to noise ratio is still large and thus the errors do not significantly affect the results.

FIELD SITE

This work focuses on a two phase scheme of rubble mound detached breakwaters situated at Sea Palling, Norfolk, on the East coast of the United Kingdom (Figure 1).

Figure 1: A map of the UK with Sea Palling marked by a black dot.

The site is situated on an eroding coastline that has historically suffered from storm surge induced flooding. The coastline is characterized by a narrow beach with a single offshore bar and backed by a single dune line. D_{50} at the site is 430μm (Bacon et al., 2005), although the beach also has a very sparse armoring of pebbles. The majority of the low lying hinterland is farmland but at Sea Palling, a village is situated directly behind the dune line. The dune line was protected by a concrete sea wall in 1953 and narrowing beach widths lead to the construction of 9 breakwaters between 1994 and 1997 (Hamer, 1998). Two

phases of rubble mound breakwaters were built: phase one consisting of 4 fully emergent breakwaters; phase two, five smaller tidally submerged breakwaters. The dimensions of the breakwaters are displayed in Table 1.

Table 1: Dimensions of the two designs of detached breakwater

	Breakwater length (m)	Gap length (m)	Distance offshore (m)	Spring HW freeboard (m)
Phase one	270	160	270	1.3
Phase two	160	160	270	-0.5

Figure 2 shows a merged rectified view of the breakwaters system at mean low tide with the two phases marked. The different breakwaters have different accretionary features in their lee. The larger phase one breakwaters have produced tidal tombolos (salients at high tide, tombolos at low) in their lee and phase two has produced salients. The large size of the tombolo at the far left of the plot is partially due to the longshore sediment direction and partially due to beach re-charge. The phase one bays are still observed to be infilling suggesting that the scheme is not yet in equilibrium.

Figure 2: A merged rectified view of the breakwater system, showing the different breakwaters and the different morphological features produced

Hydrodynamic conditions are typical of the southern North Sea. The spring tidal range is ~3.1m and characterized by a progressive tidal wave meaning peak currents occur at high and low tides. Tidal currents alone are sufficient to mobilize sediment (Bacon et al., 2005) and the tide is asymmetric leading to a net current towards the south east. A description of the wave climate is displayed in Figure 3. The plot shows a wave rose of mean wave height against wave period based on 7 years of UK met-office hind cast data. The data has been linearly transformed inshore to just offshore of the breakwaters, only waves incident to the site were transformed hence the lack of waves propagating in an offshore direction. Two peaks in mean wave height can be seen approaching the site from oblique NNE and ENE directions. These represent the two most common storm directions, Northerly events, caused by low pressures tracking eastward from the Atlantic into the North Sea, are the most prevalent storms. The longest period waves approach the site from a shore normal (NE) direction. The prevalence of northerly wave events, along with the asymmetry in the tidal current, lead to a net longshore sediment transport direction to the South East which has been estimated at 100 m^3yr^{-1} (Clayton, 1983).

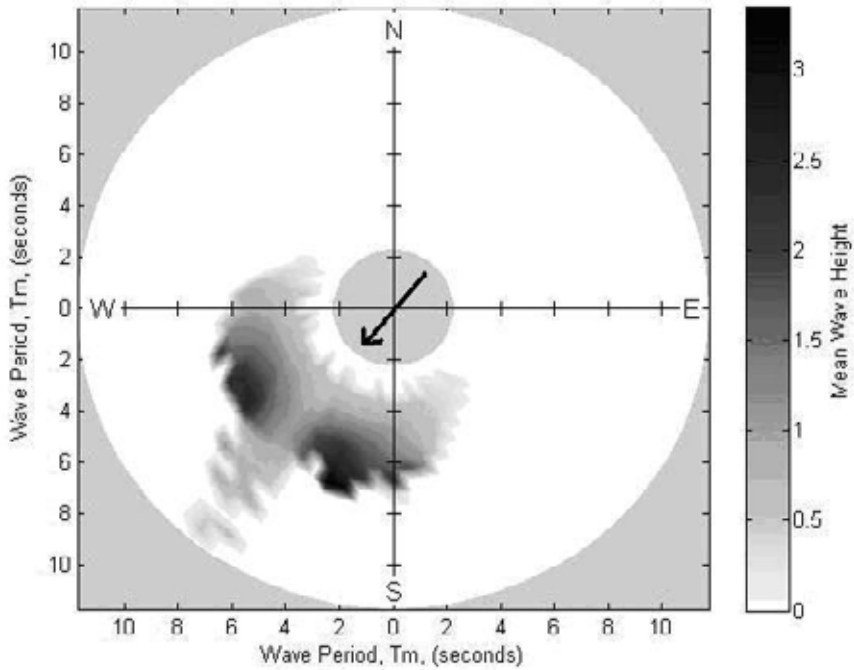

Figure 3: A figure showing mean incident wave height for different wave periods and directions. The wave period increases from 2 at the centre of the rose to 12 on the outside. North is at the top of the plot and the arrow in the centre points to shore normal at Sea Palling.

METHODOLOGY

Six high resolution digital video cameras are positioned on a guyed tower on top of the dune line at an elevation of 27m above mean sea level. A local computer allows for remote access both for image upload and camera control. The cameras are situated in between phase one and phase two and provide coverage of the whole scheme. Accuracy is reduced due to pixel footprint size increasing with distance and hence analysis is restricted to within ~1250m from the camera position. This means that the northernmost and southernmost embayments are excluded.

Three-dimensional intertidal bathymetries are produced by picking shorelines (x, y) at known water elevations (z) from images collected at half hourly intervals over a half tidal cycle. Ten minute time averaged images are used in this analysis. Time averaged images remove short term shoreline variation due to individual swash motions and produce a more stable shoreline feature. Water elevations were measured using a pressure transducer attached to the northern breakwater marker pile. Surface elevation at the shoreline also contains a component due to wave driven set-up, however the sheltering effect of the breakwaters mean that the wave set-up varies around the embayments and

calculation of these differences would have been difficult. Instead the wave set-up component was neglected and images only picked on days with minimal wave heights (sub 0.1m). This leads to maximum set-up based vertical errors of ~0.02m.

Shorelines were extracted manually using a point and click graphical user interface. Manual picking was found to be the most accurate and user efficient method of shoreline extraction: automatic routines routinely frequently failed for the Sea Palling images. Shorelines were picked pre- and post-storm on the closest days to the storm with low waves and good visibility. The *x, y, z* coordinates from the shorelines were interpolated to a regular grid of 1m spacing to create pre- and post-storm intertidal bathymetric maps. From these, erosion accretion maps and cross-shore profiles were produced. Erosion-accretion maps produce valuable descriptions of the spatial distribution of change but some information is lost due to non-overlapping regions, hence it is useful to visualize the morphological change in a variety of ways.

RESULTS

Storms with different angles of incidence, different durations and different surge levels were investigated. An annotated wave power time series for the period evaluated is displayed in Figure 4, and the basic storm parameters are described in Table 2. The directional convention used in the table is 0 being shore normal, positive wave angles represent waves incident from the north and negative angles from the south. Surge level is determined from the NTSLF gauge at Cromer, 15miles from Sea Palling.

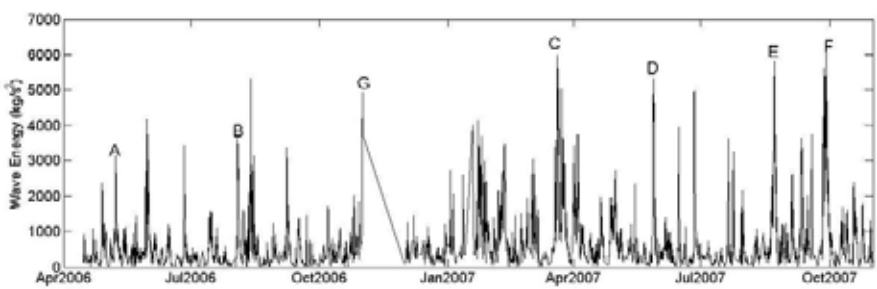

Figure 4: A wave energy time series with the evaluated storms labeled.

Table two: Basic storm parameters for the storms analyzed.				
Storm	Duration	Max. Hsig	Wave Direction	Surge level
A	2	2.6	40	0.5
B	2	2.4	30	0.5
C	6	3	30	1.3
D	1	2.5	-25	0.15
E	4	3	30	0.5
F	4	3	±10	0.4
G	17	3	40	1.3

Erosion-Accretion plots

Erosion accretion plots for the seven storms are shown in Figure 5. The co-ordinate system for this figure is based on the camera location. The *x*-axis is the longshore distance in meters from the camera location. The *y*-axis is cross-shore distance from the camera location in meters. Phase one of the scheme is positive in a longshore direction and phase two negative. Negative *z* values indicate erosion and positive *z* values accretions. The longshore movement of the tombolos and salients is clearly displayed in storm A, with erosion on the updrift and accretion on the down drift side of the tombolos.

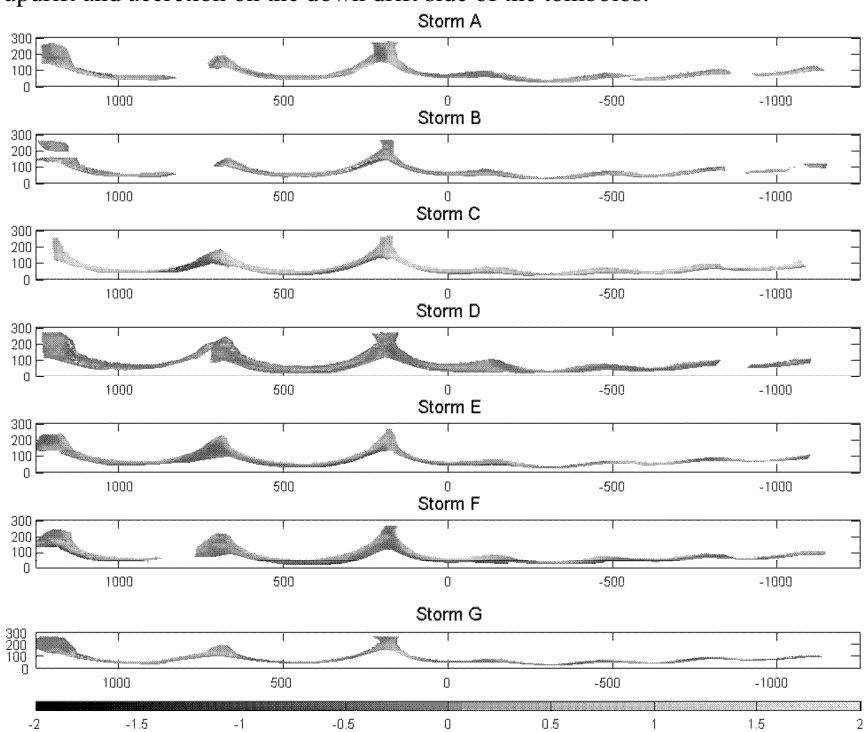

Figure 5: Erosion-Accretion plots for the seven storms analyzed. Erosion is negative and accretion positive.

The salients show less defined displacement although still in the same direction. The same trend is evident, but to a lesser extent in storms B and C. Storm D, where waves are incident from the opposite direction, shows the opposite displacement of the salients and tombolos. Storm F, with shore normal wave incidence shows the tombolos staying at the same longshore location, but flattening, with erosion on the upper horn and accretion either side. The salients show some accretion on their northern flanks corresponding to the waves being incident from south at the tail of the storm and suggesting the salients respond more rapidly to changes in wave direction. Storm E which has waves incident from the same direction as A, B and C and has longer duration and larger wave height does not show the same longshore movement. Both phases show some general accretion over most storms. Phase one shows more accretion in the lower intertidal region and on the tombolos. Phase two shows more uniform accretion over the entire intertidal region. Storm G, with the longer duration shows erosion over the entire phase two and much of phase one. It is only on the tombolo horns that accretion is observable.

Detailed look at changes to a tombolo

Figure 6 shows a tombolo pre- and post-storm for a northerly storm. The movement displayed is characteristic of tombolo movement under such storms and allows elucidation of the changes to the tombolo over the storm. As shown in the erosion accretion plots, the tombolo is moved in a down drift direction, this movement is constrained to the tombolo itself with little movement at the extremes (x>300 and x<100). The movement of the crest centre line is approximately 25m. Also noticeable is an accretion on the horn of the tombolo, this is particularly evident further seaward (200-275m cross-shore) where the salient crest accretes by ~0.5m. A skewness in the tombolo form is induced by the oblique waves. Pre-storm the tombolo displays a symmetrical plan-form, whereas post-storm the plan-form is skewed in a down drift direction. The cross-section in a longshore direction of the tombolo horn is very slightly skewed in a down drift direction pre-storm but this skewness is increased post-storm.

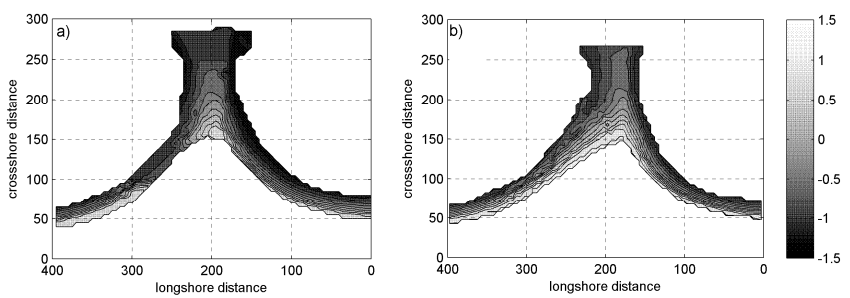

Figure 6: Contour maps of one tombolo a) pre-storm and b) post-storm.

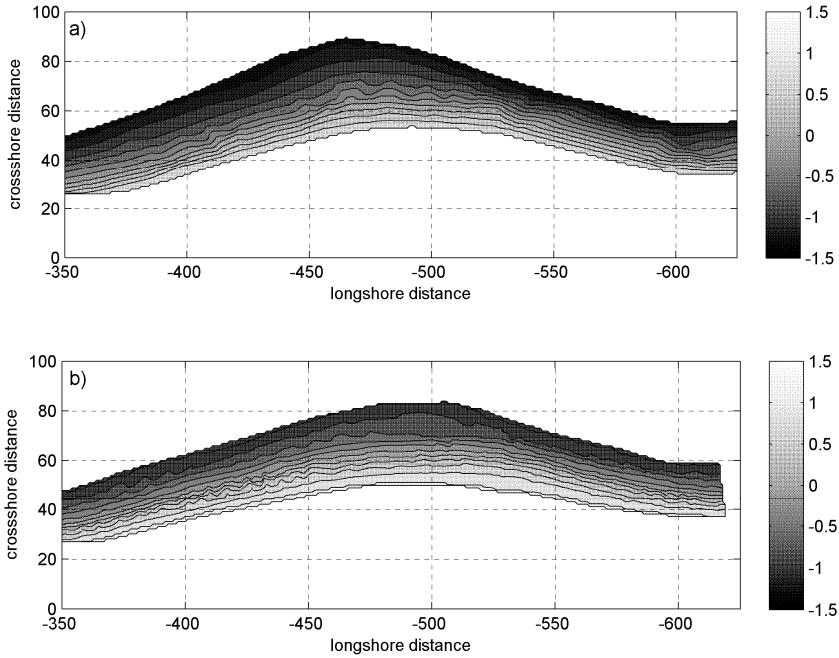

Figure 7: Contour plots of a salient a) before and b) after a northerly storm event.

Detailed look at changes to a salient

Pre- and post-storm contour plots for a phase two salient from the same northerly storm as the previous plots of the tombolo are shown in Figure 7.

It can be seen that there is a similar southward shift of the feature to that displayed in the tombolo (Figure 7), however, the movement is much less defined in the salient. Similar to the tombolo, accretion occurs over the storm but the accretion is over the entire region rather than specifically on the horn of the tombolo. The skewness displayed by the tombolo is not observable in the salient response.

Cross-shore profile changes

Pre and post storm cross-shore profiles from the bay centres are displayed in Figure 8. The profile numbers refer to longshore distance from the cameras; the left hand two columns are phase one embayments, the right two columns phase two and the middle column the transition embayment between phases. Profiles were only taken in the bay centers to minimize the impact of the longshore movement of the salients /tombolos on the cross-shore profile changes. It can be seen that the cross-shore profile gradients in phase two remains similar regardless of wave height or storm duration. Flattening of the beach gradient is more prevalent in phase one. It is only for the storm C with the largest surge level (1.4m) that significant flattening of the beach gradient is

observed, for this storm phase two shows some slight flattening also. The storm with shore normal wave approach (storm F) shows more beach flattening than the other storms with large surges. Storms A, B and C show a general accretion through the intertidal region of both phases, as is shown in the erosion-accretion plots.

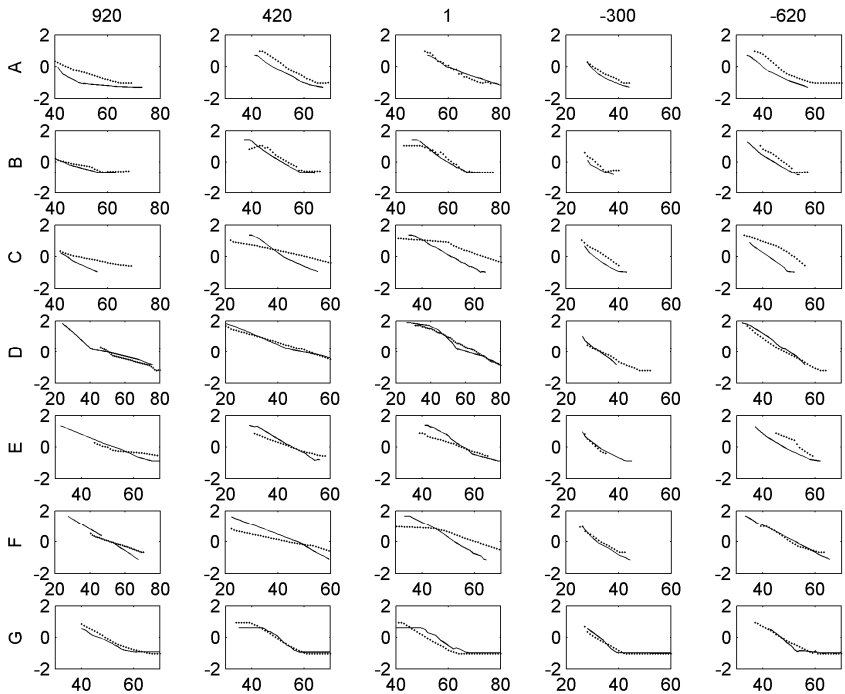

Figure 8: Cross-shore profiles from bay centers, pre- (solid line) and post- (dotted line) storm. Each row is a different storm (A-G) and each column a different profile location (numbered in terms of longshore distance.

DISCUSSION

The southward movement of the tombolos under northerly storm has previously been reported by Dolphin et al (2005) who used GPS surveys to measure morphological changes under two storms in phase one. As expected, the video analysis corroborates these previous findings and shows that for waves from the opposite direction the reverse moment takes place. Whilst such reversal in tombolo movement might seem obvious, the asymmetry in the strong tidal current means such movement cannot be assumed a priori. This work extends the investigation into phase two where the same direction of feature movement is displayed in the salients. The salient movement is more diffuse, this can be explained by the lesser difference between sheltered and unsheltered regions in phase two, cause both by the shorter breakwater lengths and the increased overtopping and wave transmission. The emergent phase one

breakwaters provide much more refined gradients in wave exposure and hence the more defined response in the longshore movement of the features. The nature of features themselves exacerbates this: the tombolo horn positions are more firmly 'tied' to the structure locations. This concept can be used to explain the lack of longshore tombolo movement in storm E: if previous storms from one direction have displaced the tombolos to the limit of the sheltered region, no further storms from that direction will produce further longshore movement since the tombolos cannot exist in the exposed regions due to increased wave attack. It appears that the phase two salients respond more readily to changes to wave direction, this, it is believed, is due to the wave overtopping of the phase two structures reducing the amount of diffraction through the gaps and hence waves approach the shore more obliquely than for phase one.

Dolphin et al (2005) pose the question of storm recovery of tombolo position due to the dominance of northerly waves and the asymmetry in tidal transport giving a net south easterly transport, meaning that sediment transport to the north is not favoured. This work helps to address this: firstly, as expected, southerly events return the features northward; secondly, observed changes to the tombolo shape allow postulation of a return mechanism. The tombolo actually accretes over the storm period and becomes more asymmetric in cross section. This means that in order to return to the original position further accretion is not required, instead erosion of tombolo crest and smoothing of the asymmetry could return the tombolo to its original from. Flow compression of the tidal currents over the tombolos and scour caused by hydraulic jump induced turbulence in the lee of the feature may well be sufficient to affect this change

Cross-shore gradients remain similar in phase two whereas phase one show greater evidence of beach flattening. This is counter-intuitive since the phase one beaches are better protected, it is postulated here that sediment abundance potentially explains this difference. The beaches in phase two are narrower both due to the lesser sheltering of smaller breakwaters and since they are down drift of phase one and suffer from reduced sediment supply. High tide shorelines are constrained by the sea wall, which is reached most high tides, and hence further shoreline recession is impossible. This fact probably restrains the changes to beach gradient. The wider phase one beaches allow for upper-intertidal and supra-tidal erosion and associated flattening of the beach gradient.

It is thought that the sediment deposited for the observed intertidal accretion over the storm could well be taken from the supra-tidal beach, the other likely source is increased longshore sediment transport under storm conditions. Since, as previously stated, there is little supra-tidal sediment in phase two (unless surge levels are high enough to allow erosion of the dune above the sea wall), the general intertidal accretion of phase two is supposed in be due to increased longshore sediment supply. In phase one, larger storm waves intensify circulation patterns and lead to greater deposition on the

tombolo horns where circulation diverges; overtopping of the phase two breakwaters reduces this effect which leads to lesser accretion behind the structures.

CONCLUSIONS

A coastal imaging system has been used to investigate the storm scale responses of beaches protected by detached breakwaters. The use of video remote sensing has allowed for isolation of storm changes from other types of beach response.The beaches protected by the two different designs of rubble mound breakwater show both differences and similarities in storm scale response. This can largely be attributed to differences in breakwater geometry, particularly the presence or absence of overtopping, although abundance of sediment must also be taken into account. Under oblique waves the tombolos and salients are moved in a down drift direction due to alteration of the longshore location of the breakwater induced circulation patterns. Both designs of breakwater produce the same direction of longshore movement under oblique waves but the larger structures constrain this movement giving better defined regions of change. Accretion is observed in the intertidal region over storm periods, but this could well be at the expense of the supra-tidal beach. In phase one this accretion is focussed on the tombolos whilst phase two exhibits a more general accretion over the intertidal area. The beaches protected by the smaller lower breakwaters show little changes to beach gradient over the storm, whereas the beaches protected by the large structures show beach flattening. It is believed that is more related to the presence of the sea wall and lack of sediment than the breakwater geometries.

ACKNOWLEDGMENTS

This work was conducted as part of a PhD attached to the LeaCoastII project and funded by the UK EPSRC. Thanks must go to all members of the LeaCoastII project, especially Tony Dolphin, John Bacon and Roger Phillips of the UEA.

REFERENCES

Ahrens, J.P., Cox, J., 1990. Design and performance of Reef Breakwaters. Journal of Coastal research, 51(7): 61-75.

Archetti, R., Lamberti, A., 2006. Study of hydrodynamic induced by low crested structures through image processing. In: J. Mckee Smith (Editor), Proceedings of the 30th international conference on coastal engineering. World Scientific, San Diego, pp. 5021-5033.

Bacon, J.C. et al., 2005. The offshore breakwater scheme at sea palling, England; Sand transport generated by tidal currents. In: J.M. Smith (Editor), Coastal Engineering 2004, Vols 1-4, pp. 1896-1908.

Clayton, K.M., McCave, I.N., Vincent, C.E., 1983. The Establishment of a sand budget for the East Anglian coast and its implications for coastal stability Shoreline Protection. Thomas Telford, London, pp. 91-96.

Dolphin, T., Taylor, J., Vincent, C., Bacon, J., Pan, S. Q., O'Conner, B., 2005. Storm-scale effects of shore-parallel breakwaters on beaches in a tidal setting (Leacoast). In: J.M. Smith (Editor), Coastal Engineering 2004, , pp. 2849-2861.

Fairley, I., Davidson, M., Kingston, K.,, 2007. Video monitoring of overtopping of detached breakwaters in a mesotidal environment, Coastal Structures '07, Venice.

Fairley, I., Davidson, M., Kingston, K., Dolphin, T., Phillips, R., in Prep. Empirical Orthogonal Function Analysis of Shoreline Changes Behind Two Different Designs of Detached Breakwaters. submitted to Coastal Engineering.

Hamer, B.A., Hayman, S.J., Elsdon, P.A., Fleming, C.A.,, 1998. Happisburgh to Winterton Sea Defenses: Stage Two, Coastlines, Structures and Breakwaters. Thomas Telford, London.

Holman, R.A. and Stanley, J., 2007. The history and technical capabilities of Argus. Coastal Engineering, 54(6-7): 477-491.

Loveless, J., Debski, D., Macleod, B., 1998. Sea level set-up behind detached breakwaters 26th International Conference on Coastal Engineering, Copenhagen, pp. 1665-1678.

McCormick, M.E., 1993. Equilibrium Shoreline Response to Breakwaters. Journal of Waterway, Port, Coastal and Ocean Engineering, 119(6): 657-670.

Pilarczyk, K.W., Zeidler, R.B.,, 1996. Offshore breakwaters and shore evolution control. Balkema, Rotterdam.

Pope. J., D., J. , 1986. Development of Design Criteria for Segmented Breakwaters. In: B. Edge (Editor), Coastal Engineering. ASCE, Taipei, Taiwan, pp. 2144-2158.

Thomella, F., Vincent, C.E.,, 2004. Designing Offshore Breakwaters Using Empirical Relationships: A Case Study from Norfolk, United Kingdom. Journal of Coastal research, 20(4): 1224-1230.

Van Der Meer, J., Briganti, R., Wang, B., Zanuttigh, B., 2004. Wave transmission at low-crested structures, including oblique wave attack, Coastal Engineering 2004, pp. 4152-4164.

GEOTECHNICAL ASPECTS IN INTEGRATED DESIGN OF SEA- AND ESTUARY DIKES

Carsten Pohl[1], Lars Vavrina[1] and Werner Richwien[1]

With publishing of the 3rd IPCC report in May 2007 seriously discussion about climate change and consequences for coast protection like secular rise and intensifying waves resumed. With this background, soil mechanical processes at storm tide, like erosion and infiltration, accompanied with changes in water content and in stress state, are analyzed exhaustively. Structuring by propagation of cracks as well as strength softening due to weakening are quantified. Rules for functional and structural design are deduced, based on an integrated consideration of local hydrodynamic impacts and specific soil resistance. The design concept is based on failure equations for well defined failure situations, which allow the declaration of state of safety as well as an optimization of the structure with respect to probability of load and load combinations.

1 Introduction

After the storm-tide in 1953, Germany has changed from responsive to preventive coast protection. One element of prevention is the design of sea- and estuary dikes with regard to expected secular rise. This demand is still only applied on determination of the dike height, which is the sum of the design water level and the wave run-up. The design water level includes a safety surcharge to consider consequences of climate change. With respect to the predictions of the 3rd IPCC report some German administrations have decided to double the safety surcharge from 25 cm/100 years to 50 cm/100 years. Large scale tests in the Netherlands (ComCoast, 2007) and in Germany (Weißmann, 2003) have detected unexpected high resistance against wave overtopping. Perhaps, a lot of dike sections will already show an adequate buffer to fit with the new safety surcharge.

Design in terms of engineering means determination of building material and its required properties as well as dimensioning of components with the aim of a technical and economical optimization. Conceptual transfer on design of sea- and estuary dikes includes an integrated view on the hydrodynamic impacts and the specific soil resistance. Current design praxis of the dike components is based empirically (fig. 1). The installed soils are only classified by empirically defined limits. Hence, up to now, the soil properties have no influence on dike height or on dimensions of the dike components. Comparison of impacts and resistance provides utilization in an iterative process.

[1] Institute of Soil Mechanics and Foundation Engineering, Department of Building Sciences, Faculty of Engineering, University Duisburg-Essen, Universitätsstr. 15, 45117 Essen, Germany

The performance of this procedure is objective of the research project "Integrated Design of Sea- and Estuary Dikes". Research partners are the Institute of Soil Mechanics and Foundation Engineering of University Duisburg-Essen and the Coastal Research Station of Lower Saxony Water Management, Coastal Defence and Nature Conservation Agency. The Coastal Research Station calculates wave run-up and wave overtopping at modular dike geometries, taking the respective location into account. At the University Duisburg-Essen the stability of dikes under these hydrodynamic impacts is analyzed.

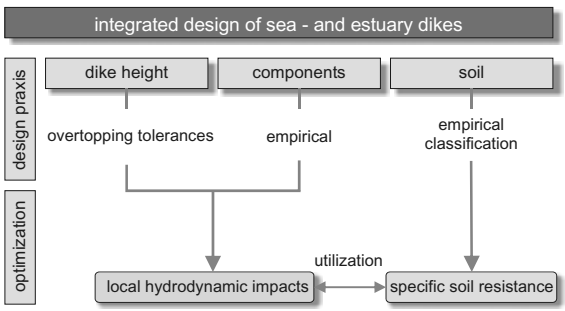

Figure 1. Integrated design.

2 Soil mechanical processes

Most dikes along the North-Sea have been reconstructed in the last four decades as sand-core dikes with a grassy cohesive layer, which is often made of marine clay. The specific resistance of the dike section depends on the composition and the structure of cohesive layer. Permeability and strength are influenced by the aggregate size essentially. Water could infiltrate straight through the macro-pores and weaken the cohesive layer. Thus, resistance against hydrodynamic impacts at storm-tide is decreased.

2.1 Soil structure

The structure of the cohesive layer is characterized by longstanding influence of climate and animal impacts. Extraction of moisture at desiccation causes volume shrinkage, the loss of volume is compensated by formation of cracks. Near to the surface, cracking is intensive enough to separate the layer into small aggregates, which become larger and larger with distance to the surface. Single cracks reach deeper than the layer desiccates and divide the lower part in monolithic blocs. Hence, according to fig. 2 the cohesive layer typically shows a topsoil of heavy cracking, a cracked subsoil with single cracks and an uncracked subsoil where the structure of installation remains. Physical processes at shrinkage are complex. Anisotropy and inhomogeneity distinguish initiation and progress of cracking. Nevertheless, analysis of stress-strain behavior enables to predict depth and distribution of shrinkage cracks.

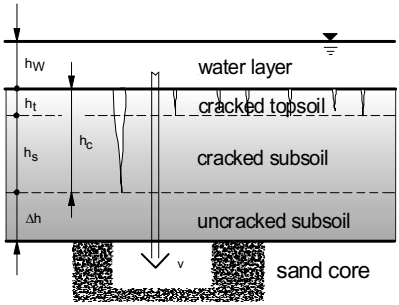

Figure 2. Structuring.

At desiccation is not enough water available to satisfy the storage capacity of the soil and suction pore water pressure arises. Ability of the turf to extract moisture is limited in pedology to a suction of 1585 kN/m². Measurements of suction (TAW, 1996) at cohesive layers in the Netherlands, made of marine clay, confirmed a stress of more than 1000 kN/m² near to the surface, which subside with depth. A suction pore water pressure of 100 kN/m² is stated as representative. These measurements indicate rather a logarithmic decrease of suction with depth, but other distributions could be decisive as well.

Suction acts isotropic and causes therefore a 3-dimensional volume change. Taking overburden pressure by geostatic load into consideration, tension stress at depth z could be estimated to:

$$\sigma_h = \frac{\nu}{1-\nu}(\gamma z) - \frac{E}{H(1-\nu)} 10^{\left(1-\frac{z}{z_A}\right)\log 1585} \quad [\mathrm{kN/m^2}] \qquad (1)$$

Tension stress has negative algebraic sign. The dead weight is represented by the specific weight γ [kN/m³] and the depth of desiccation by z_A [m]. E/H reflects the relation of compression modulus with reference to normal stress and to suction and is approximately conform to (1 - 2ν) at saturated state, with ν [-] as Poisson's ratio. Cracks develop, if tensile strength σ_t [kN/m²] is exceeded by tensile stress σ_h. They will deepen, until stress and strength at the crack tip are in equilibrium:

$$\sigma_t = \frac{\nu}{1-\nu}(\gamma z) - \frac{E}{H}\frac{1}{1-\nu} 10^{\left(1-\frac{h_t}{z_A}\right)\log 1585} \quad [\mathrm{kN/m^2}] \qquad (2)$$

Transition from topsoil to cracked subsoil could be provided by dissolving eq. 2 iteratively for h_t [m].

Tensile stress cannot be transferred via cracks and redistribute to the crack tips. As consequence, an infinitesimal crack extension could release more energy than it is required by the additional crack surface. The crack will deepen suddenly, until balance of energy is restored again. Therefore sometimes single cracks reach deeper than the cohesive layer desiccates. Assuming linear elastic stress-strain behavior and neglecting loss of energy for releasing aggregate bonding and for their rearrangement, stress concentration could be described within linear elastic fracture mechanics (LEFM) by the stress intensity factor K_I:

$$K_I = Y\,\sigma_h\,\sqrt{\pi h_c} \quad [\mathrm{kN/\sqrt{m^3}}], \qquad (3)$$

The soil resistance is expressed by the critical stress intensity factor K_{Ic} as material characteristic. If K_I becomes smaller or equal than K_{Ic}, no further crack extension is possible. The depth h_c of single cracks is concluded to:

$$h_c = \frac{K_{Ic}^2 \pi}{Y^2 \sigma_h^2} \quad [m] . \tag{4}$$

The coefficient Y reflects the distribution of tension stress and could be taken from literature (Konrad/Ayad, 1997). However, determination of critical stress intensity factor and prediction of crack depth by LEFM are still difficult.

Stability of cracks is limited by shear strength as well. At a certain depth $h_{crit.}$ the shear strength is no longer sufficient to resist the earth pressure by dead weight. Cracks, which grow up to this depth, will close. In drained conditions pore water suction supports stability of crack flanks. The slightest crack depth is therefore provided at saturated state by the undrained shear strength c_u [kN/m²] and by the dead weight γ_r [kN/m³] of the saturated soil:

$$h_{crit.} = \frac{2\, c_u}{\gamma_r} \quad [m] . \tag{5}$$

Structuring of the topsoil cannot be avoided, but it could be reduced by adjustment of installation conditions on specific soil properties.

2.2 Infiltration

Dammed up water, wave overtopping and rainfall infiltrates through the cracks and saturates the macro pores without retardation. The uncracked part of the cohesive layer offers a much lower permeability than the cracked part. Thus, only the uncracked subsoil contributes to reduce difference of potential head between surface and sand-core. Total potential head is sum of gravitational and pressure potential ($h_c + h_W$). If infiltration has progressed up to the sand-core, gravitational potential will comply with thickness of uncracked subsoil Δh. The gradient of potential head is given by:

$$\text{grad}\, \psi = \frac{h_W + h_c + \Delta h}{\Delta h} \quad [-] . \tag{6}$$

Weißmann (2003) has shown that a discontinuous sequence of surface run-off in the course of overtopping might be replaced by a continuous average flow rate. In accordance to Darcy's law, flow velocity is the product of hydraulic conductivity k_r [m/s] and gradient of total potential head grad ψ [-]:

$$v = k_r \cdot \text{grad}\, \psi \quad [m/s] . \tag{7}$$

2.3 Strength softening

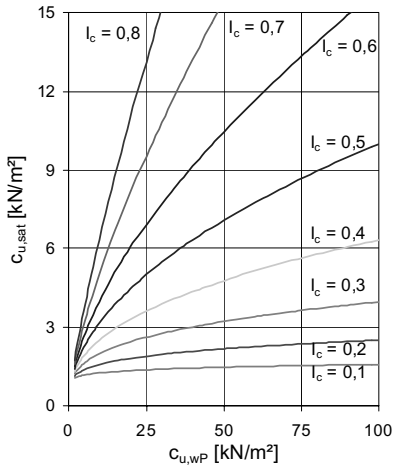

Figure 3. Strength weakening.

Infiltrated water fills first the cracks and macro pores while water login into the aggregates lasts some time. Nevertheless, the surface of the aggregates gets smeary. Consequently, consistency of the cohesive layer softens and strength weakens.

With variation of water content, a cohesive soil will take all possible consistencies from solid to liquid. The softest consistency exists, when the pore volume is saturated and no further increase of water content is possible:

$$w_{sat} = \rho_W \left(\frac{1}{\rho_d} - \frac{1}{\rho_S} \right) \quad [-], \qquad (8)$$

with ρ_W [g/cm³] as density of water, ρ_d as density of dry soil and ρ_S as grain density.

Consistency at actual water content w in relation to plastic limit w_P and liquid limit w_L is reflected by the consistency index I_C:

$$I_c = \frac{w_L - w}{w_L - w_P} \quad [-]. \qquad (9)$$

Obviously there is a significant undrained shear strength at plastic limit and no sufficient shear strength at liquid limit. Strength weakening could be appreciated by a well known logarithmic tendency of undrained shear strength c_u to consistency index:

$$c_{u,w} = c_{u,w_P}{}^{I_c} \quad [kN/m^2]. \qquad (10)$$

By implementation of the consistency index at saturated state, eq. 10 provides the minimum undrained shear strength, which keeps always available, even after saturation:

$$c_{u,sat} = c_{u,w_P}{}^{\left(\frac{w_L - \rho_W \left(\frac{1}{\rho_d} - \frac{1}{\rho_S} \right)}{w_L - w_P} \right)} \quad [kN/m^2]. \qquad (11)$$

Fig. 3 presents the practical range of strength, depending on the consistency index. If the cohesive layer offers an undrained shear strength of 100 kN/m² at plastic limit, there remains just a strength of 10 kN/m² at a consistency index of 0.5.

2.4 Erosion

Wave overtopping as well as wave run-up create a bed shear stress on the dike surface. Soil particles are detached and transported away by the water. Consequently, local damages by erosion holes or channels develop. The blades of the turf roughen surface and decrease velocity of flowing water. At high discharge the blades lie down and protect the slope. Based on small-scale experiments in the Stillwater Hydraulic Laboratory in Oklahoma, Temple et al. (1987) present an approach to describe the erosive shear stress on grassy layers:

$$\tau_0 = \gamma_W \, h_W \left(1 - C_F\right)\left(\frac{n_B}{n}\right)^2 I_E \quad [\mathrm{kN/m^2}]. \tag{12}$$

The empirical parameter C_F reflects density of plant cover, for very dense grass it is around 0.75. Influence of surface roughness is included by the relation of soil roughness to roughness of grass (n_B/n). The energy gradient I_E [-] is in the order of the slope inclination for little overtopping rates.

No erosion will occur before a critical bed shear stress τ_C is exceeded. Only higher shear stress will erode the slope. Erosion progresses approximately linear to integral of erosive load, which is the difference of impacting shear stress τ_0 and critical shear stress τ_C:

$$\varepsilon = k_d \cdot \int_0^t \left(\tau_0 - \tau_c\right) dt \quad [\mathrm{m}]. \tag{13}$$

The parameters k_d and τ_C are soil characteristics and can be determined by complex laboratory tests, e. g. with the rotating erosion cylinder device (INTBEM, 2008).

3 Functional and structural design

Dikes in tidal areas are exposed to serious hydrodynamic impacts, which are generated by breaking waves and wave run-up as well as by wave overtopping. These impacts only appear for a few hours. Nevertheless, they affect soil mechanical processes like erosion and infiltration, accompanied with soil deformations by sliding or local slope damages. The aforementioned processes are not equivalent owing to their consequences. For that reason, infiltration and erosion have to be restricted to provide functionality of the dike section. Incompatible deformations of the cohesive layer have to be prevented to ensure its structural stability.

3.1 Functional design

Functional design includes all processes which does not endanger stability of the dike but which are important for maintenance.

a) Infiltration

Infiltrated water generates temporary an internal water pressure in the sand-core. The resultant uplift forces become hardly ever dangerous for slope

stability during one storm-tide. However, infiltration rate has to be limited to ensure just subordinate changes of saturation line. The cracked part of the layer is marked by a high system permeability. To reduce the infiltration rate strongly, the layer thickness has to exceed depth of cracks h_c [m] by an additional depth Δh [m]:

$$h \geq h_c + \Delta h \quad [m] . \tag{14}$$

Adherence to a critical infiltration rate $q_{crit.}$ is given by:

$$\Delta h \geq \frac{k_r}{q_{crit.} - k_r} \left(h_W + h_c \right) \; [m] . \tag{15}$$

With practical background and with respect to the specific infiltration conditions Δd should not fall below 0.5 m for the seaside slope and 0.25 m for the inner slope. The infiltration rate has to comply with efficiency of drainage and with volume of water which can be tolerated backwards the dike. Weißmann and Richwien (2004) suggest a moderate rate of $q_{crit.} = 1 \cdot 10^{-5}$ m³/(sm²), taking short duration of damming and overtopping into account.

b) Erosion

Erosion resistance is dominated by the turf. First, loose aggregates are transported away by running down water, subsequently by roots connected aggregates follow, but the plants remain for a while. Erosion has to be restricted to guarantee mode of operation of the turf at any time. It is assumed that the turf regenerates itself, if erosion depth d_E does not exceed 1/3 of rooting depth d_R:

$$d_E \leq \frac{1}{3} d_R \; [m] . \tag{16}$$

The rooting depth has to be estimated in advance. Conformity with the presumption has to be attested within dike inspection. Design against erosion provides quality standards for the turf.

3.2 Structural design

During the storm-disaster in 1962 at many dikes sliding of the inner slope and local deformations of the seaside slope have been observed (e.g. fig. 4 and 5). These mechanisms compromise overall stability of the dike.

a) Stability against sliding

Sliding of the inner slope was the most common failure mechanism during former flood disasters. Saturation of the cohesive soil by infiltrating water increases the dead weight G. Additionally wave overtopping generates flow forces S and F inside the cohesive layer and on the slope surface.

If the weakened strength C is too less, the combined action of these loads could cause sliding. Weißmann (2003) has modeled this failure mechanism with a slope parallel sliding plane.

Figure 4. Sliding of the steep inner slope at Grothusenkoog 1976 (Petersen/Rohde, 1991).

Figure 5. Deformations of the seaside slope at Friedrichskoog 1962 (Petersen/ Rohde, 1991).

Formally stability against sliding is verified, as shown in fig. 6, by equilibrium of forces in the sliding plane. Keeping in mind, strength at saturated state $c_{u,sat}$ [kN/m²] according to eq. 11, the utilization of resistance results to:

$$\alpha_S = \frac{G_{II} + S_{II} + F}{C} = \frac{d \sin\beta(\gamma_r \gamma_G + \mathrm{grad}(\psi)\gamma_w \gamma_Q) + \gamma_w h_w I_E \gamma_Q}{\frac{1}{\gamma_{cu}} \left(c_{u,w_P} \left(\frac{w_L - \rho_W (1/\rho_d - 1/\rho_S)}{w_L - w_P} \right) \right)} \quad [-]. \tag{17}$$

In eq. 17 d [m] accords to the depth of the sliding plane and γ_r [kN/m³] to the specific weight of the saturated soil. The parameter h_w [m] corresponds to thickness of the water layer and I_E [-] to the gradient of energy. The gradient of potential head is included by grad ψ. So far as permeability is homogeneous, the flow force S will follow the gravitation ($\alpha = 0°$). But, if the layer shows dense horizons by densification, the flow force will be deflected.

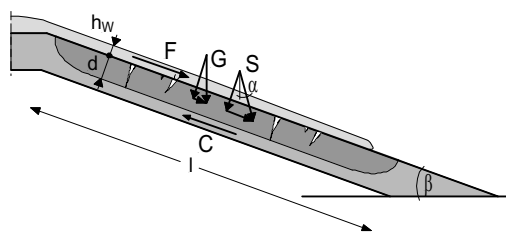

Figure 6. Stability against slope parallel sliding.

b) Stability against breaker induced pressure impacts

Damages of the seaside slope trace back to wave induced pressure impacts. Shocking pressures multiply the hydrostatic water load. Sparboom (1991) specifies the maximum pressure p_{max} by the wave height H_S [m], the specific weight of the water γ_W [kN/m³] and an empirical constant C_i:

$$p_{max} = C_i \cdot \gamma_W \cdot H_S \quad [\mathrm{kN/m^2}]. \tag{18}$$

European standards demand a probability of 95 % for characteristic values of loads and resistances. For this request the empirical constant C_i could be estimated from Sparboom (1991) for a 1 : 6 inclined slope to approximately 3.7.

A closed slope surface in combination with an elastic turf cushions the shocking pressure in most cases. But if the cohesive layer offers water filled cracks or holes from mice or moles, the shocking pressure could propagate into the structure and destroy it from inside to outside. This may cause the very first damage of the cohesive layer.

Führböter (1966) introduced a very simple model of a rigid sliding body. He assumed that the pressure p_{max} in the crack still acts in full magnitude, while the surface has been relaxed. This idea has been enhanced, as illustrated in fig. 7, by implementation of the crack length l_r and by adding the strength of roots.

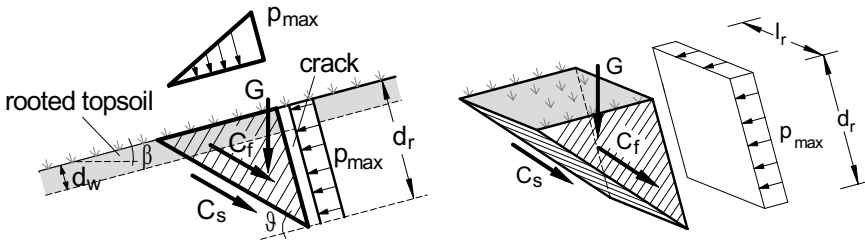

Figure 7. Verification of stability against breaker induced pressure impacts.

The resistance is given by undrained shear strength c_u [kN/m²] in the sliding plane (C_S) and at the flanks (C_f) as well as by root cohesion c_W [kN/m²] in the rooted topsoil. The utilization of resistance against breaker induced pressure impacts complies with:

$$\alpha_D = \frac{p_{max}\cos\vartheta\tan\vartheta\,\gamma_Q}{\frac{1}{2}\gamma_r d_r \gamma_G \sin(\vartheta-\beta) + \frac{c_{u,d}}{\gamma_{cu}}\left(\frac{1}{\cos\vartheta}+\frac{d_r}{l_r}\right) + \frac{c_w d_w}{\gamma_{cu}}\left(\frac{2}{l_r}+\frac{1}{d_r\cos\vartheta}+\frac{d_w}{d_r l_r}\right)}\,[-] \quad (19)$$

The dead weight G of the saturated soil, which is reflected in eq. 19 by the specific weight γ_r [kN/m³], contributes to stabilize the sliding body. Inclination of the sliding plane is in undrained conditions around $\vartheta = 45°$. As consequence to very short duration of shocking pressure and to low permeability of the soil, viscosity of pore water increases strength. Thus, undrained shear strength $c_{u,d}$, which could be twice of static undrained shear strength c_u, has been adopted.

Partial safety factors γ_G, γ_Q and γ_{cu} in eq. 17 and 19 correspond to limit state 1C of German standard DIN 1054.

4 Exemplarily design

Exemplarily, procedure of integrated design has been tested for a dike without foreland, located at East-Frisian Coast in Lower Saxony. Fig. 8 shows the cross section, consisting of a sand-core and a cohesive layer. Additionally,

the toe of the seaside slope is protected by a wedge, made of the cohesive cover soil. The crest level is situated at 7.80 m above mean sea level (MSL).

Wave run-up and wave overtopping have been calculated for scenarios of anticipated design water levels (DWL) ranging from 5.0 to 7.5 m MSL. The present design water level constitutes to 5.75 m MSL. In the investigated range increases the mean overtopping rate from 0 to more than 200 l/(sm), see fig. 9.

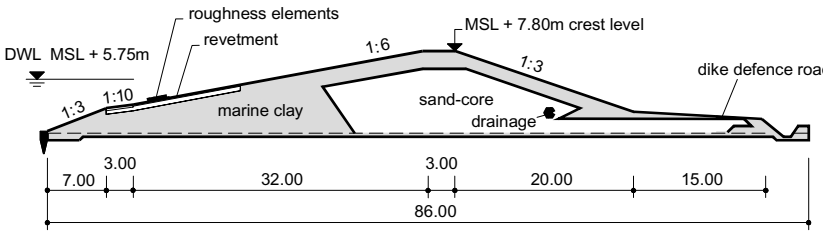

Figure 8. Dike without foreland.

To give an idea about consequences of soil quality on required dimensions and on structural utilization, the dike has been designed for 6 typical cohesive soils. In the following, 2 marine clays have been picked out, a clay of high plasticity, called Hohenkirchen, and a clay of low plasticity, named Elisabethgroden. Both soils have been taken landwards from North-Sea. According to evaluation practice of Weißmann (2003) is the soil Hohenkirchen "very well qualified" as dike material, whereas the soil Elisabethgroden only offers a "less qualified" suitability. Basis soil characteristics are tabulated in table 1. Details and results for the other 4 soils are summarized in INTBEM (2008).

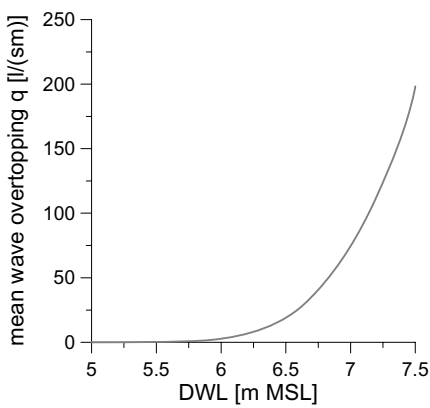

Figure 9. Mean wave overtopping.

4.1 Functional Design

The soil Hohenkirchen is susceptible to shrinkage at desiccation. The maximum crack depth has been estimated to 0.80 m. Eq. 2 provides the height of cracked topsoil to 0.45 m. In contrast to this limits little strength at saturated state durable crack depth of Elisabethgroden to 0.22 m.

To reduce the infiltration rate, the cohesive layer has to exceed crack depth. Due to low permeability of uncracked soil and to protection by the wedge is the required thickness almost independent from the design water level (see fig. 10), assuming a moderate critical infiltration rate of 1 - 10^{-5} m³/(sm²). In the case of a

higher permeability or without the wedge, the required dimensions of the layer would increase with the design water level.

Table 1. Basic soil characteristics.

	Hohenkirchen	Elisabethgroden
w_L [-]	0.514	0.2528
w_P [-]	0.201	0.1879
γ [kN/m³]	17.5	18.5
γ_r [kN/m³]	20.0	20.5
k_r [m/s]	$1.9 \cdot 10^{-10}$	$2.64 \cdot 10^{-6}$
$c_{u,sat}$ [kN/m²]	17.9	2.3
$c_{u,d}$ [kN/m²]	35.8*	4.6*
k_d [m³/(Ns)]	$5 \cdot 10^{-7}$	-
τ_c [N/m²]	10	-
h_t [m]	0.45	> 0.22
h_c [m]	**0.80***	> 0.22
$h_{crit.}$ [m]	1.80	**0.22**

*estimated values

Astonishing smaller thickness of the poor soil Elisabethgroden attributes to dominant cracking of the soil Hohenkirchen.

Wave overtopping erodes the inner slope. Fig. 11 demonstrates the influence of the turf. A good turf decreases erosion rate of the soil Hohenkirchen within an overtopping of 3 hours up to 6 times compared to bare soil. The proposed design criteria of eq. 16 led for example at design water level of +6.5 MSL in combination with a medium turf to a required rooting depth of 15 cm. However, only the erosion parameters of the soil Hohenkirchen have been determined. The soil Elisabethgroden has been too less resistant against erosion to perform erosion tests (de Groot, 2003). At the seaside slope erosion by wave run-up is of subordinate importance as result to flatter slope inclination.

4.2 Structural design

The stability of the slopes depends essentially on the available strength at saturated state. First, the heavy cracked topsoil weakens. Therefore, demarcation from topsoil to subsoil will be a frequented sliding plane. The flow force inside the layer could be deflected along this horizon to a slope parallel direction.

The soil Hohenkirchen keeps a stiff consistency, even at saturated state. For the soil Elisabethgroden remains only a soft consistency. Increase of utilization of resistance against sliding is illustrated in fig. 12. An utilization of resistance smaller than 1.0 indicates reserves in loading capacity. If the utilization exceeds 1.0 the dike has to be reinforced. The utilization of the soil Hohenkirchen is always smaller than 1.0 as well, although the utilization is doubled in the investigated range of overtopping. If the soil Elisabethgroden is installed, the available resistance is already exceeded at DWL +5.0 m MSL without any overtopping.

The results for verification of stability against shocking pressure are comparable. The wave height corresponds with the design water level. Hence, the utilization rises with intensifying wave impacts, see fig. 13. Nevertheless, for a crack length of 1 m the soil Hohenkirchen still shows an utilization smaller than 1.0 at DWL +7.5 m MSL, while the resistance of the soil Elisabethgroden

is already fully passed at DWL +5.0 m MSL. A root cohesion of 7 kN/m² up to a depth of 20 cm has been presumed. However, the presented failure equation (eq. 19) for verification of stability against breaker induced pressure impacts has to be improved concerning the spatial geometry of the failure body and the conservative pressure distribution inside the crack.

Obviously, the very well qualified soil Hohenkirchen would offer reserves in loading capacity with regard to secular rise. On the other hand, the less qualified soil Elisabethgroden has to be excluded as cover material for this dike or the cross section has to be changed.

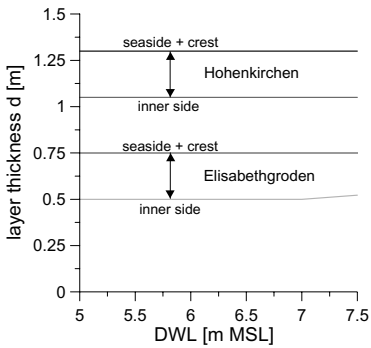

Figure 10. Infiltration.

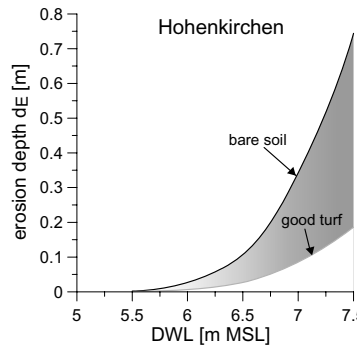

Figure 11. Erosion.

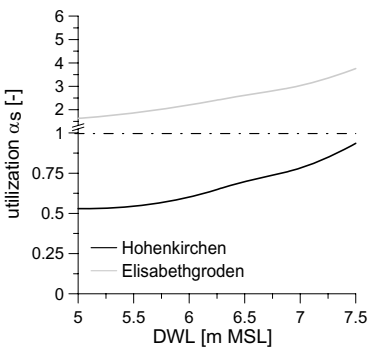

Figure 12. Sliding.

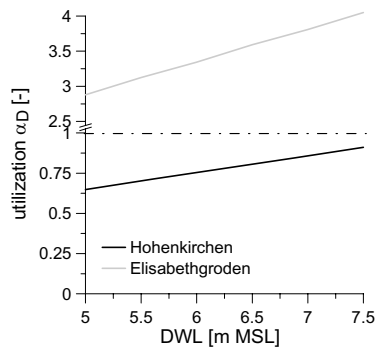

Figure 13. Shocking pressure.

5 Conclusions

Stability of dikes at storm-tide depends essentially on soil mechanical properties of the cohesive layer. In contrast to current design praxis, the presented failure equations enable to take all relevant processes like structuring and weakening into consideration. Thus, design of dikes with respect to specific resistance of disposable soils is possible. All dike components can be executed with the same level of safety. Regarding to expected accelerated secular rise, the integrated design provides valuable information to develop more effective

strategies for adjustment as up to now available. Reserves in loading capacity can be quantified and potential for optimization can be shown.

ACKNOWLEDGMENTS

The work presented has been conducted under the KFKI-research project "Integrated Design of Sea- and Estuary Dikes" (INTBEM) sponsored by the German Federal Ministry of Education and Research (BMBF). The support is gratefully acknowledged.

REFERENCES

ComCoast 2007. *Wave Overtopping Erosion Tests at Groningen Sea Dyke*. Report by Royal Haskoning and Infram (Workpackage 3). http://www.comcoast.org/ (07/04/08)

De Groot, M.B., van Essen, H.M. 2003. *Erosion Tests on Hannover Clay*. Report of the Institute for Geosciences Delft.

Führböter, A. 1966. *Der Druckschlag durch Brecher auf Deichböschungen*. Mitteilungen des Franzius-Instituts der TU Hannover. Heft 27 (in German)

INTBEM 2008. *Integrierte Bemessung von See- und Ästuardeichen – Statusbericht 9/2008*. Ed.: Institut für Grundbau und Bodenmechanik der Universität Duisburg-Essen and Forschungsstelle Küste des NLWKN. Essen/Norderney (in German)

Konrad, J.-M., Ayad, R. 1997. An Idealized Framework for the Analysis of Cohesive Soils undergoing desiccation, *Canadian Geotechnical Journal*, Vol. 34, p. 477-488

Petersen, M., Rohde, H. (1991). *Sturmflut: Die großen Fluten an den Küsten Schleswig-Holsteins und in der Elbe*. Wachholtz Verlag. Neumünster (in German)

Sparboom, U., 1991. Full-scale investigations on wave loadings of sea dyke structures. *Proc. 3rd Int. Conf. on Coastal and Port Eng. in Developing Countries (COPEDEC III)*, Mombasa, Kenya

TAW. Technical Advisory Committee for Flood Defence in The Netherlands. 1996. *Technical report Clay for Dikes*

Temple, D.M., Robinson, K.M., Ahring, R.M., Davis, A.G. 1987. *Stability Design of Grass-Lined Open Channels*. U.S. Dep. of Agriculture. Agriculture Handbook 667.

Weißmann, R. 2003. *Die Widerstandsfähigkeit von Seedeichbinnenböschungen gegenüber ablaufendem Wasser*. Universität Duisburg-Essen. Mitteilungen aus dem Fachgebiet für Grundbau und Bodenmechanik. Heft 30. Essen (in German)

Weißmann, R., Richwien, W. 2004. Funktionale und statische Bemessung der Abdeckung von Deichbinnenböschungen. *HANSA*. 141. Vol. 6, p. 69-75 (in German)

IMPOUNDED WATER IN SEA DIKES

Karsten Peters[1,5], Magnus Geduhn[2],
Holger Schüttumpf[3,5] and Helmut Temmler[4,5]

Impounded water in modern sea dikes with a sand core can cause significant reduction of the structural safety. The phenomenon of impounded water in sea dikes with a sand core was observed at several locations along the dike line at the North Sea Coast. This phenomenon is described and resulting consequences are discussed. The corresponding hydraulic and geotechnical processes are analyzed and responsible influence parameters are appointed. Possible countermeasures against impounded water are presented and recommendations are given.

INTRODUCTION

Geology of Coastal Region at the North Sea Coast

The geology along the German North Sea Coast is mainly characterized by the Pleistocene and Holocene (see Fig. 1).

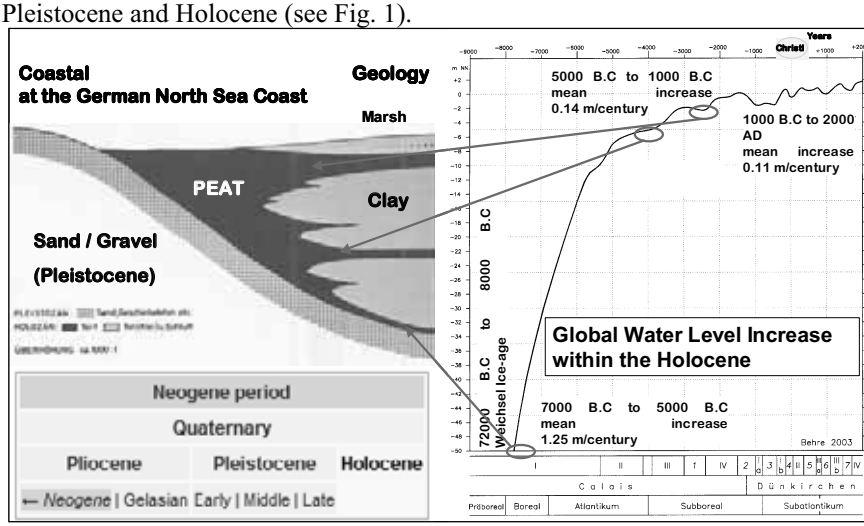

Figure 1. Geology along the German North Sea Coast and its development during Pleistocene and Holocene

[1] IMS Ingenieurgesellschaft mbH, k.peters@ims-ing.de, Stadtdeich 5, D-20097 Hamburg
[2] IMS Ingenieurgesellschaft mbH, m.geduhn@ims-ing.de, Stadtdeich 5, D-20097 Hamburg
[3] RWTH Aachen University, schuettrumpf@iww.rwth-aachen.de, Mies-van-der-Rohe Strasse 1, D-52056 Aachen
[4] temmler@gmx.de, Ahornallee 6, D-24161 Altenholz
[5] Member of the *German Committee of Coastal Structures*, HTG (*German Port Technology Association*)

In the Holocene (post-glacial age) climate changes caused a global sea level rise of more than 52 m in the last 11 000 years. In the coastal regions the transport of fine sediments were forming layers of peat and clay covering the sand and gravel layers created by the glacial period (Pleistocene). A detailed description on the geological development is given by SCHWARZER et al. in KfKI (2008).

Coastal Protection at the North Sea Coast

Coastal protection along the North Sea Coast has a strong relation to the coastal development and geology and the need of protection against flooding. The mainland (mostly marsh area) is mainly protected by dikes. Islands offshore mostly have a geological foundation of sand originating from the Pleistocene. A schematic cross section of the coastline is given in Fig. 2. A detailed description of the German Coast and its protection measures is given in KfKI (2008).

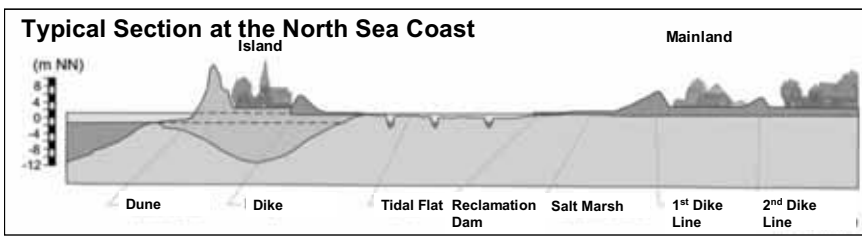

Figure 2. Schematic cross section at the North Sea Coast (Lower Saxony)

History of Sea Dikes in Germany

The construction and building of dikes as a coastal defence structure especially in the marsh areas has a very long history and tradition. Fig. 3 shows the development of the dike profile during the last 400 years.

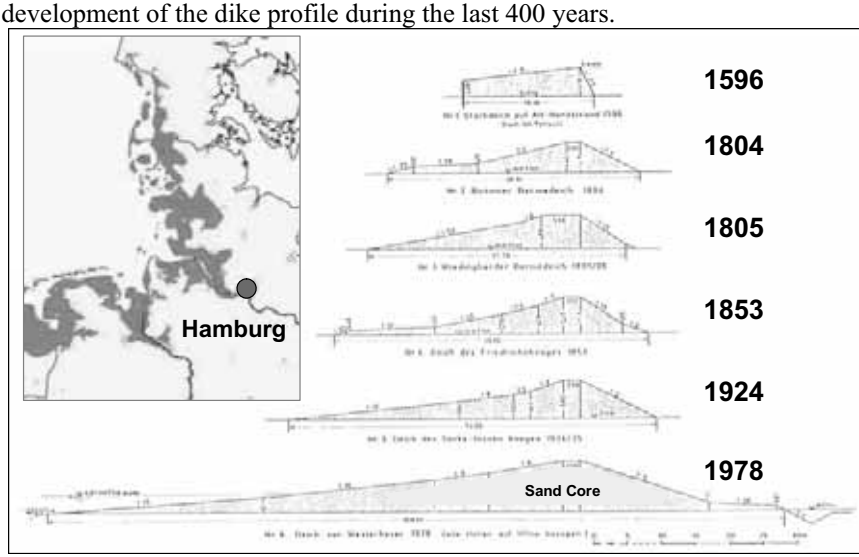

Figure 3. Development of dike profiles in the last 400 years

The development of the sea dikes goes along with the history of storm flood events, the increase of storm surge water levels in the past and the development of building and construction techniques.

While older dikes were build completely out of clay with relatively steep seaward slopes, modern sea dikes consist of a sand core with a covering clay layer of 1.0 m to 1.5 m thickness. The seaward slopes flattened up to 1:6 mainly as a result from dike failures during the most severe storm flood in 1962 in the Elbe estuary and along the German North Sea coast. In EAK (2002) recommendations are given for the planning and construction of modern sea dikes and examples of actual dikes profiles are documented (see KfKI, 2008).

IMPOUNDED WATER IN SEA DIKES

Problem

Depending on the local boundary conditions, modern sea dikes with a sand core were build under different soil conditions. This means that in some cases the sand core of the dike was constructed either on a permeable or on a impermeable subsoil depending on the local geology (see Fig. 4).

Field measurements in the latest years indicated increased water tables inside existing clay dikes as well as inside modern sea dikes with sand core (see TEMMLER, 2004). These levels of impounded water were measured with an altitude significantly higher than the mean tidal high water level, while a level slightly above mean water should be the normal case caused by the hydraulic connection to the estuary and its tidal conditions.

Consequences

This phenomenon of impounded water leads generally to geotechnical problems with regard to structural stability and safety. The water table inside the sand core causes a lifting force against the covering clay layer and reduces the weight of the dike, which is needed for structural stability. This means that in case of storm surges and corresponding increased water levels the calculated structural stability of the whole dike and the resulting safety factor can be lower than defined critical values, so that sufficient protection cannot be guarantied.

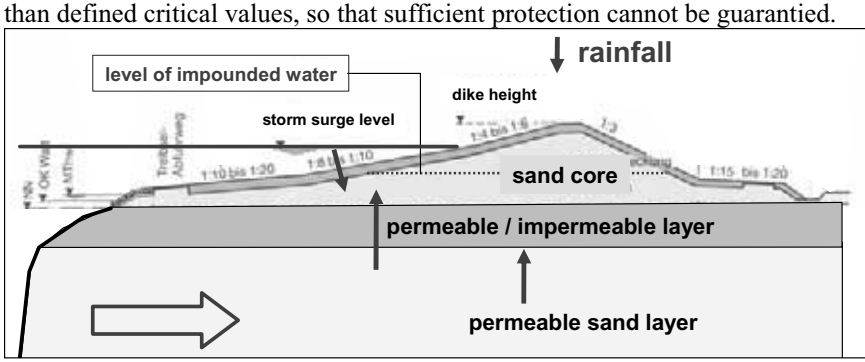

Figure 4. Modern sea dike with sand core as schematic cross section with a typical soil layer structure and relevant parameters

Indication of impounded water

Impounded water in sea dikes with sand core is a local and spatially limited phenomenon, which causes a percolation of water from the inner sand core through the clay covering layer. Therefore the discharge of the percolating water is sometimes visible at the lower parts of the inner or seaward dike slope or at the foot of the dike together with a weak clay layer (see TEMMLER, 2007).

ANALYSIS OF IMPOUNDED WATER IN SEA DIKES

With respect to the high importance of the intact dike line and its flood protection task the phenomenon of impounded water was further analyzed within several projects.

Relevant influence parameters

The percolation of water into the dike core and the development of impounded water in sea dikes can generally have different reasons, like

meteorological conditions
hydraulic boundary conditions
- rainfall
- tidal conditions
- wave run-up and overtopping
- storm surges

geometrical conditions
- general topography
- dike geometry and slopes
- thickness of covering layer

geotechnical boundary conditions
- subsoil layers and conditions
- quality of the soil

specific conditions
- dike construction technique
- damages and holes in the covering clay layer

In case of detected impounded water in sea dikes the different influence parameters have to be investigated in order to abbreviate adequate countermeasures.

Process Analysis

Numerical investigations of the governing processes resulting to impounded water with a permeable and non-permeable subsoil layer below the sand core dike have been conducted. The simulation results are shown in Fig. 5.

The simulations with a permeable subsoil and the hydraulic impact in case of a storm surge (Fig. 5, upper part) showed that ground water percolates continuously through the subsoil into the sand core of the dike. As far as a sufficient hydraulic gradient towards the dike is existing the percolation processes continues and water penetrates into the sand core. But as long as the hydraulic connection works properly the water inside the dike core also

discharges again on the same path with decreasing storm surge level and opposing hydraulic gradient.

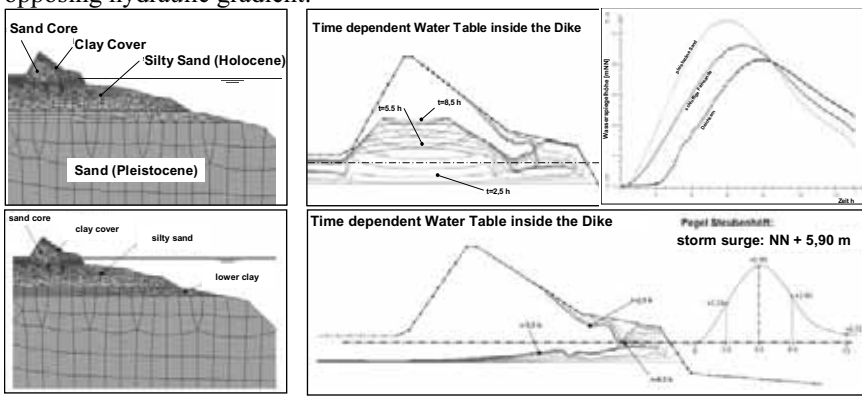

Figure 5. Simulation results of percolation process in case hydraulically permeable soil conditions (above) and hydraulically non-permeable soil conditions (below)

In case of an impermeable (or partly impermeable) subsoil below the dike (see Fig. 5, lower part) no hydraulic connection exists so that consequently no or only reduced ground water can flow into the sand core of the dike.

These investigations lead to the result that impounded water in sea dikes with an impermeable subsoil is mainly caused by the infiltration of water through the covering clay layer in case of rainfall and storm surges over quite long time steps. This is supported by the fact that the phenomenon of impounded water in sea dikes mostly appears decades and years after dike building.

Numerical Investigations on relevant Parameters

SCHÜTTRUMPF and REINHARDT (2004) focussed their investigations on percolation processes inside the dike during storm surges. The most important parameters with respect to impounded water in sea dikes are

- thickness and quality of the covering clay layer
- storm surge level
- existence of impermeable soil layers and bodies inside and under the dike contour

Reasons for impounded Water in Sea Dikes

The old clay dike was often cut and used as bordering dike for the sand spilling process within the construction phase (see Fig. 6) and later as cover layer for the modern sand core dike. As a result of the construction technique vertical and horizontal barriers of impermeable clay layers can form an internal basin inside the dike. In this basin water is stored from the construction process but also from inflow through the cover layer or coming out of the ground caused by high water levels. With progressing time more and more impounded water can be hold in a “closed” sand core – the so-called bathtub effect.

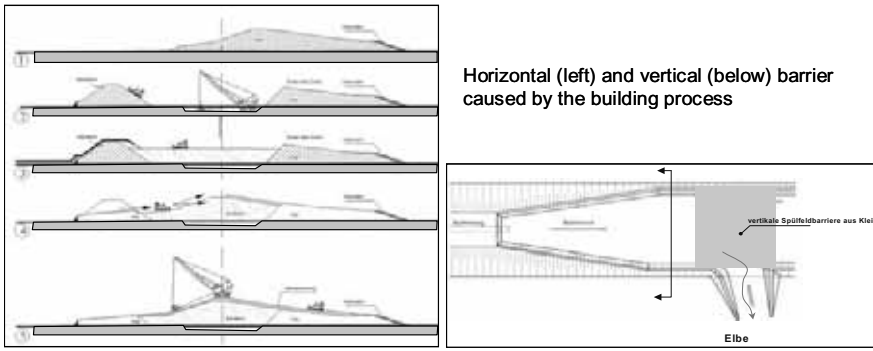

Figure 6. Construction works of a modern sand core dike (EAK, 2002)

The bathtub effect becomes visible in the following Fig. 7. The vertical barriers resemble the clay dikes used in the spilling process. The horizontal barrier resembles an impermeable soil layer, which has not removed before the sand core was build.

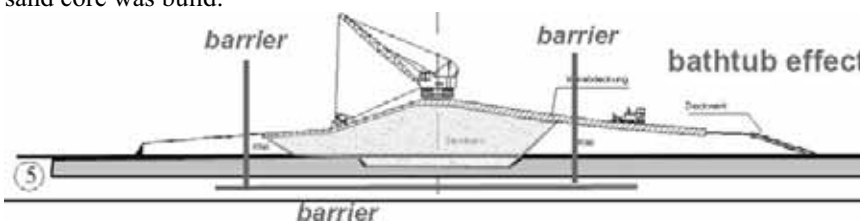

Figure 7. Bathtub effect caused by construction works

RECOMMENDATIONS AND COUNTERMEASURES

There are a number of different possibilities to deal with impounded water. At first the detection of impounded water and the checking of the structural stability and safety under design conditions is very important. In case of a significant reduction of the structural safety countermeasures have to be taken into consideration.

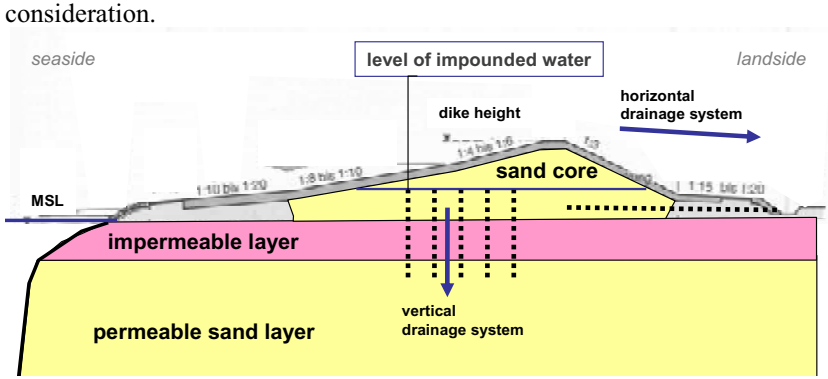

Figure 8. Possible drainage systems as countermeasures against impounded water

The aim of the countermeasures is to facilitate a discharge of the impounded water, normally to the landward side of the dike or to the subsoil beneath the dike. This can be realized with different artificial or mineral drainage systems (see Fig. 8).

REFERENCES

EAK (2002) Empfehlungen für die Ausführung von Küstenschutzwerken, Archive for Research and Technology on the North Sea and Baltic Coast, Die Küste, Heft 65, Editor: Kuratorium für Forschung im Küsteningenieurwesen (*Coastal Engineering Research Council*), Westholsteinische Verlagsanstalt Boyens & Co.

KfKI (2008) Archive for Research and Technology on the North Sea and Baltic Coast, Die Küste, Heft Nr. 74, Editor: Kuratorium für Forschung im Küsteningenieurwesen (*Coastal Engineering Research Council*), Westholsteinische Verlagsanstalt Boyens & Co.

Schüttrumpf and Reinhardt (2004) Untersuchungen zu Sickervorgängen in See- und Ästuardeichen bei instationären Randbedingungen, Bundesanstalt für Wasserbau *(Federal Waterways Engineering and Research Institute)*.

Temmler (2004) Über Grundwasserstandsbeobachtungen in Deichen, Die Hansa, 141. Jrg, Heft Nr. 8.

Temmler (2007) Neue Untersuchungen zur Schrumpfung, Durchsickerung und Aufweichung von Deichabdeckböden bei Extremsturmfluten in Schleswig-Holstein, Archive for Research and Technology on the North Sea and Baltic Coast, Die Küste, Heft Nr. 72, Editor: Kuratorium für Forschung im Küsteningenieurwesen (*Coastal Engineering Research Council*), Westholsteinische Verlagsanstalt Boyens & Co.

ON THE RUN-UP OF BREAKING SOLITARY WAVES

Yu-Hsuan Chang[1], Kao-Shu Hwang[1] and Hwung-Hweng Hwung[2]

The run-up of solitary waves was investigated experimentally and theoretically in this study. Based on the asymptotic solution of water depth close to the run-up tip, a theoretical approach considering hydraulic pressure in the run-up process of breaking solitary waves was developed. Experimental investigations into the validity of this theoretical approach were conducted in the Super Tank at Tainan Hydraulics Laboratory. Experimental measurements clearly show that the proposed depth equation can reasonably describe the swash depth near run-up tip. Good agreement between modeled and observed swash behavior suggest that the present model can adequately estimates the maximum run-up height.

INTRODUCTION

Solitary waves propagating on plane beaches are frequently used to simulate the behavior of tsunamis as they approach the sea shore. There have been a number of analytical and numerical studies concerning the propagation and run-up of solitary waves. As a solitary wave propagates shoreward over a sloping sea-floor it increases in height and may eventually break, running up onto the beach.

The formation of a bore in breaking solitary waves has given rise to a theoretical consideration where it is treated as a moving discontinuity in water depth and velocity. Wave motions in surf and swash zones can be approximated well as bores, as shown in the solutions of nonlinear shallow-water equations by Whitham (1958) and Shen & Meyer (1963). Whitham (1958) first proposed a characteristic rule to solve the problem of bore propagation over a sloping sea-floor. At the shoreline, however, a singularity exists. During shoreline approach the predicted height of a bore tends to vanish. At the shoreline the fluid and bore front velocities approach their common finite value, but their acceleration becomes singular. This rapid conversion of potential to kinetic energy is also called 'bore collapse'. To address the wave run-up that occurs after bore collapse, Shen & Meyer (1963) analytically investigated a characteristic boundary-value problem using the mathematical solution of nonlinear shallow-water theory proposed by Ho & Meyer (1962). They formulated an equation that describes water depth thinning near the run-up front as time increases. In their study, asymptotic behavior is completely governed by gravity. Thus, the shoreline moves up and down the beach under the force of gravity as though it was a freely moving particle.

---

[1] Tainan Hydrauics Laboratory, National Cheng Kung University, Tainan, 709, Taiwan
[2] Department of Hydraulics and Ocean Engineering, National Cheng Kung University, Tainan, 701, Taiwan

Yeh *et al.* (1989) experimentally analyzed the entire process of bore propagation, collapse and run-up. They emphasized that the acceleration in bore-collapse is caused by a 'momentum exchange' process rather than a mathematical singularity, as described in shallow-water wave theory. The 'momentum exchange' process is the interaction between a bore and the initially quiescent water along a shoreline. In a fully developed bore, run-up deceleration is slower than what is predicted using only gravity. In contrast to the appreciable deceleration caused by viscosity, this adverse trend suggests that gravity is not the only dominant force. Yeh *et al.* (1989) pointed out that the pressure gradient force can also influence run-up motion and that this force is important in the early stages of run-up.

In the study presented here, we experimentally and theoretically investigated the run-up of solitary waves on gentle slopes. The pressure gradient force is considered in the kinematic run-up process description by adding a pressure term in the force balance. This term is added on the leading edge within the run-up tongue. A depth equation is proposed as the description of the swash depth near run-up tip, and is further applied to calculate the pressure gradient force acting on the thinning leading edge. An initial-value problem of run-up motion was constructed and solved using a semi-analytical solution technique. Results were compared with experiments performed in the Tainan Hydraulics Laboratory Super Tank.

METHODOLOGY

Consider that a solitary wave propagates on a sloping beach, as shown in Fig. 1. After breaking, a generated shoreward-propagating bore arrives at the initial shoreline and then climbs onto the rigid plane beach, which has a slope indicated by the angle α .

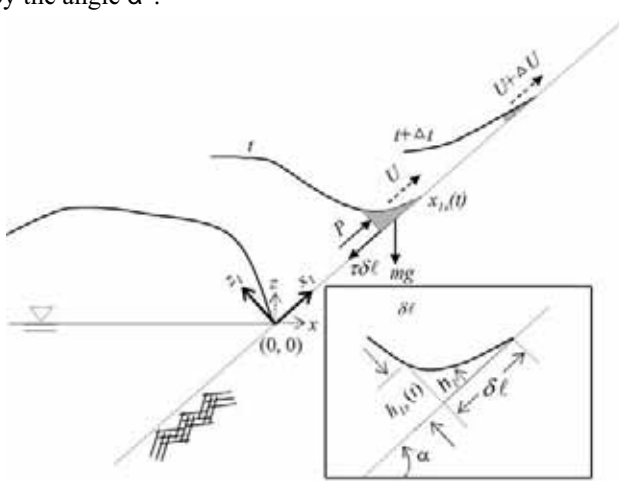

Figure 1. A schematic diagram of run-up motion.

To formulate the governing equation of momentum for the run-up tip along a sloping beach, the tip is taken to be a leading edge of fixed length $\delta\ell$ (see the magnified section in Fig. 1). The stream-wise coordinate is denoted by x_1, where $x_{1s}(t)$ is the shoreline position and t is the time counted from when the run-up front begins to climb the sloping beach. Thus, the rear boundary of the leading edge is at $(x_{1s}(t) - \delta\ell)$. Here, x and z indicate the two-dimensional Cartesian coordinate system. If $M(t)$ is the total momentum of fluid in the leading edge, then the system can be written (by Newton's second law) in the form:

$$\frac{dM}{dt} = F \tag{1}$$

where F is the sum of all external forces acting on the leading edge, and it includes the gravitational force, hydrostatic pressure and resistant force. To account for the balance of atmospheric pressure acting over the free surface of the tip region, the resultant pressure force across the rear boundary is ($\rho g h_{1s}^2/2$), where ρ is the fluid density, g denotes gravitational acceleration, and h_{1s} is the water thickness measured perpendicular to the rear boundary slope. The resistant force is due to bottom shear stress (τ). Thus, the total external force F can be represented as:

$$F = -m(t)g\sin\alpha + \frac{1}{2}\rho g h_{1s}^2 - \tau\delta\ell \tag{2}$$

Furthermore, the leading edge volume can be calculated by integrating water thickness (h_1) with respect to x_1. The mass of the leading edge is then:

.

$$m(t) = \rho\int_{x_{1s}-\delta l}^{x_{1s}} h_1 dx_1 \tag{3}$$

Considering the initial system at time t, a leading edge has mass $m(t)$. We assume there is no cross-stream variation in the run-up flow and that interior particles are moving with velocity U along the x_1 axis. Notably, the leading-edge mass decreases as the tip climbs onto the beach. Although there is local fluid piling up immediately behind the shoreline due to hydraulic resistance (Whitham, 1955 and Hogg & Pritchard, 2004), the whole sheet of run-up flow becomes thinner as time increases. At a period of time (Δt) later, the decrease in leading edge mass is Δm, reducing the leading edge mass to $[m(t) - \Delta m]$. Therefore, at time $(t + \Delta t)$, the original system will be divided into a thinner leading edge with the loss of Δm. In this final system, the leading edge velocity changes to $(U + \Delta U)$ and that of Δm is assumed to be the velocity u. The required expressions for the initial system momentum $M(t)$, and the final system momentum $[M(t + \Delta t)]$ are thus:

$$M(t) = m(t)U \tag{4}$$

$$M(t+\Delta t) = (m(t) - \Delta m)(U + \Delta U) + \Delta mu \tag{5}$$

For the time interval Δt, the dM/dt in Eq. 1 can be written as $[(M(t+\Delta t)\text{-}M(t))/\Delta t]$. After substitution of Eq. 4 and Eq. 5, this leads to:

$$m(t)\frac{\Delta U}{\Delta t} = F - \frac{\Delta m(u - U - \Delta U)}{\Delta t} \tag{6}$$

The quantity $[u - (U + \Delta U)]$ in Eq. 6 is simply the relative velocity (u_{rel}) of Δm with respect to the leading edge. If we suppose that mass flow across the rear boundary in time interval Δt is equal to Δm, then u_{rel} can be derived via dividing the flow flux by a time-average surface. On the one-dimensional rear boundary, the time-average area is given compactly by $[(h_{1s}(t) + h_{1s}(t + \Delta t))/2]$. The relative velocity of Δm can then be written as:

$$u_{rel} = \frac{2\Delta m}{\rho \Delta t(h_{1s}(t) + h_{1s}(t + \Delta t))} \tag{7}$$

Because the change in mass (dm) is intrinsically negative in this case, the positive quantity Δm is replaced by –dm in the limit. With these changes, Eq. 6 in the limit as Δt approaches zero can be written as:

$$m(t)\frac{dU}{dt} = F + \frac{u_{rel}dm}{dt} \tag{8}$$

Furthermore, the force balance equation with substitution of Eq. 2 is given as:

$$m(t)\frac{dU}{dt} = -m(t)g\sin\alpha + \frac{1}{2}\rho g h_{1s}^2 - \tau\delta\ell + u_{rel}\frac{dm}{dt} \tag{9}$$

and the equation of motion is:

$$\frac{dx_{1s}}{dt} = U \tag{10}$$

Eq. 9 and Eq. 10 construct an initial-value problem for the run-up motion of a breaking solitary wave. Given the initial conditions and the water thickness (h_1), which will be further introduced in later analyses, the simultaneous solution of these two equations can be accomplished using the Runge-Kutta fourth order method.

LABORATORY EXPERIMENTS

Wave Flumes and Setup

A series of experiments was conducted in the 300 m (L), 5 m (W) and 5.2 m (D) Super Tank at Tainan Hydraulics Laboratory (*THL*), National Cheng Kung University. Two plane beaches of slopes 1:20 and 1:60 were constructed respectively at the end of wave tank. The plane beach of slope 1:60 was constructed with a smooth layer of concrete that started 54 m from the neutral wave paddle. The still water depth, h_0, at the toe of the plane beach was 2.25 m. In the case of 1:20 slope, the position of the toe and the still water depth at the toe are 201 m and 1.75 m, respectively.

Time series of local water surface elevations were recorded by capacitance-type wave gauges distributed at 96 stations along the tank. Among the wave gauges, fourteen were located beyond the initial shoreline. In addition to these fourteen wave gauges, run-up sensors were also used to detect shoreline motion. Because the up-rush zone of this experiment stretched over 20 m, six run-up sensors (each 5 m long) were necessary to measure the entire run-up process. These sensors were installed lengthwise at 0, 9.4, 18.4, 25.2, 33.1 and 41.7 cm above the still-water-level on the sloping bottom. Each sensor was placed at a fixed distance of 1 cm above the bottom. With these gauges, the maximum run-up heights can be compared to those made using direct visual observation. All surface displacements were recorded simultaneously at a 50 Hz sampling rate using a Microsoft NT based Multi-Nodes-Data-Acquisition-System (MNDAS), which was developed by *THL*.

Figure 2. A generated solitary wave in the Super Tank.

Solitary Wave Generation and Test Conditions

Fig. 2 shows a typical solitary wave propagation in the Super Tank. The solitary wave was generated by applying Goring's (1978) method, from which the wave-board motion was computed using a nonlinear algorithm and then

inputted into the programmable controller for managing the hydraulically driven wave-maker. With a maximum stroke limit of 2 m and a maximum velocity limit of 1 m/s, this large-scale laboratory facility was validated for the function of solitary-wave generation as in Hwang *et al.* (2007) and Hsiao *et al.* (2008). Table 1 lists all of the initial solitary wave height and conditions measured at the still shoreline, where H_b/h_0, $U_0/\sqrt{gH_b}$, and λ gcosα correspond to the dimensionless bore height, initial Froude number and the relative value of determined λ to the coefficient of Peregrine & Williams (2001) [1/gcosα], and will be further introduced in later analyses. In experiments of slope 1:60, relative wave heights (H/h_0) of the wave condition ranged between 0.019 and 0.152, with an identical water depth of 2.25 m in the constant-depth region (h_0). In experiments of slope 1:20, relative wave heights (H/h_0) of the wave condition ranged between 0.054 and 0.235, with an identical water depth of 1.75 m.

Table 1. Initial conditions at the still shoreline position.

cotα	h_0 (m)	H/h_0	H_b/h_0	$U_0/\sqrt{gH_b}$	$\lambda g\cos\alpha$
60	2.25	0.152	0.076	1.853	2.247
		0.134	0.075	1.724	1.691
		0.117	0.070	1.799	2.842
		0.100	0.050	1.671	1.583
		0.084	0.048	1.741	4.367
		0.066	0.056	1.625	2.306
		0.050	0.048	1.470	2.349
		0.040	0.038	1.633	2.149
		0.029	0.036	1.772	2.047
		0.019	0.030	1.751	6.050
20	1.75	0.235	0.198	1.870	1.868
		0.173	0.122	2.283	1.721
		0.094	0.081	2.551	1.117
		0.054	0.056	2.121	2.466

RESULTS AND DISCUSSION

The Water Thickness of Run-up Flow

The measured water surfaces at eight times prior to the maximum run-up of a solitary wave on a 1:60 sloping bottom are presented in Fig. 3. Here the initial wave condition was H/h_0 = 0.152, with a water depth of h_0 = 2.25 m. The simultaneous data of run-up sensors and wave gauges is denoted as open circles. Data is further compared with two swash depth equations. One of these is the theoretical solution of Peregrine & Williams (2001), and is presented in dimensional units as:

$$h_1(x_1,t)=\frac{1}{g\cos\alpha}\frac{\left(x_{1s}(t)-x_1\right)^2}{(3t)^2},\quad 0<x_1\le x_{1s}(t) \tag{11}$$

It is conveniently abbreviated to "PW (2001)". As an extension of the swash solution given by Shen & Meyer (1963), Eq. 11 is also singular at (x_1, t) = 0 and is only expected to be accurate near the moving shoreline. The other depth equation is a semi-empirical formulation proposed by Baldock & Holmes (1997) and is shortened as "BH (1997)":

$$h_1(x_1,t) = H_b\left(\frac{x_{1s}(t)-x_1}{x_{1s}(t)}\right)^{C^*}\left(\frac{T_s-t}{T_s}\right)^{D^*}, \tag{12}$$

where H_b is the terminal bore height, T_s is the swash period, and C^* and D^* are empirical coefficients in the range of C^* = 0.5 to 0.75 and D^* = 1 to 2. When x_1 is greater than $x_{1s}(t)$, h_1 = 0. To compare this with measured data, results of PW (2001) and that of BH (1997) were transformed in the xz-coordinate system, as shown by dash lines and the × marked lines, respectively. Unlike the concave-up swash profile of PW (2001), BH (1997) yielded a convex water surface profile. This agreed with the experimental observation at t = 10 sec using an optimum determination of C^* = 0.5 and D^* = 1. The depth equation of BH (1997) yields a much greater water volume in the up-rush than that of Shen & Meyer (1963) or PW (2001), but it overestimates the swash depth in the early stage of run-up.

In the present run-up prediction model, h_1 must be equated to describe water thickness. The two swash depth equations (shown above) must first demonstrate utilization of the present model. The PW (2001) apparently underestimated water thickness; on the other hand, BH (1997) overestimated swash depth in the early run-up stage. These types of problems would cause significant deviations when estimating the pressure gradient force. Also, in calculation of this initial problem, another comes about. Namely, the swash period (T_s) in BH (1997) is unknown and can not directly refer to $T_s = 2U_0/g\sin\alpha$, which is used in the ballistic solution. Therefore, a swash depth equation is proposed here, which was based on the asymptotic water depth by Shen & Meyer (1963):

$$h(x,t) \to \frac{\left(x_s(t)-x\right)^2}{\left(3t\right)^2}, \; t > 0 \tag{13}$$

Note that it is defined in the xz-coordinate system, where x_s is the shoreline position and h is the swash depth above the sloping bottom. To unify the dimensions, Eq. 13 was transformed into the swash depth equation:

$$h(x,t) = \lambda\frac{\left(x_s(t)-x\right)^2}{\left(3t\right)^2}, \; t > 0 \tag{14}$$

where the dimension of λ has units of ($L^{-1}T^2$) and is identical to the dimension of $1/g\cos\alpha$, which is a coefficient in Eq. 11. To yield a much greater water thickness than given by PW (2001), λ was used to force the maximum

computational surface elevation at the still shoreline to match the measurement. Given the shoreline position (x_{sb}) and the time (t_b), which were measured when the maximum surface elevation reached the still shoreline, this produced:

$$\lambda = H_b \frac{\left(3t_b\right)^2}{\left(x_{sb}\right)^2} \tag{15}$$

where H_b is the maximum surface elevation at the still shoreline and is the same as the terminal bore height. In the sample case where H/h_0 = 0.152 and cotα = 60, the maximum surface elevation at the still shoreline (H_b) was 17.1 cm at t_b = 2.5 sec, while the run-up tip reached position x_{sb} at 6.462 m. With substitution into Eq. 15, this yielded a λ of 0.23. Thus, the spatial profiles of Eq. 14 are plotted as solid lines.

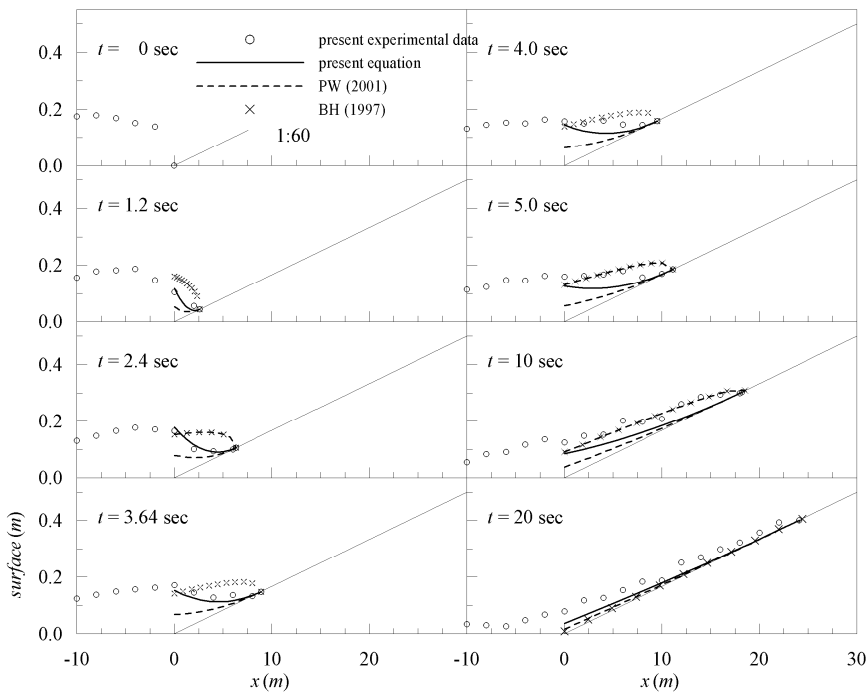

Figure 3. Snapshots of the water surface during the run-up process (H/h_0 = 0.152, cotα = 60, h_0 = 2.25 m).

Note that in Fig. 3, these three equations were forced by specifying $x_{1s}(t)$ or $x_s(t)$ from measurements. Comparisons made here serve to demonstrate Eq. 14 as a reasonable depth equation for the run-up tip. Owing to the T_s limit in applying the depth equation of BH (1997) for the present prediction model, the present depth equation i.e., Eq. 14 was determined to be an alternative way to

equate the swash depth. From comparisons depicted in Fig. 3, Eq. 14 clearly produces a much greater water thickness than PW (2001), owing to the function of λ. There is, however, a slight burst immediately after t = 0, owing to the singularity in shallow-water theory (Pritchard & Hogg 2005). Within such a narrow region of invalidity, the water thickness (h_{1s}) of the present model was forced to zero in order to not overestimate hydraulic pressure. Despite this simplification, it is reasonable to state that a sheet of run-up water becomes thinner as time increases, as described in Eq. 14. Furthermore, in the early stages of run-up, water-depth fitness near the run-up front is exceedingly important in order to estimate the pressure gradient force.

Run-Up Computation of the Present Prediction Model

A representative comparison between actual shoreline motion and predicted swash behavior is shown in Fig. 4, using the case where H/h_0 = 0.152, h_0 = 2.25 m, and cotα = 60. Given the initial run-up velocity (U_0), the ballistic solution space-time trajectory (i.e., the projection of $[U_0 t - g \sin\alpha\, t^2/2]$ at the x-axis) is shown as a dashed line. The trace of actual shoreline motion is clearly more complex than the parabolic curve produced with the ballistic solution, which is only governed by gravity force. Measured maximum run-up (inundation) distance is also farther than that produced in the ballistic solution. Therefore, in models extended from a ballistic solution, the pressure gradient force has to be considered to support the existence of an extra driving force for the actual run-up motion.

Although the presented prediction model yield a form that is similar to the equation of Kirkgöz (1981), it extends the model of ballistic motion by adding a term to represent hydraulic pressure behind a variable mass leading edge, which drives it forward despite friction. Hydraulic pressure was estimated via incorporation of Eq. 14, which approximates the evolving swash depth. For bottom shear stress (τ), which causes flow resistance, the term is typically represented as a quadratic equation (i.e., $\tau = \rho f U^2$). The f coefficient is a Chézy friction coefficient and is usually assumed to be constant. Typical values of the friction coefficient are in the range of 0.01 to 0.001 (Moody 1944), depending on the boundary roughness. On the other hand, the lower resultant run-up of ballistic solutions implies that the bottom shear stress term can amplify underestimation, owing to its excessive dissipative effect on the run-up process. Even when we assumed a smooth, artificial slope, the value of f was constant (0.001) and the resultant swash behavior was greatly dissipated, as indicated by the × marked line. Hogg & Woods (2001) suggested that the initial motion of this gravity flow may be independent of bottom drag. Thus, the case of f = 0.001 may overestimate the drag force during the initial stages of large flow velocity. As indicated by Hibberd & Peregrine (1979), the commonly used Chézy friction term is unsuitable for unsteady flow problems. Without an exact formulation for bottom shear stress during unsteady flow, we found it difficult to correctly simulate it in the present model. In this prediction model there are

also some weaknesses in the proposed depth equation and in the run-up velocity determination. With its simpler depth equations, the present prediction model may substantially underestimate water thickness of the fluid element at times longer than those discussed in Fig. 3. In addition, the run-up velocity determination was not exactly the depth-average flow velocity used in the Chézy friction term. In contrast, with a weak, stream-wise hydraulic pressure force, the friction term could cause apparent dissipation. Based on the comparison of results with $f = 0$ and $f = 0.001$, the bottom shear stress (τ) was excluded in the present prediction model.

Before the present model can be used to predict swash behaviors, an estimate for $\delta\ell$ is required. Given $\delta\ell = 0$ m, the present prediction model using $\tau = 0$ is identical to the ballistic solution. However, the present model meets the sensitivity of computational run-up height to $\delta\ell$. Resulting durations and inundation distances of the present prediction model become higher as $\delta\ell$ increases. When $\delta\ell$ is equal to the 2% inundation distance incurred as the maximum surface elevation reaches the still shoreline [i.e., $\delta\ell = 0.02x_{sb}\sec\alpha$], a computational swash behavior approaches experimental observations, as represented by the solid line. Similar to the ballistic solution, computational maximum run-up heights occur on shorter timescales relative to real shoreline motion. Despite the above deficiencies, this approach can reasonably estimate the maximum run-up heights of breaking solitary waves.

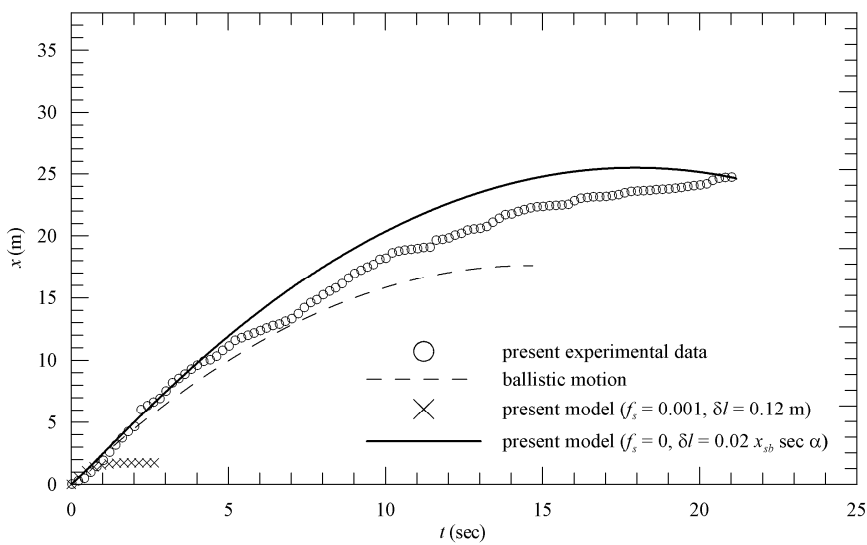

Figure 4. Computed and measured swash trajectories for a solitary wave, where H/h_0 = 0.152, h_0 = 2.25 m, and cotα = 60.

Ultimately, further verification on the omission of bottom shear stress and leading edge length $\delta\ell = 0.02x_{sb}\sec\alpha$ is necessary to place the matter beyond

doubt. More studies on a 1:60 sloping bottom, with relative wave heights (H/h_0) ranging from 0.029 to 0.134, are shown in Fig. 5. Examinations conducted with a beach of slope 1:20 are shown in Fig. 6. Relative wave heights (H/h_0), for this series of experiments ranged from 0.054 to 0.235. As for the case where H/h_0 = 0.152 and cotα = 60, good agreement are observed in the comparisons between the computational swash behavior and measurement.

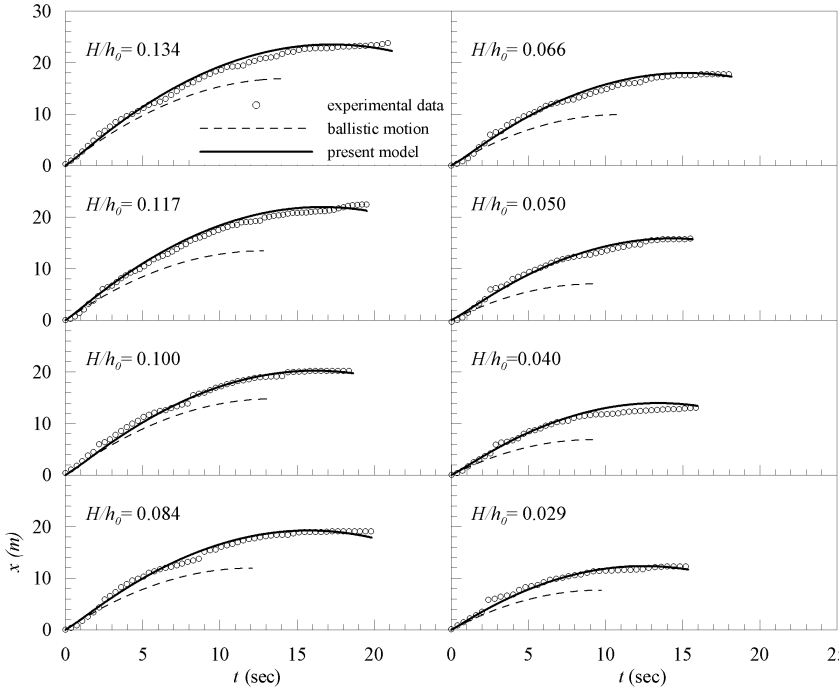

Figure 5. Computed and measured swash trajectories for a solitary wave, where H/h_0 = 0.134 ~ 0.029, h_0 = 2.25 m, and cotα = 60.

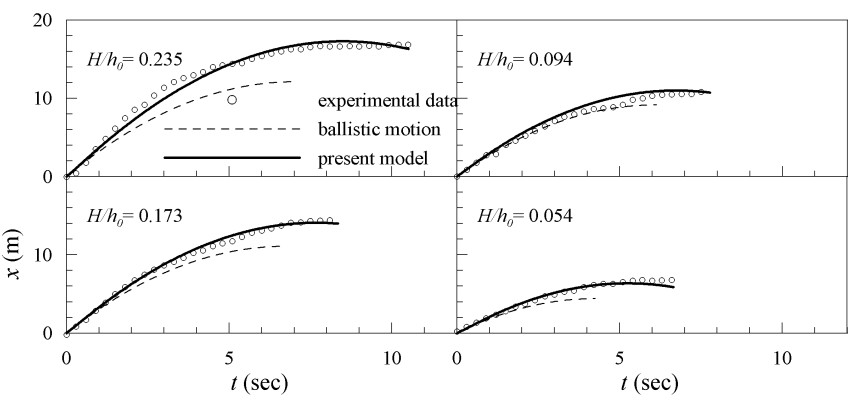

Figure 6. Computed and measured swash trajectories for a solitary wave, where H/h_0 = 0.235 ~ 0.054, h_0 = 1.75 m, and cotα = 20.

CONCLUDING REMARKS

In this study an approach was developed, considering hydraulic pressure effects, for the run-up process of breaking solitary waves on plane beaches. Detailed measurements of water surface elevation and shoreline motion were presented. We draw the following conclusions based on this study:

(1) Experimental measurements clearly show that the proposed depth equation, Eq. 14, can reasonably describe the swash depth near run-up tip in the early stages of run-up while the water-depth fitness near the run-up front is exceedingly important in order to estimate the pressure gradient force. The coefficient λ was determined by forcing the maximum computational surface elevation at the still shoreline to match the measurement, and the higher value, $\lambda g\cos\alpha > 1$, indeed yield a much greater water thickness than given by the equation of Peregrine & Williams (2001). Consequently, hydraulic pressure term in the present model can be well estimated via incorporation of Eq. 14.

(2) The present model meets the limit in applying Chézy friction term and the sensitivity of computational run-up height to δℓ. Because that the run-up velocity determination was not exactly the depth-average flow velocity used in the Chézy friction term and the apparent dissipation was caused by the friction term, the bottom shear stress (τ) was, therefore, excluded in the present prediction model. From the agreement in the comparison with experiments, the leading edge length, $\delta\ell = 0.02x_{sb}\sec\alpha$, is recommended for use with conditions in the present prediction model of solitary wave run-up.

(3) By adding the pressure term into the force balance on a variable mass leading edge, an initial-value problem of run-up motion was constructed. The kinematic description of solitary wave run-up can be solved by a semi-analytical solution algorithm. Through comparison with experiments, this theoretical approach considering hydraulic pressure was found to not only reasonably predict maximum run-up heights, but also to describe the shoreline motion of breaking solitary waves.

ACKNOWLEDGMENTS

The authors would like to express sincere gratitude to the "NCKU Project of Promoting Academic Excellence & Developing World Class Research Centers", which was supported by the Ministry of Education, Taiwan. In addition, many thanks are due to the Senior Design Engineer, Lambert N.G. Romijnders Development & Control of Bosch Rexroth B.V., and research staff of Tainan Hydraulics Laboratory for performing a series of experiments.

REFERNCES

Baldock, T. and P. Holmes. 1997. Swash hydrodynamics on a steep beach, *Proc. Conf. Coastal Dynamics* '97, ASCE, 784-793.

Goring, D. G. 1978. Tsunami: the propagation of long waves on a shelf, *Rep. KH-R-38*, W. M. Keck. laboratory of hydraulics and water resources, California Institute of Technology, Pasadena, CA. 337 pp.

Hibberd, S. and D. H. Peregrine. 1979. Surf and runup on a beach: A uniform bore, *J. Fluid Mech.*, 95, 323-345.

Ho, D. V. and R. E. Meyer. 1962. Climb of a bore on a beach. Part 1. Uniform beach slope, *J. Fluid Mech.*, 14, 305-318.

Hogg, A. J. and D. Pritchard. 2004. The effects of hydraulic resistance on dam-break and other shallow inertial flows, *J. Fluid Mech.*, 501, 179-212.

Hogg, A. J. and A. W. Woods. 2001. The transition from inertia- to bottom-drag dominated motion of turbulent gravity currents, *J. Fluid Mech*., 449, 201-224.

Hsiao, S.-C., T.-W. Hsu, T.-C. Lin and Y.-H. Chang. 2008. On the evolution and run-up of breaking solitary waves on a mild sloping beach, *Coastal Engineering*, doi: 10.1016/j.coastaleng.2008.03.002.

Hwang, K.-S., Y.-H. Chang, H.-H. Hwung, and Y.-S. Li, 2007. Large scale experiments on evolution and run-up of breaking solitary waves, *J. Earthquake and Tsunami*, 1, 257-272.

Kirkgöz, M. S. 1981. A theoretical study of plunging breakers and their run-up, *Coastal Engineering*, 5, 353-370.

Moody, L. F. 1944. Friction factors for pipe flows, *Trans.* ASME, 66, 671.

Peregrine, D. H. and S. M. Williams. 2001. Swash overtopping a truncated plane beach, *J. Fluid Mech*., 440, 391-399.

Pritchard, D. and A. J. Hogg. 2005. On the transport of suspended sediment by a swash event on a plane beach, *Coastal Engineering*, 52, 1-23.

Shen, M. C. and R. E. Meyer. 1963. Climb of a bore on a beach. Part 3. Run-up, *J. Fluid Mech.*, 16, 113-125.

Whitham, G.B. 1955. The effects of hydraulic resistance in the dam-break problem, *Proc. R. Soc. Lond. A*, 227, 399-407.

Whitham, G.B. 1958. On the propagation of shock waves through regions of non-uniform area of flow, *J. Fluid Mech*., 4, 337-360.

Yeh, H., A. Ghazali, and I. Marton, 1989. Experimental study of bore run-up, *J. Fluid Mech*., 206, 563-578.

DESIGN AND CONSTRUCTION OF WATERFRONT STRUCTURES WITH SPECIALLY DESIGNED NONWOVEN GEOTEXTILES

G. Heerten[1], J. Klompmaker[2], H. Pohlmann[1] and Janne Kristin Pries[2]

Coastal and hydraulic engineering problems were the starting point of the technical development of geotextiles. Nearly 60 years ago first trials with sandbags made of synthetic textiles were realized in coastal and hydraulic engineering in the USA, the Netherlands and in Germany. First extensive investigations have been in done in the 1970ies at the German North Sea Coast in order to safeguard and expand the knowledge on long-term resistance of geotextiles applied in coastal protection applications. This early investigation programme dealt with geotextiles being installed from 5 up to 21 years at 13 different locations of the North Sea coast at the German Bight. Results of these field investigations will be presented. Due to lack of information relating design criteria extensive laboratory investigations have been carried out on geotextile containers as dune reinforcement. Results from German large scale model tests are presented and design approaches which have been derived based on these tests, will be presented. Finally international case studies will be presented, where the encapsulation of sediments in geotextile sand containers dominates but other functions as e.g. reinforcement and filtration cannot be neglected.

INTRODUCTION

Encapsulating or wrapping sand into geotextile units provides a variety of flexible, economical and ecological coastal applications. Especially at indifferent dynamic sandy beaches, where the use of rocks, steel and concrete as "hard coastal structures" is contrary to the soft coastal protection philosophy, geotextile sand filled containers made of needle- punched nonwovens offer more advantages as "soft rock structures". As flexible construction elements geotextile containers behave advantageously relating cyclical hydrodynamic loads and morphological sea bed changes. In recent years, geotextile container technology has experienced great success at highly visible projects. Nowadays geotextile sand containers find their application as construction elements for erosion control, scour protection, reefs, groynes, dams, breakwaters and dune revetments.

FIELD INVESTIGATIONS

The main reason for the carried out field investigations on coastal structures was the examination of the long-term behaviour of the installed geotextile products under service conditions. In the framework of the carried out investigations multi-filament fabrics, tape fabrics and nonwovens made from

[1] NAUE GmbH & Co. KG, Gewerbestraße 2, 32339 Espelkamp-Fiestel, German
[2] BBG Bauberatung Geokunststoffe GmbH & Co. KG, Gewerbestraße 2, 32339 Espelkamp-Fiestel, Germany

different polymers (PET, PA, PP, PP/PE) were examined. At 13 locations on the North Sea coast of the German Bight sampling operations were carried out. Altogether 39 samples were taken. 16 samples were dug out from revetments of sea dikes and 23 samples of woven fabrics were taken from sandbags and sand filled tubes. Figure 1 gives an impression of the sampling operation at the revetment of the sea dike located at the Dithmarscher Bight on the North Frisian coast. In figure 2 a nonwoven fabric is shown after removing the cover layers (riprap and gravel) of the revetment.

Figure 1. Digging out a filter fabric underneath rip rap of revetment

Figure 2. Nonwoven fabric after removing the revetment cover layers

The picture in figure 3 gives an example of the application of sand filled tubes. It shows a small dam in land reclamation fields in the tidal flats in front of the sea dikes. From the sandbags and sand filled tubes two different samples were taken, one of the weathered upper side and one of the protected bottom

side. Thus it is possible to calculate the influence of weathering on the long-term resistance of the fabrics.

Figure 3. Sand filled tube in a land reclamation field

For geotextile samples dug out of revetments the following individual investigations were carried out:

1. Condition and change of the profile of the revetment
2. Condition of the geotextile
3. Testing the tensile strength
4. Testing the filtration properties
5. Testing the fabric weight and soil content
6. Grain-size analysis and permeability test of the subsoil

For geotextile samples of sand bags and sand filled tubes the research program is reduced to the following individual investigations:

1. Condition of the fabric
2. Testing the tensile strength
3. Estimation of effective opening size
4. Grain-size analysis of packed soil

An essential result of the investigations of the sea dike revetments was the detected extensive filling of the riprap layers with sand and mud particles and the considerable incorporation of soil in the nonwoven fabrics. Caused by the filling of the riprap layers with sand and mud, the boundary layer of fabric and subsoil was protected against dynamic wave attack. This situation also gave stability to revetment sections with fabrics of too large opening size according to actual knowledge.

The extensive incorporation of soil in the nonwoven fabrics leads to the assumption to doubt about the similarity to nature of laboratory test with nonwoven fabrics and soil. Figure 4 gives and example of a nonwoven fabric with a filling rate of about 9,000 g/m² by a fabric weight of about 1,000 g/m².

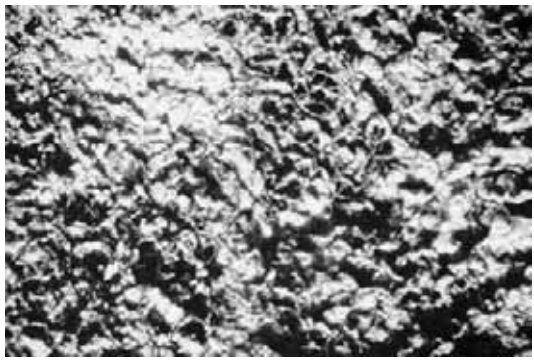

Figure 4. Nonwoven fabric filled with sand and mud particles

Additional investigations lead to the perception that the sand and mud particles in the coarse-layers mostly came from the seaside of the construction and not from the bottom side. Some significant profile changes with a flatter slope of the revetment were perhaps caused by soil-liquefaction under wave impact but certainly not by a washout through the filter-fabrics.

RESULTS ON LONG-TERM RESISTANCE

A usual method to give some information about the long-term resistance of geotextiles is a comparison of the tensile strength of the virgin and of the aged material based on standard tensile testing methods, as e.g. EN ISO 10319. In the following some examples of the results of investigations about long-term resistance of the synthetic filter geotextiles are presented. For different multifilament fabrics made of nylon (PA 6.6) the minimum value of residual strength after 20 years of free, unprotected exposure was about 20%. Protected samples showed a residual strength of about 70% after the same exposure time.

The next examples give an impression about the long-term resistance of all fabrics examined in the research program. The residual strength values of the exposed products (no protection) were determined as follows:

PE/PP Tape fabric, high titre (85 % after 5 years)
PE Tape Fabric, high titre (68 % after 15 years)
PP Multifilament woven, low titre (32 % after 15 years)
PP/PE Tape fabric, high titre (49 % after 8 years)
PET Multifilament woven, low titre (60 % after 2 years)
PA 6.6/PA 6 Multifilament woven, low titre (67-19 % after 2.5-21 years)

The results for residual strength of protected geotextile products were determined as follows:

PE/PP Tape fabric, high titre (100 % after 5 years)
PE Tape Fabric, high titre (97 % after 15 years)
PP Multifilament woven, low titre (91 % after 15 years)
PP/PE Tape fabric, high titre (91 % after 8 years)
PET Multifilament woven, low titre (86 % after 7 years)
PA 6.6/PA 6 Multifilament woven, low titre (56-68 % after 8.5-21 years)

To be able to interpret the summarized results it needs to be considered that the fibre fineness (titre) has a great influence on the long-term resistance of geotextiles. Therefore the good result of the tape-fabrics, produced of relative thick tapes, is no surprise. The fibre fineness of the tapes is about some hundred dtex whereas the fibre fineness of filaments is only 5 to 10 dtex. In addition it needs to be considered that the results determined on samples of the salt-water region could be influenced by a lot of parameters like suspended load of the seawater, duration of tidal overflow, covering of the fabrics by mud, seaweed, micro-organism or rubble and their temporary variation. The damage of fabrics could also be caused by wave-action, drifting-wood, ice, shipping or tourists.

Most of the parameters only influenced the sections with unprotected weathering like the upper sides of the sand filled tubes. Geotextile filter fabrics in revetments protected by several cover-layers are less endangered but attention must be paid so that not damage of the fabrics occurs during construction time. Also it can be concluded that the most important parameter influencing the long-term resistance of fabrics in the saltwater region of the North Sea coast is the ultra-violet radiation and the raw material and fibre fineness of the fabric. Finally it has to be considered that the fabrics have been produced with the technical knowledge of their production time up to 20 years before the research programme was carried out. Actual produced and sufficiently stabilized geotextiles will service even better.

Ageing by biological and chemical damages is of much lower importance and could not be identified. Attention has to be paid that no damage of fabrics occurs during the construction period. These results show fair agreement with the results of investigations carried out on the woven geotextile filter fabric used as a construction element of protection against scouring at the Eider storm surge barrier. The protection against souring was damaged but the first assumption that the damage was caused by insufficient long-term resistance of the woven fabric could not be confirmed but damage already during installation took place because of the low fabric weight of only 200 g/m^2 compared to ≥ 600 g/m^2 based on actual coastal and hydraulic engineering practice in Germany. These early findings are completely transferable to needle-punched staple-fibre nonwoven geotextiles, which are used for already 30 years in coastal and hydraulic engineering applications as sand filled tubes and containers under free/exposed weathering conditions. Especially the area weight and the huge

pore volume (90% pores), which is especially receptive for sediment particles and algae growth, effectively protects the synthetic fibers in addition to the today's commonly added stabilizers.

PREPARATION OF LARGE-SCALE MODEL STUDY IN A WAVE FLUME

In the framework of an applied research programme at the Leichtweiss-Institute for Hydrodynamics and Coastal Engineering of the Technical University Braunschweig, Germany, the large scale model tests were recently conducted, particularly focussing on the hydraulic stability of nonwoven geotextile containers used as dune protection. The results are described in the following.

OBJECTIVE

The main purpose of this study was the detailed testing of the stability of sand containers under wave load. Within three test phases a 1:1 sloping barrier composed of sand container of different sizes (150 l and 25 l) with and without fixation belts were investigated. A picture of the typical test-setup of the 1:1 inclined dune made of geotextile containers is given in Figure 5.

Figure 5. Large-scale model tests with geotextile containers

RESULTS OF LARGE-SCALE MODEL TESTS

The sand containers at the crest of the structure started to move earlier than the elements on the slope due to the different load conditions on the crest and on the slope. For the investigated geometry, design formulae have been developed which can distinguish between crest and slope elements. The main loading of the crest elements is induced by wave run-up and overtopping whereas the load of the slope elements is principally induced by the uplift and suction during the wave run-up and run-down. The results of the three test phases are summarised below:

TEST PHASE I WITH SAND CONTAINERS (150 LITERS)

The analysis of the data from test phase I using 150 l geotextile containers (1.50 m x 0.75 m unfilled) showed a large scatter of the stability number Ns from which a clear threshold between movement and no movement can hardly be identified. Relating the initiation of movement to the number of container layers it was however possible to obtain a distinction with respect to the stability behaviour of crest and slope elements. Therefore, two stability formulae were developed to distinguish between the stability of crest and slope elements. For the slope elements the following formula was obtained (Figure 6):

$$N_s = \frac{H_s}{(\rho_E / \rho_W - 1) \cdot D} = \frac{2.75}{\sqrt{\xi_0}} \quad (1)$$

- D = characteristic diameter of sand container defined as $D = l \cdot \sin\alpha$
- l = length of sand container (container dimensions in wave direction) [m]
- H_s =significant wave height in front of the structure [m]
- ρ_w,. ρ_E = density of water and sand container, respectively [kg/m^3] with
- $\rho_E = \rho_s(1-n) + \rho_w$,
- n= porosity of sand,
- ρ_s= density of sand grain (2650 kg/m^3),
- ξ_0 = surf similarity parameter.

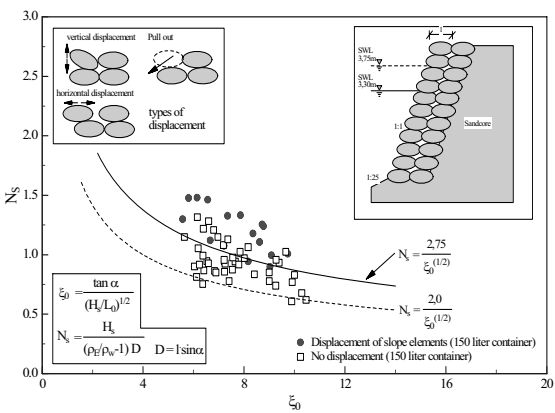

Figure 6. Stability of containers in slope section-Test phase I (Oumeraci et al., 2002b)

As already mentioned, the crest elements start to move earlier than the elements on the slope (Figure 7). It was observed that the stability behaviour of the crest elements was clearly dependent on the relative freeboard Rc/Hs.

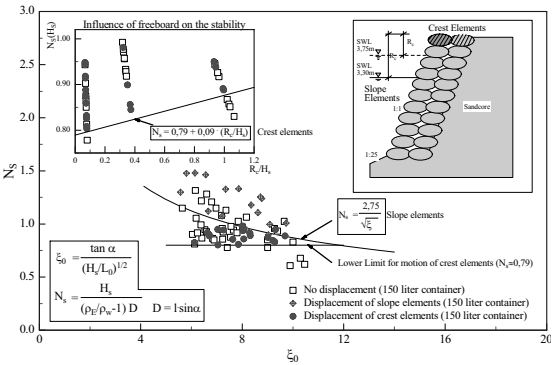

Figure 7. Stability of sand containers at slope crest-Test phase I (Oumeraci et al., 2002b)

From these observations a linear relation of the stability number N_s from the relative freeboard R_c/H_s was obtained:

$$N_s = \frac{H_s}{(\rho_E/\rho_W - 1)\cdot D} < 0,79 + 0,09 \cdot \frac{R_c}{Hs} \qquad (2)$$

where Rc = freeboard [m].

TEST PHASE II WITH SAND CONTAINERS (25 LITERS)

In general, a similar behaviour of the small sand containers as compared to the 150 l sand containers was observed, i.e. the crest elements started to move earlier than the slope elements (Figure 8).

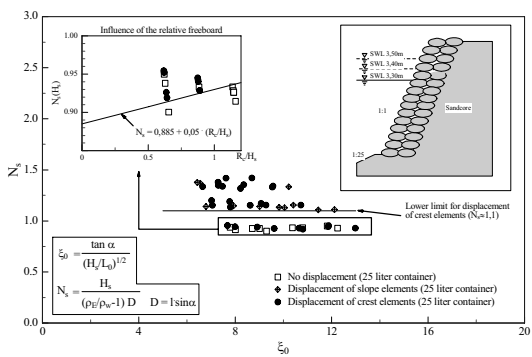

Figure 8. Stability of sand containers in test phase II (Oumeraci et al., 2002b)

No wave period effect on the stability could be observed for the stability number N_s for the slope elements.

$$N_s = \frac{H_s}{(\rho_E/\rho_W - 1)\cdot D} < 1,1 \qquad (3)$$

A more detailed analysis of the movement of the crest elements has shown that a similar relationship between stability number N_s and relative freeboard R_c/H_s exists:

$$N_S = \frac{H_S}{(\rho_E / \rho_W - 1) \cdot D} < 0{,}885 + 0{,}05 \cdot \frac{R_c}{H_S} \quad (4)$$

Comparing these results with the results found with 150 l sand containers the smaller containers are relatively more stable.

TEST PHASE WITH VELCRO TAPES

In test phase III, each layer of sand containers was connected to the neighboring layer by means of a self-adhesive Velcro tapes which were fixed approximately at the front one third of the higher layer.

Generally, it was found that the velcro tapes increase the stability of the sand containers considerably (Oumeraci et al., 2002b).

Moreover it was observed that the filling material is removed from the front part of the containers to the back part. Consequently, the front parts of the containers were folded backwards up to the position of the Velcro tapes, but still kept in position.

The effect of Velcro tapes should however not be overestimated since the percentage of fastened container length was rather high due to the width of the fixation belts used. Furthermore, there is a strong need to carefully fix the belts. When re-using the Velcro tapes the fastening characteristics significantly decrease. Generally, new Velcro tapes should be used.

CASE STUDY

HOUSE "KLIFFENDE", GERMANY

After a series of storm tides in 1990 which had caused severe erosion problems at the western coast of the island Sylt in Germany the historical house “Kliffende“ was at risk to being lost to the sea during further tidal storm surges. The authorities rejected hard rock structures such as concrete revetments at these natural sandy beaches. On this basis, the consulting engineers (Knabe + Knabe, Germany) developed a new system consisting of geotextile sand cushions (wrapped sand into geotextiles).

The installed geotextiles fulfill two requirements. On the one hand the geotextiles function as a filter-effective protection against sediment wash-out and on the other hand the terraced layered geotextiles work as reinforcement for stabilization of the dune embankment.

The construction required knowledge about the hydrodynamic loads. In combination with beach nourishment this soft coastal construction was designed as “second defense line“and sand should cover the structure again after severe eroding storm periods:

According to Figure 9 the achieved total height of the construction is 8 m (inclinations of V:H = 1:2 and V:H = 1:4).

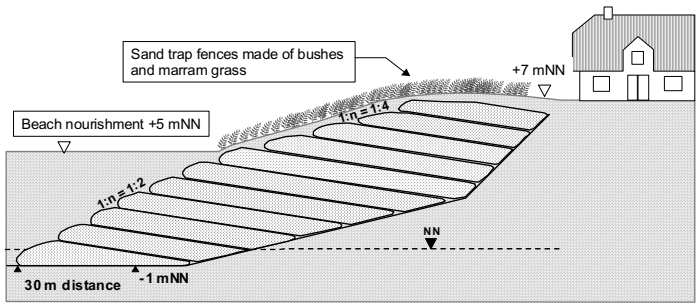

Figure 9: Island Sylt, 1990, Invisible dune reinforcement with wrapped-around geotextile sand cushions as second line of coastline erosion defense

A stability analysis was conducted by the BAW Germany (Federal Waterways Engineering and Research Institute) and was based on the decisive load case for possible deformations resulting from down drift waves with the pore-water pressures acting from the inside of the structure. In order to achieve a quick relaxation towards the front of the construction, it was necessary to match the permeability of the sand, the permeability and drainage effect of the geotextiles.

As biological accompanying measures, sand trap fences made of bushes were put up and beach grass served as stabilization. Thus, the construction looked like a natural dune and survived the winter storms of the last nearly 20 years despite repeated exposure and direct wave attack.

A needle-punched composite consisting of a polypropylene slit film woven and a polyester nonwoven was selected. The seaward faces of the sand cushions were accurately formed with the aid of temporary concrete shuttering elements. Parts of beach nourishment were mechanically re-deposited on the geotextile sheets and compacted. The geotextile sheets were folded up and back. The sand cushions are laid on top of each other to form a stabilized beach section.

The soft geotextile structure proved worthwhile several times during winter storms in 1993/94 and was exposed during these storm tides, but not severely damaged (Figure 10). These sand cushions even survived the second largest storm surge in December 1999, showing superior effectiveness compared to all other structures being used on the island. Thus the geotextile soft coastal structure survived storm surges with a still water level at 2.5 m above normal and severe wave action which could reach more than 5.0 m.

Figure 10: After storm surges in the year 2000, the second defense line is exposed to wave attack again since construction in 1990

JETTY "MUARA KARANGSONG", INDRAMAYU-CIRABON, INDONESIA

Under the direction of the Ministry of Public Works, West Java, Indonesia, it was planned in 2004 to rehabilitate a heavily eroded jetty (Figure 11), which was originally used as docking station for local fishermen.

Figure 11: Old Jetty – heavily eroded

The design for the rehabilitation of the old jetty considered the use of rock as core fill and riprap, stabilized in wire baskets, as cover layer in the slope area. In addition to a very tight project budget, problems with regard to the availability of rock, which was needed to construct the core of the jetty, occurred. The fact that quarries were only available hundreds of kilometers away from the site opened the existing design for alternative solutions. For these reasons an alternative solution was finally selected, which was based on the theory of encapsulating on-site available soil using nonwoven geotextile (600 g/m^2) sand containers.

Soft soil layers underneath the new jetty were improved by using 4m long wooden piles, which were driven down to the firm subgrade. The piles, which had a diameter of approx. 0.1 m were arranged in a triangular pattern with horizontal pile distances of about 1m. On top of the wooden piles a working platform made of a laid and welded geogrid in combination with the first layer of sand containers was created. Altogether approx. 15,000 geotextile containers with a filling volume of 0.6 m^3 were installed. Figure 12 shows the installation of aggregate subbase material for the final access road on top of the jetty.

Figure 12: Installation of aggregate for access road on top of geotextile sand containers

By using geotextile sand containers as core fill, the stability of the whole structure is ensured, as the geotextile component acts as a filter and separator to the coarse riprap cover layer, which prevents erosion in the long run. The alternative design reduced the planned construction time compared to the conventional solution and most important the total costs were nearly half of the original budget.

CONCLUSION

Geotextile nonwoven sand containers as "soft rock structures" for flexible coastal protection measures provide significant advantages over "hard coastal structures" made of concrete, steel and rocks. Geotextile "soft rock structures" are variable or even removable if necessary and they can easily be combined with conventional elements like rip-rap or rock revetments. Geosynthetic solutions provide greater efficiency relating costs, time and equipment if compared to conventional methods

Investigations on the long-term resistance of up to 21 years installed geotextiles in hydraulic applications at the German North Sea have shown, that they will survive typical stresses and maintain their functions (filtration,

separation & reinforcement) over the desired design life of approx. 30 to 50 years, if they are properly designed and installed.

The analysis of large-scale model tests in the Large Wave Flume of Hannover (GWK) has allowed identifying the most heavily loaded parts of sand container barrier systems. It could be shown that the stability of the crest elements is generally dependent on the relative freeboard and the corresponding design weight, whereas the stability of the slope elements is mainly governed by the wave height, the wave period and the slope of the structure. The latter has a major influence since it directly affects the degree of overlapping of the slope elements. Subsequently, the length of the sand containers should be large enough to ensure a proper overlapping.

The "fixation" of the sand container by self-adhesive Velcro tapes resulted in a substantial stability increase. Due to the type of fixation used in the tests which is associated with a large "fixation area", caution is recommended when trying to transfer these results to other conditions in prototype.

REFERENCES

Heerten, G. 1980. Long-term experience with the use of synthetic filter fabrics in coastal engineering. Proceedings of the 17. Conference on Coastal Engineering, Sydney

Oumeraci, H.; Bleck, M.; Hinz, M., 2002a. Untersuchungen zur Funktionalität geotextiler Sandcontainer. Berichte Leichtweiß-Institut für Wasserbau, Technische Universität Braunschweig, Nr. 874, Braunschweig, Germany, unpublished (in German).

Oumeraci, H.; Bleck, M.; Hinz, M.; Kübler, S.. 2002b. Großmaßstäbliche Untersuchungen zur hydraulischen Stabilität geotextiler Sandcontainer unter Wellenbelastung. Berichte Leichtweiß-Institut für Wasserbau, Technische Universität Braunschweig, Nr. 878, Braunschweig, Germany, unpublished (in German)

Oumeraci, H.; Bleck, M.; Hinz, M.; Möller, J.. 2002C: Theoretische Untersuchungen zur Anwendung geotextiler Sandcontainer im Küstenschutz. Berichte Leichtweiß-Institut für Wasserbau, Technische Universität Braunschweig, Nr. 866, Braunschweig, Germany, unpublished (in German).

STABILITY OF SINGLE-LAYER CONCRETE ARMOUR UNITS ON THE CREST OF LOW STRUCTURES

Nicolas Garcia and Arnaud Sallaberry[1]

A study of the stability of single-layer concrete armour units placed on wide horizontal berms has been conducted, in the frame of the Busan-Geoje (South Korea) fixed link project. The structure in study is part of the immersed tunnel protected with CORE-LOC™ and ACCROPODE™ II units. Placing methods have been tested in dry conditions at a scale ~1:10-1:8, with the aim of analysing packing density and quality of unit placement. The hydraulic stability of the armour units under different wave conditions was verified in 3D model tests at a scale ~1:69.

CONTEXT AND PURPOSE OF THE STUDY

The advantages of complex single-layer concrete units for breakwater armouring are well known and recognised, together with the peculiarities of the behaviour of these units under wave attack compared to conventional two-layer systems. The response under wave attack of armour slopes made of complex single-layer concrete units has been assessed through a number of physical model test studies, but the behaviour of these units placed horizontally on the crest of submerged or highly overtopped structures has not been much investigated. In the context of an increasing demand for low-crested structures, among which structures armoured with single-layer systems, an analysis of the placement and of the hydraulic stability of single-layer concrete units on horizontal berms in the frame of a real-world project is presented here.

This research has been conducted in the frame of the Busan-Geoje fixed link project, designed by COWI (Denmark) for the Daewoo Company (South Korea). The project consists of the construction of a fixed link between the Busan city and the Geoje Island in South Korea. This link will consist of two bridges and an immersed tunnel. The structure being studied here is the protection of the tunnel made of CORE-LOC™ and ACCROPODE™ II units of different sizes (5 m^3 CORE-LOC™ units, 11, 15 and 20 m^3 ACCROPODE™ II units) and including large flat areas, with a width varying from approximately 30 m up to 100 m.

The objective of the study is to investigate the placing method and the hydraulic stability of the single-layer armour units on this wide horizontal berm.

DRY TESTS

The first step of the analysis has consisted in dry tests on the placement of large model units, conducted at the Laboratory of SOGREAH (near Grenoble,

[1] SOGREAH Consultants, 6, Rue de Lorraine, 38 130 Echirolles, France.
nicolas.garcia@sogreah.fr

France) on two types of units: 35 kg ACCROPODE™ II and 22 kg CORE-LOC™ units, corresponding to scales between 1:10 to 1:8 for the unit sizes considered for the project and indicated above. The objective of the dry tests was to investigate different types of placement, to analyse the resulting packing density and quality of unit placement and eventually to define the placing methodology for both the hydraulic laboratory tests and the construction on site.

Figure 1. Dry tests on armour unit placement (~1/8, 1/10 scale): tests on 35 kg ACCROPODE™ II units.

The tests were performed on an existing flat concrete platform covered by stone material representing the underlayer (see Figure 1). The units were placed using a gantry crane equipped with an electrical hoist. A rotating semi-automatic release hook, equipped with a cable sling, was used. The units were placed on the testing area according to specific theoretical (X, Y) coordinates. A first series of tests has consisted in placing the units seeking the highest possible packing density, interlocking them by hand, to assess the maximum theoretical value of packing density. The second series of tests has consisted in placing the units with the crane according to the theoretical pre-defined coordinates. With the aim of reproducing as much as possible the site conditions, the units were placed using a sling, comparing good/low visibility conditions, including or not the possibility to control the orientation of the unit being placed and a lateral pulling of the units by crane. Two placing methods were investigated: a random

placement and a systematic placement (all the units placed with the same orientation). Except for the unit orientation for the latter method, both methods followed the ACCROPODE™ II and CORE-LOC™ placing method standards defined by CLI (Concrete Layer Innovations, Tours, France). The packing density was measured at the end of each test, taking into account the surface area of placement and the total number of placed units, and compared to the theoretical value.

The tests have shown that both methods could be suitable for the placement on wide flat areas of the tunnel protection. The analysis of packing density and risks of unit rocking led to the validation of the standard grid for the random placement and the definition of a slightly modified grid for the systematic placement. Recommendations were made for the building of the rock underlayer and the use of systems for unit orientation and positioning. Full scale tests were performed on a dry test area on site to complement and verify the outputs of the scale model tests, and the systematic placement mode was chosen on site for building the root area of the structure (see Figure 5).

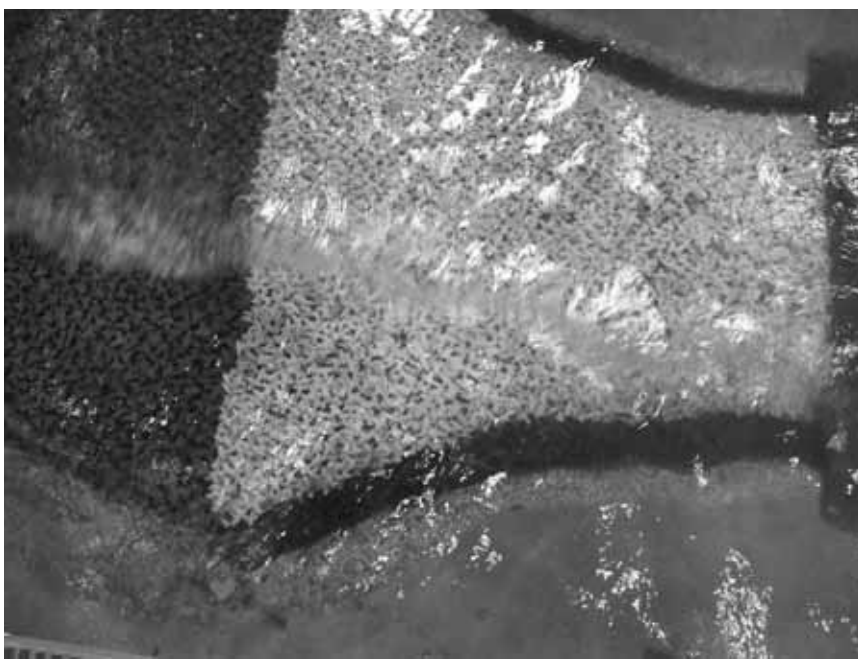

Figure 2. 3D physical model tests on hydraulic stability (1/69 scale): top view of the immersed tunnel, CORE-LOC™ armour layer.

3D HYDRAULIC MODEL TESTS

Subsequently to the dry tests, a hydraulic model of part of the Busan-Geoje fixed link project was studied in one of the wave basins of the Laboratory of SOGREAH. The model tests, at a scale of 1/69, were mainly aimed at verifying the stability of the tunnel's protection in concrete units. The complete surrounding bathymetry, topography (including islands and cliffs) and structure under study were reproduced. The two types of placement investigated during the dry tests were considered: a systematic placement of the units at the root of the tunnel's protection, where the structure is mostly emergent, and a random placement for all the remaining parts.

Figure 3. 3D physical model tests on hydraulic stability (1/69 scale): top view of the immersed tunnel, ACCROPODE™ II armour layer.

Irregular wave tests were conducted, with one wave direction (corresponding to a 15° incidence offshore with respect to the tunnel's main axis) and five wave conditions. The design significant wave height is 8.7 m for a peak period of 16.2 s. Overload conditions, with significant wave height and peak periods up to 10.7 m and 20.1 s were also tested. Three water levels were considered: 0, -1.55 and -1.72 m MSL. The minimum seabed level in front of the structure is -20 m approx. The structure's freeboard varies from +1 m at the root to -13 m. The methodology for the assessment of the stability of the modelled structure has consisted of visual observations supported by analysis of photographs. A total of ~4000 model units were placed on the model. The key stability parameters of the study were unit settlement, extraction and rocking. The 3D tests have shown a satisfactory stability of the armour units, placed either systematically or randomly, on the wide horizontal berm, even under critical overload wave conditions. These units, submitted to strong breaking-induced leeward flows in a region where gravity does not contribute to improve the interlocking, were proved to behave well, for all the tested wave conditions and water levels.

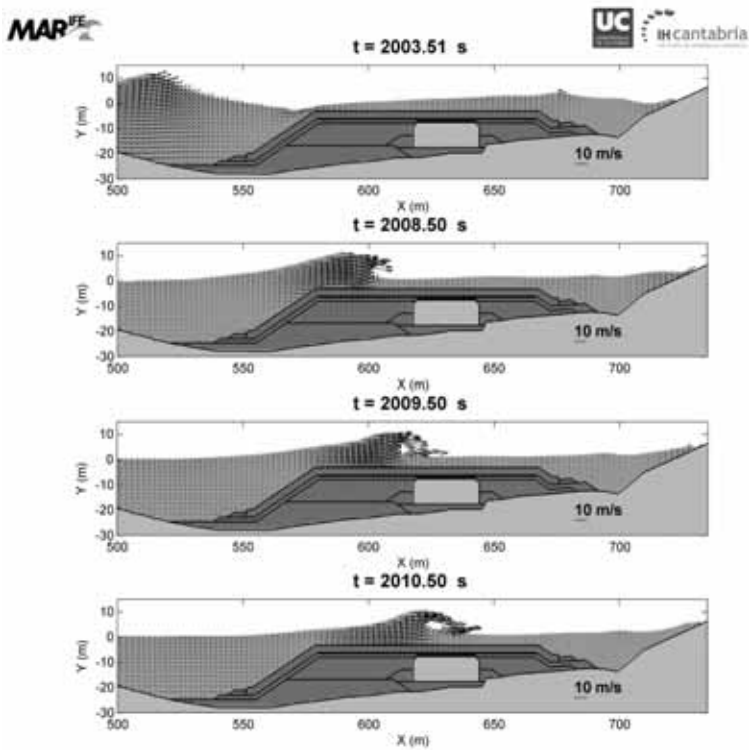

Figure 4. Numerical simulation of wave/structure interaction. Computed instantaneous velocity field under wave breaking conditions.

To complement the physical model tests, a numerical simulation was performed with the 2D VOF-type COBRAS-UC code (Losada *et al.*, 2008) in order to characterize in a 2D approximation the breaking-induced flow conditions on the horizontal berm. The COBRAS-UC code has been validated for the analysis of wave interaction with different kinds of coastal structures, including submerged structures, see e.g. Garcia *et al.* (2004). Figure 4 shows snapshots of the computed instantaneous velocity field at breaking around the structure, for a section located near the interface between the CORE-LOC™ and the ACCROPODE™ II units (respectively white and dark model units on Figures 2 and 3). The crest's width is ~90 m wide. The simulation, performed at real scale on the 100-year wave conditions (Hm0 = 8.7 m, Tp = 16.2 s) and a water level of -1.55 m giving a structure's freeboard of -5.6 m, showed that horizontal velocities up to 10 m/s could be achieved on the horizontal berm under these conditions.

The physical model tests also demonstrated 3D effects that caused unit movements on the leeward half of the crest and leeside slope of the structure. In that region, complex flow conditions resulting mainly from the combination of the horizontal flow above the crest and lateral currents related to the water piling-up behind the structure took place. Still, no units were extracted out of the armour layer and a very limited number of rocking units on the wide flat area of the protection was registered. Minor losses of packing density in the leeward half of the crest's width were observed. A few unit extractions due to wave concentration effects took place in the sloping seaward area of the structure close to the root, which led to the replacement of a small percentage of the 15 m^3 units by 20 m^3 ACCROPODE™ II units. Another key aspect of the hydraulic tests was to verify the stability of the transitions between units of different types and sizes, which proved to be satisfactory, including on the horizontal berm.

Figure 5 illustrates the ongoing construction works, and in particular the systematic placement (carried out from sea with barges) of 15 m^3 ACCROPODE™ II units.

Figure 5. In situ systematic placement of ACCROPODE™ II units at the root of the structure.

ACKNOWLEDGMENTS

The numerical investigation was carried out by Dr Javier L. Lara of IH Cantabria (Santander, Spain).

REFERENCES

Garcia N., Lara J.L., Losada I.J. (2004). 2D numerical analysis of near-field flow at low-crested breakwaters. Coastal Engineering, 51: 991-1012.

Losada I.J., Lara J.L., Guanche R., Gonzalez-Ondina J.M. (2008). Numerical analysis of wave overtopping of rubble mound breakwaters. Coastal Engineering, 55 (1): 47-62.

COMPARISON OF SEDIMENT TRANSPORT FORMULAE REGARDING ACCELERATED SKEWED WAVES

Tiago Abreu[1], Paulo Silva[2], Francisco Sancho[3]

As waves travel and shoal towards a beach, their surface elevation becomes peaky (sharp crests) and asymmetric relative to the vertical. Within a wave period, the flow acceleration shows an asymmetry, which is responsible for onshore net sediment transport. This work presents a comparison of different sediment transport formulae with a new set of experimental data in accelerated skewed waves. Some experiments have a collinear net current, opposing the wave direction. The performance and accuracy of the sediment transport formulae in predicting sediment fluxes are analysed. Results indicate that most formulae perform reasonably well (within a factor of two), with the model of Soulsby and Damgaard (2005) being the most accurate for the majority of the flow conditions.

Introduction

As waves travel and shoal towards a beach, their surface elevation becomes peaky (sharp crests) and asymmetric relative to the vertical. Within a wave period, the corresponding orbital velocity near the bottom shows a similar (time) variation. Under the steep front face, between the past wave trough and the following wave crest, the velocity varies rapidly from a maximum negative (offshore) value to a maximum positive (onshore) value, giving rise to rapid fluid accelerations. The accelerations during the rear face are smaller due to a slower variation in the velocity. This asymmetry in the flow acceleration as been recognized as responsible for onshore net sediment transport (eg., King, 1991; Elgar *et al.*, 2001; Watanabe and Sato, 2004; Houser and Greenwood, 2007). Though the importance of accelerated skewed waves is acknowledged, a very scarce number of experiments have been performed (e.g., King, 1991; Dibajnia and Watanabe, 1998; and Watanabe and Sato, 2004). As measurements in the field in and above the wave boundary layer concerning sand transport are very difficult to acquire, experiments in facilities like wave flumes or water tunnels are usually carried out. To fulfill the lack of data on the sediment transport rates in the sheet flow under accelerated skewed waves, a new series of experiments were performed by Silva *et al.* (2008) in the Large Oscillating Water Tunnel (LOWT) of WL|Delft Hydraulics.

[1] Civil Engineering Department, Polytechnic Institute of Viseu, ESTV Campus de Repeses, Viseu, 3504-510, Portugal
[2] University of Aveiro & CESAM, Physics Department, Campus de Santiago, Aveiro, 3810-193, Portugal
[3] LNEC-DHA, National Civil Engineering Laboratory, Av. do Brasil, 101, Lisboa, 1700-066, Portugal

The knowledge and description of the hydrodynamics and sediment transport in the nearshore zone is very important to coastal managers dealing with morphological problems. Their work relies increasingly on models of sand transport and morphology that can predict with accuracy the sediment dynamics. In this study the attention is focused on how different existing practical sediment transport formulae perform in comparison with the net sediment transport rates obtained from the new set of laboratory data.

"TRANSKEW" Experiment

Under storm conditions high near-bed orbital velocities and shear stresses are created near and inside the surf zone. If shear stresses are high enough to move a layer of bed-load particles in a thin layer (thickness on the order 10mm), the so-called sheet-flow regime is attained. In this layer, extremely large sediment concentrations develop and the combination of large sediment concentrations and velocities can cause high sediment transport rates.

In the Large Oscillating Water Tunnel (LOWT) of WL|Delft Hydraulics a new series of experiments in sheet flow conditions, under accelerated skewed waves, was performed by Silva *et al.* (2008). The tunnel as the shape of a U-tube, consisting of a long (14m) rectangular horizontal section connected to a vertical cylinder at each end (Figure 1). The tunnel was designed for full-scale simulation of the near-bed horizontal oscillating water motion, which can be combined with a steady current. The desired motion in the test section is created by the movement of the piston in one of the cylinders. Detailed descriptions of the facility can be found in Ribberink and Al-Salem (1994).

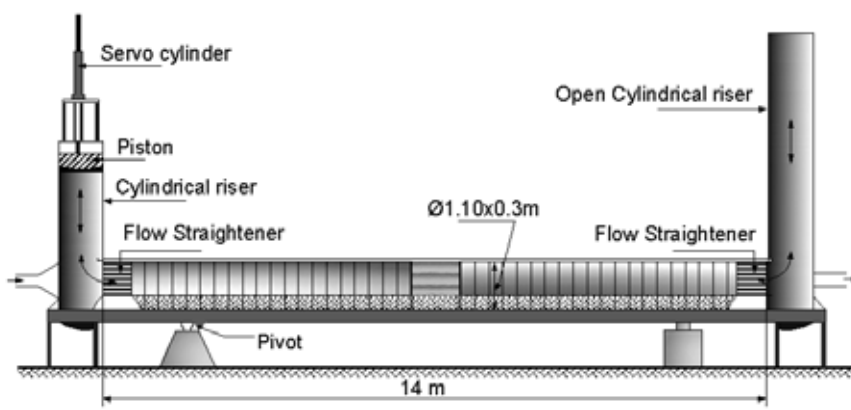

Figure 1. General outline of the wave tunnel.

The purpose of the present experiments was to obtain measurements of the net transport rates in certain hydraulic conditions. These consisted on a repetition of regular oscillatory flows with the same velocity root-mean-square

value ($U_{rms} \approx 0.9\,m/s$), different wave periods ($T = 7$ and 10s), different velocity and acceleration asymmetries (R and β, defined below) and different superimposed net currents (opposite to the wave propagation direction). R is the velocity skewness, defined as $R = u_{max}/(u_{max} - u_{min})$, where u is the flow velocity, and β is the acceleration skewness, $\beta = a_{max}/(a_{max} - a_{min})$, where a is the flow acceleration.

Table 1 synthesizes the characteristics of the several experiments performed:

- Series A (A1 to A4) consisted of regular oscillatory flows with different degrees of acceleration skewness;
- Series B (B1 to B4) considered acceleration-skewed oscillatory flows with a collinear net current, opposing the wave direction;
- Series C (C1 to C3) considered both velocity- and acceleration- skewed oscillatory flows.

The bottom of the tunnel was covered with a 30 cm layer of well-sorted sand with a median diameter of $d_{50} \approx 0.20mm$

Table 1. Hydraulic characteristics obtained for the test conditions

Condition	U_{rms} (m/s)	β	R	T (s)	U_0 (m/s)
A1	0.90	0.64	0.50	7	0.00
A2	0.88	0.63	0.49	10	0.00
A3	0.88	0.72	0.50	7	0.00
A4	0.86	0.72	0.49	10	0.00
B1	0.89	0.64	0.50	7	-0.22
B2	0.88	0.64	0.50	7	-0.44
B3	0.86	0.71	0.50	7	-0.22
B4	0.86	0.71	0.51	7	-0.44
C1	0.86	0.61	0.59	7	0.00
C2	0.94	0.60	0.59	10	0.00
C3	0.87	0.53	0.59	7	0.00

The flow velocity measurements (u) above the wave boundary layer were performed using an Electromagnetic Flow Meter (EMF). The sampling frequency was 100Hz and the signals were collected 30cm above the bed. As an example, in Figure 2, the target velocity time series for Tests A1, B1 and C1 are shown against the ensemble-averaged and low-pass filtered measured values by the EMF. It can be verified that the target velocities were accurately reproduced inside the LOWT. The corresponding acceleration time series were obtained by numerical differentiation of the filtered velocity time series, and are also plotted in Figure 2. The accelerations obtained by this procedure are local accelerations at each point $(a = \partial u/\partial t)$.

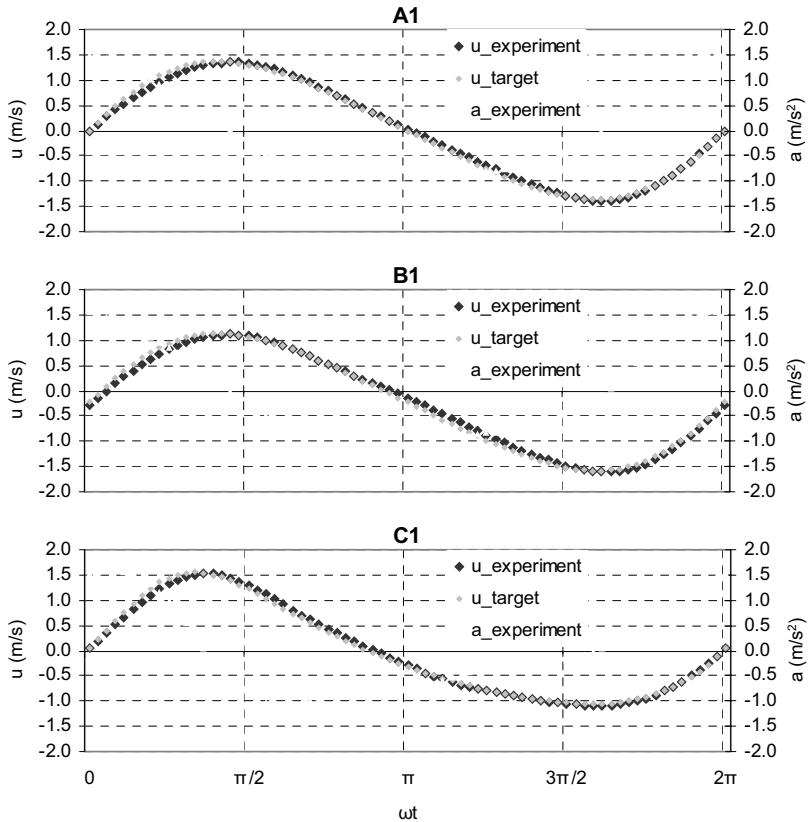

Figure 2. Time series of the measured (ensemble averaged) and target velocities, and the corresponding accelerations for the experimental conditions A1, B1 and C1.

Sediment Transport Models

Different formulations found in the literature were applied to the hydrodynamic conditions described in Table 1 in order to verify its ability to predict the net sediment transport rates in accelerated, skewed, oscillatory motions. The measured and predicted transport rates are non-dimensionalized by:

$$\Phi = \frac{q_s}{\sqrt{(\rho_s/\rho - 1) g {d_{50}}^3}}, \tag{1}$$

where q_s is the net sediment transport rate, ρ and ρ_s represent the water density and sediment density, respectively, and g is the gravitational acceleration.

These formulations are briefly described in the following. Further details can be found in the original papers.

Meyer-Peter-Müller (1948)

The well known Meyer-Peter and Müller's (1948) bedload formula, based in the Shields parameter, θ, was selected for this study as a reference:

$$\Phi(t) = 8\left[\theta(t) - \theta_{cr}\right]^{3/2} \frac{\theta(t)}{|\theta(t)|}, \qquad \theta(t) > 0.05 \cdot \tag{2}$$

The Shields parameter $\theta(t)$ is defined by $\theta(t) = \tau_0(t)/(\rho(\rho_s/\rho - 1)gd_{50})$, where $\tau_0(t)$ is the instantaneous bottom shear stress. This is computed as a function of the free stream velocity, u_∞:

$$\tau_0(t) = \frac{1}{2}\rho \, \mathrm{f} \, |u_\infty(t)| \, u_\infty(t) \tag{3}$$

where *f* represents the friction parameter. In Equation (2) θ_{cr} is the critical value of θ, at the threshold of motion. A value of $\theta_{cr} = 0.05$ is typical for the present sediments. This formulation supports, like other practical sediment transport models, that the bottom shear stress is the most important parameter input for sediment transport computations. However, the Meyer-Peter and Müller's formulation provides a zero net transport rate for the pure accelerated skewed waves, as the one depicted in figure 3 (Series A), because the maximum and minimum absolute values of the velocity are equal.

Nielsen (2006)

The limitation presented with Meyer-Peter and Müller's (1948) formula took several investigators to introduce some modifications. As an example, Nielsen (2006) has incorporated the combined effect of the bottom shear-stress, proportional to u_∞, and the pressure gradient, proportional to the near-bed flow acceleration, in the computation of a sediment mobilizing velocity which is considered in Equation (3). This results in a more precise estimation of the Shields parameter. The agreement of the phase difference between bottom shear stress and the free stream velocity ($\varphi = 51^o$) concerning the Watanabe and Sato (2004) data was also considered in his work. Nielsen's formulation to calculate the instantaneous transport rate can be written as:

$$\Phi(t) = 12\left[\theta(t) - \theta_{cr}\right]\theta(t)^{1/2} \frac{\theta(t)}{|\theta(t)|}, \qquad \theta(t) > 0.05 \cdot \tag{4}$$

Drake and Calantoni (2001); Hoefel and Elgar (2003)

Drake and Calantoni (2001) have suggested a modification of the classical formulations of the energetics-type sediment transport models (Bagnold, 1963, Bowen, 1980, and Bailard, 1981, models) to incorporate the acceleration effects (q_{ba}). According to Drake and Calantoni, the bed load (q_b) is given by:

$$q_b = k\langle u^3 \rangle + q_{ba}, \tag{5}$$

with

$$q_{ba} = \begin{cases} K_a \left(a_{spike} - a_{cr} \right) & , a_{spike} > a_{cr} \\ 0 & , a_{spike} < a_{cr} \end{cases}. \tag{6}$$

The angle brackets denote a time averaging and a_{cr} is the critical value of a_{spike} that must be exceeded before acceleration enhances transport. This acceleration descriptor can be calculated in terms of the near-bed statistic moments of the acceleration ($a_{spike} = \langle a^3 \rangle / \langle a^2 \rangle$). The values of K_a and a_{cr} were determined by fitting the computed sediment transport rates with the ones obtained with a discrete-particle model simulations in sheet flow, yielding: K_a= 2.64×10^{-5} ms and a_{cr}= 1 m/s^2.

Hoefel and Elgar (2003) have extended Equation (5) to account for random waves and take into account the sign of a_{cr}:

$$q_{ba} = \begin{cases} K_a \left(a_{spike} - a_{cr} \times \left(a_{spike} / \left| a_{spike} \right| \right) \right) & , \left| a_{spike} \right| > a_{cr} \\ 0 & , \left| a_{spike} \right| < a_{cr} \end{cases}. \tag{7}$$

Through the comparison of model results with observed data (Duck94 field campaigns) they have determined the optimal values of K_a = 1.4×10^{-4} ms and the critical threshold a_{cr}=0.2 m/s^2.

Soulsby and Damgaard (2005)

Soulsby and Damgaard (2005) analysed the general form of some formulae applied to compute the bedload transport and derived a number of analytical formulae for the cases of current alone, current with sinusoidal waves and current with asymmetric waves.

The algebraic approximation for the net transport by a steady current superimposed on asymmetrical waves can be predicted according to the following equations:

$$\Phi = max\left(\Phi_{x1}, \Phi_{x2} \right) \tag{8}$$

with

$$\Phi_{x1} = A_2 \theta_m^{1/2} \left(\theta_m - \theta_{cr} \right), \tag{9}$$

and

$$\Phi_{x2} = A_2\left(0{,}9534 + 0{,}1907\cos\left(2\phi\right)\right)\theta_w^{1/2}\theta_m + A_2\left(0{,}229\Delta\cdot\theta_w^{3/2}\cos\left(\phi\right)\right)\cdot \quad (10)$$

In these equations, A_2 is a coefficient normally considered in the range of 8 and 12 (here assumed to be 10, equal to the default value proposed in Soulsby and Damgaard's conclusions), θ_m is the modulus of the time-mean Shields parameter, θ_w is the amplitude of the oscillatory part of the Shields parameter, ϕ is the angle between the wave propagation and the current direction and Δ is the ratio between the amplitude of the second harmonic, $\theta_{w,2}$, and the amplitude of the basic harmonic, θ_w. Here the algebraic approximation of the Soulsby and Damgaard (2005) model is validated for the case of asymmetrical waves with a current with the "TRANSKEW" data. The particular case of asymmetric waves without a current is obtained by setting $\theta_m = 0$ in either Eq. (9) or (10).

Silva et al. (2006)

Silva *et al*. (2006), based in the work of Dibajnia and Watanabe (1992), developed a semi-unsteady, practical model, to predict the total sediment transport rates in wave or combined wave-current flows. The predicted transport rates, Φ, are computed from:

$$\Phi = \alpha\ |\Gamma|^{\beta}\frac{\Gamma}{|\Gamma|} \quad (11)$$

with

$$\Gamma = \frac{u_c T_c(\Omega_c^3 + \Omega_t'^3) - u_t T_t(\Omega_t^3 + \Omega_c'^3)}{u_c T_c + u_t T_t}. \quad (12)$$

In these equations T_c and T_t represent, respectively, the time duration of the positive and negative half cycle of the near bed velocity, *u(t)*, with equivalent velocities u_c and u_t (the subscript *c* stands for crest and *t* for trough). The quantities Ω_i and Ω_i' (i = *c, t*) represent, respectively, the amount of sediment which are entrained, transported and settled in the *i* half cycle, and the amount of sediment still in suspension from the *i* half cycle that will be transported in the next half cycle. The values of Ω_i are computed from the total bottom shear stress. The non-steady processes are taken into account through the exchange of sediment fluxes between the two half cycles (Ω_i' quantities). α and β are two empirical constants; their best values were determined by fitting the numerical solutions to a large data set, yielding $\alpha = 3.2$ and $\beta = 0.55$.

Results

The predicted net sediment transport rates from the models described earlier are compared in Figure 3 against the laboratory data. Note that in Meyer-Peter and Müller (1948) and Nielsen's (2006) formulae (equations 2 and 4) the computed transport rates are averaged over the oscillatory period T to retrieve the net transport rate. In Figure 3, the oblique non-diagonal lines define a region where the predicted transport is within 50 and 200% of the measured transport.

It is perceivable that, except the Meyer-Peter and Müller's (1948) formula, and despite some discrepancies in reproducing mainly the series A, the overall formulae are able to predict, almost within a factor of 2, the laboratory data. The comparison shows that the model of Soulsby and Damgaard (2005) performs generally better. It is followed by Nielsen's model which gives very close results. Both models underpredict the transport magnitudes in the presence of currents (tests B), though. The model of Silva *et al.* (2006) is particularly sensitive to small changes in the velocity, as shown for A2 and A4 results, predicting sediment transport in opposite direction relative to the measured one for those cases. The model of Hoefel and Elgar (2003) appears to slightly overestimate the transports. Results evidence that the Meyer-Peter and Müller's (1948) formula is unable to predict the transport rates for most cases of waves only (tests A and C), but performs well when a current is super-imposed on the wave motion (tests B).

Conclusions

In this paper the net sediment transport rates obtained in the Large Oscillating Water Tunnel (LOWT) of WL|Delft Hydraulics, under sheet flow conditions, are compared with predictions from five simple sediment transport models. The experiments performed in the tunnel contemplate different wave periods and different conditions of velocity and acceleration skewnesses. Also, superimposed net currents opposing the wave direction were tested.

The accuracy of some practical sediment transport formulae, useful in coastal applications, to the new available data is analyzed.

Models like Meyer-Peter-Müller (1948) fail to predict net transport rates under accelerated skewed waves (series A), and in combination with sharp-crested waves (series C).

The net transport rates computed from Hoefel and Elgar (2003), Soulsby and Damgaard (2005), Silva *et al.* (2006) and Nielsen (2006) models show an overall good agreement with the new experimental results, despite some discrepancies in reproducing mainly the results of series A.

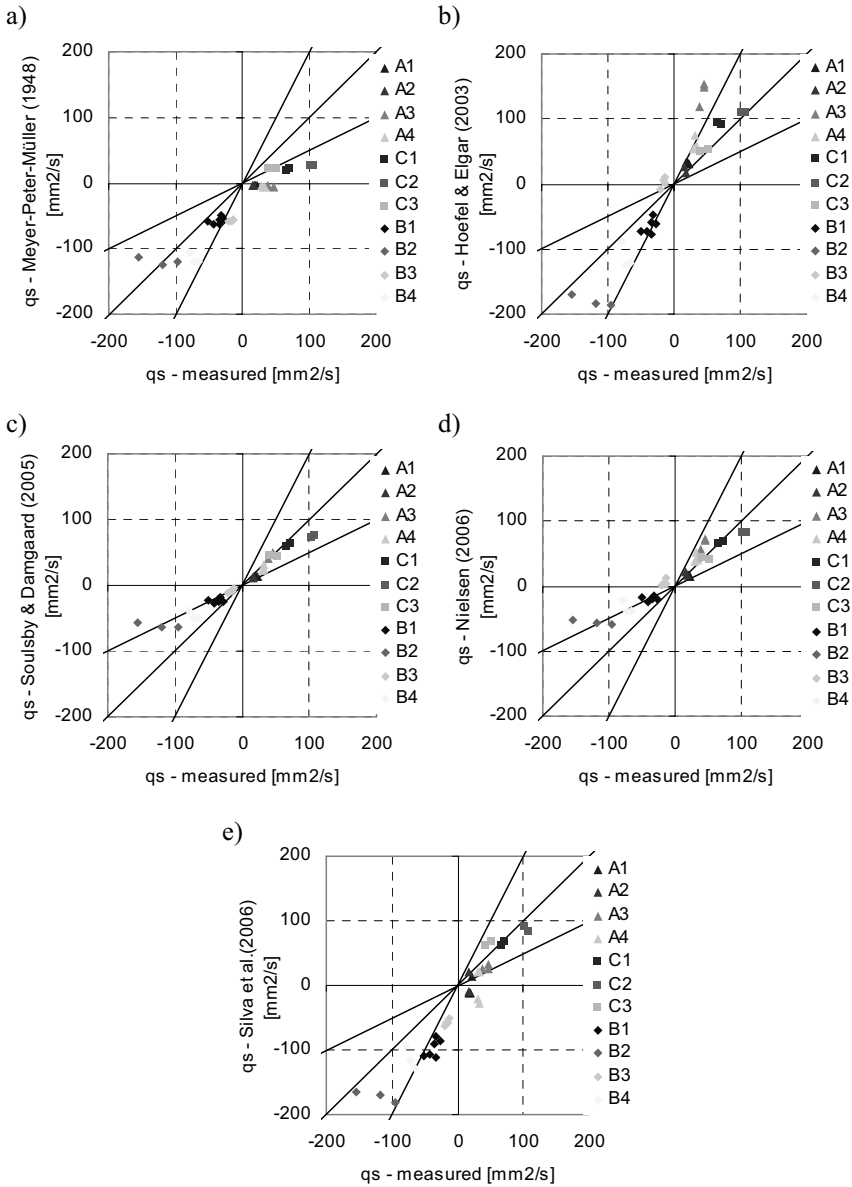

Figure 3. Comparison between measured and computed transport rates (a) Meyer-Peter-Müller (1948), (b) Hoefel and Elgar (2003), (c) Soulsby and Damgaard (2005), (d) Nielsen (2006) and (e) Silva *et al.* (2006). Envelope lines represent transports within a factor of ½ and 2.

All models (except Meyer-Peter-Müller) are able to predict onshore net transport rates only as a function of skewed accelerations. The effect of

increasing the acceleration skewness, the addition of an opposing net current and the added effect of velocity skewness on net sediment transport rates are also reasonable replicated by the models.

Finally, the model of Soulsby and Damgaard (2005) performs generally better, but underpredicts the transport magnitudes in the presence of currents, although it should be remarked that this model only computes bedload transport.

ACKNOWLEDGMENTS

The experimental work was supported by the European Community's Sixth Framework Programme through the grant to the budget of the Integrated Infrastructure Initiative HYDRALAB III, Contract no. 022441(RII3).

The first author of this work has been supported by FCT through a PhD grant (SFRH/BD/41827/2007).

REFERENCES

Bagnold, R. 1963. An approach of marine sedimentation, in: *Hill, M.N. (Ed.), The Sea*, vol. 3, Interscience, New York, 507–528.

Bailard, J.A. 1981. An energetics total load sediment transport model for a plane sloping beach, *Journal of Geophysical Research*, 86, C11, 10938-10954.

Bowen A.J. 1980. Simple models of nearshore sedimentation; beach profiles and longshore bars, in *The Coastline of Canada*, edited by S.B. McCann, Pap. Geol. Surv. Can., 80-10, 1-11.

Dibajnia, M. and Watanabe, A. 1992. Sheet flow under non-linear waves and currents. *Proc. 23rd Int. Conf. on Coastal Eng.*, 2015-2028.

Dibajnia and Watanabe 1998. Transport rates under irregular sheet flow conditions. *Coastal Engineering*, 35, 167-183.

Drake, T.G. and J. Calantoni. 2001. Discrete particle model for sheet flow sediment transport in the nearshore, *Journal of Geophysical Research – Oceans*, 106, C9, 19859-19868.

Elgar, S., E.L. Gallagher, R.T. Guza. 2001. Nearshore sand bar migration, *Journal of Geophysical Research*, 106, C6, pp. 11623-11627.

Hoefel. F. and S. Elgar. 2003. Wave induced sediment transport and sand bar migration, *Science* 299, 1855-1887.

Houser, C., B. Greenwood. 2007. Onshore migration of a swash bar during a storm, *Journal of Coastal Research*, 23, 1, 1-14

King, D.B. 1991. Studies in oscillatory flow bed load sediment transport, *University of California*, Ph.D. thesis, San Diego.

Meyer-Peter, E. and R. Müller. 1948. Formulas for bed-load transport, *Proc. 2nd Congress of the Int. Ass. Hydraulic Structures Research*, Stockholm.

Nielsen, P. 2006. Sheet flow sediment transport under waves with acceleration Skewness and boundary layer streaming, *Coastal Engineering*, 53, 749-758.

Ribberink, J.S. and A.A. Al-Salem. 1994. Sediment transport in oscillatory boundary layers in case of rippled beds and sheet flow, *Journal of Geophysical Research*, 99, C6, 12707-12727.

Silva, P., A. Temperville and F. Seabra Santos. 2006. Sand transport under combined current and wave conditions: a semi-unsteady, practical model, *Coastal Engineering*, 53, 897-913.

Silva, P., T. Abreu, P. Freire, G. Kikkert, H. Michallet, T. O'Donoghue, S. Plecha, J. Ribberink, G. Ruessink, F. Sancho, K. Steenhauer, A. Temperville, D. Van der A., J. Van der Werf. 2008. Sand transport induced by acceleration-skewed waves and currents – The TRANSKEW project, *PECS08 – Physics of Estuaries and Coastal Seas*, Liverpool, UK.

Soulsby, R.L. and J.S. Damgaard. 2005. Bedload sediment transport in coastal waters, *Coastal Engineering*, 52, 673 – 689

Watanabe, A. and S. Sato, 2004. A sheet flow transport formula for asymmetric forward-leaning waves and currents, *Proceedings of 29th International Conference on Coastal Engineering*, Lisbon, Portugal, 1703-1714.

DETERMINING LITTORAL TRANSPORT RATE ON MIXED BEACHES USING AN IMPOUNDMENT TECHNIQUE

Inés Martín-Grandes[1], David J. Simmonds[2], Abdulla Kizhisseri[3], Andrew J. Chadwick[4], Dominic E. Reeve[5] and Mark Davidson[6]

The determination of the longshore sediment transport (LST) rate plays a fundamental role in any study related to the solution of coastal engineering problems. Detailed knowledge of the LST is necessary for the assessment of the beach evolution in response to the wave climate and due the presence of coastal protection structures. Amongst the most typical formulations that have been proposed to determine the LST rate are the well known CERC formula (SPM 1984), and those proposed by Kamphuis et al. (1986), Kamphuis (1991, 2002) and Bayram et al. (2007). However, most of these empirical equations have been derived from investigations related to sandy environments. In the UK gravel and mixed (gravel and sand) beaches are common coastal features along the South Coast and these have great significance for the protection of coastal communities and environmental and agricultural resources (Mason and Coates, 2001). Yet, only few research efforts have been carried out on this type of beaches (Chadwick 1989). In the present study, an impoundment technique has been employed to measure LST rates in a mixed (gravel-sand) beach with the aim of calibrating existing formulae for estimating the LST developed for sandy beaches.

INTRODUCTION

Coastal environments are natural systems susceptible to change under the actions of coastal processes and the development of communities in littoral boundaries. Indeed, the effect of climate change raises the vulnerability of coasts to damage. Nowadays more information about shoreline changes or beach morphodynamics is requested by local authorities to integrate sustainable activities within the environment under the frame of coastal management plans.

Beaches are the most efficient mechanism for protection the coast and their configuration is the result of the balance between the action of waves and tides and the sediments moving along the coast. In the south of the UK mixed and shingle beaches are common features along the coast, but are less well understood than sandy environments despite being of considerable interest to coastal authorities (López de San Román-Blanco, 2003). Indeed, most empirical equations for longshore transport have been derived from investigations related to sandy environments (Chadwick 1989).

[1] Coastal Engineering Research Group, University of Plymouth, Drake Circus, Plymouth, Devon, PL4 8AA, U.K.
[2] Coastal Engineering Research Group, Drake Circus, Plymouth, Devon, PL4 8AA, U.K.
[3] Coastal Processes Research Group, Drake Circus, Plymouth, Devon, PL4 8AA, U.K.
[4] Coastal Engineering Research Group, Drake Circus, Plymouth, Devon, PL4 8AA, U.K.
[5] Coastal Engineering Research Group, Drake Circus, Plymouth, Devon, PL4 8AA, U.K.
[6] Coastal Processes Research Group, Drake Circus, Plymouth, Devon, PL4 8AA, U.K.

Quantification of coastal sediment transport, specially the longshore sediment transport, LST, constitutes the most essential information for beach management in coastal engineering. Spatial and temporal changes in LST along a coastline are inextricably linked to beach profile changes over both the short and long term (Horikawa, 1988). Measurements of beach profiles are used to estimate variability in relation to meteorological forcing and to monitor the changes of beach volume and the shoreline position. The latter "line of demarcation between the water and the exposed beach" Komar (1976) is variously defined parametrically (Farris and List 2007).

In the work presented here, a field experiment has been executed to attempt to calibrate the CERC Equation (USACE, 1984) for a mixed beach. Other well known formulations for the sediment transport as Kamphuis (1991) and Van Wellen et al. (2000) will also be looked at.

Mixed beaches are complex systems where the hydrodynamic processes affect different due to the mixture of sediments and their hydraulic properties than pure sand or gravel beach (Kirk, 1980; Mason et al. 1997). Again examples of research into mixed beaches in terms of their dynamics and predictive tools for their behaviour are few and far between: Kirk, 1980; Mason et al., 1997; Mason et al., 2001; Bradbury et al., 2003; López de San Román-Blanco, 2003; López de San Román-Blanco et al., 2006; Buscombe et al., 2006. In these, there is much mention of the need for further research, including the calibration of existing methods derived from laboratory experiments or physical models.

We thus present our study of a mixed (gravel and sand) beach on the south UK coastline. The aim here is to measure the littoral transport and develop a modelling approach for understanding the longer-term shoreline behaviour at this beach.

FIELD SITE

The field site is Milford on Sea, located in Christchurch Bay (Hampshire, UK), see Fig. 1. The work forms part of a project, RF-PeBLE: Risk-based Framework for Predicting Long-term Beach Evolution. This stretch of coastline contains many typical coastal elements: cliff erosion to the western side near Barton on Sea; natural beach at Hordle Cliff; coastal defence structures comprising timber groynes and seawall between Milford on Sea and Hurst Spit. The coastline from Barton on Sea to Hurst Spit is also designated a Site of Special Scientific Interest (SSSI). Milford on Sea is a Coastal Area of Outstanding Natural Beauty (AONB) (SCOPAC, 2003). In terms of coastal planning, Milford is subject to New Forest District Council and is covered by the Solent Strategic Guidance Plans and Local Authority Coastal Management Plans.

A sediment transport study (SCOPAC, 2003) revealed the relative recent geological origin of Christchurch Bay. Its configuration has been formed by the coastline retreat during the mid to late Holocene transgression in the Quaternary Period. Sediment inputs come from cliff or coastal slope erosion of gravel, sand and clay and in general the littoral drift pattern is west to east transporting gravel

and sand in the bay. Also onshore-offshore sand transport is seen in Hordle Cliff.

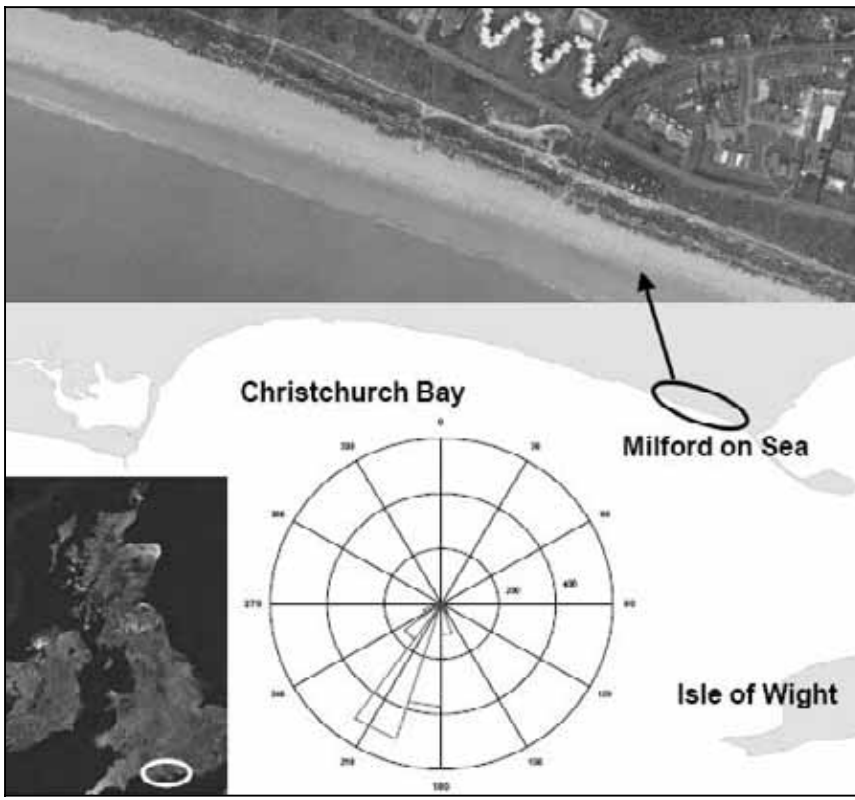

Figure1. Field site location, Christchurch Bay, South U.K. (Google; SANDS Database, Halcrow)

Focusing in on the Hordle Cliff beach , see Fig. 2, this can be seen to be of shingle and sand, dominated by an upper berm of coarse shingle which acts as the main toe protection for the cliffs. Well-defined cusps are often evident on this berm. Below the berm is a sandy terrace with a bar that is exposed at low tide. Two further bars are evident in energetic wave conditions.

The predominant wave direction is SSW and the mean tidal range of 2m is low in comparison with other coastal zones around UK. This and the double tide cycle may be due to the combination of shallow waters and the location near to an amphidromic point (Komar, 1976). During a tide the beach can be considered to move from being reflective at high tide to dissipative at low tide in line with Davidson et al's (2004) observations. This changes the nature of processes acting upon the berm and those acting on the lower terrace.

Coarse grained beaches are characterized by their narrow, high energy surf and swash zones over a steep, reflective beach face (Kirk, 1980). The reflective nature is related to the size and hydraulic properties of material. The permeability controls the beach slope, which in turn controls the breaker type, which is typically surging or plunging for mixed beaches (Van Wellen et al., 2000; López de San Román-Blanco, 2003). At low tide, dissipative conditions are evident with the wider surf-zone typical of a sandy beach.

Figure2. Milford on Sea: on the top, left-hand panel, sand bar exposed during spring tide; right-hand panel, experimental structure and cusps formed at the beach face; at the bottom, mixed sediments.

METHODOLOGY

In a review of the LST equations for gravel beaches, Van Wellen et al. (2000) point out the lack of data and information related to coarse and mixed beaches due to the limitations of deploying delicate instrumentation on energetic and erosive shingle shores. They noted only three studies of relevance: Nichols and Webber (1987) and Nichols and Wright (1991) at Hurst Castle Spit (1981 & 1982) and Hengisbury Head respectively; Chadwick (1989) at Shoreham Beach.

Because the lack of field data on coarse grain beaches, the estimations of LST rates have to rely on data collected by tracers, traps and profile or shoreline changes (Van Wellen et al. 2000). In general tracers and traps tend to overestimate the LST and present limitations regarding to the shingle sediment size and it is associated with more variability in space and time rather sandy beaches. They conclude that the most appropriate and reliable method for assessing the beach response in the long term and also from the engineering point of view seems to be an impoundment technique. In this, a shore- normal structure acting as a barrier is studied as it traps the longshore sediment transport. It is assumed that no sediments pass through the structure and the

profile change is due to the longshore transport. Nichols and Wright (1991) noticed that loss of shingle seaward is generally minimal on mixed and gravel beaches and thus this approach can be effective for estimating LST rates.

This approach was adopted in the work presented here.

One of the most familiar formulae for LST in coastal engineering is the CERC equation (SPM 1984) which has been developed for sandy beaches. . This empirical equation is based on the Energy Flux method which considers the immersed weight of the alongshore moving sediment is proportional to the alongshore wave power per unit length of beach, Eq.1, (Kamphuis et al. 1986).

$$I_l = KP_l \tag{1}$$

P_l is the alongshore component of wave power in the breaking zone and it is defined as Eq. 2:

$$P_l = (C\ )_b (E_b) \cos\alpha_b \sin\alpha_b = \frac{1}{16}\rho g H_b^2 C_b \sin 2\alpha_b \tag{2}$$

Further investigations to attempt reliable estimations of the LST rate applying the CERC formula for different locations identified the need of modify the equation considering other parameters that affect sediment transport processes. Those formulae proposed include beach slope and sediment size (Kamphuis et al., 1986), later on wave period or wave steepness (Kamphuis, 1991) or wind, tide and breaking wave (Bayram et al., 2007).

In order to provide a calibration for sediment transport at the field site a temporary groyne was used to impound sediment. The impoundment technique then relies on the principle of mass conservation applied with the assumption that the shore normal temporary structure functions as a total barrier for the sediments. Any observed changes in beach volume between two arbitrary profiles lines are then assumed equal to the difference between the sediment flux into and out of the section under consideration. Against the groyne, any volume change is simply equal to the flux towards or away from this barrier. The sediment fluxes in any section must be related to the wave conditions through appropriate LST equations, see Fig. 3. An assessment of the accuracy of the technique can be achieved by balancing accretion on the up drift side with erosion on the down drift side (Wang and Kraus, 1999).

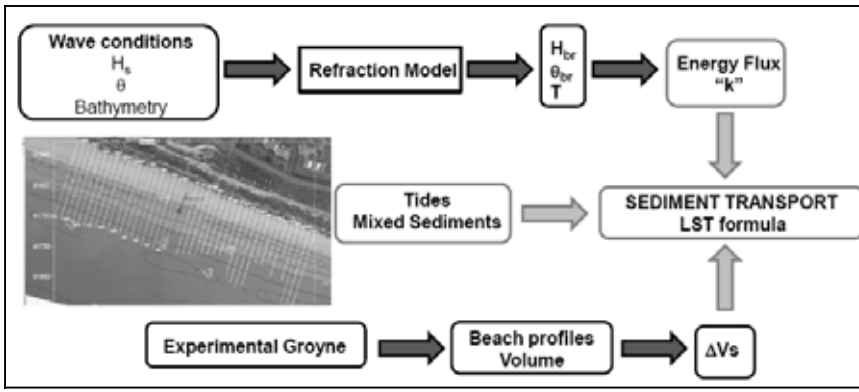

Figure3. Scheme of the project methodology for the calibration including an experiment site image with hydrographic data and topographic survey grid overlaid.

Bodge (1987) and Bodge and Dean (1987) (Wang and Kraus, 1999) have used an impoundment technique to study LST on sandy beaches. However, this work is the first to apply the technique in the UK and on a mixed beach to the authors' knowledge.

The impoundment experiment at Hordle Cliff lasted for 2 months. A location was chosen free from existing structures and overlooked by a low cliff from which an Argus Beach Monitoring System (ABMS) could be used to observe the experiment.

The 40m groyne was constructed directly in front of an Argus camera tower from approximately 200 customised geobags, see Fig. 4. These 1m x 1m x 1m size were designed to carry 2 Tonnes, are of the kind commonly used to transport sediment and granular materials. The design was modified with a top closing to keep the sediment contained inside. The bags were filled up with native beach material from the berm. Subsequent to the experiment the bags were emptied and the contents spread along the beach to fill in the shallow borrow pit from whence it was taken.

USACE, 1992 specifies groyne design in terms of specific wave parameters and tidal range. However in this case, the structure length was dictated by the tidal excursion and position of the sediment interface. The 40m length was selected to ensure that the coarse material from the berm would be totally impounded over the spring tidal range of 2m. It was not practical to trap the sand on the lower terrace. However, at this site it was assumed that the shingle upper beach appears to determine the performance of the beach as a defence and, furthermore, that the sand and shingle appear to behave as two distinct morphological systems, with the shingle overlaying a compacted and stable horizon of sand (see below).

Figure4. Top left: Geobag filled with beach material. Top right: view of structure from top of cliff. Bottom left: western elevation. Bottom right: view shorewards showing accretion-erosion across the structure with some damage evident.

A survey grid, 300m in extent, was defined with 15 profile lines on either side of the groyne location, spaced at 10m intervals. This distance exceeded that recommended in the SPM (1984) "on the order of two or three groyne length where this length is specified from the beach berm crest to the groyne seaward. Surveys were conducted daily over this grid for the duration of the 2 month deployment of the structure, 28th September to 24thNovember 2007. Surveys were conducted at low tide using a Differential Global Positioning System (DGPS). Contemporary measurements of wave climate were obtained using a Nortek AWAC acoustic Doppler current profiler providing wave height and directional spectrum.

Additionally, tidal observations were taken from RBR TWR-2050 Series gauges located at the groyne head and on a nearby waste water outfall along the coast. This provided tidal elevation and spot measurements of surface elevation and wave period. Additional hydrographic surveys were obtained before and after the experiment to enable accurate wave transformation calculation and assessment of nearshore sediment dynamics. Grain size samples were also taken regularly during the experiment.

The groyne was pulled out of the beach on 26th November 2007, the sediment replaced and the beach regraded.

PRELIMINARY RESULTS

The slope and shape of the beach face is a function of grain size, sorting, wave energy and tidal range (Komar, 1976). As mentioned above, we concentrate on the dynamics of the gravel upper beach, which appears to determine the function of the beach as a coastal defence. Thus the LST we are interested in is that of the gravel and the sandy bar and lower beach is not considered. That is not to say that the bar does not have noticeable influence on the shoreline position (Farris and List, 2007).

Having decided this, the changing volumes of sediment need to be determined either side of the groyne in order to infer the LST. We adopted the approach of defining a master profile above which the cross-sectional area at each profile line is calculated. The base of the master profile was found to be well described by a compacted sand horizon observed during excavation of the beach during groyne installation. Furthermore this can be demonstrated by consideration of the position of the seaward limit of the gravel for each profile line over time, ie where the sand "outcrops" the gravel. A good linear correlation (R^2=0.97) is observed in this position indicating a sand beach/horizon slope of about 1:7.

Fig. 5 represents the area changes at the MHWS (Mean high water spring) of the beach profiles respect to the mean area for the survey grid for 56 days. Changes are related with the wave conditions in terms of wave angle and alongshore wave energy calculated with the significant wave height at 6m depth. In general on the west side the accretion was more important than on the eastern side, however longshore sediment transport events in both directions were frequent as well as cross-shore events caused by normally incident waves.

With reference to Fig. 5, changes on the beach profiles due to longshore sediment transport can be seen at the start of November up to 17th November. The combination of energetic wave conditions and an angle from the SSW accumulated sediments on the west side and caused erosion on the east side of the groyne. Then, on 18th November, normal wave incidence and storm wave conditions moved the sediment seaward at the same order of magnitude for both sides of the structure.

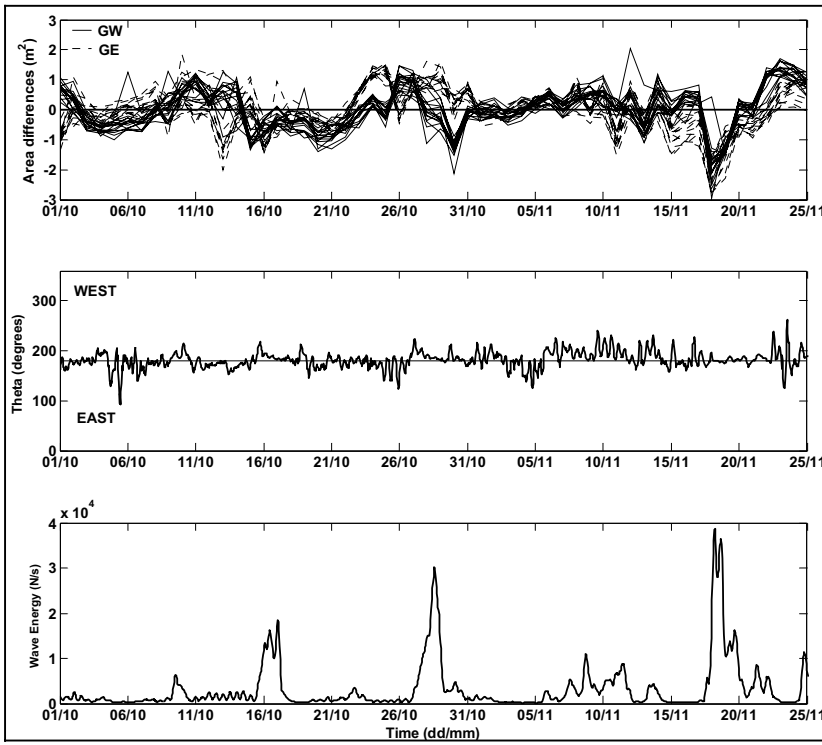

Figure5. Top panel: solid lines represent area changes on the west side of the groyne and dashed lines the eastern profile lines. Middle panel: wave angle corrected respect to the beach orientation, greater than 180° is from the west and less than 180° from the east. Bottom panel: longshore wave energy.

Table 1. Area differences (m^2) respect to the mean and MHWS

Date	GW01	GE01
2102007	0.3885	1.0921
8112007	0.8332	-0.1551
13112007	0.8289	-1.0876
17112007	0.8343	-1.0937
18112007	-2.9437	-2.7836

A significant difference between volume estimations on the updrift and downdrift sides of the temporary groyne for specific wave conditions demonstrates the applicability of the technique, see Table 1 and Fig. 6; in this case the shoreline change is explained by the longshore sediment transport

although cross-shore transport is taking place daily with important changes too (Horikawa, 1988).

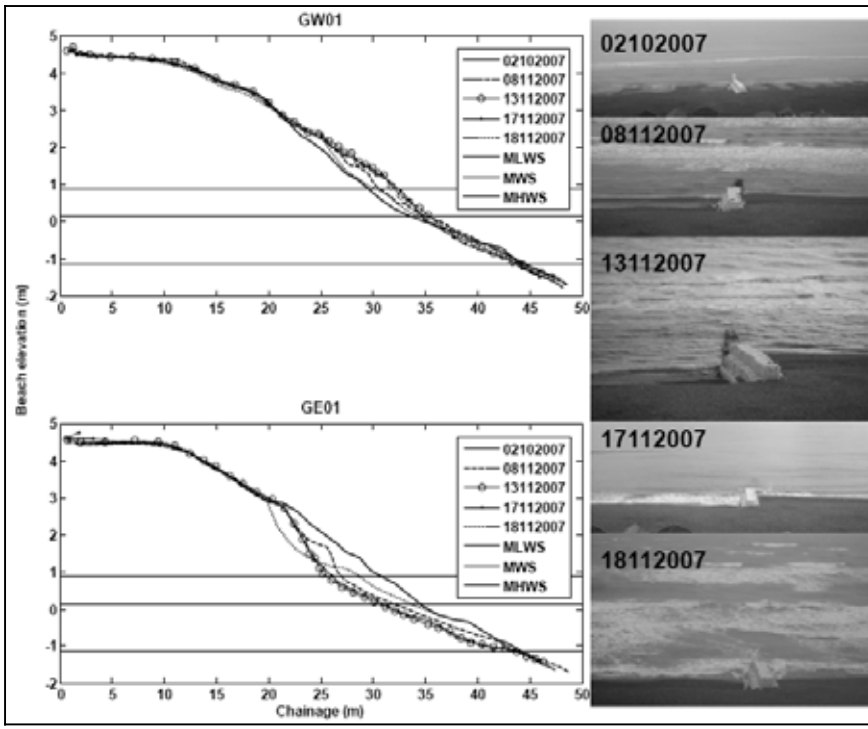

Figure6. On the left-hand panel, graphs represent the cross-section of the beach profile for five dates for the profile lines GW01 (on the west side of the groyne) and GE01 (on the east side of the groyne), both at a distance of 10m alongshore from the experimental structure. Changes shown in the graphs can be compared at the field site with the photos of the right-hand panel.

FUTURE WORK

Future research is focus on the field data analysis in order to develop a methodology for calibration of the formula for the longshore sediment transport rate. From the calibration, a new formula for the LST rate will be derived and fit in a One-line model to predict long-term mixed beach behavior.

As a first approximation, volume calculations are being analyzed in order to calibrate the CERC equation. Afterwards, the aim is to examine the calibration of other formulae, such as Kamphuis (1991, 2002), Bayram et al (2007) and Van Wellen et al. (2000). The latter was developed specifically for gravel beaches and for use in the BORESED LST model (Chadwick 1991, Van Wellen et al, 2000).

Preliminary observations from the beach profile data related to the wave conditions indicate that this technique has worked successfully. This should provide an effective demonstration for the coastal authorities as a good method for evaluating morphological changes and quantifying LST rates. This builds upon Wang and Krauss' (1999) short term impoundment study on a sandy beach. Validation of the new formula with data sets from other mixed beaches will assess its applicability as suggested by Schoonees (2000) for extending its applicability.

ACKNOWLEDGMENTS

This research was funded by the Faculty of Technology of the University of Plymouth and the EPSRC (Engineering and Physical Sciences Research Council) under Grant EP/C005392/1. The first author also acknowledges support from ENCORA to make possible the attendance at ICCE 2008.

REFERENCES

Bayram, A., Larson, M., Hanson, H. 2007. A new formula for the total longshore sediment transport rate. *Coastal Engineering* 54, 700-710.

Bradbury, A. P., McCabe, M. 2003. Morphodynamic response of shingle and mixed sand/shingle beaches in large scale tests- preliminary observations. Towards a Balance Methodology in European Hydraulic Research, *HYDRALAB II*, Budapest 2003.

Buscombe, D., Masselink, G. 2006. Concepts in gravel beach dynamics. *Earth-Science Reviews*, 79, 33-52.

Chadwick, A. J. 1989. Field measurements and numerical model verification of coastal shingle transport. BHRA, The Fluid Engineering Centre, UK, *Advances in water modelling and measurements*, 381-402, Chapter 27.

Dean, R. G., Dalrymple, R. A. 2002. *Coastal processes with engineering applications*. Cambridge University Press.

Farris, A. S., List, J. H. 2007. Shoreline change as a proxy for subaerial beach volume change. *Journal of Coastal Research* 23 (3), 740-748.

Halcrow Group Ltd., SANDS, Shoreline And Nearshore Data System.

Horikawa, K. 1988. *Nearshore dynamics and coastal processes: Theory, measurement and predictive models*. University of Tokyo Press.

Kamphuis, J. W., Davies, M.H., Nairn, R.B., Sayao, O.J. 1986. Calculation of littoral sand transport rate. *Coastal Engineering* 10, 1-21.

Kamphuis, J. W. 2000. *Introduction to coastal engineering and management. Advance series on ocean engineering*, Vol 16. World Scientific.

Kirk. R. M. 1980. Mixed sand and gravel beaches: morphology, processes and sediments. *Progress in Physical Geography*. 4, 189-210.

Komar, P.D. 1976. *Beach processes and sedimentation*. Prentice- Hall, Inc.

López de San Román-Blanco, B. 2003. Development of Predictive Tools and Design Guidance for Mixed Beaches-Stage 2 Final Report, PhD Thesis. HR Wallingford.

López de San Román-Blanco, B., Coates, T. T., Holmes, P., Chadwick, A. J., Bradbury, A., Baldock, T. E., Pedrozo-Acuna, A., Lawrence, J., Grune, J. 2006. Large scale experiments on gravel and mixed beaches: experimental procedure, data documentation and initial results. *Coastal Engineering* 53, 349-362.

Mason, T., Voulgaris, G., Simmonds, D. J., Collins, M. B. 1997. Hydrodynamics and sediment transport on composite (mixed sand/shingle) and sand beaches: a comparison. *Coastal Dynamics* 1997.

Mason, T., and Coates, T. T. 2001. Sediment transport processes on mixed beaches: a review for shoreline management. *Journal of Coastal Research* 17 (3), 645-657.

Schoonees, J. S. 2000. Annual variation in the net longshore sediment transport rate. *Coastal Engineering* 40, 141-160.

SCOPAC, 2003. Standing Conference on Problems Associated with the Coastline.

USACE. 1984. Shore Protection Manual. Department of the Army, U.S. Corps of Engineers, Washington, DC 20314.

USACE. 1992. CEM, Coastal Engineering Manual. Department of the Army, U.S. Corps of Engineers, Washington, DC 20314.

Van Wellen, E., Chadwick, A. J., Mason, T. 2000. A review and assessment of longshore sediment transport equations for coarse - grained beaches, *Coastal Engineering* 40, 243-275.

Wang, P., and Kraus, N.C. 1999. Longshore sediment transport rate measured by short-term impoundment, *Journal of Waterway, port, coastal and ocean engineering* 125 (3), 118-126.

BED-LEVEL CHANGE OVER INDIVIDUAL SWASH CYCLES ON SAND AND GRAVEL BEACHES

Turner, I.L.[1], Masselink, G.[2], Russell, P.E. [3] and Blenkinsopp, C.E.[1]

This paper describes two large field campaigns designed to obtain the most comprehensive dataset to date of morphodynamic change in the swash zone and the associated hydrodynamic processes. Experiments were undertaken at a sand and gravel beach to provide complimentary data from contrasting beach types. An initial analysis of the data revealed that relatively large bed-level changes (1 – 2 cm) were observed to occur in response to individual swash events. Indeed, it was found that the net morphological changes over a 2-hour section of data were not caused by the gradual accumulation of small bed-level changes, but in fact the morphological response was dominated by a small number of large events which had the same order of magnitude as the overall bed-level change during the entire time-series.

INTRODUCTION

The swash zone marks the transition between the submerged surf zone and the dry beach and can be loosely defined as the region where the beachface is intermittently submerged by wave runup, over time-scales ranging from a few seconds to a few minutes. Along tidal coasts, the swash zone translates landward-seaward across the intertidal profile.

Seas, swells and breakpoint- or swash-driven infragravity energy, cause water to rush up and back across the beachface, resulting in the destabilisation and movement of sediment. It is the integration of this wave-by-wave sediment movement that causes beaches to erode or accrete, over time-scales ranging from a few minutes to a single tide cycle, and from individual storm events to chronic and longer-term coastal erosion. Some significant differences exist in sediment dynamics between the swash zone and the adjacent surf zone, and these differences have inhibited direct application of existing surf zone sediment transport models to the swash zone. Several recent reviews (Butt and Russell, 2000; Elfrink and Baldock, 2002; Masselink and Puleo, 2006) have assisted in clarifying the dominant hydrodynamic and sediment transport processes that occur in the swash zone of natural beaches, and the degree to which these may differ from the adjacent surf zone.

Fundamentally, beachface erosion is characterised by a general flattening of the profile, and is sometimes accompanied by the rapid formation of vertical erosion ‘scarps’ up to several metres in height. During calmer periods, steepening of the beachface often occurs, caused by the accumulation of

[1] Water Research Laboratory, School of Civil and Environmental Engineering, University of New South Wales, Sydney, NSW 2052, Australia.

[2] School of Geography, University of Plymouth, Plymouth, PL4 8AA, UK.

[3] School of Earth, Ocean and Environmental Sciences, University of Plymouth, Plymouth, PL4 8AA, UK.

sediment to form a 'berm' above the high-tide still water line. In general, hydrodynamic models tend to be able to reproduce the velocity and depth variations in the swash zone quite well (e.g. Raubenheimer, 2002; Raubenheimer et al., 2004). In contrast, large-scale morphodynamic models, used in both research and industry to predict the evolving nearshore morphology, are less successful at predicting the flattening and steepening of the beachface. Indeed, in the majority of operational models the swash zone is usually excluded, with the land-ocean boundary represented numerically by a vertical 'wall' at the shoreline. More advanced treatments include predictions of long-wave swash motions only, with short-wave swash energy and asymmetries being estimated from (untested) surf zone parameterizations.

It is generally acknowledged that our understanding of swash zone sediment transport processes lags equivalent knowledge of the surf zone and must be improved. To meet this challenge, in September 2004 the '1st International Workshop on Swash Zone Processes' (Puleo and Butt, 2006) was held, to coincide with the 29th International Conference on Coastal Engineering (McKee Smith, 2005). The purpose of this benchmark meeting was to bring together key research groups working in the swash zone, to discuss ideas, share concerns and to formulate future directions for research. At the conclusion of the meeting it was highlighted that in-situ and continuous beachface bed-level measurements at the fundamental time-scale of individual uprush-backwash events were yet to be achieved. The meeting participants identified the need to measure swash zone morphology on a swash-by-swash basis, to quantify the relative contributions of suspended and bedload transport, and to examine the net effect of sediment transport patterns (Puleo and Butt, 2006).

Previous studies of bed-level change in the swash zone have been undertaken, but such measurements are fairly sparse and generally not at sufficiently high frequency to characterise wave-by-wave bed-level change. The methods employed in these studies have included manual measurements of a series of stakes with a graduated rule (Sallenger & Richmond, 1984; Howd & Holman, 1987; Horn & Walton, 2004; Weir et al., 2006), the use of video to measure bed elevations against a series of stakes (Larson et al., 2004) and capacitance probe techniques (Waddell, 1976; Waddell, 1980). These studies suggest that considerable morphological changes can be observed in the swash zone on relatively short timescales. However, significantly more detailed information with corresponding measurements of the processes that drive morphodynamic change (sediment transport and hydrodynamics) are needed.

The work reported herein describes two separate field programmes that were undertaken at a sandy beach in France and a gravel barrier beach in England to provide unique simultaneous measurements of bed-level change and hydrodynamics on two contrasting beach types. To demonstrate the nature of the data obtained from these experiments we then go on to present some initial analysis of two short time-series from the sandy beach experiment. Future work will go on to compare the similarities and differences in swash zone processes

for the two different beach types. Additional measurements were also made at prototype scale in the large-scale Delta Flume facility in the Netherlands, which will be reported elsewhere.

FIELD SITE AND INSTRUMENTATION

Le Truc Vert – Sandy Beach Field Programme

The first set of field data was obtained at Le Truc Vert beach, France over 27 tidal cycles between 19th March and 4th April, 2008. The experiment was undertaken within the structure of the multi-institutional ECORS project (Senechal et al., 2008) and forms part of a large collaborative swash zone research project between the Universities of New South Wales and Plymouth. Le Truc Vert is an exposed beach located on the Atlantic Coast of France to the west of Bordeaux (Figure 1). The beach experiences a mixture of high-energy Atlantic swell and locally generated wind-waves with an average significant wave height of 1.3 m. During the experiment, the significant offshore wave height varied in the range 0.9 m to 4.1 m. The beach is macrotidal, with a spring tidal range of 4.3 m and a beachface gradient of approximately 1:18. The median sediment size D_{50} is approximately 0.35 mm.

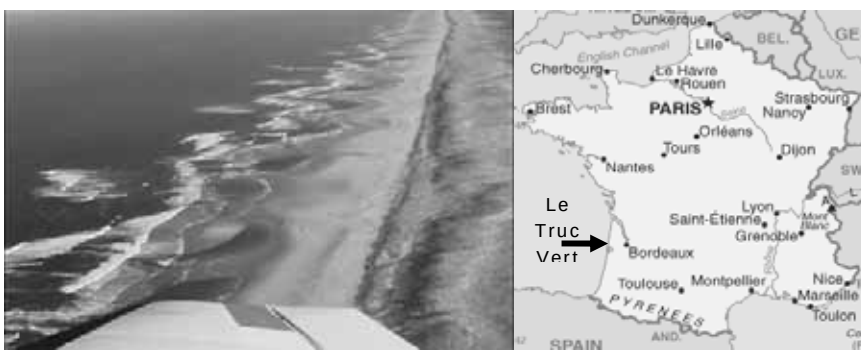

Figure 1 – Aerial photograph of Le Truc Vert beach, and map showing the location of Le Truc Vert on the Atlantic coast of France.

High frequency bed-level data were recorded using a large array of 45 ultrasonic bed-level sensors sampled at a rate of 4 Hz. The sensors were mounted on a large scaffolding rig approximately 1 m above the bed in 3 cross-shore lines with a spacing of 1.9 m (Figure 2). The bed-level sensors are described by Turner *et al*. (2008) and when mounted perpendicular to the bed, make non-intrusive Eulerian measurements of the vertical distance to the closest target (bed-level when the bed is dry and swash height when the bed is wet) based on the time of flight of a reflected signal. Offshore wave data was recorded by a waverider buoy in a water depth of 20m, while nearshore wave and water level data was measured by an ADV positioned 20 m offshore of the

main scaffold rig. Additional measurements of current velocity, suspended sediment concentration, water depth and infiltration/exfiltration gradients were made to complement the bed-level measurements but are not discussed here. To put the high-frequency bed-level measurements into the context of the wider beach area, topographic surveys were completed on every low tide along 11 cross-shore transects, spaced 20 m apart and extending from the foredunes to the mean low tide line.

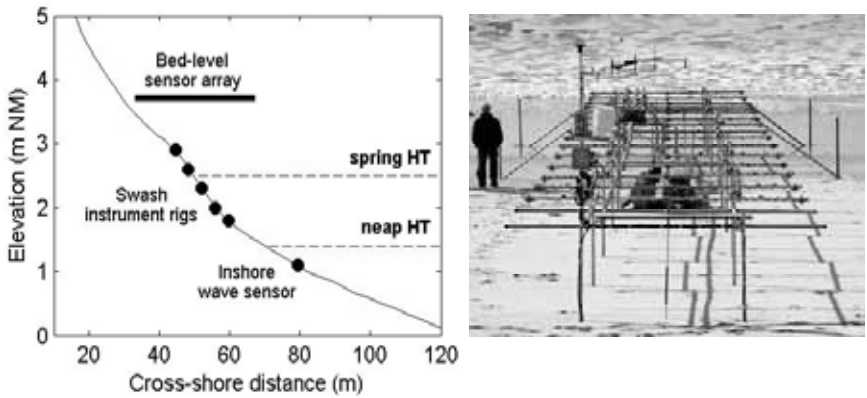

Figure 2 – Beach profile at the start of the field experiment with instruments locations, and photograph showing the scaffolding structure used for mounting the instruments. The three cross-shore lines of bed-level sensors can be seen down each end, and down the middle, of the scaffold array.

Slapton Sands – Gravel Beach Field Programme

Additional data to complement that from Le Truc Vert was recorded during a 10 day field deployment at Slapton Sands, England between 31/4/08 and 9/5/08. Slapton Sands is a 4 km long gravel barrier beach in South Devon, South West England. The Barrier has a width of 100-140 m, a crest-elevation of 6-7m and is backed by a freshwater lagoon (Slapton Ley). The beach is composed of fine to medium gravel with a D_{50} sediment size of 4-10 mm. Slapton faces East up the English Channel and is protected from Atlantic swells by a large headland (Figure 3). Consequently the wave climate at Slapton consists mostly of small, short period waves with a mean significant wave height of just 0.3 m. During the experiment, the significant wave height at the site varied in the range 0.3 m to 1.3 m.

Figure 3 – Photograph of Slapton Sands and Slapton Ley freshwater lagoon, and map showing the location of Slapton Sands in the South West of England.

The experimental instrumentation was similar to that used at Le Truc Vert, but due to the challenging nature of working on a gravel beach, a few modifications were made. The beachface gradient at Slapton was approximately 1:5 and consequently the swash zone width (the distance from the rundown limit to the point of maximum uprush) was considerably smaller than that at Le Truc Vert. Consequently the 45 ultrasonic bed-level sensors were deployed at 0.5 m spacings along a single cross-shore transect on a modified scaffolding rig (Figure 4). The hydrodynamic measurements were the same as those at Le Truc Vert with the exception that due to the coarser nature of the sediment at Slapton, no suspended sediment concentration measurements were possible. As at Le Truc Vert, topographic surveys of the beach were undertaken at every low tide.

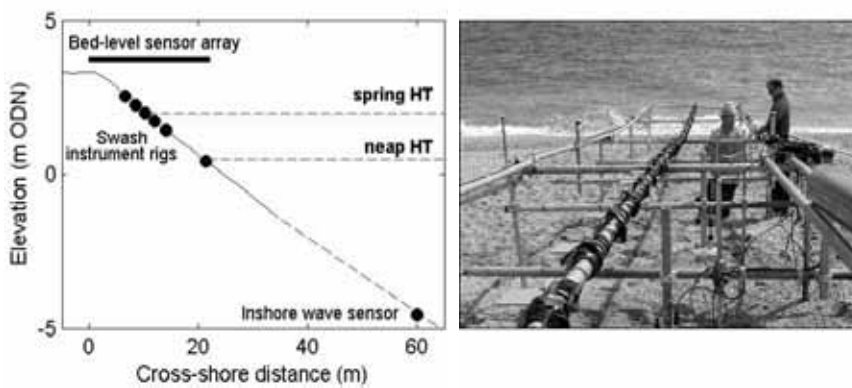

Figure 4 – Beach profile at the start of the gravel beach field experiment with instruments locations and photograph showing the scaffolding structure used for mounting the instruments.

BED-LEVEL MEASUREMENTS

To demonstrate the nature of the data obtained from these experiments and highlight some very interesting preliminary findings, the following section presents some initial analysis of two short time-series from the sandy beach

experiment. Comparable data is also available from the gravel beach experiment and future work will go on to examine the similarities and differences in swash zone processes for the two different beach types.

Bed/Swash Elevation Data

Figure 5 shows a 30 minute segment of data obtained from a single bed-level sensor located in the upper swash (x = 50.02 m) during the Truc Vert experiment. The values on the plot represent the elevation of the uppermost surface beneath the sensor (bed-level when the bed is dry and swash elevation when the bed is wet) and have been corrected for temperature effects. Examining this trace, the vertical spikes represent the raised water depth when a swash passes beneath the sensor and have a saw-tooth profile typical of swash (Hughes, 1992), while between these events 'flat' regions correspond to *in-situ* measurements of the bed and it is possible to estimate the bed-level change caused by a single swash event.

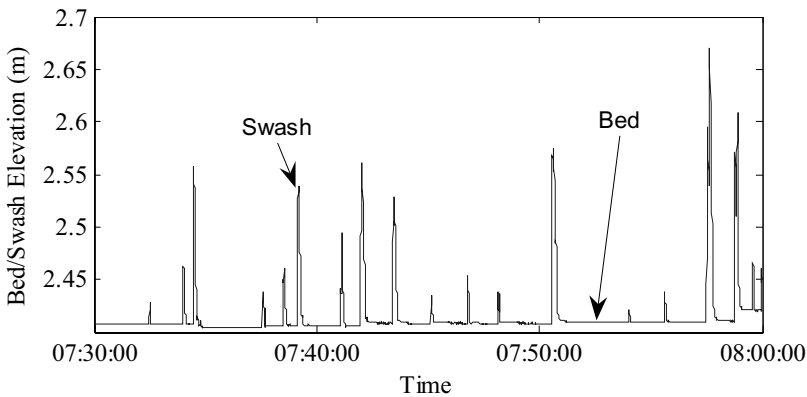

Figure 5 - 30 minute time-series of data obtained from a single bed-level sensor located in the upper swash (x=50.02 m) during the Truc Vert experiment.

Figure 6 presents the same 30 minute time period as the previous figure, but now pre-processed to separate the individual 'bed-level events' from swashes. For the example data included here, detection of the bed was defined by the following two criteria based on observations of the physical processes and some trial and error (after Turner *et al*, 2008):

$$|z(t+\delta t) - z(t)| \times f < 0.0005 \text{ ms}^{-1}$$
$$T_{bed} > 2 \text{ seconds}$$

where $z(t)$ and $z(t+\delta t)$ are the observed bed/swash elevations at two successive time-steps, f (= $1/\delta t$) is the sampling frequency (4 Hz) and T_{bed} is the duration of a suspected 'bed-level event'. Simply stated, the sensor was deemed to be detecting the bed when the elevation of the closest target (swash or bed)

changed at a rate less than 0.5 mm per second and this condition persisted for a minimum of 2 seconds in duration. Applying these simple pre-processing criteria, Figure 6(a) depicts the individual bed inundation events, with the peak of each bore indicated. Note that a single inundation event may consist of one or more individual bores traversing the beach face. Figure 6(b) shows the intervening time periods when bed-level measurements were achieved. These particular bed-level data suggest a net accretion of 11 mm through the 30 minute sampling interval shown, much of which was achieved by a single swash event just before 0800 hrs.

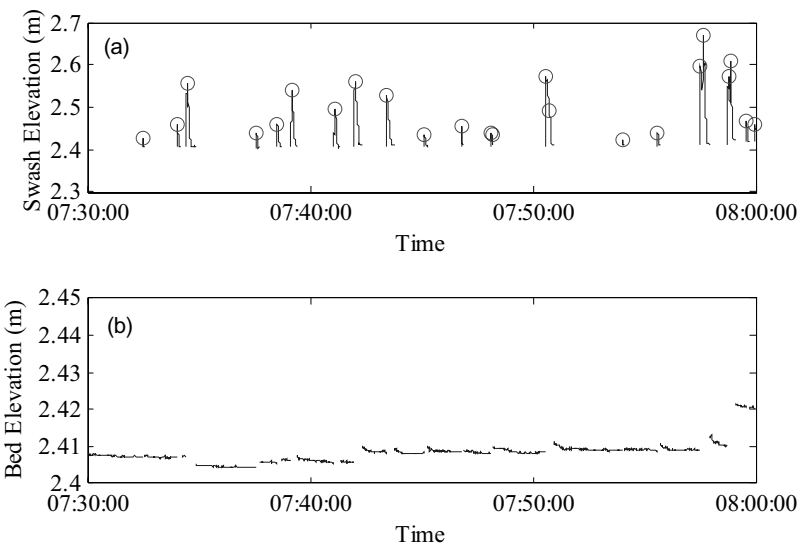

Figure 6 – (a) Time-series of extracted swash elevation data recorded during inundation events with the peak of each bore marked with a circle, and (b) a time-series of extracted bed-level data recorded between swash events.

Bed-Level Measurements

The ability to measure wave-by-wave bed-levels continuously and repeatedly enables, for the first time, subtleties in beach face adjustment to be observed and quantified. To illustrate, Figure 7 presents two time-series of bed/swash elevation data obtained during two consecutive tides (Tide 22 and Tide 23) at Le Truc Vert. The time-series are taken from the same sensor, mounted in both cases in the mid high-tide swash zone (x=50.02 m) and during approximately the same part of the tidal curve. In both cases, the ebb tide was observed to fall through the location of the sensor and this can be seen in the gradual reduction of swash heights through the time-series. During Tide 22 the incident wave conditions, measured by a waverider buoy in 20 m water depth, were significant wave height, H_s = 2.82 m and peak spectral period (T_p) = 12.5

s. During Tide 23, the wave conditions were very similar to that during Tide 22, with an offshore significant wave height, H_s = 3.12 m and T_p = 12.5 s.

Comparison of these two datasets reveals a different bed-level response despite the similar physical conditions and the identical location of the sensor on the beachface. During Tide 22 an erosional trend was observed, with the beach face eroding by approximately 50 mm, the majority of which occurred during the first 15 minutes due to a small number of large swashes. In contrast, a slight net beach face accretion of 15 mm was observed during Tide 23. Closer inspection of the two time-series shows that relatively large bed-level changes (1 – 2 cm) were observed to occur intermittently in response to individual swashes. Indeed, further examination of the time-series suggests that the observed net erosion or accretion are not caused by the gradual accumulation of small erosive and accretionary changes for Tides 22 and 23 respectively, but in fact the morphological change is dominated by a small number of large events which have the same order of magnitude as the overall bed-level change during the full time-series. This idea is reinforced by the histograms of bed-level change events presented in Figure 8 which show that for both cases there are approximately equal numbers of small erosive and depositional bed-level change events. These small events approximately balance out and the majority of net change in both cases occurs due to the small number of bed-level changes greater than 10 mm. The high significance of a small number of events means that even the direction of net bed-level change at a single point on the beachface will be difficult to predict as it depends on a very fine balance between positive and negative changes.

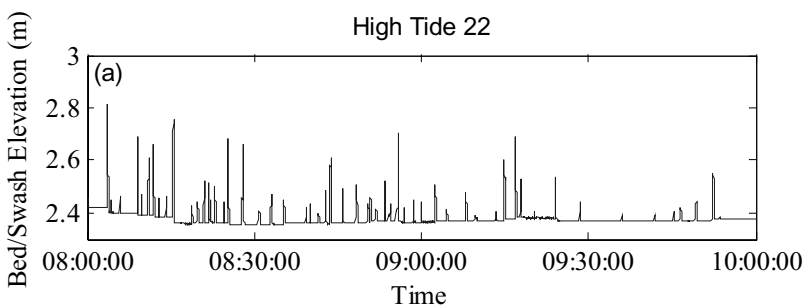

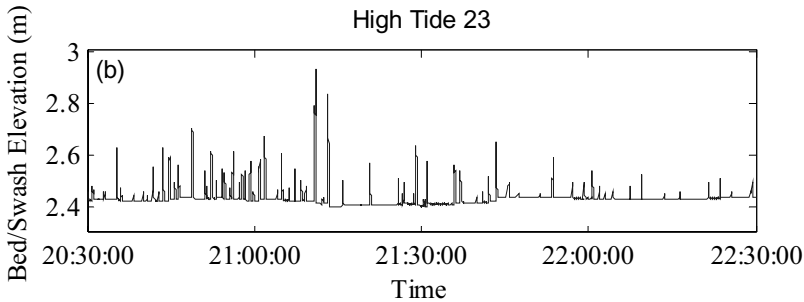

Figure 7 – Two hour time-series of data during two consecutive ebb tides, (a) Tide 22 and (b) Tide 23, recorded at the same sensor position (x=xx) in the mid high-tide swash zone.

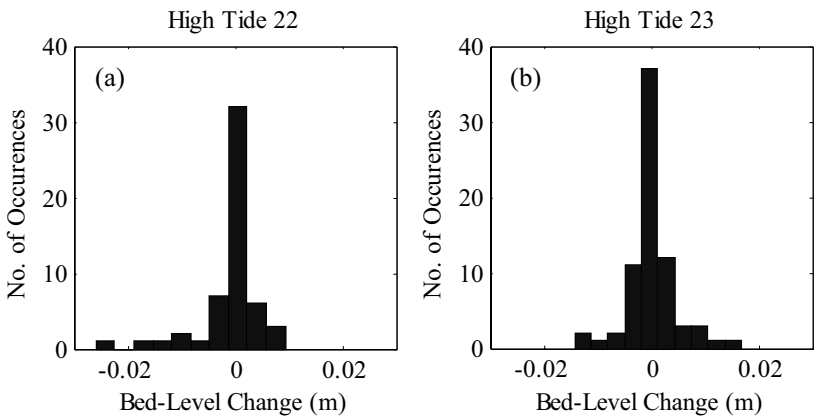

Figure 8 – Histograms of the individual bed-level change events during the measurement periods shown in Figure 6 for (a) Tide 22 and (b) Tide 23.

To synthesise and compare these observations, Table 1 presents a basic summary of the two bed-level time-series depicted. Note that the net bed-level change per swash event was defined by calculating the difference between each measured bed elevation immediately prior to an individual swash, to the measured bed elevation immediately prior to the next swash. Referring to Table 1, the mean bed-level change per uprush-backwash cycle was extremely small, at least two orders of magnitude smaller than the largest changes. This observation attests to the fact that in neither case the beach face was observed to dramatically erode or accrete (< 50 mm net change) during each of the two-hour measurement periods. However, the standard deviation of wave-by-wave bed-level changes was an order of magnitude greater, and the magnitudes of the largest bed-level accretion/erosion per wave were 18 mm and -24 mm respectively. To place this magnitude of single-wave bed-level change in context, at this rate and for a 10 second wave period, the beach face would

erode-accrete by more than 9 m vertical elevation per hour! The fact that single-wave bed-level changes of the order of centimetres are measured (Figure 8), but that time-integrated bed-level changes of corresponding magnitude are generally not observed in nature suggests there is a form of dynamic equilibrium operating which limits rapid change at the beachface and the nature of this equilibrium is of great interest.

Table 1: Summary of bed-level observations during Tides 22 and 23 (refer Figure 4).

Tide No.	Net Bed-Level Change (mm)	No. of Events	Mean Bed-Level Change Per Event (mm)	Standard Deviation (mm)
22	-50	54	-0.078	0.56
23	15	73	0.015	0.45

CONCLUSIONS

Recent reviews of the state of swash zone research have suggested that the swash zone is critical area for further research as it is currently poorly understood, yet of great importance to successful coastal modelling and management. To predict and model coastal erosion and accretion, the nearshore research community has identified it as a basic requirement that wave-by-wave sediment movement within this most active region of the beach be first quantified and elucidated (Puleo and Butt, 2006). The work presented here describes two large scale field experiments designed to obtain continuous field measurements of wave-by-wave beach face evolution in order to fill this knowledge gap.

The results from these experiments demonstrate that an array of ultrasonic bed-level sensors can be used to successfully obtain high quality measurements of bed and swash elevation at sufficient resolution to observe morphological change at the beachface at the timescale of individual waves. The data obtained from these field experiments provides us with a unique dataset which reveal rather complex fluctuations of the bed observed over time periods of minutes to hours. In particular, gross bed-level changes are shown to be many times greater than the observed rate of net morphodynamic change at the beachface.

The data obtained during the experiments described in this paper will enable bed-level adjustment at the beachface of sand and gravel beaches to be analysed in detail over short timescales in order to elucidate the processes that dominate morphodynamic response in the swash zone for two constrasting beach types.

ACKNOWLEDGEMENTS

The authors would like to acknowledge the financial assistance provided by the Australian Research Council (ARC) and the Engineering and Physical Sciences Research Council (EPSRC). We would also like to thank the following for their assistance with the fieldwork described in this paper: Peter

Ganderton, Tim Scott, Dan Buscombe, Amaia Ruiz de Alegria Arzaburu, Tim Poate, Jon Tinker, Will Hibberd, James Moon, Guillaume Dodet, Martin Austin, Richard Hartley and Andre Pacheco.

REFERENCES

Butt, T. and Russell, P.E., 2000. Hydrodynamics and cross-shore sediment transport in the swash-zone of natural beaches: a review. *Journal of Coastal Research*, 16(2), 255-268.

Elfrink, B. and Baldock, T., 2002. Hydrodynamics and sediment transport in the swash zone: a review and perspectives. *Coastal Engineering*, 45, 149-167.

Horn, D.P. and Walton, S.M., 2004. Sediment-level oscillations in the swash zone of a mixed sand and gravel beach. *Proceedings, 29th International Conference on Coastal Engineering,* ASCE, 3, 2390-2402, World Scientific Publishing Co, New Jersey.

Howd, P.A. and Holman, R.A., 1987. A simple model of beach foreshore response to long-period waves. *Marine Geology*, 78, 11-22.

Hughes, M.G., 1992. Application of a non-linear shallow water theory swash following bore collapse on a sandy beach. *Journal of Coastal Research*, 8 (3), 562-578.

Hughes, M.G. and Turner, I.L., 1999. The Beach face. In: Short, A.D. (ed), *Handbook of Beach and Shoreface Morphodynamics*. Wiley Scientific Publishers, London.

Larson, M., Kubota, S., and Erikso, L., 2004. Swash-zone sediment transport and foreshore evolution: field experiments and mathematical modelling. *Marine Geology*, 212, 61–79.

Masselink, G. and Puleo, J.A., 2006. Swash zone morphodynamics. *Continental Shelf Research,* 26(5), 661-680.

McKee Smith (ed.) 2005. *Proceedings of the 29th International Conference on Coastal Engineering*, Lisbon, 2004. World Scientific. 4840pp.

Puleo, J.A. and Butt, T., 2006. First international workshop on swash zone processes. *Continental Shelf Research*, 26(5), 556-560.

Raubenheimer, B., 2002. Observations and predictions of fluid velocities in the surf and swash zones, *J. Geophys. Res*., 107, 3190, doi:10.1029/2001JC001264.

Raubenheimer, B., Steve Elgar, and R.T. Guza, 2004. Observations of swashzone velocities: a note on friction coefficients, J. Geophys. Res., 109, C01027, doi:10.1029/2003JC001877.

Sallenger, A.H. and Richmond B.M., 1984. High-frequency sediment level oscillations in the swash zone. *Marine Geology*, 60, 155-164.

Sénéchal, N., F. Ardhuin, and others, 2008. ECORS-TRUC VERT 2008, Qualification des modèles de houle et de morphodynamique. Paper presented at Genie Côtier, Génie Civil (2008) (in French).

Turner, I.L., Russell, P.E. & Butt, T. 2008. Measurement of wave-by-wave bed-levels in the swash zone. *Coastal Engineering*, doi:10.1016/j.coastaleng.2008.09.009

Waddell, E.,1976. Swash-groundwater-beach profile interactions. In Davis, R.A. and Etherington, R.L. (eds), *Beach and Nearshore Sedimentation*. Society of Economic and Paleontological Mineralogists Special Publication, 24, 115-125.

Waddell, E., 1980. Wave forcing of beachgroundwater. *Proceedings of 17th International Conference on Coastal Engineering*, ASCE, Sydney, Australia, 1436-1452.

Weir, F.M., Hughes, M.G. & Baldock, T.E. 2006. Beach face and berm morphodynamics fronting a lagoon. *Geomorphology*, 82, 331-346.

EVALUATING THE VOLUME OF MIXED SAND AND GRAVEL BEACHES ON RAPIDLY ERODING CLIFFED SHORELINES

Mark Dickson[1], Charlie Bristow[2], Murray Hicks[3], Harry Jol[4]

A method is described for calculating the volume of mixed sand and gravel beaches on rapidly eroding cliffed shorelines. This is important because the volume of available sediment determines the capacity of the beach to protect the cliff toe from wave attack. At a study site in southeast New Zealand, ground penetrating radar (GPR) is used to image sub-surface beach stratigraphy. Particular attention is focused on identifying the contact between beach sediments and an underlying substrate that is composed of the same Pleistocene sediments as the cliff face (i.e. the bedrock). This contact is clear on the radar facies as a broadly concave reflection that slopes steeply (~15°) from near the cliff toe where it is about 3-4m above mean sea level (MSL) and veneered by a thin sequence of beach sediment. Several metres from the cliff toe the substrate slopes more gently (5-9°) toward the sea and is covered by thicker sequences of beach sediments. The substrate is rarely observed, but a storm six months after the GPR survey stripped beach sediments seaward and exposed the substrate at one site. Survey of the storm beach profile provides a ground truth to the interpretation of the substrate profile on the radar facies.

INTRODUCTION

Beaches on cliffed shorelines form the principal natural defence against coastal recession. Given a certain wave climate, sediment characteristics and other parameters, the volume of available sediment determines the protective capacity of the beach. Hence, accurate measures of beach volume are important for coastal management, but these are rarely straight-forward. On sandy coasts, beach profiles may be wide and largely subaqueous. Often the thickness of beach sediment overlying rock substrate is unknown and beach volume calculations are made with respect to an assumed base level. Several properties of gravel and mixed sand/gravel beaches allow for a more accurate volume calculation: (1) wave asymmetry causes coarse sediments to pile up at the shoreline meaning that a much larger portion of gravel beaches are subaerial; (2) this effect is exaggerated on cliffed shorelines where the occurrence of a bedrock surface, sloping seaward from the cliff toe, forms an intertidal to supratidal platform on which beach sediments are deposited; (3) coarse

[1] School of Geography, Geology & Environmental Science, University of Auckland, New Zealand
[2] School of Earth Sciences, Birkbeck College, University of London, Malet Street, London WC1E 7HX, U.K.
[3] National Institute of Water & Atmospheric Research, Christchurch, New Zealand
[4] Department of Geography and Anthropology, University of Wisconsin - Eau Claire, 105 Garfield Avenue, Eau Claire, WI, U.S.A., 54702-4004.

sediments result in beaches that have an abrupt beach step which forms a distinct boundary between beach sediments and the nearshore seabed; (4) coarse sediments are relatively freely draining, meaning that at low tide it may be possible to image beach stratigraphy as well as any underlying basal substrate using ground penetrating radar (GPR) (e.g. Neal et al., 2002).

This paper describes the use of GPR for calculating the volume of thin mixed sand and gravel beaches that occur in front of rapidly eroding cliffs along a section of the east coast of South Island, New Zealand (Fig. 1).

STUDY SITE

The study area on the east coast of the South Island, New Zealand, is part of the Waitaki coast between Oamaru in the south and the mouth of the Waitaki River in the north (Fig. 1). This section of the coast has a relatively narrow gravel beach (width between 20 and 30m) at the base of 10–20m high cliffs that have been cut into the Quaternary alluvial fan of the Waitaki River.

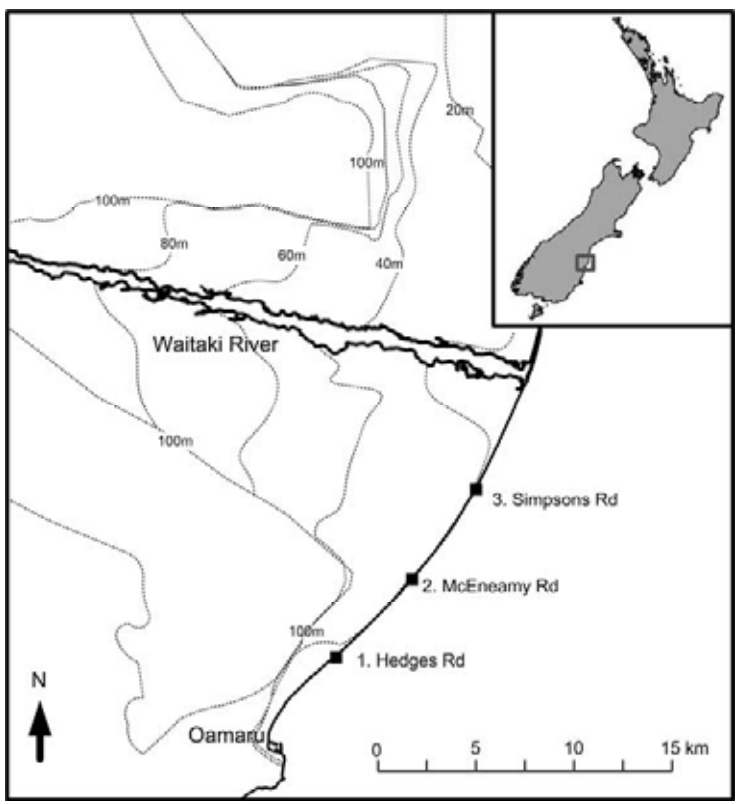

Fig 1. Location map showing study sites (1-3) on the southern side of the prograded fan of the Waitaki River.

In recent decades cliffs in the study area have been eroding at rates of 0.5-2m/yr (Gibb, 1978) which has resulted in the loss of agricultural land and commercial property along the coast north of Oamaru. This trend of erosion has been occurring for several thousand years of Holocene high sea level which has trimmed the fan creating a cliffed coastline. The eroding cliffs are composed of pebble to cobble grade conglomerates capped by loess.

Fig. 2 illustrates typical features of the cliffs and mixed sand and gravel beaches that have formed along the study site (also see Fig. 3). Cliffs 10-20m high are generally close to vertical in profile, and beaches are steeply sloping (4-6°) across a distance of 20-30 between the storm berm which is 3-5m above MSL and the still water level. A characteristic feature of these beaches is a pronounced beach step that occurs just below the water line and slopes steeply to an abrupt juncture between the step sediments (gravel and cobbles) and a seabed composed of fine sediment (Kirk, 1980). Under most conditions there is no surf zone and waves plunge or collapse on the beach step and swash up the lower beach face. During storms the convex beach-face is considerably altered by seaward cross-shore sediment movement. Berms are removed and if the storm is of sufficient duration, the cliff toe and substrate may be exposed to direct wave attack.

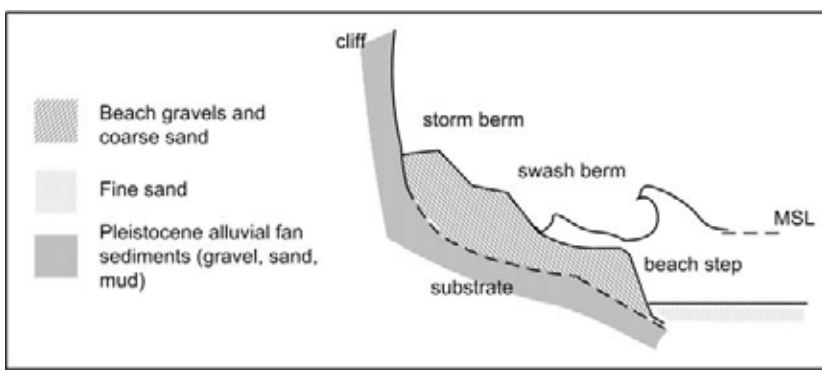

Fig. 2. Schematic profile view of a mixed sand and gravel beach overlying a substrate that is composed of the same sediments as the cliff.

On the east coast of the South Island of New Zealand the prevailing swell comes from the southerly quadrant generating a regional northeasterly longshore drift (Pickrill and Mitchell, 1979).

The focus of the present study was on determining the shape of the substrate. Some details of the nature of the substrate have been provided through a previous study by Stapleton (2005) in which trenches were excavated at two sites in front of cliffs north of the Waitaki River. Here the substrate was identified visually based on the contrasting colour of beach and substrate

sediments, and secondly by analysis of bulk sediment samples. Pleistocene sediments are exposed in the cliff face, with in-situ cobbles distinctly brownish in colour due to surface weathering. By contrast, beach sediments are grey and generally have a fresh appearance having been moved and abraded by wave action (see Fig. 3). Stapleton's (2005) bulk samples showed that Pleistocene alluvial sediments are composed of a mixture of sand and gravel with minor (<5%) mud, whereas surficial beach samples are 100% gravel, and sub-surface beach samples are mixed sand and gravel with mud typically absent. Samples from the substrate are sedimentologically similar to those exposed in the cliff face, implying that the substrate has formed from the cliffs as the cliffs have eroded.

A primary objective of the present study was to identify the volume (per unit shore length) of beach sediments overlying the Pleistocene substrate. It was hypothesized that the sedimentological boundary between beach and substrate sediments might be apparent in GPR images owing to changes in dielectric permittivity, which in sediments is primarily controlled by water content, which is itself mainly controlled by the porosity, fabric and grain size of the beach and substrate sediments (van Dam and Schlager 2000, van Dam et al. 2003).

METHODS

GPR surveys were conducted in Nov 2006 using Pulse EKKO 100 and Pulse EKKO 1000 GPR systems (Fig. 3) with antennae frequencies of 100, 200, 225, 450, and 900 MH).

Fig. 3. Photographs showing Pulse EKKO radar systems, near-vertical cliffs at site 2 (right), and contrasting beach and cliff sediments (left).

Profiles were surveyed across the beach perpendicular to the cliff face and the two-way travel-time from surface to subsurface reflections was converted to depth using a velocity of 0.15 mns^{-1} calculated from common mid-point surveys. Ground control was provided by RTKGPS and established survey marks, and beach profiles were surveyed with RTKGPS or automatic level. GPR surveys

were conducted under fair-weather conditions and at low tide. However, survey was restricted to within several metres of the beach step, beyond which the signal became attenuated by salt-water intrusion (often observed in instrument "ringing" on the profile images). Topographic survey was restricted to a similar range as the beach-step is hazardous even in fair-weather conditions. Interpretation of GPR profiles follows the methodology described in Bristow and Jol (2003). Several sites were surveyed during the study, but we focus on three sites (Fig. 1) that were subject to a storm six months after the survey which, on one of the profiles, transported beach sediments seaward and exposed the substrate on which beaches overlie. The post-storm profile was resurveyed providing an opportunity to verify the GPR interpretation.

RESULTS

Fig. 4 shows GPR images from site 3 utilising 225MHz and 450MHz antennae. The stratigraphy interpretation is overlaid on the 225MHz profile on the bottom panel.

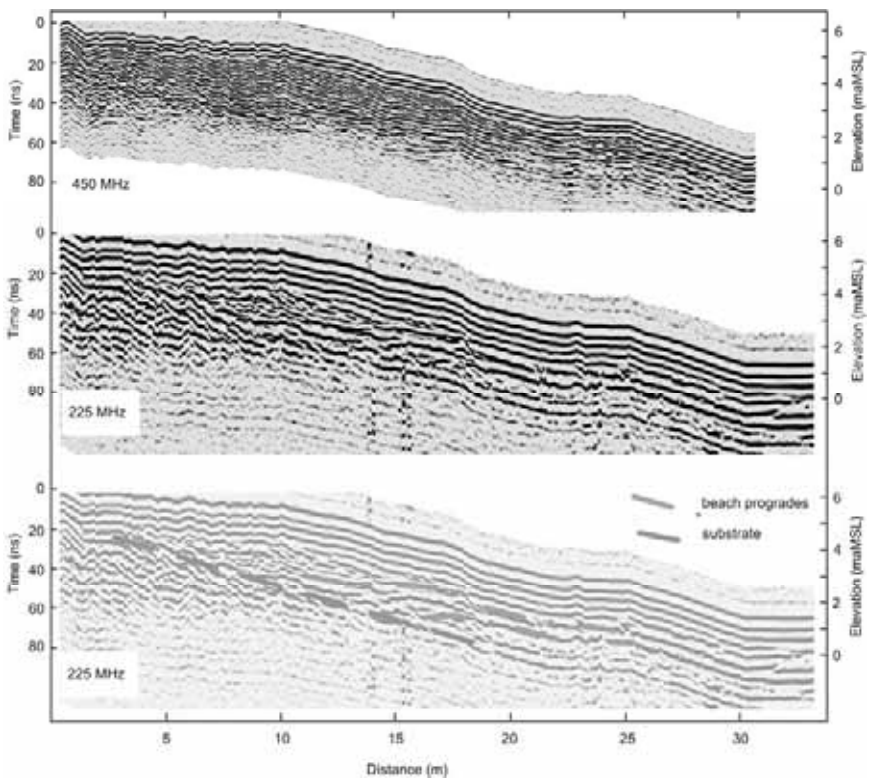

Fig. 4. GPR images at 225 and 450 MHz conducted at site 3. Distance is measured from the cliff toe. Interpretation of the substrate is difficult owing to poor topographic controls.

Of the three sites surveyed for this study, the interpretation of the substrate profile is least clear on Fig. 4 owing to the loss of DGPS control on topographic survey near the cliff toe. Despite this, the stratigraphy shows a basal reflection that that slopes seaward relatively steeply from near the cliff toe, where it is 3-4m above MSL. This surface is down-lapped by prograded beach surfaces and associated berm-shaped features. The beach surfaces slope more gently than the substrate and approximately parallel the modern beach surface.

The topographic control on the beach profile is very good at sites 2 and 1. Fig. 5 shows GPR profiles from site 2. Profiles returned from surveys at 225MHz and 450MHz are once again shown, with stratigraphy overlaid on the 225MHz profile.

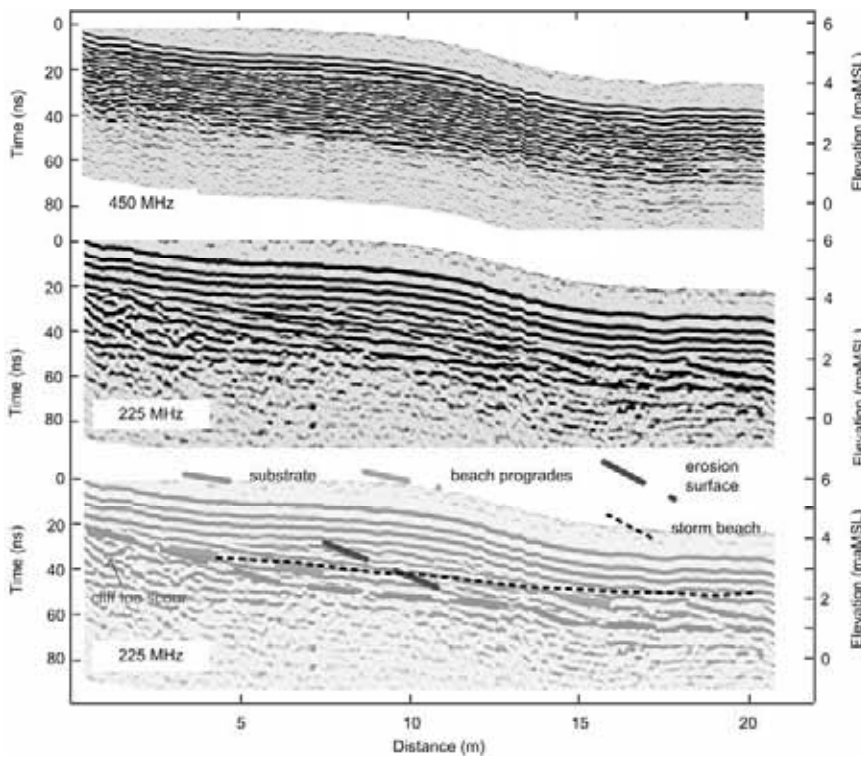

Fig. 5. GPR images at 225 and 450 MHz conducted at site 2.

Fig. 5 once again shows a basal reflection, interpreted as the substrate, sloping relatively steeply from near the cliff toe where it is about 4m above

MSL. The reflection has a concave shape in which the initial steep slope flattens about 5m across the profile. A second steeply sloping portion of the reflection can be seen about 14m across the profile. Overlying and down-lapping the basal substrate reflection there are more gently sloping reflections that parallel the beach face and which are interpreted as beach progrades. Approximately 6-11m across the profile a steeply sloping reflection is apparent, particularly in the 450MHz survey. This is interpreted as a beach erosion surface.

A storm occurred six months after the GPR survey and resulted in significant seaward movement of beach sediments. As Fig. 6 shows, this storm was particularly notable in that at site 2 the substrate was exposed at the cliff toe and in places it remained exposed as far as 4m seaward of the cliff toe.

Fig. 6. Photographs from site 2 looking north (left) and south (right). The substrate has been exposed by seaward movement of beach sediments during a storm.

The beach profile was resurveyed at site 2 and has been overlaid on Fig. 5. The profile contacts the reflection that was interpreted to be the substrate about 4m from the cliff toe. This supports the interpretation of the substrate shape based on analysis of the radar facies.

Fig. 7 shows GPR profiles at site 1. Once again a basal reflection can be seen sloping relatively steeply from the cliff face. On the high resolution (450 MHz) profile a series of shallow scours are apparent in the GPR reflections above the basal reflection. Likewise, small beach progrades are apparent down-lapping on to the basal reflection, particularly in the 225 MHz profile. The facies from this site therefore show phases of beach erosion and accretion. At this site the storm six month after the GPR survey did not expose the substrate. The storm beach profile was resurveyed, and the survey results show that the beach surface elevation was lowered by almost 2m. However, this was insufficient to expose the substrate and when the topographic survey data are overlaid on the GPR image it would appear that after the storm a thin (<50cm) veneer of beach sediment probably remained on top of the substrate.

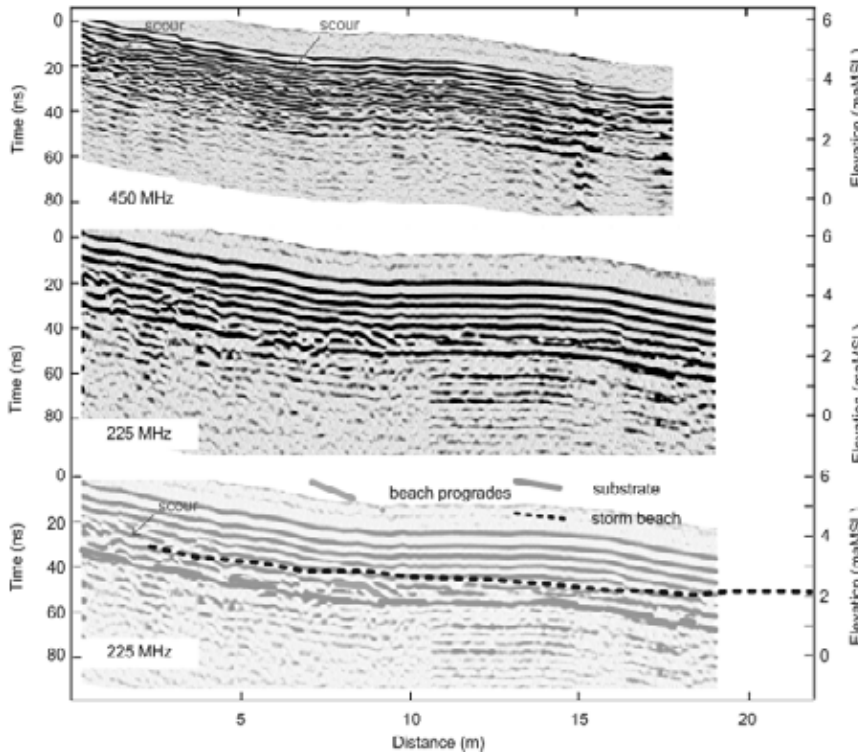

Fig. 7. GPR images at 225 and 450 MHz conducted at site 1. The storm did not expose the substrate.

DISCUSSION

GPR has been used to investigate the structure of prograding beaches (e.g. Neal et al., 2002; Moore et al., 2004; Engels and Roberts, 2005), but there has been little effort to use its ability to image the shallow subsurface in beach deposits. This paper demonstrates that the technique can be used to characterize the rarely-observed substrate on eroding mixed sand and gravel shorelines. Ground truthing in a previous study suggests that the substrate is composed of the same alluvial Pleistocene sediments as the cliff face (Stapleton, 2005). In the present study the substrate is apparent as a continuous reflection that slopes steeply (~15°) from the cliff face across several metres, and then more gently (5-9°) toward the sea.

If the substrate can be reliably imaged with GPR, then it is straightforward to accurately determine the volume of beach sediment overlying the substrate. For the present study beach volumes were evaluated simply using polygons with upper and lower bounding surfaces provided by measured beach profile surfaces and substrate profiles digitised from GPR images. Calculated in this way, the

volume of beach sediments (per metre length of shoreline) increases northward from site 1 (~30m^3/m), to site 2 (~45m^3/m), to site 3 (~75 m^3/m) in the direction of dominant longshore sediment transport. This calculation is limited by the seaward extent of both topographic and GPR surveys. As a result, the seaward edge of the beach polygon is open as the substrate and beach surface merge well below water level. We have not attempted to estimate this portion of the beach volume.

A storm that followed six months after the GPR survey provided an opportunity to ground-truth the stratigraphic interpretation because sediments were stripped away from the substrate near the cliff toe (Fig. 5 and Fig. 6). On average the storm removed a 2m-thick wedge of beach sediment. Using an approach combining GPR survey and beach profiling, an opportunity exists to calculate the volume of sediments that are eroded seaward by storms of different magnitudes. This is important because on mixed sand and gravel shorelines, cliff erosion by wave undercutting can occur only when beach sediments are removed from the cliff toe.

CONCLUSIONS

At a study site along the east coast of the South Island, New Zealand, GPR has been shown to be an effective method of profiling the substrate that underlies mixed sand and gravel beaches on eroding cliffed shorelines. Confirmation of the facies interpretation was provided by a storm which stripped beach sediments from one site exposing the substrate. Once the substrate has been reliably profiled, beach volume per metre length of shoreline can be easily calculated by constructing a polygon composed of the beach profile surface and the digitizing substrate reflection. The method is limited to the subaerial beach, both owing to the attenuation of radar signal on seaward parts of the profile, and the difficulty of beach profiling beyond the beach step.

ACKNOWLEDGMENTS

Funding for this research was provided by a Postdoctoral Fellowship to MED by New Zealand's Foundation for Research Science and Technology, Environment Canterbury, the University of Wisconsin – Eau Claire (Provost Office, Office of Research and Sponsored Programs, Department of Geography and Anthropology), and Birkbeck College, University of London, Faculty Research Grant.

REFERENCES

Engels, S. and Roberts, M.C., 2005. The Architecture of Prograding Sandy-Gravel Beach Ridges Formed During the Last Holocene Highstand: Southwestern British Columbia, Canada. *Journal of Sedimentary Research*, 75(6): 1052-1064.

Gibb, J.G. 1978. Rates of coastal erosion and accretion in New Zealand. *New Zealand Journal of Marine and Freshwater Research*, 12: 429-456.

Jol, H.M., and Bristow, C.S., 2003, GPR in Sediments: Advise on data collection, basic processing and interpretation, a good practice guide. In Bristow, C.S., and Jol, H.M., (Eds.) 2003, *Ground Penetrating Radar in Sediments*. Geological Society Special Publication 211. p.9-27.

Kirk, R.M., 1980. Mixed sand and gravel beaches: morphology processes and sediments. *Progress in Physical Geography*, 4(2): 189-210.

Moore, L.J., Jol, H.M., Kruse, S., Vanderburgh, S. and Kaminsky, G.M., 2004. Annual layers revealed in the subsurface of a prograding coastal barrier. *Journal of Sedimentary Research*, 74: 690-696.

Neal, A., Pontee, N.I., Pye, K. and Richards, J., 2002. Internal structure of mixed-sand-and-gravel beach deposits revealed using ground-penetrating radar. *Sedimentology*, 49(4): 789-804.

Pickrill, R.A., and Mitchell, J.S., 1979. Ocean wave characteristics around New Zealand. New Zealand Journal of Marine and Freshwater Research 13: 401-520.

Stapleton, J.M., 2005. Form and Function of the Waihao-Wainono Barrier, South Canterbury, *MSc Thesis. Department of Geography*, University of Canterbury, 216 pp.

van Dam, R.L. and Schlager, W., 2000. Identifying causes of ground-penetrating radar reflections using time-domain reflectometry and sedimentological analyses. *Sedimentology*, 47: 435-449.

van Dam, R.T., van den Berg, E.H., Schaap, M.G., Broekema, L.H. and Schlager, W., 2003. Radar reflections from sedimentary structures in the vadose zone. In: C.S. Bristow and H.M. Jol (Editors), *GPR in Sediments*, Geological Society of London Special Publication 211, pp. 257-273.

NUMERICAL SIMULATION OF GRAIN-SIZE SORTING AT BEACH CUSPS

Tatsuya SHIMIZU[1], Akio KOBAYASHI[2], Takaaki UDA[3], Takayuki KUMADA[4], Yasuhito NOSHI[1] and Masumi SERIZAWA[5]

The topography of beach cusps and grain-size sorting were investigated at four coasts and the backwash flow in the bay of a cusp was observed, i.e., the movement of seawater flowing obliquely from the apex to the bay resulting in the generation of a backwash flow. On the basis of these observations, two pairs of a sink and source were assumed and the three-dimensional cusp topography was predicted using the contour-line-change model considering the effect of grain-size changes developed by Kumada *et al.* (2006). The formation of a cusp and the associated accumulation of coarse material around the apex were accurately predicted.

INTRODUCTION

Cusps observed on a coast can be classified into giant, large and beach cusps (Komar, 1998). In addition to three categories, beach cusps have been further separated into two types: edge-wave cusps and swash cusps. Regarding the modeling of these cusps, Guza and Inman (1975) and Werner and Fink (1993) developed the edge-wave model, in which the forcing function is due to run-up waves with subharmonic edge waves, and the self-organization model, in which the interaction between the run-up waves and beach topography is the main forcing function, respectively. Shimada *et al.* (1995) experimentally showed that a backwash flow is induced by superimposing backwash waves in the bay in the case of forming a swash cusp; this backwash flow becomes a jet near the breaking point, causing the retardation of the wave run-up in the bay. Shibazaki *et al.* (2005) explained the development of cusps under a dynamically stable condition by introducing a term representing a pair of a sink and source of sand in the contour-line-change model (Serizawa *et al.*, 2003) and by replacing the effect due to the backwash flow by this term. When fluid motion around cusps is observed, the assumption of offshore sand transport due to the

[1] Graduate student, Department of Oceanic Architecture & Engineering, College of Science & Technology, Nihon University, 7-24-1 Narashinodai, Funabashi, Chiba 274-8501, Japan
[2] Dr. Eng., Professor, Department of Oceanic Architecture & Engineering, College of Science & Technology, Nihon University, 7-24-1 Narashinodai, Funabashi, Chiba 274-8501, Japan
[3] Dr. Eng., Executive Director, Public Works Research Center, 1-6-4 Taito, Taito, Tokyo 110-0016, Japan
[4] Dr. Eng., Laboratory of Aquatic Science Consultant Co., Ltd., Meishin Building, 1-14-1 Kami-ikedai, Ota, Tokyo 145-0064, Japan
[5] Coastal Engineering Laboratory Co., Ltd., 301, 1-22 Wakaba, Shinjuku, Tokyo 160-0011, Japan

backwash flow in the bay is considered to be appropriate, but seawater flowing to the apex of the cusps flows obliquely down into the bay, forming a backwash flow in the bay, instead of returning to the original position by the oscillatory flow. Taking this fact into account, it is assumed that shoreward sand transport also takes place and that the transport may be given by the combination of a sink at a seaward point and a source at a landward point relative to the apex of the cusps. Thus, two pairs of a sink and source of sand are considered and their effect is investigated in this study. On the other hand, it is often observed on coasts that coarse (fine) sand accumulates at the apex (in the bay), but the mechanism of grain-size sorting around the cusps has not yet been studied. Here, a model for predicting beach topography and grain-size sorting around beach cusps is developed while improving the contour-line-change model considering grain-size change by Kumada *et al.* (2006).

FIELD OBSERVATION

To investigate the topography and the grain-size sorting of bed material around cusps of various spatial scales, field observations were carried out at four coasts, as shown in **Fig. 1**: a lakeshore in Lake Biwa, Odaiba beach park in Tokyo Bay, and the Chigasaki and Isumi coasts.

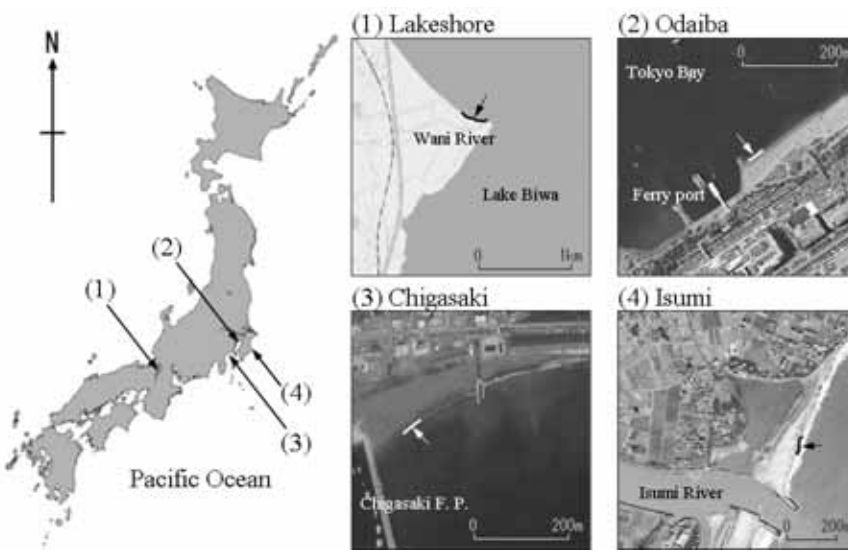

Figure 1. Locations of field observation of a cusp.

(1) Lakeshore in Lake Biwa

On February 9, 2007, beach cusps at Lake Biwa were studied near the mouth of the Wani River flowing into the west shore of the lake. **Figure 2** shows a cusp with a wavelength of approximately 50 cm. Although cusps regularly develop along the shoreline, coarse sand and gravel accumulate landward of the shoreline. Setting points A, A', B and B' at and away from the

apex, as shown in **Fig. 2**, the width of the accumulation zone of fine sand becomes narrow at points B and B', whereas the width increases between them, forming an out-of-phase shape with respect to the shoreline configuration of the cusp. Furthermore, offshore of the boundary line connecting B and B', the lake bed is completely covered with gravel with a large grain size, and cusps are formed on this lake bed. Under the ordinary wave conditions, no beach changes occur on the lake bed offshore of the boundary line connecting B and B', suggesting that the offshore lake bed is a solid bed. This implies that the water depth at B and B' is equivalent to the depth of closure at this lakeshore. The bed slope in the bay is gentler than that at the apex, and the lake bed is covered only with fine sand.

Figure 3 shows another example of a cusp at the same lakeshore. In this example, the bed of the bay is deeply eroded, and gravel with a large grain size, which had been deposited to form the lower layer, was exposed. These topographic changes explain why a strong outflow always develops in the bay that causes fine sand to be transported offshore.

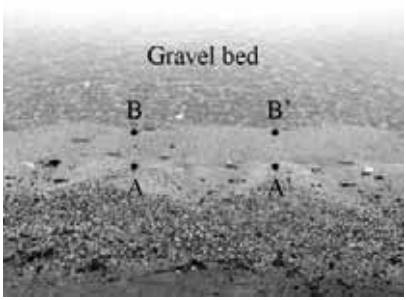

Fig. 2. Beach cusp observed at lakeshore near mouth of Wani River in Lake Biwa.

Fig. 3. Another example of beach cusp in Lake Biwa

(2) Odaiba beach park in Tokyo Bay

On April 7, 2007, beach cusps at Odaiba beach park in Tokyo Bay were observed. Because this beach park is located deep in Tokyo Bay, the action of wind waves is weak compared with that on the other open coasts, but ship waves with a significant wave height are generated because this beach is close to a harbor. Beach cusps are generated by these ship waves. **Figure 4** shows the beach cusps and wave run-up. The grain size significantly changes across the dotted line in the figure, and coarse sand is distributed only in the zone shoreward of this dotted line. **Figure 5** shows the beach cusps immediately before the wave run-up. The timing of the wave run-up in the bay at the cusps is delayed compared with that at the apex, causing the formation of a concave wave crest line. The topography of the beach cusps shown in **Fig. 5** was measured. We also carried out bottom sampling. **Figure 6** shows the results of bottom sampling as well as the bottom contours. The wavelength of the cusps is approximately 100 cm, and coarse sand is accumulated at the apex, whereas the

seabed in the bay is covered with fine sand. The accumulation pattern of coarse and fine sand at the apex and in the bay, respectively, is similar to the observation results at the lakeshore, as shown in **Fig. 3.**

Fig. 4. Wave run-up at cusps (Odaiba beach park).

Fig. 5. Beach cusps immediately before wave run-up (Odaiba beach park).

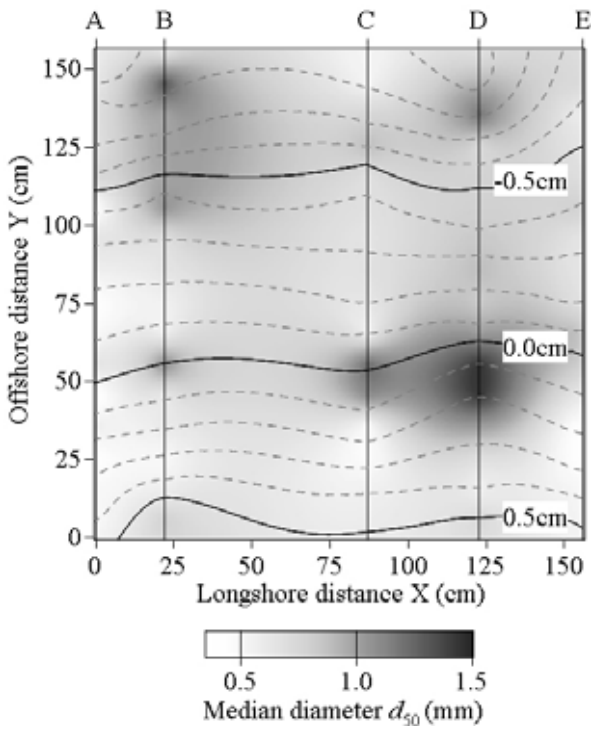

Fig. 6. Beach topography and distribution of median diameter (Odaiba beach park).

(3) Chigasaki coast

Field observation at the Chigasaki coast, which faces Sagami Bay, was carried out on January 18, 2007. The beach material is composed of fine and medium sand, and beach cusps with a regular spacing were observed, as shown in **Fig. 7**. A backwash flow was clearly observed in the bay, as shown by the arrows in the figure. Part of the seawater, which flowed toward the apex of the cusp, quickly returned to the sea as a backwash, but the movement of the remaining seawater, which flowed from the apex down to the bay, had a phase shift with the run-up waves because of the long return distance, resulting in the occurrence of the backwash flow. **Figure 8** shows another example of backwash flow, taken from the foreshore shoreward of the backwash flow. It was realized that the backwash flow is formed by accumulated seawater that flows from both apices toward the bottom of the bay.

Fig. 7. Beach cusps and backwash flow observed at Chigasaki coast.

Fig. 8. Backwash flow concentrated in the bay.

(4) Isumi coast

The observation of beach cusps on the Isumi coast, which faces the Pacific Ocean, was carried out on June 28, 2006. The topography and grain size distribution of the beach material were measured along nine survey lines, as shown in **Fig. 9**. The beach elevation was measured at the locations shown by an open circle, whereas the beach materials were sampled at the locations indicated by a solid circle. **Figure 9** also shows the measured beach topography of a beach cusp with a 30 m wavelength. Comparing the intervals of survey lines with the wavelength of a beach cusp, it was realized that the observation of the beach topography and the sampling of beach materials were carried out with sufficiently high accuracy. **Figure 10** shows the configuration of cusps with a wavelength of 30 m, along with the distribution of d_{50}. It was found that coarse sand accumulates at the apex, whereas fine sand accumulates in the bay. These results are similar to those measured at Odaiba beach park.

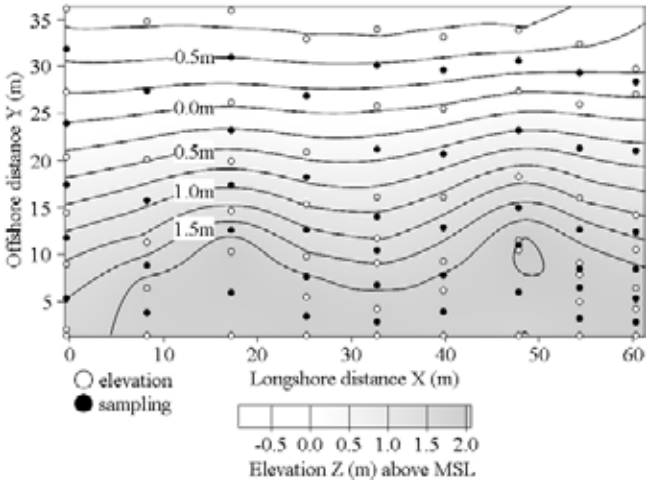

Fig. 9. Topography of beach cusp and measuring points at Isumi coast.

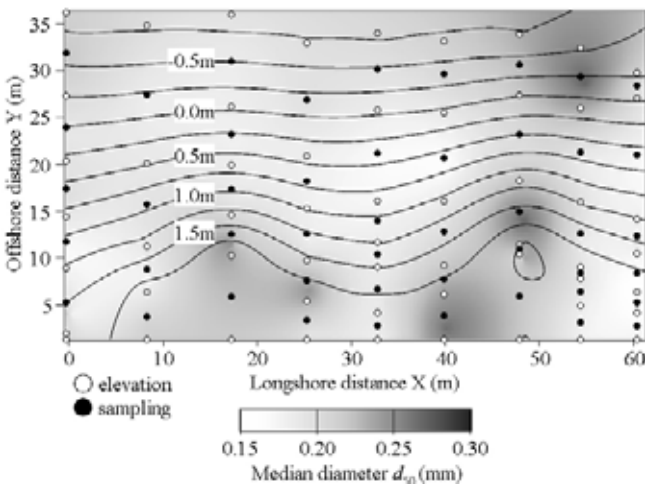

Fig. 10. Distribution of median diameter of beach material and configuration of cusps at Isumi coast.

MODEL

From the observations at the four coasts, the relationship between the flow in the bay and at the apex, and the sink and source of the sand can be summarized as shown in **Fig. 11**. Regarding the fluid motion around the cusps, the assumption of offshore sand transport in the bay is appropriate since a backwash flow develops, as observed on the Chigasaki coast. In contrast, it is assumed that the seawater flowing to the apex flows obliquely down into the bay, resulting in the formation of a backwash flow, instead of returning to the

original position by the oscillatory flow. In this case, it is assumed that shoreward sand transport is also triggered by the combination of a sink at a seaward point and a source at a landward point relative to the apex of the cusps, as schematically shown in **Fig. 12**. Out of the sand of mixed grain size transported by this fluid motion, coarse sand accumulates at the apex because the run-up wave energy dissipates on the foreshore, and fine sand, which can be easily transported by the decreased wave energy, is transported into the bay. The repetition of this motion results in the accumulation of coarse sand at the apex and fine sand in the bay.

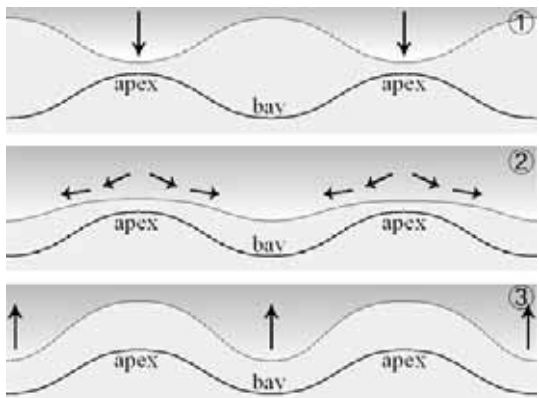

Fig. 11. Topography of cusps and concept of flow development around cusps.

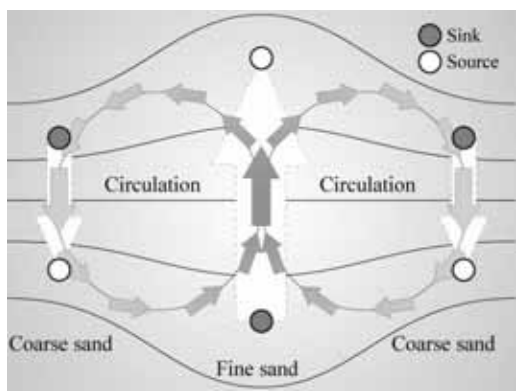

Fig. 12. Development of circulating sand transport.

On the basis of this concept, a model for predicting both the topography and grain-size sorting of a beach cusp under a dynamically stable condition (Uda *et al.*, 2006) can be developed, by applying the contour-line-change model considering grain-size changes developed by Kumada *et al.* (2006). An additional term representing a sink and source of sand is included in the continuity equation of the model, as given in Eq. (1).

$$\frac{\partial y^{(k)}}{\partial t} = -\frac{\partial q_x{}^{(k)}}{\partial x} - \frac{\partial q_z{}^{(k)}}{\partial z} + q_s{}^{(k)} \quad ; \quad k = 1, 2, ..., N \tag{1}$$

$$q_s{}^{(k)} = K_1{}^{(k)} \cdot \mu^{(k)} \cdot q_{all} \tag{2}$$

$$K_1{}^{(k)} = \frac{A}{\sqrt{d^{(k)}}} \tag{3}$$

Here, $\Delta y^{(k)}$ is the change in each contour line corresponding to each grain size , x is the longshore distance, z is the seabed elevation , $q_z{}^{(k)}$ and $q_x{}^{(k)}$ are the cross-shore and longshore sand transport of each grain size , respectively, $q_s{}^{(k)}$ is the sink and source of the sand, $\mu^{(k)}$ is the content of each grain size in the exchange layer and $d^{(k)}$ is the grain size in mm. A is a constant depending on the condition of the coast . q_{all} is the sink and source of sand per unit width and unit depth, and is given so that the sand budget in the entire calculation domain is satisfied. The total change, ΔY, in each contour line corresponding to all the grain sizes can be calculated by Eq. (4) by the summation of the change, $\Delta y^{(k)}$, in the contour line corresponding to each grain size.

$$\frac{\partial Y}{\partial t} = \sum_{k=1}^{N} \frac{\partial y^{(k)}}{\partial t} \tag{4}$$

The other equations and the methodology of the calculation are the same as those given in Kumada *et al.* (2006).

RESULTS

To realize the fundamental features of the formation of cusps, two cases of numerical simulation were carried out; in case 1, basic features were investigated given a model topography of beach cusps, and in case 2, predicted results were compared with the cusps measured at the Isumi coast. **Table 1** shows the calculation conditions.

In case 1, sand composed of two grain sizes (d=0.5 mm for fine sand and d=5 mm for gravel) is considered. The initial content of each grain size is assumed to be 60 % and 40 %, respectively. The equilibrium slope of the sand population is set at a constant 1/10. The berm height and the depth of closure are assumed to be 1.5 m and 3 m, respectively, taking into consideration the fact that cusp formation occurs in extremely shallow water. The location and intensity of the sink and source of sand are also shown in **Table 1**. Two pairs of a sink and source of sand were distributed as shown in **Fig. 12**. The sinks and sources of sand were located at symmetrical points with respect to the shoreline.

Waves are incident from the normal to the shoreline, and the solution under a dynamically stable condition was predicted.

Table 1. Calculation conditions.

Initial slope	1/10
Initial grain size and content of sand	0.5 mm: 60 %, 5.0 mm: 40 % (case 1) 0.25 mm: 70 %, 1.5mm 30 % (case 2)
Equilibrium slope	1/10
Width of exchange layer	B=0.27 m
Breaker height	1.0 m
Tide level	Mean sea level
Depth range of beach changes	h_R=1.5 m and h_C=-3 m (case1) h_R=2.0 m and h_C=-4 m (case2)
Critical slope of sand on land and sea bottom	1/2 and 1/3
Grid size	Δy=2.5 m and Δz=0.5 m
Intensity of sink and source of sand	1.0×10^{7} $m^3/m^2/yr$ (case1) 5.0×10^{6} $m^3/m^2/yr$ (case2)

Figure 13 shows the result of the model calculation. The formation of concave and convex contour lines landward and seaward of the shoreline, respectively, are clearly predicted, as well as accumulation of fine sand in the bay and coarse sand at the apex. Furthermore, coarse sand continuously accumulates along the offshore marginal area of the cusp, which is in good agreement with the results measured, as shown in **Fig. 3**.

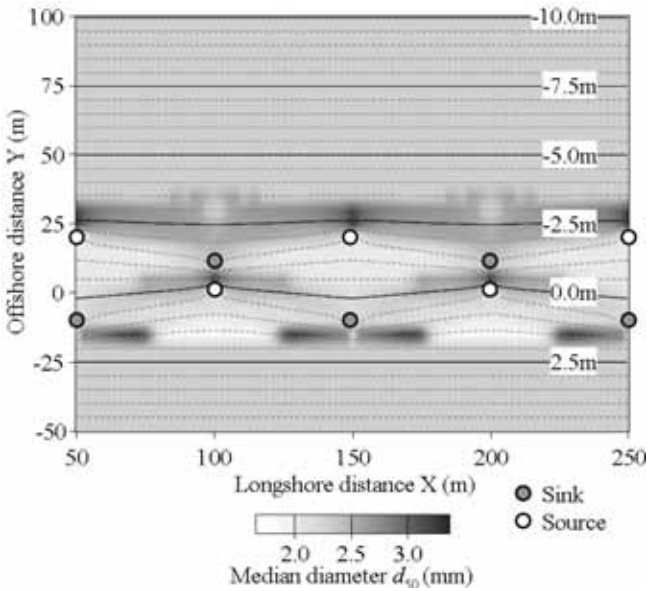

Fig. 13. Predicted beach topography of cusps and distribution of median diameter of beach material.

Figure 14 shows the longshore distribution of the contents of fine sand and gravel after 0, 1,000, 5,000, 10,000 and 50,000 steps. Initially, the contents of fine sand and gravel were constant along the shore with the proportions of 40 % and 60 %, respectively, but the content of gravel gradually increased in the central part of the bay up to 1,000 steps, whereas it decreased in the vicinity of the apex. By 5,000 steps, the content of gravel had increased to 60 % in the center of the bay, and the location of the peak in the content of fine sand, which was located near the apex after 1,000 steps, moved toward the center of the beach cusp. Finally, by 50,000 steps, the peak content of fine sand, which was located between the bay and the apex after 10,000 steps, had moved to the center of the bay. The content of fine sand markedly decreased at the apices, whereas it was high in the bay. The grain size composition reached a stable condition at 50,000 steps. Thus, the accumulation of coarse sand at the apex and fine sand in the bay over time was predicted well.

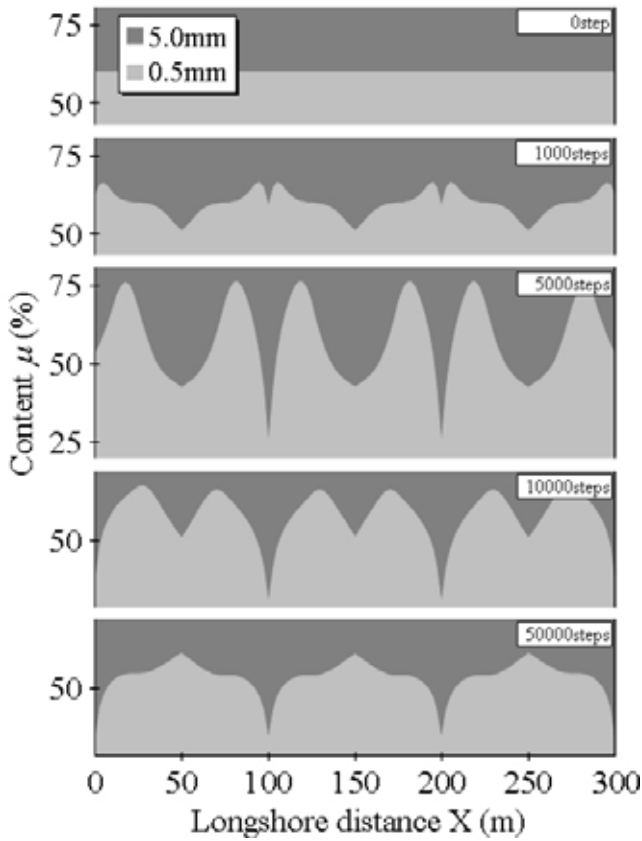

Fig. 14. Longshore distribution of content of each grain size.

The numerical model was applied to the cusps at the Isumi coast. As the calculation condition, the grain sizes (contents) of the beach material were set to 1.5 mm (30 %) and 0.25 mm (70 %), on the basis of the grain size analysis of sand samples taken from the site. The equilibrium slope of the grain size population was assumed to be 1/10. The berm height and the depth of closure were assumed to be 2 m and 4 m, respectively, because beach cusps are formed in the shallow water zone. The conditions of the sink and source of sand are shown in **Table 1**. **Figure 15** shows the reproduced results of the cusps measured on the Isumi coast. The predicted topography of the cusps with the apex and the bay are in good agreement with the measured topography, as shown in **Fig. 10**. The accumulation of fine sand in the bay and coarse sand in the apex was also reproduced.

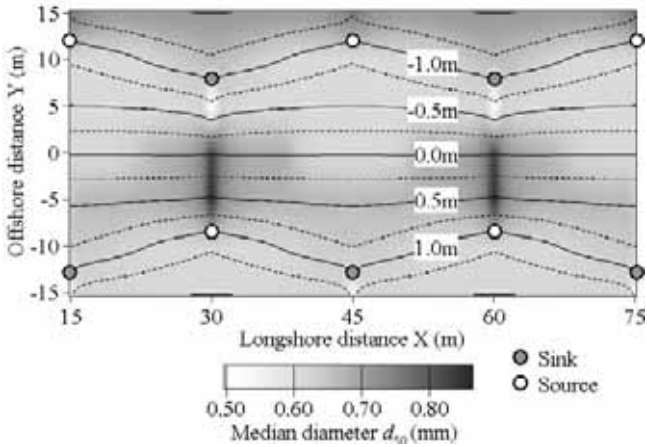

Fig. 15. Predicted beach topography of cusps and distribution of median diameter of beach material at Isumi coast.

CONCLUSIONS

The topography of beach cusps and grain-size sorting were investigated at four coasts. It was found that seawater in the apex flows obliquely down from the apex to the bay, forming a backwash flow, as schematically shown in **Fig. 12**. On the basis of this concept, a model for predicting both topographic changes and grain-size sorting around a beach cusp was developed by applying the contour-line-change model considering grain-size changes developed by Kumada *et al.* (2006), and by introducing two pairs of a sink and source of sand. Not only the configuration of the cusp, but also the accumulation of coarse sand at the apex and fine sand in the bay were accurately predicted. Predicted results were in good agreement with the measured ones.

REFERENCES

Guza, R. T. and D. L. Inman. 1975. Edge waves and beach cusps, *JGR*, Vol. 80 (21), pp. 2997-3012.

Komar, P. D. 1998. Beach Processes and Sedimentation, Second Edition, *New Jersey, Prentice-Hall*, p. 544.

Kumada, T., T. Uda, M. Serizawa and Y. Noshi. 2006. Model for predicting changes in grain size distribution of bed materials, *Proc. 30th ICCE*, pp. 3043-3055.

Serizawa, M., T. Uda, T. San-nami, K. Furuike and T. Kumada. 2003. Improvement of contour line change model in terms of stabilization mechanism of longitudinal profile, *Coastal Sediments '03*, pp. 1-15.

Shibazaki, M., T. Uda, M. Serizawa, A. Kobayashi and T. Maeda. 2005. Formation and maintaining mechanism of beach cusps, *Annual Jour. Coastal Eng. in Japan*, Vol. 52. pp. 416-420. (in Japanese)

Shimada, H., H. Takano and Y. Mizuguchi. 1995. Formative mechanism of beach cusps, *Annual Jour. Coastal Eng. in Japan*, Vol. 42. pp. 586-590. (in Japanese)

Uda, T., M. Serizawa, T. San-nami and K. Furuike. 2006. Model for predicting dynamically stable beach based on analogy with two-dimensional potential flow, *Proc. 30th ICCE*, pp. 3911-3923.

Werner, B. T. and Fink, T. M. 1993. Beach cusps as self-organized patterns, *Science*, Vol. 260, pp. 968-971.

ANALYSIS OF TURBIDITY DATA TO DESCRIBE THE SUSPENDED SEDIMENT DYNAMICS IN THE GERMAN ESTUARIES EMS AND ELBE

Habermann Christine[1] and Theis Heinz[2]

Changes in the hydromorphologic conditions have led to an altered sediment budget and shifts in sedimentation and erosion processes in the German estuaries Ems and Elbe. These changes call for improved and ecologically sound sediment management concepts with the aim to diminish dredging rates. Analysis of long term turbidity data from point measurements at different stations along the estuaries provide a powerful tool to learn more about the transport processes of sediments as a basis for developing new mamagement strategies.

Introduction

A better understanding of the long-term, large-scale suspended sediment dynamics is needed. To gain more knowledge on suspended sediment behaviour, turbidity datasets with a high temporal resolution from various measuring stations along the two estuaries Elbe and Ems were analysed. The turbidity in an estuary shows a great variation that depends on the longitudinal position in the estuary and the system characteristics of the estuary. It is influenced by different natural parameters. The aim of the here presented studies was to identify these relevant parameters and to quantify their effect on turbidity using different statistic methods. An important question examined is the impact of anthropogenic measures such as dredging and dumping activities on the long-term, large-scale turbidity distribution. In this paper, results are shown for the Elbe estuary. For the Ems Estuary, results are presented in BfG Report No. 1488.

Data Basis (Elbe)

For the tidal Elbe turbidity datasets from 3 point measurement stations that are operated by the NLWKN (Niedersächsischer Landesbetrieb für Wasserwirtschaft, Küsten- und Naturschutz) and the BSU (Behörde für Stadtentwicklung und Umwelt, Hamburg) were analyzed. This data plays an important role for the description of the transport characteristics of the Tidal Elbe as it has a high temporal resolution with one data point every 5 minutes. On the other hand, the datasets cover a long time period of approximately 10 years. The turbidity is measured with a turbidity sensor at 1.5 meters below the

[1] Federal Institute of Hydrology, Postfach 200253 D-56002 Koblenz, Germany
[2] Group, Laboratory, Address, City, State, ZIP/Zone, County

water surface. In the following drawing, the different turbidity measurement stations along the Tidal Elbe are presented. In the here presented study, the datasets from the station Grauerort, Seemannshöft and Blankenese were analyzed.

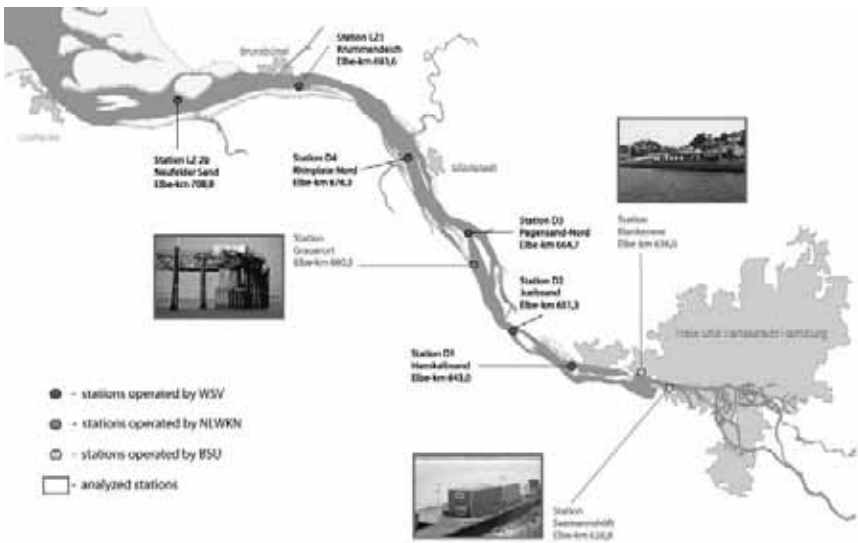

Figure 1. Map of the Elbe estuary with point measurement stations of turbidity.

Results (Elbe)

In the following graph, the general characteristics of sediment dynamics and their dependence from the river discharge are shown exemplary for station Grauerort.

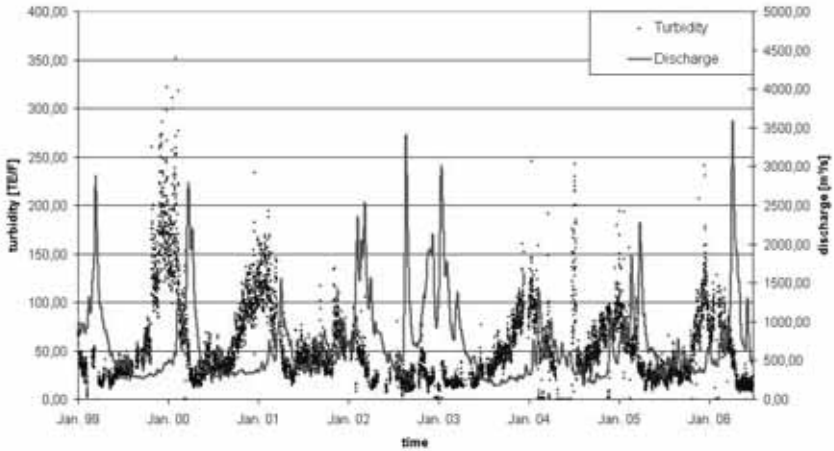

Figure 2. Time variation curve of turbidity at station Grauerort and discharge at Neu Darchau.

It can be seen that a constant material accumulation takes place over several weeks in periods of low discharge. A seaward shift of suspended sediments in the upper reach of the estuary leads to a decrease of turbidity when a certain discharge is exceeded.

Information on sediment transport characteristics can be obtained by using a Ratio of mean turbidity during flood to mean turbidity during ebb tide. The results for this analysis are shown exemplary for station Seemannshöft.

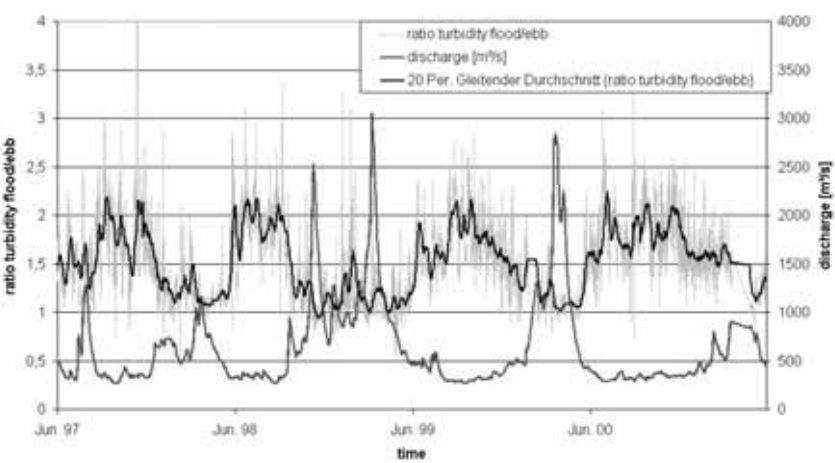

Figure 3. Time variation curve of mean turbidity ratio at station Seemannshöft and discharge at Neu Darchau.

In this graph, a ratio > 1 can be regarded as an indicator for resulting net upstream transport of sediments as more material is transported upstream during flood then during ebb tide.
A ratio < 1 is an indicator for resulting net downstream transport of sediments as more material is transported during ebb tide.

High discharge from the inland leads to balanced sediment transport with a Ratio of approximately 1 whereas low discharge leads to higher sediment concentrations during flood tide which is an indicator for resulting net upstream transport.

This characteristic behaviour is superimposed by higher ratio values in spring phases and lower ratio values in neap phases.

At station Blankenese, the same behavior can be observed:
By this it can be concluded that it is characteristic for the reach downstream of the harbor of Hamburg.

Another goal of the study was to investigate the influence of dumping activities on the large scale, long term sediment concentration. Results are shown exemplary for station Seemannshöft:

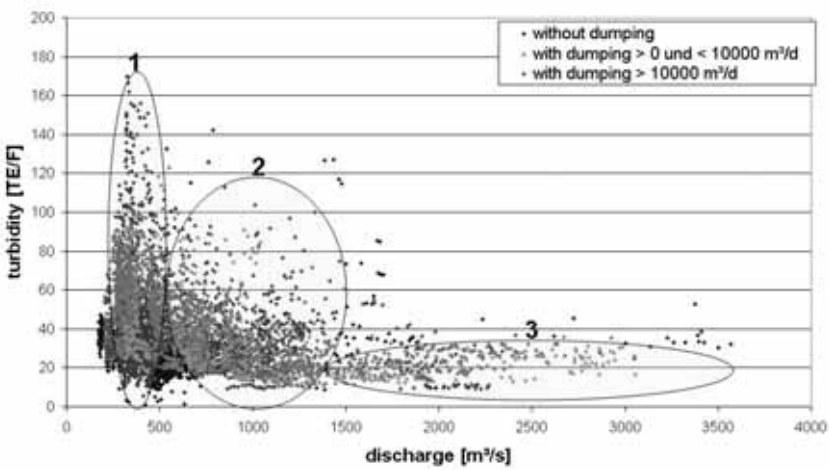

Figure 4. Turbidity at station Seemannshöft versus discharge at Neu Darchau. The different colors indicate dumping events close to the station.

It can be seen that low discharge leads to high sediment concentrations with strong fluctuations that are not influenced by Q. With medium discharge, a transition area can be observed where the sediment concentration depends on

the discharge history. High discharge leads to a low sediment concentration as a clearing takes place in the upper part of the Tidal Elbe.

Neither in the Tidal Elbe nor in the Ems estuary could a connection be detected between the long-term, large-scale sediment concentration and dredging and dumping activities.

REFERNCES

Habermann, C., 2006. Einfluss von Unterhaltungsbaggerungen auf die Schwebstoffdynamik der Unterems – Monitoring während eines baggerungsfreien Zeitraumes, *BfG Bericht BfG 1488*, Koblenz.

NEW TURKISH SEISMIC DESIGN CODE FOR PORT STRUCTURES: A PERFORMANCE-BASED APPROACH

M. Nuray Aydınoğlu[1], Ayşen Ergin[2], Işıkhan Güler[3], Yalçın Yüksel[4], Esin Çevik[5] and Ahmet Yalçıner[6]

A new seismic design code is being enforced in Turkey, effective September 1, 2008, for transportation structures officially administered by General Directorate for Construction of Railways, Harbors and Airports (RHA) of Ministry of Transportation. The aim of this contribution is to describe the main aspects of the RHA Seismic Code with special emphasis given to port structures. The most important aspect of the code rests on its main approach incorporating "performance-based design". In this context, port structures have been classified with respect to their expected seismic performance, usage and functional importance, namely, special, nominal, simple and unimportant structures. This is followed by standard definition of performance levels, namely "Minimum Damage Performance Level", "Controlled Damage Performance Level" and "Excessive Damage Performance Level" prior to state of collapse. On the other hand, design earthquakes have been specified in three levels with probability of exceedance of 50%, 10% and 2% in 50 years, respectively. Minimum performance objectives are then specified for each class of structure under different earthquake levels. Two different classes of design methods have been specified in the code, namely, Strength-Based Design (SBD) and Deformation-Based Design (DBD). The latter includes practice-oriented nonlinear analysis, namely pushover analysis as well as nonlinear response history analysis in the time domain. Acceptance criteria are specified in terms of nonlinear deformation quantities for multi-level performance objectives. In view of a very limited number of seismic codes available for port structures, the new Turkish Seismic Code is expected to attract a special attention with its modern approach.

INTRODUCTION

Rapid development of international sea trade in the last few decades has eventually led to questioning of seismic safety of port structures. Heavy damage occurred in Port of Kobe in disastrous Kobe Earthquake of 1995 was a costly reminder to the engineering community regarding the lack of modern seismic design guidelines and codes specifically addressed to port structures. In 2001, a notable attempt was made by International Navigation Association (formerly Permanent International Association for Navigation Congresses – PIANC) Working Group 34 through the publication of Seismic Design Guidelines for Port Structures (PIANC 2001). In the following years, first generation of modern seismic codes for port structures emerged from California, USA. In this respect, Port of Los Angeles seismic code (POLA 2004) and Marine Oil Terminal Engineering and Maintenance Standards (MOTEMS 2005) are the

[1] Department of Earthquake Engineering, Boğaziçi University, Kandilli Observatory and Earthquake Research Institute, Istanbul, Turkey
[2] Ocean Engineering Research Center, Middle East Technical University, Ankara, Turkey
[3] Yüksel Proje International Co., Ankara, Turkey
[4] Civil Engineering Department, Coastal Engineering Laboratory, Yıldız Technical University, Istanbul, Turkey
[5] Civil Engineering Department, Coastal Engineering Laboratory, Yıldız Technical University, Istanbul, Turkey
[6] Ocean Engineering Research Center, Middle East Technical University, Ankara, Turkey

most recent examples. The latter is based on extensive preparatory studies by Ferrito et al (1999).

The common design philosophy behind all the above-mentioned codes is the *performance-based design*. As opposed to traditionally used prescriptive *strength-based approach*, performance-based design rests on an explicit *deformation-based approach*, where damage is *quantified* in terms of inelastic deformation demand quantities on element level under specified multi-level earthquakes and such *ductile* demand quantities are then evaluated against prescribed *deformation capacities* for selected *performance objectives* under each earthquake level. In the mean time internal force quantities corresponding to *brittle* behavior modes are ensured not to exceed the specified *strength capacities*.

The General Directorate for Construction of Railways, Harbors and Airports (RHA) of Ministry of Transportation of Turkish Republic has commissioned a group of experts in 2005 for the preparation of a seismic code applicable to transportation structures officially administered by RHA. The aim of this contribution is to describe the main aspects of the RHA Seismic Code (Ministry of Transportation 2007) with a special emphasis given to port structures. The code, as a whole, rests completely on a performance-based design philosophy, as explained in this paper.

PERFORMANCE – BASED DESIGN PARAMETERS

As in any performance-based design code, the RHA code for port structures starts with the definition of the following performance-based design parameters:

1. Structural classes associated with the expected performance, usage and functional importance,
2. Seismic performance levels associated with expected damage levels,
3. Earthquake levels associated with frequent, rare and very rare earthquakes,
4. Seismic performance objectives under different earthquake levels.

The above-listed parameters are explained in the following paragraphs.

Structural Classes

Port structures are classified as special, nominal, simple and unimportant structures.

Special Structures:

- Structures to be used for rapid response and evacuation immediately after an earthquake,
- Structures to be used for toxic, flammable or explosive materials.

Nominal Structures:

- Structures where the loss of life and property must be avoided,
- Structures of economic and social significance,
- Structures with difficult and time-consuming post-earthquake repair and retrofit needs,

Simple Structures:

- Less important structures other than those classified in Special and Nominal Structures,
- Structures other than those classified as Unimportant Structures.

Unimportant Structures:

- Easily replaceable structures,
- Structures not causing life safety risk even extensively damaged,
- Temporary structures.

Seismic Performance Levels

Seismic performance levels of port structures are defined with respect to expected damages during an earthquake.

Minimum Damage (MD) Performance Level:

This performance level corresponds to a state where no or a very limited damage occurs in port structures and/or in their elements under an earthquake. In this case, port operation continues uninterrupted or if any, service interruptions are limited to few days.

Controlled Damage (CD) Performance Level:

This performance level corresponds to a state where non-extensive, repairable damage occurs in port structures and/or in their elements under an earthquake. In this case, short-term (few weeks or months) interruptions in related port operations may be expected.

Extensive Damage (ED) Performance Level:

This performance level corresponds to a state where extensive damage occurs in port structures and/or in their elements under an earthquake. In this case, long-term interruptions or even closures in related port operations may be expected.

State of Collapse (CS):

This corresponds to the collapse state in port structures and/or in their elements under an earthquake. Related port operation is terminated.

Earthquake Levels

Three different levels of earthquakes are defined in terms of their intensity, representing frequent, rare and very rare seismic events. Response spectra ordinates of the relevant earthquakes are given for the entire country in an annex of the code.

(E1) Earthquake Level:

This earthquake level represents relatively frequent but low-intensity earthquake ground motions with a high probability to occur during the service life of port structures. The probability of exceedance of (E1) level earthquake in 50 years is 50%, which corresponds to a return period of 72 years.

(E2) Earthquake Level:

This earthquake level represents the infrequent and high-intensity earthquake ground motions with a low probability to occur during the service life of port structures. The probability of exceedance of (E2) level earthquake in 50 years is 10%, which corresponds to a return period of 475 years.

(E3) Earthquake Level:

This earthquake level represents the highest intensity, very infrequent earthquake ground motions that port structures within the scope of the code may be subjected to. The probability of exceedance of (E3) level earthquake in 50 years is 2%, which corresponds to a return period of 2475 years.

Seismic Performance Objectives

Minimum performance objectives are specified as shown in Table 1 for each class of port structure under different earthquake levels defined above.

Table 1. Minimum performance objectives for port structures

Structure Class	(E1) Earthq. Level	(E2) Earthq. Level	(E3) Earthq. Level
Special	–	MD	CD
Nominal	MD	CD	(ED)*
Simple	CD	(ED)*	–
Unimportant	(ED)*	(CS)*	–
* Implied objectives not requiring design verification.			

ANALYSIS AND DESIGN PROCEDURES

Being a performance-based code, the new Turkish seismic code for port structures mainly rests on a *deformation-based design (DBD)* approach, which in turn requires the implementation of nonlinear seismic analysis procedures. However, linear analysis procedures within the framework of traditional *strength-based design (SBD)* are allowed for the verification of *Minimum Damage (MD) Performance Objective* where structural behavior is at or near the elastic limits. Linear procedures are further allowed for the verification of *Controlled Damage (CD) Performance Objective* with relatively conservative design parameters. Table 2 indicates the design approaches to be used for different classes of structures under multi-level earthquakes. The table should be read with Table 1 where the corresponding performance objectives are given.

Table 2. Applicable design approaches to port structures

Structure Class	(E1) Earthq. Level	(E2) Earthq. Level	(E3) Earthq. Level
Special	–	SBD / DBD	DBD
Nominal	SBD	SBD / DBD	–
Simple	SBD	–	–
Unimportant	–	–	–

In the following both *strength-based design* approach and *deformation-based design* approach are explained as implemented in the code with particular reference to pile supported wharves and piers.

Strength-based design approach for pile supported structures

In *strength-based design* (SBD) approach for piled systems, the structure is analyzed linearly under reduced seismic loads, as similar to the standard building seismic design codes. Seismic load reduction factor $R_a(T)$ is defined in terms of period of vibration, T, as

$$\begin{aligned} R_a(T) &= 1.5 + (R-1.5)\frac{T}{T_S} && (0 \le T \le T_S) \\ R_a(T) &= R && (T_S < T) \end{aligned} \qquad (1)$$

where T_S represents the transition period of the response spectrum at the intersection of constant acceleration and constant velocity regions, and R is the structural behavior factor given in Table 3 for pile supported wharves and piers.

For the linear analysis under reduced seismic loads, the Equivalent Seismic Load Method based on single-mode response as well as multi-mode Spectral Mode Combination Method have been specified in the code.

Table 3. Structural Behavior Factors (*R*)

Structure	Pile arrangement	Performance Level	
		MD	CD
Wharf	Vertical piles	1.5	2.5
	Batter piles	1.0	1.5
Pier	Vertical piles	2.5	4.0
	Batter piles	1.0	1.5

Inadequacy of strength-based design for batter piled structures

Batter piles are commonly preferred in piers and wharves, in particular for their satisfactory performance under breasting and mooring loads. However, batter piled systems perform very poorly in earthquakes because of their inherent lack of ductility. In fact majority of strength-based designed batter piled piers and wharves have exhibited very poor performance in recent earthquakes, namely 1989 Loma Prieta earthquake and 1995 Kobe earthquake (Ferrito et al 1999, PIANC 2001), and 1999 Izmit earthquake in Turkey (Boulanger et al 2000). It is for this reason that the design and construction of batter piles are virtually prohibited in the current Californian code practice unless special measures are taken or specially designed structural fuse systems are used (POLA 2004, MOTEMS 2005).

As observed from Table 3.2, batter piled systems were assigned very low R factors in the new Turkish code, i.e., R=1 is specified for MD level and R=1.5 for CD level. Note that, as opposed to Californian practice, the intention of the

code is not to avoid the use of batter piles completely. Instead, the designer is strongly discouraged to employ the strength-based approach and fictitious linear analysis under artificially reduced seismic loads to simulate highly complex nonlinear behavior of such systems in earthquakes. In fact, recently Harn (2004[a,b]) showed that the complex seismic behavior of batter piles can only be explained with nonlinear analysis, and advocated the use practical nonlinear analysis procedures for a rational seismic design of batter piled structures. The so-called *pole vaulting* phenomenon is shown to be the major source of failures in pile-to-deck connections and in deck elements (Fig.1).

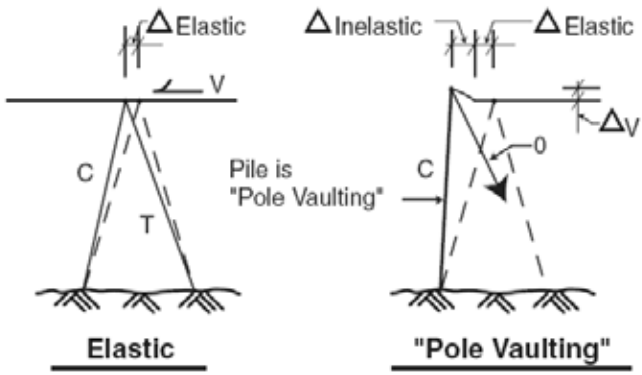

Figure 1. Pole vaulting mechanism in batter piles (Harn 2004[a,b])

Thus, by assigning very low values to *R* factors for batter piles, the new Turkish code effectively pushes the designer to use deformation-based design approach in batter piled systems with or without structural fuse systems (Harn 2004[b]), or otherwise to choose vertical pile systems for an efficient seismic design.

Deformation-based design approach for pile supported structures

Deformation-Based Design (DBD) approach based on nonlinear analysis is essentially required for *nominal* and *special* class structures to verify the Controlled Damage (CD) performance objective. Recommended nonlinear analysis procedures include response-history analysis in the time domain as well as practice oriented nonlinear analysis procedures based on single-mode and multi-mode pushover analyses (Aydınoğlu 2003, 2004), which are recently included as well in the Turkish seismic design code for buildings (Ministry of Public Works and Settlement 2007). Traditional plastic hinge model, as well as fiber models are recommended for nonlinear pile and pile-to-cap beam dowel connection modeling. In piled structures, soil is recommended to be modeled with nonlinear p-y, t-z and Q-z springs.

Regarding the plastic hinge at the pile-to-cap beam/deck *dowel connection*, the plastic hinge length, L_p , is specified as the sum of strain penetration lengths into the pile and cap beam or deck:

$$L_p = 0.044\, f_y\, d_b \tag{2}$$

where f_y and d_b represent the yield strength and diameter of the dowel, respectively. In-ground plastic hinges are characterized with a plastic hinge length of twice the section depth.

Regarding the reinforced concrete dowel connection at the pile/pile cap interface, the yield surface of the section may be piecewise linearized and strain hardening effect may be neglected as shown in Fig.2. In constructing the yield surface of the connection, concrete compressive strain and dowel reinforcement tensile strength may be taken as 0.004 and 0.015, respectively (Priestley 2003). The normality condition is to be considered for plastic deformation vector.

Estimation of deformation demands

Inelastic deformation demands obtained from the nonlinear analysis are verified against the corresponding capacities given for various performance objectives, as explained in the following.

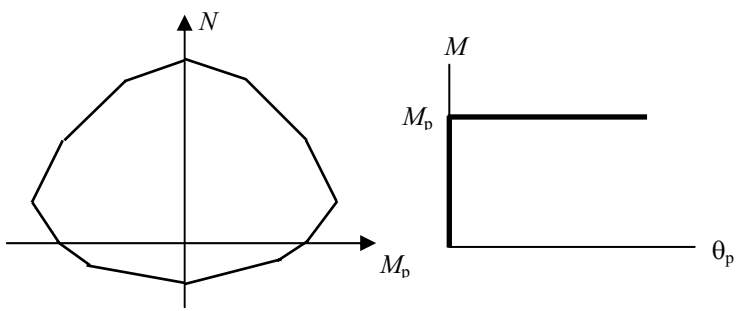

Figure 2. Linearized yield surface and elasto-plastic moment-plastic rotation relationship

In pile supported piers and wharves, nonlinear deformation demands are obtained either directly in terms of strains (in fiber analysis) or in terms of plastic rotations through plastic hinge analysis. Since deformation capacities have been defined in the code in terms strains, any plastic rotation, θ_p , has to be converted first to plastic curvature, ϕ_p , through an appropriately defined plastic hinge length, L_p , followed by the calculation of total curvature, ϕ_t , by adding the yield curvature, ϕ_y (Fig.3).

$$\phi_p = \frac{\theta_p}{L_p} \qquad ; \qquad \phi_t = \phi_y + \phi_p \tag{3}$$

Concrete and reinforcing steel strain demands in reinforced and prestressed concrete piles, and steel strain demands in steel piles are then estimated from the corresponding curvatures under prevailing axial force demands.

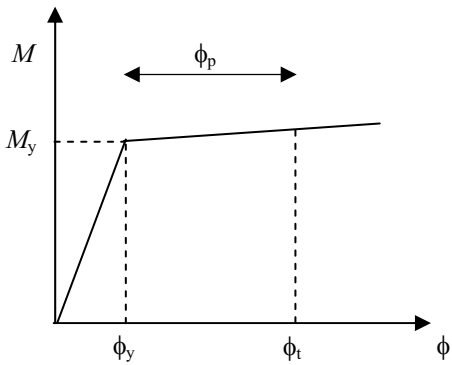

Figure 3. Bi-linearized moment-curvature relationship

Acceptance criteria for damage limits: Strain capacities

The estimated strain demands as above, are checked against below given strain capacities, which correspond to accepted damage limits for a given seismic performance objective. The criteria basically follow those given in POLA (2004) and MOTEMS (2005).

Table 4. Strain capacities for piles

Strain	Performance Objective	
	MD	CD
Reinforced and prestressed concrete pile		
Plastic section at pile-to-pile cap/deck connection:		
Concrete compressive strain	0.005	0.020
Reinforcing steel tensile strain	0.010	0.040
Prestressed concrete pile		
In-ground plastic section:		
Prestressing steel strain	0.005(1)	0.040
Steel pipe pile		
Plastic section at reinforced concrete pile-to-pile cap/deck connection:		
Concrete compressive strain	0.008	0.025
Reinforcing steel tensile strain	0.010	0.040
Compressive or tensile steel strain at in-ground plastic section:		
Hollow steel pipe pile	0.008	0.025
Concrete infilled pipe pile	0.008	0.035

(1) Strain increment due to earthquake action

Shear strength capacities

In addition to specifying deformation capacities of ductile members, brittle force capacities, such as shear capacities, have been defined as well to compare with the shear demands in piles, pile-to-deck connections and deck elements.

CONCLUSIONS

General Directorate for Construction of Railways, Harbors and Airports (RHA) of Ministry of Transportation has recently issued a new seismic design code applicable to railways, harbor/port structures and airports in Turkey. In this paper, main aspects of the code are explained with particular reference to the seismic design requirements for port structures.

As its main feature, the code rests on a performance-based seismic design philosophy. In this context, classification of port structures, definition of damaged-based performance levels, multi-level earthquake actions and performance objectives are briefly described in the paper as the essential parameters of the performance-based design. Applicable analysis and design procedures are explained with a special emphasis given to the requirements of deformation-based nonlinear design of pile supported port structures.

In view of a very limited number of seismic codes available for port structures, the new Turkish Seismic Code is expected to attract a special attention with its modern approach.

ACKNOWLEDGMENTS

The authors gratefully acknowledge the generous support of Ms. Ülker Yetgin, Head of Marine Structures Engineering Department of General Directorate for Construction of Railways, Harbours and Airports, Ministry of Transportation, Ankara, Turkey.

REFERENCES

Aydınoğlu, M. N. 2003. An incremental response spectrum analysis based on inelastic spectral displacements for multi-mode seismic performance evaluation. *Bulletin of Earthquake Engineering*; **1(1)**: 3-36.

Aydınoğlu, M. N. 2004. An Improved Pushover Procedure for Engineering Practice: Incremental Response Spectrum Analysis (IRSA). International Workshop on Performance-based seismic design – Concepts and implementation, Eds. P. Fajfar and H. Krawinkler, June 28-July 1, 2004, Bled, Slovenia, PEER Report 2004/05, September 2004.

Boulanger, R.W., Iai, S., Ansal, A., Çetin, K.Ö., Idriss, I.M., Sunman, B., Sunman, K. (2000). Chapter 13: Performance of Waterfront Structures. Special Issue on 1999 Izmit Earthquake, *Earthquake Spectra,* EERI, **16**, 295-310.

Ferrito, J., Dickenson, S., Priestley, N, Werner, S., Taylor, C. 1999. Seismic Criteria for California Marine Oil Terminals, Technical Report TR-2103-SHR, Volumes 1,2,3, *Naval Facilities Engineering Service Center*, California.

Harn, R.E. 2004[a]. Have Batter Piles Gotten a Bad Rap in Seismic Zones (Or Everything You Wanted to Know About Batter Piles But were Afraid to Ask, *Proceedings ASCE Ports 2004*, May 23-26, Houston, Texas.

Harn, R.E. 2004[b]. Displacement Design of Marine Structures on Batter Piles. *Proc. 13th World Conference on Earthquake Engineering*, Paper No.543, August 1-6, Vancouver, B.C., Canada.

Ministry of Public Works and Settlement. 2007. Specification for Buildings to be Constructed in Seismic Zones, Ankara, Turkey.

Ministry of Transportation. 2007. Seismic Code for the Constructions of Harbor and Coastal Structures, Railways and Airports, *General Directorate for Construction of Railways, Harbors and Airports (RHA)*. Ankara, Turkey.

MOTEMS – The Marine Oil Terminal Engineering and Maintenance Standards. 2005. Chapter 31F (Marine Oil Terminals), Title 24, California Code of Regulations, Part 2, California Building Code, *California Building Standards Commission*, California.

PIANC – International Navigation Association 2001. Seismic Design Guidelines for Port Structures, *Working Group 34 of the Maritime Navigation Commission*, A.A.Balkema Publishers.

POLA – Port of Los Angeles. 2004. Code for Seismic Design, Upgrade and Repair of Container Wharves. Los Angeles, California.

Priestley, M.J.N. 2003. Myths and Fallacies in Earthquake Engineering, Revisited. *The Mallet Milne Lecture*, 2003. IUSS Press, Pavia, Italy.

NATURAL VERSUS ANTHROPOGENIC FACTORS IN CANCUN BARRIER EROSION

J. Javier Diez[1], M. Dolores Esteban[1], Jose S. Lopez[1], V. Negro[1] and Rosa M. Paz[2]

During the first half of 2006 important sand nourishment was done along the barrier shore face of Cancun Nizuc (Quintana Roo, Mexico). It was quickly decided and constructed after that the hurricane *Wilma* swept the barrier and under the recent general impression of the devastating *Katrina* effects on New Orleans region. That decision interrupted a long time of discussions about the better Project to recover the great erosion of the barrier beach. This paper discuss the role of the different natural agents on the coastal erosion in this Cancun barrier under strictly natural conditions, trying to discern the relative importance of the common maritime weather versus the hurricanes; and the role of the different anthropogenic agents of development in both the generation of new erosive coastal processes (strictly anthropogenics) and the strengthening of the previous and natural processes (partially anthropogenics). The later being more significant, the paper looks at the different importance of their synergies with the, respectively, common weather versus hurricanes effects on the barrier erosion.

INTRODUCTION

The Cancun-Nizuc (Benito Juarez, Quintana Roo, Mexico) coastal barrier (Figure 1) has suffered dramatic reduction since 1970. An important and hasty tourist development has been taking place, by the alongshore occupation with condominiums, hotels and other facilities of a great part of the barrier; this occupation affected in many stretches most of its wideness including dunes and even, some times, part of the beach. This way of development had as consequence the onset of a permanent unsteadiness of the beach, and the subsequent setting of the erosion conditions on, at least, some of its stretches, though they were not well noticed for some not specially storming time (Diez and Esteban, 2006). The erosive situation became suddenly and dramatically evident in 1988 after the *Gilbert* event. Among the effects of hurricane *Gilbert* the erosions suffered by the beaches of the Nizuc-Cancun barrier acquired special meaning, although they had to be presumable taking into account the placement of the buildings of the excessive tourist development, doubtless too much close to the shoreline, even built on the active profile of the beach.

[1] School of Civil Engineering, Universidad Politecnica de Madrid, Profesor Aranguren, s/n, Madrid, Spain
[2] Biology Faculty, Universidad Complutense de Madrid, Madrid, Spain

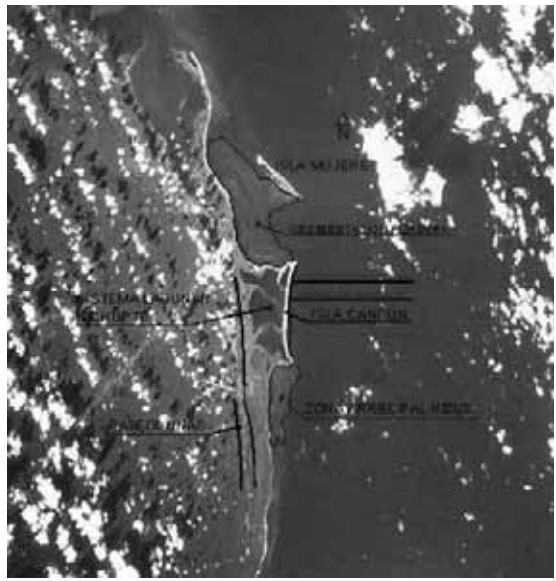

Figure 1. Localization of the Cancun-Nizuc beach barrier (CFE, 2000-2001).

The effect on tour operators became important, reducing local incomes and becoming to have a main effect on socio-economic activity of the whole estate. As a result of the *Gilbert* impact some studies were immediately undertaken by UNAM (1989-1991) looking for adequate knowledge of the problem and processes to aboard a well founded regeneration project for the whole barrier; it delayed and some local owners, mainly hotels, projected a few small constructions, for local protection in different few short stretches of the barrier beach, with little satisfactory results.

By the turn of the past century most of the barrier length scarcely had permanent beach and the wave attacks on the hotel structures became very frequent. Socioeconomic damages by the affection of tourism were already important at that time and environmental impacts were presumed to be happening, not only on the coastal barrier and its beaches but in the ecosystem of Nichupte lagoon as well if the barrier became broken. Therefore local authorities promoted new studies to understand as accurately as possible the behaviour of the whole barrier system and surroundings. Several additional studies were so developed until 2004 (CFE, 2000-2001; CFE, 2003), initially aiming to come forward with a solution for the recovery of the beaches and the permanent protection of the barrier.

The erosion (Figure 2) was even more serious after passing new different hurricanes throughout the zone, especially *Ivan* (2004) and *Wilma* (2005). *Wilma* trajectory run parallel onto the barrier from south to north and had a notorious impact on the whole barrier installations, probably being determinant

of the beach recovery decision, taken at the beginning of 2006. The regeneration was developed along the fist half of the same year, apparently as a simple nourishment of the whole barrier beach, although no professional information could be obtained about it.

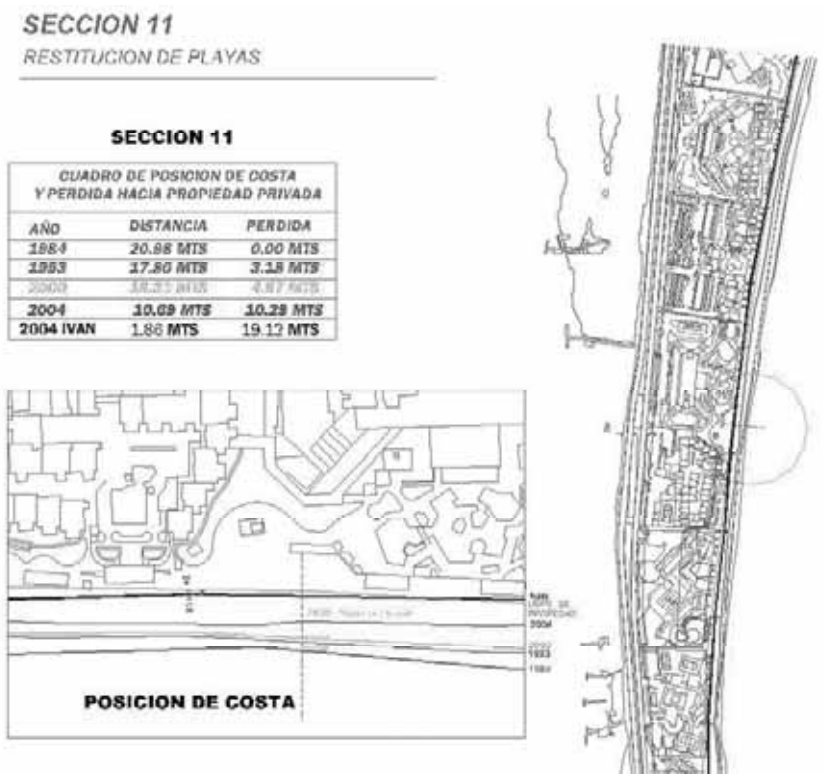

Figure 2. Typical evolution of shoreline in Cancun. The regression of the shoreline is practically continuous in all sections and had reached dramatic reduction of the beach in many of them.

ZONE DATA

The continental part linked to the Cancun-Nizuc area has the same nature than the rest of the Yucatan Karstic formation since the Pliocene (Diez, Esteban and Paz, 2009). The sea platform is so from Karstic origin and constituted of calcareous material. The present landscape began to take shape in the late Pleistocene; Nizuc and Cancun have initially constituted islands and the littoral barrier between them was developed under Aeolian and northward littoral actions, probably induced by an underlying reef system that could be extended as far as the Mujeres Island. The bay between it and the continental shoreline became a coastal lagoon which evolved to the current Nitchupte lagoon.

Former barrier was extended as a spit as result of the longshore transport, probably till Mujeres Island, changing later northwestward its direction as a consequence of a colder climate (Diez, Esteban and Paz, 2009)**.** Lagoon, barrier and spit have been submitted to sea level and other climatic conditions along the Holocene permitting the formation of two *tombolos* respectively sheltered by Cancun and Nizuc points. The Cancun and Nizuc island system became, thus, to prevent the sea water flowing to the lagoon and allowed a freshwater/estuarine ecosystem. This former barrier, of about 17 km. length and 100 – 400 m. width initially, has evolved loosing the sandy spit and reducing its length to 12 km. Part of the ancient barrier and spit still remain as sand banks and islands (Diez, Esteban and Paz, 2009)

Current water circulation is restricted in the lagoon system only flowing seaward through a few narrow tidal channels between both *tombolos*. The barrier had accumulated Aeolian materials reaching significant heights in some dunes, but most of the sandy material was removed afterwards. The beach had before fine sands but now, due to the erosions, the sediments show a triple origin: the notably gross sands and coarser materials are from the reefs, the carbonated finest sands deposited by saturation, and the organogenic sands and shell rests; the three can be identified in the size grain distribution curves of these studies.

It is necessary to separate in this area the so called ordinary or common wind waves, corresponding to the regular maritime climate, with its extremal wind regime, corresponding to the storm waves, and the regime due to hurricanes. Although the effect of extreme common storm waves is important respect to the rest of the common waves, is quite small in relation to the effect of hurricanes when directly affecting the study point. The analysis of the average wind wave distribution seems to clearly show a certain climatic bi-seasonality (winter-summer), much more illustrative and meaningful than the division in the four classic seasons (astronomical), which have not only climatic meaning. The winter spans from September to mid February, with storms coming from the NE, and the summer goes from February to mid September, with storms coming from SE. February and September are transitory periods with the respective roles of spring and autumn (Diez and Esteban, 2006).

The effect of hurricanes does not depend in fact only on their magnitudes, but also on their trajectories and diameters. And according with the continental shelf shape the refraction is always important, being maximum for the north-eastern offshore waves (CFE, 2000-2001) (Figure 3). The referred studies show that the potential transport of sediments due to hurricanes such as *Gilbert*, that only lasted a few days, are not much greater than those due to common wind waves, that run along the whole year.

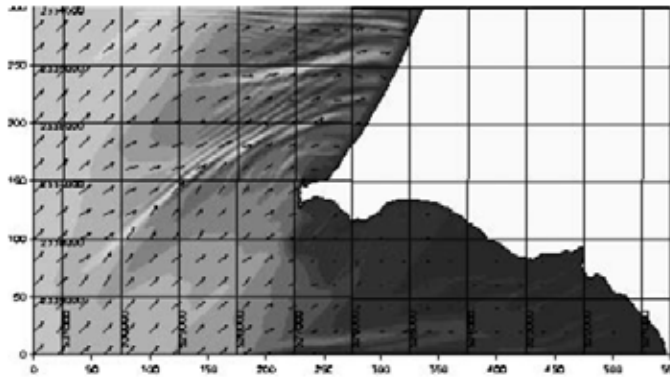

Figure 3. Application of the Model refraction of northeast waves (CFE) showing a strong, but likely insufficient, change of the waves direction. The northward drift is dominant.

A northwards net longshore littoral transport throughout the barrier seems to be obvious, and a natural feeding of sediments to the barrier system takes so place from the south in front of Nizuc point, but this feeding is lesser than the northward losses in front of Cancun point, whose rocky support is not able to hold the littoral transport. It also shows the existence of a transversal swing of the beach cross profile moved by the transversal littoral transport and whose net balance is estimated seawards, mainly due to the difficulty for the recovery of the sand material (difficulty mainly caused to the dyke effect of the natural reefs, outcropped by erosion and still rather unknown, not researched nor sufficiently mapped in the studies, and whose destabilizing role on the beach profile cannot be ignored. These outcrops do not appear reflected in charts and bathymetries before Gilbert event and only begin to be increasingly noticed in bathymetries and cross profiles made since UNAM studies (CFE, 2003).

Most of cross profiles along the beach are monoparabolic; only in some zones in the barrier, those placed in its extremes, a little "step" can be distinguished like a reminiscence of the bar. Bathymetric data managed make us think a loss of that "step" since 1985 (CFE, 2000-2001; Diez and Esteban, 2006). The sedimentologic analysis let us to recognize a close relationship between the materials from extraction banks and the materials from the beaches and dunes, and between all of them and the materials of the reefs (Diez and Esteban, 2006).

DEVELOPMENT OF THE STUDIES

The Institute of Engineering of the UNAM conducted a research from 1989 to 1991 at the request of the *Fomento Nacional de Turismo* (FONATUR). They determined topographic and bathymetric characteristics, coastal and maritime weather and storm surges, and the refraction of the wind waves; they also studied the nature and behaviour of the sediments. A solution to solve the

erosion problem was proposed. This study separated already the so called ordinary/common wind waves from those produced by hurricane conditions and referred to as cyclonal waves (the hurricanes Gilbert, Carla, Carmen, Beulah and Allen are likewise mentioned) (CFE, 2000-2001). They might have assumed that the wave distribution of the latter could be considered as the extreme wave distribution of the former. This hypothesis would not be entirely appropriate because they actually are two different types of climatic phenomena.

As a consequence of the recovery phase of the natural cycle of any beach (Copeiro, 1978) the initially (1989) apparent recovery of beaches soon after Gilbert was expected to continue. Nevertheless, later observations recognized that this natural recovery stopped soon, if it actually happened at all, and was only confirmed in the ends of the barrier. As a matter of fact, this accretion of the barrier ends could be due to the combination of both the barrier and the sheltering effects of the rocky extremes of the barrier during the time of intense longitudinal transport caused by Gilbert. The slowness of this natural recovery of the beach up to 1990/91 determined an early change in the initial diagnostics, notably about the need for some artificial way of protection or regeneration was taken into consideration (CFE, 2000-2001).

Wave refraction was calculated using diagrams obtained by means of numerical models and it results maximum for north-eastern waves. However, no special meaning was given to this finding. In our opinion, this strong refraction of the first quadrant waves can be estemated merely observing the bathymetry in deep waters in front of the barrier (Figure 4); and this significant refraction explains the predominance of the northward longshore littoral transport.

The littoral transport (CFE, 2000-2001) is obtained in those studies by empirical formulas that, although generally accepted, provided hardly consistent results, perhaps due to the problems of a suitable modelling of the wave refraction. Ordinary waves generate a littoral transport that widely depends on the formulations made and on the considered stretch of the barrier (net longshore transport: between 7,000 m^3/year northward and 610,000 m^3/year southward; seaward transversal transport: between 1000,000 and 1700,000 m^3/year). *Gilbert,* however would have generated 130,000 m^3 net offshore transport and between 6,500 and 256,000 m^3 northward longshore transport, also depending on the applied formulas and estimated waves (CFE, 2000-2001). On the other hand, the calculated littoral transport is just potential (i.e. capability of transport) and the studies do not show the availability of sedimentary materials which could allow this calculated transport to actually take place.

New studies (developed in three stages) to establish a diagnosis and to provide and update the data were made by CFE (2.000-2.001). They reviewed and extended the studies made by UNAM in order to draft a project for “integral rehabilitation of the beaches between Punta Cancun and Punta Nizuc”. And CFE proposed a later and final report in December 2003. Oceanographic, geotechnical, topographic and hydrographical research was conducted in the first stage of these studies in order to complete the information about sediments.

UNAM's conclusions were reviewed and a first diagnosis critically revised its previous assumptions. In a certain way, studies at this stage followed the working lines of the research made by UNAM, but correcting and completing them thoroughly.

Figure 4. Bathymetry in front of the barrier (CFE). Notice the differences in the slope from the north to the south, that favour a stronger northwesternwards refraction under practically any wave conditions.

The second stage of these studies were finding alternatives for the beach recovery works and nourishment, studying the beach profiles and evaluating the sandbanks nearby (Diez, Esteban and Paz, 2009). The data obtained in the previous stage was reviewed and taken into account to make an analysis of the movement of the coastline. Erosion limits were established, and a good analysis of the variability of the beach cross profiles is also incorporated.

The third stage contains new sediment data of the banks of extraction and of beach and dune sands, new wind wave and surge studies and a satellite photograph showing the sediment passage in front of Cancun point towards the Bay of Mujeres Island. At this stage a construction project was proposed, consisting of beach nourishment and some stabilizing works (Diez, Esteban and Paz, 2009). CFE proposed in its later report (December 2003), however, a new construction project totally free of rigid works, consisting of just sand nourishment.

This final report made evident the existence of a net longshore littoral transport northwards throughout the barrier, and of both a natural feeding of sediments to the barrier system from the south in front of Nizuc point and a drainage of the sands in front of Cancun. That feeding had to be smaller than the northward losses through Cancun section, whose rocky support cannot hold the material from the littoral transport. It also showed the existence of a transversal swing of the beach cross profile caused by the transversal littoral transport and

whose net balance was estimated seawards. The difficulty for the recovery of the sediments (possibly caused by the dike effect of natural reefs, outcropped by erosion of the sands around) had a destabilising role on the beach profile which cannot be ignored. This presumptive outcropping was not reflected in the charts and bathymetries before *Gilbert* and only began to be increasingly noticed in bathymetries and cross profiles after the UNAM studies, but they have never been evaluated before (Figure 5).

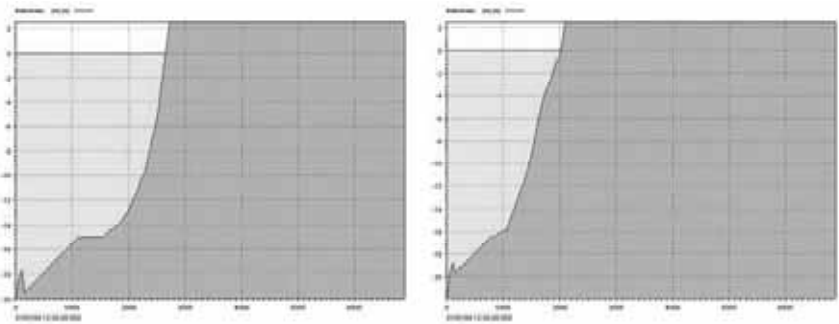

Figure 5. Typical cross profiles: monoparabolic till farer than common Cornaglia point, showing however residual and witness reefs.

HURRICANES

Hurricanes are frequent phenomena in the Cancun-Nizuc barrier. This barrier has suffered the consequences of different hurricanes (Table 1). Due to the influence in the erosion of the Cancun-Nizuc barrier, events are deserved to be emphasized are *Gilbert*, *Ivan* and *Wilma*.

Table 1. Critic features and critic time of several hurricanes in the zone in 1961-1988 (CFE).

Hurricane	Date	Direction	P_o (mb)	H_s (m)	T_s (s)
Gilbert	September, 1988	71,5º NE	675,17	12,00	13,83
Carmen	September, 1974	69º SE	755,44	2,19	9,89
Carla	September, 1961	77º NE	751,69	5,23	9,1
Beulah	September, 1967	26º SE	751,69	5,18	9,06
Allen	August, 1980	11º SE	747,94	6,64	10,27

Gilbert happened in 1988 and it has been the most devastating hurricane on the beaches of the Cancun-Nizuc littoral barrier due to its force and extension, but also due to it path (Figure 6). This event made evident the erosion in those beaches.

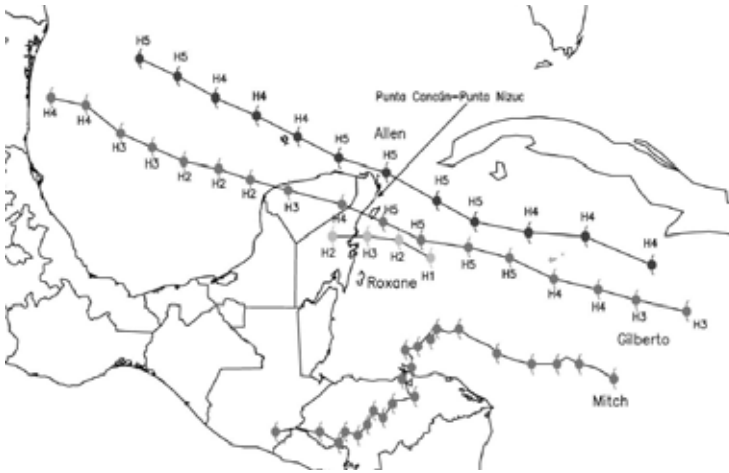

Figure 6. Trajectories and forces of different hurricanes: Gilbert, Allen, Match & Roxane (according CFE)

Ivan (2004) affected Cancun beaches from faraway, generating wind waves with relative southeastern incidence and causing northward littoral transport on the barrier, just the worst case for it. Although the damages could be worse, in the worst moment, the position of *Ivan* generated a very powerful wind wave storm with northeastern incidence permitting the recovery of the beach barrier. Also, its path (Figure 7) turned north before reaching the barrier, generating a smaller storm tide (surge level) on Cancun than *Gilbert*.

Figure 7. Trajectory of *Ivan* in last position over Cancun area

Wilma (2005), whose trajectory was parallel to the barrier, from south to north (Figure 8), had a greater effect than *Gilbert*, especially because of the permanence and longshore evolution of the waves, and in spite of a lesser degree of intensity in front of this coast. During faraway trajectory, *Wilma* could be more aggressive against Cancun beaches because wind waves incidence was even more southeastern than *Ivan*'s but the worst situation was produced during

the time when *Wilma* slowly evolved in front of and over coastal zone (Figure 9). All this time, incidence of the waves remained from the southeastern.

Besides, the intensity and magnitude of erosion on the beaches and dunes had already caused (even previously to *Gilbert)* important damage on the whole barrier, affecting tourism, with risk for its stability and its integrity at some points.

Figure 8. Trajectory of *Wilma* hurricane over Cancun area

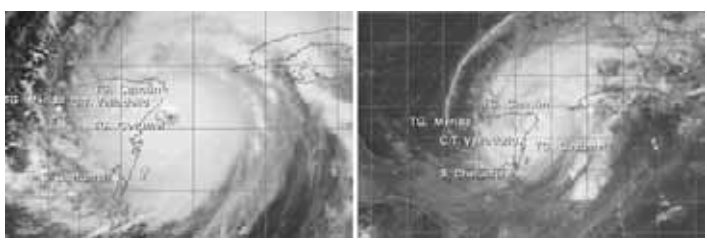

Figure 9. Three pictures of the evolution of *Wilma* in a stretch path in front of Yucatan peninsula, in Cancun area

DISCUSSION

The analysis of the average wind wave distribution clearly shows a certain climatic biseasonality (winter-summer), more illustrative and meaningful than the division in the four classic seasons (astronomical). Winter spans from September to mid February, with storms coming from the NE. Summer goes from February to mid September, with storms coming from SE. February and September are transitory periods playing the respective roles of spring and autumn. This biseasonal grouping allows a better analysis of the real coastal processes. The same climatic features take place in many zones of the planet (Diez, Esteban and Paz, 2009) and should be taken into account in similar studies.

The ordinary waves are not statistically related to the hurricane waves. They have an annual average distribution and an extreme value distribution; the former (*wave regime*) is appropriate to analyze sediment transports and coastal

processes and the latter is appropriate to estimate stress and other mechanical design variables. Statistical estimates of the hurricane wind wave regime in a determined point of the coast may not make much sense due to the lack of data, as the number of hurricanes in zones of similar situation, geographically assimilable to the observation point, is very scarce. The hurricane analysis conducted in these studies may be correct, and valid for a generic point of observation in the Gulf of Mexico. However, it must be avoided for specific areas, such as Cancun barrier; and cannot be used instead of the extreme value distribution of the ordinary waves because hurricanes (tropical conditions) have different climatic circumstances than the extratropical cyclones or trade winds.

The previous assessment is relevant in the analysis and design of littoral rigid works and also in the problem analysed here. The significant variables for the management of this kind of coastal processes come from either ordinary waves or hurricane analysis: the former in the "prevailing" coastal processes and the latter in the processes under hurricane conditions.

The potential littoral transports were calculated using average wave distribution that is different from the classic regimes based on exceeding along the average year. The obtained littoral transport values obtained are smaller when formulations like Coastal Engineering Research Center ones are used. There is a threshold wave height necessary to move each grain of sediment, and a non-lineal relation between the transport and the wave heights. Because of this, the transport generated by waves below the average wave is smaller than that due to the waves above the average one. This can imply the existence, under ordinary waves, of capacities of transport greater than those that had been calculated before.

The effects of extreme common storm waves, although significant in relation to the rest of the common waves, are quite small in comparison with the effect of hurricanes. The CFE study omits their extreme wave distribution, making hurricanes the determinant cause of the extreme impacts; not only for surging level estimation but also for the forecasting of catastrophic wave processes on beaches. As Cancun barrier has already undergone the powerful *Gilbert* effects, however, its observed values must be more appropriate than the lesser regime values determined with any pseudo-statistical method. The statistical analysis of the hurricane surge level and waves is perhaps appropriate, and undoubtedly convenient for the whole Caribbean area and for its different zones. Nevertheless, it does not have a relevant meaning here because it is based on a small number of hurricanes (Table 1) and also because all of them have different statistical parameters in the study point. Therefore, the recurrence determined for *Gilbert* can be considered worthless.

Waves suffer an intense refraction, greater than that anticipated by theoretical models, (Figure 3), which are commonly accepted and do not correspond sufficiently to the bathymetry of the continental slope and shelf in front of the Cancun barrier. It affects negatively both the evaluation of the sediment transport and the risk of the beach erosion.

Some geomorphologic data of these studies are also remarkable and it is possible to conclude observing the bathymetries that reef outcropping has been increasing after *Gilbert*, as a result of the erosion and the descent of the profiles. Besides, the erosion of the reefs themselves obviously increases when they outcrop, providing thus the gross fractions of the sediments and samples. These studies do not supply so far, though, any accurate information about the presence or outcropping of reefs and the possibility of obtaining it now, after the nourishment of the beach, has become very low until posterior erosion, but it is still very convenient. The knowledge of the distribution and nature of reefs, announced by the comparison of the bathymetries of 1985 and 1989 could certainly be improved. That comparison permits, however, to conclude that the reefs increasingly outcropped in those years and that the erosion of the beach profile along the entire barrier was also more significant then. The reefs affect the natural changes and evolution of the cross profiles and may have been playing a destabilising role on them. The available studies have not taken into account the effect of such reefs on the transversal transport processes.

Marine climate in these latitudes is characterized by a bimodal wave distribution in deep waters, with dominant waves from NE from mid September to early February (period that can be called winter), and dominant waves from SE from mid February to early September (summer). The wave propagation until breaking implies a change of direction according to the bathymetry of the zone next to the coast, and the change is greater with NE waves. Therefore there is a net northward alongshore transport with loss of sediments in front of Cancun. Cancun point cannot retain all of them, and the transversal transport caused by hurricanes can aggravate the problem. Sediment supply to the system, run by SE waves, takes place mainly in summer coming from the south in front of Nizuc.

The alongshore transport under common waves is generally restricted to a limited band which permits Cancun point to retain a great part of sediments. Before the development of the barrier, the losses in front of Cancun due to the transversal transport along the barrier were limited, because of the fast recovery of “prevailing” profiles after the storms. Before the appearance of reef outcroppings, hurricanes implied a large swing of the profile, with a strong incidence in the longshore transport and losses of sand, but with a fast recovery of the profile. The normal loss of sediments in front of Cancun could be easily compensated each year with the increase of sediments in front of Nizuc point; and the extraordinary losses under hurricane conditions could be also compensated in a few years.

Development has increased along the shoreline, even on berm and dunes, reducing the “resilience” of the beach profile for the different sea states. As a consequence, a continuous erosion of the coast was unavoidably induced and made worse when hurricanes appeared (Figure 2). The possibility of cross profile recovery diminished, its bar reducing and its slope increasing, and the reef outcrops probably appeared. Under these conditions the sea level reaches

more easily and frequently the (rigid) structures that confine the hotel facilities, which accentuates wave reflections undermining the profile. The removal of the sediments facilitated their transport towards the barrier in front of Cancun. Common waves, in addition to hurricanes, were, to sum up, increasing their efficiency on beach erosion.

CONCLUSIONS

When the *Gilbert* hit the coastline, the beach was already eroded, its bar very reduced, its profile sloping and getting deeper and, perhaps, with multiple outcropped reefs for that time. The transversal off-shore transport due to *Gilbert* storm and surge moved away a significant volume of sediments offshore beyond the reefs. *Gilbert* could have stricken the zone prior to the profile transformation; then the recovery of the beach would have been probably greater and faster: It took place however after that the slope had deepened and, possibly, that a remarkable amount of reefs had already outcropped, so that the common waves were not able to return the sediments towards the land again.

The problem of beach erosion apparently manifested for the first time in Cancun after *Gilbert*, but these studies permit to state that the hurricane only magnified a problem that had been livilng for a long time. Its origin would be attributed to the occupation process of the barrier. The idea that climatic sea level rise could have unleashed the process must not be taken yet sufficiently consistent hypothesis, otherwise it would have been proposed before. The study does not provide any sign of submersion in this coast.

REFERENCES

CFE, 2.000-2.001. *Estudios y Modelos de Simulación y Proyecto Ejecutivo para la rehabilitación Integral de las playas en el tramo entre Punta Cancún y Punta Nizuc. Primera, Segunda y Tercera Etapa,* Technical reports and projects.

CFE, 2.003. *Presentación y Mantenimiento de la Zona Federal Marítimo Terrestre entre Punta Cancún y Punta Nizuc,* Project.

Copeiro, E., 1.978. Los ritmos naturales de nuestras playas, *Revista de Obras Públicas*, 3157, 361-378.

Diez, J.J. and Esteban, M. D., 2.006. Barrera litoral de Cancun, *Proceedings of XXX Pan American Convention of Engineers, UPADI, 16 pp.*

Diez, J.J., Esteban, M. D. and Paz, R., 2.009. Cancun-Nizuc Coastal Barrier, *Journal of Coastal Research, 12 pp.*

NUMERICAL SIMULATIONS OF TURBULENT BORE RUN-UP AND RUN-DOWN

Mathieu Mory[1], Sylvain Mauriet[1], Stéphane Abadie[1] and Pierre Lubin[2]

The collapse of a turbulent bore propagating inshore on a sloping beach and the subsequent run-up and run-down flow is simulated using a RANS VOF model. The results are compared to experimental results of Yeh *et al.* (1989). The phenomenon of bore collapse is first studied and the transition between bore collapse and run-up is characterized. The run-up flow is then described with a focus (i). on the shear stresses applied in the swash layer and on the bottom, and (ii). on the maximum height of run-up.

INTRODUCTION

Dynamic processes occurring in the swash zone have a significant impact on the shore area evolution. Because of wave breaking, a significant part of the cross-shore sediment transport occurs in this zone, especially in the area where wave run-up and run-down take place. Up to the shore line, a comprehensive understanding is given by existing numerical models based on the non linear shallow water equations or the Boussinesq equations. The wave decay is well reproduced, but the subsequent modelling of the sediment transport requires a parameterisation of the friction coefficient on the sea bed. The paper presents the results of RANS numerical simulations of a bore propagating on a sloping beach and resulting in a run-up/run-down phenomenon. Numerical results are compared to the results of a laboratory experiment by Yeh *et al.* (1989).

THE MODEL

Numerical simulations were carried out using the AQUILON model, developed at the TREFLE laboratory (Bordeaux, France) (Vincent and Caltagirone, 1999; Lubin *et al.*, 2006). This code includes a Navier-Stokes Volume Of Fluid (NS-VOF) model solving the two-phase flow (air and water). Two different methods (VOF-PLIC method, TVD method) are implemented in the model to compute the interface between fluids. Although the PLIC method is more precise than the TVD method, its use was found to be inappropriate for the present computations due to the small size of grid elements. The interface broke in drops at the head and it could finally not be reconstructed. The TVD technique was finally employed. Its disadvantage is the enhancement of diffusion across the interface. Diffusion was artificially reduced by taking the physical properties of fluids (density, viscosity) to be those of water in a grid

[1] LASAGEC[2], Université de Pau et des Pays de l'Adour, 1 allée du parc Montaury , Anglet, 64400, France
[2] UMR CNRS 8508 TREFLE, ENSCPB,16 avenue Pey-Berland, Pessac, 33607, France

element when the colour function was C>0.5, and those of air when C<0.5. Turbulence modelling was achieved using a RANS approach. The eddy viscosity is computed using the V2F model (Durbin, 1991). This model does not require a parameterisation at the wall. This is a clear advantage for the present study which aims in particular at focusing on the computation of shear stresses applied on the bed.

CASE STUDY

We study the bore generated from a dam-break condition with initial water depths h_0 and h_1 (Fig. 1). The bore properties are sketched in Fig. 2, using the water depths h_0 and h_m at the foot and at the head of the bore, respectively, and the propagation velocity U. The quantities are related through the Froude number F_0 by the usual relationship

$$F_0 = \frac{U^2}{gh_0} = \frac{1}{2}\frac{h_m}{h_0}\left(\frac{h_m}{h_0}+1\right) \qquad (1)$$

The water depth h_m below the bore head varies with the initial water depths h_0 and h_1 before dam-break using (Stoker, 1957, §10.8)

$$\sqrt{h_1} = \sqrt{h_m} + (h_m - h_0)\sqrt{\frac{h_m + h_0}{8h_m h_0}} \quad . \qquad (2)$$

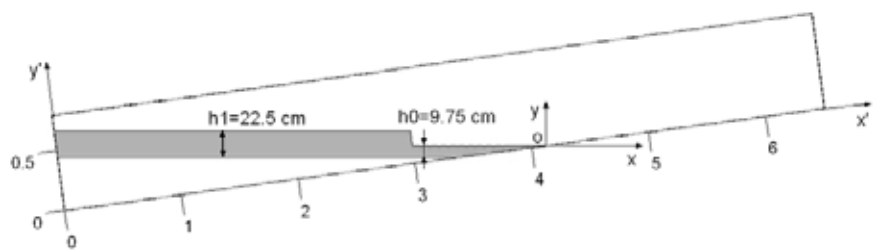

Figure 1. Initial conditions of the Yeh *et al.* (1989) experiment and calculation domain.

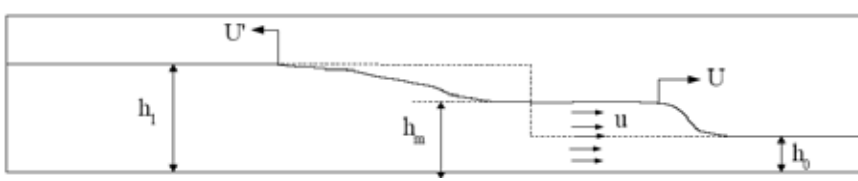

Figure 2. Properties of a bore generated from a dam-break conditions.

Shortly after its generation the bore propagates over a sloping beach. The geometry considered for numerical simulations is the same as for the experiments by Yeh *et al.* (1989). The initial shoreline is the origin of the (O,x,y) co-ordinate system. The only parameter modified in computations is the

water depth h_1. The different conditions investigated in this work are given in Table 1. The Froude number F_0=1.43 corresponds to the Yeh *et al.* experimental conditions.

The grid mesh in the domain is made of 1300x180 elements in the x' and y' directions, respectively. Square grid element are used ($\Delta x'=\Delta y'=5$ mm), except in the vicinity of the bottom where the $\Delta y'$ size is progressively reduced to 0.0243 mm, in order to capture the boundary layer properties.

Table 1. Conditions of cases computed

h_0	h_1	h_m	F_0	u_*
9.75 cm	18.7 cm	13.8 cm	1.31	2.07 m/s
9.75 cm	19.9 cm	14.3 cm	1.35	2.19 m/s
9.75 cm	22.5 cm	15.4 cm	1.43	2.42 m/s
9.75 cm	26.0 cm	16.8 cm	1.53	2.70 m/s
9.75 cm	27.4 cm	17.3 cm	1.57	2.81 m/s

BORE COLLAPSE AT THE SHORE LINE

The theory of Whitham (1958), based on the shallow water equations, predicts the collapse of the bore at the shoreline. In this framework, "bore collapse" means that the water depth goes to zero when the bore reaches the position of the shoreline at rest (x=0). However, fluid particles have a non zero velocity u_* which initiates the run-up flow. The theory of Shen and Meyer (1963) is up to date the reference model of the run-up flow. It is discussed in the present paper.

Following Whitham's theory, numerous studies have considered that the bore collapses at the position of the shoreline at rest, although the experimental results of Yeh *et al.* (1989) clearly show a different phenomenon. This is seen in Figure 3 where the water depth h_c below the head and the height η_c of the head above the shoreline at rest are plotted as a function of the position of the head along the x axis. The x position is made dimensionless using the velocity u_*, in order to help for a comparison with Yeh *et al.* experimental results, superimposed in Fig. 1. The height of the head η_c remains approximately at the same level for x<0, as observed in Yeh et al. experiment. The water depth decreases rapidly when the bore head approaches the shoreline, but at the position of the shoreline at rest (x=0), the water depth below the head is still of the order of h_0. It continues to decrease at a roughly constant rate until the position $g.x.tg\beta / u_*^2 \approx 0.07$ (β is the angle of the slope), after which the decay of the water depth is significantly slower. From this position the height of the bore crest increases rapidly in relation with the upward run-up on the beach. This indicates a different behavior of the swash flow on each side of the position $g.x.tg\beta / u_*^2 \approx 0.07$.

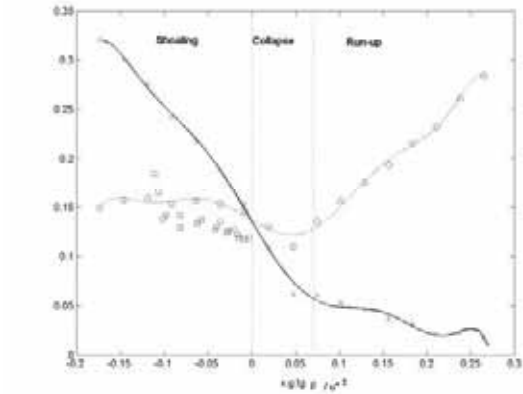

Figure 3. Variations of water depth h_c below the head (x , continuous line) and of the height η_c of the head (o, dotted line) above the still water level during bore collapse and run-up. Squares are experimental data by Yeh *et al.* (1989). Case conditions : F_0=1.43.

We examined in more detail the properties which may distinguish the bore collapse phenomenon from the subsequent run-up down. Figure 4 shows the displacement in time of the positions of the foot and of the head of the swash layer for the Yeh et al. initial flow conditions. The position of the crest was determined at different times from the analysis of the air/water interface obtained from the numerical simulation. The line joining the data was fitted using a polynomial interpolation from which the velocities of the head and foot (also plotted) were determined.

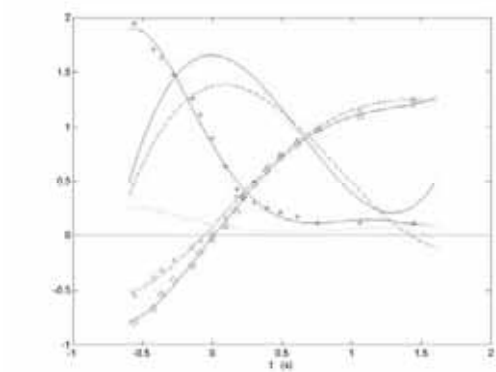

Figure 4. Time displacement of the head (x) and of the foot (o) of the swash layer and variation of the distance between the two (…). The time evolution of the speed of the head (cont line), of the foot (dashed line), and of the water depth h_c below the head (+) are also plotted. Values are in m for lengths (except for h_c plotted using dm), and in m/s for velocities. Case conditions : F_0=1.43.

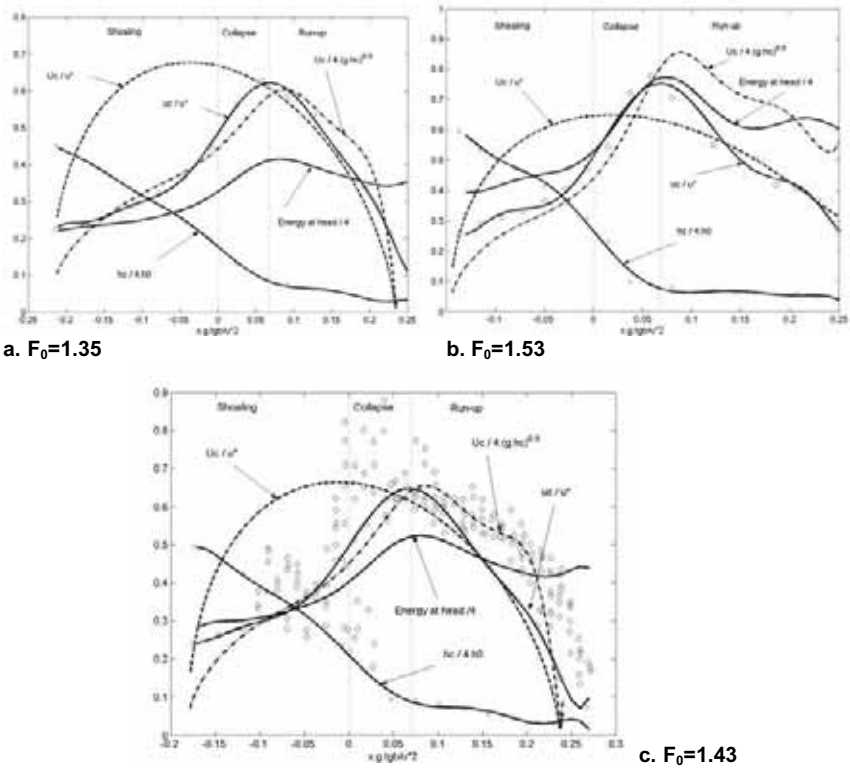

Figure 5. Variations of the bore head propagation speed, of the horizontal mean velocity, of the energy at the head, and of the water depth below the head obtained during bore collapse and run-up.

The results are analyzed in Figure 5 together with two other cases corresponding different Froude numbers. Similar observations are made for the three cases. The decay of the water depth below the head, as already discussed with Fig. 3, is similar. We also observe that the mean velocity below the head u_c, the local Froude number at the crest $U_c^2/g.h_c$ (using the head velocity U_c), and the energy at the crest $\rho g \eta_c + \rho u_c^2/2$ reach a maximum value at $g.x.tg\beta / u_*^2 \approx 0.07$. A different behavior is observed for the head velocity U_c, which reaches a maximum at x=0. The head velocity is accelerated around this position, as shown in Figure 5c where experimental data of U_c / u_* from Yeh *et al.* are also superimposed. There is considerable scatter at this point and the interpolation employed to estimate the head speed might not be appropriate there. For $g.x.tg\beta / u_*^2 > 0.07$ the velocity of the head and the flow mean velocity below the head decay in the same manner. This is a property obtained with the shallow water model (Whitham, 1958) and the Shen and Meyer (1963)

model of the run-up flow. The various observations made in Fig. 5 for the three cases considered suggest that the flow behavior is different if $g.x.tg\beta / u_*^2 < 0.07$ or $g.x.tg\beta / u_*^2 > 0.07$. This led us to distinguish three flow regime ("shoaling", "bore collapse" and "run-up") as indicated in Figs. 3 and 5 and we considered that the transition between bore collapse and run-up actually occurs at $g.x.tg\beta / u_*^2 = 0.07$. The flow properties at this point will be used to analyze in the next section the maximum height of run-up obtained from numerical simulations.

THE RUN-UP FLOW

Figure 6 shows the swash layer at different times during the run-up flow for the Yeh *et al.* case. The contour levels of the colour function are plotted and the water and air domains are shown in grey and white colours, respectively. For each time, vertical profiles of the mean velocity, of the shear stress and of the dynamics viscosity are plotted. The shear stress is defined as

$$\tau = \left(\mu + \mu_t\right)\frac{\partial u}{\partial y} . \qquad (3)$$

The eddy viscosity for the V2F model (Durbin, 1991), basically defined from the turbulent kinetic energy k and dissipation rate ε,

$$\mu_t = \rho C_\mu \overline{v'^2} T \qquad \text{with } T = \max\left(\frac{k}{\varepsilon}, 6\sqrt{\frac{\nu}{\varepsilon}}\right). \qquad (4)$$

also takes into account the anisotropy of turbulence, considering the turbulent kinetic energy $\overline{v'^2}$ of the component perpendicular to the mean flow direction. The anisotropy ratio $\overline{v'^2} / k$ is also plotted in Figure 6.

The mean velocity component parallel to the bottom is almost uniform along the direction perpendicular to the bottom, except in the boundary layer. The profiles of the total viscosity display an usual behaviour. The anisotropy of turbulence, taken into account by the Durbin model, is mostly confined in the bottom boundary layer, as expected, and in less extend in the vicinity of air/water interface.

The main conclusion given by Figure 6 is that the shear stress, which is maximum on the bottom, decreases rapidly for increasing distance from the bottom. This corresponds to the case of a developing boundary layer. For x<0 the fluid is at rest before the bore foot arrives at this position. The fluid is suddenly accelerated in the fluid layer while the bore passes and the boundary layer develops. The bottom shear stress is maximum when the bore is around the position x=0 because the acceleration is most sudden there (Figure 5). The bottom shear stress decreases progressively in the run-up flow with the advection of fluid.

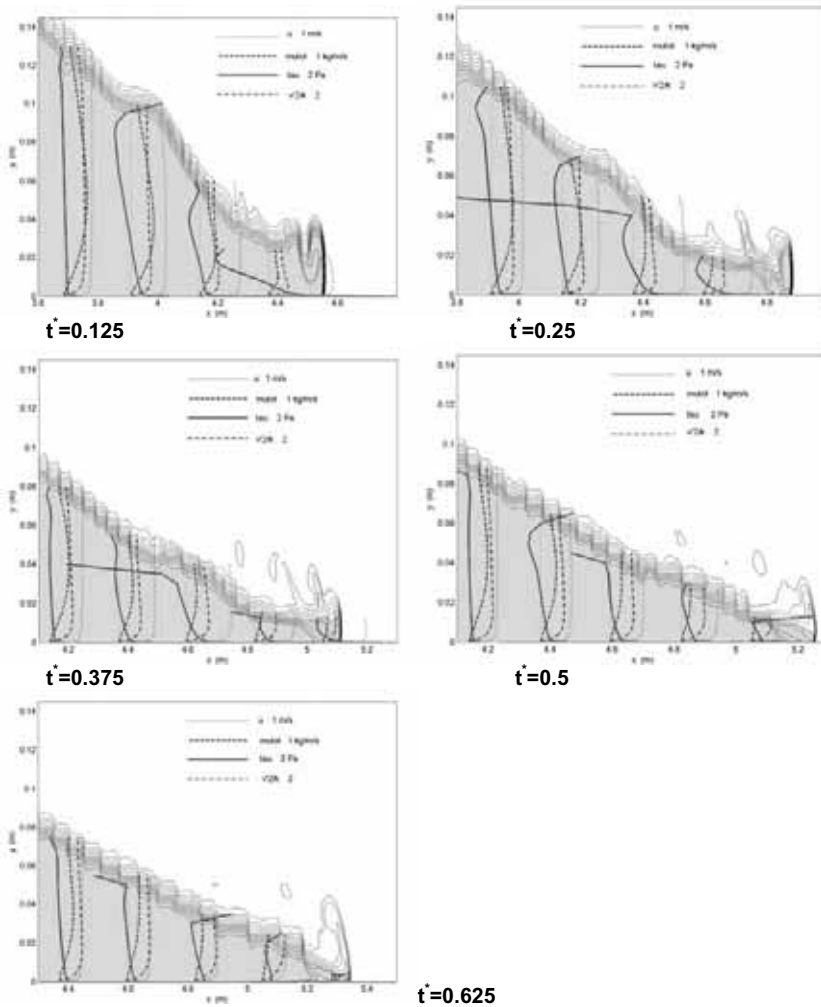

Figure 6. Plot of the isocontours of the colour function in the swash layer at different times during run-up. Density of water and air correspond to the blue and white areas, respectively. Vertical profiles of the mean horizontal velocity (….), of the total dynamic viscosity (---), of the isotropy factor $\overline{v'^2}/k$ (-.-.) and of the shear stress (continuous line) are plotted. The length of segments indicate the scales. The value is measured from the vertical dotted line. Case condition : F_0=1.43. $t^*=t/t_{max}$ is the dimensionless time using the duration t_{max} between the time the swash toe passes at x=0 and the time it reaches its uppest position on the beach.

Figure 6 shows that significant negative values of the shear stress are obtained below the free surface. On the one hand, we point out that the bed

shear stress is not directly given by the Aquilon model. It was computed as a post-processing of the velocity and turbulence data using eq. (3). In the vicinity of the interface, the assumption that the fluid is water in a grid mesh if C>0.5 and air if C<0.5 induces a significant inaccuracy in the estimates of the shear stress, and we are not much confident in the shear stress data there. On the other hand, the Aquilon model computes as well the flow inside the air. This is not shown in Figure 6, but we see a slight velocity decrease with increasing height in the upper part of the swash layer due to this interaction between the flows in the air and in the water. This is associated to significant values of the bed shear stress due to the significant level of turbulence.

The length of run-up $x_{run\text{-}up}$ and the maximum height η_{max} reached by the swash layer are quantities of practical interest. Shen and Meyer (1963) proposed an inertial model that states that η_{max} is simply determined by an energy conservation argument between the kinetic energy ρu_*^2 at x=0 and the potential energy $\rho g \eta_{max}$ at the highest position. However, the experimental results of Yeh et al. show that the kinetic energy initiating the run-up flow should be lower by a factor $(0.82)^2$ to recover the run-up height η_{max} found in the experiment. Figure 7 shows a schematic of the swash layer and defines the different parameters.

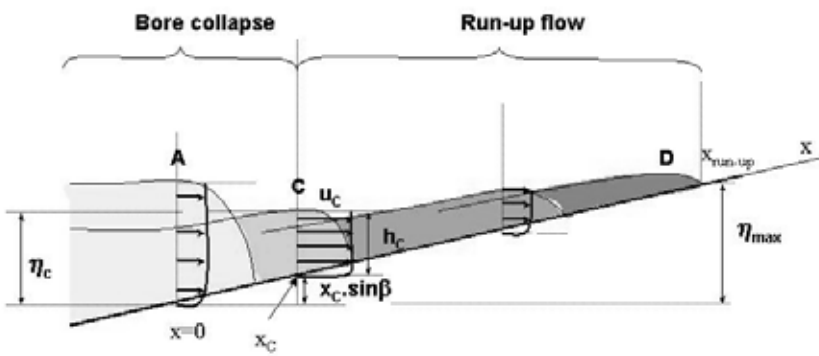

Figure 7. Schematic of the swash layer and definition of parameters.

The maximum height of run-up obtained by our numerical simulations are given in Table 2 for three values of the initial Froude number. The potential energy at the maximum height of run-up is compared to the sum of the potential energy and the kinetic energy at the transition between bore collapse and run-up. Because the transition is at the position x_c such as $g.x_c.tg\beta / u_*^2 = 0.07$ and since the water depth below the head is not zero at this point, the energy at the transition is not only made of kinetic energy as stated by Shen and Meyer (1963) but it includes a significant potential energy. The total energy at the transition is

$$\frac{2E_c}{\rho u_*^2} = 2\left\{\frac{g.x_c.\sin\beta}{u_*^2} + \frac{g.h_c}{u_*^2}\right\} + \frac{u_c^2}{u_*^2}. \quad (5)$$

This dimensionless form using the kinetic energy $\rho u_*^2/2$ does not have a physical basis. It is however useful since the various contributions to the total energy E_c at the transition are easily estimated from Figure 5. The different quantities are given in Table 2. For the three Froude number cases, the potential energy at the maximum height of run-up is slightly lower than the total energy at the transition. The ratio between the two quantities ranges between 76% and 85 %. This is consistent with the energy decrease in the run-up flow seen in Figure 5 after the bore collapse. For the Yeh *et al.* case (F_0=1.43), the energy E_c at the transition is equal to the modified kinetic energy used by Yeh *et al.* because $(0.82)^2$=0.68. The important conclusion is that the various contributions to the energy have to be taken into account since the water is not zero at the transition. Nevertheless, the numerical simulation for this case predicts a maximum height of run-up slightly lower than observed in experiments. This is rather unexpected since the shear stress is confined in the bottom boundary layer. Fluid particles reaching the maximum height of run-up are those in the vicinity of the bore head at the transition (point C in Figure 7). They are not submitted to pressure force and should conserve their energy if no shear stress is applied at the air/water interface. Although we pointed out before that the negative values of the shear stress obtained by the simulations in the vicinity of the interface (Figure 6) were not accurately determined, the existence of such shear stress at the interface and its effect on the height of run-up is an open question.

Table 2. Maximum height of run-up and comparison of the potential energy at the maximum height of run-up to the total energy at the transition between the bore collapse and the run-up flow.

F_0	η_{max}	$\frac{u_c^2}{u_*^2}$	$2\frac{g.x_c.\sin\beta}{u_*^2}$	$2\frac{g.h_c}{u_*^2}$	$\frac{2.E_c}{\rho u_*^2}$	$\frac{\rho g.\eta_{max}}{E_c}$
1.35	**13.5 cm**	**0.40**	**0.14**	**0.14**	**0.68**	**0.81**
1.43	**17.2 cm**	**0.41**	**0.14**	**0.13**	**0.68**	**0.85**
1.53	**22.6 cm**	**0.56**	**0.14**	**0.10**	**0.80**	**0.76**

SHEAR STRESSES APPLIED ON THE BOTTOM

We analyse in more detail in Figure 8 the evolution in time of the shear stress applied on the bottom along the swash water layer. It is confirmed that the maximum bottom shear stress is obtained at the beginning of the run-up flow. It increases suddenly at this time and then slowly decreases. The value of about 10 Pa of the maximum bottom shear stress obtained for t*=0.125 (the bore head is

about such as $g.x.tg\beta / u_*^2 = 0.07$) is higher than that obtained for t*=0 when the bore head passes at x=0.

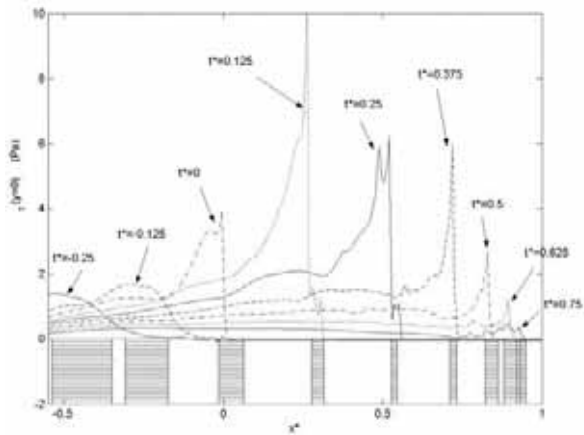

Figure 8. Evolution in time of the shear stress applied on the bottom. The dashed rectangles in the lower part of the figure indicates for each time the areas between the toe and head of the swash layer. $x^*=x/x_{max}$ is dimensionless using the maximum length of the run up x_{max} taken from the shore at rest. Case conditions of Yeh *et al.* (1989) experiment : x_{max}=1.135 m for F_0=1.43).

For each time considered in Figure 8 the maximum value of the bottom shear stress is obtained between the toe and the head of the swash layer. This is clearly indicated although the position of the toe, determined using polynomial interpolations (Figure 4) is not always accurate, especially for t* around 1 when the swash layer is around its uppest position on the beach, but the bottom shear stress is quite small at this time.

For three values of the initial Froude number F_0, Figure 9 shows the evolution in time of the maximum bottom shear stress applied on the bottom and of the dimensionless position where it is computed by the numerical model. Figure 9 includes data from the run-down flow ($t^*>1$). We observe that the bottom shear stress is much lower during run-down as compared to run-up. The flow is highly asymmetrical between run-up and run-down.

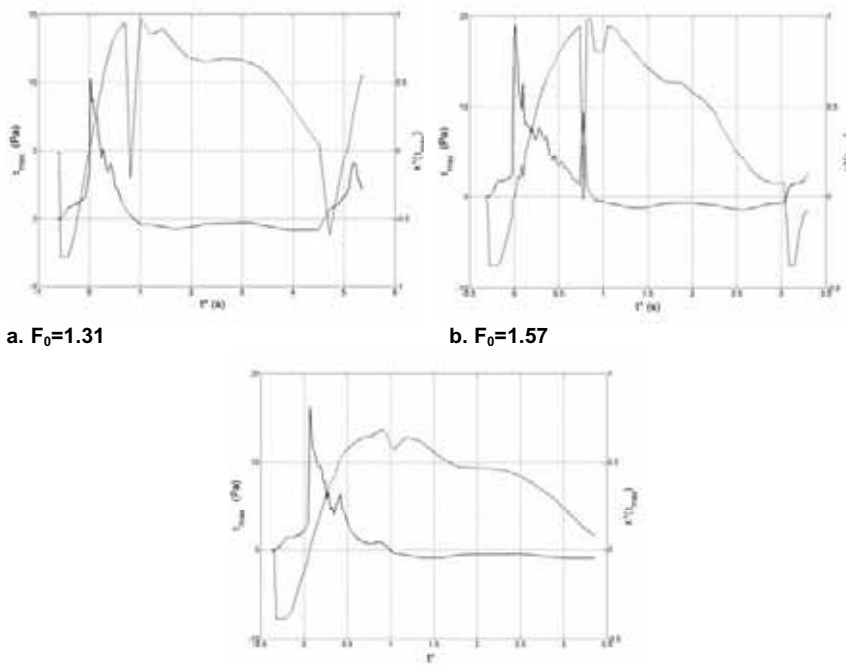

a. F_0=1.31 b. F_0=1.57

c. F_0=1.43

Figure 9. Evolution in time of the maximum shear stress applied on the bottom (continuous line) and of the dimensionless position $x^*=x/x_{max}$ (dashed line) where it is obtained.

CONCLUSION

This paper presents results of numerical simulations of a turbulent bore propagating over a sloping beach. The bore collapse at the shore line and the subsequent run-up flow were analyzed. The simulations were carried out using a RANS- VOF model. Our results demonstrate the ability of the model to simulate such a flow. This was already demonstrated by previous studies (Zhang and Liu, 2008). The results presented in this paper essentially deal with the conditions of the Yeh *et al.* (1989) experiment. We analyzed the results of numerical simulations in relationship with experimental results and the theories of bore propagation on a sloping bottom (Whitham, 1958) and of run-up (Shen and Meyer, 1963).

The results of our simulation show that the theory of Whitham does describe with sufficient detail the mechanism of bore collapse, due to the inherent shortcomings of shallow water equations. The results of our simulation are used to describe the transition between bore collapse and run-up flow and we propose that this transition occurs at the position such as $g.x.tg\beta / u_*^2 = 0.07$. At this position, however, both the kinetic energy and the

potential energy have to be taken into account to estimate the energy initiating the run-up flow.

The maximum height of run-up found in numerical simulations is slightly lower than found in the experiment of Yeh *et al.*. This is rather unexpected as the dynamics of run-up appears to be mostly inertial, as considered by Shen and Meyer (1963). A focus was made on the analysis of shear stresses. We observed that the shear stress is mostly confined in the bottom boundary layer. It should therefore not have a significant effect on the height of run-up. Significant negative shear stresses were computed in the vicinity of the interface. Although the values are not accurate, the interaction at the air/water interface is an open question.

The paper analyses the time evolution of bottom shear stress during run-up and run-down flows. Consistent evaluations of this quantity are predicted by the model. In particular, it is found that the most significant bed shear stresses are obtained at the beginning of run-up and the highest bottom shear stresses are obtained between the foot and the head of the swash layer. A strong assymetry between run-up and run-down flows is observed.

REFERENCES

Durbin, P.A.. 1991. Near-wall turbulence closure models without damping functions. *Theoret. Comput. Fluid Dynamics*, 3, 1-13.

Lubin, P., Vincent, S., Abadie, S., and J.P. Caltagirone. 2006. Three-dimensional Large Eddy Simulation of air entrainment under plunging breaking waves, *Coastal Engineering*, Volume 53(8), 631-655.

Shen, M.C., and R.E. Meyer. 1963. Climb of a bore on a beach part 3. Run-up. *J. Fluid Mech.*, 16(1),113-125.

Stoker, J.J. 1957. Water waves. Interscience publishers, Inc., New-York.

Vincent, S., and J.P. Caltagirone. 1999. Efficient solving method for unsteady incompressible interfacial flow problems. *Int. J. Numerical Methods in Fluids*, 30(6), 795-811.

Whitham, G.B., 1958, On the propagation of shock waves through regions of non-uniform area or flow, *J. Fluid Mech.*, 4, 337-360.

Yeh, H.H., Ghazali, A., and I. Marton. 1989. Experimental study of bore run-up. *J. Fluid Mech*, 206, 563-578.

Zhang, Q., and P.L.F. Liu, 2008, A numerical study of swash flows generated by bores, *Coastal Engineering*, doi:10.1016/j.coastaleng.2008.04.010.

A 2D NUMERICAL SIMULATION BY PLIC METHOD ON WAVE BREAKING OVER A SLOPING BOTTOM

Chin-Yen Tsai[1], Tai-Wen Hsu[1], Shan-Hwei Ou[2] and Yu-Jie Jhu[1]

This study presents the results of 2D numerical simulation on wave breaking over a sloping bottom by using the Reynolds Averaged Navier-Stokes (RANS) model. The RANS equations are solved with a k-ε turbulence model for model closure by Finite Volume Method (FVM). To track the complicatedly and rapidly changed water surfaces during wave breaking, piecewise linear interface calculation (PLIC) method developed based on the concept of volume-of-fluid (VOF) is chosen to achieve the interface tracking between fluid and air. A Lagrangian advection technique is adopted to appropriately advect the interface segments and evaluate the volume fluxes in the fluid cells under the mean flow field. Comparing with the existing experiments, a good agreement is found between numerical results and measured data.

INTRODUCTION

When waves reach a beach and enter water that is nearly as deep as the waves are high, they become unstable and break with the crest thrown forward as the wave disintegrates into bubbles. Wave breaking is one of the most commonly observed features of water waves propagating from deep water to shallow water, over a sloping bottom. On the other hand, submerged coastal structures are also frequently used for coastal protection from wave attack. The main purpose of this structure is to reduce the transmitted wave energy by reflecting waves and dissipating wave energy over the structure by breaking up the propagating waves.

When wave breaking occurs, a large amount of wave momentum will be released to the surface layer of surf zone. Breaking waves also play an essential role in the surf zone for an entire coastal process. For example, strong turbulence produced by breaking waves could stir up sediment particles into the flow. Changes of sediment subsequently result in sediment transport may cause beach erosion and related coastal disasters such as wave overtopping, coastal flooding and failure of coastal structures, and so on.

Notably the existing potential theories describing the evolution of wave profile of breaking waves normally neglect the effect of viscosity and turbulence. In order to simulate the process of real flow interaction which takes place on sea bottom or around submerged structures, the full Navier-Stokes equations with exact free surface boundary conditions should be solved.

[1] Department of Hydraulic and Ocean Engineering, National Cheng Kung University, 1 University Road, Tainan, 70101, Taiwan
[2] Department of Environmental Resources Management, Tajen University, 20 Wei Shin Road, Pingtung, 90741, Taiwan

Computational efficiency and reliability are key elements of the model for simulating wave breaking process. In this research, we developed a numerical model to calculate the flow dynamics and water free surface deformation for periodic waves traveling on different types of sloping bottom with breaking and energy dissipation. The feasibility of the numerical model was verified through a series of comparisons of numerical results with the existing analytical solutions and the experimental data. The good agreements demonstrate the satisfactory performance of the developed numerical model.

The purpose of this paper is to perform numerical simulations of numerical simulations in investigating the deformation of periodic waves and breaking process on a sloping bed by the VOF/PLIC method. The applicability of the PLIC method on the wave breaking problem is discussed. The mean flow pattern and turbulent kinetic energy distribution under wave breaking are explored using the developed numerical model.

MODEL DESCRIPTION

The physical problem considered in this study is the propagation of a two-dimensional periodic wave train traveling toward the sloping bed and the varying topography. The Cartesian coordinate system is employed in this study as shown in Fig. 1. Herein, h denotes the quiescent water depth in front of the sloping beach, H the wave height of incident periodic waves.

Governing Equations

The Reynolds decomposition method is applied to simulate the turbulence effect. The governing equations which describe the mean quantities of the flow field for unsteady incompressible turbulent flows are denoted as
continuity equation

$$\frac{\partial U}{\partial x}+\frac{\partial W}{\partial z}=0\,, \tag{1}$$

and momentum equations

$$\begin{aligned}\frac{\partial U}{\partial t}+U\frac{\partial U}{\partial x}+W\frac{\partial U}{\partial z}=&-\frac{\partial P}{\partial x}+(\nu_t+\nu)\nabla^2 U\\&+\frac{\partial}{\partial x}(\nu_t\frac{\partial U}{\partial x})+\frac{\partial}{\partial z}(\nu_t\frac{\partial W}{\partial x})-\frac{2}{3}\frac{\partial k}{\partial x}\end{aligned}\,, \tag{2}$$

$$\begin{aligned}\frac{\partial W}{\partial t}+U\frac{\partial W}{\partial x}+W\frac{\partial W}{\partial z}=&-\frac{\partial P}{\partial z}+(\nu_t+\nu)\nabla^2 W\\&+\frac{\partial}{\partial x}(\nu_t\frac{\partial U}{\partial z})+\frac{\partial}{\partial z}(\nu_t\frac{\partial W}{\partial z})-\frac{2}{3}\frac{\partial k}{\partial z}-g\end{aligned}\,, \tag{3}$$

in which x and z are the coordinates in a fixed Cartesian system respectively, t is the time, U and W are the mean velocity components in the x- and z-directions,

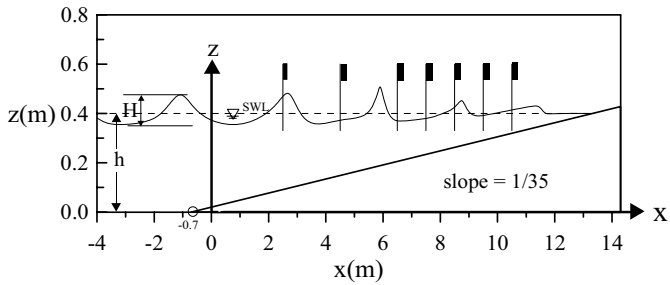

Figure 1. Schematic diagram of periodic wave train over a sloping bed.

respectively, P is pressure, g is the gravitational acceleration, ν_t is the eddy viscosity, ν is the molecular viscosity, $\nabla = (\partial/\partial x, \partial/\partial z)$ is the gradient operator; and k is the turbulent kinetic energy.

The standard k-ε model is employed here to resolve the eddy viscosity in the present study. The eddy viscosity is determined by the turbulent kinetic energy k and energy dissipation rate ε using the following formula

$$\nu_t = \frac{C_\mu k^2}{\varepsilon} \ . \tag{4}$$

The governing equations are closed by the transport equations of the Turbulent Kinetic Equation (TKE) and Energy Dissipation Equation (EDE):

$$\frac{\partial k}{\partial t} + U\frac{\partial k}{\partial x} + W\frac{\partial k}{\partial z} = \nabla\cdot\left[(\nu + \frac{\nu_t}{\sigma_k})\nabla k\right] + Prod - \varepsilon \ , \tag{5}$$

$$\frac{\partial \varepsilon}{\partial t} + U\frac{\partial \varepsilon}{\partial x} + W\frac{\partial \varepsilon}{\partial z} = \nabla\cdot\left[(\nu + \frac{\nu_t}{\sigma_\varepsilon})\nabla \varepsilon\right] + C_1\nu_t\frac{\varepsilon}{k}Prod - C_2\frac{\varepsilon^2}{k} \ , \tag{6}$$

where *Prod* term represents the production of turbulent kinetic energy denoted as

$$Prod = \nu_t\left[2(\frac{\partial U}{\partial x})^2 + 2(\frac{\partial W}{\partial z})^2 + (\frac{\partial U}{\partial z} + \frac{\partial W}{\partial x})^2\right] \ . \tag{7}$$

Herein, σ_k, σ_ε, C_μ, C_1 and C_2 are empirical coefficients and are taken to be $\sigma_k = 1.0$, $\sigma_\varepsilon = 1.3$, $C_\mu = 0.09$, $C_1 = 1.44$ and $C_2 = 1.92$ as suggested by Rodi (1980) and Hsu et al. (2004).

Initial and Boundary Conditions

For the above-mentioned initial boundary value problem, appropriate initial condition and boundary conditions are required. At the beginning of the flow simulation, the initial flow field is assumed to be still, so that the velocity components U and W are both set to be zero throughout the whole flow field. The hydrostatic pressure is utilized for the first stage of the pressure field. For

the turbulence quantities k and ε, the specification of initial condition requires more careful treatments to avoid singular terms existing in the EDE when $k = 0$. Following Lin and Liu (1998), we specify the initial value by setting $k = U_p^2 / 2$, where $U_p = A_1 C_p$, U_p and C_p are the horizontal mean velocity and wave celerity on the upstream boundary, respectively. A_1 is taken to be 2.5×10^{-3} in the present computation.

There are four boundary conditions considered in this flow, including the upstream, downstream, free surface, and solid surface boundaries. In the numerical computations the free-surface displacements and the velocity components of two kinds of periodic waves are given as the inflow conditions at $x = 0$, the upstream end of domain. The first kind of periodic wave is co-sinusoidal wave based on linear wave theory. The other incident wave is Cnoidal (Cn) wave. The wave profile can be expressed as (Isobe et al. 1978)

$$h_s = h + \eta = h\sum_{n=0}^{3} A_n \,\mathrm{cn}^{2n}\left[2\kappa(\frac{x}{L} - \frac{t}{T})\right], \tag{8}$$

where $\kappa = 2\pi / L$, L is the wave length, and

$$U = \sqrt{gh}\sum_{n=0}^{3}\sum_{m=0}^{2} B_{nm}\left(\frac{h+z}{h}\right)^{2m} \mathrm{cn}^{2n}\left[2k(\frac{x}{L} - \frac{t}{T})\right], \tag{9}$$

$$\begin{aligned} W = {} & \sqrt{gh}\cdot \mathrm{sn}\left[2\kappa\left(\frac{x}{L} - \frac{t}{T}\right)\right]\cdot \mathrm{dn}\left[2\kappa\left(\frac{x}{L} - \frac{t}{T}\right)\right]\times \\ & \frac{4\kappa h}{L}\sum_{n=1}^{3}\sum_{m=1}^{2}\frac{n}{2m+1} B_{nm}\left(\frac{h+z}{h}\right)^{2m+1}\cdot \mathrm{cn}\left[2\kappa(\frac{x}{L} - \frac{t}{T})\right] \end{aligned}. \tag{10}$$

Coefficients A_n and B_{nm} in Eqs. 8 to 10 are determined according to Isobe et al.'s theory. cn, sn, and dn are Jacobian elliptic function. On the other hand, a radiation condition proposed by Orlanski (1976) is imposed at the downstream to let progressive waves outgoing without reflection.

The boundary conditions on the solid surfaces including the bed and the undulation surfaces are assumed to be impermeable and non-slip. That is, the velocity components U and W are equal to zero at those boundaries. On the free surface boundary, one kinetic and two dynamic boundary conditions are used. They are denoted as,

$$\frac{\partial h_s}{\partial t} + U\frac{\partial h_s}{\partial x} = W \text{ , at } z = h_s(x,t) \text{ ,} \tag{11}$$

$$2\frac{\partial h_s}{\partial x}(\frac{\partial U}{\partial x} - \frac{\partial W}{\partial z}) + \left[(\frac{\partial h_s}{\partial x})^2 - 1\right](\frac{\partial U}{\partial z} + \frac{\partial W}{\partial x}) = 0 \text{ , at } z = h_s(x,t) \text{ ,} \tag{12}$$

$$P/\rho = \frac{2(\nu+\nu_t)}{1+(\frac{\partial h_s}{\partial x})^2}\left[(\frac{\partial h_s}{\partial x})^2\frac{\partial U}{\partial x} - \frac{\partial h_s}{\partial x}(\frac{\partial U}{\partial z}+\frac{\partial W}{\partial x})\frac{\partial W}{\partial z}\right], \text{ at } z = h_s(x,t) \ , \quad (13)$$

Boundary conditions for k and ε on a free surface are (Launder 1989)

$$\frac{\partial k}{\partial n} = 0 \ , \ \frac{\partial \varepsilon}{\partial n} = 0 \ , \quad (14)$$

where n is the normal direction of a free surface.

Interface Calculation

Like other studies of free surface flows, we also encounter difficulties in treating the free surface boundary conditions. Thus an suitable way of finding the free surface is important in numerical calculation. The piecewise linear interface calculation (PLIC) method developed based on the concept of VOF is adopted in this study to track the complicatedly and rapidly changed water surfaces during wave breaking.

The main principle of VOF is established according to the material transport conservation theory (Hirt and Nichols 1981). Based on this theory, we can define a variable called the VOF function, $F(x,z,t)$ which represents the fractional volume of fluid occupied on every cell and the mechanism can be described by the following formula

$$\frac{\partial F}{\partial t} + U\frac{\partial F}{\partial x} + W\frac{\partial F}{\partial z} = 0 \ . \quad (15)$$

The variable F ranging from 0 to 1 is also defined at the center of a computational cell. That is, the computational cells can be divided into three kinds. A cell full of fluid is called a fluid cell and has the value of 1. On the other hand, if a cell does not contain any fluid, it will be called an empty cell and has a zero value. Lastly, cells that are partially filled with fluid are called surface cells and have the values between 0 and 1.

To solve Eq. 15 and reconstruct the free surface, Gueyffier et al. (1999) proposed a VOF/PLIC algorithm with second order accuracy. The procedure for this algorithm is divided into two steps: a reconstruction step and a propagation step. The first step is the determination of the orientation of the segment and the area occupied by water in a surface cell with the known volume fraction F. After reconstructing the free surface, its motion by the underlying flow field need to be modeled appropriately in the propagation step. In the present study, a Lagragian advection technique is utilized to advect the interface segments and evaluate the corresponding volume fluxes in the fluid cell.

The RANS equations were solved numerically by a finite volume method with a staggered system. All the velocity components are defined at the midpoints of a cell face; the pressure, the turbulent kinetic energy, the dissipation rate of energy, and the wave profile are defined at the center of the

cells. For a detailed description of the numerical procedure, the readers may refer to Hsu et al. (2004).

MODEL VALIDATION

The physical problem considered here is the propagation of a two-dimensional periodic wave train shoaling on a sloping bottom. Three cases of different bottom types including uniform slope, bar type and step type are chosen to validate the developed model. Table 1 shows the numerical conditions for each test case.

Fig. 1 shows the schematic view of the numerical wave channel for case A where the distance between x = 0 m and the begin of the slopping bed is 0.7 m and z = 0 m is located at the bottom. Ting and Kirby (1994) performed experiments to investigate the evolution of a spilling breaking Cn wave over the 1/35 slope. The incident wave heights H_i and period T in the constant water depth are 0.125 m and 2.0 s for the spilling breaker, respectively. They measured time histories of surface elevation at 4 various locations over the bed. In the numerical simulation, the computational domain is 20 m long and 0.8 m high. Fig. 2 is the comparison of the water elevations at the shoaling regions and a bore region. It reveals very close agreements existed between the predicated elevations shown in solid line and the measurements denoted as circles.

Fig. 3 shows the comparison of the predicated wave crest, trough and mean water level distribution, among Ting and Kirby's data, and numerical results given by Bradford (2000) and present model. The predicated wave crest profile agrees with other's results except for the values in the region x = 5~7 m. The wave breaking happens at x = 6.4 m, so it is a critical region to compare. Furthermore, the predicated wave trough profile agrees with their data well. The mean water level profile is very interesting, because it is lower then the still water level before the wave breaking point x = 6.4 m and arises gradually after the breaking point.

The comparison of the averaged velocity components are presented in Fig. 4. The overall agreements between computed and measured results are found to be good at different locations in the surf zone. From Figs. 2 and 4, it is demonstrated that the developed model is capable to simulate the wave transformation and flow field for spilling breaking wave on a uniform slope bottom.

At the post-breaking stage, the wave energy may recover followed by another occurrence of wave breaking if the local water depth does not decrease

Table 1. Numerical conditions of test cases for model validation.

Case	Bottom type	Wave height H (m)	Wave period T (s)	Wave profile
A	Uniform slope	0.125	2.0	Cnoidal wave
B	Bar type	0.07	0.94	Co-sinusoidal wave
C	Step type	0.07	1.18	Co-sinusoidal wave

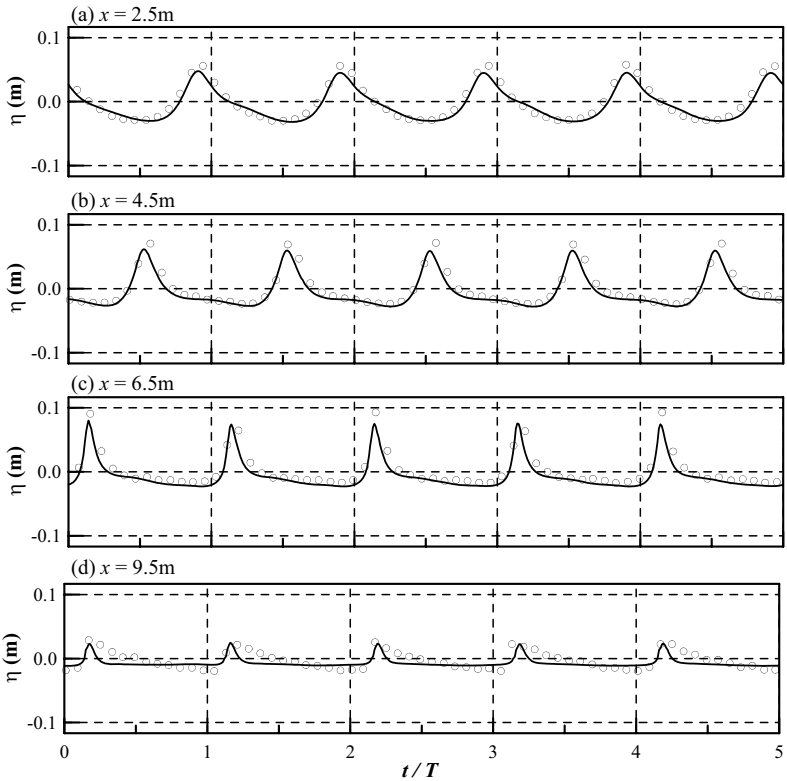

Figure 2. Comparisons of simulated (solid line) and measured (circles, Ting and Kirby 1994) water elevations at the shoaling region (a)-(c) and the bore region (d).

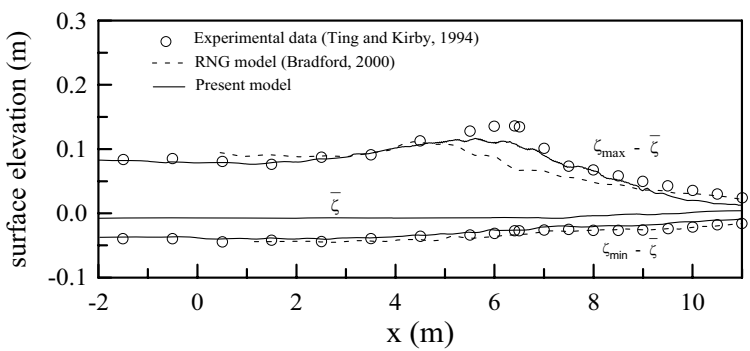

Figure 3. Computed and measured spatial distribution wave crest, mean water level, and wave trough.

gradually shoreward. Therefore, numerical simulations of periodic waves propagating on composite sloping bottoms are carried out to evaluate the performance of the present model on wave recovery. Nagayama (1983) measured the wave height variations on the bar type and the step type bottoms

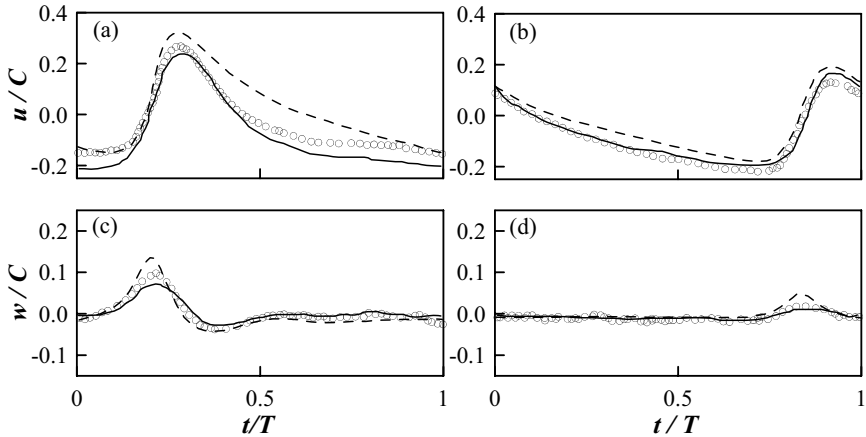

Figure 4. Comparisons of averaged horizontal (a, c) and vertical velocities (b, d) at different locations in the surf zone. Solid lines: present model; dashed lines: numerical results from Lin and Liu (1998); circles: experimental data from Ting and Kirby (1994).

as shown in the lower row of Figs.5 and 6. The wave conditions for these two laboratory experiments are listed in Table 1 as cases B and C, respectively.

Figs. 5 and 6 show the computed wave heights in upper row, the surface elevations at different time steps and the envelopes in the middle row, and the profiles of composite slope bottoms in the lower row. It is clearly seen that the recovery of wave energy takes place while the post-breaking waves propagate on the section with increasing or constant water depth. Moreover, the locations of first and second breaking points are well predicted in comparing with the experimental data. In general, the present model results agree well with the measurements but slightly overestimated in the surf zone for case C.

RESULTS AND DISCUSSION

In this section, we present some discussion on mean flow field and turbulent kinetic transport mechanism under wave breaking on sloping bottom using our numerical results. Contours of turbulent kinetic energy k are shown in Fig. 7 at different phases. The initial phases is set as the wave crest passes the breaking point, i.e. x = 6.4 m. It is found that the k is formed behind the wave crest. When it travels, the wave becomes steeper and k increases gradually. We also found that there is substantial turbulent kinetic energy generated at the solid boundary associated with the wave crest. Under the spilling breaking wave, the turbulent kinetic energy continues to dissipate in the bore region. This is due to the high shear rates at the wavefront which generates significant levels of k at the lower front face of the wave. After that, the production of k continues as the wave transforms into a bore and overtakes the decaying turbulence from the previous breaking wave.

Figs. 8 and 9 present the sequence of variation of the simulated streamlines

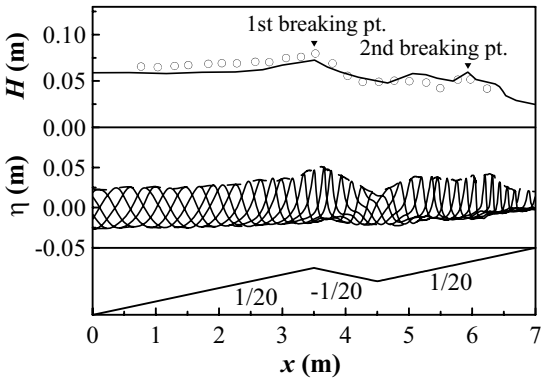

Figure 5. Computed wave height variation and wave envelope for the case of bar type bottom. Solid line: present model; circles: experimental data from Nagayama (1983).

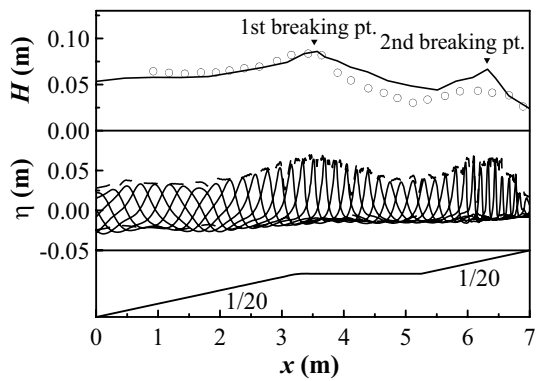

Figure 6. Computed wave height variation and wave envelope for the case of step type bottom. Solid line: present model; circles: experimental data from Nagayama (1983).

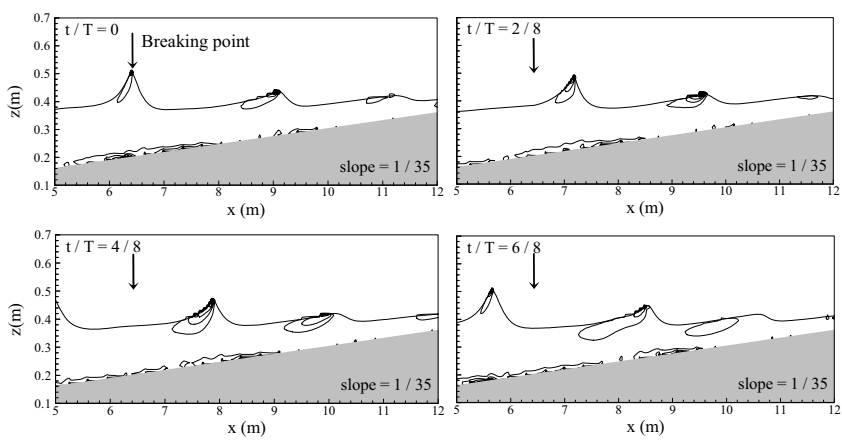

Figure 7. Sequence of variation of the simulated turbulent kinetic energy for case A in a wave period.

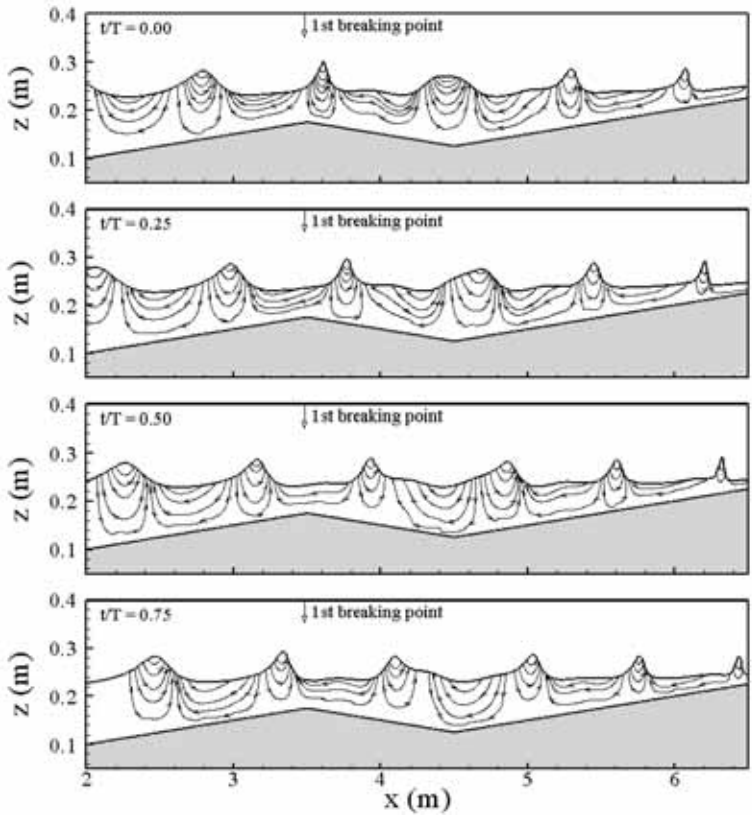

Figure 8. Sequence of variation of the simulated streamlines for case B in a wave period.

and vorticity fields for case B of bar type bottom in a wave period. The vorticity is calculated by the following equation $\Omega = \partial U / \partial z - \partial W / \partial x$. In Fig. 8, we notice that the wave profile at the recovery stage is quite different from that expected for a spilling breaker. The wave crest of recovery wave is much flatter with a relatively mild leading wavefront. Fig. 9 shows that the vorticity generated by waves is initiated at the wavefront just before the breaking point for both the first and second breaking scenarios. It is noted that the computed vorticity in the second breaking is larger that in the first breaking.

CONCLUDING REMARKS

A two-dimensional free-surface flow model used in this study is established by directly solving Reynolds averaged Navier-Stokes (RANS) equations and the continuity equation. The VOF/PLIC is adopted to track the free surface on a Cartesian grid. An explicit numerical algorithm is employed with a predictor-corrector procedure of pressure and velocity field. By applying the developed

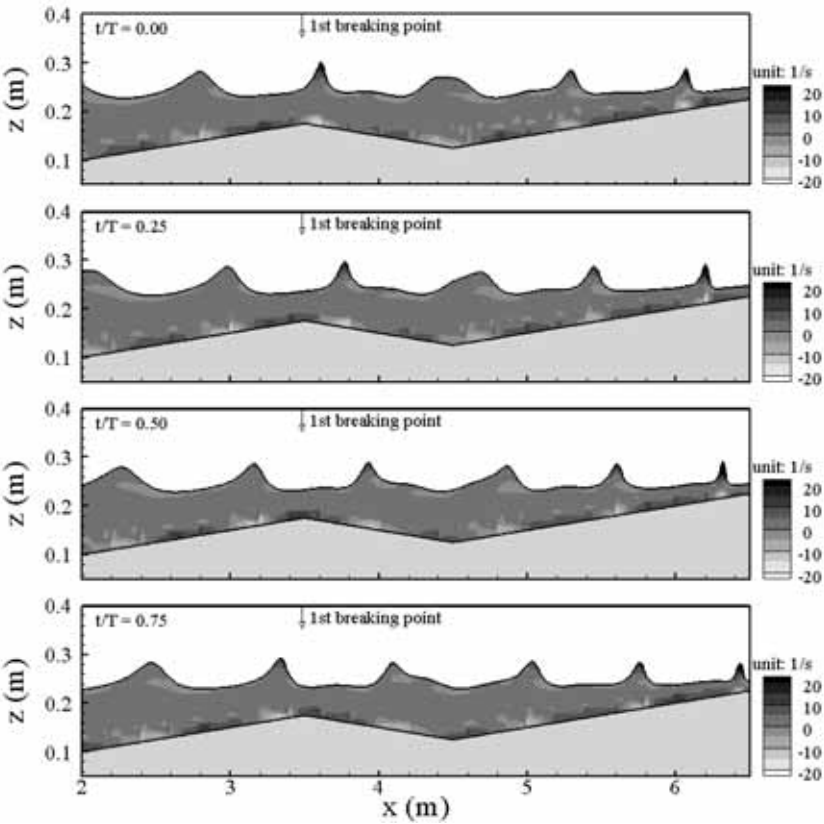

Figure 9. Sequence of variation of the simulated vorticity fields for case B in a wave period.

model to the problems of periodic waves breaking on different types of sloping bottoms, we found that the model results compare well with the experimental data. Additionally, the model is demonstrated to provide reliable information concerning wave breaking and wave recovery on a composite slope bottom.

Detailed analysis of numerical results also shows that the turbulent kinetic energy and vorticity are primarily located above the wave trough. The turbulent kinetic energy is convected and diffused to the back face of the wave, and continues to dissipate while the breaking wave moves towards the shore. As the second wave breaking takes place after the recovery of wave energy, note that the vorticity in the bore region is larger than those in other regions.

ACKNOWLEDGMENTS

This research was supported by the National Science Council and the Landmark Project of National Cheng-Kung University, Taiwan, under the Grants No. NSC-96-2221-E-127-006-MY3 and A0162.

REFERNCES

Bradford, S.F. 2000. Numerical simulation of surf zone dynamics, *Journal of Waterway, Port, Coastal, and Ocean Engineering*, 126, 1-13.

Gueyffier, D., J. Li, A. Nadim, R. Scardovelli, and S. Zaleski. 1999. Volume-of-Fluid interface tracking with smoothed surface stress methods for three-dimensional flows, *Journal of Computational Physics*, 152, 423-456.

Hirt, C.W., and B.D. Nichols. 1981. Volume of fluid (VOF) method for dynamics of free boundaries, *Journal of Computational Physics*, 39, 201-225.

Hsu, T.W., C.M. Hsieh, and R.R. Hwang. 2004. Using RANS to simulate vortex generation and dissipation around impermeable submerged double breakwaters, *Coastal Engineering*, 51, 557-579.

Isobe, M., H. Nishimura, and K. Horikawa. 1978. Expressions of perturbation solutions for conservative waves by using wave height, *Proceedings of 33rd Annual Conference of* JSCE, 760-761 (in Japanese).

Launder, B.E. 1989. Second-moment closure and its use in modeling turbulent industrial flows, *International Journal for Numerical Methods in Fluids*, 9, 963-985.

Lin, P., and P.L.F. Liu. 1998. A numerical study of breaking waves in the surf zone, *Journal of Fluid Mechanics*, 359, 239-264.

Nagayama, S. 1983. Study on the change of wave height and energy in the surf zone, Bachelor thesis, Yokohama National University, Japan, 80 pp (in Japanese).

Orlanski, I. 1976. A simple boundary condition for unbounded hyperbolic flows, *Journal of Computational Physics*, 21, 251-269.

Rodi, W. 1980. *Turbulent models and their applications in hydraulics - a state of the art review*, IAHR, Delft, 104 pp.

Ting, F.C.K., and J.T. Kirby. 1994. Observation of undertow and turbulence in a laboratory surf zone, *Coastal Engineering*, 24, 51-80.

SAND PIT INDUCED HYDRODYNAMICS BY A TWO-DIMENSIONAL BOUSSINESQ TYPE OF MODEL FOR BREAKING WAVES

Antonino Viviano[1,2], Rosaria E. Musumeci[2], Felice Arena[1], Enrico Foti[2]

In the present contribution a two-dimensional weakly dispersive fully nonlinear Boussinesq type of model is developed and applied. The model takes into account breaking terms by means of the surface roller concept. More precisely, the velocity is influenced by the effects of vorticity due to breaking, which is modelled by means of the "roller 3D" concept, defined as a volume of water in which vorticity is generated and "pumped" into the water column. Such a model has been validated for simple one-dimensional cases and then it has been applied for studying the behaviour of wave motion and its generated currents over a nearshore submarine cave. The results of this application seem in a fairly good agreement with what has been observed and reported in the available literature field data.

OVERVIEW

Boussinesq type of models have been widely applied to accurately describe nearshore waves dynamics at a reasonable computational costs. It is worth pointing out that Boussinesq equations permit to extract information about the vertical distribution of the horizontal velocities despite they are managed as depth integrated equations. Such equations were first derived by Peregrine (1966), for the constant water depth case, and by Peregrine (1967) for the variable depth case. However, even though the Boussinesq models are able to handle very efficiently several nearshore phenomena, such as refraction, diffraction, shoaling, dispersion and nonlinear interactions, they cannot deal with wave breaking. To face such a problem, in the last two decades several approaches have been studied with the aim of including both wave breaking criterion and, in turn, the surf zone energy dissipation. For example Madsen et al. (1997) applied the concept of the surface roller, first defined by Svendsen (1984) as the 'volume of water carried by the wave with the wave celerity' on the front of a breaking wave. The corresponding momentum equations derived in their model contain some additional terms that account for the excess of momentum originating from the nonuniform velocity distribution due to the presence of the roller. As regards the breaking onset criterion, usually it is assumed that incipient breaking occurs when the local slope of the surface elevation exceeds an initial critical value. Another approach to study wave breaking within a Boussinesq type of model is the one adopted by Chen et al.

[1] Department of Mechanics & Materials, 'Mediterranea' University of Reggio Calabria, Loc. Feo di Vito, Reggio Calabria, 89060, Italy
[2] Department of Civil and Environmental Engineering, University of Catania, V.le A. Doria 6, Catania, Italy

(2000), which use weakly nonlinear equations written in terms of both the horizontal velocity vector $\mathbf{u}_a = (u_a, v_a)$ at a reference elevation z_a in the water column and the free surface elevation. The wave breaking dissipation is modelled by the above mentioned author by means of a quite simple formulation somewhat similar to the 'eddy viscosity' formulation of Zelt (1991). The attempt to provide a more realistic description of the onset and cessation of wave breaking is implemented as well. Such a formulation consists in adding a new term to the momentum equation in which the eddy viscosity appears as a function of space and time.

In all the above mentioned models the assumption of irrotational motion is assumed, whereas after the onset of breaking a lot of vorticity from the surface is introduced inside the domain. In order to overcome such a limit by means of a more physical approach, Veeramony and Svendsen (2000) removed the hypothesis of irrotational motion and solved analytically the vorticity transport equation coupled with a weakly nonlinear Boussinesq model with enhanced dispersive characteristics. In their contribution the similarity between the hydraulic jumps and the wave breaking has been assumed in order to specify both the boundary condition on vorticity and the roller geometry; in fact they used the results of the experimental investigations on three hydraulics jumps with low Froude number (Svendsen et al., 2000) to get the values of vorticity at the lower edge of the roller. The importance of knowing in detail the shape of the velocity pattern in the breaking region leaded Musumeci et al. (2005) to provide an accurate description within the roller region through the implementation of a self-adaptive-time varying subgrid.

In the present work the above mentioned one-dimensional approach by Musumeci et al. (2005) has been extended to the two-dimensional case in order to study an intrinsic 3D problem as the nearshore hydrodynamics induced by a pit. In the following sections the analytical derivation of the proposed equations, the adopted numerical scheme and results relative to some case studies are shown.

DERIVATION OF THE PROPOSED EQUATIONS

The Boussinesq type of model adopted in the present work is two-dimensional and fully nonlinear; moreover the model can be applied to study the hydrodynamics induced by breaking waves approaching the surf zone. In particular such a model does not assume the flow as irrotational. By considering an incompressible fluid, impermeable and fixed bed, gentle beach slope and by neglecting the effects of the bottom boundary layer and, moreover, by using the free slip condition at the bottom, the equations of motion are integrated over depth. The pressure term is here expressed as a function of the velocity and therefore eliminated from the equations. An expression for the horizontal velocity as a function of the horizontal depth averaged velocity vector $\overline{\mathbf{u}} = (\overline{u}, \overline{v})$ must be provided. This last variable and the free surface elevation

ζ are the unknowns of the problem, which are defined in accordance to the sketch shown in Figure 1.

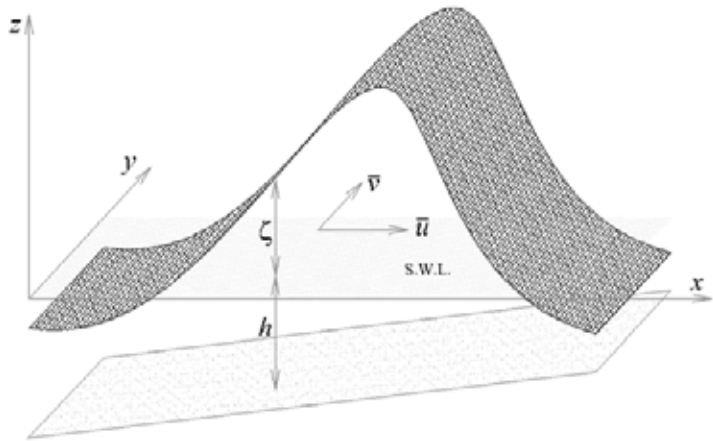

Figure 1. Reference system and schematization of the problem: h is the local water depth, ζ is the free surface elevation, $\overline{u}$ and $\overline{v}$ are the two components of the horizontal depth averaged velocity vector.

In the following derivation it is important to define two dimensionless parameters in order "to measure" the magnitude of the different terms in the momentum equations and therefore in order to allow some simplifications to be introduced:

$$\mu = kh\,;\quad \delta = \frac{a}{h} \tag{1}$$

These two parameters represent the dispersiveness and the nonlinearity properties of the waves respectively, in which k is the wave number, h is the water depth and a is the wave amplitude.

The approach followed to solve the Boussinesq equations, namely the depth averaged momentum and continuity equations, is to specify some reference velocity, such as the depth integrated velocity, the bottom velocity, the surface velocity or the velocity at a reference level, which are in some way representative of the entire velocity profile over the water column. Since the aim of this work is to deal with breaking waves, the horizontal velocity $\mathbf{u} = (u, v)$ can be expressed as an irrotational component, called potential velocity $\mathbf{u}_p$, plus a term in which the contributions due to the vorticity are collected, called rotational velocity $\mathbf{u}_r$. It is worth to point out that if breaking does not start, $\mathbf{u}_r = 0$, since the vorticity is negligible; therefore in such a case the present

model is comparable to the other irrotational Boussinesq models. In presence of breaking the proposed equations can model more physically the related dissipation, by including terms which are function of the wave breaking generated vorticity.

The continuity equation is integrated along the water column; then, by applying the fixed bottom and free surface kinematic boundary conditions, in dimensionless form it can be written as

$$\frac{\partial \zeta}{\partial t} + \nabla \cdot [(h + \delta\zeta)\bar{\mathbf{u}}] = 0 \tag{2}$$

Starting from the three Cartesian components of the momentum equation expressed in conservative form and with the Reynolds averaged turbulent terms, integrating the horizontal components along the water column, it is possible to obtain the so called combined momentum equations in the two horizontal dimensions, which, in vectorial form read:

$$\begin{aligned}
&\bar{\mathbf{u}}_t + \delta(\bar{\mathbf{u}}\cdot\nabla)\bar{\mathbf{u}} + \nabla\zeta \\
&\quad + \mu^2\Big\{\left(B - \frac{1}{3}\right)h^2\nabla(\nabla\cdot\bar{\mathbf{u}}_t) - \frac{1}{2}h\nabla(\bar{\mathbf{u}}_t\cdot\nabla h) - \frac{1}{2}h(\nabla\cdot\bar{\mathbf{u}}_t)\nabla h \\
&\quad + Bh^2\nabla(\nabla\cdot\nabla\zeta)\Big\} \\
&\quad + \delta\mu^2\Big\{-\frac{1}{3}h^2\nabla[\bar{\mathbf{u}}\cdot\nabla(\nabla\cdot\bar{\mathbf{u}})] + \frac{2}{3}h^2(\nabla\cdot\bar{\mathbf{u}})\nabla(\nabla\cdot\bar{\mathbf{u}}) - \frac{1}{2}h\nabla[\bar{\mathbf{u}}\cdot\nabla(\bar{\mathbf{u}}\cdot\nabla h)] \\
&\quad - \frac{1}{2}h[\bar{\mathbf{u}}\cdot\nabla(\nabla\cdot\bar{\mathbf{u}})]\nabla h + \frac{1}{2}h(\nabla\cdot\bar{\mathbf{u}})^2\nabla h - h(\nabla\cdot\bar{\mathbf{u}}_t)\nabla\zeta - \frac{2}{3}h\zeta\nabla(\nabla\cdot\bar{\mathbf{u}}_t) \\
&\quad - \frac{1}{2}\zeta(\nabla\cdot\bar{\mathbf{u}}_t)\nabla h - \frac{1}{2}\zeta\nabla(\bar{\mathbf{u}}_t\cdot\nabla h) - (\bar{\mathbf{u}}_t\cdot\nabla h)\nabla\zeta + Bh^2\nabla[\nabla\cdot((\bar{\mathbf{u}}\cdot\nabla)\bar{\mathbf{u}})] \\
&\quad + \delta^2\mu^2\Big\{-\frac{1}{3}\zeta^2\nabla(\nabla\cdot\bar{\mathbf{u}}_t) - \zeta(\nabla\cdot\bar{\mathbf{u}}_t)\nabla\zeta + \frac{4}{3}h\zeta(\nabla\cdot\bar{\mathbf{u}})\nabla(\nabla\cdot\bar{\mathbf{u}}) \\
&\quad - \frac{2}{3}h\zeta\nabla[\bar{\mathbf{u}}\cdot\nabla(\nabla\cdot\bar{\mathbf{u}})] + h(\nabla\cdot\bar{\mathbf{u}})^2\nabla\zeta - h[\bar{\mathbf{u}}\cdot\nabla(\nabla\cdot\bar{\mathbf{u}})]\nabla\zeta \\
&\quad + \frac{1}{2}\zeta(\nabla\cdot\bar{\mathbf{u}})^2\nabla h - \frac{1}{2}\zeta[\bar{\mathbf{u}}\cdot\nabla(\nabla\cdot\bar{\mathbf{u}})]\nabla h - \frac{1}{2}\zeta\nabla[\bar{\mathbf{u}}\cdot\nabla(\bar{\mathbf{u}}\cdot\nabla h)] \\
&\quad - [\bar{\mathbf{u}}\cdot\nabla(\bar{\mathbf{u}}\cdot\nabla h)]\nabla\zeta\Big\} \\
&\quad + \delta^3\mu^2\Big\{\frac{2}{3}\zeta^2(\nabla\cdot\bar{\mathbf{u}})\nabla(\nabla\cdot\bar{\mathbf{u}}) - \frac{1}{3}\zeta^2\nabla[\bar{\mathbf{u}}\cdot\nabla(\nabla\cdot\bar{\mathbf{u}})] + \zeta(\nabla\cdot\bar{\mathbf{u}})^2\nabla\zeta \\
&\quad - \zeta[\bar{\mathbf{u}}\cdot\nabla(\nabla\cdot\bar{\mathbf{u}})]\nabla\zeta\Big\} + \{\delta\nabla(\boldsymbol{\Delta}\mathbf{M}) + \delta\mu^2\nabla(\boldsymbol{\Delta}\mathbf{M}_1) + \mu^2[\nabla(\nabla\cdot\boldsymbol{\Delta}\mathbf{P})]_t \\
&\quad - \delta\mu^2\mathbf{D}_{\mathbf{w}} - \mu^2(\mathbf{D}_{\mathbf{sv}} + \mathbf{D}_{\mathbf{sh}}) - \delta\mu^2\mathbf{D}_{\mathbf{uw}}\}(h + \delta\zeta)^{-1} = O(\mu^4)
\end{aligned} \tag{3}$$

in which B is a coefficient that has been applied to improve dispersive characteristics in deeper water. The last terms in curly brackets in Eq. 3 are the breaking terms.

Even though such equations are similar to those derived by Musumeci et al. (2005), they crucially differ from the one-dimensional case for the presence of the ∇ operator, that causes the presence of mixed spatial derivatives. Another difference is represented by the dissipative term $\mathbf{D}_{sh}$, that is related to the turbulent Reynolds stresses in the horizontal plane, modelled by an appropriate eddy viscosity.

THE ADOPTED NUMERICAL SCHEME

Due to the presence of the time derivatives of the unknown variable $\overline{\mathbf{u}}$ in Eq. 3, the momentum equation is solved as function of a new vectorial variable $\mathbf{U} = (U, V)$ defined as:

$$\begin{aligned} U &= \bar{u} + \left(B - \frac{1}{3}\right) h^2 \bar{u}_{xx} - h h_x \bar{u}_x - \frac{1}{2} h h_{xx} \bar{u} \\ V &= \bar{v} + \left(B - \frac{1}{3}\right) h^2 \bar{v}_{yy} - h h_y \bar{v}_y - \frac{1}{2} h h_{yy} \bar{v} \end{aligned} \tag{4}$$

This new variable permits to exclude the velocity time derivative of order μ^2, which causes a substantial numerical destabilization of the model. The scheme adopted to integrate numerically the continuity and momentum equations is one of the most popular predictor-corrector methods, namely the Adams-Bashforth-Moulton scheme, which has good stability properties (Press et al., 1992). In particular, the scheme here is of third order at the predictor step and of fourth order at the corrector one.

The computational grid is constituted by a rectangle in which three of the boundary are vertical walls and the other is the offshore boundary. The condition at the vertical walls is that the velocity components perpendicular to them, are set equal to zero. This is an artificial condition in a lot of nearshore systems, so in order to avoid enormous numerical domain, it is necessary to insert in front of each wall a sponge layer that absorbs the reflected flow. At the offshore boundary an absorbing-generating boundary condition is applied, obtained under the assumption of plane progressive waves of constant form, in analogy to van Dongeren and Svendsen (1997).

Wave breaking generated vorticity is obtained solving analytically the vorticity transport equation for the direction of wave propagation:

$$\frac{\partial \omega}{\partial t} + \sqrt{u^2 + v^2}\,\frac{\partial \omega}{\partial s} + w\frac{\partial \omega}{\partial z} = \nu_t \left(\frac{\partial^2 \omega}{\partial s^2} + \frac{\partial^2 \omega}{\partial z^2} \right) \tag{5}$$

in which ω is the vorticity, *s* is the direction of wave propagation, *u*, *v*, *w* are the three velocity components in the Cartesian coordinates system, ν_t is the eddy viscosity. As a matter of fact, Eq. 5 should be written in terms of the three components of vorticity, but, assuming wave breaking as a phenomenon mainly characterized by cylindrical symmetry, the vorticity can be considered as acting on a vertical plane perpendicular to the wave front. The analytical solution of this last equation is developed assuming that the introduction of vorticity is possible only from the free surface when breaking appears, generating a vorticity ω_s. Then the implementation of this analytical solution need an appropriate spatial definition of the 3D roller concept (see Figure 2), in order to determine the value of ω_s to be specified along the upper limit of the computational domain, corresponding to the lower boundary of the surface roller.

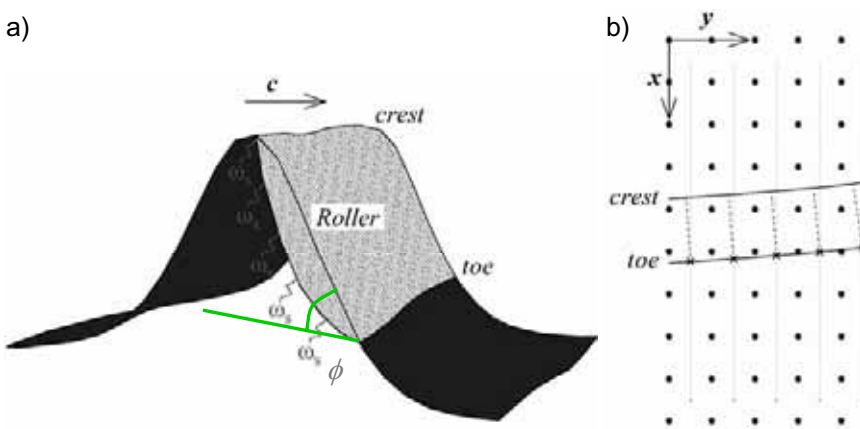

Figure 2. Physical scheme of a three-dimensional roller: a) axonometric view with injection of the vorticity ω_s at the roller lower boundary, *c* is the wave celerity, ϕ is the angle at the toe of the roller and influences the breaking onset criterion; b) top view of the numerical grid in which toe points (x) and grid nodes (•) are showed, the red broken lines represent the sections in which injection of vorticity is computed.

As in some one-dimensional models in which the roller concept has been applied (Schäffer et al., 1993), breaking is here assumed to initiate when and where the local steepness of the wave front exceeds a certain limiting surface gradient tanϕ. Precisely, the toe of the roller is defined as the location where the wave steepness is identical to tanϕ and the roller itself is included between its toe and the wave crest. To account for the transition from the initial breaking to the bore-like stage in the inner surf zone, the critical roller angle, ϕ, is assumed to decrease from ϕ_B to ϕ_0 as function of the age *t* of each surface roller:

$$\tan\phi(t) = \tan\phi_0 + (\tan\phi_B - \tan\phi_0)\exp\left[-\ln\left(2\frac{t-t_B}{t_{1/2}}\right)\right] \quad (6)$$

where t represents the time interval measured from when the wave starts to break, $t_{1/2}$ defines the time scale for the development of the roller, and t_B is the time of incipient breaking.

In the two horizontal dimensions, the toe of the roller becomes a curve, defined as the points satisfying the condition that the absolute value of the surface elevation gradient equals the instantaneous local value of tanϕ and that the gradient in the direction of the wave propagation is negative. Moreover the roller toe angle is allowed to vary within a roller because different stages of the breaking process can be represented within the same 3D roller. The trend in time of the roller position is not correlated to the flow motion but it depends from the wave shape; then an algorithm for accurately tracking the roller position has been developed similar to the one used by Sørensen et al. (1998), but with some original differences. First of all, the discrete toe points of the roller and the tangential lines at these points are determined as shown in Figure 2b. In particular, a rectangular grid is defined, with a surface elevation computational node in the center of each grid cell. Values of the roller angle and of the surface elevation gradient are then calculated at the nodes of this grid and subgrid roller toe points satisfying the toe condition are found by interpolation at the boundary of each cell. Then the wave crest and the width of the roller in the wave propagation direction is found in the correspondence of each toe point. The roller thickness and the injection of vorticity ω_s is computed along the sections passing through the toe points (red broken lines in Figure 2b), by applying the results of the experiments of Svendsen et al. (2000). Finally the age of the roller is updated and the corresponding toe angle ϕ can be calculated according to Eq.6.

MODEL VALIDATION

A preliminary validation of the proposed model has been made considering the simple case of total reflection, i.e. by studying the interaction of an incident cnoidal wave with a vertical wall perpendicular to the propagating wave direction. From the analysis of the wave envelopment, shown in Figure 3, it is possible to argue that the model manages the generation of a stationary wave in a correct way.

The proposed model has been also tested in breaking condition with incident waves propagating orthogonal to the coastline. Precisely, the results have been validated by means of the previous one-dimensional model by Musumeci et al. (2005) and by means of the experimental data of Cox et al. (1995) and of Hansen and Svendsen (1979). Figure 4 shows a fairly good matching both within the shoaling and the surf regions with the experimental data of Hansen and Svendsen (1979).

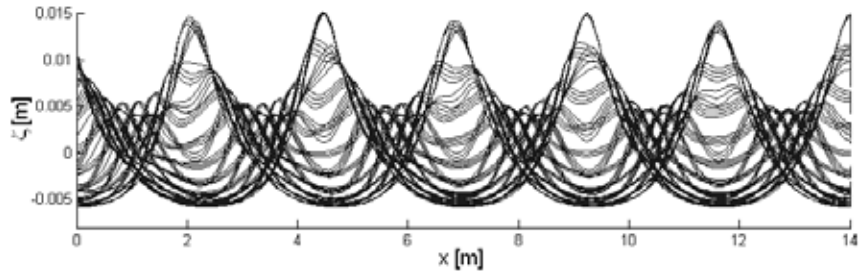

Figure 3. Wave envelope generated by cnoidal waves over a fully reflective vertical wall located at x = 14 m; input wave is cnoidal and has H = 0.01 m and T = 2.5 s.

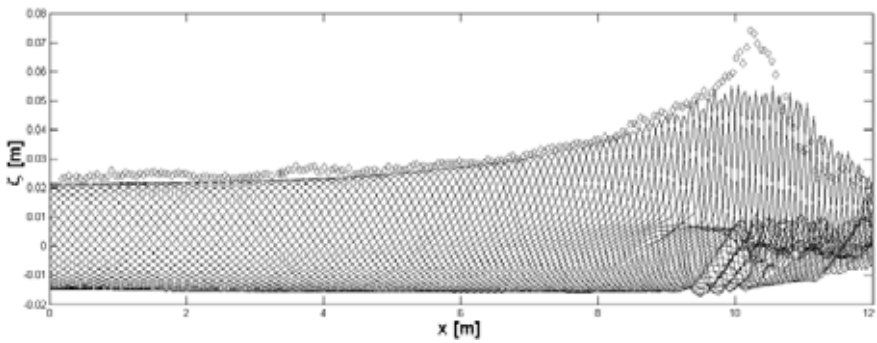

Figure 4. Proposed model results: wave envelope, registered at every 0.074 s; input wave is cnoidal and has H = 0.04 m and T = 2.5s. The red diamonds represent the maximum surface elevation obtained by Hansen and Svendsen (1979).

APPLICATION TO SUBMARINE CAVES

Two-dimensional models may be used to analyze complex situations as the ones generated by waves approaching the nearshore region, wave-structure interaction, submerged breakwaters, cuspidate beaches and submarine sand mines, which can cause the presence of macrovortices and rip currents. In particular the aim of this contribution is to better understand the behavior of wave motion and its generated currents when they propagate over nearshore submarine caves.

The reference bathymetry is based on the field data measured in the correspondence of an existing cave, called PUTMOR (see Figure 5), placed in front of the Dutch coast, which has been analyzed by Walstra et al. (2003). Such a cave is sketched as an inverted truncated pyramid, reaching a maximum depth equal to 10 m with respect to the sea bottom; its base dimensions are 900 m

along the cost and 100 m in the cross shore direction, with wall sloping 1:20. Its toe dimensions in the correspondence of the existing sea depth are 500m x 1300m, which corresponds to an excavation volume of about 3.5 Mm^3.

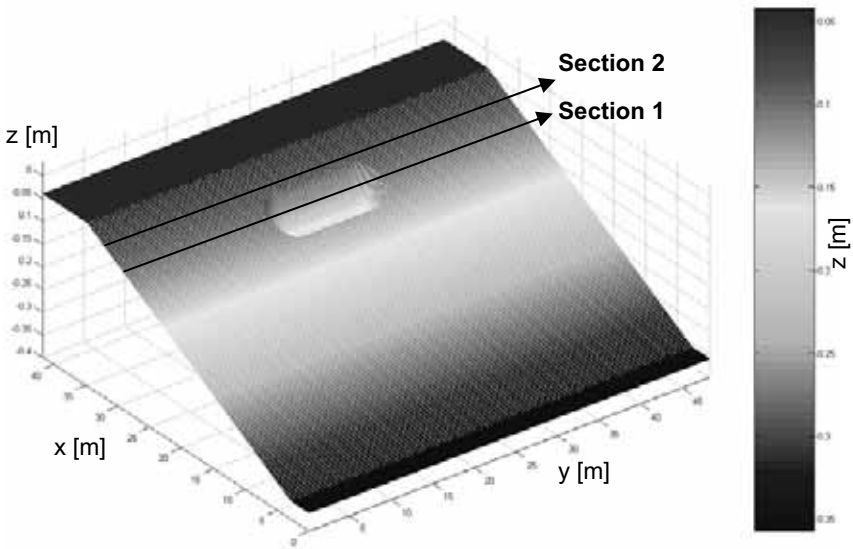

Figure 5. Bathymetry of the submerged cave PUTMOR in scale 1:100. Computational grid with the section in which results are extracted.

For computational reasons the above described bathymetry has been reported in scale 1:100 through a Froude similitude. The proposed model has been used with an incident cnoidal wave with an height equal to 0.0224 m and a wave period of 2.0 s, and direction perpendicular to the coastline, i.e. to the *y* axis of the computational grid. The presented results refer to two sections (shown in Figure 5) located on the cave and landward near the alongshore toe of the cave, respectively. The resulting free surface elevation envelop is reported for the two sections in Figure 6. From these graphics it is possible to point out that in Section 1 there is a decrease of the wave height in the middle of the cave and a sudden increase in the correspondence of the cave boundaries (i.e. *y* equals to18 m and 31 m respectively). Such an effect is amplified in Section 2 which is placed shoreward and close to the cave. Moreover here is possible to notice a greater decrease of the wave height just before the limits of the cave (i.e. *y* equals to 20 m and 29 m respectively).

This qualitative results obtained from the model can be compared with those obtained in the field along with the model results available from the SANDPIT project (van Rijn et al.; 2005), which show a small increase of the wave height, shoreward and corresponding to the middle of the cave, of about

2%, and a gradual decrease up 5% to the boundary of the cave. It is also reported an increase, equal to about 10-15%, of the wave height in the area surrounding the cave, just out of the extreme part of the pit. Moreover it has been concluded that wave height and currents have been modified no more than 5% at a distance of 1km from the cave.

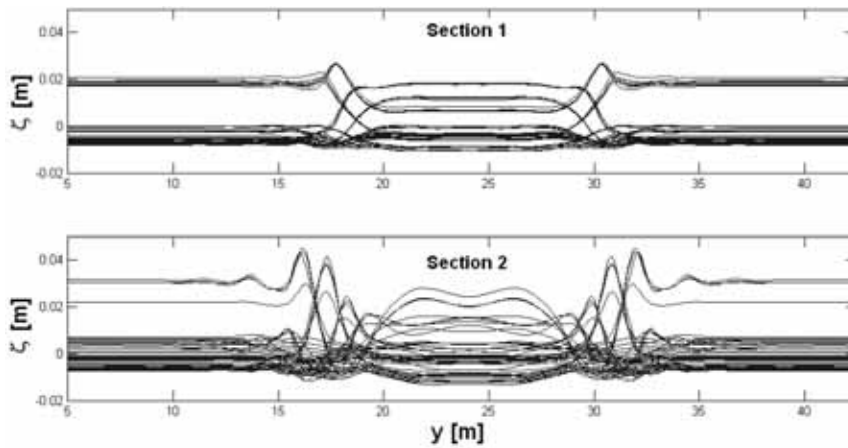

Figure 6. Model results: wave height envelope plotted every 0.2s at section 1 and 2 of the PUTMOR cave, for an incident cnoidal wave (H=0.0224m and T=2.0s).

These conclusions can be deduced also by the analysis of the distribution of the mean surface elevation and of the disturb coefficient (local wave height over incident wave height), shown in Figure 7 and Figure 8 respectively. In particular the important effect of the presence of the cave are localized shoreward, in the area just immediately out of its lateral boundaries. These effects can be summarized in a greater shoaling and set down respect to the rest of the computational domain.

Finally it has been varied the planar dimension of the cave with respect to its basic configuration, fixing the dig volume, thus obtaining as a smaller cave causes a minor impact, although caves wider than the basic case do not generate severe impacts on the wave propagation.

CONCLUSIONS

Derivation of the 2D continuity and momentum equations implemented in the proposed model highlighted the presence of new terms with respect to the corresponding one-dimensional Boussinesq model for breaking waves by Musumeci et al. (2005).

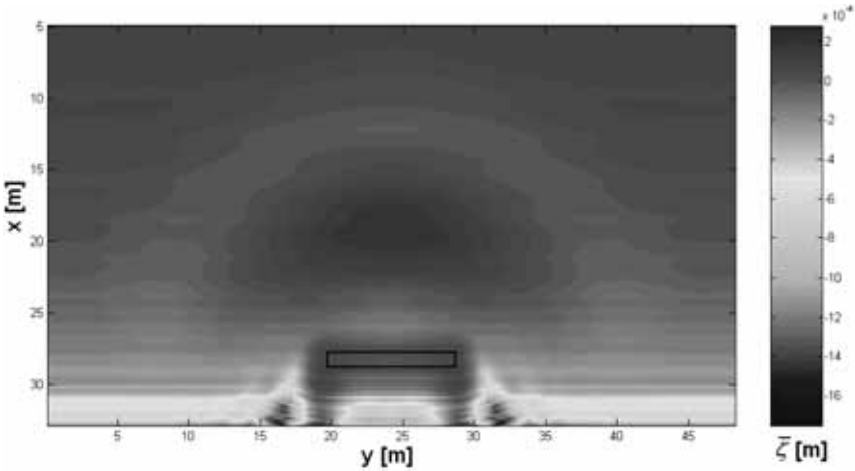

Figure 7. Model results with indication of the bottom boundaries of the cave: mean surface elevation for an incident cnoidal wave (H=0.0224m and T=2.0s).

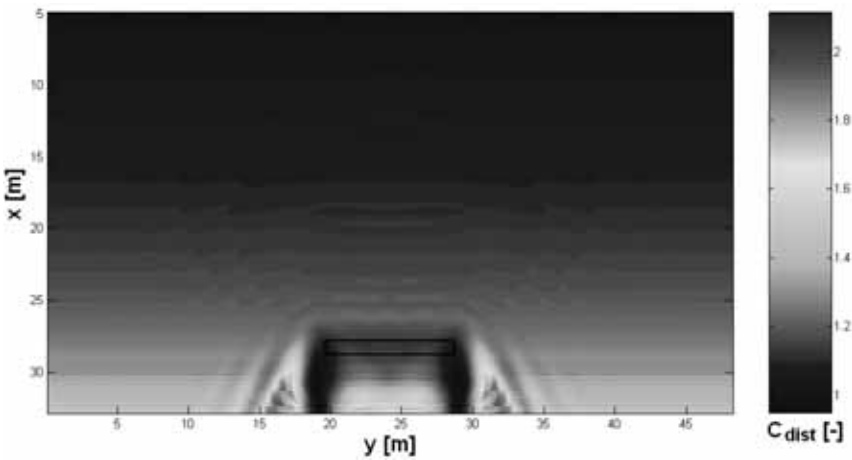

Figure 8. Model results with indication of the bottom boundaries of the cave: disturb coefficient, defined as local wave eight over incident wave (H=0.0224m and T=2.0s).

Moreover a new three-dimensional roller concept has been defined and implemented with the aim of obtaining the breaking terms included in the momentum equation. In particular, the application of the 3D roller permitted to obtain the vorticity ω_s injected in the water surface and then it was possible to compute analytically the vorticity ω in the computational domain below the

roller its self. Validation of the model to verify its correct behaviour for the case of straight and parallel contours in the presence of orthogonal incident wave, provided fairly good results also after the onset of breaking, above all in the bore-like region.

Finally the application of the proposed model to study wave motion over submarine caves, i.e. in complex hydrodynamic conditions, highlighted the increase of wave height in the area surrounding the cave, in particular close to its boundaries. Such a behaviour is in good agreement with what observed in the field and also with the numerical results obtained in the framework of the SANDPIT project.

Therefore it is reasonable to expect that the proposed model can be applied, in the near future, to study nearshore hydrodynamics generated by complex conditions of engineering interest, ever in the presence of breaking.

ACKNOWLEDGMENTS

This work has been carried out in the framework of the EU funded project HYDRALAB-III (contract no. 0224411(RII3)).

REFERNCES

Chen, Q., Kirby, J. T., Dalrymple, R. A., Kennedy, A. B., Chawla, A. 2000. Boussinesq modeling of wave transformation, breaking, and runup. ii: 2D. *J. of Waterway, Port, Coastal and Ocean Engng*., 126, 48-56.

Cox, D. T., Kobayashi, N., Okaiasu, A. 1995. Experimental and numerical modeling of surf zone hydrodynamic. Research report CACR-95-07, Center For Applied Coastal Research, University of Delaware.

Hansen, J. B., and Svendsen, I. A. 1979. Regular waves in shoaling water experimental data. Series Paper 21, Institute of Hydrodynam. and Hydraulic Engng, Technical University of Denmark.

Madsen, P. A., Sørensen, O. R., Schäffer, H. A. 1997. Surf zone dynamics simulated by a Boussinesq type model. part i. model description and cross-shore motion of regular waves. *Coastal Engng*., 32, 255-287.

Musumeci, R. E., Svendsen, I. A., Veeramony, J. 2005. The flow in the surf zone: a fully nonlinear boussinesq-type of approach. *Coastal Engng.,* 52, 565-598.

Peregrine, D.H. 1966. Calculation of the development of an ondular bore. *J. Fluid Mech*., 25, 321-331.

Peregrine, D. H. 1967. Long waves on a beach. *J. Fluid Mech*., 27, 815-827.

Press, W. H., Flannery, B. P., Teukolsky, S. A., Vetterling W. T. 1992. *Numerical recipes in Fortran (2nd ed.)*. Cambridge University Press.

Schäffer, H. A., Madsen, P. A., Deigaard, R. 1993. A Boussinesq model for waves breaking in shallow water. *Coastal Engng*., 20, 185-202.

Sørensen, O. R., Schäffer, H. A., Madsen, P. A. 1998. Surf zone dynamics simulated by a Boussinesq type model. part iii. wave-induced horizontal nearshore circulation. *Coastal Engng*., 33, 155-176.

Svendsen, I.A. 1984. Wave heights and setup in a surf zone. *Coastal Engng*., 8, 303-329.

Svendsen, I. A., Veeramony, J., Bakunin, J., Kirby, J. T. 2000. The flow in weak turbulent hydraulic jump. *J. Fluid Mech*., 418, 25-57.

van Dongeren, A.R., and Svendsen, I.A. 1997. Absorbing-generating boundary condition for shallow water models. *J. Waterway, Port, Coastal and Ocean Engng*, 123(6), 303-313.

van Rijn, L.C., Soulsby, R.L., Hoekstra, P., Davies, A. G. 2005. SANDPIT sand transport and morphology of offshore mining pits. EC Framework V Project No. EVK3-2001-00056.

Veeramony, J., and Svendsen, I.A. 2000. The flow in the surf-zone waves. *Coastal Engng*., 39, 93-122

Walstra, D.J.R, van Rijn, L.C., Boers, M., Roelvink, J.A. 2003. Offshore Sand Pits: Verification and application of a hydrodynamic and morphodynamic model. Coastal Sediment. Clearwater Beach, Florida, USA.

Zelt, J. A. 1991. The run-up of nonbreaking and breaking solitary waves. *Coastal Engng*., 15, 205-246.

WAVE REGIME COMPARISONS ON THE PORTUGUESE COAST

Rui Capitão and Conceição Fortes[1]

In this paper, two methodologies are compared, one that uses the same linear wave ray BACKTRACK-REFSPEC model for both the back-propagation transfer of observed data to offshore and for the forward-propagation of that offshore data to desired location(s) and another that uses the more sophisticated nonlinear SWAN model for the latter propagation. A verification of the methodologies was done firstly by comparing the transferred wave regimes with the measured wave regimes in front of Leixões, on the north western Portuguese coast. Then, both methodologies were used to compute representative wave regimes on two main areas of the Portuguese coast. Results on these wave regimes, which may be assumed as representative of the North and South western coast of Portugal, are compared and discussed, allowing one to also compare the numerical models included in those methodologies.

INTRODUCTION

For several years, LNEC has used the so-called TRANSFER methodology, described in Capitão et al. (2006), to solve a problem that occurs quite often in coastal engineering studies: the absence of observed wave data at locations where coastal works have to be built. To accomplish this goal, sea wave propagation models are used to transfer the available wave data or regimes at a coastal location, to offshore, and to transfer this offshore regime to the coastal site(s), not so distant from the original site, where the wave regime(s) is(are) sought. In this way, a set of significant wave heights, HS, mean wave periods, TZ, and mean wave directions, Θ, that defines a wave regime at the coastal site(s) of interest, is obtained.

The TRANSFER methodology is based on three numerical models: BACKTRACK and REFSPEC, Covas and Pontes (1988) and, more recently, SWAN, Booij et al. (1999). BACKTRACK computes the path of the wave rays reaching one point for a given bottom configuration (fan-type refraction diagrams). REFSPEC uses as input the output numerical files from BACKTRACK and the deep-water two-dimensional directional wave spectrum to compute the wave spectrum at the beginning point of the wave rays, by refracting the offshore spectrum. The well-known nonlinear spectral SWAN model (Booij et al., 1999) may used instead of BACKTRACK-REFSPEC to propagate the offshore spectrum to the shoreline taking into account the major physical processes of wave refraction, diffraction and shoaling due to bottom depth variation and to the presence of currents. It also includes wind induced wave growth, wave breaking due to bottom variation and to whitecapping,

[1] Environmental and Hydraulics Department, National Laboratory of Civil Engineering (LNEC), Avenida do Brasil 101, 1700-066 Lisboa, Portugal

energy dissipation by bottom friction, wave blocking and reflection by opposing currents as well as wave transmission. The SWAN model has recently been included into the TRANSFER methodology because of its completeness in considering more complex phenomena than the linear wave ray model BACKTRACK-REFSPEC (BR).

In this paper, a verification of both original (using BR) and improved (using SWAN) TRANSFER methodologies is first presented for a site in front of Leixões, where observed data are available. In the following, the methodologies associated with each of the models BACKTRACK-REFSPEC and SWAN will be termed "TRANSFER_BR" and "TRANSFER_SWAN", respectively, and BACKTRACK-REFSPEC model will be simply termed "BR". Both methodologies are then applied and compared in two selected sites on the Portuguese coast. These where chosen due to their relative closeness to the deployment locations of existing directional wave buoys.

METHODOLOGY

The methodologies analyzed in this paper use the linear wave ray model BR for the back-propagation transfer of the observed data to offshore (from A to B, in Fig. 1), while for the forward-propagating of that offshore data to the desired location (from B to C, D or E, in Fig. 1) two models may be used: the same BR model or the SWAN model.

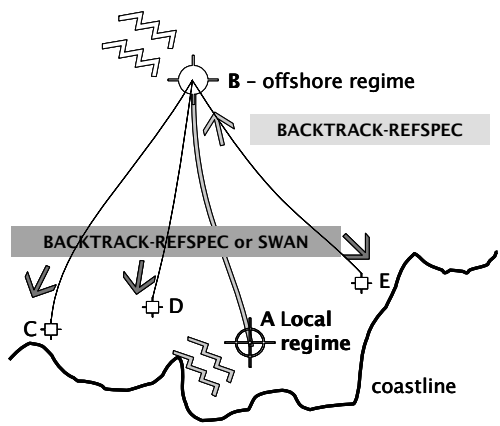

Figure 1. TRANSFER methodology

Several wave regimes along the Portuguese coast were determined by using the BR model for the offshore-inshore transfer, although only for a few sites the SWAN model was used. However, no validation with observed data was performed yet using both models, which is a fundamental aspect to be taken into account to find the "best" offshore-inshore propagation model. The following verification will give confidence on future applications to other locations along the Portuguese coast.

VERIFICATION

In this paper, a comparison between the wave regimes transferred using the two different methodologies is made for a location, in front of Leixões, on the north western Portuguese coast, where two wave buoys (C3 and C4) have simultaneously recorded data for 6 months, from Oct. 2001 to Mar. 2002, Fig. 2.

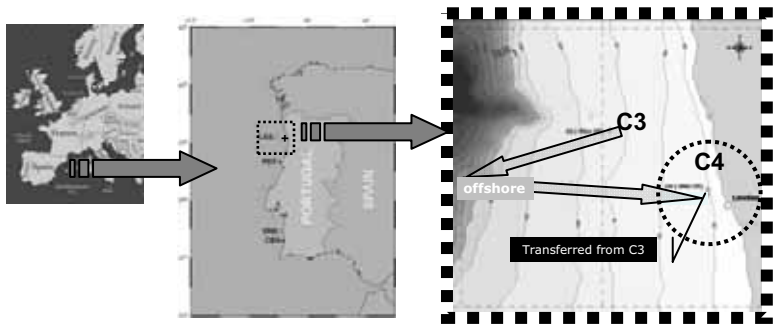

Figure 2. Verification location, in front of Leixões, Portugal

Comparisons of the local (transferred from C3 location) wave regimes with the measured (observed and not transferred, at C4 location) data were done. Fig. 3, below, shows, for a small stretch of 17 days, a comparison of the significant wave heights and periods between the observed values at C4 location and transferred C3 values using the two methodologies.

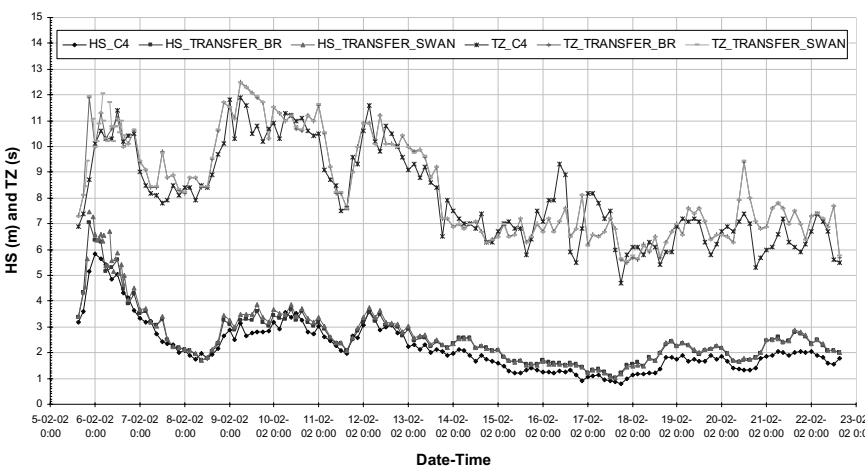

Figure 3. Comparison of observed wave data (HS and TZ) at C4 location with TRANSFER_SWAN and TRANSFER_BR results

Also histograms of the same parameters for the whole data set (6-months) are shown to enable a better assessment of the results of the two models as compared to the observed data at C4, Figs. 4 and 5.

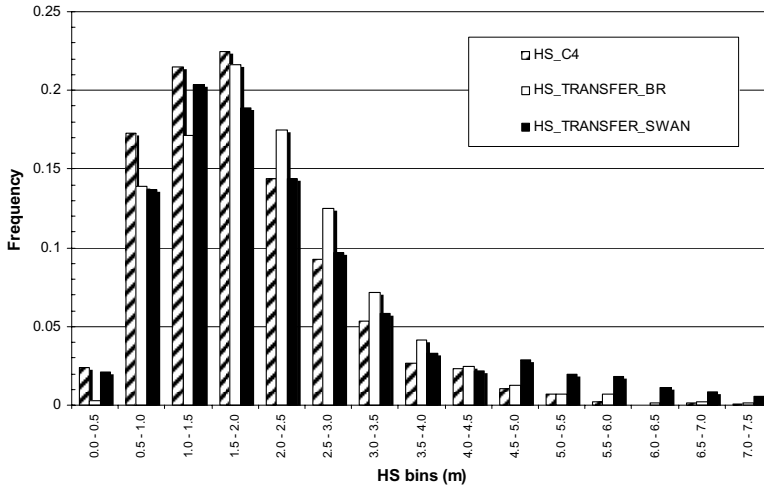

Figure 4. Comparison of observed wave data at C4 locations with TRANSFER_SWAN and TRANSFER_BR results. Histogram of HS

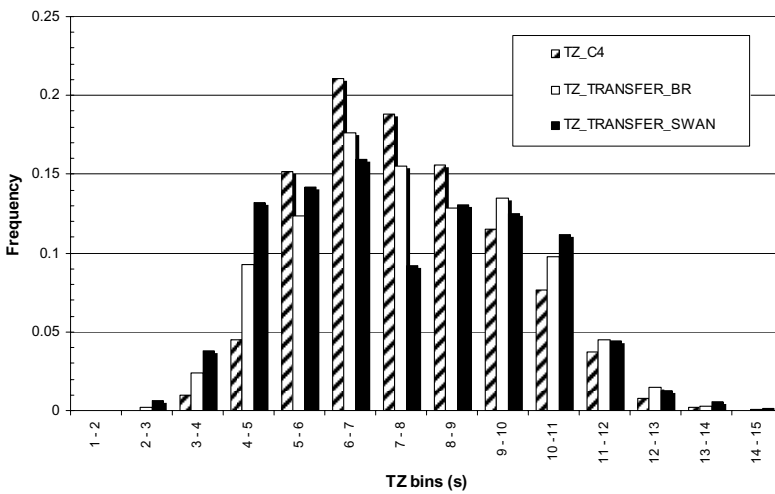

Figure 5. Comparison of observed wave data at C4 locations with TRANSFER_SWAN and TRANSFER_BR results. Histogram of TZ

This assessment of the transfer verification was made by comparing values transferred from the C3 buoy to values measured by C4 buoy, by employing time series and histograms of HS and TZ (Figs. 3 to 5). For the case of the comparison between measured C4 values and transferred values using TRANSFER_BR, the verification also included statistical comparisons using

standard tests like visual tests, run tests, rank-sum tests, Kolmogorov-Smirnov tests and $\chi 2$ tests for HS and TZ wave parameters. Θ was not considered, due to the lack of directional information at the C4 position.

For this location and for the 6-month-period, a small overestimation of both the wave heights and wave periods was obtained for both models, see Fig 3 to 5. A part of the overestimation may possibly be attributed to buoy measurement errors, which can reach 3%, for wave heights and periods, and 2º, for directions.

From these comparisons, no significant differences between the methodologies were found. This is related to the location of C4 (open-sea and near deep water conditions). However, one should note that the TRANSFER_SWAN methodology was applied using relatively simplified conditions, i.e., no wind, no non-linear effects and stationary mode were considered.

APPLICATION

The previous comparisons between the wave regimes transferred using the two methodologies showed no significant differences between them. Therefore, in the applications shown below, both methodologies were used to transfer the north western offshore regime, transferred from Leixões (LXS), and the south western offshore regime, transferred from Sines (SNS), to two inshore locations at a water depth of 10 m inside each area, Praia da Tocha (PDT) and Cabo Sardão (CBS), see Table 1 and Fig. 6.

Table 1. Location of wave buoys and target points on the western coast of Portugal

Name location	Code	Latitude (N)	Longitude (W)	Depth (m)
Leixões	LXS	41° 12' 12"	9° 05' 18"	110.0
Praia da Tocha	PDT	40º 20' 00"	8º 57' 00"	49.7
Sines	SNS	37° 55' 16"	8° 55' 44"	94.8
Cabo Sardão	CBS	37° 35' 46"	8° 50' 31"	47.0

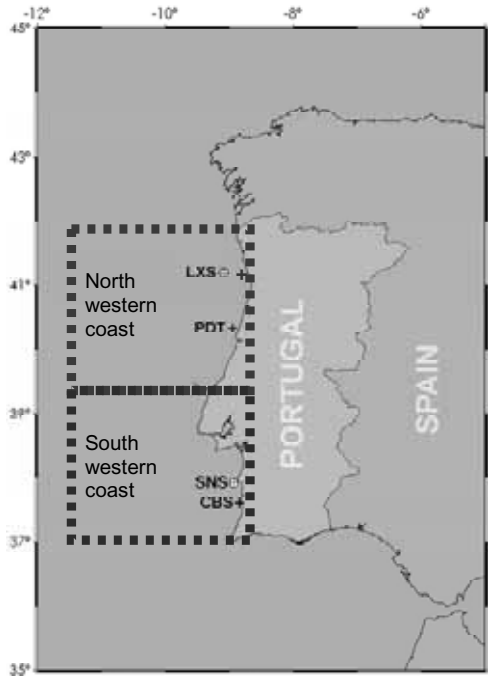

Figure 6. LXS, PDT, SNS and CBS locations on the western coast of Portugal

In the next section, comparisons will be made for the two mentioned sites: a) PDT (on the North western coast), Figs. 7 to 11, and b) CBS (on the South western coast), Figs. 12 to 16.

Wave regime at PDT (North western coast)

A first comparison is made at Praia da Tocha (PDT), on the North western coast. As an example, Figs. 7 to 9 show the comparisons, for eleven months (from 2001-10-1 to 2002-08-31), of the time series computed using the two methodologies of, respectively, HS, TZ and Θ.

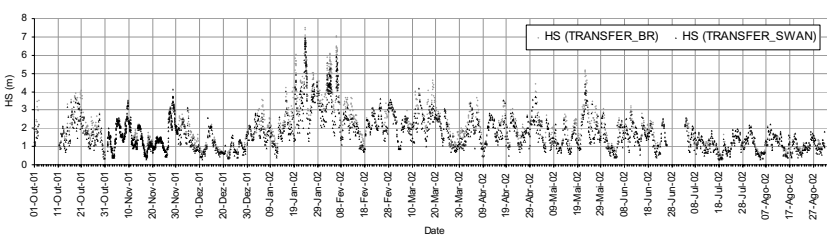

Figure 7. Time series with the comparison of HS using TRANSFER_BR and TRANSFER_SWAN for PDT location

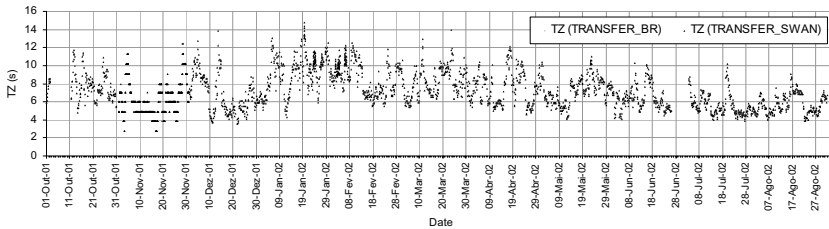

Figure 8. Time series with the comparison of TZ using TRANSFER_BR and TRANSFER_SWAN for PDT location

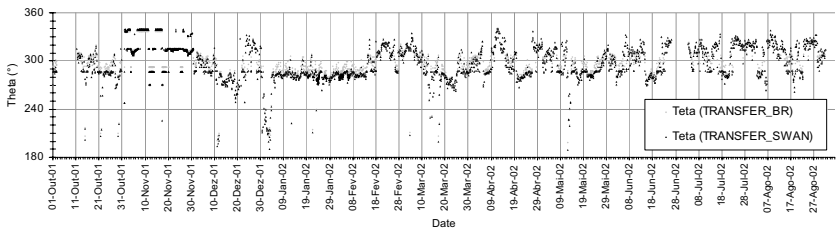

Figure 9. Time series with the comparison of Θ using TRANSFER_BR and TRANSFER_SWAN for PDT location

A comparison was made by means of histograms of the parameters HS and Θ, for the whole data that make up the wave regimes "IH+TRANSFER_BR" and "IH+TRANSFER_SWAN" at PDT, Figs. 10 and 11. The parameter TZ was not considered in these comparisons because it was assumed to be constant in the transfer process for both methodologies.

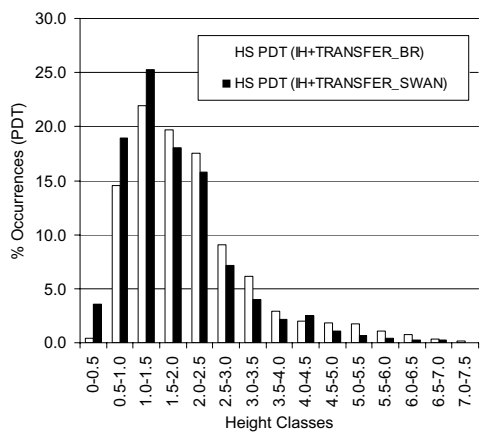

Figure 10. Histogram with the comparison of HS using TRANSFER_BR and TRANSFER_SWAN for PDT location

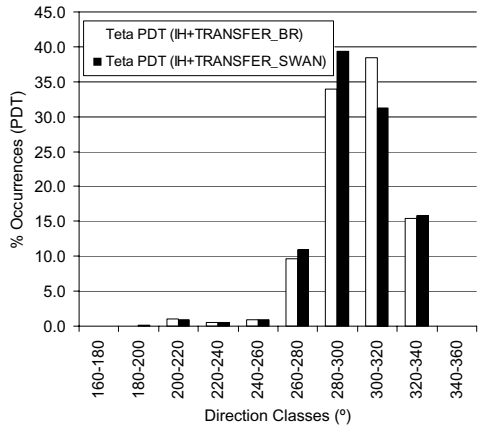

Figure 11. Histogram with the comparison of Θ using TRANSFER_BR and TRANSFER_SWAN for PDT location

Table 2 shows a summary of the results of these comparisons for PDT location.

Table 2. Summary table of the comparison of HS, TZ and Θ using TRANSFER_BR and TRANSFER_SWAN for PDT location

Parameter/method		*TRANSFER_BR*	*TRANSFER_SWAN*
Height	Mean	2.08	1.79
	Standard Deviation	1.194	1.051
	Minimum	0.41	0.29
	Maximum	7.50	6.94
	Count	3129	3129
Period	Mean	7.20	7.20
	Standard Deviation	2.075	2.075
	Minimum	2.80	2.80
	Maximum	14.82	14.82
	Count	3129	3129
Direction	Mean	301.36	298.82
	Standard Deviation	21.144	22.470
	Minimum	198.27	189.73
	Maximum	338.60	340.74
	Count	3129	3129

The following conclusions arise from the analysis of the above results:

1. In general, the parameters, computed either by TRANSFER_BR or TRANSFER_SWAN methodologies show a similar trend, that is, their variations along the studied period are quite similar, see Figs. 7 to 9;
2. The mean, standard deviations and range of the wave heights are of the same magnitude. However, TRANSFER_SWAN was found to produce higher occurrences in the smaller wave height classes than TRANSFER_BR;
3. The wave directions are scattered into two main 20° classes (280° to 320°). The major occurrences are on 300°-320° class for TRANSFER_BR while

for TRANSFER_SWAN are on 280°-300° class. TRANSFER_BR shows a smaller range of values than the TRANSFER_SWAN;

4. The wave direction range for both models is limited by the use of this type of methodologies (a back-propagation followed by a forward-propagation).

b) Wave regime at CBS (South western coast)

A similar comparison was made for the Cabo Sardão (CBS) site. Figs. 12 to 14 show the comparisons from 2001-10-1 to 2002-08-27 of the time series of HS, TZ and Θ computed at CBS, using transferred data from SNS.

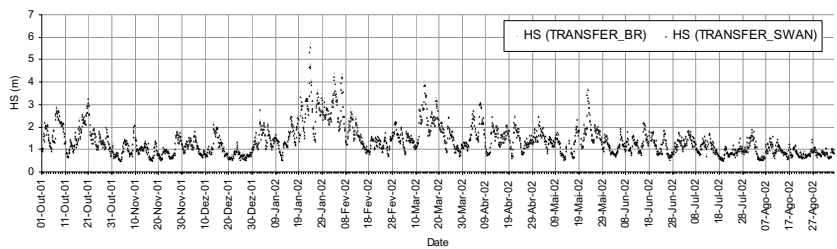

Figure 12. Time series with the comparison of HS using TRANSFER_BR and TRANSFER_SWAN for CBS location

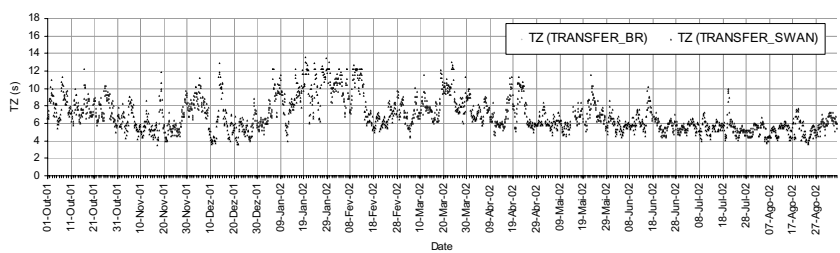

Figure 13. Time series with the comparison of TZ using TRANSFER_BR and TRANSFER_SWAN for CBS location

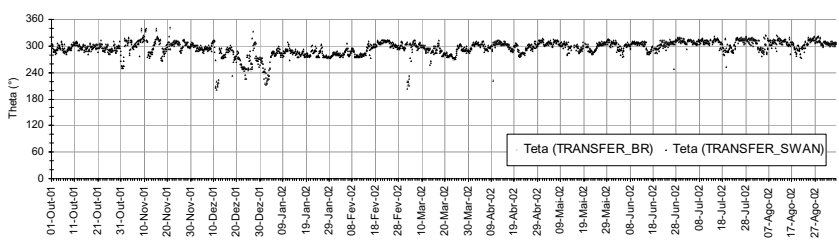

Figure 14. Time series with the comparison of Θ using TRANSFER_BR and TRANSFER_SWAN for CBS location

For CBS, a comparison was also made by plotting histograms of HS and Θ, Figs. 15 and 16. Here, TZ parameter was also not considered.

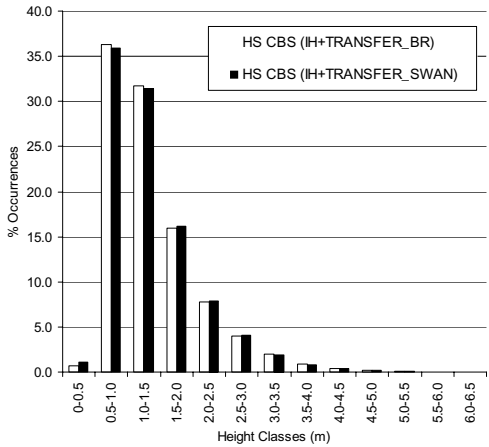

Figure 15. Histogram with the comparison of HS using TRANSFER_BR and TRANSFER_SWAN for CBS location

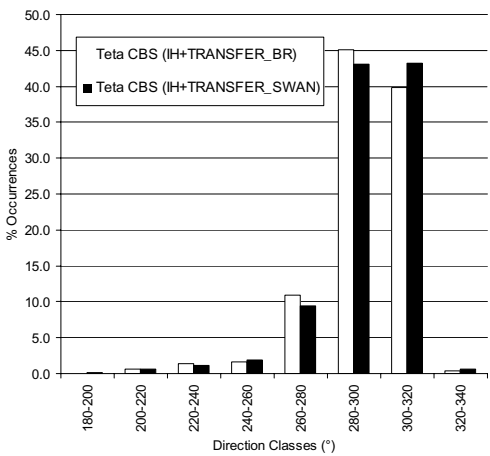

Figure 16. Histogram with the comparison of Θ using TRANSFER_BR and TRANSFER_SWAN for CBS location

Very small discrepancies were found between the methodologies for this location. This is due to the fact that this location is an open-sea area, and the

models included in both methodologies represent very well the main phenomena that may be present on the area. This can also be seen on Table 3, below.

Table 3. Summary table of the comparison of HS, TZ and Θ using TRANSFER_BR and TRANSFER_SWAN for CBS location

Parameter/method		*TRANSFER_BR*	*TRANSFER_SWAN*
Heights	Mean	1.36	1.36
	Standard Deviation	0.697	0.695
	Minimum	0.33	0.33
	Maximum	6.11	6.06
	Count	32784	32784
Periods	Mean	6.90	6.90
	Standard Deviation	1.778	1.778
	Minimum	3.32	3.32
	Maximum	15.31	15.31
	Count	32784	32784
Direction	Mean	293.81	294.68
	Standard Deviation	16.639	16.928
	Minimum	192.03	180.64
	Maximum	342.56	348.03
	Count	32784	32784

The following conclusions arise from the analysis of the above results:

1. In general, the parameters HS, TZ and Θ show a very similar trend, that is, their variations along the studied period are comparable, Figs. 12 to 14.
2. As mentioned before, the differences in the TRANSFER methodology by using either BR or SWAN are very small. It should be noted however that this location is a deep area where the refraction is the main phenomenon affecting the wave transformation.

CONCLUSIONS

In this paper, a comparison between two methodologies was done by considering wave regimes transferred using the BACKTRACK-REFSPEC (BR) and SWAN models in a location where wave data are available at two wave buoys that have been deployed for 6 months, simultaneously. The methodologies were found to be quite satisfactory, especially if a slight overestimation for parameters HS and TZ is taken into account.

Using both methodologies, the wave regime at locations at PDT (on the North western coast of Portugal), and at CBS (on the South western coast of Portugal) were determined. In summary, for the two locations, only small differences between the two methodologies were found. This is expected because the two locations are in an open area and the main phenomenon present is the wave refraction. The results on the wave regimes presented in this paper are meant to be a contribution to a better inshore wave characterization on the continental Portuguese coast.

ACKNOWLEDGMENTS

The authors acknowledge the financial support of the following projects of the “Fundação para a Ciência e a Tecnologia”: MADyCOS project, ref. PTDC/ECM/66484 /2006 and MOIA project, ref. PTDC/ECM/73145/2006.

REFERENCES

Capitão, Fortes, Coli, Pinheiro. 2006. Wave Regime Characterization on the Portuguese Coast using Hindcast and Wave Propagation Models. *Proceedings of ICCE 2006*, ASCE, San Diego, USA,

Covas, Pontes (1988). "Modelo matemático de refracção de ondas irregulares", *Joint report LNEC/LNETI*, Lisboa (in Portuguese).

Booij, Ris, Holtthuijsen (1999). A Third-generation Wave Model for Coastal Regions, Part I, Model Description and Validation, *J. Geophysics Res.*, 104.

THE MANAGEMENT OF MIXED BEACHES – DILEMMA. THE GETARES BEACH CASE (SW SPAIN)

Luis Moreno[1], G. Gómez[2], J.J. Muñoz[3], and A. De la Casa[2]

The behavior mixed beaches is still not well understood. Public perception of beach sediment composition is sometimes negative concerning the presence of gravel or of important gravel fractions. The poster discusses alternative options that were discussed during such a case in Getares Beach.

INTRODUCTION

The sediment composition of beaches plays an outstanding role in their morphodynamic behavior, while it also plays a relevant role in public perception of beaches (Buceta 2000, 2002).

Mixed beaches are formed by a mixture of sand and gravel in such fractions that it may not be considered as formed by one single sediment size "contaminated" by the other.

Sandy beaches are by far more studied, followed by gravel beaches. In the last years, however, the interest in mixed beaches has grown and their behavior has been investigated with an aim to establish its behavior pattern and to provide engineering design guidance (Blanco 2002, 2003).

MIXED BEACHES

The response of mixed beaches may be considered – as a first approximation – as half way between the response of sandy beaches and that of gravel beaches neglecting the interactions among the sediment sizes. Some "armoring" effect is anticipated due to the fact that sand grains may fill the larger holes provided by the gravel sediments.

The beach sediment very often happens to be, in a natural way, a mixture of fine sizes (sand) and coarse sizes (gravel). Whereas the former are more easily subjected to motion under certain circumstances – either seasonal or longer – the fine sediment is washed out faster, remaining the larger sized material on the beach. In this case, the coarsening of beach material becomes evident.

Taking into consideration the public perception may lead to the definition of a number of action alternatives some of them could become a success in the first instance but may be cause reverse effects in the long term. Among these actions, the removal of the large sized fraction of material or the generalized sand capping of the beach could be cited.

---

[1] INTECSA-INARSA, S.A.; Santa Leonor, 32; 28037 Madrid; Spain
[2] Ministry of Environmental Protection, Marianista Cubillo, 7; 11071 Cadiz; Spain
[3] CASEM - Facultad de Ciencias del Mar y Ambientales; 11510 Puerto Real; Cádiz; Spain

The manager's dilemma with respect to the intervention on the type of sediments that constitute the mixed beach arises when the users demand improvements in the easiness of use of the beach, explicitly rejecting the presence of coarse sediment.

The poster discusses the work undertaken in order to diagnose the gravel "appearance" in the northernmost section of Getares Beach (Figure 1). The different alternative actions studied to achieve sustainability of the beach use will be described and discussed with special emphasis in the advantages and disadvantages, works performed, and beach response monitoring of this beach restoration project.

Figure 1. Getares Beach (Algeciras, Cádiz), showing location of coarse material.

ALTERNATIVE ACTIONS

Alternative I: Sand Nourishment

The most simple action will be to cover the coarse material with finer material with a thickness of about 1.5 to 2 m. A number of different sand sources may be envisaged such as the mouth of the Pícaro River (located at the southernmost section of the beach (see Figure 2) or the dredging of a borrow site located in the center of the bay at about 20 m depth (see Figure 3). Sand volume required will add up to about 10.000 m^3 in both cases.

Advantages and disadvantages of both options are discussed below.

Alternative I.A: Sand Nourishment from the Mouth of the Pícaro River

- Execution cost will be about 40.000 €.
- Lifespan will be short, probably about one year.
- Social claims will be immediately satisfied.
- Possibility of environmental problems.

Alternative I.B: Sand Nourishment from the Dredging of a Borrow Site

- Execution cost will be about 110.000 €.
- Lifespan will be short, probably about one year.
- Social claims will be immediately satisfied.

- No environmental problems anticipated since the borrow site is located on a low ecological fragility area.

Figure 2. Alternative I.A: Sand Nourishment from the Mouth of the Pícaro River.

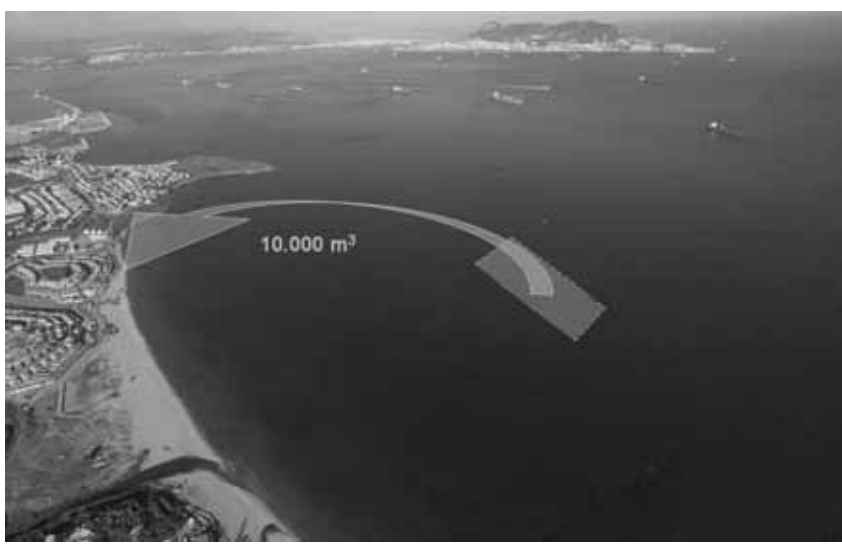

Figure 3. Alternative I.B: Sand nourishment from borrow site.

Alternative II: Gravel Nourishment

The second alternative action will be the nourishment by using rounded gravel (called locally "*garbancillo*") with nominal diameter comprised between 5 mm and 15 mm. The thickness will be of about 1.5 to 2 m. The nourished volume will be of about 10.000 m^3, so that the estimated cost will about 120.000 € (see Figure 4).

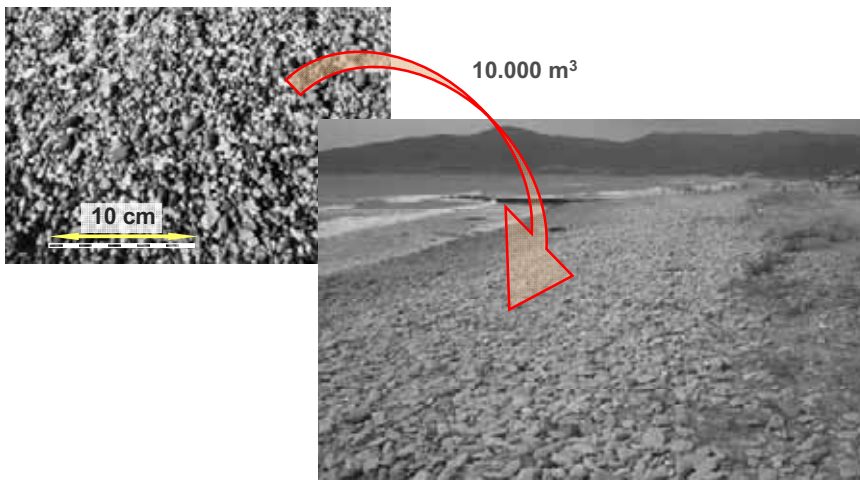

Figure 4. Gravel nourishment from quarry.

Alternative III: Integrated Management Strategy

This alternative action integrates a number of different maintenance operations and allows the combination of different actions.

The basic action will consist on the mechanical separation of gravel in a layer of about 3 m thick. A trench in the upper section of the beach profile will be filled with the gravel.

The coarse material could either be dumped in the trench in a random way or be dumped gradually according to the size (see Fig. 5).

Possible variation of this alternative option include seasonal maintenance operations in order to protect the beach during the winter storms and to make it more comfortable for the users during the summer season.

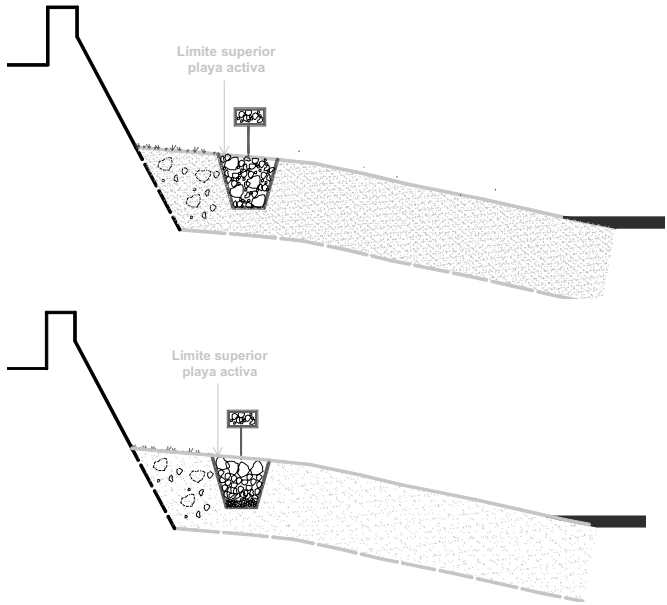

Figure 5. Example of integrated management strategy. Top: random placement of material. Bottom: selective placement of material.

REFERENCES

Blanco (2002): Further insight on behaviour of mixed sand and gravel beaches – Large scale experiments on profile development. *Proc. 28th Int. Coastal Eng. Conf.*, ASCE, pp. 2561 - 2663.

Blanco, Coates, Whitehouse (2003): Development of predictive tools and design guidance for mixed beaches – Stage 2. *Report SR 628*, HR Wallingford.

Buceta (2002): How to assess beach quality. *Ingeniería Civil*, CEDEX, nº 128, pp. 145-154. (in Spanish).

Buceta (2000): *Workshop on beach quality indexes*. Centro de Estudios de Puertos y Costas on behalf of Dirección General de Costas. (in Spanish).

INVESTIGATION OF THE EFFECT OF SHALLOWS IN THE NEARSHORE DYNAMICS BY NUMERICAL MODELS: APPLICATION TO THE MELORIA SHALLOWS AND PISA LITTORAL (ITALY)

Brunella Guida[1] and Gianluigi De Filippi[2]

The coast of Pisa is affected by strong erosion rates in most of its length. The Arno river separates this littoral in a northern part, characterised by a wildlife park, and in a southern section, where touristic beaches are present as well as the mouth of the Scolmatore waterway. In front of this tuscan coast, mainly in the south-eastern part, the Meloria Shallow is present, considered a relevant site for environmental reasons. To assess proper beach restoration projects along the coast as well as to carefully analyse the impact of the foreseen piers at the Scolmatore mouth on the surrounding littoral, a morphodynamic numerical model(*) has been applied at different spatial resolution to simulates waves, currents and sediment transport, accounting of the presence of the shallow waters of Meloria. The obtained results show the important role of the Meloria Shallow, which behaves like a filter for the incident wave energy coming from the different directions inducing a spatial redistribution of the energy, sometimes characterised by crossed sea or multi-peaked spectra, and able to modify the wind set-up along the coast, but even contribute to create a short-crested wave system between the shallows and the coast. The hydrodynamic conditions are consequently complicated and the sediment transport pattern affected by strong variations that contribute to the creation of bed dunes mainly normal to the coast.

INTRODUCTION

The coast of Pisa, extending from Livorno to Viareggio harbours, is affected by strong erosion rates in most of its length. For this reason its nearshore dynamic has been studied several times during the last decades. The Arno river separates this littoral in a northern part, characterised by a natural park, and in a southern section, where touristic beaches are present. Immediately north of the Livorno harbour the Scolmatore exists, a waterways realized in the past, subsequently the famous 1996 Arno flood to reduce the flood effects, where important projects are expected in the near future. In the 2006 we performed a detailed study in order to assess the impact of this coastal project involving. In front of the south-eastern part of this tuscan coast the Meloria Shallow is present, a protected site very relevant for environmental reasons.

It is well known that the wave propagation within coastal areas is strongly influenced by the bottom topography: in this case the main processes involved, i.e. refraction, shoaling, and energy dissipation due to bottom friction and wave breaking are in some cases strongly modified by the Meloria Shallow, placed about 10 kilometers far from the coastline, due to its large dimensions and very shallow waters.

1 Scientific Collaborator for D.E.A.M. srl, Pisa, Italy, guida@deamitalia.it

2 Professor of Coastal Oceanography, University of Pisa, Italy, defi@deamitalia.it

* Developed by D.E.A.M. srl, Via della Casina 11 56017 Pisa, Italy.

Figure 1 : The study area and the Meloria Shallow position

We hold as highly important to take into account of this morphological item in the investigation of the nearshore processes, as well as in the assessment of proper coastal engineering projects.

A morphodynamic model has been used to simulates the wave, current, sea level and transport conditions. Using nesting techniques, model grids at different spatial resolutions have been defined in order to reduce problems at the boundary conditions and carefully discretise the bottom of the Meloria. The coarse domain, in which various fine grids are nested, has been set up with a resolution of about 0.005° in longitude and 0.004° in latitude. The coarse grid results drive the fines nested, defined at high spatial resolution in various region of the whole littoral.

AVAILABLE DATA SET

The study is based on the available long term wind and wave climate: Because of a general lack of measurements along the Italian coasts, both measured and hindcasted wind and wave data have been analysed in order to assess the typical and extreme offshore meteo-marine conditions to be used as input of the nearshore models. The available sources of data are shown in Figure 2 and listed in the following:

- directional wavemeter maesurements at La Spezia (43°55.7'N, 9°49.6'E), 12 years time series (provided by the National Ondametric Net, R.O.N) ;
- ECMWF wind and wave hindcasted data, 12 years time series available at 9 different location in the Thyrrenian basin;
- offshore bathymetries extracted from nautical charts;
- nearshore bathymetries measured on 1997;

Moreover, water level time series measured at various location along the tuscany coast were available.

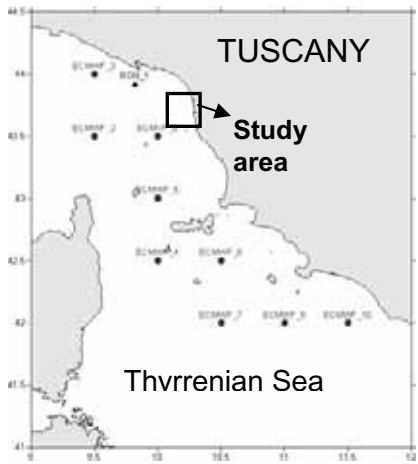

Figure 2: The available wind and wave data location points hindcasted (ECMWF grid points) and measured (RON point).

METHODOLOGY

We performed the simulations with a morphodynamic model, that is an integrated system of numerical models running on the same calculation grid and having as input the same bathymetry, that predicts waves, currents sediment transport and bathymetric changes in the nearshore area. In Figure 3 a block diagram shows the operation characteristics of the model.

The application at the coast of Pisa has been done by following the subsequent methodology:

- definition of the main characteristics of the nearshore area (morphology, bathymetry, sediment grain size distribution);
- definition of the typical and extreme meteo-marine conditions (wind, wave, sea water leve), issued from the analysis of the available data;
- wave storm selection: we selected the most frequent and most energetic storms, considering the main incoming direction inside the exposure sector;
- simulation of the wave and current field evolution during each storm;
- simulation of the bottom evolution during each storm;
- analysis and rendering of the results of each simulated storm;
- combination of the storm results on the basis of the annual climate: we assessed the mean annual bathymetric changes assuming the linear combination of the storm results;
- interpretation of the results.

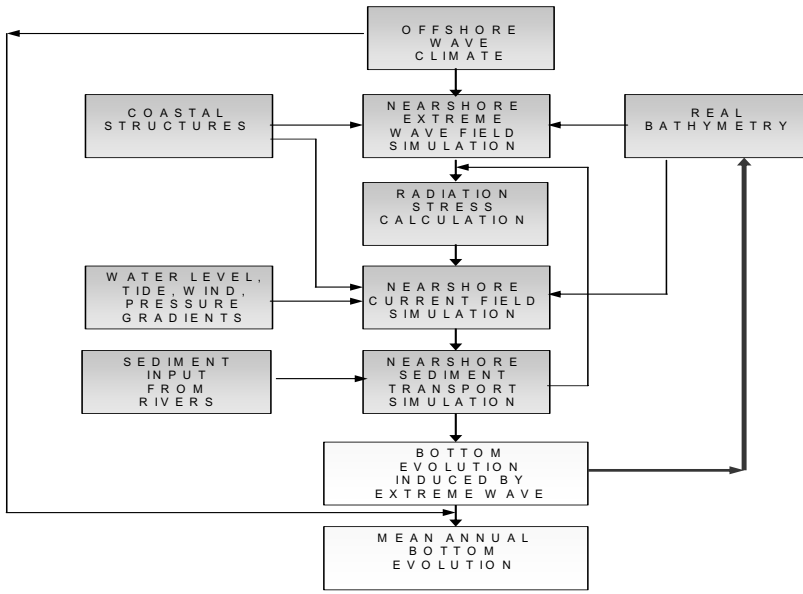

Figure 3: Block diagram showing the operation characteristics of the morphodynamic model

The SWAN model has been used as wave driver to simulate the propagation of the wave from the offshore to the nearshore area, taking into account of wave energy dissipation due to the bottom friction, white-capping, wave breaking and wave interaction processes.

The nearshore circulation patterns have been simulated by means of an hydrodynamic numerical model, forced with both wind and wave input. A wave-averaged model has been used, which is based on the integration of the Navier-Stokes shallow water equations, including the radiation stress terms.

The sediment transport induced by the current has been simulated by means of a proper numerical model based on the Bijker formulations (Bijker, 1968), which take into account of both bed load and suspended load. The model calculate the crosshore and longshore sediment fluxes in each grid mesh: the simulation of the bottom evolution is carried out by forcing the conservation of mass.

THE MODEL GRIDS

In order to investigate the influence of the Meloria Shallow on the local dynamics, we defined three different grids at different spatial resolutions:

- "district scale" domain: forced by offshore conditions issued from the available data. The grid include size of the mesh is 500x500 meters,

- "coarse scale" domain nested into the district scale one. The size of the mesh is 50x50 meters;
- "fine scale" domain nested into the big scale one. The size of the mesh is 10x10 meters.

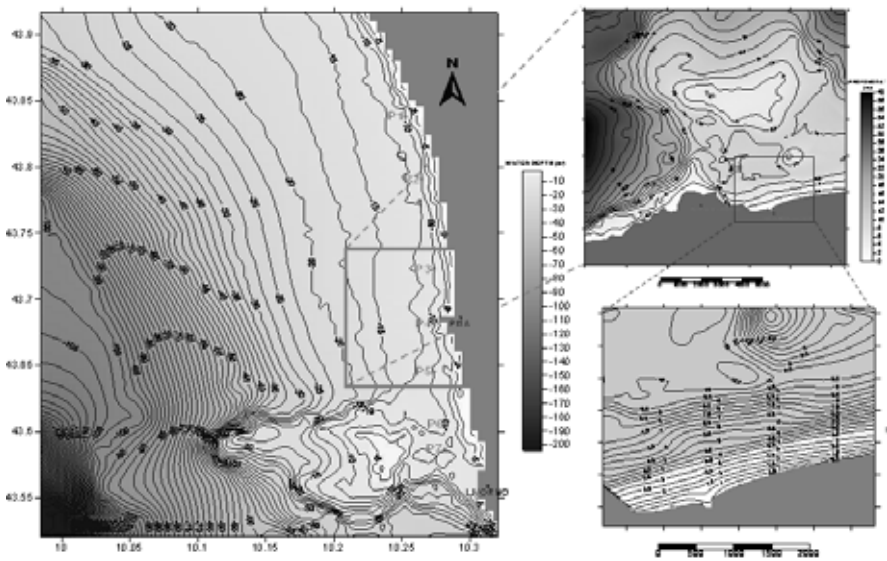

Figure 4: The system of nested model grids at different spatial resolution.

The characteristics of the defined calculation domains are briefly summarized in Tab. 1.

Table 1. Characteristics of the three defined calculation domains

	DISTRICT SCALE	COARSE SCALE	FINE SCALE
Mesh size	500x500 m	50x50 m	10x10 m
Wet mesh number	5580	71655	123396
Maximum water depth	200 m	40 m	10.5 m

INFLUENCE OF THE SHALLOW ON THE WAVE AND CURRENT FIELD

Offshore wave conditions have been applied at the boundary of the district scale grid and propagated towards the coast: the nearshore wave spectra and time series have been recorded at 6 points located at 10 m water depth along the coast, as shown in Figure 4, in order to evaluate the influence of Meloria on the nearshore wave conditions.

The results show that noticeable modification are induced on wave field by Meloria Shallow. Crossed sea conditions, with two well separate peaks in direction, are generally present in front of the southern littoral, and in some cases even 2 peaks at different frequencies appears: two-peaked wave spectrum conditions are maximum at point 6 (which is located in front of the southern littoral of Pisa) and tend to disappear gradually along the coast, moving from south to north, as shown in Figure 5. At the back of the shoals the offshore wave energy arrives splitted in direction and frequency, since the Meloria acts as a filter.

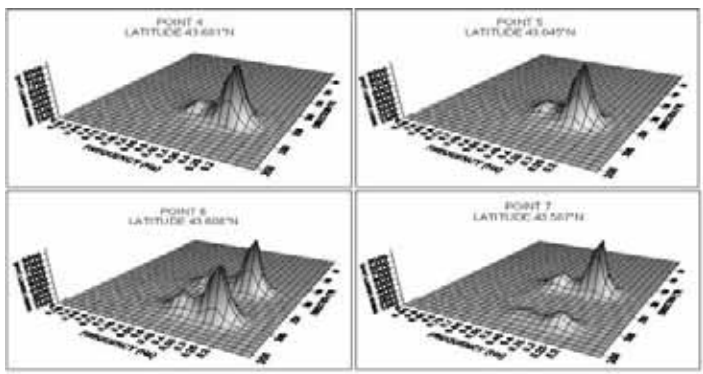

Figure 5 : Modification of the nearshore wave spectral shape moving from north to south along the coast of Pisa for extreme wave coming from south-western direction: crossed sea conditions are generated in front of the southern part of the littoral (points 7 and 6) and tend to disappear moving towards north.

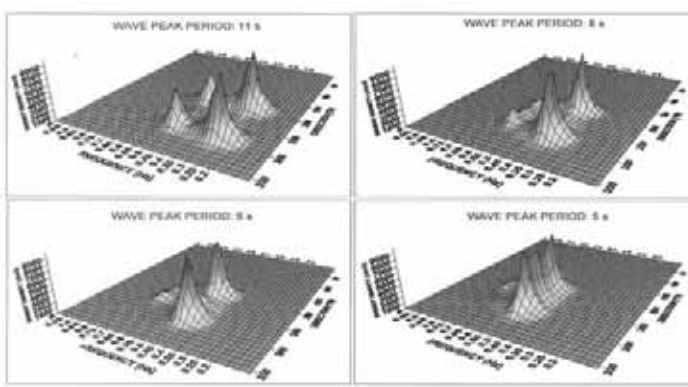

Figure 6 : Nearshore wave spectral shape with different peak period of the offshore extreme wave coming from south-western directionat point 6, located at the back of the shoals.

The model results carried out over the detailed grids show a strong spatial variability of the wave and current nearshore fields at the back of the shoals.

INFLUENCE OF THE SHALLOW ON THE BOTTOM EVOLUTION

The results of the morphodynamic model running over the fine grid show the formation of bedforms mainly normal to the beach at the end of each extreme storm as well as in the mean annual bottom evolution, assessed by combining the results of each storm in the linear superimposition assumption (Figure 7).

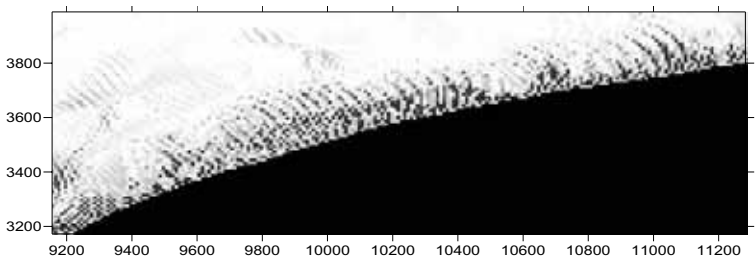

Figure 7: Mean annual sea bed evolution along the southern part of the littoral: erosion (blue) and accretion (yellow) zones form bed dunes mainly normal to the coast.

This could be due to the formation of a short-crested wave system (Hsu, 1979), which develops in this area during crossed sea storm conditions, as the waves arrive strongly angled to each other. In a short-crested wave system very complex orbital motions of the water particles occur under the synchronous wave crests genearted in the area (see Figure 8), which induce large oscillations of the velocity at the bed with greater suspension of sand grains.

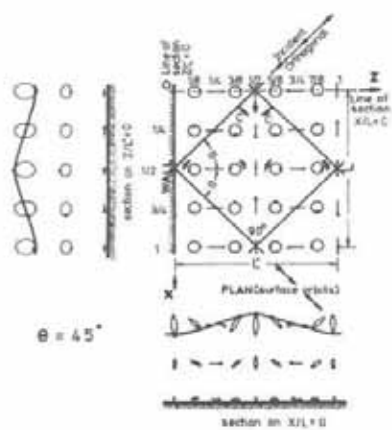

Figure 8: Orbital motions of water particles within a short-crested wave system (from Hsu, 1979).

We compared the bottom evolution results with detailed bathymetry measurements obtained during a survey done in 2006 with multibeam thecniques, shown in Figure 9. The measurements show that in this area the bottom is strongly irregular, and tend to become regular moving toward north.

The linear dimensions of the bedforms (20-30 centimeters) are very similar to that carried out by the morphodynamic model simulations. Unfortunately the measured data do not cover the shoreface area, where the bedforms normal to the beach occur.

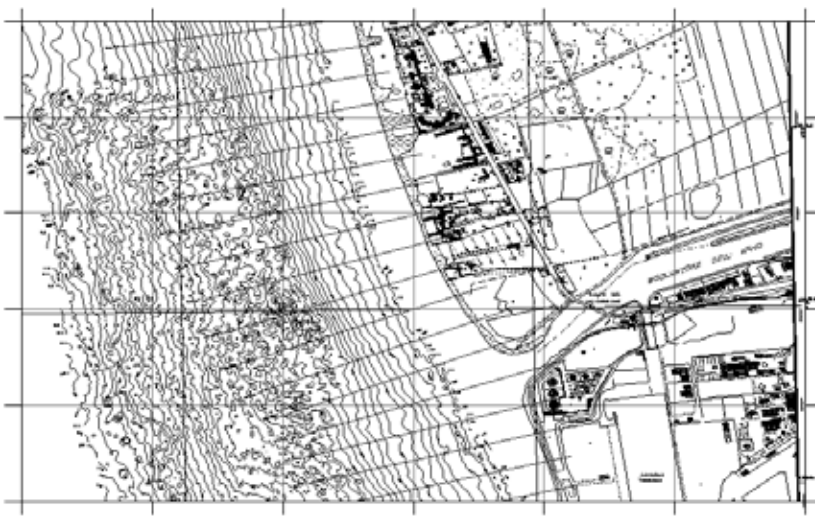

Figure 9 : Real bathymetry detected by multibeam survey (2006) shows that the southern part of Pisa littoral is chracterised by bedforms (about 20-30 cm of amplitude) which disappear moving toward north

CONCLUSION AND FUTURE DEVELOPMENT

In conclusion, it turns out from the results that Meloria Shallows play an important role on the nearshore dynamics of the southern part of Pisa littoral, determining crossed sea conditions and a consequent irregular spatial distribution of the fine materials over the bottom in the nearshore zone.

The future developments of the study will be focused on the assessment of the spatial distribution of the variations on nearshore current due to the interaction between general longshore current and the estuarine circulation induced by the Arno river.

With the aim of a good coastal management, which should also be directed to the preservation of the environmental value of the site, we will evaluate the coastal stabilization after the fullfillment of the ongoing projects involving the Scolmatore waterway mouth .

REFERENCES

Bijker E.W., 1968, "Littoral Drift as Function of Waves and Current", Delft Hydraulics Laboratory, publ. n. 58;

Bijker E.W., 1971, "Longshore Transport Computations", Proc. A.S.C.E., Journal of Waterways, Harbours and Coastal Eng. D.V., WW4;

Hsu, Tsuchiya, Silvester: Third-order approximation to short-crested waves, Journal of Fluid Mechanics(1979), 90: 179-196 Cambridge University.

Booij, N., R.C. Ris and L.H. Holthuijsen, 1999, A third-generation wave model for coastal regions, Part I, Model description and validation, J.Geoph.Research, 104, C4, 7649-7666

Ris, R.C., N. Booij and L.H. Holthuijsen, 1999, A third-generation wave model for coastal regions, Part II: Verification, J.Geoph.Research, 104, C4,7667-7681

MORPHODYNAMICS OF A WADDEN SEA AREA – FIELD MEASUREMENTS AND MODELLING

Thorsten Albers[1] and Nicole von Lieberman[1]

The tidal flats of the German North Sea coast are affected by intense morphodynamics. Especially in the mouths of the estuaries sedimentation and erosion occur on different temporal and spatial scales and therefore challenge the decision-makers. To satisfy the requirements, which modern cargo ship industry demands, a concept for sediment management has to be developed to grant an economic and ecologic balanced system. To evaluate different actions and their effects, e.g. by means of numerical models, an improved knowledge of morphodynamic processes on tidal flats is required. The Institute of River and Coastal Engineering at the Hamburg University of Technology runs detailed measurements to collect hydrodynamic and morphodynamic data of tidal flats in the estuary Elbe that is the approach to the port of Hamburg. Water levels, flow and wave parameters and the concentration of suspended sediments are recorded in high resolution. Furthermore, the bathymetry is determined in frequent intervals with a multi-beam echo sounder.

INTRODUCTION

The North Sea is a border sea of the Atlantic Ocean. Thus, the oscillation of the Atlantic affects the North Sea from the north and through the British Channel. Huge tidal flat areas, long tidal channels and creeks, ripples and dunes have an effect on the view of the German North Sea coast. Especially the areas of the Wadden Sea underlie sediment relocations on different scales.

The most important waterways at the German coast are the estuaries Elbe, Weser, Ems and Jade. In spite of several measures, that stabilize the waterways, strong morphodynamic changes occur. Especially in the mouth of the estuary Elbe these permanent displacements challenge the stakeholders and decision-makers. The Elbe is the approach to the port of Hamburg and thus it may be called a lifeline of a whole region. The harbor of Hamburg is a turntable of the international container shipping, the largest port in Germany and the second largest in Europe. To live up to expectations of many different parties a holistic and innovative estuary management is necessary. A main issue of a new concept for a sustainable development of the tidal area of the Elbe River is to decrease the energy caused by tidal flow into the estuary (HPA and WSV 2006).

A broad process-knowledge is necessary to assess the resulting risks and to find an agreement between utilization demand and ecological meaning of the affected coastal zone. Due to its high sensitivity against hydro- and morphodynamic changes tidal flat areas, especially in the mouths of estuaries,

[1] Institute of River and Coastal Engineering, Hamburg University of Technology, Denickestr. 22, 21073 Hamburg, Germany

move over to the center of scientific activities. Big challenges in this interrelation are the impacts of the climate change.

In spite of great successes in numerical modeling it was not possible to generate reliable forecasts of morphodynamic changes of tidal flats in consequence of short and long-term impacts. This is founded in both, the lacking resolution of the models and the insufficient process knowledge. For instance secure perceptions about the effect of tidal flats as a sediment reservoir of estuaries are missing. The function of wave-induced processes in tidal creeks and channels and of higher spring tides or lower storm surges is not yet completely understood. Frequently phases of sedimentation and erosion in tidal flat areas change patchwork-like over different seasons without any visible pattern.

INVESTIGATION AREA

The aim of the research project discussed in this paper is the analysis of morphodynamic and hydrodynamic changes in the investigation area "Neufelder Watt" in the mouth of the estuary Elbe. Supported by the Hamburg Port Authority (HPA) the Institute of River and Coastal Engineering of the Hamburg University of Technology runs extensive field measurements to improve the process knowledge on tidal flats. The results may provide a secure theoretical background for the mathematical multi-dimensional modeling of morphodynamic processes on tidal flats.

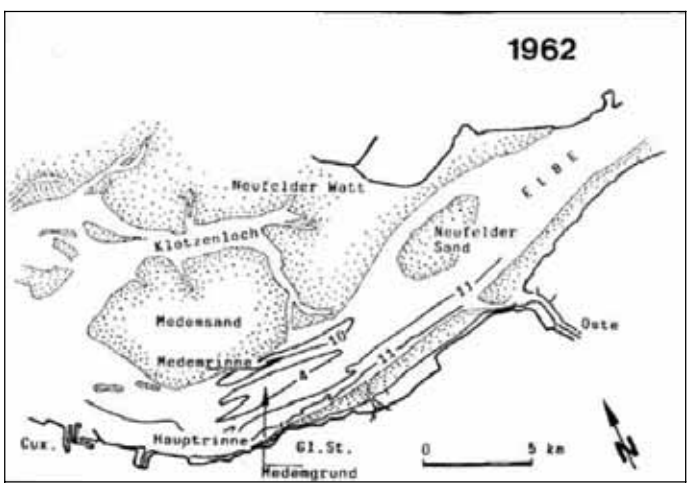

Figure 1. Historical sea chart of the Elbe mouth from the year 1962.

The field investigations take place in the Neufelder Watt with the "Neufelder Sand" in the mouth of the estuary Elbe. The area under investigation is in close interaction with the main stream of the Elbe. The Neufelder Sand started to develop in the years after 1926 when a shallowness formed in the south of the Neufelder Watt. The ebb stream ran along the south banks of the Neufelder Watt. While the "Neufelder Channel" (= "Neufelder Rinne", cf. Fig. 2) deepened, the tidal flat area Neufelder Sand grew. Figure 1 shows a map of the investigation area from the year 1962.

After 1960 at the south bank of the Neufelder Watt a groin was built to stabilize the inter-tidal area. The ebb stream was refracted to the main channel and the Neufelder Rinne decreased in depth. In the following decades the area under investigation grew increasingly and the Neufelder Rinne changed to a creek with smaller depth. Yet it is still of high importance for a huge part of the Neufelder Watt due to its dominating role in flooding and dewatering of the tidal flat area.

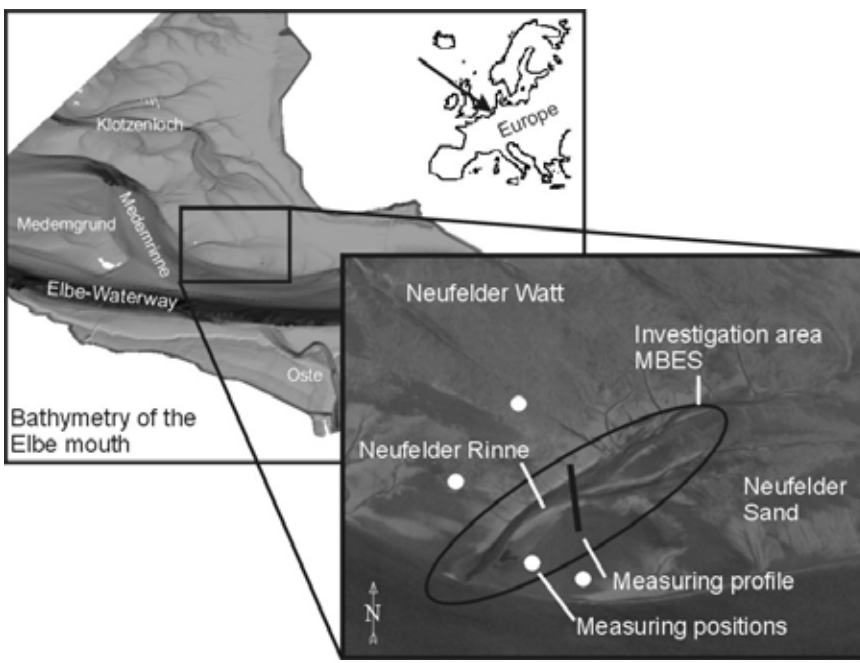

Figure 2. Investigation area and measurement positions in the mouth of the estuary Elbe.

The average tidal range in the investigation area is about 3 meters. The Wadden Sea areas around the Neufelder Rinne fall dry during a longer period around low tide. The water depths during an average tidal high water amount to 1 m to 1.5 m northwest of the channel and 1.5 m to 2 m southeast of the channel. The largest water depths in the main part of the channel add up to 4.5 m at mean high tide according to measurements in September 2008. The inlet was silted up highly at that time so that the water depths in that area are only a few centimeters at mean tidal low water.

Figure 2 shows the bathymetry in the mouth of the estuary Elbe with the Wadden Sea areas and the "Medemgrund" as the most important shallowness.

FIELD MEASUREMENTS

In summer 2006 firstly a cross section in the Neufelder Rinne was selected to install the measurement devices (Fig. 2). The equipment was positioned in the middle of the creek as well as on both banks. Flow parameters, sediment concentrations and waves were measured permanently in a high resolution. In the following phases of the project the measuring positions were installed at areas of higher elevation northwest and southeast of the channel. In the process three Acoustic Doppler Current Profilers (ADCP) were used as well as six pressure sensors and three Optical Backscatter Profilers, which allowed an assessment of the suspended sediment concentration. Additional to the permanent installed instruments multi-beam echo sounder (MBES) measurements were performed in the channel and on the surrounding areas in frequent intervals of three to five weeks and after extreme events. Furthermore, soil samples were taken. They were completed to a sediment register of the area under investigation. Also the temporal changes of the top layer of certain positions were analyzed.

The arrangement of the measuring devices in one position is shown in figure 3. Flow parameters were recorded continuously and in a high resolution with three RDI ADCP Workhorse Sentinel. Over a period of 5 minutes an ensemble of 50 pings was collected, whereas the accuracy of the flow velocity is ± 0.3 cm/s and the one of the flow direction ± 2°. Suspended sediment concentrations were measured with three Argus Surface Meters (ASM) by ARGUS Environmental Instruments. In that innovative measuring instrument 100 optical backscatter sensors mounted in a steal bar assessed the sediment concentration over a one-meter column above the sea bottom. Before the deployment the device was calibrated with the suspended matter occurring in the area under investigation. Every 5 minutes 5 samples were collected and averaged, whereas the accuracy is ± 10 %. Regularly suspended matter samples were taken and compared with the results of the ASM. Six pressure sensors recorded waves with a measurement frequency of 10 Hz. Those sensors are a self-construction of the institute. Data can be collected self-sustainingly over a period up to three months and is stored on a MMC memory card. All other devices work autarkic as well.

In regular intervals of three to five weeks the bathymetry of the marked investigation area was analyzed with a multi-beam echo sounder. Furthermore, measuring tours were attempted as soon as possible after extreme events. Therefore the research vessel “Nekton” of the Institute of River and Coastal Engineering comes into operation (Fig. 4). To survey the bathymetry a built-in multi beam sonar Elac Nautik Seabeam 1185 with a frequency of 180 kHz is used. It is especially appropriate for surveys in shallow water but also applicable for water depths up to 300 m. The tide correction is done by Real Time Kinematics (RTK Tides) and the vessel’s movements are compensated by an Octans gyrocompass.

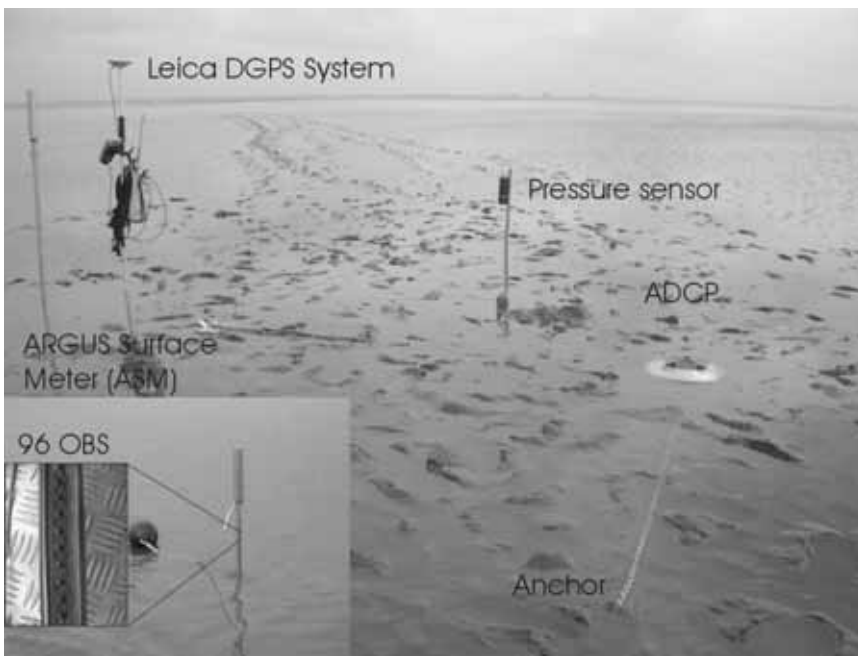

Figure 3. Measuring position with installed devices. DGPS-System to level the devices.

Figure 4. Research vessel "Nekton". Photo: Albers.

RESULTS

Flow parameters and sediment concentration

Figure 5 shows the field data from June 8th and 9th 2007 measured at a position on the Neufelder Sand to the east of the inlet. In the figure the wind velocities and directions, water levels, flow velocities and directions, sediment concentrations and wave parameters are shown. Flow parameters and sediment concentrations are specified depth averaged. Due to the relative high elevation the devices fall dry around low water and the data is not continuous. The flow velocities do not reach the peaks that were recorded in the channel, however with values up to 0.8 m/s they are reasonably high for Wadden Sea areas. The diagram shows a comparatively calm weather situation with wind of 3 Beaufort from east-southeast, which leads to small waves with significant wave heights of maximum 0.20 meters. The displayed flow parameters are characteristic for calm weather conditions. The depth averaged sediment concentration is marked with the continuous line. The dashed line shows the 10 bottom backscatter sensors, the dotted line shows the 24 sensors at the top of the device, one meter above the bottom. The concentration of suspended sediments (SSC) at the bottom is higher than one meter above the bottom. The course of the SSC is similar, if the course of the flow velocity is comparable (see 1st and 3rd, 2nd and 4th branch). In the first and third branch of the plotted period the influence of even small waves is visible. The sediment concentration increases already at small flow velocities especially at the bottom sensors. This phenomenon occurs basically only during tides with lower tidal high water levels.

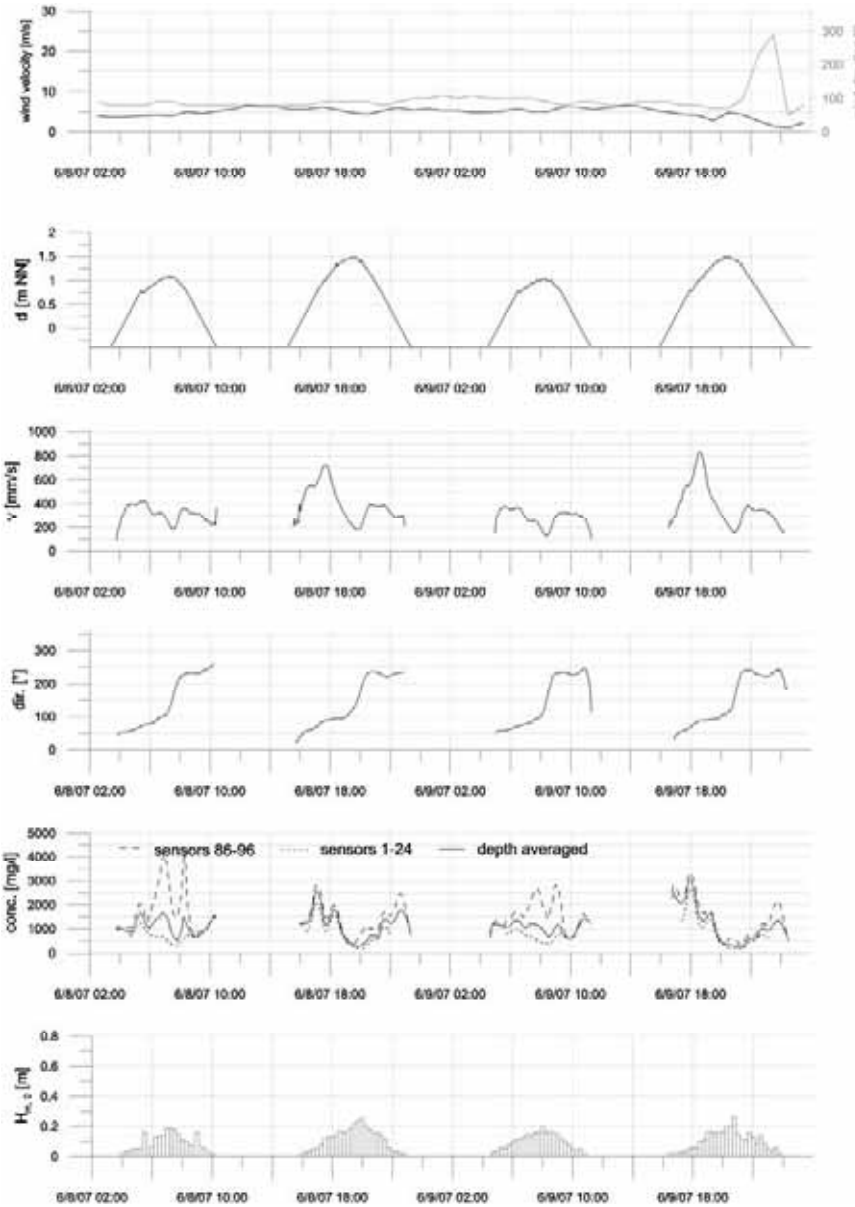

Figure 5. Field data from June 8th - 9th 2007.

In the course of the sediment concentration on the tidal flats over a tidal cycle a flow dependent pattern consisting of four maxima is constituted. The first maximum develops at increasing flow velocities at the beginning of the flood phase. If the flow velocity has a clear peak the maximum of the sediment concentration normally is reached before that peak. If the flow velocity has a saddle point the maximum of the sediment concentration lies at the beginning of that saddle. A second maximum of the sediment concentration results afterwards from decreasing flow velocities, whereas higher concentrations occur especially at the bottom sensors. After slack water the before deposited particles are re-mobilized at increasing flow velocities and cause a third maximum, which lies as a rule at the beginning of the saddle point of the flow velocity of the ebb phase. At the end of this saddle a fourth maximum of sediment concentration develops at decreasing flow velocities.

This described pattern is more or less pronounced depending on the measuring position and the course of the corresponding tide. It is visible most clearly during tides with a mean high tide water level. During tides with lower or higher high water levels the peaks are damped, whereas the mean level of the sediment concentration increases during tides with lower water levels. During distinct east wind dominated weather conditions with low water levels the level of the sediment concentration is considerable above the concentrations during normal and increased tides. Then there is no maximum, which can be constituted as dominant. At certain measuring positions the maxima are essentially stronger developed and sediment plumes are flowing along the bottom sensors at recurring points in time. The sediment samples at those positions show a very heterogeneous grain size distribution with increased silt and coarse sand rates and a very low compactness of the packing.

In general the sediment concentrations during eastward directed flow velocities are higher than the ones during westward directed flow velocities. Furthermore, the period of the eastward directed flow lasts longer.

Within the framework of the research project PROMORPH, done by several research institutes in Germany in the years 2000 to 2002, field measurements were performed in tidal channels of the central Dithmarscher Bight at the west coast of the federal state Schleswig-Holstein. The measurements covered a wide range of tidal conditions whereas the widths of the surveyed tidal channels were up to ten times larger than the Neufelder Rinne and the water depths were up to 18 meters (Poerbandono and Mayerle 2005). Although the areas under investigation have different hydrological and morphodynamic characteristics, a comparison between the results of the current project described in this article and the results of PROMORPH could be used to verify the deliverables from the Neufelder Watt.

Multi-beam sonar

Figure 6 shows a cross section at the inlet of the Neufelder Rinne with the results of different multi-beam echo soundings. There the strong dynamics of that area is obvious. Essentially the inlet moves east, whereas a simultaneous increase in elevation of the surrounding tidal flat areas occurs. That relocation can be up to one hundred meters per month. It continuous until the inlet branches off from the deeper main part of the channel, that relocates less, in a very acute angle. Then at the undercut slope of the ebb stream of the main part of the channel a new inlet is formed. For a short while two inlets exist, until the older one is silted up. This reversible development is visible between August 20th and October 2nd. Subsequent the process begins again.

The horizontal displacement especially of smaller creeks was already discovered by Ehlers (1988). Different observations showed that those creeks may changes their position about a few decimeters per tide. These changes are reversible and do not lead to large medium-term changes.

From the different multi-beam soundings the morphological changes in the investigated area of the Neufelder Rinne can be derived. The most dynamic part is the inlet. The main part of the channel also underlies an eastward directed relocation, which however is less strong than at the inlet. Hence the main part is comparatively stabile in its position. The described and relatively continuous relocations occurred both during summer and winter months. Direct impacts of three recorded heavy storm surges on the bathymetry could not be observed.

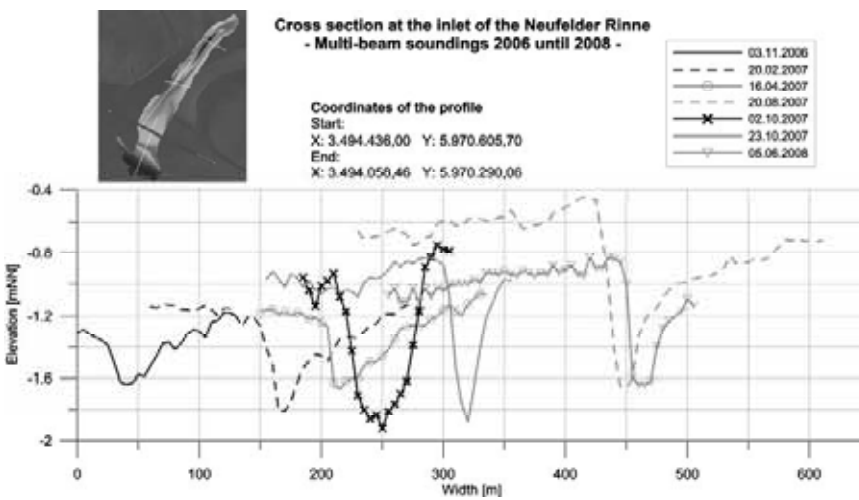

Figure 6. Cross section at the inlet.

CONCLUSIONS

From the recorded and analyzed sediment concentrations and flow parameters the residual transport was calculated by balancing the transported material. In the Neufelder Rinne the residual transport during ebb tide overbalanced (Q_{ebb}, Fig. 7). The suspended sediment is carried out of the creek and forms an ebb delta, which is clearly visible on the sonar soundings.

On the tidal flats the sediment transport during flood phase overbalanced (Q_{flood}). The Neufelder Rinne interrupts this eastward directed transport. Material deposits at the western slope and pushes the creek's axis to the east. There an interrelation of the morphodynamics with the spatial location of the considered structures exists. Largest changes occur if the creek's course runs orthogonal to the main transport direction. The more the creek's course follows this direction the smaller are the relocations.

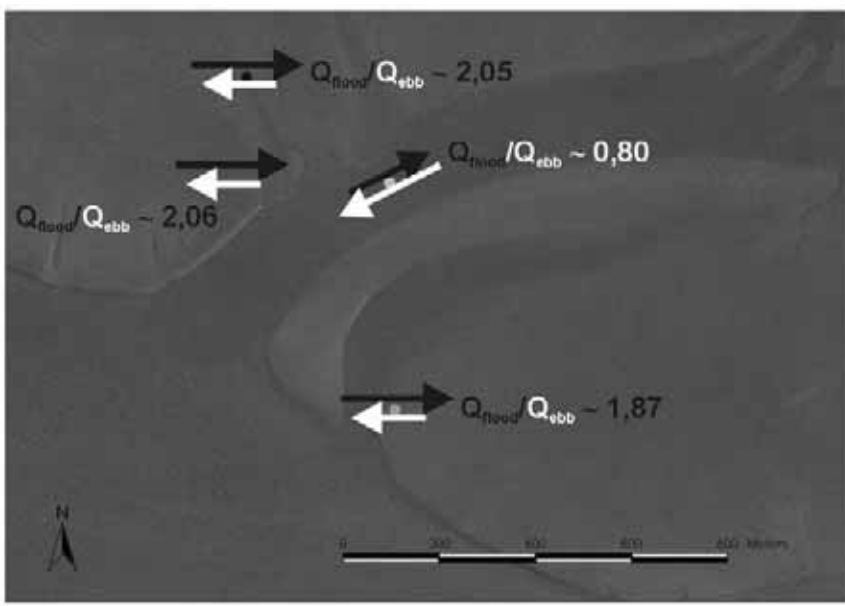

Figure 7. Residual transport in the investigation area.

NUMERICAL MODELING

The morphodynamic modeling is done with the numerical model RMA 10S (King 2006). Firstly a larger surrounding model was set-up and calibrated. This model is controlled exclusively with water level boundary conditions. The finite element network for the hydrodynamic calculation in RMA 10S consists of 35,000 triangular elements. The resolution is not only high in the investigation area but also in all areas that are of importance for the flooding and drainage of

the Wadden Sea areas. The navigation channel on the other hand is discretized by larger elements.

The surrounding model passes water level and flow boundary conditions to a detailed model, which covers the investigation area Neufelder Watt with the Neufelder Sand. Here the Wadden Sea structures are dissolved very accurate to be able to model the morphological changes as detailed as possible. For the time being the scale transfer from the surrounding model to the detailed model is determined, so that no current model results can be compared with the field measurements.

SUMMARY AND OUTLOOK

Facing the high importance the free approach to the port of Hamburg means to the economic development of Northern Germany, a sustainable estuary management is required. In particular the knowledge about morphodynamic processes on tidal flats needs to be improved.

On the basis of extensive high-resolution field investigations the Institute of River and Coastal Engineering at the Hamburg University of Technology analyzed morphodynamic processes in a tidal flat area in the mouth of the estuary Elbe. It is the intention to implement the results in a detailed morphodynamic model and to improve the process knowledge of sediment transport on tidal flats.

Certain conclusions about morphodynamic processes in the Neufelder Watt can be drawn on the basis of the present investigations. Therefore historical data and maps as well as the executed field measurements were considered.

Morphodynamic tendencies and displacements were recorded in the channel Neufelder Rinne and the nearer surroundings with a multi-beam echo sounder. During the complete observation period large dynamics – essentially an eastward directed movement – especially at the inlet of the channel could be determined. In the main part of the channel the displacement was articulately smaller. Three recorded heavy storm surges did not have any significant impact on the bathymetry of the investigated area.

The course of the sediment concentration over a tidal cycle is primarily related to the flow velocity. The level of the sediment concentration thereby is dominated by the tidal high water level. During east wind dominated weather conditions with higher wind velocities the sediment concentrations increased compared with tides with mean high water levels. During tides with increased high water levels the sediment concentration level lies below the mean level.

A calculation of the residual transport at different positions showed, that the sediment transport on the tidal flats during flood phase overbalances and therefore is eastward directed. The Neufelder Rinne interrupts this transport band. Inside the channel the sediment transport during ebb phase overbalances and transported matter deposits at the inlet and forms an ebb delta. The eastward directed transport causes the described relocation of the creek structure.

The stationary field measurements are only punctual. Due to the shallow water in the investigation area even the multi-beam soundings only can cover limited areas. By the choice of the measuring positions information about spatial processes can be derived from the punctual information. This counts only inside the boundaries of the investigated area, whereas this area often cannot be looked at detached from the surrounding.

To gain comprehensive information about Wadden Sea areas remote sensing methods become more important. The strengthened use of those methods is aimed for in the future. In addition the knowledge derived from the field measurements will be implemented into the morphodynamical model.

ACKNOWLEDGMENTS

The authors thank the Hamburg Port Authority for the fruitful cooperation and the extensive support.

REFERNCES

Ehlers, J. 1988. The Morphodynamics of the Wadden Sea. Balkema. Rotterdam, The Netherlands.

HPA and WSDN (Eds.) 2006. Konzepte für eine nachhaltige Entwicklung der Tideelbe als Lebensader der Metropolregion Hamburg. Brochure. In German.

King, I. 2006: A finite element model for stratified flow and cohesive sediment/sand transport – RMA 10s Users Guide; Version 3.5E.

Poerbandono and Mayerle, R. 2005. Composition and Dynamics of Sediments in Tidal Channels of the German North Sea Coast. In: Kuratorium für Forschung im Küsteningenieurwesen (Ed.): *Die Küste, Heft 69*. Boyens Medien GmbH & Co. KG. Heide, Germany.

STOCHASTIC BEHAVIOUR OF BEACH POSITION NEAR A GROYNE

Adrián Pedrozo-Acuña[1], Dominic E. Reeve[1] and Mark Spivack[2]

[1]Centre for Coastal Dynamics and Engineering, School of Engineering, University of Plymouth, Drake Circus, PL4 8AA, United Kingdom apedrozoacuna@plymouth.ac.uk ; dreeve@plymouth.ac.uk

[2] CMS, University of Cambridge, CB3 0WA, United Kingdom ms100@cam.ac.uk

This work uses a simple model of shoreline evolution to investigate the stochastic behaviour of beach position near a groyne. The diffusion coefficient, which depends on the wave conditions, is treated as a stochastic variable. This allows the theoretical framework to be developed extending the solution from the deterministic to the stochastic domain. It is illustrated how the deterministic analytical solution can be used to derive an expression for the ensemble average moments of shoreline position. The proposed simplifications are tested against Monte Carlo simulations based on data from the field.

INTRODUCTION

Coastal landscapes are the product of processes and responses over a variety of temporal and spatial scales. Changes in the character and position of the coast occur as it evolves in response to waves, tides and movement of sediment. To the casual observer the beach response can be seen as benign fluctuations about some mean shape. However, extremes of variation about the mean can have serious repercussions. The coastal environment is further complicated by the fact that these controls, feedbacks and subsequent responses act over a range of different spatial and temporal scales.

The ability to predict changes in coastal morphology is hampered by a lack of observational data, and by the prohibitive computational complexity of applying deterministic dynamical equations for fluid flow and sediment transport over even relatively short periods of a single storm (De Vriend et al. 1993).

A deterministic approach was pioneered by Pelnard-Considère (1956) who proposed an equation to forecast changes in coastline position and which has become known as 'the one-line model'. Despite its simplicity, the one-line model has proved robust and reliable, and is used widely in design today (eg. Hanson and Kraus 1989; Larson et al. 1997).

In recent years there has also been a growing interest in probabilistic prediction, whereby rather than obtaining a single answer by solving the equations in a deterministic manner, the equations are solved to find some measure of the probability of beach position. Such methods are becoming

commonplace in operational weather forecasting and provide means of estimating the uncertainty in the predictions which is helpful for planning and risk management.

As it is schematized in Figure 1, probabilistic models can be divided into two general categories. Firstly, the Monte-Carlo type approach where a deterministic model will be run repeatedly with slightly different initial and/or boundary conditions to generate a family or 'ensemble' of possible outcomes. This ensemble is treated as a sample of possible futures and sample statistics can be computed directly from the predictions. Secondly, equations describing the evolution of the moments or probability density function.

Figure 1. Probabilistic methods schematization.

Under this framework, the one-line model provides a suitable vehicle from which to develop a probabilistic approach for coastal management. Vrijling and Meier (1992) presented one of the first applications of the one-line model to probabilistic shoreline modelling in a Monte-Carlo analysis of beach evolution near a port. Reeve and Spivack (2004) used the one-line model to develop a probabilistic theory which accounts for temporal correlation in the wave climate, and presented solutions to moment equations of the shoreline position. The equations describe the ensemble-averaged movement of the beach and its dependence on wave climate.

Despite their simplicity, analytic solutions of the one-line equation have proved to be of great practical use. Not only can they be a quick means of calculating estimates of shoreline change, but they may also provide a reliable and independent check for numerical models.

One of the least realistic aspects of this approach is that a constant diffusion coefficient is often adopted in analytical studies. This corresponds to

unchanging and perpetual wave conditions, which in reality it is obviously not the case.

To overcome this limitation, Reeve (2006) presented analytical solutions to a beach evolution equation obtained for the case where the initial beach shape may be an arbitrary function of position and where the forcing conditions may be a known function of time. Explicit solutions were obtained using an integral transform technique. The solutions are found in terms of closed-form integrals which, for all but the simplest cases, require numerical evaluation.

In this paper, we employ the methodology outlined by Pedrozo-Acuña et al. (2006) to determine, in a direct manner, the ensemble average shoreline evolution in the vicinity of a single groyne. We also employ Monte-Carlo methods to investigate the statistical dependence between terms in the analytical solution, and thereby to support simplifying assumptions that allow approximate direct evaluation of the ensemble solution. This paper is organised as follows; firstly, the mathematical background to derive ensemble averaged solutions from the analytical solution is presented. Next the selected case study, wave conditions and hypothesis are introduced. To finalise with the presentation of the results from the statistical reliability test of our hypothesis along with some conclusions.

MATHEMATICAL BACKGROUND

At its simplest, the one-line equation for the position of the shoreline (or a single depth contour) from a fixed datum line takes the form of a linear diffusion equation with constant coefficient it is given by the following equation:

$$\frac{\partial y}{\partial t} = K \frac{\partial^2 y}{\partial x^2} \qquad (1)$$

Where, y is the distance of the reference contour from a datum line (usually taken to be the x axis), t = time; and K = diffusion coefficient that represents the factors affecting the rate at which sediment is transported along the shoreline. It is therefore defined as ($2 \times Q_0$ divided by the active profile depth). The sediment transport rate (Q_0) is then calculated with the widely used formula known as the "CERC equation" (US Army Corps of Engineers 1984).

Following Reeve (2006) the general solution for the evolution of the beach plane in the vicinity of a groyne is given by

$$y = -\frac{1}{\sqrt{\pi}} \int_0^t \left(\int_w^t K(u)du \right)^{-1/2} e^{\left(-\left(\frac{x^2}{4\int_w^t K(u)du} - \int_w^t r(u)du \right) \right)} K(w)h(w)\, dw \qquad (2)$$

Given a sequence of wave conditions (Hs, T and θ) we can construct a corresponding sequence of *K(t)*, (and *h(t)*), to then evaluate the solution at any particular time using numerical integration. The closed-form nature of this solution enables several options to determine the statistics of the beach position. These are:

1.Use the solution to generate a 'Monte Carlo' simulation, from which statistics can be computed, and

2. Use the solution to estimate statistical moments directly.

Both procedures require long sequences of wave data, or a means of generating these with the correct statistics. However, if the estimation of the statistical moments is possible then a time-dependent ensemble averaged solution can be found without the need for computationally intensive 'Monte-Carlo' simulations. Moreover, when applying 'Monte-Carlo' techniques to the one-line equation, it is necessary to make some assumptions about the statistics of the forcing conditions that restrict the application of this method to more general situations (Vrijling and Meijer 1992; Dong and Chen 1999).

The route to the Monte-Carlo solution is straight forward once we have established a suitable wave climate and means to create statistically accurate realisations of this. We now consider the second option of direct estimation. To simplify the analysis we set an initially straight beach and no external sediment sources. The solution given in Equation (2) denotes the temporal variation of the shoreline position in the vicinity of a groyne.

Thus the ensemble average of this expression over all possible sequences of wave conditions the first moment (the mean of the solution) can be written as

$$\langle y \rangle = -\frac{1}{\sqrt{\pi}} \int_0^t \left\langle \left(\int_w^t K(u)du \right)^{-1/2} e^{\left(-\left(\frac{x^2}{4\int_w^t K(u)du} - \int_w^t r(u)du \right) \right)} K(w)h(w) \right\rangle dw \qquad (3)$$

where the $\langle\ \rangle$ denote the ensemble average. This is difficult to treat analytically because it involves a cross-correlation of three terms. If the

quantities $e^{\left(-\left(\frac{x^2}{4\int_w^t K(u)du}-\int_w^t r(u)du\right)\right)}$, *K(w)* and *h(w)* are approximately statistically independent, then we may approximate the ensemble of the product of functions by the product of the ensemble averages, thus:

$$\langle y\rangle = -\frac{1}{\sqrt{\pi}}\int_0^t \left\langle \left(\int_w^t K(u)du\right)^{-1/2} e^{\left(-\left(\frac{x^2}{4\int_w^t K(u)du}-\int_w^t r(u)du\right)\right)} \right\rangle \langle K(w)\rangle\langle h(w)\rangle\, dw \tag{4}$$

This will significantly simplify the evaluation of the solution. The extent to which such a simplification is justifiable can be investigated on a site by site basis by checking the approximate answers obtained in this way against the full solution.

If the hypothesis is not true, the ensemble average of the whole integral defined by Equation (3) must be computed from time series (in a Monte-Carlo fashion). Therefore, the need of wave data alongside with beach surveys is clear for the testing of the proposed hypothesis. In the following section we introduce the case study that has being employed to extract time series of the forcing conditions.

CASE STUDY

The forcing conditions consist of hourly hindcast wave conditions for the coast of Aberystwyth, a town on the Welsh coast of the United Kingdom (UK). This time-series have been furnished by Royal Haskoning and Aberystwyth City Council and correspond to offshore hindcast wave heights, wave periods and directions at a water depth of 32 metres. In order to construct a continuous time series of nearshore wave climate, the offshore waves were transformed inshore to a fixed water level contour (2m) using a wave transformation model (SWAN).

To characterise the wave climate resulting from this procedure, we estimated the probability density functions (PDF's) for wave height and period, as well as the wave rose for the wave directions. These results are shown in Figure 2 where the top panel presents the wave rose for the wave direction and the middle and bottom panels show the PDF's for the wave height and period, respectively.

From this figure it is possible to determine that the probability distribution function (PDF) of wave heights does not resemble a Rayleigh distribution, i.e. does not have a bell shape. This is understandable as the wave transforms from deep to shallower waters changing its shape, and wave breaking is included in the modelling. In contrast, it can be observed that the PDF for wave periods has a bell-shape distribution.

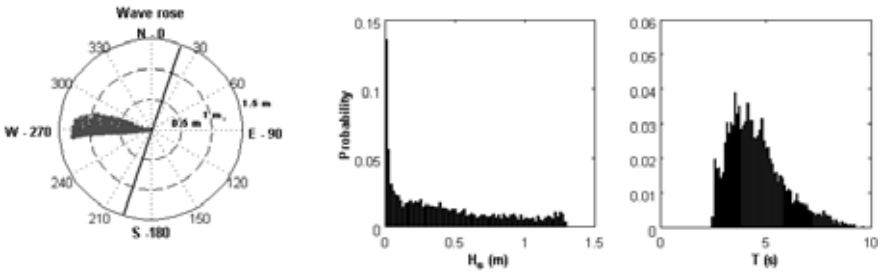

Figure 2. Left panel – Wave rose for inshore waves transformed by the SWAN model. Middle and right panels – Probability density functions (middle – wave height and right - period).

In order to estimate ensemble averaged quantities we require numerous wave sequences. The 4 years of hindcasted waves may be considered a single realisation of wave conditions. However, we use this to generate more sequences with similar statistical properties, in order to generate an ensemble of solutions.

Borgman and Scheffner (1991) proposed a statistical procedure that allows the generation of wave sequences with the same statistical properties as the input data set. The procedure uses as a basis an empirical normal scores transformation which maintains the first-order multivariate and higher order univariate moments of the data. We have used this technique to generate 600 sequences, with a length of 4 years, of wave height, period and direction which preserve the statistical properties of our original time series shown in Figure 2. Time series of wave height and period, as well as the wave angles were determined for all the wave sequences generated.

Figure 3 presents an example of these results, where the wave height record of the original data is presented along with 10 synthetic time series. Top panel show the original sequence of wave heights the rest of the panels show samples for 10 different realisations. From the comparison of the plots and the PDF's of the synthetic data against those obtained for the original data (not shown), it is clear that the technique preserves the distributional properties reasonably well.

The PDF's of wave height and period, as well as the wave rose were determined for all the wave sequences generated. This confirmed the

conservation of the statistical properties of the generated data. Figure 4 presents an example of these results, where the wave rose and PDF's of 3 synthetic time series are illustrated.

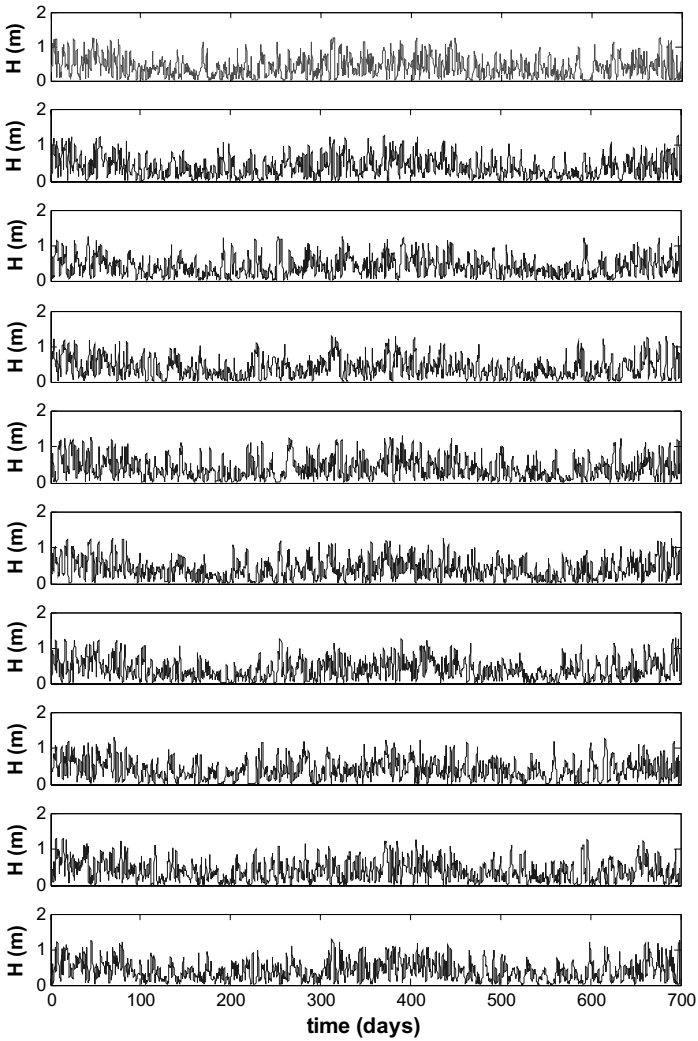

Figure 3. Wave height records for the original data set (top panel) and 10 samples of simulated wave data.

Right panels in this figure show the wave rose and the middle and left panels show the probability distribution functions for wave heights and periods respectively. From the comparison of these plots against those obtained for the

original data (Figure 3), it is clear that the technique preserves the distributional properties reasonably well.

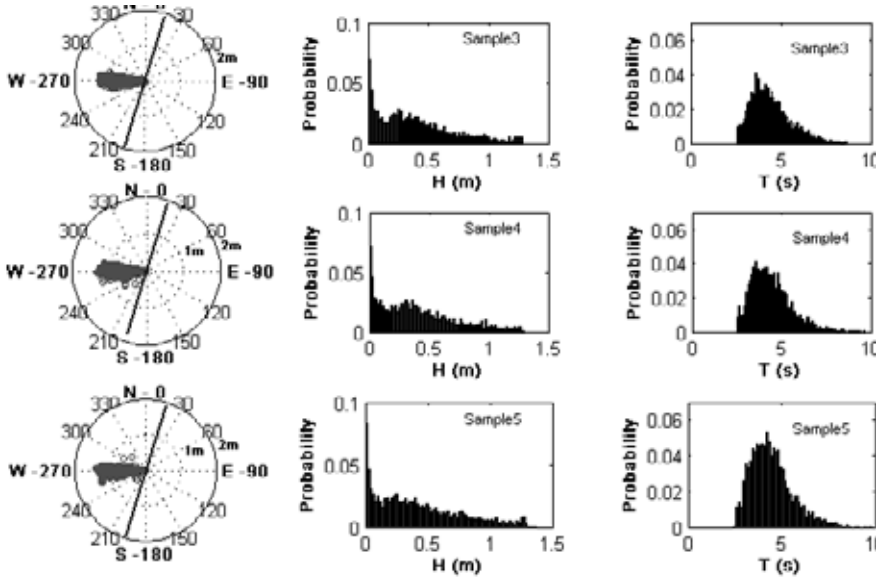

Figure 4. Wave rose and probability distribution functions for wave angles, wave heights and periods for 3 samples of simulated data. Left panel – Wave rose for directions; Middle and right panels – Probability distribution functions for wave height and period.

INITIAL ASSESSMENT OF HYPOTHESIS

The key test in this work consists in estimating the ensemble average with Eq. (3) and Eq.(4). If the results obtained through both expressions are approximately similar then this will pave the road towards a simplification of the procedure which accounts for the variability of the forcing conditions in the solution of the one-line equation.

Figure 5 shows the results of initial tests, using 200 realisations, of estimating the ensemble average via Eq. (3) and Eq. (4). The plot shows the ensemble average beach position at a fixed point in time (4 years after the start from an initially plane beach). From the visual comparison of both panels it is clear that both results are very similar.

This demonstrates that the results are very close, and also that there is a persistent but small difference between them. This result also suggests that an assumption of independence between the terms in the integrand could provide a

useful approximation to the full solution. This also implies that analytical solutions for idealised cases could be sought in order to provide checks on the numerical procedures that are needed to evaluate solutions for cases of more practical application.

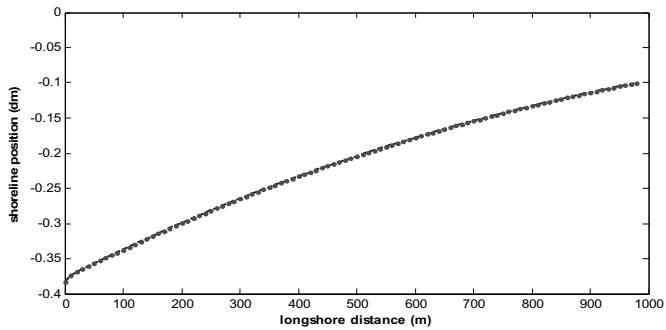

Figure 5. (solid line) Ensemble average of the solution estimated with Eqn 3; (dotted line) Ensemble average of the solution estimated with Eqn 4.

CONCLUSIONS

An analytical solution for shoreline evolution under time dependent wave conditions has been used as the basis for investigating the direct evaluation of the evolution of the ensemble average shoreline near a groyne. Site-specific wave conditions have been used to generate statistically similar wave sequences in order to create an ensemble of forecasts over a four year period. These have been used to investigate the statistical characteristics of the ensemble of the analytical solution.

The results indicate that the terms in the analytical solution may be treated as being statistically independent to a good degree of accuracy. This result greatly simplifies the evaluation of the first moment (mean) of the shoreline, because the ensemble averaging can be performed separately for each term in the integrand. This also implies that analytical solutions for idealised cases can be sought in order to provide checks on the numerical procedures that are needed to evaluate solutions for cases of more practical application. Further work is ongoing to perform further tests and check the robustness of the conclusions.

ACKNOWLEDGMENTS

The support of EPSRC through grant number (EP/C002172/1) is gratefully acknowledged.

REFERNCES

Borgman, L.E. and Scheffner, N.W. (Editors), 1991. Simulation of time sequences of wave height, period, and direction. Thechnical report DRP-91-2. Dredging Research Progam, Vicksburg, Mississippi.

De Vriend, H.J., Capobianco, M., Chesher, T., de Swart, H.E., Latteux, B. and Stive, M., 1993. Approaches to long-term modelling of coastal morphology: a review. Coastal Engineering, 21: 225-269.

Dong, P. and Chen, H., 1999. Probabilistic predictions of time-dependent long-term beach erosion risks. Coastal Engineering, 36: 243-261.

Hanson , H. and Kraus, N.C., 1989. Genesis: Generalised Model for simulating Shoreline Change. CERC Report 89-19, US Corps of Engineers, Vicksburg.

Larson, M., Hanson, H. and Kraus, N.C., 1997. Analytical solutions of oneline model for shoreline change near coastal structures. Journal of Waterways, Port, Coastal and Ocean Engineering, ASCE(July/Aug): 180-191.

Pedrozo-Acuña, A., Reeve, D.E. and Spivack, M., 2006. Beach variability near groynes. In: J.M. Smith (Editor), International Conference on Coastal Engineering. World Scientific, San Diego.

Pelnard-Considère, R., 1956. Essai de thèorie de l'evolution des formes de rivage en plages de sables et de gâlets. rappt 1, Société Hydrotech. de France.

Reeve, D.E., 2006. Explicit Expression for Beach Response to Non-Stationary Forcing near a Groyne. Journal of Waterways, Port, Coastal and Ocean Engineering, ASCE, 132(2): 125-132.

Reeve, D.E. and Spivack, M., 2004. Evolution of shoreline position moments. Coastal Engineering, 51(8-9): 661-673.

US Army Corps of Engineers, (1984). Shore protection manual, Coastal Engineering Research Center, Washington, D.C.

Vrijling, J.K. and Meijer, G.J., 1992. Probabilistic coastline position computations. Coastal Engineering, 17: 1-23.

MARINE INFORMATION SYSTEM FOR MITIGATION OF COASTAL FLOODING

Dong-Jiing Doong[1] Laurence Zsu Hsin Chuang[2] and Chia Chuen Kao[3]

This report presents a web-based integration information system for the purpose of coastal flooding warning. The components of this system includes in-situ field data and forecast results on sea states, live video images and the historical records of coastal flooding events. The in-situ data and field images are linked to the nationwide coastal monitoring network of Taiwan. Nested models including NWW III, SWAN and POM are used to forecast the wave and storm surge conditions. The key technology of this study is to integrate all these components to form an operational system. This system was daily run and attracted a lot of interests during typhoon period. This system has been operated for more than three years by governmental institutions in Taiwan and did play an important role on the decision making for the mitigation of coastal flooding.

BACKGROUND

Flood, inundation, and erosion disasters in coastal areas are becoming severer with increasing uncertainty of global meteorological system. For more accurate prediction and risk reduction of these disasters, research techniques of field investigation, numerical modeling, and to study the causes of disaster cases are strongly required. Taiwan is an island located in the Western Pacific. The island is situated on typhoon tracks. Typhoon always brings heavy rainfalls and severe sea states. On the land, rogue streams are formed because of the steep slope of rivers from their sources in the very high mountain and the short distance to the river mouths. On the other hand, Taiwanese coasts receive direct impacts by huge waves especially in the eastern part of the island as well as large surge heights in the western part. In the past 100 years, there were average 3.5 typhoons attacking Taiwan per year. Coastal flooding events happen very often. Lives and properties lost very much within every year. To warn, even to prevent and reduce the damages of lives and properties induced by severe weather conditions especially by typhoons, have already become one of the present primary works of Taiwanese government.

To mitigate the damages induced by typhoons, it is necessary to understand the nature since it's very difficult. The flooding events in Taiwan are always happened in the coastal area. The causes of coastal flooding are from two directions. One is because of the high water level in the river which the other

[1] Department of Marine Environmental Informatics, National Taiwan Ocean University, 2, Beining Rd., Keelung 20224, Taiwan ROC
[2] Institute of Ocean Technology and Marine Affairs, National Cheng Kung University, 1, Da-Hsueh Rd., Tainan 70101, Taiwan ROC
[3] Department of Hydraulic and Ocean Engineering, National Cheng Kung University, 1, Da-Hsueh Rd., Tainan 70101, Taiwan ROC

reason is because of the high sea level elevation and high waves. The water in the river is choked by high sea level to flood the coastal area. In addition, direct coastal flooding will be probably happened if the sea level rises by storm surge or by the overtopping of huge waves or their joint effects.

In-situ measurement and numerical modeling are both the approaches to understand the sea. Since 1998, the Central Weather Bureau and Water Resources Agency in Taiwan have been established a coastal monitoring network around Taiwan coast and developed several numerical models in order to implement the sea-state forecasts. However these projects were separated having less links. In this study, we would like to try to assemble those exist project outcomes to form a useful production in practical need for the governmental decision marker. The purpose of this production is to provide real-time information and prospective message for the references of coastal flooding mitigation decision. It should be a very simple use but rich data production. We developed such a production called the Coastal Watch Information System (CWIS). It is a web-based system to make it can be maintained and improved easily. This is an integration system. It includes 4 components, the Real-time in-situ sea states, the forecast sea-states, the field live video images, and the historical records and data of coastal flooding. They are introduced in next sections.

SYSTEM COMPONENTS

The Real-Time and In-Situ Data

Generally speaking, sea-state monitoring can be distinguished into two major categories: one is short-term observation of research or engineering orientation; the other is long-term operational routine monitoring. The object of long-term operational monitoring is to build national marine meteorology and coastal hydrology database to satisfy present and potential future needs, which include navigation, weather prediction, fisheries, ocean and coastal engineering design and planning, water sport safety, coastal hazard warning, disaster mitigation and coastline management, etc. From these needs a guiding principle for developing a comprehensive marine environment monitoring system can be derived, namely the system shall be able to operate on long-term basis and has capable of real-time data transmission in providing data for decision marking as well as for marine weather prediction.

Based on said guiding principle, the nationwide coastal monitoring network as shown in Fig. 1 was jointly established by Central Weather Bureau, Water Resources Agency and Tourist Bureau around Taiwan's coast waters (Kao et al., 1999; 2006). The basic observation items in this network include: wave height, period and direction, tidal elevation, surface current, wind speed and direction, air temperature, water temperature and barometer. The observation time interval is 1 hour. All the measured data are transmitted to a data quality check center via GSM, GPRS, Satellite or long distance wireless technologies in real-time, depending on the location of the stations (Doong et al., 2007). This network has

been started to be built since 1997. By the operation in the 10 years, it has been identified that these systems have high sea resistance to forestall any potential interruption. In addition, when hazardous weather systems such as typhoons approach, the system can accept remote control in shorten the time interval to increase the monitoring intensity and maintain the integrity of long-term database. By 2008, there are 11 data buoys, 32 tide stations, 11 coastal weather stations and 6 camera stations to form a 60 stations network. All the in-situ data and images are imported to the presented system in real-time to display on the screen and to store in the MS SQL-Server constructed database.

Figure 1. The real-time and in-situ measurement network around Taiwan. The buoy-like symbol is the locations of data buoys. Circle symbol represents the tide stations. Triangular symbol represents the coastal weather stations.

The Numerical Forecasting Models

Projection of future possibility is an important task in the presented system. Numerical models are used to implement this objective. A large scale NWW III wave model nested to a regional scale SWAN model is constructed to forecast waves at Taiwan's coast (Ou et al., 2002). In addition, POM model is used to forecast storm surge height. The flowchart of the calculation within this presented system is shown in Fig.2. The import of wind field is one of the critical processes to maintain the operation of the models and influence the accuracy of forecasting results. The other factor is the setup of numerical models. For research purpose, the grid size is generally arranged to very fine in

order to obtain very fine resolution results. However, fine grid calculation always represents long calculation time. Calculation with proper large size grid sometimes reduces the accuracy of the results but save time. High resolution results but long time calculation has no meaning for a quick-reply required system. To balance the model setup such as the grid arrangement with the calculation time is a critical issue in such as an operational and practical system (Yeh et al., 2005). By the practical experiences, to forecast waves and storm surges for Taiwanese coast (about 35 default locations to be outputted) by mentioned three models need to be completed within 45 minutes.

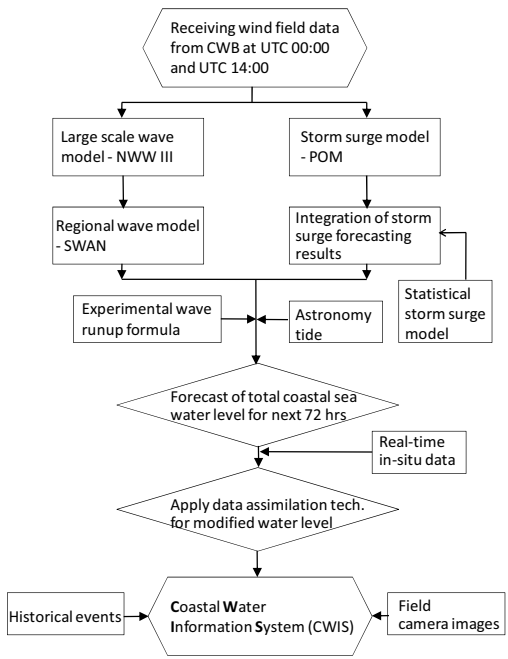

Figure 2. Components and flowchart of the presented system.

The Field Video Images

CWIS is designed for decision maker use. Most of these decision markers are not major in coastal engineering or even they are not in the field of engineering or science. It is difficult for them to understand the 3 meter wave height or 1 meter storm surge. The best way is to show them the real images. Therefore CWIS includes the component of field video images as auxiliary information. High resolution cameras are installed at the high building or on a pile at the coastal area. High intensity light or infrared light is equipped in order to make it visible in the night. It needs high flow channel to transmit image sequences to CWIS. A long distance wireless data transmission technology was applied. The camera observation systems are allowed to manually adjust the

looking direction, focal length, and to record the interests. This camera component is always the attraction in CWIS, especially for decision markers.

The Historical Record of Coastal Flooding Events

People says that historical experiences are sometimes more useful than scientific results. CWIS collected historical record of coastal flooding events of past 20 years. The records cover the description of coastal flooding events, the tracks and parameters of induced typhoon and the meteorological and oceanographic data. When a typhoon alarm announces, CWIS will search in the database of historical events to find typhoons with similar tracks and intensity together with their induced disasters. CWIS shows these data in the system to provide the historical experience.

THE SYSTEM AND ITS OPERATION

Fig. 3 shows the main page of CWIS. As previous mentioned, it is a web-based system providing information for potential coastal flooding mitigation. People can visit to CWIS if they are able to access to the Internet. Presented four components in previous section are shown in the main page of CWIS. The first component is located in the middle of the page. They are real-time in-situ data which are measured from the nationwide coastal ocean monitoring network. This component shows the real-time sea-states such as wave, tide, wind, water temperature, air temperature and pressure. They are updated each hour when new data are transmitted to the server. The second component is the total sea water levels (TSWL) at the coast which are separately estimated from numerical models. The total sea water level (TSWL) is estimated by the summation of astronomical tide height, storm surge height, half of significant wave height and the setup height. TSWLs at some special locations are shown in the upper left and right tables on the page. In the tables, the TSWL is compared with the elevation of sea dyke (the second column in the table) to assess if it will be overtopped and flooded. When there is a potential to flood, the status display a red color warning notice. Second component is the kernel of CWIS. Above the tables, there is a function scroll entitled Forecast Time which shows the time of these forecasting results. CWIS is designed to the forecasting results of three hours ahead. The third component, i.e. the field live video images is arranged at the down left and right windows. The system manager and the decision marker have the right to remote control the cameras when they press on the image window and input user data. The component of historical record of coastal flooding events due to typhoons is shown at the bottom area of CWIS page.

CWIS is now applied by Water Resources Agency of Taiwan and the technical support is from the Coastal Ocean Monitoring Center of National Cheng Kung University. The system was developed using Microsoft ASP.NET technology with a MS SQL-Server. Real-time data are updated hourly and the field images are updated every minute. According to the time of wind field

received from Central Weather Bureau, the numerical models run twice in a day. For each run, the models provide the results for next 72 hours but only the forward few hours results are used because next run overlaps the hind results. On the regular days, CWIS has less attention because the coastal damages and flooding events in Taiwan always happen during typhoon period (Hsu et al., 2007; 2008). Therefore CWIS trains itself to check the stability and accuracy of forecasting results for the period. Few days before typhoon comes, high concern goes to CWIS. Since 2005, CWIS started to be operated and improved. It did provide very much information for the governmental offices to make necessary decisions, such as to withdraw habitant when their town is under flooding potential and to arrange pumping machine when one area's natural drainage capability is not sufficiency.

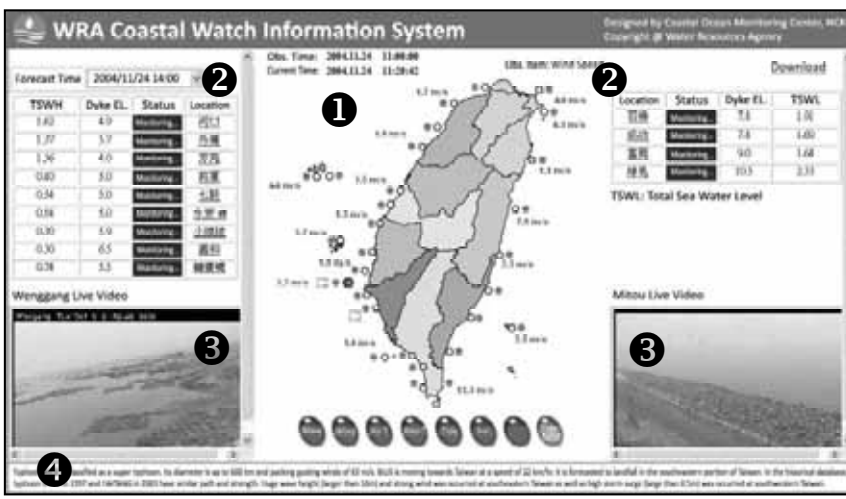

Figure 3. Main page of CWIS. ①Real-time data display area. ②Numerical Forecasting results of total sea water level for next few hours at special locations. ③Field live image display. ④Historical records of coastal flooding events.

SUMMARY

The engineering of warning system is a critical means to effectively mitigate disaster damages. As technologies for monitor and surveillance, data transmission, forecast and calculation progressively developed, to certain extent information of disaster occurrence and evolution can be quickly sent to the prevention and rescue decision-makers as well as the concerned public, and through direct assessment, arriving at effective rescue decision to prevent losses and accelerate rebuilding.

CWIS (Coastal Water Information System) is a web-based information system developed by Water Resources Agency in Taiwan in order to provide wide data for decision marker for making necessary decisions for coastal flooding damages. This information system includes real-time sea-states display,

future sea-states forecast and records and experiences of historical events. CWIS plays an important role to understand the sea conditions during typhoons. This paper reports the idea and contents of CWIS. Since it doesn't pay too much attention on the technical calculation, however CWIS has its very high value to assemble several exist works such as measurements, modelling and the information technology. CWIS has been operated for many years and did assist decision marker knowing the sea-states and making necessary decisions by its training and improvement.

ACKNOWLEDGMENTS

Development of CWIS was funding supported by Water Resources Agency in Taiwan. In-situ data imported to CWIS are also from Central Weather Bureau and Tourist Bureau. Prof. T.W. Hsu at National Cheng Kung University and his team members supported the development of numerical modeling in the CWIS. Writing this article is also supported by National Science Council (NSC 96-2611-M-019-012). The authors would like to offer their great thanks to these authorities and persons.

REFERENCES

Doong, D.J., S.H. Chen, C.C. Kao, and B.C. Lee. 2007. Data quality check procedures of an operational coastal ocean monitoring network, *Ocean Engineering*, 34, 234-246.

Hsu, T.W., I.F. Tseng, T.Y. Lin, C.Y. Shin, and S.H. Ou. 2008. Review of countermeasures against beach erosion on the Taiwanese coast, *Coastal Management*, Vol. 36, Issue 3, 274-293.

Hsu, T.W., T.Y., Lin, and I.F. Tseng. 2007. Human impact on coastal erosion in Taiwan, *Journal of Coastal Research*, Vol. 23, Issue 4, 961-973.

Kao, C.C., K.C. Jao, D.J. Doong, and C.L. Kuo. 2006. Buoy and Radar Observation Network around Taiwan, *Prof. OCEANS'06 Asia Pacific IEEE*.

Kao, C.C., Laurence Z.H. Chuang, Y.P. Lin, and B.C. Lee. 1999. An Introduction to the Operational Data Buoy System in Taiwan, *Proceedings of the International MEDCOAST Conference on Wind and Wave Climate of the Mediterranean & the Black Sea*, 33-39.

Ou, S.H., J.M. Liau, T.W. Hsu, and S.Y. Tzang. 2002. Simulating Typhoon Waves by SWAN wave model in Coastal Waters of Taiwan, *Ocean Engineering*, Vol. 29, No. 8, 947-971.

Yeh, S.P., B.C. Lee, D.J. Doong, C.L. Kuo, and C.C. Kao. 2005. The Coastal Hazards Warning System Based on the Operational Wave and Storm Surge Models, *Proceedings of the 15th International Offshore and Polar Engineers Conferences (ISOPE 2005)*, 440-445.

LARGE AND SMALL SCALE EXPERIMENTS ON WAVE TRANSMISSION AT SUBMERGED WIDE-CRESTED BREAKWATERS

Cappietti L.[1], Aminti P.[2], Sanchez-Arcilla A.[3], Gironella X.[4]

In this paper we present a series of laboratory experiments about the process of wave transmission at submerged wide-crested rubble-mound breakwaters. The experimental activities were conducted using a composite laboratory process modeling that is characterized by large-scale and small-scale physical model tests. Description and motivation of this methodology, of the experiments, and some preliminary data analysis are reported.

INTRODUCTION AND MOTIVATIONS

The use of detached, surface piercing, rubble-mound breakwaters has been one of the most common approach to assure shore protection. Often these structures have been build during contingency situations, just after dramatic coastal flooding episodes, with the main objective of assuring a proper protection level but paying less attention to environmental aspects. If on one hand, they successfully guaranteed their primary objective, thus stabilizing the shoreline, on the other hand, they posed some environmental impacts (see Fig. 1).

Figure 1. Marina di Pisa, Tuscany, Italy. The defense of the coast on the left side of Arno river mouth has been assured by emerged rubble-mound breakwaters since 1938. On the opposite, the right side of the coast is unprotected and has been

[1] DICeA, University of Florence, Via S. Marta 3, Florence, 50139, Italy
[2] DICeA, University of Florence, Via S. Marta 3, Florence, 50139, Italy
[3] LIM, Universitat Politècnica de Catalunya, Campus Nord-UPC, Edif. D1, Barcelona, 08034, Spain
[4] LIM, Universitat Politècnica de Catalunya, Campus Nord-UPC, Edif. D1, Barcelona, 08034, Spain

eroding at a rate of about 20 m/yr for a total retreat of approximately 1400m.

Nowadays, the increasing interest on environmental aspects leads coastal managers to prefer submerged breakwaters due to their own advantages like a better water renewal, reduced impact on the landscape, and the allowed navigability of small support boats for the safety of bathers. Moreover, obsolete coastal protection systems are widespread along the European coasts and the theme of the rehabilitation of these structures is emerging in the scientific community (European Coastal Action Plan 2008, Cappietti and Aminti 2005). For the case at hand a possible approach could be the conversion of existing emerged breakwaters into the submerged kind.

In any case, the use of submerged breakwaters, leads to an increment in wave transmission, with respect to the emerged kind, but in principle this inconvenience can be controlled by increasing the breakwater crest width. From this perspective, the influence of the crest width in wave transmission at submerged breakwater is of certain importance. It is worth to note that, at present, most of the experimental data on wave transmission at submerged breakwaters concern the case of relatively small crest width parameter, B/Hi. It exists a reduced amount of small-scale laboratory experiments where the crest width parameter has been uniformly changed, in a wide range, up to very large values (Seabrook and Hall 1998, Gómez and Valdes 1990).

A new data set of wave transmission, at submerged wide-crested rubble-mound breakwaters, has been obtained in the present work. The experiments were conducted using a composite approach based in large-scale and small-scale physical models. This paper is devoted to the description of the whole experimental activity and to the discussion of some results emerging from preliminary data analysis.

EXPERIMENTAL METHODOLOY

Our objective was to study, by means of a laboratory process modeling, the effect of the crest width of a submerged rubble-mound breakwater in the control of the wave transmission. We planned to investigate the phenomenon exploring a wide range of variability of the crest width parameter and assuring an high resolution of this range. The experimental activity resulting from this goal, can rarely or can not practically achieved in large-scale facilities due to a limited amount of resources. This is not the case for a small-scale facilities but small-scale measurements suffer in principle of higher scale distortions. The key question is, how much does the wave transmission is affected by scale distortions? Obviously to answer to this question we need an accurate measurement of the phenomenon in absence of scale distortion and then compare this reference measurement with the small-scale measurement. Measurements not affected, or poorly affected, by scale-effects can be conducted only in large-scale models that are the needed tool in order to reproduce, in a controlled way (not possible in the field), the multi-scale

interactions of wave transmission. This is the main reason that imposes large-scale experiments to enhance the quality of laboratory experiments in the future. The synergetic use of large-scale and small-scale experimental facilities leads to a research tool that enhances the positive features and decreases the negative aspects of both infrastructures thus increasing their value of use. A wider discussion concerning the motivation of the so called "Composite LAboratory PROcess Modelling" (CLAPROM) is reported in Cappietti et al. 2007.

DESCRIPTION OF THE EXPERIMENTS

The large-scale model tests, were conducted in the wave-flume at Laboratori d'Enginyeria Maritìma (LIM) of the Universitat Politecnica de Catalunya, Barcelona, Spain (Kramer et al 2005).

The experiments include two sections of a rubble-mound breakwater of trapezoidal shapes that differ about the values of the crest width. The structures were composed by an internal core of finer material and a armor layer of bigger material. To assure the stability of the elements of the armor layer, a metallic net was installed on top of the breakwaters. The barriers were tested under five irregular wave attacks in a fixed bottom. The waves were run under three different water depths in the flume, in order to change the barrier freeboards, so that emerged and submerged breakwaters were tested.

The small-scale breakwater models were tested in the medium-scale wave-current-flume of the Coastal Laboratory of the University of Florence, Italy (CL) at a ratio of 1/10. The tests at CL were reproduced with the main objective to minimize the differences between the large-scale and the small-scale experiments concerning: i) the flume set-up, ii) the breakwater geometries, iii) the breakwater materials, iii) the wave gauge positioning, iv) the wave conditions, v) the experimental methodology, vi) the data analysis. The actual conditions at UPC were used as target conditions at CL. The results have shown a satisfactory agreement between the transmission coefficients measured at both scale levels, under the same test conditions, for submerged as well as emerged breakwaters.

However, for emerged breakwaters, the water set-up on the rear of the barriers that were measured at small-scale were considerably higher than those measured at large-scale, whereas for submerged breakwater the measurements were much more closer.

This discrepancy suggests that the hydraulic resistance, exerted at the return flow that filtrates through the armor of the emerged breakwater, is much higher in the small-scale experiments than in the large-scale. Considering that the transmission coefficients measured at both scale are in good agreement, it is likely that a second kind of scale-effect has to compensate the reduced trasmissibility of the small-scale rubble-mound. It is so reasonable that the wave run-up and the resulting overtopping are higher at the small-scale model of emerged breakwater. A detailed description of these experiments and a

comparison of the transmission coefficients, measured at large-scale and small-scale models, is reported in Cappietti et al. 2007.
After this first set of experimental results, that proved the validity of the use of small-scale model, to study the wave transmission at submerged breakwaters, we expanded the test conditions by means of a new set of experiments carried out at the small-scale level in order to study the effect of the different crest width.

We conducted new measurements of wave transmission, under the same wave conditions approaching the tested submerged breakwater section but with the new aspect that the width of its crest was increased step by step. The description of this new set of experiments is reported hereinafter only for those aspects different from the previous experiments described in Cappietti et Al. 2007; the interested readers are referred therein concerning the aspects not described hereinafter,

A total of 13 submerged rubble-mound breakwater were tested. The crest width was varied in the range B=35cm-150cm (increments of about 12cm) and the freeboard was R_c=2.6cm (note that the freeboard for submerged barriers is considered positive hereinafter). The structures were characterized by an internal core made of finer material (D_{50}=0.2cm), an armor layer (D_{50}=1.0cm) and a metallic net to assure the stability of the elements. The water depth in front of the barrier was d=18.5cm, (note that it is higher than the maximum level that was tested in the cited reference, F3=17.2cm), moreover, two extra wave conditions were added to those tested in Cappietti et al. 2007, one of which (code I0 in Table 1) has the lower wave height and the other has the highest wave height (code I6 in Table 1).

Table 1. incident wave conditions measured in absence of the barrier at the gage couple 6-7 (Goda and Suzuki, 1976), and dimensionless parameters

H_{m0} [cm]	T_p [s]	$H_{m0}/L_{m-1,0}$	$\xi_{m-1,0}$	H_{m0}/d	H_{m0}/R_c	H_{m0}/D_{50}	B/H_{m0}	$B/L_{m-1,0}$
I0=2.7	0.8	0.036	2.6	0.16	1.0	2.7	4.4-55	0.16-1.99
I1=3.3	1.1	0.028	3.0	0.18	1.3	3.3	3.6-45	0.10-1.27
I2=4.1	0.8	0.054	2.1	0.22	1.6	4.1	2.9-37	0.16-1.99
I3=5.0	1.0	0.048	2.3	0.27	1.9	5.0	2.4-30	0.11-1.44
I4=5.3	1.0	0.051	2.2	0.29	2.0	5.3	2.3-28	0.11-1.44
I5=6.0	1.1	0.051	2.2	0.33	2.3	6.1	2.0-25	0.10-1.27
I6=9.1	1.6	0.049	2.3	0.49	3.5	9.1	1.3-17	0.06-0.81

All waves had a JONSWAP spectrum with peak enhancement factor of 3.3. The wave motion was measured by using 10 resistive wave gages. The wave gages were positioned, as depicted in Fig. 2, in order to check for the wave generation and to obtain the incident and the transmitted wave parameters. The spectral analysis was employed and the resulting wave parameters are reported in Table 1. All incident waves were of the kind of non-breaking or at the onset of breaking (wave I6); each wave breaks when propagating on the barrier and

the breaking process approaches the surging type. The dimensionless barrier width B/H_{m0} ($B/L_{m-1,0}$) is in the range 1.3-55.6 (0.06-1.99) and the relative freeboard R_c/H_{m0} is in the range 0.28-1.0

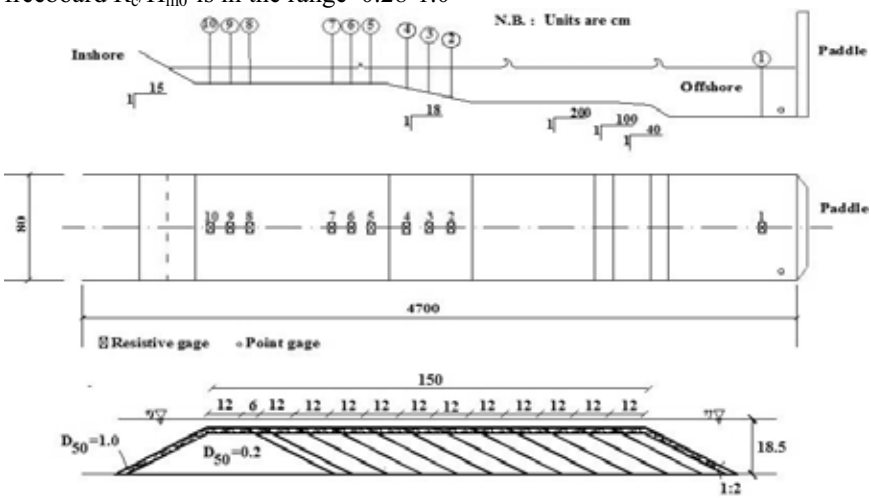

Figure 2. Layout of the wave-flume and wave gages position. The breakwaters were positioned on the horizontal part of the profile between wave gages 5 and 8.

PRELIMINARY ANALYSIS OF THE DATA

The wave transmission is, in principle, a function of several dimensionless characteristic parameters. Traditionally, the relative freeboards R_c/H_{m0} has been one of the most important parameter as demonstrated by Van der Meer and Daemen (1994) that based their regression formula on this parameter. Subsequently, D'Angremond et al. (1996) proposed a new regression formula pointing out also the influence of the dimensionless crest width B/H_{m0} and of the breaker parameter $\xi_{m-1,0}$. Later on, Van der Meer et al. (2005) noted that the formula of D'Angremond et al. (1996) gives worth predictions in the range $B/H_{m0}>12$ so that they have proposed a recalibration of the same formula, to be used in this range, but limiting the computed transmission coefficient in the intervals $0.05 \le kt \le 0.93 - 0.006 \cdot (B/H_{m0})$. For the clarity of the readers, the proposal of Van der Meer et al. (2005) is reported in Eq. 1.

$$k_t = \begin{cases} -0.4\dfrac{R_c}{H_{m0}} + 0.64\left(\dfrac{B}{H_{m0}}\right)^{0.31}\left(1 - e^{-0.5\xi_{0p}}\right) \;\; if \;\; \dfrac{B}{H_{m0}} < 8 \\ -0.35\dfrac{R_c}{H_{m0}} + 0.51\left(\dfrac{B}{H_{m0}}\right)^{0.65}\left(1 - e^{-0.41\xi_{0p}}\right) \;\; if \;\; \dfrac{B}{H_{m0}} > 12 \end{cases} \quad (1)$$

The transmission coefficient in the range $8< B/H_{m0} <12$ is obtained interpolating the values obtainable by the 2 equations.

Our experimental range of variability of the dimensionless crest width and

of the dimensionless barrier freeboard is quite large whereas the breaking parameter $\xi_{m-1,0}$, can be considered relatively constant. The behavior of the transmission coefficient as a function of these two former parameters is highlighted in Fig. 3. It clearly confirms that the transmission coefficient decreases for increasing crest width and decreasing barrier freeboard.

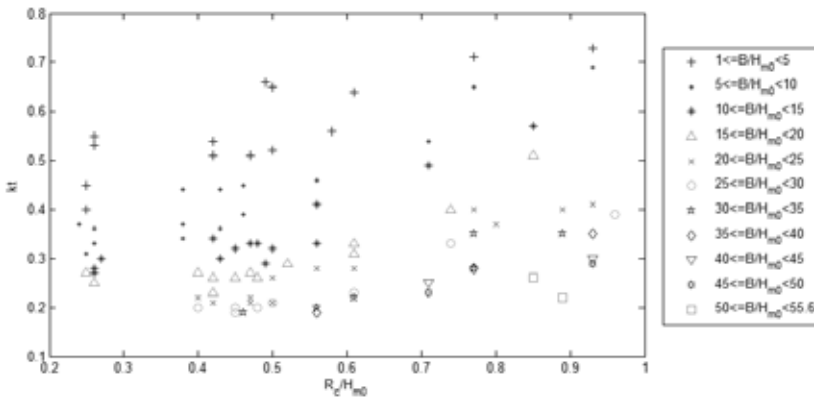

Figure 3. Measured transmission coefficients as a function of the dimensionless crest width and the dimensionless barrier freeboard. In the picture, the freeboard is considered positive for submerged barriers.

A preliminary comparison of our experimental data set with the prediction of the wave transmission, obtainable by means of the regression formula proposed by Van der Meer et al. (2005), is summarized in Fig. 4. The spreading, around the measured values, seems to increase for increasing the width of the breakwaters. The discrepancy between the predicted and the measured transmission coefficients, as a function of the crest width, is more clearly highlighted in Fig. 5 that is related to the wave attacks named I0 and I6 in Table 1.

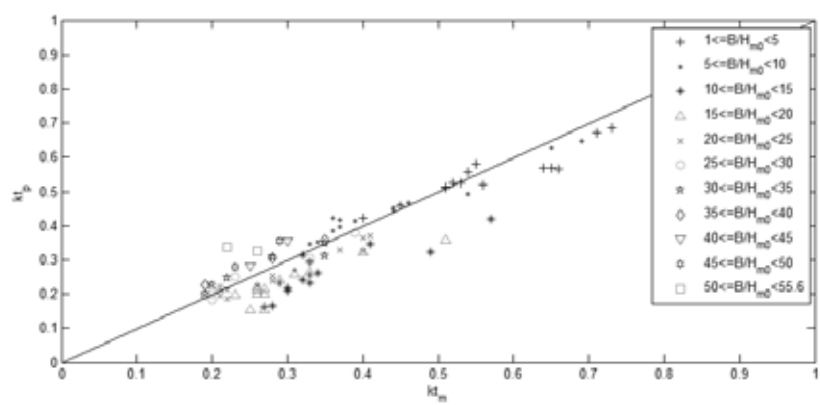

Figure 4. Measured transmission coefficients kt_m versus the predicted transmission coefficients kt_p.

The predicted rate of attenuation of the wave transmission seems quite different from the measurements, at least if only our data set is used for the comparisons.

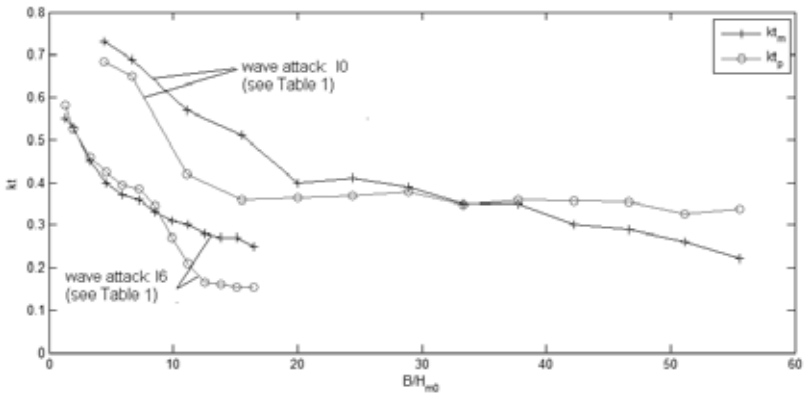

Figure 5. Measured transmission coefficients kt_m versus the predicted transmission coefficients kt_p for the wave attacks named I0 and I6 in Table 1.

CONCLUDING REMARKS

A new date set of experimental values about wave transmission at submerged wide-crested rubble-mound breakwaters has been obtained. The first part of the experiments have been conducted in physical models at large-scale and small-scale levels (at a ratio of 1:10). The measurements conducted in the large-scale models have been used to calibrate the small-scale experiments. The comparison between the measurements conducted at both scale levels has demonstrated that the wave transmission reproduced in the small-scale model is, for the case at hand, close to the large-scale measurements. The range of variability of the crest width parameter has been expanded, up to the value B/H_{m0}=55.6, by means of a new set of experiments that have been conducted using small-scale models. The results show that the sensitivity of the wave transmission to the crest width is characterized by the decreasing of the k_t for increasing the width of the crest of the barrier (and also for decreasing its submergence), thus confirming previous findings.

The measured power law, concerning this attenuation, has been compared to the prediction obtainable by a recent regression formulation that has been proposed for wide-crested breakwaters by Van der Meer et Al. 2005. The results show that the prediction is quite satisfying for the estimation of the phenomenon as a first approximation; however, the preliminary data analysis here presented, suggest that the proposed power law is partially inadequate to capture the exact rate of attenuation that has been measured in the present experiments.

ACKNOWLEDGMENTS

The support of the Ministerio de Educatiòn y Ciencia under the program

Instalacion Cientifico Tecnologica Singular (ICTS) Canal De Investigación Y Experimentación Marítima (CIEM), Laboratori D'enginyeria Maritima (LIM), Universitat Politecnica De Catalunya (UPC), project title: *Composite Hydraulic Models – CHYM*, Lorenzo Cappietti, is gratefully acknowledged .

REFERENCES

Cappietti L. and P.L. Aminti. 2005. Rehabilitation of highly protected\beaches by using environment-friendly structures", *Environmental Friendly Coastal Protection,* Nato Sciences Series, Vol. 53, 163-175.

Cappietti L., Aminti P., Sánchez-Arcilla A., Gironella X. 2007. Toward A Composite Hydraulic Model For Wave-Flume Experiments, *Coastal Structures 2007 International Conference.*

d'Angremond K., J.W. Van der Meer, R.J. De Jong. 1996. Wave transmission at low crested structures" *Proc. of 25th Int. Conf. on Coastal Engineering*, 3305–3318.

ENCORA. 2007. *European coastal action plan for strengthening the knowledge base of sustainable coastal and marine management*. Paris Conference, 5-7 December 2007, 104 pp.

Goda Y. and Y. Suzuki. 1976. Estimation of incident and reflected waves in random wave experiments, *Proc. of 15th Int. Conf. Coastal Engineering*, 828-845.

Gómez Pina G. and J.M. Valdés. 1990. Experiments on coastal protection submerged breakwaters: a way to look at the results. *Proc. of 22th Int. Conf. Coastal Engineering*.

Kramer M., B. Zanuttigh, J.W. Van Der Meer, C. Vidal, X. Gironella. 2005. Laboratory experiments on low-crested breakwaters. *Coastal Engineering*, Vol. 52, 867-885.

Van der Meer J.W. and I.F.R. Daemen. 1994. Stability and wave trasmission at low crested rubble-mound structures. *Journal of the Waterway Port Coastal and Ocean Engineering*, 120.

Van der Meer J.W., R. Briganti, B. Zanuttigh, B. Wang. 2005. Wave trasmission and reflection at low crested structures: Design formulae, oblique wave attack and spectral change. *Journal of Coastal Engineering*, Vol. 52.

PHYSICAL AND NUMERICAL MODELLING OF WAVE TRANSFORMATION OVER A SUBMERGED RUBBLE-MOUND STRUCTURE

Scott Baker[1], Ioan Nistor[1], Andrew Cornett[2], Pedro Lomonaco[3]

Physical and numerical modelling of the interaction of irregular waves with a large-scale three-dimensional submerged structure was performed, with the purpose of understanding the structure's influence on the wave and hydrodynamic field, the wave-induced velocities along the structure crest, as well as on the wave-induced currents. Extensive processing and analysis was performed for a multitude of data and experimental scenarios, including – but not limited to – wave heights, wave periods, wave energy spectra, energy transfer functions, wave reflection, and wave-induced velocities.

INTRODUCTION

Submerged rubble-mound structures are widely used for coastal defence against severe hydrodynamic conditions generated by the combined action of waves and currents. Understanding energy dissipation and wave transformation over submerged structures is essential in assessing their structural reliability and in determining their impacts on the environment. The objective of this research program was to investigate and quantify, both experimentally and numerically, the wave transformation and hydrodynamic field induced by the presence of a steeply-sloped, deeply submerged structure with a varying cross-section and varying submergence depth. The project is a component of an extensive collaborative research program established between the Department of Civil Engineering at the University of Ottawa, Canada, and the Canadian Hydraulics Centre (CHC) of the National Research Council of Canada.

PHYSICAL MODELLING

The large scale three-dimensional physical model of the submerged structure was designed and constructed in the Coastal Basin at the Canadian Hydraulics Centre in Ottawa, Canada. The basin measures 63 m long by 14 m wide by 1.5 m in height, and is equipped with a computer controlled multi-mode wave generator capable of producing irregular long-crested waves with significant wave heights of up to approximately 0.35 m at model scale. The

[1] Department of Civil Engineering, University of Ottawa, 161 Louis Pasteur, CBY A-115, Ottawa, Ontario, K1N 6N5, Canada
[2] Canadian Hydraulics Centre, National Research Council 1200 Montreal Road, Building M-32, Ottawa, Ontario, K1A 0R6, Canada
[3] Environmental Hydraulics Institute, University of Cantabria, Avda de los Castros, 39005 Santander, Spain

basin is fitted with highly efficient wave absorbers for minimizing undesired wave reflections back into the model area.

The physical modelling study was conducted at an undistorted 1 to 50 length scale (based on Froude scaling). A 7.2 m wide central testing channel was created by constructing two parallel solid vertical walls and leaving two 3.4 m wide side-channels on either side of the central channel. A rigid model bathymetry was constructed within the central testing channel, which included a 0.32 m deep by 6 m long trench that was filled with fine sand used to simulate the seabed beneath the submerged structure. Two thrusters were placed in each of the side channels in order to generate reversing currents within the central channel (simulating tidal currents). Steady currents could be generated flowing both with and against the direction of wave propagation. Test cases involving currents will not be discussed in the present paper.

Wave conditions in the model were measured at 10 locations, distributed up-wave, down-wave, and along the crest of the submerged structure using capacitance wire gauges. The arrangement of the wave gauges remained constant throughout the calibration and testing stages so that further comparison of the impact of the structure on the wave field could be properly assessed.

The magnitude and direction of the orbital velocities and currents were measured using two 2-axis electromagnetic current meters (ECM) installed along the channel centerline up-wave and down-wave from the structure, and three 3-axis acoustic Doppler velocimeters (ADV) placed above the structure crest. Similarly, the location of the current meters remained constant throughout the calibration and testing phases. Once the structure was constructed, the locations of the ADVs were set approximately 5 cm above the longitudinally-varying crest elevation of the submerged structure.

A series of tests were conducted prior to constructing the submerged structure in order to calibrate and verify the waves and currents within the central test channel. Once the undisturbed tests were competed, dredging works were replicated in the mobile sand bed and the model structure was constructed. The submerged rubble-mound structure had a longitudinally varying freeboard, from approximately half the water depth at the high end (-14.8 m), sloping down to just above the seabed (-30.3 m) at the lower end (see Figure 1).

Figure 1. Physical model of the submerged structure in CHC's Coastal Basin.

Once the structure was completed, a series of tests were carried out with varying significant wave heights, wave periods, and water levels (see Table 1). The generated waves were irregular and long-crested, defined by the JONSWAP spectrum, with a γ parameter of 3.3. Each time series of waves had a duration corresponding to a 5 hour storm at full scale (approximately 43 minutes at model scale), and each wave train consisted of more than 1000 individual waves.

Table 1. Test Series – Extreme (storm) wave conditions

Test	Wave Height (m)	Wave Period (s)	Water Level from MSL (m)	Storm Duration (hrs)	Presence of Tunnel
Case 0	4.5	16.2	-1.55	5	No
Case 1	4.5	16.2	-1.55	5	Yes
Case 2	6.0	20.1	-1.72	5	Yes
Case 3	6.0	20.1	-5.00	5	Yes
Case 4	7.0	20.1	-5.00	5	Yes

NUMERICAL SIMULATIONS

Numerical modelling was undertaken to verify and compare the computational results with the data collected during the experiments. To properly simulate the propagation and transformation of waves over a steeply sloping submerged structure, a highly non-linear numerical model was required. In this study, the 2DH (two-dimensional horizontal) numerical model WaveSim (Nwogu 1993, 1996) was employed. WaveSim is an extended Boussinesq-type model, based on the depth-integrated mass and momentum equations for nonlinear dispersive waves. The model is capable of simulating the nonlinear transformation of irregular multidirectional waves in water of varying depth, incorporating at the same time the effects of shoaling, refraction, diffraction,

full/partial reflection and transmission, bottom friction, nonlinear wave-wave interactions, wave breaking and runup, and wave-induced currents.

The computational domain (see Figure 2) was a replica of the central test channel from the physical modelling study. The domain included the initial bathymetry and the submerged structure. Since currents were not simulated, the lateral channels were omitted from the computational domain. The numerical wave generator was placed at the left side of the computational domain, with 200 m long sponge layers placed behind the wave generator and also down-wave of the submerged structure in order to absorb all outgoing wave energy and prevent any undesirable reflections from the front and back walls.

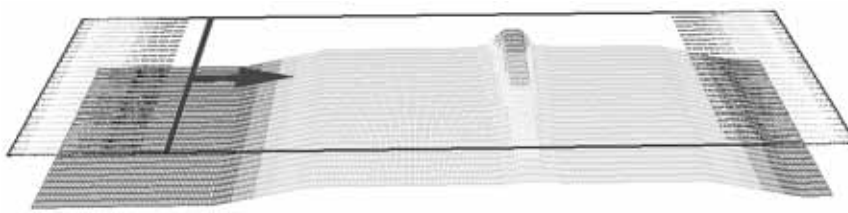

Figure 2. Overview of the computational domain.

The computational domain was discretized using grid steps of $\Delta y = 5.25$ m by $\Delta x = 14.4$ m (prototype) yielding a grid with 245 steps in the direction of wave propagation and 25 steps in the transverse direction. A time step of 0.1 s was found to maintain stability of the numerical solution. The model's strong non-linearity and wave-breaking options were both utilized for all the numerical simulations. The same test conditions listed above (refer to Table 1) were simulated using the numerical model so that direct comparisons of the computational and experimental results could be performed.

RESULTS

The authors performed significant processing and analysis on both the experimental and numerical data sets. This included comparisons of the wave statistics and spectra, the transfer function (describing changes in spectral shape across the structure), and orbital velocities between the physical and numerical results. The numerical simulations alone were used to investigate the spatial distribution of significant wave height around the structure, the wave-induced current field, and level of wave reflection.

For the undisturbed test condition (before the structure was constructed, refer to Table 1 -- Case 0) the comparison of the wave spectra showed that the experimental and numerical results matched very well. When the submerged structure was included in the physical and numerical model, a significant change in the wave conditions was observed. The gauges located up-wave of the structure measured higher waves than was observed during the undisturbed case due to wave reflections from the submerged structure. As expected, the readings

showed that the influence of the structure was more significant at the right side of the channel, where the submergence depth was smaller (the structure was taller). A similar trend was observed for the gauges located at the structures crest (see Figure 3). Figure 3a shows the measured wave spectra at the left side of the channel, where the submergence depth was greatest (the structure was shorter). Only a small increase in measured wave height was observed in this location. However, Figure 3d demonstrates a significant increase in the measured wave height, for the location where the submergence depth was smallest. The submerged structure forces the approaching waves to undergo shoaling as they pass over it.

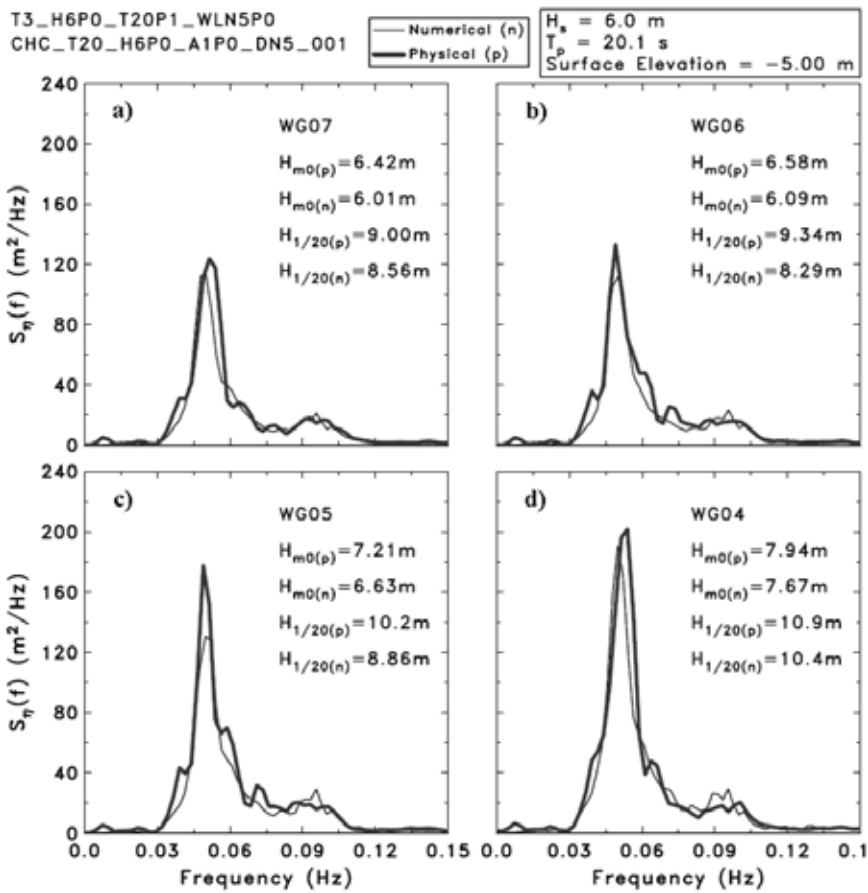

Figure 3. Comparison of wave spectra above the crest of the submerged structure from numerical simulations and physical experiments of Test Case 3.

The wave heights observed at all the down-wave located gauges, for both the physical and numerical model were nearly identical, suggesting, as expected, that the submerged structure increases wave energy dissipation with decreasing submergence depth.

A transfer function provides a measure of the transfer of energy into and out of a system. Transfer functions were defined relating the wave spectra measured down-wave from the submerged structure to spectra measured on the up-wave side. These transfer functions describe the frequency-dependent changes in wave energy due to the presence of the submerged structure. In this case, a distinct pattern in energy transfer across the structure was revealed by the analysis of variance spectra of the wave conditions. Specifically, a significant reduction in energy is observed at the spectral peak frequency f_p, and a significant increase in energy is observed at roughly 1.8 times the spectral peak frequency (see Figure 4).

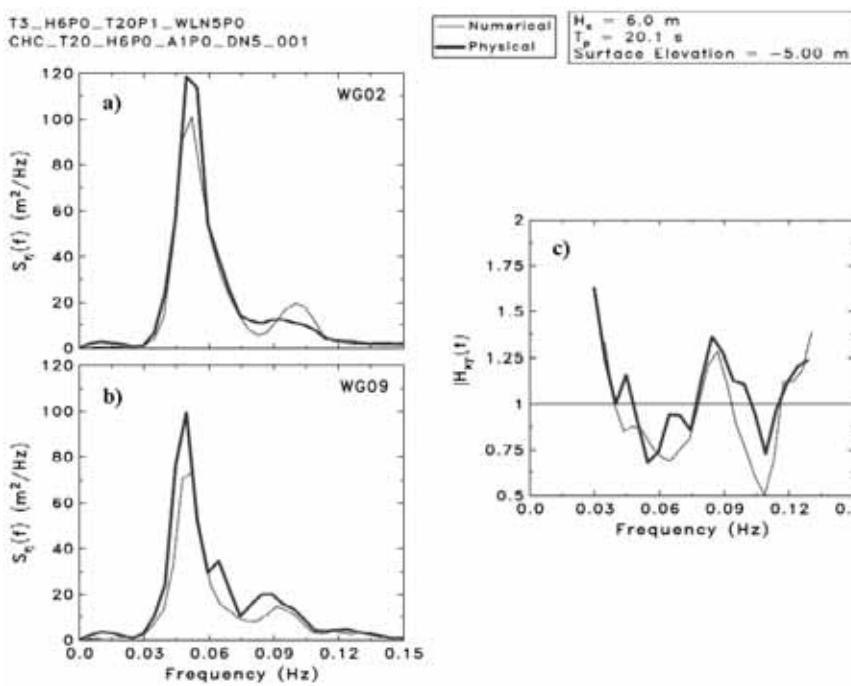

Figure 4. Comparison of transfer functions from numerical simulations and physical experiments of Test Case 3.

Figures 4a and 4b show the up-wave and down-wave spectra respectively, while Figure 4c shows the computed transfer function. Although the results were much more clearly visible in the numerical modelling results, the "W" shape of the computed transfer function was repeatedly observed in both the

numerical and physical modelling results. Also, as expected, the "W" shape was accentuated where the structure freeboard was least, that is, where more energy transfer occurred.

Orbital velocities were measured above the structure's crest at three locations. The influence of the submerged structure was consistently observed in both the physical and numerical model. Figure 5 shows the cumulative distributions of orbital velocities for the three measurement locations.

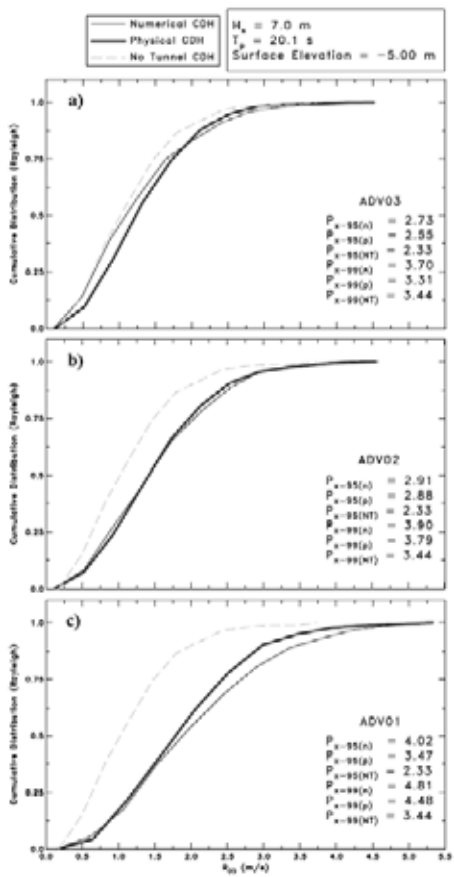

Figure 5. Comparison of orbital velocities above the crest of the submerged structure from physical experiments and numerical simulations of Test Case 4.

The dotted lines show the measured velocities during the undisturbed case before the structure was introduced. In Figure 5a, where the crest of the submerged structure was almost even with the sea floor, there is little difference between the measured and simulated velocities with and without the structure. However, in Figure 5c, both the physical measurements and numerical

simulations show that velocities measured over the crest of the structure increased with increasing crest elevation. As the wave heights increased with each progressive test case, the observed orbital velocities also increased in magnitude.

A reflection analysis was also performed using data from the numerical simulations. For the undisturbed case, no wave reflection was observed since there were no obstructions in the path of the incident waves. However, once the structure was included, a steady increase in reflected wave energy was observed as the freeboard of the structure decreased. In other words, the reflected wave energy was roughly proportional to the submergence depth (height) of the structure. Figure 6 shows an example of the incident and reflected wave trains in front of the part of the structure with lowest freeboard (greatest height) for Test Case 4. The overall reflection coefficient for this case was 35%.

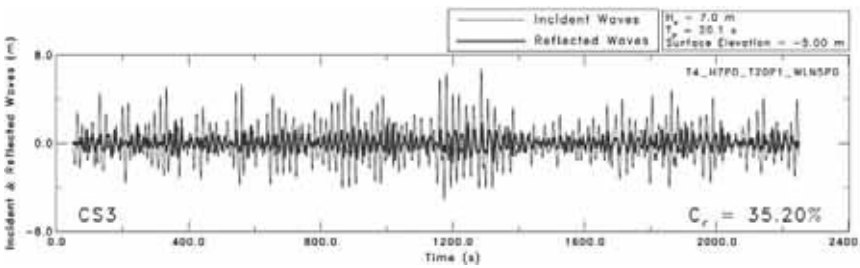

Figure 6. Wave reflection analysis from numerical simulations of Test Case 4.

These results confirm some of the findings of previous researchers. Twu *et al.* (2001) conducted research on deeply submerged breakwaters and developed an equation for calculating wave reflection from such structures. In general, the reflection coefficients computed from the numerical simulations in this study agree very well with the relationship proposed by Twu *et al*.

The spatial distribution of time-averaged wave height around the submerged structure was also examined. The numerical simulations clearly showed the formation of a partial standing wave field in front of the submerged structure, with peaks occurring approximately every half-wavelength. The numerical results also showed that the longitudinally sloping submerged structure induced a circular time-averaged residual current with flow in the direction of wave propagation over the lower part of the structure, balanced by flow in the opposite direction over the higher part (see Figure 7).

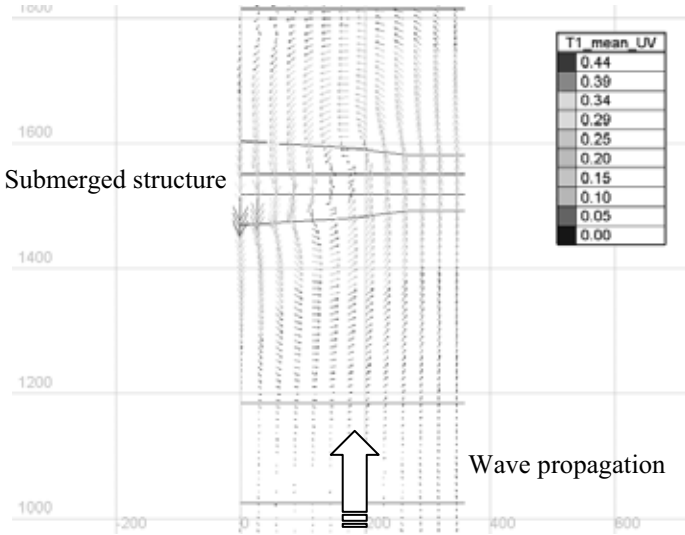

Figure 7. Circular time-averaged current.

Although the WaveSim model has its limitations, the numerical model provided an excellent tool for studying the wave field transformation over a steeply-sloped, three-dimensional submerged structure.

Weston *et al.* (2004) modelled wave groups passing over a shoal and observed the release of free waves as the wave groups returned to deeper water. This phenomenon was clearly reproduced in the present numerical simulations as well. As particularly large waves passed over the submerged structure, the rapid change in water depth induced the waves to steepen and take on a highly non-linear shape associated with the growth of high-frequency harmonics. A portion of this high-frequency energy was released as free waves on the down-wave side of the structure.

Burcharth *et al.* (2006) observed that the freeboard has a large influence in regards to the initiation of damage for low-crested structures. The pattern of damage observed in the physical model study was entirely consistent with this finding. A significant increase in observed damage to the outer armour layer was observed as the freeboard of the structure decreased (as the crest elevation increased).

CONCLUSIONS

Submerged structures are increasingly being considered for use in coastal engineering applications. However, past research has focused on low-crested structures while relatively few studies have specifically dealt with deeply submerged structures. In addition, unlike this study, most previous research considered structures with uniform cross-section and constant submergence

depth (Van der Meer & Daemen (1994), d'Angremond et al. (1996), Seabrook & Hall (1998), Briganti et al. (2003), etc.).

The present study showed that the wave-structure interactions were intense and significantly affected the local hydrodynamic conditions. The submerged structure induced significant transformations to the wave characteristics and generated substantial orbital velocities at the crest of the structure. As expected, the maximum increases in wave height and wave-induced velocities were observed where the submergence depth of the structure was smallest (where the structure crest was highest).

The present study showed that even deeply submerged structures can have complex and important effects on waves and orbital velocities. These effects can be important considerations for the design of the submerged structure itself, the design of other structures nearby, and the assessment of the structure's impact on the surrounding marine environment. The three-dimensional sloping nature of the submerged structure considered herein spawned a circular residual current that would not occur in cases with a uniform crest elevation.

ACKNOWLEDGMENTS

The authors wish to express their gratitude to the Canadian Hydraulics Centre, National Research Council Canada, for providing the experimental facilities and to the Natural Sciences and Engineering Research Council of Canada (NSERC) for its partial financial support for this project.

REFERENCES

Baker, S. 2007. Physical and Numerical Modelling of Wave Interaction with a 3-D Submerged Structure, *M.A.Sc. Thesis, Department of Civil Engineering*, University of Ottawa, 223 pp.

Briganti, R., Van der Meer, J., Buccino, M., & Calabrese, M. 2003. Wave Transmission Behind Low-Crested Structures, *Proceedings of the Conference on Coastal Structures*, 580-592.

Burcharth, H.F., Kramer, M., Lamberti, A., & Zanuttigh, B. 2006. Structural Stability of Detached Low Crested Breakwaters, *Coastal Engineering*, 53, 381-394.

d'Angremond, K., Van der Meer, J.W., & de Jong, R.J. 1996. Wave Transmission at Low-Crested Structures, *Proceedings of the 25th International Conference on Coastal Engineering*, 2418-2427.

Nwogu, O. 1993. Alternative Form of Boussinesq Equations for Nearshore Wave Propagation, *Journal of Waterway, Port, Coastal and Ocean Engineering*, 119(6), 618-638.

Nwogu, O. 1996. Numerical Prediction of Breaking Waves and Currents with a Boussinesq Model, *Proceedings of the 25th International Conference on Coastal Engineering*, 4807-4820.

Seabrook, S.R., & Hall, K.R. 1998. Wave Transmission at Submerged Rubblemound Breakwaters, *Proceedings of the 26th International Conference on Coastal Engineering*, 2000-2013.

Twu, S.-W., Liu, C.-C., & Hsu, W.-H. 2001. Wave Damping Characteristics of Deeply Submerged Breakwaters, *Journal of Waterway, Port, Coastal, and Ocean Engineering*, 127(2), 97-105.

Van der Meer, J.W., & Daemen, I.F.R. 1994. Stability and Wave Transmission at Low-Crested Rubble-Mound Structures, *Journal of Waterway, Port, Coastal, and Ocean Engineering*, 120(1), 19 pp.

Weston, B.P., Taylor, P.H., Borthwick, A.G.L., Hunt, A.C., & Stansby, P.K. 2004. Boussinesq Modelling of Wavegroup Propagation over a Shallow Shoal and the Release of Second Order and Higher Harmonics. *Proceedings of the 29th International Conference on Coastal Engineering*, 1277-1289.

WAVE REFLECTION AT RUBBLE MOUND BREAKWATERS RANGING FROM SUBMERGED TO EXPOSED

Mario Calabrese[1], Pasquale Di Pace[1] and Mariano Buccino[1]

An empirical method is presented to predict wave reflection at permeable rubble mound breakwaters ranging from well submerged to exposed (non-overtopped). It has been validated against a wide ensemble of both regular and random wave experiments and proved to be rather robust. The model can be used for a range of water depths included between 0.01 and 0.25 the deepwater wavelength and for a wave height to depth ratio less than 0.56.

INTRODUCTION

Wave reflection is a major variable to be considered in the design of rubble mound breakwaters (Figure1), as it controls wave velocity in front of the structures and, consequently, scour events and disturbances at the harbour entrance.

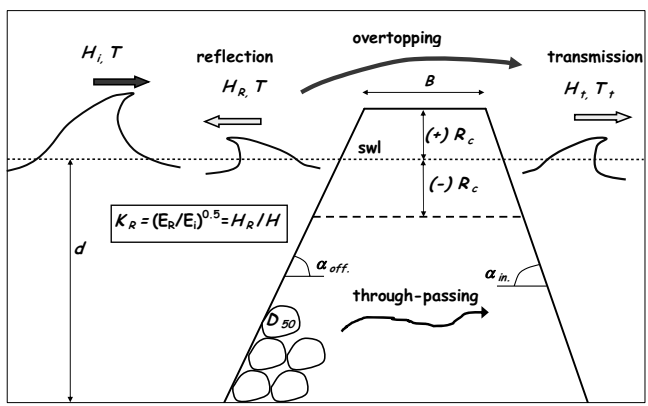

Figure 1. Scheme of wave-structure interaction and definitions.

In the frame of a linear analysis, the most used index to measure wave reflection is the so-called *reflection coefficient* K_R, i.e. the root square of the reflected to incident wave energy ratio.

In the past many authors provided design equations that predicted K_R at straight slopes and non-overtopped breakwaters. Among them, the leading

[1] University of Napoli Federico II, Department of Hydraulic, Geotechnical and Environmental Engineering D.I.G.A., Via Claudio 21, Napoli, 80125, Italy.

works by Miche (1951), Battjes (1974), Seelig (1983) and Postma (1989) have to be mentioned.

Recently, with growing interest in low crested and submerged breakwaters as measures for shore erosion control, many researchers attempted at extending predictive formulae to include this kind of structures; the most interesting examples are those by Garcia Govea (2000) and Zanuttigh and van der Meer (2006). In particular, the latter relies on results of both the European research projects *DELOS* and *CLASH* and likely represents, nowadays, the most robust available design formula.

However some additional efforts on this topic might be still meaningful, mainly with purpose of rendering the equations suited to a range of structural configurations as wide as possible; in fact Garcia Govea formula holds only for surface piercing structures (R_c>0), whereas Zanuttigh and van der Meer doesn't apply to well submerged breakwaters (R_c≤-1). In addition, this formula requires the knowledge of the mean period T_{-10}, based on the spectral moment of order "-1", that may be not ever available, especially at the first stages of design process.

This paper proposes a method for calculating reflection coefficient at rubble mound breakwaters of whatever crest height, ranging from deeply submerged to exposed. It includes two simple expressions, for underwater and surface piercing barriers respectively, that meet each other at $R_c = 0$. The formulae have been calibrated on a large regular wave data base, but proved to be effective also for irregular waves. When applied to random seas, the predictive model uses the peak period as input parameter, which is always known to the designer. In conclusion the proposed tool might be used as an alternative to Zanuttigh and van der Meer formula, either when it is not applicable (R_c≤-1) or when the mean spectral period T_{-10} is not available.

THE CALIBRATION DATA BASE

The predictive formulae presented below are of a pure empirical nature and have been calibrated on two data sets, coming from regular wave experiments, conducted at the University of Naples and at the University of Caen.

Tests at the University of Naples, Italy

The experiments have been carried out at the small scale wave channel of the *D.I.G.A.* Department laboratory, of the University of Naples "*Federico II*". The flume is 23.50m long, 0.80m wide and 0.75m deep and is provided with a piston-type wave-maker capable of generating both regular and spectral waves. Moreover it is equipped with an online active absorption system, which allows minimizing the effects of any undesired reflections or disturbances.

Homogeneous models of rubble mound breakwaters at an approximately 1:20 Froude scale were used. Five crest freeboard R_c (-0.05m, -0.025m, 0m, 0.025m,

0.05m), two crown width B (0.35m and 0.80m) and two front slopes $tan\alpha_{off}$ (1:2 and 1:5) have been employed, to get twenty different models on the whole. Rear slope (1:1.5) and grade of rock (D_{50} = 0.061 m) were kept constant; near half of the tests were conducted with a 0.315m still water depth (d), whereas 350 experiments were performed using either 0.29m or 0.34m. In situ porosity of the breakwater resulted around 0.45. For each structure model, 3 series of regular wave attacks were run, using 3 different periods, namely 1s, 1.5s, 2s. For each period, wave height was increased from 0.02m to 0.12m, at a step of 0.01m.

Tests at the University of Caen, France

The channel where these experiments have been carried out, is 22.0m long, 0.80m wide and 1.0m deep and is provided with an *Edinburgh Design* wave generator. These tests were used to calibrate the Garcia Govea formula. An unique homogeneous cross section 0.40m height has been used, with D_{50} = 0.039m, B = 0.20m and $tan\alpha_{off}$ = 3:4. Water depth at the breakwater toe was varied to get three different crest freeboards, namely -0.10m, 0m and 0.05m. Other tests were conducted using a smooth impermeable structure as well as by inserting an impermeable plate in the body of the porous model; these experiments will be not considered in the following. Regular wave trains were run with 8 different periods, ranging from 1s to 2.5s. Wave heights were varied (not uniformly) from 0.02 m to 0.16m.

As far as techniques for calculating K_R are concerned, both the Mansard and Funke (1980) and the Goda and Suzuki (1976) methods have been used, for both data series, to separate incident and reflected wave spectra. In this paper the two values have been averaged to get a more robust estimate of reflection.

Table 1 summarises main characteristics of data sets.

Table 1. Main characteristics of calibration data base

TEST	#	R_c/H_i	d/L_0	$S_0=H_i/L_0$	$tan\alpha_{off}$	ξ_0	B/D_{50}
NAPLES	660	-2.7 +2.7	0.046 0.218	0.0032 0.0769	0.2 & 0.5	0.72 8.84	5.74 13.11
CAEN	149	-4.3 +1.3	0.036 0.321	0.0021 0.1026	0.75	2.34 16.23	5.13

Note that relative crest freeboard R_c/H_i varies from -4.3 (deeply submerged breakwaters) to 2.7 (nearly non overtopped breakwaters)

THE ALTERNATIVE FORMULA

Emerged breakwaters ($R_c \geq 0$)

The reference scheme for wave reflection at emerged breakwaters is sketched in Figure 2 .For exposed, non-overtopped, barriers the potential energy of the run-up wedge is converted to reflected energy, via run-down (Figure 2-a). However Cross and Sollitt (1972) reasoned this process to be highly un-effective, even for smooth slopes. When the breakwater crest becomes low, compared to run-up height, wave overtopping conveys a certain amount of energy off the structure (Figure 2-b). Yet, it is intuitively clear the latter is not entirely subtracted to reflection, as a certain share would have been dissipated within the conversion process. Finally the role of water depth, d, has to be carefully considered. If we suppose that waves don't break on the foreshore, then we may reasonably assume wave run-up to be independent of the water depth at the toe of the slope (Battjes, 1974). That is, the energy potentially disposable for reflection remains the same for a given seaward slope, wave height and wave period. However, with reducing water depth, the proportion of run up energy disposable for reflection has to spread over a shorter wavelength and, accordingly, the reflected energy per unit of horizontal area, E_R, has to increase. As a consequence, reflection coefficient might increase with reducing water depth, as previously reasoned by Muttray and Oumeraci (2006).

As a result of the above discussion we may set:

$$K_R \cong f\left[\left(\tan\alpha_{off}, \frac{H_i}{L_0}\right); \left(\gamma_f, P\right); \frac{R_c}{H_i}; \frac{d}{L_0}\right] \tag{1}$$

where L_0 is the deepwater wavelength.

The first two variables of Equation (1) govern the run-up height, whereas relative crest freeboard, R_c/H_i, is the primary parameter for wave overtopping. γ_f and P respectively represent a friction factor, that depends mainly on the shape of amour unit, and the notational permeability coefficient (van der Meer, 1988), which is a function of the number of layers the structure consists of. These parameters diminish both wave run up and overtopping rate; consequently they are expected to be relevant primarily for exposed barriers. Obviously our data base (homogeneous rock breakwaters) is not suited to weight the influence of such variables; however, as far as rock armored breakwaters are concerned, Postma's formula indicates reflection coefficient to grow by some 0.15, on average, moving from homogeneous breakwaters (non overtopped with $P = 0.6$) to structures with an impermeable core ($P = 0.1$). On the other hand, as permeable barriers are considered (P from 0.4 to 0.6), the increment becomes rather small, (0.02-0.03). More details on this item are given in a next section.

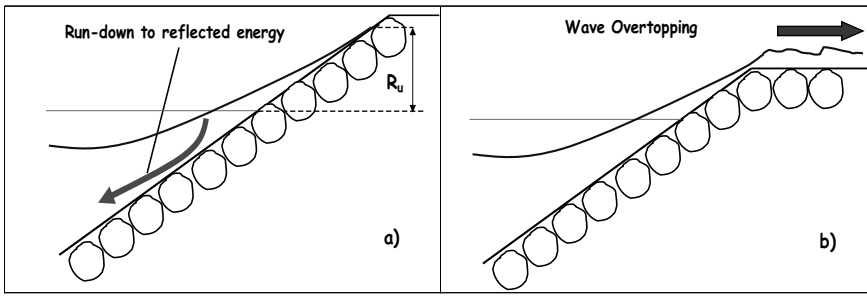

Figure 2. Scheme for reflection at emerged breakwaters.

Regarding the friction factor, an extensive experimental study has been recently published by Bruce et al. (2006), which aims at providing engineers with the most appropriate value of γ_f, for each type of armor unit. Zanuttigh and van der Meer (2006) researched on the relationships between friction parameter and reflection coefficient. However, since present work considers only rock breakwaters, γ_f can be likely assumed to be invariant.

Finally, the following expression has been found to best fit our data:

$$K_R = \left(r + K_{R0}\right) \tag{2}$$

where:

$$\begin{cases} r = 0.44 \cdot \tan\alpha_{off} \cdot exp\left(-30.82 \cdot \dfrac{H_i}{L_0}\right) \cdot tanh\left(\dfrac{R_c}{H_i}\right) \\ K_{R0} = 6.35 \cdot exp\left[1.85 \cdot \tan\alpha_{off} - 5{,}34 \cdot \left(\dfrac{d}{L_0}\right)^{0.1}\right] - 0.28 \cdot \tan\alpha_{off}^{\,2.29} \end{cases} \tag{3}$$

in which K_{R0} represents the reflection coefficient for structures with crest at the mean sea level. This quantity has been found to be nearly independent of the incident wave height. From the freeboard correction factor, r ,we see reflection coefficient to attain its maximum value when R_c/H_i is about 3. It is easy to check, from literature formulae, this relative crest freeboard corresponds to a negligible overtopping discharge.

Submerged breakwaters ($R_c/H_i \leq 1$)

For structures with the crest well below the mean water level ($R_c/H_i \leq 1$), only a weak dependence on relative crest freeboard and front slope angle has been found. Actually in these cases waves travel across the barrier without breaking and wave reflection is dominated by the capability of the barrier of

"absorbing" the incoming wave energy. The higher this capability the lower reflection. In this regard, a similitude with acoustic phenomena suggests the main variables to be likely the wave frequency, the voids amplitude as well as the structure height, h_c, and the porosity, n. Accordingly, the following non-dimensional parameters have been selected:

$$K_{RS} \cong f\left[\frac{L_0}{d};\frac{L_0}{D_{50}};\frac{h_c}{d};n\right] \tag{4}$$

where the median armour diameter, D_{50}, has been thought to be proportional to the voids amplitude.

Comparison with data yielded to the following tentative expression:

$$K_{RS} = 0.0027\frac{L}{D_{50}} \tag{5}$$

where L is the local wavelength at the depth d. Note $\frac{L}{D_{50}}$ includes both $\frac{L_0}{d}$ and $\frac{L_0}{D_{50}}$, because of the linear dispersion relationship. Clearly, effects of structure porosity couldn't be analyzed, even if they might be expected to be some less than for exposed (non overtopped) breakwaters . As far as the structure height to water depth ratio is concerned, no significant influence has been found; this likely because in our data base it fell within a quite narrow range, between 0.8 and 0.9.

When $0 \le R_c/H_i \le 1$, a reasonable estimate of reflection coefficient can be obtained by a simple linear interpolation between K_{RS} (Equation (5)) and K_{R0} (Equation (3)). This also ensures the continuity of the predictive curve. Hence we have, for a generic submerged breakwater:

$$K_R = K_{R0} + \left(K_{R0} - K_{RS}\right)\cdot max\left(\frac{R_c}{H_i};-1\right) \tag{6}$$

The comparison with data (Figure,3) shows a reasonable agreement, although the value of determination index (R^2 = 0.71) suggests the formula to possess only a moderate predictive power. However the standard error is about 0.037; this means 90% of point are expected to fall into an interval with a 0.061 semi-band about the predicted values (dashed-lines). That is quite acceptable to empirical formulae.

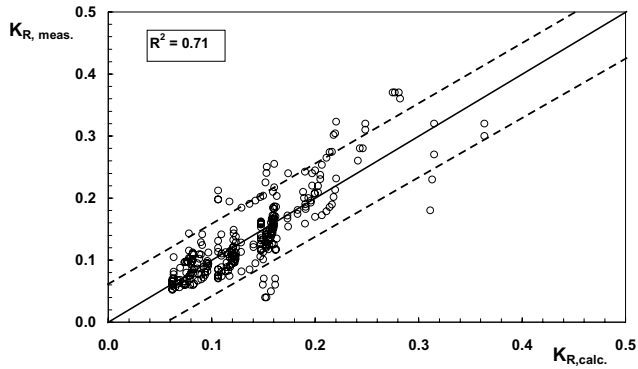

Figure 3. Comparison between experimental data and Equation (6).

General performances of the predictive model

Figure 4 compares design equations and experimental data, keeping together both submerged and emerged barriers. The agreement is quite good and the overall determination index, R^2, is about 0.82. Although the predictive model is made up on two different formulae, the scatter can be considered as coming from an unique Gaussian distribution, with a mean equal to zero and a standard deviation equal to 0.046. This implies that measured values of reflection coefficient fall within intervals of semi-band ± 0.075 (around the predictions), with a 90% probability. In the case of surface-piercing structures ($R_c > 0$), present model performs slightly worse than Garcia Govea formula; the former has a standard error 0.055, while the latter has 0.051 (Figure 5-a). However, when "no-freeboard" breakwaters are considered ($R_c = 0$, Figure 5-b), Equation (3) still gives good predictions, whereas Garcia Govea performs poorly in most of cases (note that the author suggested to use the formula only for $R_c > 0$). A further check of reliability has been performed by comparing the prediction model to the results of physical model tests recently carried out at the University of Florence; the experiments are described in Clementi et al. (2006). Regular and random waves have been run on both submerged and emerged homogeneous breakwaters. Two front slope angles have been used, namely $tan\alpha_{off}$ 0.25 and 0.5. For regular waves (Figure 6), the agreement is quite good; the number of points exceeding the confidence bands equals 4 over 40, that was numerically expected. However those four data all indicate under-prediction. For random waves (Figure 7) results are unexpectedly satisfying; no outliers have been found. Note for spectral waves, the design formulae have been applied by using as wave parameters the incident significant wave height H_{si} and the peak period, T_p.

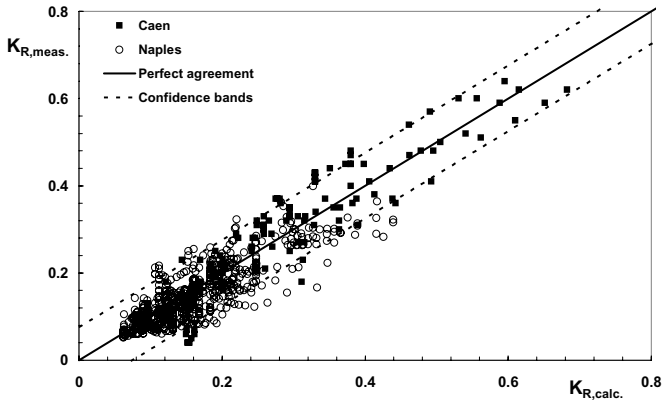

Figure 4. Predictive model vs. calibration data base

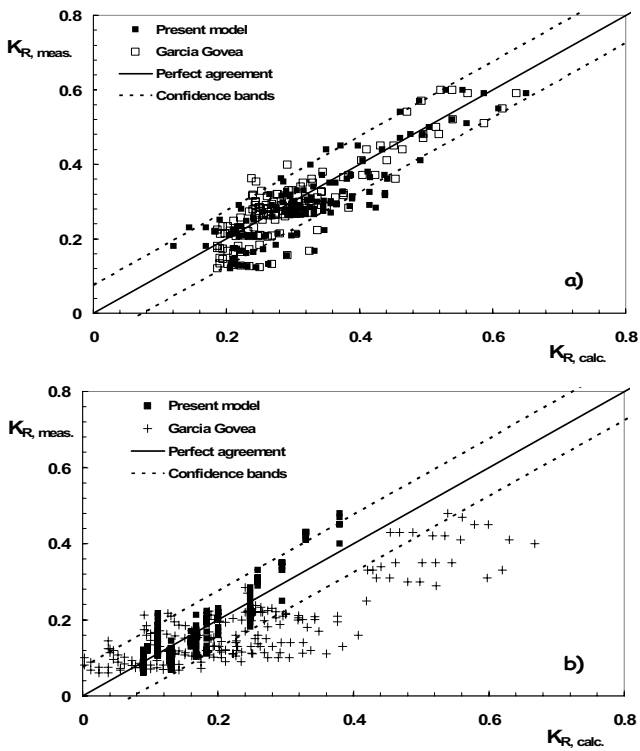

Figure 5. Present model vs. Garcia Govea formula: a) R_c>0; b) R_c= 0

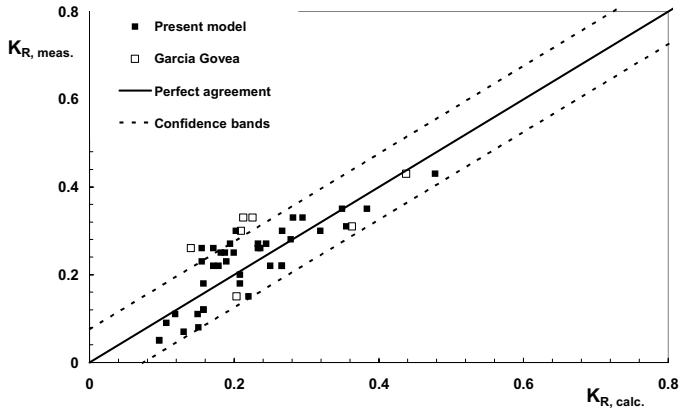

Figure 6. Present model vs. Clementi et al. (2006) data. Regular waves

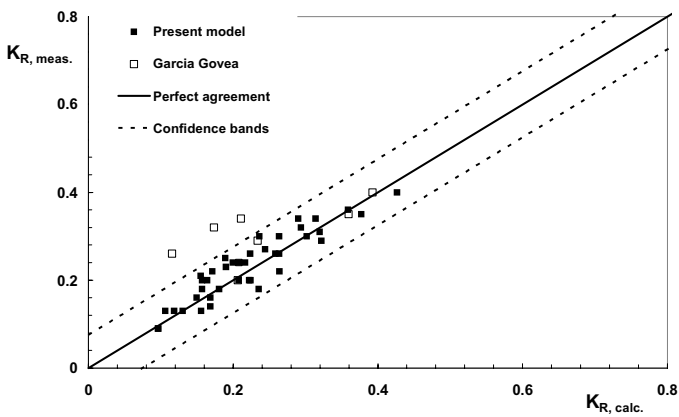

Figure 7. Present model vs. Clementi et al. (2006) data. Random waves.

Accounting notational permeability, P

As a supplementary check of the robustness of proposed method, Equation (3) has been tested against the experiments used by Postma (1989) in developing his formula for conventional non-overtopped rock breakwaters. Since wave overtopping was prevented and no information on crest freeboard is provided in the report, a fictional value R_c/H_{si} =3 has been set for calculations. For homogeneous structures (P = 0.6) Equation (3) has been found to compare pretty well with data, while some underestimation has been detected for the cases

P = 0.5 and P = 0.1. Thus a correction has been introduced in the freeboard

factor *r*, to tentatively account the effects of permeability. The new formulation reads:

$$r = \tan\alpha_{off} \cdot exp\left(-30.82 \cdot \frac{H_i}{L_0} - 1.3P\right) \cdot tanh\left(\frac{R_c}{H_i}\right) \tag{7}$$

The comparison with data is shown in Figure 8, which reveals a substantial equivalence between present (modified) model and Postma formula:

$$K_R = 0.081 \cdot P^{-0.14} \cdot \tan\alpha_{off}{}^{0.78} \cdot s_{0p}^{-0.44} \tag{8}$$

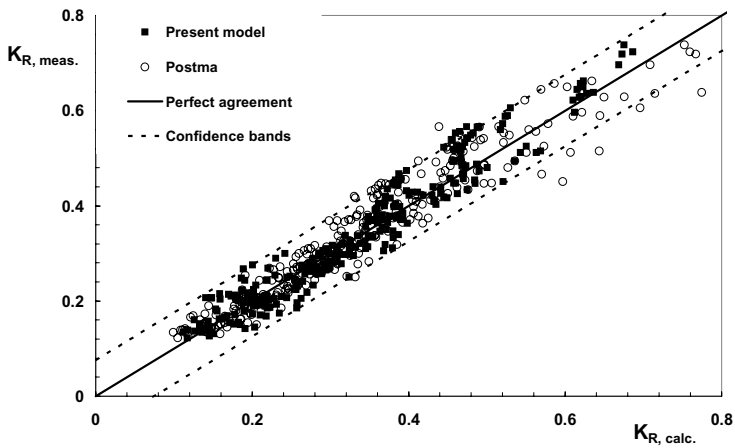

Figure 8. Present model vs. Postma data.

As a final remark it should be noted that no comparison with Zanuttigh and van der Meer formula has been presented due to the lack of knowledge about the mean wave period T_{-10}.

SUMMARY AND RECOMMENDATIONS

The paper has presented a method to predict wave reflection at rubble mound rock armoured breakwaters, ranging from well submerged to non overtopped. The analysis of nearly 1300 random and regular wave experiments led to the following final equations:

$$\begin{cases} K_R = K_{R0} + r & for \quad R_c \geq 0 \\ K_R = K_{R0} + \left(K_{R0} - K_{RS}\right) \cdot max\left(\frac{R_c}{H_{si}}; -1\right) & for \quad R_c \leq 0 \end{cases} \tag{9}$$

where:

$$\begin{cases} r = tan\,\alpha_{off} \cdot exp\left(-30.82 \cdot \frac{H_{si}}{L_{0p}} - 1.3P\right) \cdot tanh\left(\frac{R_c}{H_{si}}\right) \\ K_{R0} = 6.35 \cdot exp\left[1.85 \cdot tan\,\alpha_{off} - 5{,}34 \cdot \left(\frac{d}{L_{0p}}\right)^{0.1}\right] - 0.28 \cdot tan\,\alpha_{off}^{\,2.29} \\ K_{RS} = 0.0027 \cdot \frac{L_p}{D_{50}} \end{cases} \tag{10}$$

Equations (9-10) are written with reference to the random wave variables H_{si} (incident significant wave height), L_{0p} (peak deep water wavelength) and L_p (local peak wavelength). Structural quantities are crest freeboard (R_c), front slope angle ($tan\alpha_{off}$), water depth at the toe of the structure (d), armour median diameter (D_{50}) and notational permeability (P).

In some cases K_{RS} can give values of reflection coefficient larger than K_{R0}; this may be not considered as un-reasonable, because when the structure height approaches the mean sea level, waves may break onto the seaward slope, dissipating a significant amount of energy. However the model could be further simplified by using K_{R0} for submerged breakwaters ($R_c \leq 0$) and maintaining, at the same time, an acceptable degree of accuracy. Although some rock armoured barriers with an impermeable core have been used in the calibration (P = 0.1 in the Postma data), the formulae apply essentially to structures with a permeable core (P = 0.5 and 0.6). Finally Equations (9-10) must be used within the ranges:

$$\begin{cases} 0.01 \leq \frac{d}{L_{0p}} \leq 0.25 \\ \frac{H_{si}}{d} \leq 0.56 \end{cases} \tag{11}$$

ACKNOWLEDGMENTS

The authors gratefully acknowledge Dr. Garcia Govea for having kindly provided results of experiments conducted at the University of Caen.

REFERENCES

Battjes, J. A., 1974. Surf similarity, ASCE, *Proc. of 14th International Conference on Coastal Engineering*, Copenhagen, Denmark, 1: 446-480.

Bruce, T., van der Meer, J. W., Franco, L., Pearson, J. M., 2006. A comparison of overtopping performance of different rubble mound breakwater armour, ASCE, *Proc. of 31th International Conference on Coastal Engineering*, San Diego, USA.

Clementi, E., Cappietti, L., Martinelli, L., 2006. Analisi sperimentale di tracimazione, piling up e filtrazione per scogliere a cresta bassa. *Atti del XXX° convegno di Idraulica e Costruzioni Idrauliche – IDRA 2006*, Roma, Italia, 2006.

Cross, R. H., Sollitt, C. K., 1972. Wave Transmission by Overtopping., ASCE. *Journal of the Waterways, Port, Coastal and Ocean Engineering*, vol. 98, n. 3: 295-309.

Garcia Govea, M.C., 2000. Etude expérimentale de l'action de la houle sur les digues semi-summersibles. Ph.D Thesis, U.F.R.: Sciences de la terre et amenagement regional, Universite de Caen, France.

Goda, Y., Suzuki, Y., 1976. Estimation of incident and reflected waves in random wave experiments, ASCE, *Proc. of 15th International Conference on Coastal Engineering*, Honolulu, Hawaii, 1: 828-845.

Mansard, E.P.D., Funke, E.R., 1980. The measurements of incident and reflected wave spectra using a least square method, ASCE, *Proc. of 17th International Conference on Coastal Engineering*, Sydney, Australia, 1:154-172.

Miche, M., 1951. Le pouvoir réfléchissant des ouvrages maritimes exposés à l'action de la houle. Annales des Ponts et Chaussées, Paris.

Muttray, M., Oumeraci, H., ten Over, E., 2006. Wave reflection and wave run-up at rubble mound breakwaters, ASCE, *Proc. of 30th International Conference on Coastal Engineering*, San Diego, California, USA.

Postma, G. M., 1989. Wave reflection from rock slopes under random wave attack. Master thesis, Delft University of Technology, Department of Civil Engineering, pp. 106.

Seelig, W.N., 1983. Wave reflection from coastal structures, Balkema, *Proc. of the Int. Conference on Coastal Structures 1983*, Arlington, Virginia, USA, 1: 961-973.

van der Meer, J.W., 1988. Rock slopes and gravel beaches under wave attack. PhD thesis, Delft University of Technology, Department of Civil Engineering.

Zanuttigh, B., van der Meer, J.W., 2006. Wave reflection from Coastal Structures, ASCE, *Proc. of 30th International Conference on Coastal Engineering*, San Diego, California, USA.

OPTIMUM REPAIR PLAN FOR DETACHED BREAKWATERS INCLUDING INFLUENCES OF WAVE GROUPING CHARACTERISTICS OF INCIDENT WAVES

Susumu Araki[1], Gou Urai[2], Hirotoshi Makino[3], Mamoru Arita[1] and Ichiro Deguchi[1]

This paper describes the estimation of maintenance costs during the lifetime for detached breakwaters. In estimating the cost, the influences of wave grouping characteristics in incident waves is included. The repair criterion is determined on the basis of the decrease in the hydraulic performance of the detached breakwater. The authors show that the total cost is higher in the case where the mean length of the run of the high waves in the incident wave is larger.

INTRODUCTION

Maintenance cost of coastal structures during their lifetime should be minimized. Too frequent repair needs high repair cost; however, insufficient repairs may lead to catastrophic damage to coastal structures and surrounding area. The percentage of the coastal structures constructed more than 30 years ago is increasing in Japan. Therefore, effective repair of the coastal structures is very important.

Repair of coastal structures, *e.g.*, breakwaters, should be determined on the basis of the decrease in the breakwater performances; this will help reduce the maintenance costs of the breakwaters during their designed lifetime, *i.e.*, life cycle cost. However, the repair of breakwaters is currently determined on the basis of the degree of the displacement or the deformation of breakwaters because the change in breakwater performances with their deformation has not been investigated sufficiently.

Matsubuchi and Yokota (1999) investigated the life cycle cost of berthing facilities. Nagao and Matsubuchi (1999) investigated the life cycle cost and allowable failure probability of composite breakwater. Nanba *et al*. (2003) pointed out the necessity of regular and effective maintenance of coastal structures, *i.e.*, life cycle management. Yoshioka and Nagao (2004) investigated a design method for minimizing the life cycle cost and they compared the life cycle cost of a breakwater designed by such a design method with that designed by the present design method. Takayama *et al*. (2007) proposed a procedure for determining the optimum size of armor units by selecting the minimum life cycle cost.

[1] Dept. of Civil Eng., Osaka University, 2-1 Yamada-oka, Suita, Osaka, 565-0871, Japan
[2] Matsushita Systems Software, Co. LTD, Japan
[3] Dept. of Management of Industry and Technology, Osaka University, Japan

The authors have investigated the deformation of rubble mound structures and the change in the hydraulic performances of rubble mound structures (Araki *et al*., 2002; Araki *et al*., 2004; Araki *et al*., 2005). The authors have also proposed a method for estimating the repair costs for rubble mound breakwaters (Araki *et al*., 2007). In this study, the method proposed by Araki *et al*. (2007) is improved and the optimum repair criterion for detached breakwaters is investigated. In the estimation of the expected total repair cost, the influences of wave grouping characteristics in incident waves on the total cost of detached breakwaters are taken into account.

MODEL FOR ESTIMATING TOTAL REPAIR COST

Outline of the Model

The authors estimated the total repair cost of rubble mound breakwaters (Araki *et al*., 2007). The total repair cost was assumed to be composed of the cost of repairing the breakwater body and the cost equivalent to the amount of damage to the coastal zone. The total repair cost over a designed lifetime was estimated from the probability distribution of occurrence of the incident wave height, the criteria for repairing the breakwater body, the criteria for damage to the coastal zone and the relationship among the incident wave heights, transmitted wave heights and deformation of breakwater bodies.

In this study, the method for estimating the total repair cost was improved by considering the influence of wave grouping characteristics. The procedure for estimating the performances of breakwaters was also improved.

Procedure for Estimating Total Repair Cost

The lifetime of breakwaters is assumed to be 50 years. The total cost over a designed lifetime is estimated by Monte Carlo simulation. The procedure for estimating the total repair cost is as follows:

(i) The probability distribution of occurrence of the incident wave height is determined by using the annual maximum wave height measured in the ocean.
(ii) The annual maximum wave height of the incident wave is determined by generating a random number that satisfies the probability distribution.
(iii) The degree of wave grouping in the generated incident wave is determined (highly grouped wave or less grouped wave).
(iv) The degree of deformation caused by the wave attack of the incident wave is estimated.
(v) The transmitted wave height behind the deformed breakwater is estimated.
(vi) If the criteria for repairing the breakwater body are satisfied or if damage occurs to the coastal zone, the cost of repairing the breakwater body or the cost equivalent to the amount of damage to the coastal zone is estimated.

(vii) The above procedure, from steps (i) to (vi), is performed annually. Therefore, the steps are annually iterated until the end of the designed lifetime of the breakwater.

(viii) Steps (i) to (vii) are iterated with different random numbers (Monte Carlo simulation).

The probability distribution of occurrence of the incident wave height in Step (i) was determined to be a Weibull distribution with parameters A=1.87, B=4.20 and k=2.0 from the measured wave height (NOWPHAS data, Nagai *et al*., 1994). This probability distribution does not correspond to waves in front of the rubble mound breakwater but also to deep water waves. Therefore, the wave heights generated from this probability distribution were reduced by using the assumed physical model scale in hydraulic experiments.

The degree of the deformation of the breakwater and the transmitted wave height behind the detached breakwater were measured in the hydraulic experiments. The details of the hydraulic experiments are mentioned later.

Index of Breakwater Performance

As mentioned above, repair of breakwaters should be determined on the basis of the decrease in the breakwater performance. One of the major functions of detached breakwaters is to advance the shoreline by maintaining tranquility behind the detached breakwaters. Therefore, the degree of the transmitted wave height behind the breakwaters is the index of the performance of detached breakwaters.

Araki *et al*. (2007) used two types of transmitted wave height to express breakwater performances. The first one was the transmitted wave height for estimating costs of repairing the breakwater body, and the other one was the transmitted wave height for estimating costs equivalent to the amount of damage to the coastal zone behind the breakwater. In this study, the transmitted wave height is used only for estimating the costs equivalent to the amount of damage to the coastal zone behind the breakwater. In order to estimate the cost of repairing detached breakwater bodies, the degree of the deformation of the breakwater bodies is used because the degree of the deformation of the breakwater bodies can be related to the change in the transmitted wave height.

HYDRAULIC EXPERIMENTS

Experimental Setup

Hydraulic experiments were conducted in a two-dimensional wave flume shown in Fig. 1 in order to investigate the relationship among the incident wave height, the deformation of the detached breakwater body and the transmitted wave height. The detached breakwater was constructed on a fixed flat bed in the wave flume. The core of the detached breakwater consisted of crushed stones with nominal diameter D_{50}=1.59cm and it was armored with wave dissipating blocks of 14.5g. The crest width B was 24cm, the crest height above the still

water level h_c was 5cm and the depth at the toe of the breakwater h was 25cm. The slope of the surface of the breakwater was 1:4/3. The scale was assumed to be approximately 1/25.

Water surface elevations in front of and behind the detached breakwater were measured by using a capacitance wave gauge. The profile of the detached breakwater was measured by using a laser profiler in a 3cm interval along the cross-shore direction after the incidence of every 2000 or 4000 waves.

Incident Waves

Irregular waves were used as incident waves. The target spectrum of the incident wave was Bretschneider-Mitsuyasu spectrum. The significant wave period was $T_{1/3}$=1.5s and the significant wave height was $H_{1/3}$=6.2–8.0cm in front of the wave paddle. Irregular waves with different wave grouping characteristics were generated by changing the phase between component waves in the irregular waves. The incident waves used in the hydraulic experiments are shown in Table 1. The mean length of the run of the high waves was defined as a sequence of wave heights which exceeded the threshold. In this study, the threshold was the significant wave height $H_{1/3}$. Fig. 2 shows the measured time series of water surface elevations of Waves 3 and 4 under the condition that breakwaters were not installed in the wave flume.

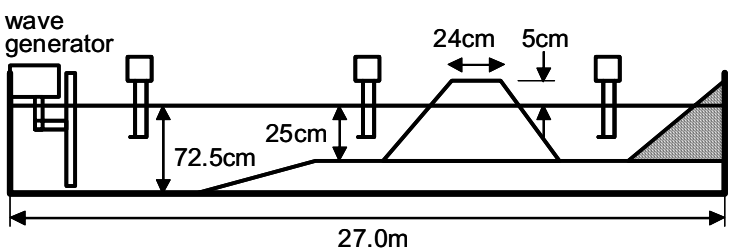

Figure 1. Experimental setup

Table 1. Incident waves.

	$H_{1/3}$ (cm)	$T_{1/3}$ (s)	Mean length of run of high waves
wave 1	6.2	1.5	1.73
wave 2	6.3	1.5	1.00
wave 3	7.7	1.5	1.28
wave 4	7.7	1.5	1.00
wave 5	8.0	1.5	1.62
wave 6	8.0	1.5	1.00

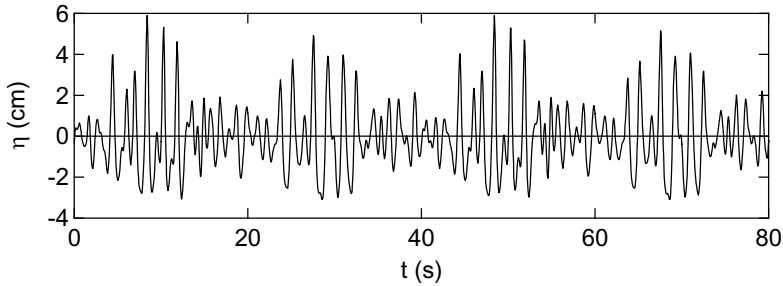

(a) Wave 3

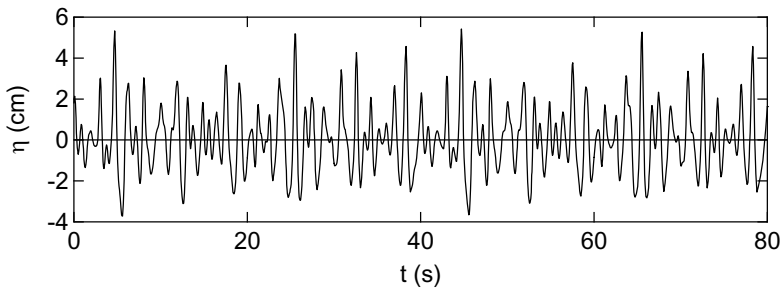

(b) Wave 4

Figure 2. Time series of water surface elevation

Deformation of Breakwater Body

Figs. 3(a) and (b) show the deformations of the breakwater bodies caused by Waves 3 and 4, respectively. The horizontal axis shows the cross shore distance normalized by the wavelength at the toe of the breakwater for the significant wave period $L_{1/3}$. The vertical axis is normalized by the depth at the toe of the breakwater h. The thin solid line shows the initial profile of the breakwater. The thick solid lines in Figs. 3(a) and 3(b) show the deformed profiles after the generation of 8,000 waves and 16,000 waves, respectively. The magnitude of the deformation caused by Wave 3 was much larger than that caused by Wave 4. The mean length of the run of the high waves has a great influence on the deformation of the rubble mound structures as indicated by Johnson *et al*. (1978).

However, the difference between deformations caused by Waves 1 and 2 was very small because the incident wave heights in these cases were not sufficiently large to cause deformation in the breakwater body. The difference between deformations caused by Waves 5 and 6 was also small because the incident wave heights in these cases were so large that the wave dissipating

blocks moved easily. In other words, the influence of the incident wave height on the breakwater deformation was larger than that of the mean length of the run of the high waves in these cases.

When the significant wave height of the incident wave was less than 6cm, no or little deformation in the detached breakwater body was confirmed in advance.

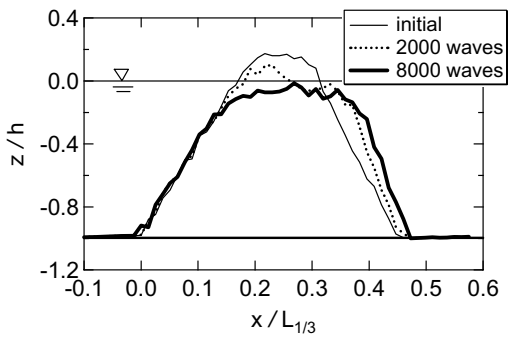

(a) Deformation caused by Wave 3

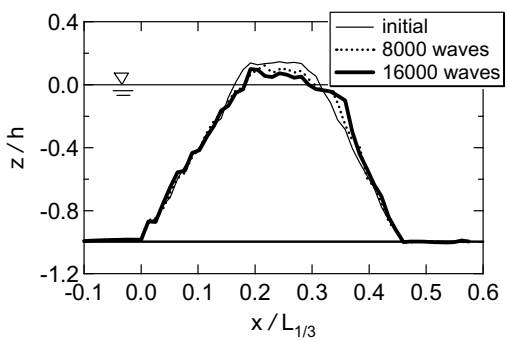

(b) Deformation caused by Wave 4

Figure 3. Deformation of breakwater body

Figs. 4(a) and 4(b) show the relationships between the damage level S ($S=Ae/D_{50}^2$, Ae: eroded area in the cross section of the breakwater, D_{50}: nominal diameter of the armor unit) and the number of the incident wave N under the influence of Wave 3 and Wave 4, respectively. The value of damage level S increases with the increase in the number of the incident wave N. In particular, the rate of increase in the number of the incident wave N at the beginning of the

wave generation is large. Therefore, the measured damage level was fitted into a square root function. The fitted curves are illustrated in Figs 4(a) and 4(b).

Figs. 5(a) and 5(b) show the relationship between the transmitted wave height behind the breakwater H_t and the damage level S under the influence of Wave 3 and Wave 4, respectively. The vertical axis shows the transmitted wave height normalized by the crest height above the still water level h_c. Under the condition of no deformation (S=0), the incident wave was transmitted behind the detached breakwater because the detached breakwater used in this experiment was permeable and had a low crest. The transmitted wave height for the incident wave of Wave 3 was larger than that of Wave 4 because the decrease in the crest height of the breakwater under the influence of Wave 3 was larger than that under the influence of Wave 4. The measured transmitted wave height was fitted into a linear function. The fitted lines are illustrated in Figs 5(a) and 5(b).

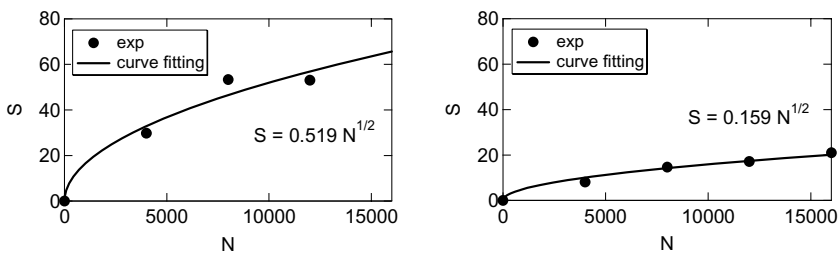

(a) under Wave 3 **(b) under Wave 4**

Figure 4. Relationship between *S* and *N*

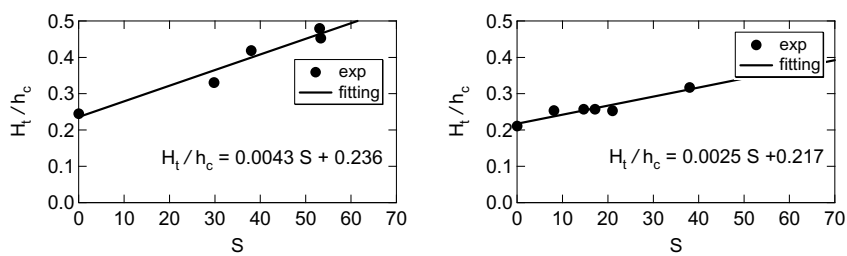

(a) under Wave 3 **(b) under Wave 4**

Figure 5. Relationship between H_t and S

DETAIL OF ESTIMATING TOTAL REPAIR COST

Detailed Procedure

As mentioned before, the detached breakwater body was repaired when the damage level S exceeded the allowable deformation, *i.e.*, the threshold for repairing the breakwater body, S_c in this study. The coastal zone behind the detached breakwater was damaged when the transmitted wave height H_t exceeded the threshold of the damage to the coastal zone H_{tc}. The detailed procedure for estimating the total repair cost is given as follows:

(i) The annual maximum incident wave height is generated on the basis of the probability distribution of occurrence.
(ii) The generated annual maximum incident wave height is classified into the 6 waves shown in Table 1 (Wave 1 – Wave 6).
(iii) The difference in the mean length of the run of the high waves, *e.g.*, the difference between Wave 1 and Wave 2, is determined by using another uniform random number.
(iv) The duration of the incident wave is assumed to be 2,000 waves and the damage level S after the generation of 2,000 waves is estimated from Fig. 4 (Fig. 4 shows the graphs for Waves 3 and 4).
(v) The transmitted wave height behind the detached breakwater H_t is estimated from Fig. 5 (Fig. 5 shows the graphs for Waves 3 and 4).
(vi) If the estimated damage level S exceeds the allowable deformation, the cost of repairing the breakwater body is estimated.
(vii) If the estimated transmitted wave height H_t exceeds the threshold of damage to the coastal zone behind the detached breakwater, the cost equivalent to the amount of damage to the coastal zone is estimated.

History of Incident Wave

If the magnitude of the deformation of the breakwater body is less than the criterion for repairing the breakwater body, the detached breakwater is not repaired. As a result, the incident waves attack the deformed breakwater. In the model described in this study, the history of the incident waves is taken into account as follows:

Consider an example of the incidence of 2,000 waves of Wave 4 after the incidence of 2,000 waves of Wave 3.

(i) The damage level S after the incidence of 2,000 waves of Wave 3 is estimated from Fig. 4(a) (S=0.519$N^{1/2}$).
(ii) The number of the incident waves of Wave 4 equivalent to the estimated damage level S is calculated from Fig. 4(b) (N'=(S/0.159)^2).
(iii) The calculated number of the incident waves N' is added to the number of the next incident waves of Wave 4 (N_0=2,000). Then, the damage level after the incidence of N'+N_0 of Wave 4 is estimated from Fig. 4(b).

Estimation of Cost of Repairing Breakwater Body and Cost Equivalent to Amount of Damage

The cost of repairing the breakwater body C_r was assumed to be proportional to the volume of the eroded area of the detached breakwater body and it was estimated as follows:

$$C_r = C_{ru} \times A_e \times b + C_{r0} \qquad \text{for } S > S_c \tag{1}$$

$$C_r = 0 \qquad \text{for } S < S_c \tag{2}$$

where S_c represents the non-dimensional allowable deformation which represents the wave absorbing performance of the detached breakwater, *i.e.*, the repair criterion, C_{ru} represents the cost of repairing the breakwater body per unit volume of the breakwater body, A_e the eroded area in a cross-section, C_{r0} the cost of repairing the breakwater body independent of the volume of eroded area and b is the longshore distance of the eroded area (in this study, b=1.0m because of the two-dimensional investigation)

The cost equivalent to the amount of damage to the coastal zone behind the detached breakwater C_d was assumed to be simply proportional to the transmitted wave height because it varies according to the circumstances. The cost C_d was estimated as follows:

$$C_d = C_{da} \times \left(H_t / h_c - H_{tc} / h_c \right) + C_{db} \qquad \text{for } H_t > H_{tc} \tag{3}$$

$$C_r = 0 \qquad \text{for } H_t < H_{tc} \tag{4}$$

where C_{da} and C_{db} are the constants that depend on the condition of land use in the coastal zone behind the detached breakwater, and H_{tc} is the transmitted wave height that represents the threshold of the damage to the coastal zone behind the detached breakwater.

The total repair cost C_t during the designed lifetime of the detached breakwater was estimated by summing up the cost of repairing the breakwater body and the cost equivalent to the amount of damage to coastal zone behind the detached breakwater in every year. In summing up both the costs, the interest was assumed to be 0.04.

ESTIMATED RESULTS

Change in C_r and C_d

Fig. 6 shows an example of the estimated results. The horizontal axis shows the non-dimensional allowable deformation, *i.e.*, the repair criterion, and the vertical axis shows the costs C_r and C_d and the total cost C_t (the sum of the C_r and C_d). In the figure, the thin solid, dotted and thick solid lines show the costs C_r, C_d and C_t, respectively. The probability of occurrence of the waves in which the mean length of the run of the high waves is larger γ was 50%. The non-

dimensional transmitted wave height that represents the threshold of damage to the coastal zone behind the detached breakwater was H_{tc}/h_c=0.39. The constant for estimating the breakwater body C_r was C_{ru}=74.6 thousand JPY/m^3 (JPY: Japanese Yen). The constants for estimating the cost equivalent to the amount of damage C_d were C_{da}=95 million JPY/m and C_{db}=222.4 thousand JPY/m.

In the range of smaller S_c, the cost of repairing the breakwater body C_r is higher because a slight deformation in the detached breakwater is repaired immediately. The cost equivalent to the amount of damage to the coastal zone behind the detached breakwater C_d is nearly zero because the transmitted wave height never increases. In the range of larger S_c, the cost of repairing the breakwater body C_r is lower because the frequency of repairing the breakwater body is lower. The cost equivalent to the amount of damage to the coastal zone behind the detached breakwater C_d is higher because the transmitted wave height increases. From these characteristics, the lowest total cost (optimum criterion) can be found at S_c=36 in the figure.

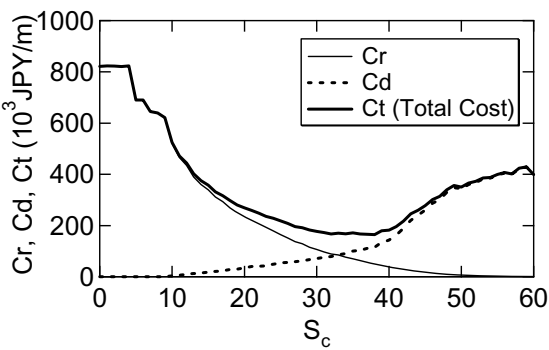

Figure 6. Example of estimated C_r, C_d and C_t

Influence of γ on Total Cost C_t

Fig. 7 shows the influence of the probability of occurrence of the mean length of the run of the high waves γ on the total cost C_t. The non-dimensional transmitted wave height that represents the threshold of the damage to the coastal zone H_{tc}/h_c and the constants C_{ru}, C_{da} and C_{db} used in this estimation were the same values used in Fig. 6. The total cost C_t increases with the increase in the probability of occurrence of the mean length of the run of the high waves γ. Under such condition, the influence of the probability of occurrence of the mean length of the run of the high waves γ on the total cost C_t is higher in the range of the larger non-dimensional allowable deformation S_c. In the case where

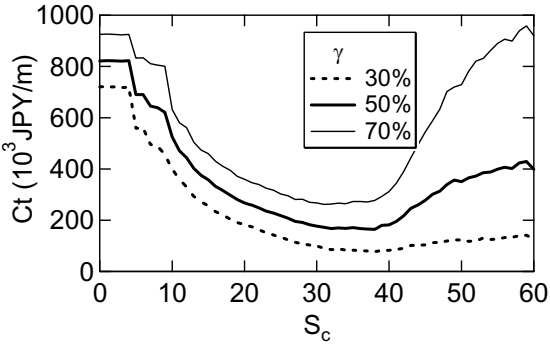

Figure 7. Influence of γ on total cost C_t (H_{tc}/h_c=0.39)

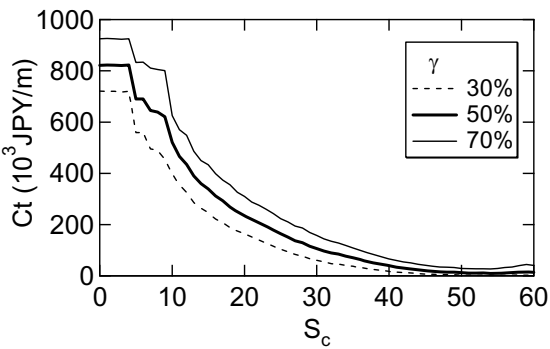

Figure 8. Influence of γ on total cost C_t (H_{tc}/h_c=0.45)

the mean length of the run of the high waves in the incident wave is large, *i.e.*, Waves 1, 3 and 5, the total cost is high because of the large deformation of the breakwater body and the large transmitted wave behind the breakwater as shown in Fig. 3. Therefore, the total cost C_t increases with the increase in the probability γ. There is no significant difference between the allowable deformations at which the total cost is the lowest for three different values of probability γ.

Fig. 8 shows the influence of the probability of occurrence of the mean length of the run of the high waves γ on the total cost C_t under the condition of the non-dimensional transmitted wave height that represents the threshold of the damage to the coastal zone H_{tc}/h_c=0.45. The constants C_{ru}, C_{da} and C_{db} were the

same values used in Fig. 6. The total cost C_t also increases with the increase in the probability of occurrence of the mean length of the run of the high waves γ as shown in Fig. 7. However, the variation in the total cost C_t is different from that shown in Fig. 7. The influence of the probability of occurrence of the mean length of the run of the high waves γ on the total cost C_t is higher in the range of a smaller non-dimensional allowable deformation S_c. In the range of the larger non-dimensional allowable deformation S_c, the total cost C_t is low. The lower total cost in this range results from the lower cost equivalent to the amount of the damage to coastal zone because the threshold of the damage to the coastal zone behind the detached breakwater is higher (H_{tc}/h_c=0.45).

SUMMARRY

In this study, the total repair costs (the sum of the cost of repairing the breakwater body and the cost equivalent to the amount of damage to coastal zone behind the detached breakwater) during the designed lifetime for detached breakwaters were estimated including the influence of the wave grouping characteristics of the incident waves. In the case where the mean length of the run of the high waves in the incident wave was larger, the total cost was higher because the deformation of the breakwater body and the transmitted wave height behind the detached breakwater were larger. However, it is noted that the detailed variation in the total cost depended on the value of the threshold of the damage to the coastal zone behind the detached breakwater and the constants in the equations by which the costs were estimated.

ACKNOWLEDGMENTS

Several parts of this research were financially supported by the Grant-in-Aid for Young Scientists (B) (No. 19760340) of The Ministry of Education, Culture, Sports, Science and Technology of Japan, for which the authors express their appreciation. The authors also express their sincere gratitude to Fudo Tetra Corporation for permitting them to use the model of wave dissipating blocks.

REFERENCES

Araki, S., Y. Kotake, T. Kanazawa, A. Matsumura and I. Deguchi. 2002. Development of Numerical Simulation Method for Predicting Deformation of Rubble Mound Seawall. *Proc. of 28th Int'l Conference on Coastal Engineering*, ASCE, 1485–1497.

Araki, S., T. Yanagihara, H. Niijima, H. Fumoto and I. Deguchi. 2004. Differences between Deformations in Two- and Three-dimensional Experiments. *Proc. of 14th Int'l Offshore and Polar Engineering Conference*, ISOPE, 636–642.

Araki, S., H. Niijima, H. Fumoto, H. Miyoshi and I. Deguchi, 2005. Change in Transmission Coefficient with Deformation of Submerged Breakwater. *Proc. of 15th Int'l Offshore and Polar Engineering Conference*, ISOPE, 606–611.

Araki, S., R. Tanaka, G. Urai and I. Deguchi. 2007. Estimation of Repair Cost and Optimum Repair Plan for Rubble Mound Breakwater, *Proc. of Coastal Structures 2007* (in press)

Johnson, R. R., E. P. D. Mansard and J. Ploeg. 1978. Effects of Wave Grouping on Breakwater Stability, *Proc. of the 16th Int'l Conference on Coastal Engineering*, ASCE, 2228–2243.

Matsubuchi, S. and H. Yokota, 1999. Life Cycle Cost Analysis of Berthing Facilities and Development of a Decision Support System during their Maintenance Work. *Report of the Port and Harbour Research Institute*, Vol. 38, No. 2, 423–473. (in Japanese)

Nagai, T., K. Sugahara, N. Hashimoto, T. Asai, S. Higashiyama and K. Toda. 1994. Introduction of Japanese NOWPHAS System and its Recent Topics, *Proc. of the Int'l Conference on Hydro-Technical Engineering for Port and Harbor Construction (HYDRO-PORT'94)*, PHRI, 67–82.

Nagao, T. and S. Matsubuchi. 1999. Studies on Life-Cycle Cost and Allowable Failure Probability of Breakwaters. *Report of the Port and Habour Research Institute*, Vol. 38, No. 2, 395–422. (in Japanese)

Nanba, K., H. Yokota, Y. Tachibana, K. Tanaka and K. Iwata. 2003. Introductory Examination of "LCM" in Coast Preservation Institution. *Proc. of Coastal Engineering*, JSCE, Vol. 50, 916–920. (in Japanese)

Takayama, T., T. Yasuda, D. Tsujio and J. Inoue. 2007. Optimum Design for Armor Units Based on the Minimum Life Cycle Cost, *Proc. of Coastal Structures 2007* (in press)

2ND ORDER WAVE TRANSMISSION PAST A SUBMERGED BREAKWATER

Mariano Buccino[1], Mario Calabrese[1],
Francesco Ciardulli[1] and Francesco Pasanisi[2]

A 2nd order scheme for wave transmission past a submerged breakwater is presented, considering harmonic generation and change in wave form due to nonlinear wave-barrier interaction. Experimental tests in wave flume were performed using different structure layouts. Harmonic amplitudes in incident and transmitted wave were separated using a 4 wave gauges method. Empirical formulae were derived for prediction of fundamental, 2nd order free wave and 2nd order bound wave amplitudes leeward of the barrier. Results show that proposed scheme provides a realistic description of transmitted wave profile.

INTRODUCTION

A key issue in functional design of submerged breakwaters is predicting the wave field leeward of the barrier resulting from wave transmission.

A "classical" approach describes wave transmission at barrier in terms of the transmission coefficient K_t, i.e. the ratio between transmitted and incident significant wave height. The importance of this main parameter is obvious, since it globally expresses the wave energy dissipation due to wave-barrier interaction, where mitigating incident wave climate is the main goal of coastal protection projects. The transmission coefficient has been deeply investigated in the past, mainly by means of experimental studies, and a number of empirical formulae are available, in which K_t is expressed as a function of wave and structure parameters (Tanaka 1976, d'Angremond et al. 1996, Seabrook and Hall 1998, van der Meer et al. 2005, Buccino and Calabrese 2007).

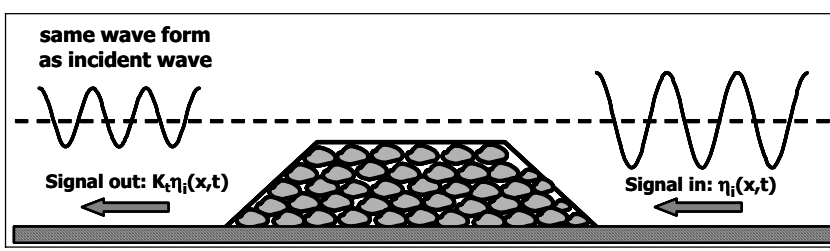

Figure 1. Linear scheme for wave transmission at submerged barrier.

[1] University of Napoli Federico II, Department of Hydraulic, Geotechnical and Environmental Engineering, Via Claudio 21, Napoli, 80125, Italy.
[2] ENEA, Department Environment, Global Changes and Sustainable Development, Portici Research Center, Località Granatello, Portici (NA), 80055, Italy.

However, by using the only transmission coefficient to describe wave transmission, a linear hypothesis is implicitly assumed, as any change of wave shape across the barrier is disregarded. Thus, the transmitted wave profile is assumed to be simply scaled from incident wave profile by using K_t as a reduction factor (Fig. 1).

On contrary, the interaction between a wave and a submerged structure is a non-linear process and change of wave form due to harmonic generation at barrier should also be considered. Namely, in the shallow water region above the breakwater multiple-frequency harmonic components are generated, either as "bound waves" or "free waves". The first waves have same celerity and initial phase as the incident fundamental harmonic, the latter have their own initial phase and celerity, obeying dispersion equation. Both types of super-harmonic components are propagated in the sheltered area, giving rise to a complex wave profile that is generally very different from incident wave.

Harmonic generation at a submerged step was theoretically described by Massel (1983) and Goda et al. (1999) using Stokes' 2nd order theory. Further investigations were conducted using both mathematical and physical models, mostly dealing with non-breaking waves (Ohyama and Nadaoka 1994, Losada et al. 1997, Huang and Dong 1999). In works dealing with breaking waves over the barrier, a reduction of transmitted super-harmonic amplitudes compared to non-breaking waves was generally reported (Grue 1992, Yamashiro et al. 1999, Brossard and Chagdali 2001). It can be argued that wave breaking would induce a saturation in non-linear wave-barrier interaction, even if the mechanism is not yet clearly defined.

In recent experimental works wave breaking over submerged barriers and its effects on transmitted wave field was investigated. Calabrese et al (2008) described wave breaking macro-features at submerged rubble-mound breakwaters with different geometry and permeability and proposed a tentative classification/parameterization of breaking forms. Same authors (Pasanisi et al. 2007) investigated changes in frequency distribution of transmitted wave energy for both non-breaking and breaking waves over the structure.

In the present work, results of an extensive experimental investigation on interaction between waves and submerged breakwater are reported. Main aim of the work is to propose a 2nd order scheme to describe wave transmission, including effects of harmonic generation and propagation at barrier and considering the role of wave breaking.

EXPERIMENTAL SETTINGS

Experiments were performed in the small scale wave flume at University of Napoli Federico II, Department of Hydraulic, Geotechnical and Environmental Engineering. The flume is about 24.50m long, and is made of two different sections; the first, closer to the wavemaker, has converging walls, and width varying from 0.80m at the wavemaker to 0.50m at a distance of 8.50m; the second section, with glass walls, is about 13.00m long, with a constant width of

0.50m (Fig. 2). The height of the flume is 0.75m. Waves were generated by a piston-type wavemaker, provided with dynamic wave absorber; absorbing shingle beaches with appropriate profile were placed at both ends of the flume.

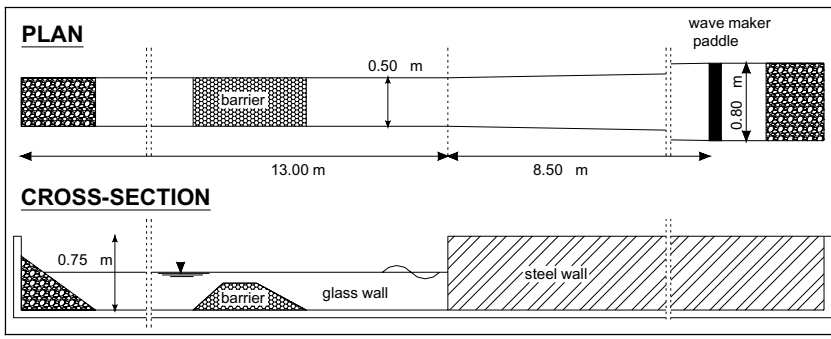

Figure 2. Wave flume at University of Napoli Federico II.

Six different layouts of submerged rubble-mound breakwater were tested, as shown in Fig. 3. ST1, ST2, ST4 and ST6 had a homogeneous cross-section with D_{50}=5.0cm, while ST3 and ST5 had a armour layer with D_{50}=5.0cm and a core of finer material (D_{50}=2cm). Crown width was 80.0cm for ST1, ST2 and ST3, 25.0cm for ST4, ST5 and ST6; freeboard above the crest was 6.5cm for all layouts except ST2, for which a 2.6cm freeboard was used. Seaward slope was 1:5 for ST4 and 1:2 for all the other structures; rear slope was 1:1.5 for all layouts.

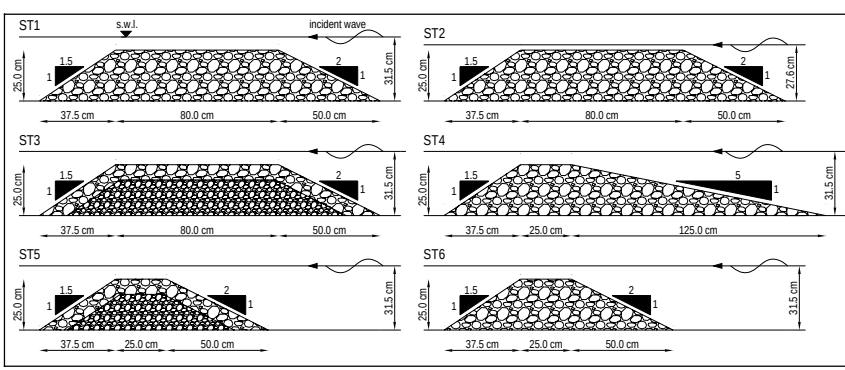

Figure 3. Layouts of structures used for tests.

Regular waves were used for tests, with target wave heights at wavemaker ranging from 2.0cm to 11.0cm, with step 1.0cm, in order to simulate both non-breaking and breaking conditions over the barrier.

As regards incident wave period *T*, results hereby reported pertains to tests with *T*=1.0s, for which the following conditions were satisfied:

•negligible wave reflection at the end of the flume;
•negligible higher order secondary waves at wavemaker;
•constant breaker types at barrier (S*pilling-to-Plunging*, according to Calabrese et al. 2008).

DATA ACQUISITION AND ANALYSIS

An array of four resistive twin-wire wave gauges was used to measure surface elevation as shown in Fig. 4. Sample frequency was 25Hz. Acquired data were analyzed in frequency domain using FFT technique and wave spectra for each station were derived.

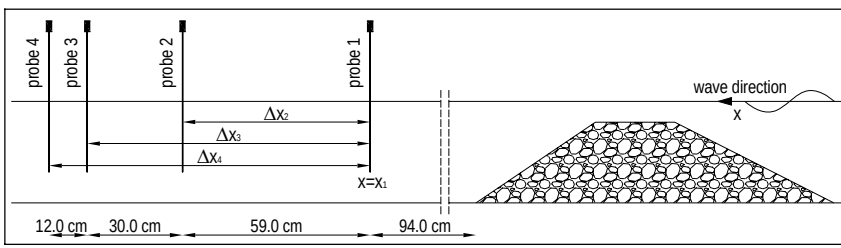

Figure 4. Data acquisition leeward of the submerged breakwater.

From 4-gauges array data, different harmonic components of transmitted wave were separated using the technique proposed by Lin and Huang (2004).

The main assumption is that, considering a regular wave traveling along x direction, surface elevation at abscissa x_m can be described by linear superposition of an infinite number of discrete harmonic components, each with its own frequency, wave height, and phase speed, as given in Eq. 1:

$$\begin{aligned}\eta(x_m,t) &= a_I\cos(kx_m-\sigma t+\phi_I)+a_R\cos(kx_m+\sigma t+\phi_R)+\\ &+\sum_{n\geq 2}a_{I,B}^{(n)}\cos[n(kx_m-\sigma t)+\phi_{I,B}^{(n)}]+\sum_{n\geq 2}a_{I,F}^{(n)}\cos[k_n x_m-n\sigma t+\phi_{I,F}^{(n)}]+\\ &+\sum_{n\geq 2}a_{R,B}^{(n)}\cos[n(kx_m+\sigma t)+\phi_{R,B}^{(n)}]+\sum_{n\geq 2}a_{R,F}^{(n)}\cos[k_n x_m+n\sigma t+\phi_{R,F}^{(n)}]+e_m(t)\end{aligned} \quad (1)$$

where:

•a_I and a_R denote, respectively, incident and reflected fundamental harmonic, with frequency f, pulsation $\sigma=2\pi f$ and wave number k ;
•$a_{I,B}^{(n)}$ and $a_{R,B}^{(n)}$ denote, respectively, amplitudes of incident and reflected nth order bound wave, with frequency $n\cdot f$;
•$a_{I,F}^{(n)}$ and $a_{R,F}^{(n)}$ denote, respectively, amplitudes of incident and reflected nth order free wave, with frequency $n\cdot f$ and wave number k_n ;
•the terms ϕ denote initial phases;

• $e_m(t)$ expresses the error arising from the signal noise in the measurement or the extraordinary terms owing to the nonlinear wave interactions, such as evanescent modes.

Wave numbers k and k_n are expressed by dispersion equation as a function of water depth h and wave pulsation σ:

$$\sigma^2 = g\,k\tanh(k\,h);\quad (n\sigma)^2 = g\,k_n\tanh(k_n\,h) \tag{2}$$

In order to decompose complex wave into individual harmonic components, the Fourier Transform is applied to surface elevation at different positions:

$$\hat{\eta}^{(n)}(x_m) = \frac{\sigma}{2\pi}\int_0^{2\pi/\sigma}\eta(x_m,t)\cdot e^{-in\sigma t}dt \qquad n=1,2,... \tag{3}$$

Considering the orthogonal properties of the trigonometric function and substituting expression in Eq. 1 into Eq. 3, we obtain:

$$\hat{\eta}^{(n)}(x_m) = C_{I,B}^{(n)}\,X_{I,B}^{(n)} + C_{R,B}^{(n)}\,X_{R,B}^{(n)} + C_{I,F}^{(n)}\,X_{I,F}^{(n)} + C_{R,F}^{(n)}\,X_{R,F}^{(n)} + \Omega_m^{(n)} \tag{4}$$

In Eq. 4 the term $\Omega_m^{(n)}$ is the Fourier Transform of $e_m(t)$. Terms C are known quantities and can be regarded as "coefficient", whilst terms X contains unknown harmonic amplitudes and initial phases. Expressions are given in Table 1:

Table 1. Expressions of terms in Eq. 4

UNKNOWNS	COEFFICIENTS
$X_{I,B}^{(n)} = a_{I,B}^{(n)}\exp[-i(nkx_1+\phi_{I,B}^{(n)})]$	$C_{I,B}^{(n)} = 0.5\cdot\exp[-i(nk\Delta x_m)]$
$X_{R,B}^{(n)} = a_{R,B}^{(n)}\exp[i(nkx_1+\phi_{R,B}^{(n)})]$	$C_{R,B}^{(n)} = 0.5\cdot\exp[i(nk\Delta x_m)]$
$X_{I,F}^{(n)} = a_{I,F}^{(n)}\exp[-i(nkx_1+\phi_{I,F}^{(n)})]$	$C_{I,F}^{(n)} = 0.5\cdot\exp[-i(nk\Delta x_m)]$
$X_{R,F}^{(n)} = a_{R,F}^{(n)}\exp[-i(nkx_1+\phi_{I,F}^{(n)})]$	$C_{R,F}^{(n)} = 0.5\cdot\exp[-i(nk\Delta x_m)]$

Eq. 4 can be written, for a given order, at different positions, obtaining an algebraic system. Obviously, for n=1 locked and free modes are not present, and the system is simplified. Applying the least squares method one simple linear system of equation for solving the complex wave for each order of approximation can be obtained. The outputs of this method are the incident and reflected fundamental wave amplitudes and the incident and reflected wave amplitudes for higher order bound and free waves.

In the present work, for sake of simplicity, analysis was limited at 2nd order approximation. Incident wave conditions were measured in absence of the structure; the accurate profile of absorbing beach at the end of the channel allowed to neglect reflected components in both incident and transmitted waves; 2nd order free wave amplitudes in incident wave were negligible.

Moreover, the incident and transmitted significant spectral wave heights were calculated, from average of the 4 wave gauges data; then, the spectral transmission coefficient was derived.

Altogether, for each run the following wave parameters were derived:

- $a_i^{(1)}$, $a_t^{(1)}$ *:* incident and transmitted 1st order (fundamental) wave amplitudes;
- $a_{ib}^{(2)}$, $a_{tb}^{(2)}$ *:* incident and transmitted 2nd order bound wave amplitudes;
- $a_{tf}^{(2)}$ *:* transmitted 2nd order free wave amplitudes;
- H_i , H_t : incident and transmitted spectral significant wave heights;
- $K_t = \frac{H_t}{H_i} = \sqrt{\frac{m_{0t}}{m_{0i}}}$ *:* global (linear) transmission coefficient, being m_{0i} and m_{0t}, respectively, the 0th order moment of incident and transmitted wave spectrum ;

Occurrence of wave breaking and, possibly, breaker type were detected for each run using a video camera.

RESULTS AND DISCUSSION

2nd order scheme for wave transmission

In the present work, a 2nd order scheme for wave transmission is proposed; the wave profile leeward of the barrier is expressed as the sum of three harmonic components:

$$\eta_t(x,t) = a_t^{(1)} \cos(k x - \sigma t) + a_{tb}^{(2)} \cos\left[2(k x - \sigma t)\right] + \\ + a_{tf}^{(2)} \cos(k_2 x - 2\sigma t + \varphi_2) \tag{5}$$

The first term in Eq. 5 is the fundamental transmitted harmonic; the second term is the 2nd order transmitted bound wave; the third term is the transmitted 2nd order free wave. Beside known symbols, φ_2 expresses the relative phase shift of the 2nd order free wave for x=0 and t=0 compared to fundamental and 2nd order bound waves.

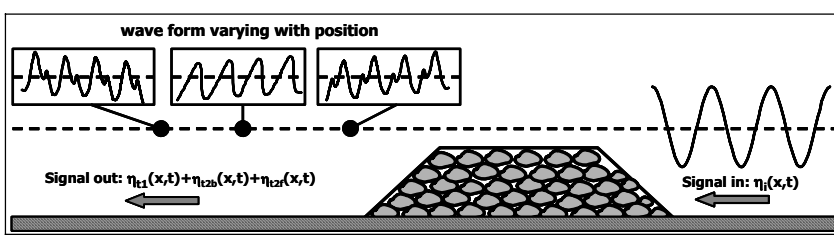

Figure 5. 2nd order scheme for wave transmission at submerged barrier.

From Eq. 5, it is to be observed that, for a given time t, phase shift among harmonic components significantly varies with abscissa x, due to difference in wave number of 2nd order free waves compared to other components. The

physical reason is that 2nd order free wave travels with a celerity that, obeying dispersion equation, is different from other components.

As a consequence, non-permanent wave forms are to be expected leeward of the breakwater, with a resulting wave profile significantly varying as wave propagates in the sheltered area (Fig. 5).

Comparing Fig. 1 and Fig. 5 it can be argued that classical linear scheme can be considered only as a rough approximation of wave transmission process, that is strongly affected by non-linear wave-structure interaction.

In the following, based on experimental data, empirical formulae for predicting transmitted wave amplitudes are proposed, considering wave and structure parameters.

Transmitted 1st order wave amplitude

For each structure layout, the amplitude of transmitted fundamental harmonic was found to increase with incident wave height. Experimental data show that transmitted 1st order amplitude is generally higher for homogeneous structure compared to structure with core, with a more significant effect for wider breakwater crown.

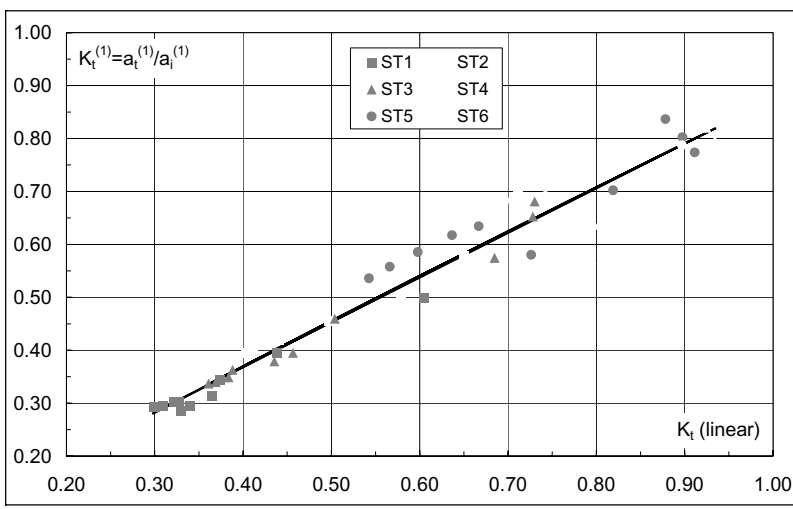

Figure 6. 1st order transmission coefficient.

The following parameter was introduced, as a "1st order transmission coefficient", ratio between transmitted and incident fundamental harmonic amplitudes:

$$K_t^{(1)} = \frac{a_t^{(1)}}{a_i^{(1)}} \tag{6}$$

In Fig. 6 experimental values of $K_t^{(1)}$ are plotted against linear transmission coefficient K_t. Experimental points are fitted by the following nearly linear function with a very good correlation factor (R^2=0.95).

$$K_t^{(1)} = 0.8727 \cdot \left(K_t\right)^{0.9376} \tag{7}$$

Result is not surprising, given that, as discussed before, both coefficients can be considered descriptive of the linear processes in wave-structure interaction. Obviously, in the 2nd order approach, the amount of wave energy transmitted at fundamental frequency is lower than value predicted using the simple linear scheme.

Transmitted 2nd order free wave amplitude

As well established in literature (Grue 1992, Brossard and Chagdali 2001, Pasanisi et al. 2007) free waves transmission leeward of the barrier strongly depends on whether wave breaks over the structure or not. Generally, for non-breaking waves, super-harmonic components grow in the shallow water region above the barrier and propagate in the sheltered area as free waves with no significant loss of energy. On contrary, as wave breaking occurs at barrier, transmitted free waves amplitudes reduce, suggesting that breaking-induced dissipation, which is more intense as wave frequency increases, induces a saturation in harmonic generation. The saturation process above described is also affected by characteristics of wave breaking at structure, such as breaker form and position of plunging point over the barrier; as a consequence, the effect on the amount of transmitted super-harmonic components can be significantly different from case to case.

In the present work the analysis focused on cases of breaking waves over the barrier, which are more frequent and more interesting for technical application. The following parameter was introduced, as a "2nd order free wave transmission coefficient", ratio between transmitted 2nd order free wave and incident fundamental amplitude:

$$K_{tf}^{(2)} = \frac{a_{tf}^{(2)}}{a_i^{(1)}} \tag{8}$$

Based on the above considerations on wave-breaking induced saturation, the main wave and structure parameters were arranged in the following dimensionless product:

$$\Xi = K_t \left(\frac{h_c}{h}\right)^3 \left(\frac{B}{L_0}\right)^{0.4} \left(\tan\alpha\right)^{0.3} \tag{9}$$

being:

- h_c : height of the breakwater crown over the bottom;
- h : water depth at seaward and leeward side of the barrier;

- B : width of barrier crest;
- L_0 : deep water wavelength for fundamental frequency;
- α : seaward face slope of the barrier.

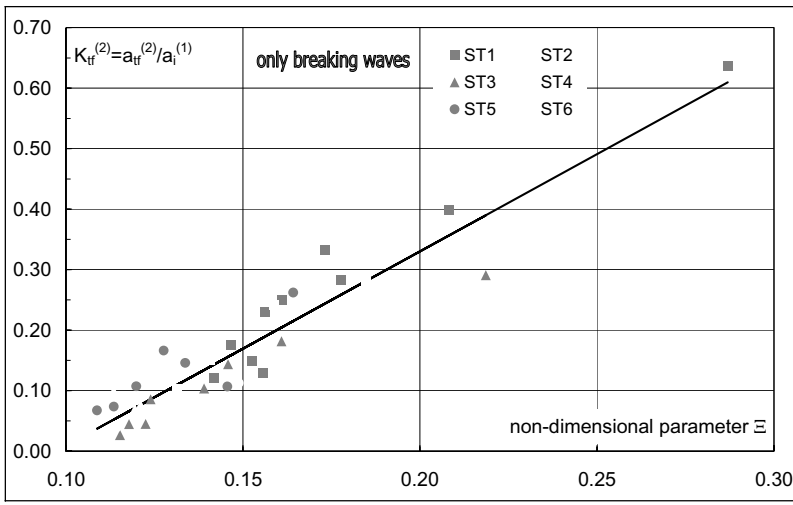

Figure 7. 2nd order free wave transmission coefficient.

In Fig. 7 experimental values of $K_{tf}^{(2)}$ are plotted against parameter Ξ above introduced. The following linear interpolation function was found, with a good correlation (R^2=0.86):

$$K_{tf}^{(2)} = 3.2146 \cdot \Xi - 0.3128 \tag{10}$$

Transmitted 2nd order bound wave amplitude

Incident and transmitted 2nd order bound wave amplitude were compared with values predicted by Stokes' theory. For incident waves, results showed a good correlation between predicted and measured values. On contrary, transmitted bound wave amplitudes resulted systematically greater than values predicted by Stokes' theory, as a consequence of non-linear effects at barrier; super-harmonic bound wave amplitudes were found to grow as the crest width or the seaward slope grows, and as barrier freeboard reduces.

The experimental data analysis data showed a reasonable correlation between transmitted bound/free wave amplitudes and fundamental harmonic. Results generally showed that bound wave amplitude tends to reduce as free wave amplitude grows.

Experimental points are plotted in Fig. 8. The following exponential formula was empirically derived, with correlation coefficient R^2=0.81:

$$\frac{a_{tb}^{(2)}}{a_{tf}^{(2)}} = 0.25 + 7.99 \cdot \exp\left(-15.457 \frac{a_{tf}^{(2)}}{a_t^{(1)}} \right) \tag{11}$$

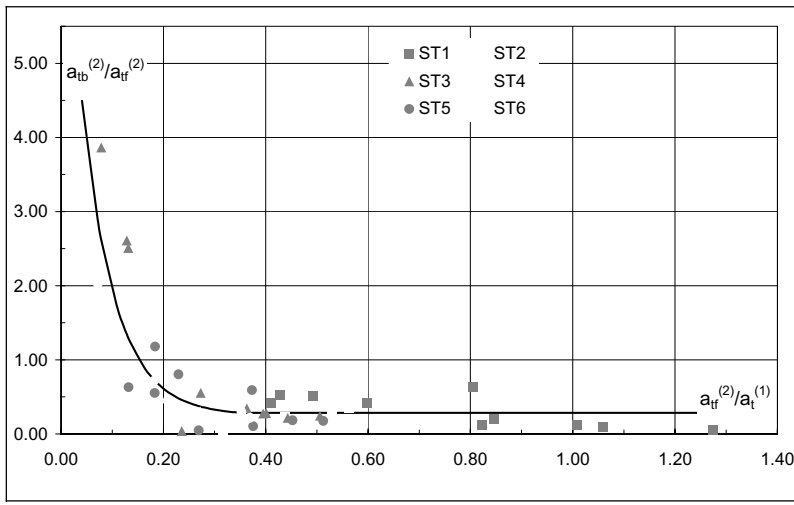

Figure 8. 2nd order bound wave amplitudes leeward of the barrier.

CONCLUSIONS

A 2nd order scheme for wave transmission at a submerged breakwater was presented and discussed. The proposed method includes generation and propagation of higher order harmonics due to non-linear wave-barrier interaction and saturation due to wave breaking over the structure. Based on experimental results, empirical formulae for prediction of transmitted harmonic amplitudes were derived. The 2nd order scheme seems to provide a more realistic description of wave conditions leeward of the barrier, compared to classical linear scheme based on the only transmission coefficient. Results seem encouraging, though more investigations are needed, considering a wider range of wave conditions and different barrier layouts.

APPENDIX - NUMERICAL EXAMPLE

For example purpose, the proposed 2nd order scheme for wave transmission is used to predict wave profile for test n. 7, with layout structure ST1; predicted and incident wave profile are then compared.

Incident wave conditions are: H_i=7.44cm, T=1.0s. 2nd order components can be neglected in the incident wave.

The global (linear) transmission coefficient is K_t=0.50.

The transmitted fundamental wave amplitude is derived from Eq. 7, obtaining $a_i^{(1)}$=1.69cm; the value of transmitted free wave amplitudes, estimated using Eq. 10, is $a_{tf}^{(2)}$=0.69cm; finally, applying Eq. 11, a transmitted bound wave amplitude $a_{tb}^{(2)}$=0.18cm is obtained.

The transmitted wave profile, in the 2nd order scheme, is expressed by the following function:

$$\eta_t(x,t) = 1.69\cos(k\,x-\sigma\,t) + 0.18\cos\left[2(k\,x-\sigma\,t)\right] + \\ + 0.69\cos(k_2\,x-2\sigma\,t+\varphi_2) \tag{A-1}$$

in which wave profile is determined regardless of phase shift φ_2, that cannot be predicted using the method above described.

Comparison between measured and predicted transmitted wave profile is illustrated in Fig. 9. Regardless of inevitable phase shift, wave forms are consistent, indicating that proposed method is sufficiently realistic in predicting transmitted wave profile.

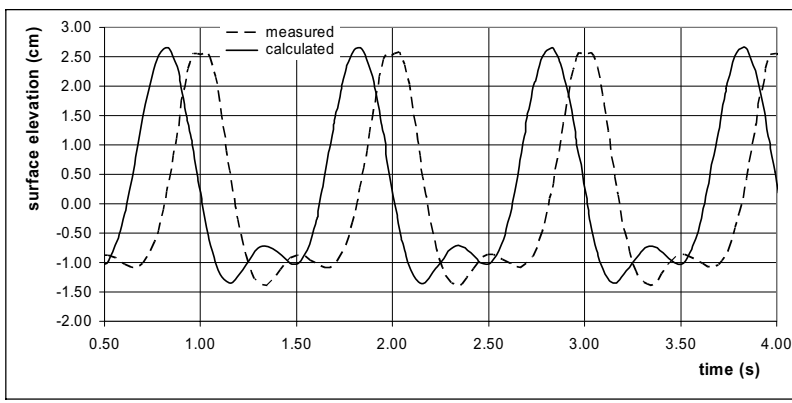

Figure 9. Comparison between measured and predicted wave profiles leeward of the barrier, according to 2nd order scheme for wave transmission.

It is worth observing that assuming the classical linear scheme for wave transmission, the transmitted wave profile would be unrealistically described by a simple cosine function, obtained by scaling incident profile by coefficient K_t.

REFERENCES

Brossard, J. and Chagdali, M. 2001. Experimental investigation of the harmonic generation by waves over a submerged plate. *Coastal Engineering*, 42, 277-290.

Buccino, M. and Calabrese, M. 2007. Conceptual approach for prediction of wave transmission at low-crested breakwaters, *Journal of Waterways, Port, Coastal and Ocean Engineering*, 133, 213-224.

Calabrese, M., Buccino, M., Pasanisi, F. 2008. Wave breaking macrofeatures on a submerged rubble mound breakwater. *Journal of Hydro-environment Research*, 1, 216-225.

d'Angremond, K., van der Meer, J.W., de Jong, R.J. 1996. Wave transmission at low crested structures. *Proceedings of 25th International Conference on Coastal Engineering*, ASCE, 3305–3318.

Goda, Y., Okazaki, K., Kagawa, M. 1999. Generation and evolution of harmonic wave components by abrupt depth changes. *Proceedings of 3rd International Conference on Coastal Structures*, ASCE, 649-658.

Grue, J. 1992. Nonlinear water waves at a submerged obstacle or bottom topography. *Journal of Fluid Mechanics*, 244, 455-476.

Huang, C.-J. and Dong, C.-M. 1999. Wave deformation and vortex generation in water waves propagating over a submerged dike. *Coastal Engineering*, 37, 123-148.

Lin, C.-Y. and Huang, C.-J. 2004. Decomposition of incident and reflected higher harmonic waves using four wave gauges. *Coastal Engineering*, 51, 359-406.

Losada, I.J., Patterson, M.D., Losada, M.A. 1997. Harmonic generation past a submerged porous step. *Coastal Engineering*, 31, 281-304.

Massel, S.R. 1983. Harmonic generation by waves propagating over a submerged step. *Coastal Engineering*, 7, 357-380.

Ohyama, T. and Nadaoka, K. 1994. Transformation of a nonlinear wave train passing over a submerged shelf without breaking. *Coastal Eng*ineering, 24, 1-22.

Pasanisi, F., Buccino, M., Calabrese, M. 2007. Macrofeatures and engineering properties of wave breaking at submerged rubble-mound breakwaters. *Proceedings of 5th International Conference on Coastal Structures*, ASCE.

Seabrook, S.R. and Hall, K.R. 1998. Wave transmission at submerged rubble mound breakwaters, *Proceedings of 26th International Conference on Coastal Engineering*, ASCE, 2000–2013.

Tanaka, N. 1976. Effects of submerged rubble-mound breakwater on wave attenuation and shoreline stabilization, *Proceedings of 23rd Japanese Coastal Engineering Conference*, 152-157.

van der Meer, J.W., Briganti, R., Zanuttigh, B., Wang, B. 2005. Wave transmission and reflection at low-crested structures: design formulae, oblique wave attack and spectral change, *Coastal Engineering*, 52, 915-929.

Yamashiro, M., Yoshida, A., Irie, I. 1999. Experimental study on wave field behind a submerged breakwater. *Proceedings of 3rd International Conference on Coastal Structures*, ASCE, 675-682.

A MITIGATION PLAN FOR THE RECLAMATION ON THE TIDAL FLAT IN GWANGYANG BAY

Bumshick Shin[1], Kyuhan Kim[2] and Chongkun Pyun[3]

As economic development in Korea has led to an increase of usage of the coast, coastal reclamation and construction of breakwaters have been increased. However, because of the development in coastal areas, marine environment has been deteriorating and the necessity of adaptive management on the mitigation plan is emphasized. The purpose of this study is to expect some of the negative effects on the ocean ecosystem, not only to mention water quality, caused by a new on-going coastal reclamation project in Gwangyang bay, is located in the middle of the southern coast of Korea. A feasibility study is carried out based on the prediction result. In order to predict change of water quality triggered by coastal reclamation, the 3D hydrodynamic model and the material cycle model are used. As a result, while the concentration level of nutrition (NH_3, NO_3, and PO4) is relatively low, that of COD and DO is observed to be higher because of high concentration of phytoplankton. The leading cause of degradation of water quality is due to the decrease in Benthos population such as shellfish and short-necked clams. This is considered to be one of the impacts of the environmental ecosystem. In this study, mitigation ideas on the environmental ecosystem impacts acquired from the numerical simulation, artificial tidal flat, artificial beach, and eco friendly revetments have been proposed.

INTRODUCTION

Recently, reclamation on the coastal, dredging of anchoring, construction of breakwaters and structures are increasing with economic development and increase of use of the coast. However, because of the development in coastal areas, marine environment has been deteriorating and the necessity of adaptive management on the mitigation plan is emphasized. The purpose of this study is to expect some of the negative effects on the ocean ecosystem, not only to mention water quality, caused by a new on-going coastal reclamation project in Gwangyang bay it's a typical semi-closed bay makes it extremely difficult to be purified by natural process.

To predict environmental change due to reclamation, observation of natural conditions of water quality and prediction by Numerical Model using accurate observation data is required. Thus, data of the Marine Environmental Information Service Center, Automatic Monitoring Network of Seawater

[1] Research Center for Waterfront and New Ocean Energy Development, Kwandong University, 522, Naegok-dong, Gangnueng, Gangwon-do, 210-701, Korea.
[2] Dept. of Civil Engineering, Kwandong University, 522, Naegok-dong, Gangnueng, Gangwon-do, 210-701, Korea
[3] Dept. of Civil & Environmental Engineering, Myongji University, San 38-2 Namdong, Yongin, Gyunggi-do, 449-728, Korea

Quality for which long-termed observation is progressed were analyzed and current conditions of water were repeated by using a 3D Hydrodynamic model and a Material cycle model. Additionally change of environment by reclamation was investigated by predicting change of water quality and ecosystem. In this research, a mitigation idea on the number of environmental ecosystem impacts acquired from the calculation, artificial tidal flat, artificial beach, and eco friendly revetments have been proposed.

STUDY AREA

The study area, Gwangyang bay, is located in the middle of the southern coast of Korea as shown in Figure 1. Considering its geographical characteristics, the fact that it's a typical semi-closed bay makes it extremely difficult to be purified by natural process when the bay is contaminated.

Since this is regionally a closing type of sea bed but a wide tidal flat is formed, there is a natural function of purifying water quality.

Major cause of tidal current in Gwangyang Bay is tide and a type of tide is a mixing type where semidiurnal tide (tide form number; 019 ~ 0.21) prevails, and ebb and flood regularly occurs 2 times a day and the drift of the maximum ebb & food current velocity in average spring tide is 1.0~1.4kn (National Ocean Survey Center, 1995).

Moreover, about 72% of the existing tidal flats in Gwangyang bay have disappeared due to extensive coastal reclamation for the industrial estate construction since 1970.

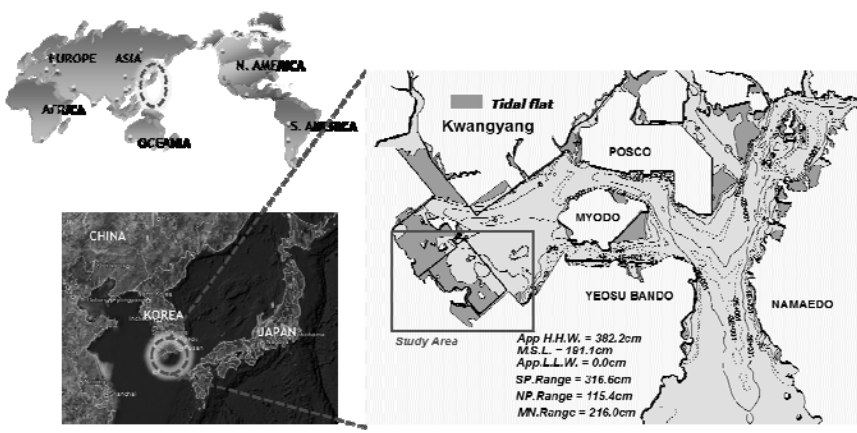

Figure 1 Study Area

Numerical Model

In predicting current status and future change of environment in the coastal area, numeric model is established, verification and a prediction is performed. A model for predicting environmental change in this study consists of two modes as shown in Figure 2.

One is a 3D Hydrodynamic model for tide and tidal current and the other is a material cycle model for predicting effect on a material circulation process, and ecosystem of coastal area can be predicted using these two models.

The first step in predicting water quality using material cycle model was to collect data of water quality was conducted by satellite images for the numerical model. The second step was to create a database and find trends for the changes in the physical oceanic environment in order to record the movement of substances. Lastly, we used the ecosystem model to predict changes in water quality.

This model is determined to be usefully used for predicting water quality in the coastal area by calculating change in time and space of the existing quantity for each component calculated in the hydrodynamic experiment into the ecosystem model.

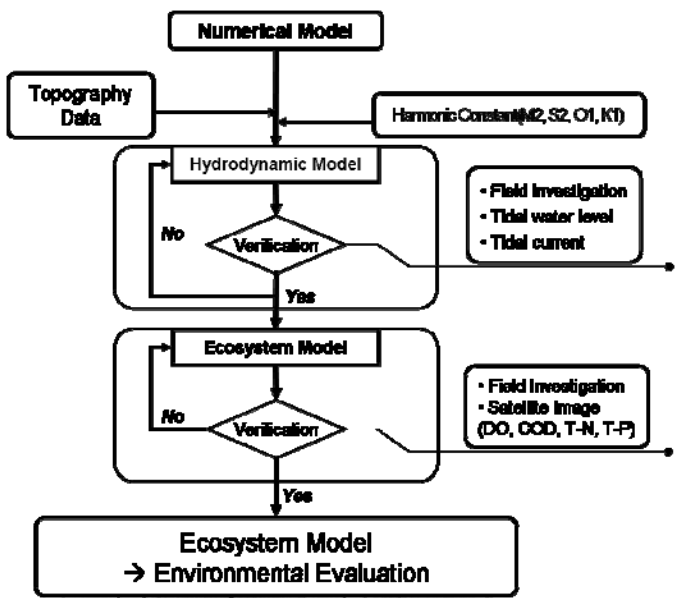

Figure 2 Material Cycle Model

Hydrodynamic Model

To simulate this circulation, we used 3D multi-level hydrodynamical equation, into which are introduced the buoyancy diffusion equation to calculate the three dimensional density structure.

The governing equations for the nutrient cycle model are as follows:

- Equation of motion

$$\frac{\partial v}{\partial t} + (v \cdot \nabla)v + w\frac{\partial v}{\partial z} + f_0 \mathrm{K} \cdot v = g\nabla\varsigma - \frac{g}{\rho_0}\int_{-H}^{0} \nabla\rho dz + \left[\nabla \cdot \left(A_H \nabla\right)\right]v + \frac{\partial}{\partial z}\left(A_z \frac{\partial v}{\partial z}\right) \quad (1)$$

- Equation of continuity

$$\nabla \cdot v + \frac{\partial w}{\partial z} = 0 \quad (2)$$

- Condition at the free surface

$$\frac{\partial \zeta}{\partial t} + \nabla \cdot \left(\int_{-H}^{\zeta} v dz\right) = 0 \quad (3)$$

where, v is the horizontal velocity, w the vertical velocity, f_0 the coriolis factor, ρ the water density, ζ the sea surface height from the mean sea level, H the depth from the mean sea level, g gravitation acceleration, A_H and A_Z are the coefficients of horizontal and vertical diffusion, t the time, z the vertical coordinate, and k the unit vector on the vertical axis.

Material Cycle Model

The material cycle model used the same grid systems as 3D hydro dynamical model and the results of hydrodynamic model are an input data. The available water quality data for Tokyo Bay were restricted to measurement of inorganic nitrogen and inorganic phosphorus (hereafter I-N and I-P are used for simplicity), and organic nitrogen (O-N) and organic phosphorus (O-P). Minimal information on biological parameters such as phytoplankton abundance or chlorophyll concentration was available.

Figure 3 is a conceptual diagram of the material cycle model in considering tidal flat ecosystem. Specially, in this study, the pollutant was divided COD(COD1) which release from the sediment, land and COD(COD2) it is primary production. The governing equations for nutrient cycle model are based on the advection and diffusion of water quality data.

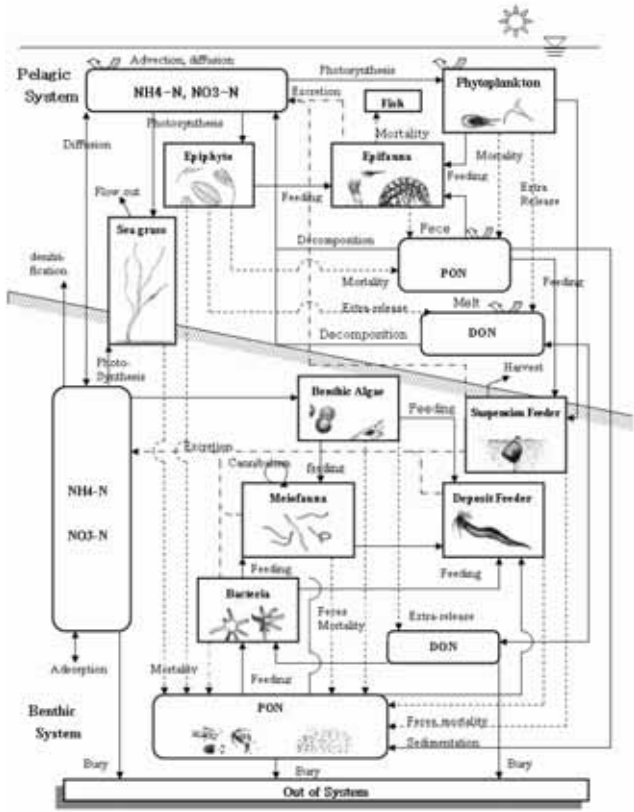

Figure 3 Model Concept

$$\frac{\partial C_k H_k}{\partial t} = -\frac{\partial M_k C_k}{\partial x} + \frac{\partial N_k C_k}{\partial y} + \left(w_f C\right)_{k-1/2} - \left(w_f C\right)_{k+1/2} \tag{4}$$
$$-\frac{\partial}{\partial x}\left(K_x H_k \frac{\partial C_k}{\partial x}\right) - \frac{\partial}{\partial y}\left(K_y H_k \frac{\partial C_k}{\partial y}\right) - \left(K_z \frac{\partial C}{\partial z}\right)_{k-1/2} + \left(\frac{\partial C_k H_k}{\partial t}\right)^* = 0$$

where, c_k is layer average concentration, w_f Fall-Velocity k_x, k_y horizontal diffusion coefficient k_z vertical diffusion coefficient.

In this study, the benthic ecosystem which was not considered in the existing study was considered in this model. Consideration of the benthos ecosystem can predict the overall change of the ocean ecosystem which is related with the pelagic ecosystem. The tidal flat ecosystem, which effect of the benthic ecosystem is largest, can be especially predicted. Thus, it is determined that tidal flat may be evaluated more effectively and quantitatively by considering both the benthic and the pelagic ecosystem.

Results of Numerical Simulation

Hydrodynamic Model

Change of tidal current in the Gwanyang Bay due to a new on-going coastal reclamation project up to 7,603,515m^2(Figure 4) was in Figure 5 in comparison it with ebb and flood tide before and after reclamation. As the results of simulation, change of tidal current around the area where reclamation will be promoted was significant. It was predicted that tidal current velocity would reduce in the front side (East side) of the reclamation, and it would increase in the side (Northern side).

Figure 4 Reclamation Plan (7,603,515m^2)

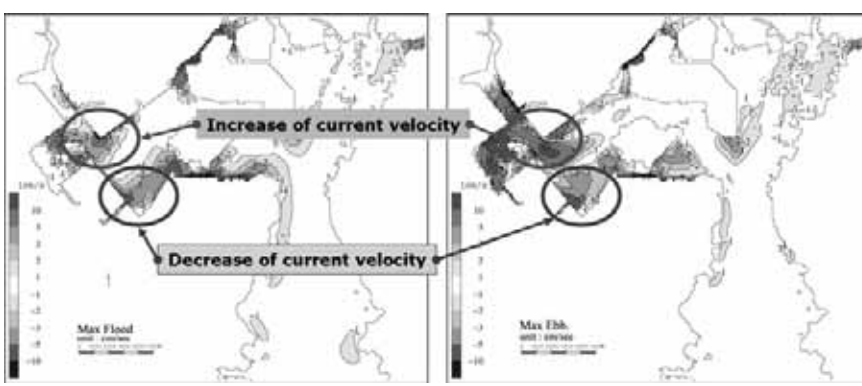

Figure 5 before and After Tidal Current simulation result

Ecosystem Model

The material cycle model was applied in the same grid system which was used in hydrodynamic model. The tide and tidal current of each grid in the model derived from simulation results of the hydrodynamic model was used as input data. As the result of numerical model, change of coastal environment around the reclamation was significant as shown in Figure 6 in comparison before and after reclamation. Drift speed reduced in the North-West side of the reclamation lands, and it increased in the East side). Nutrients (NH_3, NO_3, and PO4) show opposite trends to the Zooplankton and phytoplankton.

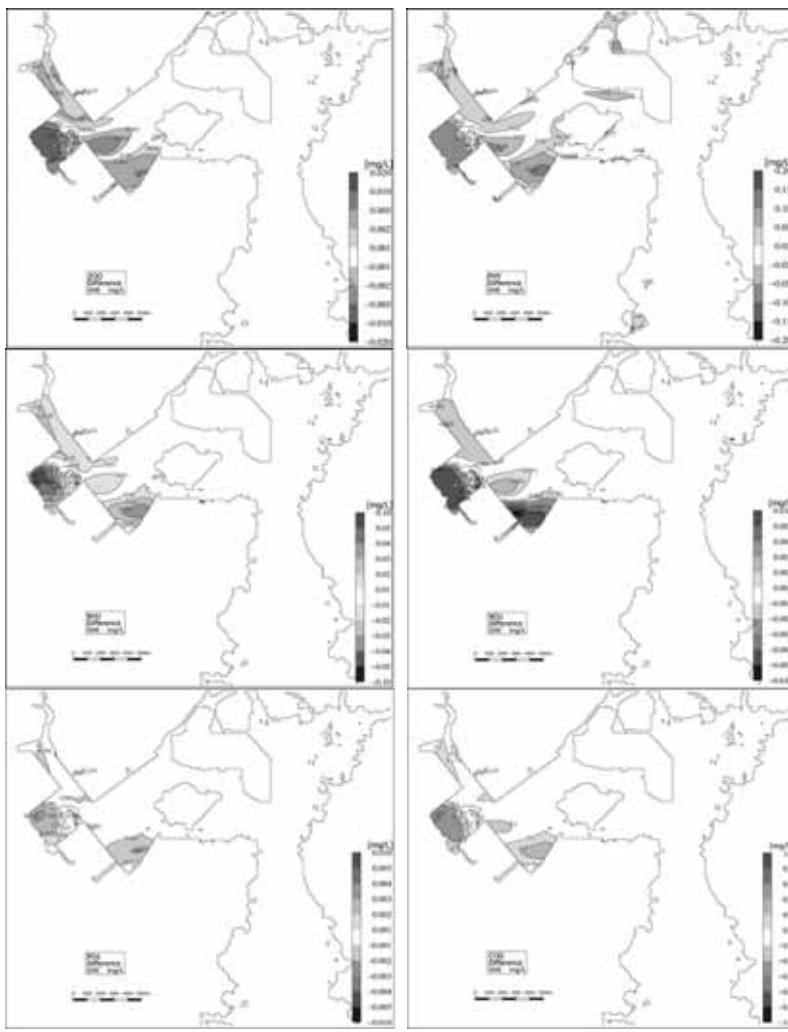

Figure 6 Results of simulation

Mitigation Plan

[Means to reduce effect on environment and restore or compensate for environment by avoid and minimize damage to sensitive coastal areas] is referred to as mitigation. It may be considered to quantitatively quantity of living things which are extinguished by large reclamation and mitigate impact to natural environment.

Calculation of natural inevitable environment caused by reclamation

The area of tidal flats existing around the sea bed which is lost by reclamation is 117ha, where short-necked clams, shells live. Since there is no clear statistics for production quantity, this study is intended to estimate and compensate for short-necked clams living this tidal flat area on the survival quantity observed in every region by now. There are survey results at Bannosu tidal flats of Chiba, Japan, which is long-term observation of relationship between existing tidal flats and short-necked clams. Its source unit is designed as follows:

Average concentration of juvenile shell naturally occurred	227EA/㎡
In short-necked clams of survival rate 100%	8g/EA
Ratio actually produced	22.1%

⇩

Area (tidal flat area of the object region)	117ha
Number of juvenile shells within given area (227EA/㎡×117ha)	26,559EA
In short-necked clams of survival rate 100%(8g/EA×26,559EA)	2,125t
Ratio actually produced (22.1%×2,125t)	470t

Thus, it is required to compensate for 470t calculated as quantity of short-necked clam damaged by reclamation.

Mitigation methods of environmental effect occurred by reclamation

Methods of mitigation to restore tidal flat and existing environment which are lost are intended to conserve, create environment and use. Before we made a mitigation plan, we have to check some important factor as follow Figure 7.

Method of creating new environment in the sea bed on full examination of development plans suggested in Figure 8 should be introduced in consideration of environmental features of the region for effective mitigation. For the reclamation plans of 7,603,515m^2, restoration methods of short-necked clams, which are major living things, to mitigate effect by damage of tidal flats of 117ha which is currently close to the coast line will be suggested.

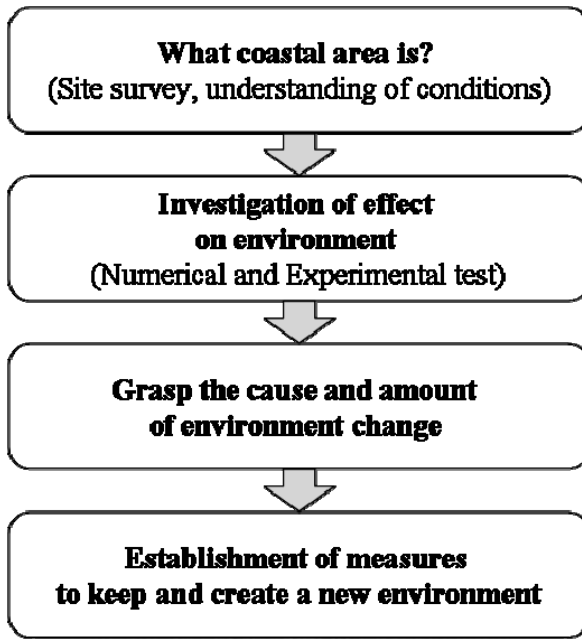

Figure 7 Check points of development plans

Figure 8 represents that eco-friendly revetments, artificial tidal flat, artificial tidal beach and biotope of fishes and seaweeds around reclaimed ground and waterways should be considered as method to restore a new environment.

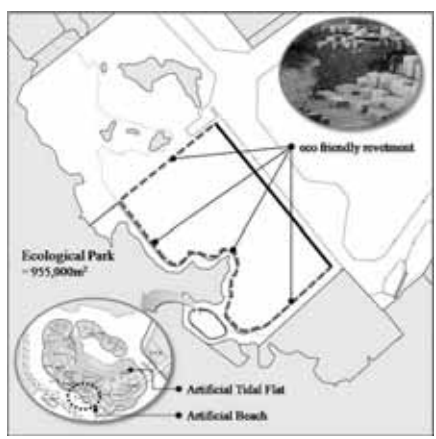

Figure 8 Outline of mitigation plan

1. Waterways: Make waterways between reclaimed ground and land as tidal flat, where short-necked clams can live.

Table 1. Mitigation method (Warerways)

Hydrodynamic expansion (4.291m+2,105m)	6,396m
Width of waterway	150m
Area (6,291×150m)	959,400m^2

Benthos in artificial tidal flat increase as 2 ~ 4 times as natural coast. Here 2 times are applied, namely the area newly created is 95.94ha.

2. Quantity of short-necked clams produced from artificial tidal flat

Table 2. Mitigation method (Artificial Tidal Flat)

Average concentration of juvenile shell naturally occurred	227EA/㎡
Area (tidal flat area of the object region)	95.95ha
Number of juvenile shells within given area(227EA/㎡×117ha)	21,780EA
In short-necked clams of survival rate 100% (8g/EA×26,559EA)	1,742t
Ratio actually produced (22.1%×2,125t)	385t
Premium ratio of artificial tidal flat (2×385t)	770t

Quantity is Benthos to be compensated is 470t but production of 770t is expected by creating waterways as tidal flat, which can sufficiently compensate lost quantity

3. Biotope(fishes)
: Block with aperture (side or flat installed at mount of inner wall)

4. Biotope(seaweeds)
: Adjusted slope of substrate capable of increasing the insertion ratio of spore

Conclusion

In this study both 3D hydrodynamic model and material cycle model were used for predicting change of water quality which is caused by reclamation. Results of experiment showed that the concentration of phytoplankton reduces and the concentration of nutrients (NH_3, NO_3, and PO_4) increase since tidal flat disappears after reclamation as results of experiment.

The leading cause of degradation of water quality is because of the decrease in Benthos population such as shellfish and short-necked clams due to reclamation in tidal flat. This is considered to be one of the impacts of the environmental ecosystem.

In this study, artificial tidal flat, artificial beach and eco-friendly revetments were considered as mitigation ideas against environmental ecosystem impact quantity which was obtained as result of numerical simulation.

It is thus determined that use of various methods is more required to minimize effect on environment than reduce a development plan in order to preventing environment from damage by development. Adaptive management plans to monitor environmental change of before and after construction must be had application

ACKNOWLEDGMENTS

This work was partly supported by the RIC program of Ministry of Knowledge and Economy of Korea.

REFERNCES

Baretta, J. and Ruardij P., 1988. *Simulation and Analysis of the EMS Estuary*. Springer Verlag pp.353.

Nakata, K., 1993. Ecosystem model, Its formulation and estimation method for unknown rate parameters. *Journal of Advanced Marine Technology Conference*. Vol.1, No.8, pp 99-138.

Shin B.S., Kim K.H., Pyun C.K., 2006. " The Evaluation of Water Quality in Shallow Water using the 3D Physical-Biochemical Coupling Model." *The 16th International Offshore and Polar Engineering Conference.* pp 548-555.

WATER RENOVATION IN MESO-TIDAL HARBOURS. THE BILBAO CASE

M. Espino[1], M. Grifoll[1,3], M. Hernáez[2], I. Rodríguez[4], J.P. Sierra[1], L. Ferrer[3], M. González[3] and A. Sánchez-Arcilla[1]

This contribution deals with water renovation in the Bilbao harbour. Hydrodynamic conditions are obtained from numerical simulations and compared with hydrographical surveys for a specific period, from which field data were available. From the results, a strong influence of the tidal-forcing in the water circulation is detected. Due to the complex lay-out of the harbour, non-persistent topographic eddies are observed in the velocity field. Apart from this, the freshwater influence of the Nervión River that discharges in the harbour can be observed in residual currents. On the other hand Lagrangian Particle Tracking Method (LPTM) has been used in order to analyze the water renovation. Residence time distribution in the water domain has been obtained, observing their sensitivity to instant release of the particles (*i.e.* low or high tide).

INTRODUCTION AND OBJECTIVES

Background knowledge on marine dynamics is important for harbour managers in terms of the control of pollution, dredging management and traffic operative conditions. In this study, hydrodynamics and water renovation conditions within the Bilbao Harbour (Spain), located at the mouth of the Nervión Estuary (Southeastern corner of Bay of Biscay), are investigated. The Nervión River Estuary, at its lower reaches, has a surface area of about 20 km^2, an average depth of 30 m and a mean flow of about 36 $m^3 \cdot s^{-1}$ (Figure 1). For the specific period of February 2005, hydrodynamic modelling has been carried out to determine the inner harbour currents using ROMS (Regional Ocean Modelling System). From the current field obtained, the renovation is evaluated through a Lagrangian Particle Tracking Method (LPTM). This study contributes to the advance in the application of numerical tools in a complex geometrical domain. The objective was to get a better understanding of the behaviour of the marine system in meso-tidal harbours (e.g. Bilbao) to provide engineering applications for the harbour and coastal management.

[1]Marine Engineering Laboratory (LIM), Technical University of Catalonia, Jordi Girona s/n, 08023, Barcelona, Spain
[2]Bilbao Harbour Authority, Campo Volantín, 37, 48007, Bilbao- Bizkaia, Spain
[3]Marine Research Division, AZTI-Tecnalia, Herrera Kaia – Portu aldea z/g, 20110, Pasaia – Gipuzkoa, Spain
[4]Puertos del Estado, Avda. del Partenón 10, 28042, Madrid, Spain

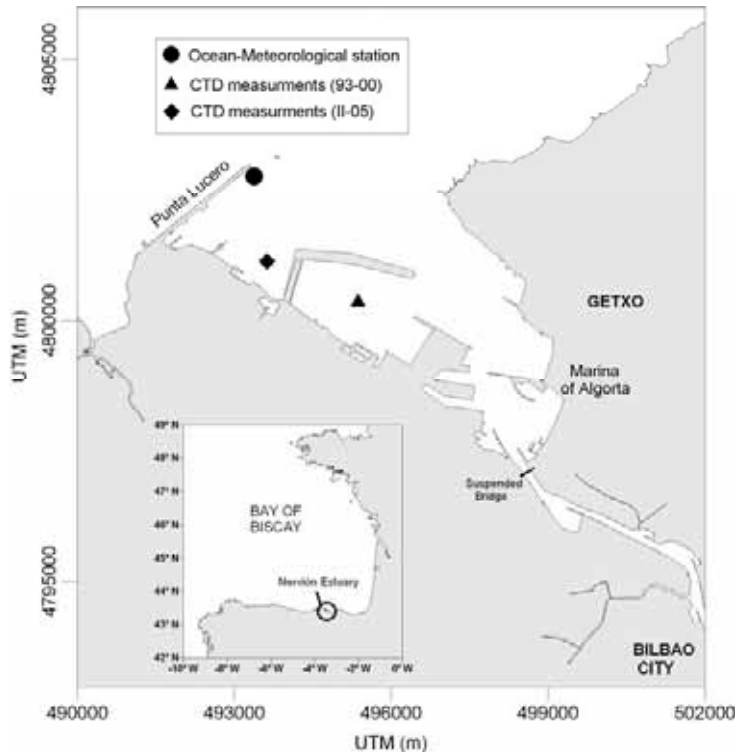

Figure 1. Schematization of the Bilbao Harbour and Nervión Estuary in Northern Spain. The map shows CTD measurements and oceano-meteorological stations used in this contribution. The Keys ♦ and ▲ show the CTD location and period measurements.

HYDRODYNAMIC CHARACTERIZATION

The hydrodynamic model used in the present study is the ROMS (Shchepetkin and McWilliams, 2005). The mean horizontal resolution was 32 m whilst vertically, the water column was divided into 5 sigma coordinate levels. The atmospheric surface forcing used in the model was six-hourly NCEP reanalysis data (provided by the NOAA/OAR/ESRL PSD, Boulder, Colorado, USA, from their web site at www.cdc.noaa.gov). Wind conditions were obtained and introduced into the model from a meteorological station situated in the external breakwater (see Figure 1). For tidal forcing, data from the OSU TOPEX/Poseidon Global Inverse Solution version 5.0 (TPXO.5) have been used. The simulation period has been February 2005. The velocity field for a tidal cycle is observed in Figure 2. In Figure 3, the comparison between the measured and computed u and v time series is shown. The calibration coefficient that has the best fit line between computed and measured velocities (data from Acoustic Doppler Current Profiler, see Figure 1) is 0.0023 for drag coefficient (using quadratic friction law).

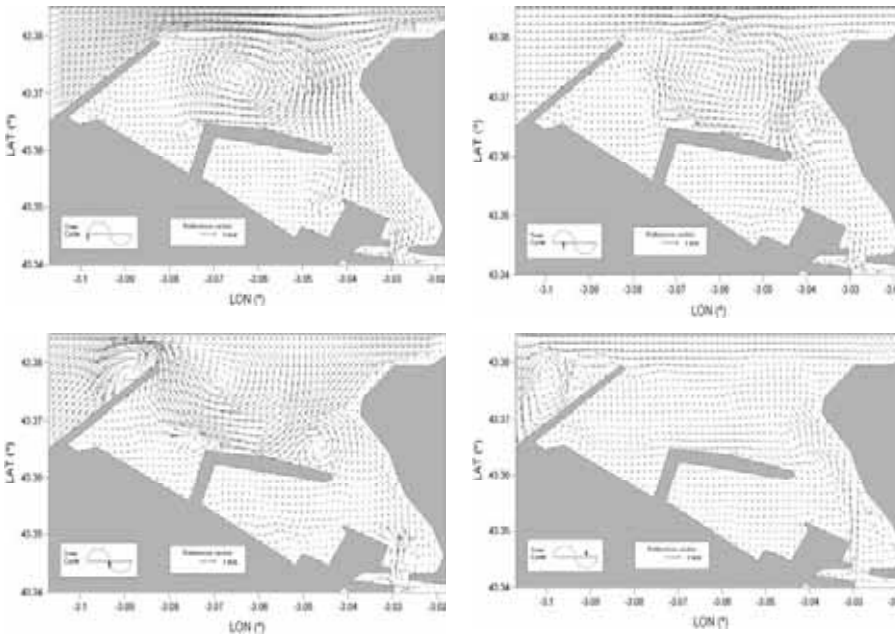

Figure 2. Velocity field obtained from numerical simulations in Bilbao Harbour during a typical spring tidal cycle at 4 m depth.

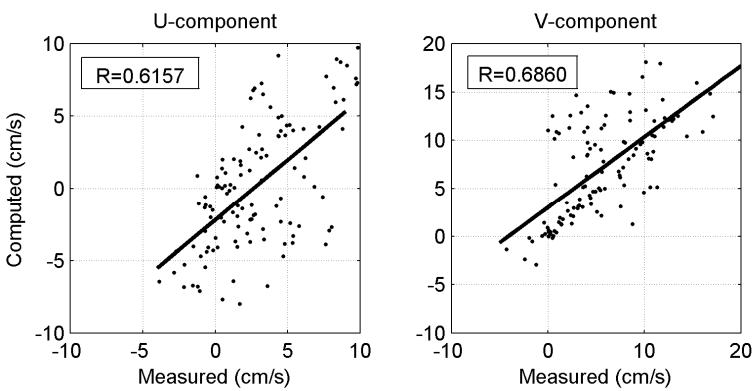

Figure 3. Comparison between the measured and computed u and v components for a characteristic period of February of 2005. The depth considered is 12 m.

Sea level variations, obtained from the model output and the field measurements, are plotted in Figure 4, during a neap-spring cycle. Good agreement between both signals was found. According to these figures, the

velocities and the sea level time-series measured were considerably influenced by the astronomical tide. Considerable disturbances are visible in the instantaneous velocities predicted by the model for the ebb-flood tidal phase. Non-persistent micro-scale eddy structures are formed laterally within the basins inside the harbour, referred to as the topographic small-scale eddies. These eddies are generated during the instantaneous change in the flood-ebb direction and persist generally during the tidal period. Tidally-driven flow separation and transition eddy developments behind headlands are well-known phenomena from elsewhere (Lee et al., 1999). Observing the predicted results, eddy formation is associated outside of the main tidal propagation pattern, as provided by the high currents; these follow the axis of the estuary in the inner zone and within the deepest (bathymetric) part in the harbour mouth.

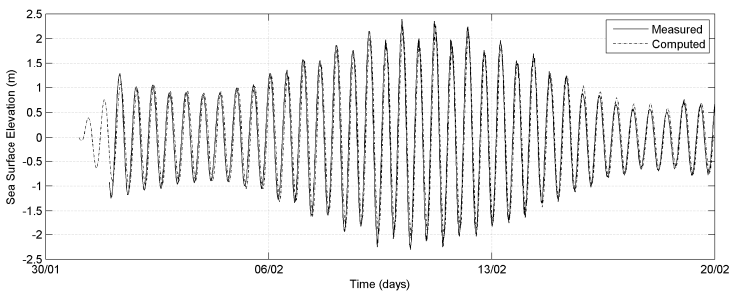

Figure 4. Comparison between sea level variations measured (sea level gauge in the inner harbour) and computed by the model.

RESIDUAL CURRENTS

The residual flow has been obtained by averaging the computed currents over a typical tidal cycle. Such currents are important in the long-term transport of pollutants or suspended material; they are induced by non-linear interactions of the flow, with variable bathymetry. The tidally-averaged velocities are shown in Figure 5, where several residual eddies are observed clearly. It has been widely reported that the tidally-driven circulation is induced within a basin, with a narrow channel, by the nonlinearity of the tidal current flowing through the "river channel". The channel path is suggested in residual current patterns; these "asymmetric" currents are induced by the non-linearity generated by river flow discharge. In this case, tidal-residual eddies are formed on both sides of the central channel path (see Figure 5 corresponding to residual currents).

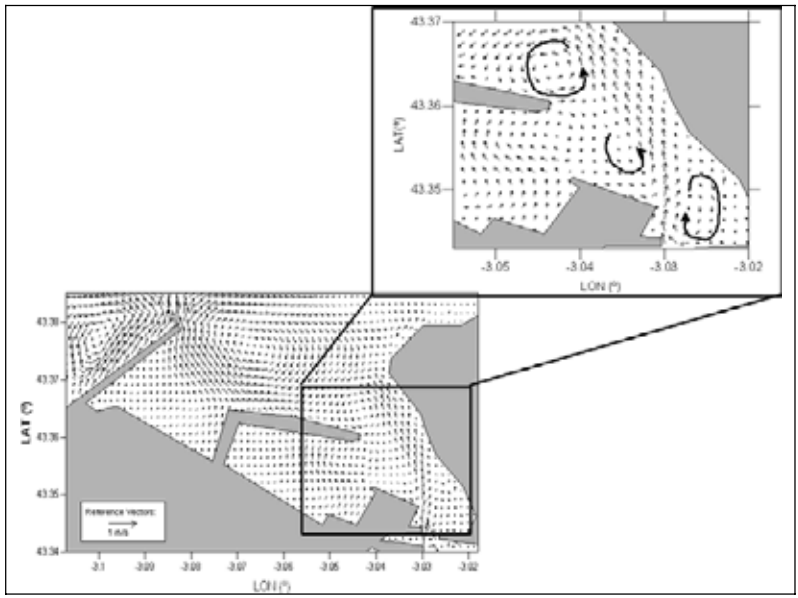

Figure 5. Residual currents obtained at 12 m layer depth.

WATER RENOVATION ANALYSIS

A Lagrangian Particle Tracking Model (LPTM) has been used in order to analyze the water renovation. Particles are deployed in different points of the water domain to evaluate their trajectories. The advective component of transport is solved using a 4th Order Runge-Kutta Method, that allows to minimize the numerical error for cases of particularly complex flows (García-Martínez and Flores-Tovar, 1990). The diffusion part is solved using Random-Walk Algorithm (Al-Rabeh and Gunay, 1992) which simulates the stochastic process of the diffusion as a function of a random process. A collection of numerical experiments has been carried out to evaluate the transport behaviour in the inner harbour. Different trajectories are shown in Figure 6 in order to analyze the following issues:

- Influence of diffusion in the Lagrangian trajectories. Due to the high level of kinetic energy in the inner harbour, the diffusion has a low effect in the central channel (Figure 6, on the left and on the centre). The effect is higher in the less energetic zones, but the total time that the particle leaves the inner harbour does not vary in excess. Also, it should be considered that neglecting the diffusion component allows to save computational cost.
- Sensitivity to instant discharge (*i.e.* low or high tide). The influence of the instant release has a decisive effect on the time that a particle needs to leave the harbour (Residence Time). In Figure 6, the different trajectories for an advective-diffusive particle released in low tide (on the centre) and high

tide (on the right) are shown. In particular, the particle released during high tide takes less time than the one released during low tide.

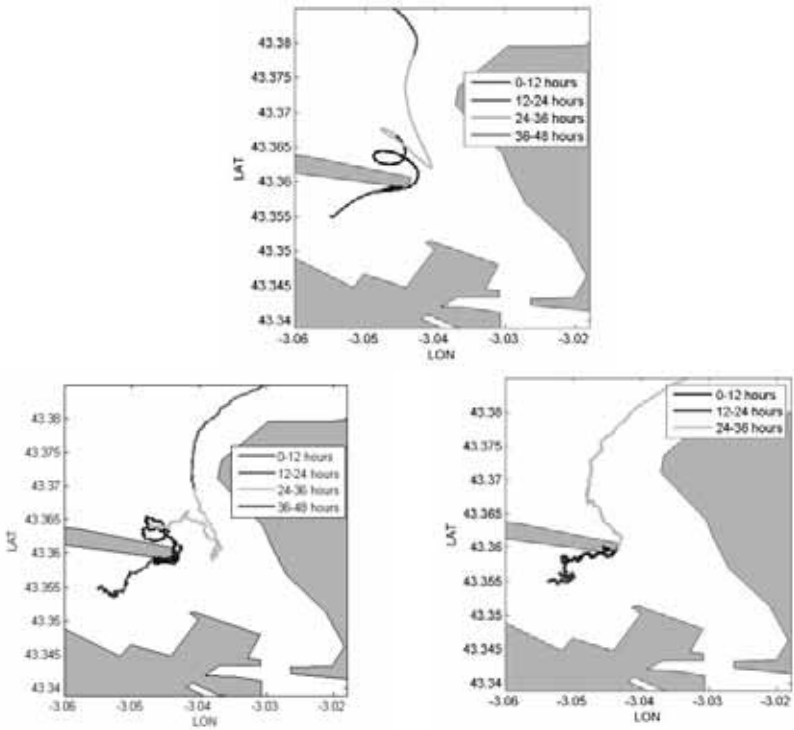

Figure 6. Trajectories of advective Lagrangian particles released in the harbour for different instants: low tide (at the top), low tide + diffusion (at the bottom on the left), high tide + diffusion (at the bottom on the right).

To parameterize the renovation behaviour in the whole domain, a finite number of advective particles distributed homogeneously have been released. The purpose was to compute the time required for each particle to leave the harbour water domain. In Figure 7, the Residence Time distribution obtained averaging the Residence Time of high-tide and low-tide releasing instant, is shown. A considerable difference among zones of the harbour is observed. This behaviour is related with the water circulation pattern: while the central channel is influenced by the Nervión flow and by the wave tide propagation, the western and innermost zones of the estuary present low water renovation.

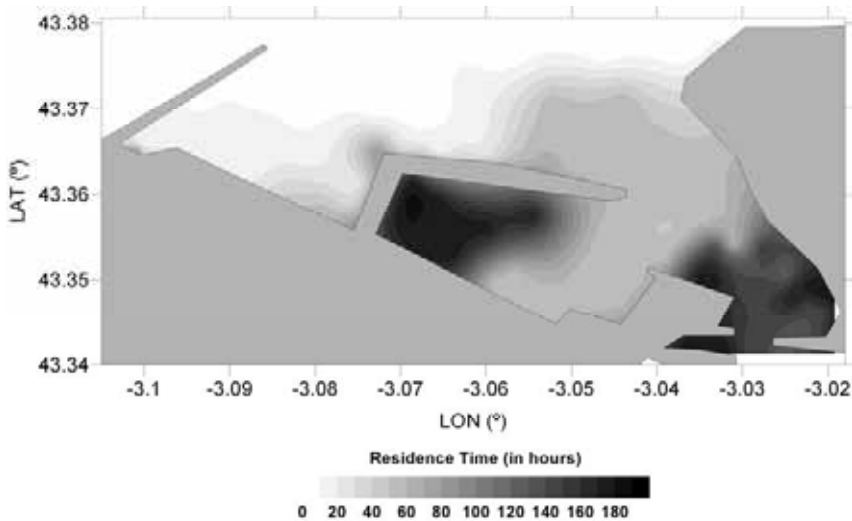

Figure 7. Residence time (in hours) distribution in Bilbao Harbour.

CONCLUSIONS

Numerical modelling of currents is a powerful tool for several applications related with harbour engineering and management. An application to water quality (*i.e.* water renovation parameterization) has been shown in this contribution. To achieve this goal, a high level of knowledge of the hydrodynamics through numerical simulation supported by field data is required. In the Bilbao harbour case, simulated with ROMS, its hydrodynamics are mainly controlled by the tide wave propagation in the estuary. From the results of Lagrangian Particle Tracking Model, different hydrodynamic zones are defined from the renovation point of view. On one side, the main channel presents an advective behaviour due to the high velocity. On the other side, the transport behaviour of substances in the west part of the inner basins and the innermost reaches of the estuary are mainly controlled by diffusion (i.e., low water renovation).

As a future work, it is worth mentioning the implementation of the system in operational mode. Also, advances in the knowledge of hydrodynamics (*i.e.* 3D effects in the transport modelling, influence of the river discharge, etc.) should be also taken into account.

REFERNCES

Al-Rabeh, A.H., Gunay, N., 1992. On the application of a particles dispersion model. *Coastal Engineering,* 17, 195-210.

García-Martínez, R. and Flores-Tovar H., 1990. Computer Modeling of Oil Spill Trajectories With a High Accuracy Method. *Spill Science & Technology Bulletin* 5, No. 5/6, pp. 323-330.

Lee, H.-J., Chao, S.Y., Fan K.-L., Kuo, T.-Y., 1999. Tide-Induced Eddies and Upwelling in a Semi-enclosed Basin: Nan Wan. *Estuarine, Coastal and. Shelf Science,* 49, 775-787.

Shchepetkin, A.F., McWilliams, J.C., 2005. The regional oceanic modeling system (ROMS): a split-explicit, free-surface, topography-following-coordinate oceanic model. *Ocean Modelling,* 9, 347-404.

RESTORATION OF THE ZWIN TIDAL INLET: HYDRODYNAMICAL AND MORPHOLOGICAL STUDY

Chantal Martens[1], Boudewijn Decrop[2], Rob Steijn[3], Annelies Bolle[2], Jelmer Cleveringa[3], Miguel Berteloot[4], Koen Trouw[2]

The Zwin is a nature reserve on the Dutch-Belgian Coast. Ever since its creation during a storm flood in 1134, the inlet has been silting up, causing a reduction in the biological diversity of the area. Moreover the existence of the Zwin is threatened as the inlet channel is closing off. In 1827 it was decided to construct a dike around the remaining (small) inlet, for safety reasons. In 2006 a multidisciplinary study was started to investigate the optimal and most sustainable way of preserving the Zwin nature reserve as a tidal inlet. Several possible solutions for the preservation of the inlet have been examined. A hydrodynamical model of the area was set up; the results provided the base for the study of the short and long term morphological effects .

INTRODUCTION

Description of the study area

The Zwin is located along the Belgian-Dutch coast, in the Southern North Sea. Its total surface is 170 ha, and the Belgian-Dutch frontier divides it in a 135 ha Belgian part, and a 35 ha Dutch part. The tidal range along the coast is 5 meters, which makes it a macro tidal coast.

Figure 1. Aerial photograph of the Zwin (Google Maps)

The inlet consists of a main channel coming from the sea, and a number of smaller subbranches that distribute the tidal water twice a day over the inlet area. Since 1952 maintenance of the area consisted mainly in

[1] IMDC, now at aMT-Maritime Access Department of the Flemish Community , Tavernierkaai 3 B-2000 Antwerpen Belgium (chantal.martens@mow.vlaanderen.be)
[2] IMDC, Coveliersstraat 15 B-2600 Berchem Belgium (ktr@imdc.be)
[3] Alkyon –PO BOX 248 8300 AE Emmeloord The Netherlands
[4] MDK –Coastal Division of the Flemish Community Vrijhavenstraat 3 8400 Ostend-Belgium (miguel.berteloot@MOW.vlaanderen.be)

keeping the channels free and relocating the inlet channel when it had migrated too far eastward, thus threatening the dune area located in the Dutch area of the Zwin. The location of the older (now disconnected) branches can still be clearly noticed on the topography of the area (figure 2).

The Zwin consists of tidal flats (located under the average high water line) and salt marshes (located above the average high water line). Due to the continuous sedimentation in the area, the ratio tidal flats/salt marshes is shrinking, and increasingly larger portions of the area are situated above the high water line, thus reducing the landscape variety.

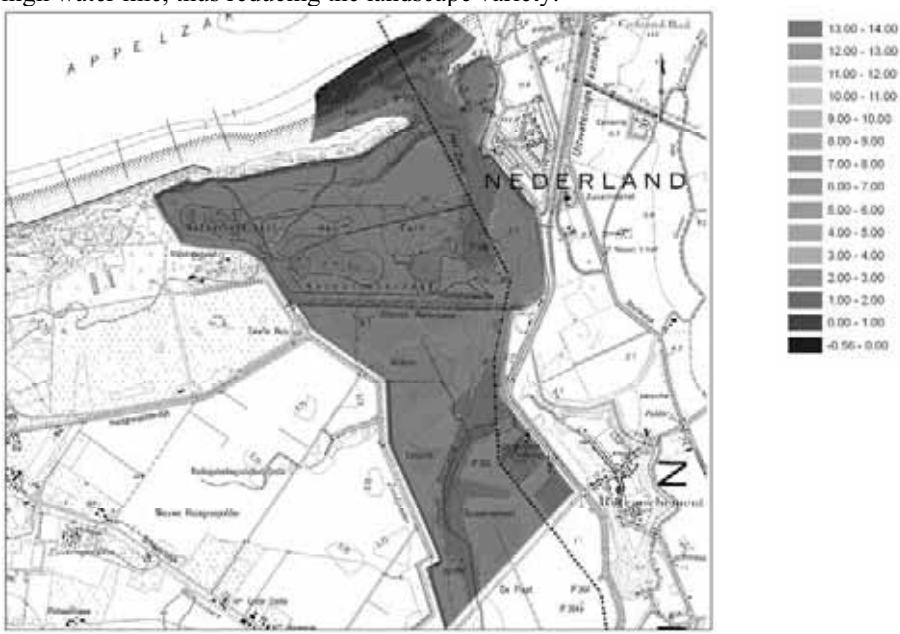

Figure 2. Topography of the study area. Landward of the current dike, the remnants of the old inlet channel can still be clearly seen

Although small maintenance works are carried out , the siltation of the inlet is progressing rapidly. The siltation is caused by two phenomena:
A first phenomenon is the surf zone longshore transport, which is running in a residual eastward direction along the entrance to the Zwin. This transport is causing the migration and subsequent narrowing of the inlet channel. It is estimated that the channel migrates at a rate of about 50-75 m/year (Econnection, 2004). Since the outlet is already at the east boundary of the area, it has to be re-located continuously westward. The tidal prism at normal tide in the Zwin is approximately 180.000 m3. The net surf zone transport is estimated tobe 200.000m3 per year in eastward direction. The ratio of these two parameters P/M is 0,75. Considering the tidal volume of a spring tide (350.000-

400.000 m3) this ratio is 3, which is still far less than the value of 20 necessary for a stable inlet (Bruun, 1960).
A second cause for the problems the Zwin is currently experiencing is the tidal asymmetry in the area, which is resulting in a flood dominated tidal current.
The outflow period being around three times longer than the inflow period (Fig 3), outflow velocities are significantly lower than during flood and insufficient to resuspend the settled sediment that has been brought into the area during flood.

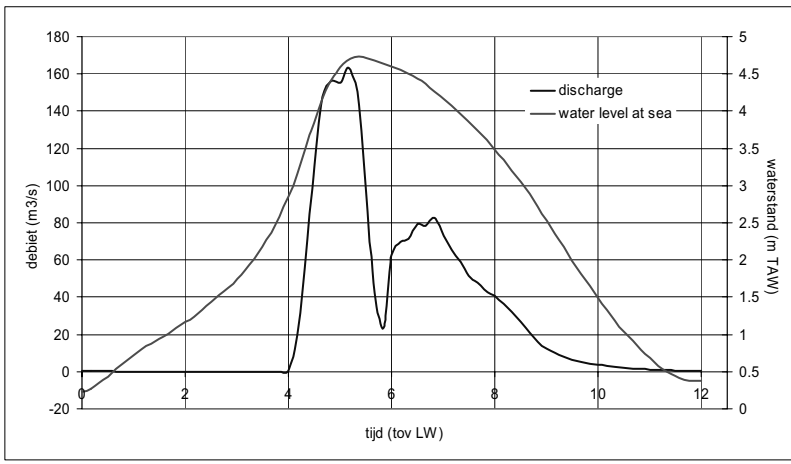

Figure 3. water inflow and outflow during a tidal cycle (model result)

Possible solutions

In order to solve the problems the area is faced with, two aims should be accomplished

1. Reduction of the tidal asymmetry to reduce the sedimentation in the area;
2. Increase of the tidal prism to stabilize the inlet;

By adding an additional area to the Zwin, the tidal prism will increase, thus helping the stabilisation of the tidal inlet. Different enlargements are examined. Not only the enlargement itself is important, but also the prediction of the new channel dimensions and the slope of the channel bed.
The enlargement can be realised in two ways:

1. constructing a low dike around the new area and connecting this area with the actual Zwin by a channel which can be closed by a barrier during storms: this has the advantage that the dikes around the extension don't need to be very high, and the visual impact on the landscape will be less. A disadvantage is that the connection between the existing Zwin and the new extension will be less clear : the dike will prevent fauna and flora migration between the two parts and a clear visual division will exist between old and new, loosening the connection with the sea;

2. remove the old dike and build a high dike around the new area. In this solution, the new extended Zwin will function as one entity, and no difference will be seen between the original and the new parts. This will however, induce the need for a relatively high dike (11 mTAW);

In addition to the basic configurations additional configurations were included:

- Enlargement of the mouth in order to reduce the flow contraction during flood, visible on figure 4, in order to reduce tidal asymmetry.

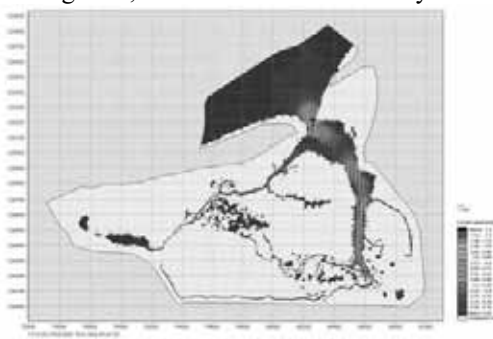

Figure 4. Flow contraction around the entrance to the Zwin during flood (model result)

- Relocation of the inlet to the utmost western location, to give it more freedom to migrate eastward, and reduce the need for frequent relocations. The relocation of the inlet would be combined with a lateral extension of the Zwin, as shown in figure 5.

Figure 5. westward relocation of the entrance channel

- The use of groynes around the inlet in order to block longshore transport
- The use of flushing, with water drained from the polders, could be used and optimized, based on the expectation that the flushing of the (fresh) polder water through the Zwin would cause an additional shear stress and

subsequent erosion of the settled material. It has however also be taken into account that the density gradient (fresh water from the flushing to salty sea water), would be causing net sediment transport into the Zwin

Figure 6. reservoir for freshwater flushing

MODELLING

A 2D hydrodynamic model was set up, to compare the different scenarios outlined above. The results of the model runs were used in a later phase as a basis for the morphodynamic assessment.

Description of the model

The model was set up in MIKE21FM (DHI, 2006), using finite volume calculations. For the scenarios where a movable barrier is constructed between the existing and new areas, a connection is established using MIKE FLOOD. Water levels and discharges are calculated by MIKE11, and the communication between both models is carried out by MIKE FLOOD. Initially, the flow field associated with water in MIKE21FM is calculated on the time step n, then an extrapolation of this flow field in time step n +1/2. The water for this "interim" time step is transmitted to MIKE11 and used for the upstream and downstream boundary conditions for the 1D model, and the discharge through the structure is calculated. This discharge is then distributed on a proportional line in the 2D model, and is thus translated into a flow velocity, taking into account the water depth. Mike21Fm has the advantage that the grid is made up of triangular elements of variable dimensions. This advantage was used to enter the thalweg of as much as possible channel systems in the structure of the grid and thus avoid the narrow gullies blocked by interpolation between channel banks. Furthermore, the resolution of the grid varies with elements of 30m on the plates and elements of 4 to 5m in and around the gullies.

Bathymetries and channel geometry

The bathymetry used is made up of the DHM Flanders (OC Gis (2003), supplemented by the DHM of the beach (VITO, 2005) and bathymetric data for the foreshore (AWK, 2003). The open seaward edge lies along the -0.5m TAW

isobath, lateral on the beach slope to the dune foot. An average spring tide curve was selected with a maximum elevation of 4m73 TAW, and two warming tides were included. For the alternatives where flushing was considered, a block function consisting of time series with a 200,000 cubic meters in 1 hour discharge was used.

The tidal system in the Zwin is in many respects not comparable with relatively larger and deeper tidal systems, such as the Wadden Sea and the Western Scheldt. The gullies are relatively shallower and much broader. The tide plays only a role in the water movement during part of the tidal cycle because of the high altitude of the area. Known relationships, to describe the characteristics of channels in relation to the catchment area or the tidal prism, are not suitable for the Zwin because of the big difference with reference areas used to establish these relationships.

Due to the large increase in the tidal prism (with more than 500%) that is expected for the scenarios, it is no longer relevant to use the current relationship between the tidal prism (P) and the channel cross-section for future situations. Due to the large increase in tidal prism, the main channel will be part of the intertidal and subtidal range for a longer part of the tide. In and outflow characteristics, and channel geometry will thus be significantly different from the current situation.

Because of the inherent unpredictability of the future situation, a number of scenarios for the future relationship between the tidal prism (P) and the surface of the cross section of the trench are described, which lie between the current situation in the Zwin and in 'real tidal basins ', such as the Wadden Sea or the Western Scheldt.

The relationship between the tidal prism (P) and the surface of the cross section of the new channel (A) is based on the formula:

$$A_c = CP^n$$

Where Ac = flow area
C = coefficient
n = coefficient, which in this situation is 1
P = tidal prism

The variable that describes the field conditions is C. In the current Zwin (without the mouth) C = 1.000 x 10-6. In the Western Scheldt C = 80 x 10-6. For the future situations, calculations will be made based on a C = 100, 200 or 300, situated between these two extremes. 200 is considered a standard value, 100 is a low value.

The relationship between the tidal prism (P) and the width of the gullies (B) in the Zwin follows the relationship B = 7.64 P + 0.0005 (see Figure 7). Based on this relationship, the width of the gullies for the scenarios would be around 900 meters. This seems to be a too broad channel for this relatively small area.

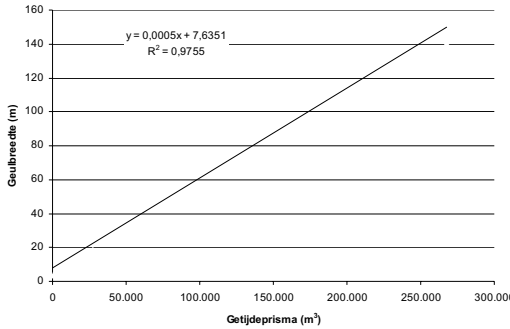

Figure 7. relation between channel width B (y) and tidal prism P (x). For the current Zwin, the relation is B = 0,0005P + 7,64P

A simple geometric model of the gullies in the current situation and future situations was used to estimate the relationship. In this model we count the channels' together ', so that the branching channel system from the real world looks like a trapezoid-shaped 'box '.
The main assumption in this geometric model is that depth of the small trench around the landward end of the basin does not change and depth of the trench on the seaward side depends on the distance to the end of the basin. The necessary wet surface in the mouth is achieved by changing the width, because the depth is only dependent on the length of the basin. The depth of the basin is considered as the distance from the mouth to the rear end of the gullies. Based on the expected tidal volumes and the distance to the rear / mouth, the new depths and widths of the channels can be calculated.

Model results

18 model runs were carried out, an overview of the different set ups is given in table 1.

Table 1. description of the model run setups	
0	Current Zwin
1a	Extension towards the south, with an additional 120 ha. Complete removal of the existing dike
1b	Id 1a, but flushing with polder water is included
2a	Extension towards the south, with an additional 180 ha. Complete removal of the existing dike
2b	Id 2a, but flushing with polder water is included
3a	Lateral expansion towards the East and West with an additional 140 ha. A siphon is used to transfer water to the western part, underneath the existing channel “Uitwateringskanaal”
3c	Lateral expansion towards the East and South with an additional 140 ha. Complete removal of the existing dike on the southward side
4a	Id 1a, but the internal dike is not removed. Instead, a

	movable barrier is installed, that will be closed during storm tide
4b	Id 1b, but the internal dike is not removed. Instead, a movable barrier is installed, that will be closed during storm tide
5c	Id 2a, but the internal dike is not removed. Instead, a movable barrier is installed, that will be closed during storm tide
5d	Id 2b, but the internal dike is not removed. Instead, a movable barrier is installed, that will be closed during storm tide
4-1->4-7	Further testing of the configuration for the removable barrier. The effect of a double width barrier is tested, as well as the impact of a half width barrier. In addition, it is tested whether a positive effect can be found from flushing with salt water, using the new expansion areas as a flushing basin, and the movable barrier as a flushing construction
3 West	Testing of the effects of the westward relocation of the entrance channel, combined with a lateral expansion of the Zwin.

For all of the modelled scenarios, the following was calculated from the model results

- Flow velocities for the study area, time and duration of maximum flow velocities
- Tidal prisms
- Evolution of the shear stresses during a tidal cycle
- Residence times for water
- Evolution of the water level during a tidal cycle.

These datasets were then used as a basis for a further morphological assessment of the alternatives. From the tidal prism data and the numbers for the longshore coastal sediment transport, the Bruun parameter for the different scenarios can be compared.

MORPHOLOGICAL ASSESSMENT

Based on the results of the hydrodynamical modeling, a morphological assessment was made of the different scenarios.

Evolution of the Zwin tidal inlet

The morphological evolution of the Zwin tidal inlet is governed by two processes

A first process is the initial formation of tidal channels in the area. It is a self-reinforcing process, which will take between 1-10 years, and will cause a local redistribution of the sediment

A second process is the filling of the (extended) basin. This will be progressing slower as the basin is filled. Depending on the size and shape of the basin, the filling will take a few decades to a hundred years.

For the stability of the mouth the ratio between the tidal prism of the basin and sediment transport along the coast is calculated. This ratio is the parameter of Bruun, said R (R = P / MTOT, where P is the tidal prism and MTOT the total longshore transport). The higher the R-parameter, the more stable the mouth will be. The Bruun parameter for different scenarios and the current situation is shown in Table 2. It is based on a value of 100,000 m3 for M, since only the longshore transport that is influencing the shallow mouth should be taken into account.

In the course of time, the tidal prism of the Zwin will diminish because sedimentation will take place in the basin. The stability of the estuary will thus gradually decrease. As an indication of this, table 2 also shows the tidal prism after 30 years and the resulting Bruun parameters.

Table 2. Tidal prism and Bruun parameter for the scenarios now and after 30 years of morphological evolution

	Current situation	1a	2a	3a	3c	4a	5c
Tidal prism at start (in 1000 m^3)	270	930	1570	570	570	900	1300
R	2.7	9.3	15.7	5.7	5.7	9	13
Tidal prism (after 30 years)	-	326	476	258	218	327	472
R (after 30 years)	-	3.3	4.76	2.58	2.18	3.27	4.72

Sedimentation processes in the extended Zwin

To determine the overall morphological development, i.e. the filling of the basin, a simple quantitative approach is used, in which the filling of the basin is calculated on the basis of the following parameters

C: the sediment concentration at the mouth of the Zwin (long-term average over the whole estuary)
P: tidal prism
ρ_s :density of sediment
E: the trapping efficiency of the basin
t: the tidal factor

The sedimentation per tide is then calculated as

$$S_{tide} = E * ((P * C) / \rho_s)$$

The sedimentation per year is given by the number of tides per year (740) and the factor t which normalises the contribution from spring and neap tides, in comparison to a normal tide:

$$S_{year} = 740 * t * S_{tide}$$

The evolution of the basin volume over time is given by

$$V_{water}^{t=n+1} = V_{water}^{n} - S_{year}$$

As long as the water volume of the basin is superior to the tidal prism, the tidal prism does not change. When the volume of water in the basin is inferior to the tidal prism, the tidal prism is equivalent to the volume of water in the basin. The water volume is determined by the local flood in the Zwin and the newly added areas.

In the above calculations quite a few uncertainties exist. For example, it is not known what the long-term average sediment concentration in the mouth of the Zwin is. Nor is it known what the trapping efficiency of the basin is and what the new situation will be. Neither the relative contribution of different water levels to the sedimentation in the Zwin is known. Therefore the sensitivity of the calculations for these factors was tested. The sediment concentration has the greatest influence on the calculations. Compared to 10 years in the basic scenario, it provides a bandwidth of - 3 and plus 10 years. The other factors influence the development to a slightly less extent, order of magnitude of a year.

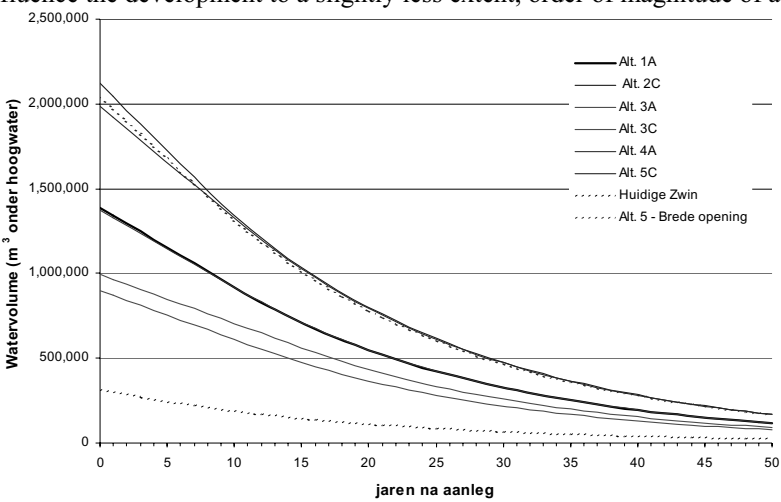

Figure 8. development of the water volume beneath high water level, over a period of 50 years, for the different scenarios.

Development of channel and salt marsh areas

Assuming that the size of the channels is in balance with the tidal prism, is universally applied in tidal basins. The relationship with the form:

$$A_c = CP^n$$

Where Ac = flow area
C = coefficient
n = coefficient, which in this situation is 1
P = tidal prism

is used to derive the equilibrium depths of the gullies in the Zwin. The length of the basin is used to determine the depth of the channels. The length of the basin also acts as a measure for the shape of the basin. Relatively more channels and therefore more gully area are required to fill a narrow and elongated basin than to do the same for a short and wide basin.
The average altitude of the basin is used as a measure for the amount of salt marsh and tidal flats. When the tidal flats at the border of the gullies are relatively low, they will function as a part of the channel for a part of the tidal cycle: at that moment the wet surface is larger then that of the channel alone. When the mud flats along the channel are higher above the water level, they will be used during a smaller part of the tidal cycle, and the channel will need a bigger wet cross-section to accommodate the greatest part of the flow by itself.
All the above mentioned relationships come together in the formula for the area gullies:

$$O_{channels} = ((C*P)*(\beta*L))/(\gamma*\sqrt{d_{mean}})$$

C * P in this relationship forms the connection to the tidal prism, where C is the same ratio as in the relationship: Ac = CPN,,
In β*L, L stands for the length of the basin and β is the length factor, which regulates the contribution of L. The effect of depth is approached by $\gamma*\sqrt{d_{mean}}$, where d_{mean} is given by the water volume of the basin below the high water level divided by the total area, and γ is the depth factor, which regulates d.
Figure 9 gives the evolution of the channel area for the different scenarios.

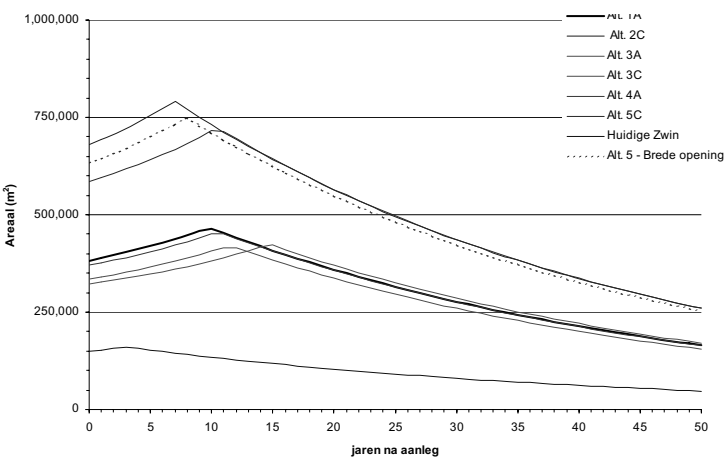

Figure 9. Development of the gullies in the area for the different scenarios, including the current Zwin.

Figure 10 gives a schematical evolution of the Zwin area, for scenario 1 (expansion of +/- 120 ha).

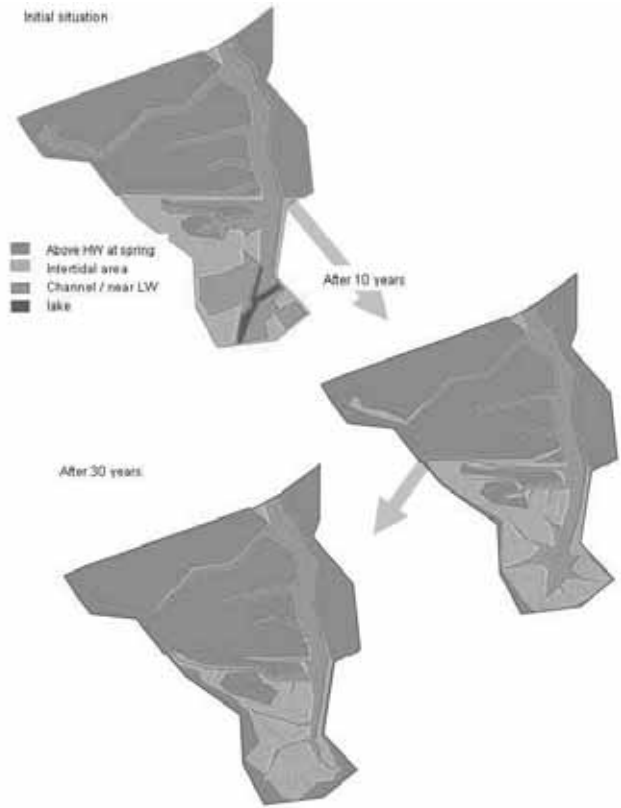

Figure 10. Estimated evolution of the expanded Zwin over a period of 30 years.

CONCLUSIONS

Effect of flushing

The use of a flushing basin at the landward side of the basin leads to a brief peak of high flow rates during flushing. These high flow rates move with the wave of flushing water towards the mouth. The highest flow rates occur in the immediate vicinity of the flushing basin and diminish in the direction of the mouth. The flow velocities in the mouth are similar to the flow velocities during the peak of the ebb tide. Admittedly, flushing creates a larger volume of water outlet, but this increase does not mean that the tidal prism (which is used to calculate the stability of the mouth) increases with the same volume: the effect on the stability is less. Moreover, the passing of a fresh water wave through the system will not create a stable gradient, but will cause a sudden transition from salty to fresh water, which will be difficult to adapt to for fauna and flora.

Effect of movable barriers

A movable barrier is a rigid element in the natural system. The sizing of the construction is aimed at a single situation and not on a continuously evolving tidal landscape. The construction can also reduce the supply of sediment. Because of these aspects a movable barrier, as opposed to a complete removal of the dike between the original, is seen as less desirable for the morphological developments. Of the different types of structures a siphon, as needed in alternative 3, is the most objectionable, because of restrictions on water and sediment supply.

Comparison of the different scenarios

The 5 main scenarios were compared for 5 parameters, as shown in table 3.

Table 3. comparison of the scenarios.

	Stability of the mouth	Movable barrier	Initial salt marsh area	Salt marsh area after 30 years	Sand/mud
1	+		+	+	Mud
2	++		++	++	Mud
3	0	-	0	0	Sand & mud
4	+	-	+	+	Mud
5	++	-	++	++	Mud

The scenarios with the greatest expansion (i.e. 2 and 5) have a higher tidal prism, and therefore a higher stability at the mouth, and a higher area of salt marsh and tidal flats both at the beginning and after 30 years of evolution. Scenarios with a lateral expansion (nr.3) have a significantly smaller increase in the tidal prism, and less opportunities for the creation of salt marsh and tidal flats.

ACKNOWLEDGMENTS

MDK Coastal Division of the Flemish Community is thanked for the funding of the project, and for the assistance during the field measurements.

REFERENCES

Bowman ,1993. Morphodynamics of the stagnating Zwin inlet, The Netherlands. *Sedimentary Geology* 84 219-239

Buonaiuto and Krauss (2003) Limiting slopes and depths at ebb tidal shoals, *Coastal Engineering* 48 (2003) 51-65

Bruun and Gerritsen 1960. *Stability of Coastal Inlets* North Holland Publishing Co.Amsterdam

DHI 2006. *Mike 21 Software Manual* Danish Hydraulic Institute, Horsholm

Econnection, 2004. *Preliminair milieuhygienisch onderzoek mbt de afgravingen ikv het beheersplan voor " het Zwin" (in Dutch)*

3D LAGRANGIAN SIMULATION OF TSUNAMI FLOOD ON BRIDGE WITH DRIFT WOODS

Hiroyuki Ikari[1] and Hitoshi Gotoh[2]

When the earthquake off the west coast of Northern Sumatra and the resultant giant tsunami in the Indian Ocean in 2004 occurred, a variety of damages were caused in countries around the Indian Ocean. For example, it was reported that a river run-up tsunami washed away a girder bridge crossing a river. In this study, numerical simulations by the particle method, which is suitable to treat a moving object and to track a water surface, are carried out. The calculated results show good agreement with previous hydraulic experiments. In addition, a washed process of a girder bridge in the case that a tsunami with drift woods collides with a bridge with handrail is also simulated.

OBJECTIVES

Countries around the Indian Ocean were damaged enormously by the earthquake off the west coast of Northern Sumatra and the resultant giant tsunami in 2004. In Sri Lanka, it is reported that bridges are destructed or disappeared due to a river run-up of tsunami and the resultant flooding. For example, a girder bridge crossing a river about 10m in width was washed away. Shoji and Mori (2006) conducted serial hydraulic experiments of washed girder bridge in a 1/100 scale model, and examined the relation of a tsunami velocity and specifications of a girder bridge. However, because it is difficult to carry out a hydraulic experiment to measure detailed physical properties in tsunami run-up flow, application of numerical analysis is effective to understand the mechanism of this kind of phenomenon.

The particle method is suitable to treat a movable object such as a girder bridge and to track a water surface in a rapidly changing flow including a fragmentation and a coalescence of water like a splash (Koshizuka et al. 1998, Gotoh et al. 2005). The particle method has a disadvantage in computational load, however, owing to development of a computer and a technique of parallel computing in these days, a 3-D calculation has been carried out (Shibata et al. 2004). Therefore, in this study, a washed process of a girder bridge by a tsunami run-up and the resultant flooding is simulated by using the MPS (Moving Particle Semi-implicit) method (Koshizuka et al. 1995). In the previous study, a girder bridge was expressed as a flatting board. In this study, in addition to the same situation as the previous study, influence of driftwoods and a handrail in the washed process of a girder bridge by a tsunami run-up is also investigated.

[1] NEWJEC Incorporation, Honjo-Higashi, Kita-ku, Osaka, 531-0074, Japan.
[2] Dept. of Urban and Environmental Eng., Kyoto University, Katsura Campas, Nishikyo-ku, Kyoto, 615-8540, Japan.

NUMERICAL MODEL

MPS Method

The equations of motion of liquid and solid particles are as follows:

$$\rho_l \frac{D\boldsymbol{u}_l}{Dt} = -\nabla p_l + \mu_l \nabla^2 \boldsymbol{u}_l + \boldsymbol{f}_{lsp} + \rho_l \boldsymbol{g} \tag{1}$$

$$\rho_s \frac{D\boldsymbol{u}_s}{Dt} = -\nabla p_s + \mu_s \nabla^2 \boldsymbol{u}_s - \boldsymbol{f}_{lsp} + \rho_s \boldsymbol{g} + \boldsymbol{f}_{colp} \tag{2}$$

where $\boldsymbol{u}$ is the velocity vector, p is the pressure, ρ is the density, $\boldsymbol{g}$ is the gravitational acceleration vector, μ is the viscosity, $\boldsymbol{f}_{lsp}$ is the interaction force vector between liquid and solid particles, $\boldsymbol{f}_{colp}$ is the collisional force vector between solid particles, mentioned later. Subscript l or s shows liquid phase or solid phase.

In the MPS method, the pressure term and the viscous term is discretized by a particle interaction model between neighboring particles of the target particle, as follows:

$$\langle \nabla p \rangle_i = \frac{D_0}{n_0} \sum_{j \neq i} \left\{ \frac{p_j - p_i}{\left| \boldsymbol{r}_{ij} \right|^2} (\boldsymbol{r}_{ij}) \cdot w(\left| \boldsymbol{r}_{ij} \right|) \right\} \tag{3}$$

$$\nu \langle \nabla^2 \boldsymbol{u} \rangle_i = \frac{2\nu D_0}{n_0 \lambda} \sum_{j \neq i} (\boldsymbol{u}_j - \boldsymbol{u}_i) w(\left| \boldsymbol{r}_{ij} \right|) \tag{4}$$

$$\lambda = \sum_{j \neq i} w(\left| \boldsymbol{r}_{ij} \right|) \left| \boldsymbol{r}_{ij} \right|^2 \Big/ \sum_{j \neq i} w(\left| \boldsymbol{r}_{ij} \right|) \tag{5}$$

$$\boldsymbol{r}_{ij} = \boldsymbol{r}_j - \boldsymbol{r}_i \tag{6}$$

$$w(r) = \begin{cases} \dfrac{r_e}{r} - 1 & for \quad r \leq r_e \\ 0 & for \quad r > r_e \end{cases} \tag{7}$$

in which D_0 is number of dimensions, $\boldsymbol{r}_i$ is the position vector and $w(r)$ is the weight function, or influencial range of particle interaction. The particle number density is defined as follows:

$$n_i = \sum_{j \neq i} w(\left| \boldsymbol{r}_{ij} \right|) \tag{8}$$

The incompressibility of fluid condition is satisfied by keeping the particle number density constant n_0.

Passively Moving Solid Model

A girder bridge and a drift wood are made by connecting some solid particles and tracked by using the passively moving solid model (Koshizuka et al. 1998). Firstly, the connections between the particles constituting a movable object are cancelled temporally, and calculations of motion are conducted with liquid particles. After that, with keeping the centroid of the movable object and its angular momentum, the positions of moving-object constituting particles are modified to keep their relative positions.

In the calculation of modification of position due to rotational motion of rigid body, the quaternion is used in the same way as Shibata et al. (2004).

At first, by using the centroid $\boldsymbol{r}_{kg}(t)$ of a movable object k at the time t, the angular momentum vector $\boldsymbol{L}_k$ is given as follows:

$$\boldsymbol{r}_{kg}(t) = \frac{1}{N_k}\sum_{i=1}^{N_k}\boldsymbol{r}_{ki}(t) \tag{9}$$

$$\boldsymbol{L}_k = \rho\sum_{i=1}^{N_k} d_{ki}^3 \boldsymbol{u}_{ki}(t+\Delta t)\times\left(\boldsymbol{r}_{ki}(t)-\boldsymbol{r}_{kg}(t)\right) \tag{10}$$

The angular velocity vector $\boldsymbol{\omega}_k$ is estimated from the equation of rotational motion as follow:

$$\boldsymbol{I}_k\boldsymbol{\omega}_k = \boldsymbol{L}_k \tag{11}$$

$$\boldsymbol{I}_k = \rho\sum_{i=1}^{N_k} d_{ki}^3 \cdot \begin{pmatrix} \left|\boldsymbol{r}_{kigy}\right|^2+\left|\boldsymbol{r}_{kigz}\right|^2 & -\left|\boldsymbol{r}_{kigx}\right|\left|\boldsymbol{r}_{kigy}\right| & -\left|\boldsymbol{r}_{kigx}\right|\left|\boldsymbol{r}_{kigz}\right| \\ -\left|\boldsymbol{r}_{kigy}\right|\left|\boldsymbol{r}_{kigx}\right| & \left|\boldsymbol{r}_{kigx}\right|^2+\left|\boldsymbol{r}_{kigz}\right|^2 & -\left|\boldsymbol{r}_{kigy}\right|\left|\boldsymbol{r}_{kigz}\right| \\ -\left|\boldsymbol{r}_{kigz}\right|\left|\boldsymbol{r}_{kigx}\right| & -\left|\boldsymbol{r}_{kigz}\right|\left|\boldsymbol{r}_{kigy}\right| & \left|\boldsymbol{r}_{kigx}\right|^2+\left|\boldsymbol{r}_{kigy}\right|^2 \end{pmatrix} \tag{12}$$

$$\boldsymbol{r}_{ig\xi} = \boldsymbol{r}_{i\xi} - \boldsymbol{r}_{g\xi} \tag{13}$$

in which subscript ξ is x, y or z.

Then, the rotational axis vector $\boldsymbol{v}_k$ and the rotational angle θ_k are calculated based on this angular velocity vector, and the quaternion $\boldsymbol{q}$ is given as follows:

$$\boldsymbol{v}_k = \frac{1}{\left|\boldsymbol{\omega}_k\right|}\left(\omega_{kx},\omega_{ky},\omega_{kz}\right) \tag{14}$$

$$\theta_k = \Delta t \left| \boldsymbol{\omega}_k \right| \tag{15}$$

$$\begin{aligned} \boldsymbol{q} &= \left(q_x, q_y, q_z, s \right) \\ &= \left(\nu_x \sin\left(\frac{\theta_k}{2} \right), \nu_y \sin\left(\frac{\theta_k}{2} \right), \nu_z \sin\left(\frac{\theta_k}{2} \right), \cos\left(\frac{\theta_k}{2} \right) \right) \end{aligned} \tag{16}$$

Finally, the positions and the velocities of the particles constituting a movable object by using the rotational matrix of the quaternion as follows:

$$\boldsymbol{r}_{ki}\left(t + \Delta t\right) = \boldsymbol{r}_{kg}\left(t + \Delta t\right) + \left(\boldsymbol{r}_{ki}\left(t\right) - \boldsymbol{r}_{kg}\left(t\right) \right) \cdot \boldsymbol{R} \tag{17}$$

$$\boldsymbol{u}_{ki} = \frac{1}{\Delta t} \left(\boldsymbol{r}_{ki}\left(t + \Delta t\right) - \boldsymbol{r}_{ki}\left(t\right) \right) \tag{18}$$

$$\boldsymbol{R} = \begin{bmatrix} 1 - 2q_y^2 - 2q_z^2 & 2q_x q_y - 2sq_z & 2q_x q_z - 2sq_y \\ 2q_x q_y - 2sq_z & 1 - 2q_x^2 - 2q_z^2 & 2q_y q_z - 2sq_x \\ 2q_x q_z - 2sq_z & 2q_y q_z - 2sq_x & 1 - 2q_y^2 - 2q_z^2 \end{bmatrix} \tag{19}$$

Distinct Element Method

In the calculation of collisional force vector $\boldsymbol{f}_{colp}$ between solid particles and solid-wall particles, the framework of Distinct Element Method (Cundall 1971), or spring and dash-pot model, is introduced, as follows:

$$\boldsymbol{f}_{colp} = \sum_j \left\{ \boldsymbol{f}_n\left(t\right) + \boldsymbol{f}_s\left(t\right) \right\}_j \tag{20}$$

$$\left.\begin{aligned} f_n\left(t\right) &= -e_n\left(t\right) \frac{\Delta \boldsymbol{\xi}_n}{\left| \Delta \boldsymbol{\xi}_n \right|} + \boldsymbol{d}_n\left(t\right) \\ f_s\left(t\right) &= -e_s\left(t\right) \frac{\Delta \boldsymbol{\xi}_s}{\left| \Delta \boldsymbol{\xi}_s \right|} + \boldsymbol{d}_s\left(t\right) \end{aligned}\right\} \tag{21}$$

$$\left.\begin{aligned} e_n\left(t\right) &= e_n\left(t - \Delta t\right) + k_n \left| \Delta \boldsymbol{\xi}_n \right| \\ e_s\left(t\right) &= e_s\left(t - \Delta t\right) + k_s \left| \Delta \boldsymbol{\xi}_s \right| \\ \boldsymbol{d}_n\left(t\right) &= \eta_n \cdot \Delta \boldsymbol{\xi}_n / \Delta t \\ \boldsymbol{d}_s\left(t\right) &= \eta_s \cdot \Delta \boldsymbol{\xi}_s / \Delta t \end{aligned}\right\} \tag{22}$$

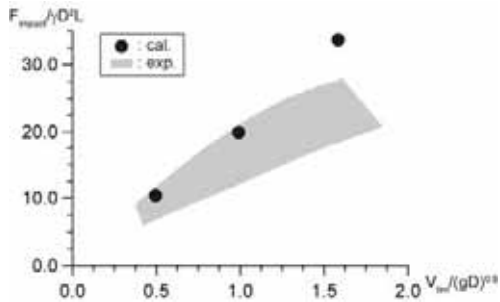

Figure 1. Collisional force

$$\left.\begin{aligned} \Delta\boldsymbol{\xi}_n &= \left(\Delta\boldsymbol{\xi}\cdot\frac{\boldsymbol{r}_{ij}}{|\boldsymbol{r}_{ij}|}\right)\frac{\boldsymbol{r}_{ij}}{|\boldsymbol{r}_{ij}|} \\ \Delta\boldsymbol{\xi} &= \Delta\boldsymbol{\xi}_n + \Delta\boldsymbol{\xi}_s \end{aligned}\right\} \tag{23}$$

where $\boldsymbol{f}$ is the force vector, k is the spring coefficient, η is the dash-pot coefficient, e is the force by spring, $\boldsymbol{d}$ is the force vector by dash-pot and $\Delta\boldsymbol{\xi}$ is the displacement vector in Δt. Subscript n or s shows normal or tangential direction.

It is popular that the model constants of DEM is determined based on the Hertzian contact theory (Kiyama and Fujimura 1973). In this study, because all the DEM particles are connected, the procedure to treat a rigid body made of many DEM particles by Tanaka et al. (2007) is applied. The coefficients of spring and dash-pot are shown as follows:

$$k_n = \alpha_{kn}\frac{m}{\Delta t^2} \quad ; \quad k_s = \alpha_{ks}\frac{m}{\Delta t^2} \tag{24}$$

$$c_n = \alpha_{cn}\frac{m}{\Delta t} \quad ; \quad c_s = \alpha_{cs}\frac{m}{\Delta t} \tag{25}$$

in which m is mass of a particle and α_{kn}, α_{cn}, α_{ks} and α_{cs} are tuning parameters.

Preparative calculations are executed to determine these parameters. The parameters of normal direction α_{kn} and α_{cn} are determined in comparison to results of a hydraulic experiment in which a collisional force of a drift wood and a rigid wall was measured (Matsutomi 1999). In Fig.1, the calculated results in the case, where the drift wood is 5.0 m in length, 0.4 m in diameter and 6.86 N/m^3 in weight per unit volume, α_{kn} is 9.0, α_{cn} is 5.0 and the angle of collision with a wall is 0°, are shown with the experimental results. In this figure, the experimental results are shown as a shaded area because it is difficult to identify each of a great many plots in the result of measurement.

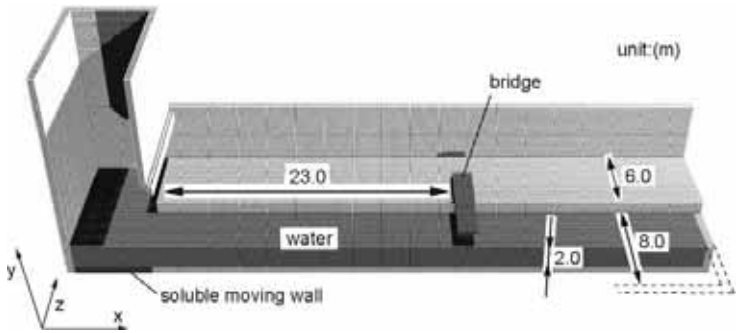

Figure 2. Calculated domain

The parameters of tangential direction α_{ks} and α_{cs}, are tuned based on the motion of an object on a slope. The critical slope angle when a still object on a slope begins to move is as follows:

$$\theta_{\lim} = \tan^{-1} \mu_f \tag{26}$$

in which θ is the slope angle and μ_f is the coefficient of static friction. When the static friction coefficient is 0.71, which is used in this study, the critical slope angle is about 35°. The parameters α_{ks}=6.0 and α_{cs}=5.0 are applied in this paper. The critical slope angle by these parameters is 31°

The model constants of each particle depend on its mass as shown in Eqs. (24) and (25). Therefore, at the collision between the particles with different mass, the model of a series connection of both model constants (Tokunaga et al. 2005) is introduced as follows:

$$k_n = k_{ni} k_{nj} / \left(k_{ni} + k_{nj} \right) \tag{27}$$

WASHED AWAY PROCESS OF GIRDER BRIDGE DUE TO TSUNAMI

Calculated Condition

In Fig.2, a calculated domain is shown. At the upper end, an inflow boundary which has 6.0 m in length and 20.0 m in width is set, and an about 43.0 m long, 8.0 m wide and 3.0 m deep model river is connected with it. A 2.0 m weir in height is arranged at the lower end, where the boundary condition is free outflow. The both shores of the model river are 6.0 m wide flat floors respectively. The initial water depth is 2.0 m. Tsunami is generated by supplying water from the inflow boundary, or the soluble moving wall (Gotoh et al. 2001). A girder bridge is set 23.0 m lower side from the inflow zone. The sizes of girder bridges are set almost same as the experiment as shown in Table1. In the previous hydraulic experiment, two kinds of static friction coefficient is used in all the cases, however, in this study, μ_f=0.71 in case1 and

Table 1. Specification of girder bridge

	length L_b(m)	width B(m)	thickness H(m)
case1	14.2	1.6	0.6
case2	12.6	4.0	0.6

μ_f=0.8 in case2 are used. The density of a girder bridge ρ_{sb}/ρ_l is 2.45. The uniform particle diameter is 0.2 m. In the experiment, a tsunami velocity is measured at 30.0 m upper side of a girder bridge, in this study, because the length from the gate to a girder bridge is set shorter to restrain the computational load, a tsunami velocity cannot be measured at the same point. Therefore, the velocity measured at 10.0 m upper side of a girder bridge is defined as the tsunami velocity.

Comparison with hydraulic experiment

In Fig.3, snapshots in the case1, or a tsunami velocity V_{tsu} is 5.4 m/s are shown. Particles in the central section of the channel are shown. In this case, the girder bridge is not moved, and the tsunami flows over the bridge. Fig.4 shows the time-dependant hydrodynamic force acting on the girder bridge, which is an ensemble averaged value among 0.05 s. The critical value of movement of a girder bridge F_{lim} is defined as follows:

$$F_{lim} = \mu_s \left(mg - F_y \right) \tag{28}$$

in which F_y is the hydrodynamic force in y-direction acting on a girder bridge. When the front of tsunami collides with the girder bridge from t=4.7 to 5.0 s, a significant force acts upward, or in the positive direction of y-axis. The hydrodynamic force in y-direction decreases rapidly after having a peak, and converges to zero around. This is because the girder bridge exists in underwater, as shown in Fig.3. The hydrodynamic force in x-direction increases quickly, and becomes constant after around the time t=6.0 s. Because it does not exceed to the critical value of movement, the girder bridge is not washed away.

In Fig.5, snapshots in the case2, or a tsunami velocity V_{tsu} is 8.1 m/s are shown. Fig.6 shows the time-dependant hydrodynamic force acting on the girder bridge. In this case, due to the steeper front of tsunami than in the case1, peaks of hydrodynamic forces in x- and y-direction come faster than the case1. Due to larger hydrodynamic force in y-direction after the collision, the critical force of movement decreases remarkably. At the time t=4.3 s, it becomes almost same as the hydrodynamic force in x-direction. The girder bridge begins to move at this time. In Fig.7, the comparison with the experiment as for a tsunami velocity and movement of a girder bridge is shown. The experimental results and calculated results shows good agreements in both cases.

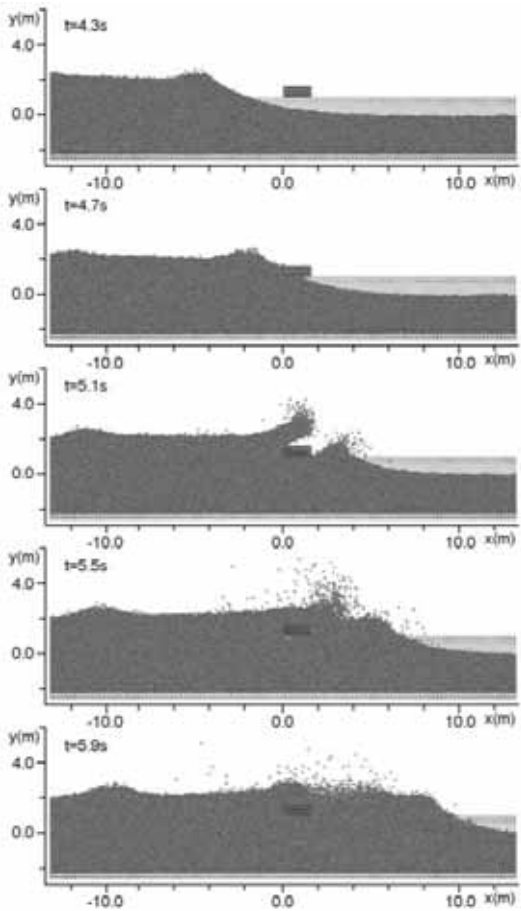

Figure 3. Snapshots (case1)

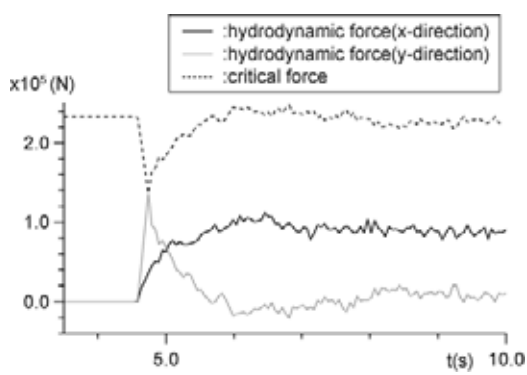

Figure 4. Hydrodynamic force acting on bridge (case1)

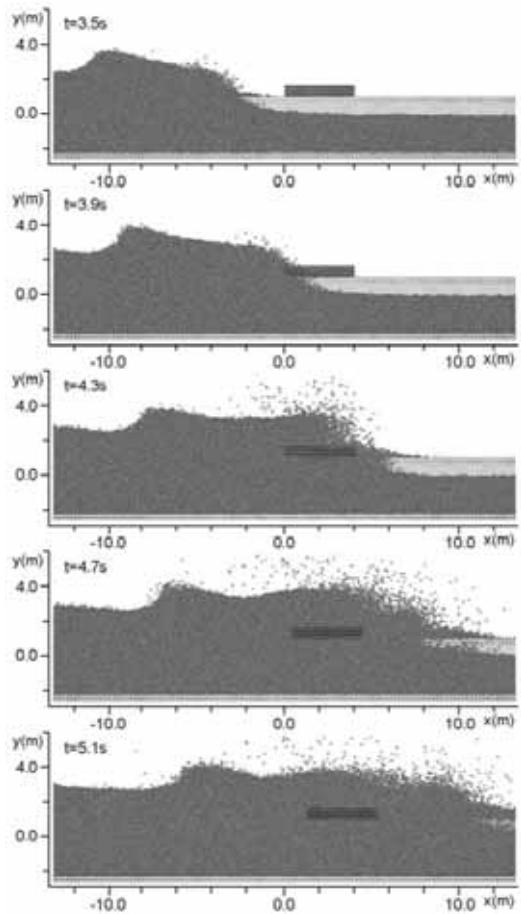

Figure 5. Snapshots (case2)

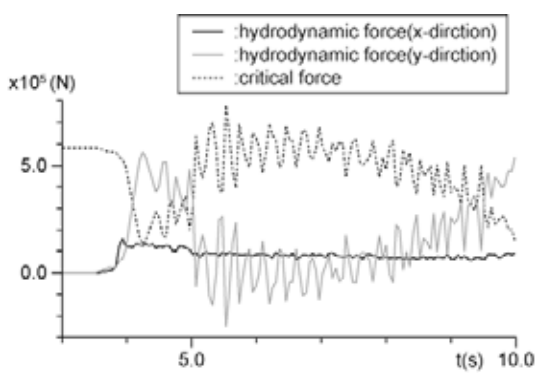

Figure 6. Hydrodynamic force acting on bridge (case2)

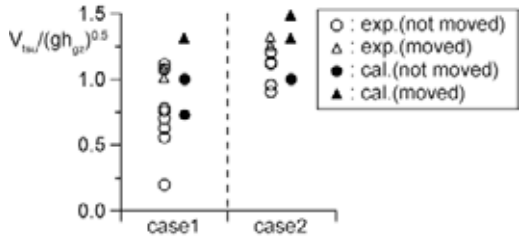

Figure 7. Tsunami velocity and movement of bridge

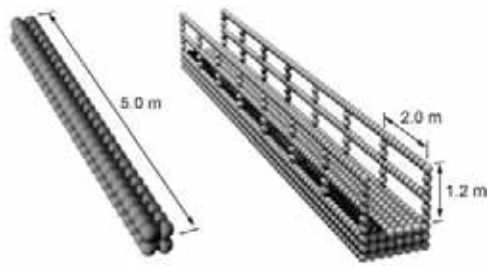

Figure 8. Drift wood and bridge with handrail

WASHED AWAY PROCESS OF GIRDER BRIDGE WITH HANDRAIL DUE TO TSUNAMI WITH DRIFT WOODS

In the former chapter, a girder bridge was treated as a flat plate in order to compare with the previous hydraulic experiment, however, an actual girder bridge usually has a handrail, and it is reported that a girder bridge washed away in Sri Lanka has also handrail. In addition, a tsunami can transport some drift woods to a girder bridge. Therefore, in this chapter, the simulation that a tsunami including some drift woods collides with a girder bridge with handrail is executed. Fig.8 shows the specifications of a drift wood and a girder bridge with handrail. A drift wood is ρ_{st}/ρ_f=0.7 in specific density, 5.0 m in length, 0.4 m in width and 0.4 m in height. Seven woods are arranged in the upper side of a girder bridge at random. Handrail consists of 1.2 m columns in height arranged at 2.0 m intervals and two beams at 0.6 m intervals, and set at both sides of a girder bridge. These columns and beams are expressed by a row of particles, which corresponds to 0.2 m in diameter. The specific density of handrail is same as a girder. The same inflow condition as the case1, under which a girder bridge was not moved, is applied.

Fig.9 shows snapshots. The water particles are shown in smaller size in this figure. The girder bridge begins to move due to the collision with drift woods carried in the front part of tsunami. The drift woods collide with the bridge one after another. Some drift woods flow down with a girder bridge after being caught by handrail. In Fig.10, the x-directional components of a hydrodynamic

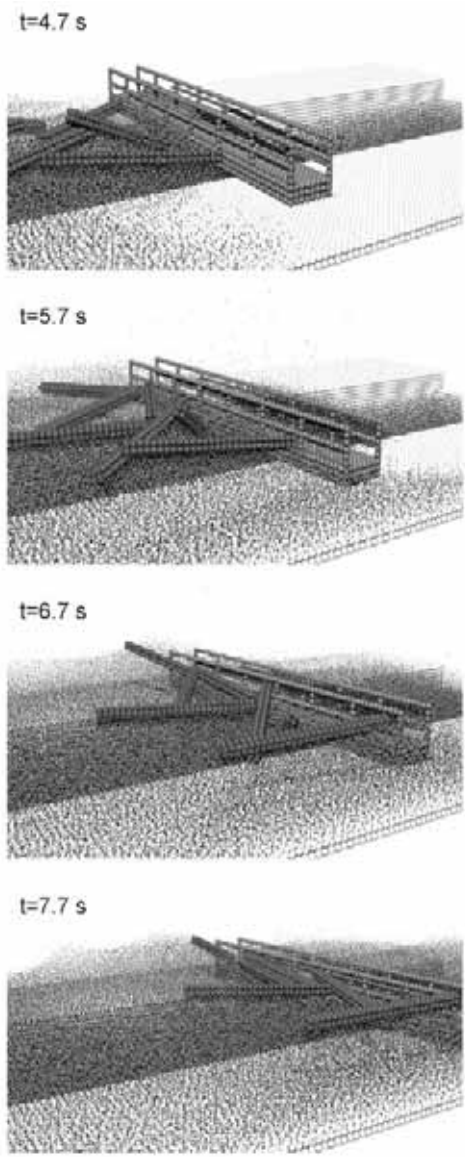

Figure 9. Girder bridge with handrail washed away due to tsunami with drift woods

force due to a tsunami and a collisional force due to the drift woods are shown. An ensemble averaging during 0.05s is applied. At the moment of attack of the tsunami, a clear peak of the collisional force with a drift wood appears, and the peak value amounts to about five times of the hydrodynamic force in *x*-direction.

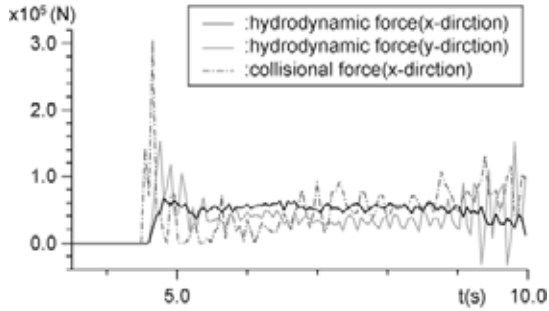

Figure 10. Hydrodynamic force and collisional force acting on bridge

CONCLUSIVE REMARKS

In this study, numerical analysis by the MPS method on a girder bridge washed away by a tsunami run-up was executed. As for a relation of a tsunami velocity and movement of a girder bridge, the calculated results showed good agreement with the previous experimental results. Furthermore, in the case where the influence of drift woods and handrail was examined, it was found that a collisional force with drift woods became more significant than a hydrodynamic force, and the movement of a girder bridge is mainly affected by the collisional force.

As the result, as a numerical tool to understand the mechanics of the washed away process of a girder bridge by a tsunami, the applicability of the particle method was clarified. In this paper, a girder bridge with comparatively simpler structure was treated. In the future, the particle method should be established as a numerical tool of analysis of this kind of phenomenon through some more examinations of the computational code on girder bridges with various structures.

REFERNCES

Cundall, P. A. 1971. A Computer Model for Simulating Progressive, Large Scale Movements in Blocky Rock System, *Symp. ISM*, Nancy, France, Proc., 2, 129-136.

Gotoh, H., T. Shibahara and T. Sakai. 2001. Sub-Particle-Scale Turbulence Model for the MPS Method –Lagrangian Flow Model for Hydraulic Engineering-, *Comp. Fluid Dyn. J.*, 9-4, 339-347.

Gotoh, H., H. Ikari, T. Memita and T. Sakai. 2005. Lagrangian Particle Method for Simulation of Wave Overtopping on a Vertical Seawall, *Coastal Eng. J.*, 47, 2-3, 157-181.

Kiyama, H. and Fujimura, H. 1983. Application of Cundall's discrete block method to gravity flow analysis of rock like granular material, *Proc. of the Japanese Society of Civil Engineering (JSCE)*, 333, 137- 146.

Koshizuka, S., H. Tamako and Y. Oka. 1995. A Particle Method for Incompressible Viscous Flow with Fluid Fragmentation, *Comp. Fluid Dyn. J.*, 4, 29-46.

Koshizuka, S., A. Nobe and Y. Oka. 1998. Numerical Analysis of Breaking Waves Using the Moving Particle Semi-implicit Method, *Int. J. Numer. Meth. Fluids*, 26, 751-769.

Matsutomi, H. 1999. A Practical Formula for Estimating Impulsive Force due to Driftwoods and Variation Features of the Impulsive Force, *Jour. of Hyd. Coast. and Env. Eng.*, 621/II-47, 111-127 (in Japanese).

Shibata, K., S. Koshizuka, Y. Oka and K. Tanizawa. 2004. A Three-Dimensional Numerical Analysis Code for Shipping Water on Deck Using a Particle Method, *Proc. 2004 ASME Heat Transfer/Fluid Engineering Summer Conf.*, Charlotte, July 11-15, HT-FED04-56477.

Shoji, G. and Y. Mori. 2006. Hydraulic Model Experiment to Simulate the Damage of a Bridge Deck Subjected to Tsunamis, *Annual J. of Coast. Eng.*, JSCE, 53, 801-805 (in Japanese).

Tanaka, M., M. Sakai and S. Koshizuka. 2007. Particle-based Rigid Body Simulation and Coupling with Fluid Simulation, *Transaction of JSCES* (in Japanese).

Tokunaga, H., K. Kaizu, K. Ikeda and O. Kobori. 2005. Impact Fracture Analysis of Thermally Tempered Glass by the Extended Distinct Element Method, *Transactions of the Japan Society of Mechanical Engineers. A*, 71, 711, 1560-1566.

NUMERICAL SIMULATION OF VISCOUS FREE-SURFACE FLOW INDUCED BY WAVE PROPAGATION OVER RIPPLED BED

Gerasimos A. Kolokythas[1] and Athanassios A. Dimas[2]

In the present study, numerical simulations of the free-surface flow, developing by the propagation of water waves over a rippled bottom, are performed assuming that the corresponding flow is two-dimensional, incompressible and viscous. The simulations are based on the numerical solution of the unsteady Navier-Stokes equations subject to the fully-nonlinear, free-surface boundary conditions and the appropriate bottom, inflow and outflow boundary conditions. The equations are properly transformed so that the computational domain becomes time-independent. For the spatial discretization, a hybrid scheme is used, in which central finite-differences, in the horizontal direction, and a pseudo-spectral approximation method with Chebyshev polynomials, in the vertical direction, are applied. A fractional time-step scheme is used for the temporal discretization. The validation of the numerical model is accomplished by comparison of the numerical results to the analytical solution for the case of laminar, oscillatory flow over a flat bed. For the rippled bed, results indicate that, close to the bottom, flow separation occurs at the ripple crests, which leads to the generation of alternating circulation regions. The amplitude of the wall shear stress distribution over the ripples increases with increasing ripple steepness, while the corresponding friction force is insensitive to this increase. The amplitude of the form drag forces due to the dynamic and hydrostatic pressure increases linearly with increasing ripple height.

INTRODUCTION

Sediment transport, induced by wave propagation in the coastal zone, results into the formation of ripples along a sandy bottom. Typical vortex ripples have a sharp crest and are symmetric with respect to their crest (Fig. 1). Their presence modifies the propagation of water waves and the development of the wave boundary layer, due to vortex generation at the ripple crests. For coastal engineering applications, the majority of corresponding studies investigate either the pure-oscillatory or wave-induced flow over ripples. For oscillatory flow, Longuet-Higgins (1981) studied the inviscid dynamics of discrete vortex shedding at the ripple crests and its effect on bed resistance, while Blondeaux and Vittori (1991) studied the viscous dynamics of vortex shedding and its effect on wall stress. Fredsøe et al. (1999) studied, experimentally, the combined waves-current and the waves-alone flow over rippled bed. Comparing results from the afore-mentioned cases, Fredsøe et al. (1999), concluded that the motion of the lee-wake vortices in the case of the combined flow is similar to that in the waves-alone case. Davies and Villaret (1999) presented a theoretical prediction for the spatial-mean drift velocity profile induced by wave

[1] Department of Civil Engineering, University of Patras, 26 500 Patras, Greece
[2] Department of Civil Engineering, University of Patras, 26 500 Patras, Greece

propagation over rippled bed, developing an analytical model. Huang and Dong (2002) studied numerically the wave propagation over ripples, utilizing the finite-analytic (FA) method, and concluded that, for solitary waves, the periodically averaged flow exhibits a current in the opposite direction of the wave propagation.

Typical sand ripples have parabolic shape, while their dimensions – length L_r and height h_r – depend on wave period, wave height and water depth, according to Fredsøe and Deigaard (1992). In the present study, the case of waves with wavelength to water depth ratio $\lambda / d_0 = 6$ and wave height to water depth ratio $H / d_0 = 0.05$ is considered, which is consistent with $L_r / d_0 = 0.25$ and $0.02 \le h_r / d_0 \le 0.05$. The objective is to numerically simulate the viscous, free-surface flow, induced by wave propagation over a rigid rippled bed, and study the behavior of wall shear stress and pressure distributions along the bed, as well as the corresponding friction and form drag forces. In the following sections, the formulation, the numerical method, and the results are presented for the propagation of the wave with the afore-mentioned characteristics, considering the two extreme values of ripple height $h_r / d_0 = 0.02$ and 0.05.

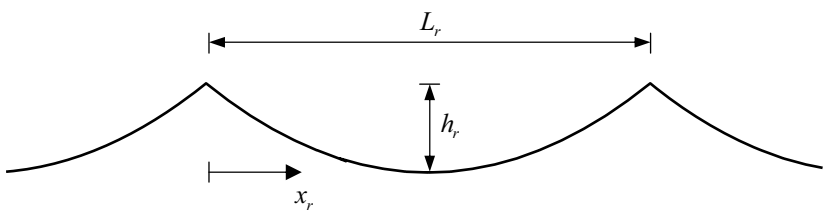

Figure 1. Sketch of a typical ripple of parabolic shape.

FORMULATION

Incompressible, viscous, two-dimensional, free-surface flow is governed by the continuity

$$\frac{\partial u_1}{\partial x_1} + \frac{\partial u_2}{\partial x_2} = 0 \tag{1}$$

and the Navier-Stokes equations

$$\frac{\partial u_1}{\partial t} + u_1 \frac{\partial u_1}{\partial x_1} + u_2 \frac{\partial u_1}{\partial x_2} = -\frac{\partial p}{\partial x_1} + \frac{1}{\mathrm{Re}} \left(\frac{\partial^2 u_1}{\partial {x_1}^2} + \frac{\partial^2 u_1}{\partial {x_2}^2} \right) \tag{2}$$

$$\frac{\partial u_2}{\partial t}+u_1\frac{\partial u_2}{\partial x_1}+u_2\frac{\partial u_2}{\partial x_2}=-\frac{\partial p}{\partial x_2}+\frac{1}{\mathrm{Re}}\left(\frac{\partial^2 u_2}{\partial {x_1}^2}+\frac{\partial^2 u_2}{\partial {x_2}^2}\right) \tag{3}$$

where t is time, x_1 and x_2 are the horizontal and vertical coordinates, respectively; u_1 and u_2 are the horizontal and vertical velocity components, respectively; p is the dynamic pressure and Re is the Reynolds number. The equations (1)-(3) are expressed in dimensionless form utilizing the inflow depth d_0, the gravity acceleration g and the fluid density ρ, therefore, $\mathrm{Re}=d_0\sqrt{gd_0}/\nu$ where ν is the kinematic fluid viscosity.

The kinematic and the dynamic – normal and tangential stress – boundary conditions must be satisfied at the free surface and they are expressed as

$$u_2=\frac{d\eta}{dt}=\frac{\partial\eta}{\partial t}+u_1\frac{\partial\eta}{\partial x_1} \tag{4}$$

$$p=\frac{\eta}{\mathrm{Fr}^2}+\frac{2}{\mathrm{Re}}\frac{1+\left(\partial\eta/\partial x_1\right)^2}{1-\left(\partial\eta/\partial x_1\right)^2}\frac{\partial u_2}{\partial x_2} \tag{5}$$

$$\left(\frac{\partial u_1}{\partial x_2}+\frac{\partial u_2}{\partial x_1}\right)\left(1-\left(\frac{\partial\eta}{\partial x_1}\right)^2\right)+4\frac{\partial u_2}{\partial x_2}\frac{\partial\eta}{\partial x_1}=0 \tag{6}$$

respectively, where $\eta\left(x_1,t\right)$ is the free surface elevation and Fr is the Froude number, which under the present dimensionless formulation is equal to one. In addition, the no-slip and non-penetration boundary conditions, which must be satisfied at the bottom, are given by the following expressions

$$u_1-u_2\frac{\partial d}{\partial x_1}=0 \qquad u_2+u_1\frac{\partial d}{\partial x_1}=0 \tag{7}$$

respectively, where $d\left(x_1\right)$ is the bottom depth measured from the still free surface level.

Given that the free surface is time-dependent, the Cartesian coordinates are transformed, in order for the computational domain to become time-independent, according to the expressions

$$s_1=x_1 \qquad s_2=\frac{2x_2+d-\eta}{d+\eta} \tag{8}$$

According to (8), the transformed domain is rectangular, $s_2 = 1$ corresponds to the free surface and $s_2 = -1$ to the bottom. The velocity components are also transformed in the following way

$$u_1 = v_1 \qquad u_2 = v_2 + rv_1 = v_2 + v_\eta \tag{9}$$

where

$$r = \frac{(1+s_2)}{2}\frac{\partial \eta}{\partial s_1} + \frac{(1-s_2)}{2}\frac{\partial h}{\partial s_1} \tag{10}$$

and $\partial h / \partial s_1 = -\partial d / \partial s_1$ is the bottom slope.

Taking into account (8) and (9), the transformed continuity equation and the Navier-Stokes equations in rotational form, respectively, are

$$\frac{\partial v_1}{\partial s_1} + \frac{2}{d+\eta}\left(\frac{\partial v_2}{\partial s_2} + \frac{v_1}{2}\left(\frac{\partial \eta}{\partial s_1} - \frac{\partial h}{\partial s_1}\right)\right) = 0 \tag{11}$$

$$\begin{aligned}\frac{\partial v_1}{\partial t} = v_2\zeta + \frac{\partial \eta}{\partial t}\frac{1+s_2}{d+\eta}\frac{\partial v_1}{\partial s_2} + r\frac{2}{d+\eta}\frac{\partial p}{\partial s_2} - \frac{\partial \Pi}{\partial s_1} + \\ \frac{1}{\mathrm{Re}}\left(\frac{\partial^2 v_1}{\partial {s_1}^2} + \left(r^2+1\right)\left(\frac{2}{d+\eta}\right)^2\frac{\partial^2 v_1}{\partial {s_2}^2} + A_1\right)\end{aligned} \tag{12}$$

$$\begin{aligned}\frac{\partial v_2}{\partial t} = -v_1\zeta + \frac{\partial \eta}{\partial t}\frac{1+s_2}{d+\eta}\frac{\partial\left(v_2+v_\eta\right)}{\partial s_2} - a_\eta - \frac{2}{d+\eta}\frac{\partial \Pi}{\partial s_2} + \\ \frac{1}{\mathrm{Re}}\left(\frac{\partial^2\left(v_2+v_\eta\right)}{\partial {s_1}^2} + \left(r^2+1\right)\left(\frac{2}{d+\eta}\right)^2\frac{\partial^2\left(v_2+v_\eta\right)}{\partial {s_2}^2} + A_2\right)\end{aligned} \tag{13}$$

where

$$A_i = -\frac{2}{d+\eta}\left(2r\frac{\partial^2 u_i}{\partial s_1 \partial s_2} + \left(\frac{\partial r}{\partial s_1} - r\left(\frac{\partial \eta}{\partial s_1} - \frac{\partial h}{\partial s_1}\right)\frac{2}{d+\eta}\right)\frac{\partial u_i}{\partial s_2}\right) \tag{14}$$

$$a_\eta = \frac{\partial v_\eta}{\partial t} + v_1\frac{\partial v_\eta}{\partial s_1} + v_2\frac{2}{d+\eta}\frac{\partial v_\eta}{\partial s_2} \tag{15}$$

where $i = 1, 2$ and

$$\Pi = p + \frac{1}{2}\left(v_1{}^2 + v_2{}^2\right) \qquad \zeta = \frac{\partial v_2}{\partial s_1} - \frac{2}{d+\eta}\frac{\partial v_1}{\partial s_2} \tag{16}$$

are the transformed dynamic pressure head and the transformed vorticity, respectively.

Finally, the free surface boundary conditions, obtained by the transformation of (4)-(6), respectively, are

$$v_2 = \frac{\partial \eta}{\partial t} \tag{17}$$

$$\Pi = \frac{\eta}{\mathrm{Fr}^2} + \frac{1}{2}\left(v_1{}^2 + v_2{}^2\right) + \frac{2}{\mathrm{Re}}\frac{1+\left(\partial\eta/\partial s_1\right)^2}{1-\left(\partial\eta/\partial s_1\right)^2}\frac{2}{d+\eta}\frac{\partial\left(v_2+v_\eta\right)}{\partial s_2} \tag{18}$$

$$\begin{aligned}&\frac{2}{d+\eta}\left(1+\left(\frac{\partial\eta}{\partial s_1}\right)^2\right)^2\frac{\partial v_1}{\partial s_2} + \left(1-\left(\frac{\partial\eta}{\partial s_1}\right)^2\right)\frac{\partial v_2}{\partial s_1} - \\ &\qquad 2\frac{\partial\eta}{\partial s_1}\left(1+\left(\frac{\partial\eta}{\partial s_1}\right)^2\right)\frac{\partial v_1}{\partial s_1} + \frac{\partial^2\eta}{\partial s_1{}^2}\left(1-\left(\frac{\partial\eta}{\partial s_1}\right)^2\right)v_1 = 0\end{aligned} \tag{19}$$

while the bottom boundary conditions, obtained by the transformation of (7), are

$$v_1 = 0 \qquad v_2 = 0 \tag{20}$$

NUMERICAL METHOD

For the numerical solution of the transformed Navier-Stokes equations, a fractional time-step scheme, consisting of three stages, is used for the temporal discretization and a hybrid scheme for the spatial discretization. Central finite differences are applied, on a uniform grid with size Δs_1, for the discretization along s_1, and a spectral approximation method with Chebyshev polynomials along s_2. For the discretization along s_2, flow variables are represented as

$$f\left(s_1, s_2, t\right) = \sum_{n=0}^{N} f_n\left(s_1, t\right) T_n\left(s_2\right) \tag{21}$$

where f is the flow variable in the physical domain, f_n is the corresponding variable in the spectral domain, N is the highest order of the Chebyshev polynomials and $T_n\left(s_2\right)$ is the Chebyshev polynomial of order n.

At the first stage of each time-step, the nonlinear and A_i terms of (12) and (13) are treated explicitly using an Adams-Bashforth scheme, in order to

compute the first intermediate velocity components. At the second stage, an implicit Euler scheme is utilized for the treatment of the transformed pressure head terms of (12) and (13), so that a second intermediate computation of the velocity components to be obtained. At this stage, the generalized Poisson's equation for the transformed pressure head is derived by satisfying the continuity equations (11) as well. The normal stress free surface condition (18) and the non-penetration condition at the bottom (20), are imposed at this stage. The transformed viscous terms of (12) and (13) are also treated implicitly, at the third stage of the time-step, where the velocity components at time-step $n+1$ are evaluated. The corresponding boundary conditions are the tangential stress free surface condition (19) and the bottom boundary conditions (20). Finally, the free surface elevation is computed by satisfying the kinematic boundary condition (17).

RESULTS

The numerical model is validated by simulating the case of laminar, viscous oscillatory flow over a flat horizontal bed. Oscillatory velocity $u_0 = U_0 \sin(\omega t)$ is imposed at the free surface, which is considered as a rigid lid symmetry plane, while no-slip condition is imposed at the bottom ($x_2 = 0$). The maximum velocity U_0 is associated with the corresponding bed velocity induced by inviscid wave propagation over flat bed, while ω is the radial frequency. Periodic conditions are applied at the streamwise boundaries. The case of Reynolds number $\mathrm{Re}_\alpha = U_0 \alpha_0 / \nu = 3258$ is considered, which corresponds to $\mathrm{Re}_\delta = U_0 \delta_s / \nu = 80$, where $\alpha_0 = U_0 / \omega$ is the amplitude of the orbital motion and $\delta_s = \sqrt{2\nu / \omega}$ is the Stokes length. The vertical dimension of the flow domain is set equal to d_0 such that $\delta_s / d_0 = 0.003$, while its length along x_1 equals to $4d_0$. The numerical parameters are $\Delta s_1 = 0.0125$, $N = 128$ and $\Delta t = 0.002$. The dimensionless streamwise velocity, obtained by the well-known analytical solution

$$u = \sin(\omega t) - e^{-\frac{x_2}{\delta_s}} \sin\left(\omega t - \frac{x_2}{\delta_s}\right) \tag{22}$$

is in excellent agreement to the numerical solution (Fig. 2).

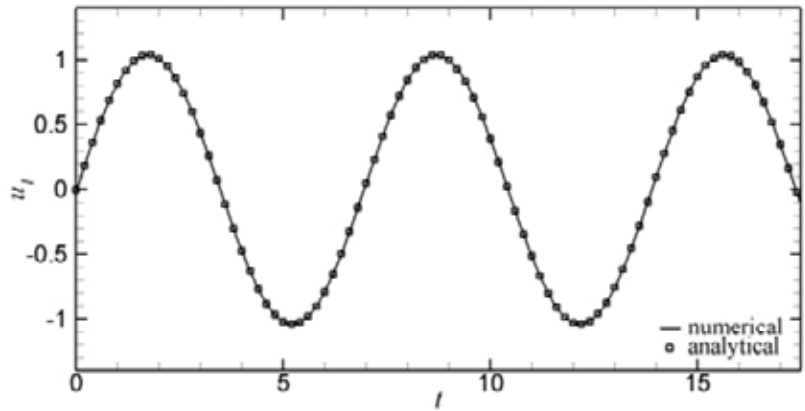

Figure 2. Time evolution of streamwise velocity of oscillatory flow over horizontal bottom, at $x_2 = 3.3\delta_s$.

For the simulation of wave propagation over rigid rippled bed, the case of waves with dimensionless wavelength $\lambda = 6$, wave period $T = 6.95$ and wave height $H = 0.3$ is considered. All variables are rendered dimensionless by g and d_0 as in (2) and (3). A sketch of the computational domain is depicted in Fig. 3. An inflow region of length λ and constant depth d_0 is placed before the ripples region of length 0.5λ, which is followed by an outflow region of length 5λ and constant depth d_0. At the inflow boundary, velocity field, dynamic pressure and free surface elevation are defined according to second order Stokes wave theory. An absorption zone is placed at the outflow region in order to efficiently minimize reflection of waves by the outflow boundary (Dimakopoulos and Dimas 2006).

The shape of the ripples is parabolic

$$h(x_r) = h_r \left(2\frac{x_r}{L_r} - 1 \right)^2 \tag{23}$$

and we consider two cases with dimensionless ripple length $L_r = 0.25$ and heights $h_r = 0.02$ and 0.05, which correspond to ripple steepness $h_r / L_r = 0.08$ and 0.2, respectively. For both of the investigated cases $\mathrm{Re} = 250000$ is considered and corresponds to $\mathrm{Re}_a = 3258$ for the equivalent oscillatory flow, which coincides with the flow simulated for validation. The numerical parameters are $\Delta s_1 = 0.0125$, $N = 128$ and $\Delta t = 0.002$.

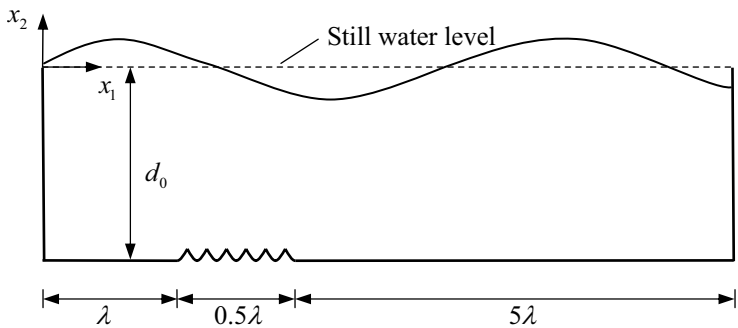

Figure 3. Sketch of computational domain for simulation of wave propagation over rippled bed.

A typical snapshot of instantaneous dynamic pressure field, for the case of $h_r = 0.05$, is shown in Fig. 4 where the efficiency of the absorption zone is also demonstrated. In Fig. 5, snapshots of the velocity and vorticity field very close to a ripple, at time instants during a wave period T, are presented. The flow separates along the wave propagation direction at each ripple crest and forms a recirculation region on the downslope side of the ripple, when a wave crest propagates above the ripple crest. Separation opposite to the wave propagation direction leads to the formation of a recirculation region on the upslope side of the ripple, when a wave trough propagates above the ripple crest. The dimensionless wall shear stress, τ_w, distribution at two time instants of a wave period is shown in Fig. 6, for both ripple heights $h_r = 0.02$ and 0.05. The amplitude of the wall stress variation, due to the presence of the ripples, increases substantially according to the increase of the ripple height and the ripple steepness h_r / L_r. The integration of the wall stress, the dynamic pressure and the hydrostatic pressure along a ripple results into the horizontal friction drag force, F_f, dynamic pressure drag force, F_p, and hydrostatic pressure drag force, F_s, on each ripple, respectively. The time evolution of these forces is shown in Fig. 7. The amplitude of both pressure drag forces, F_p and F_s, increases linearly with increasing ripple height, while the amplitude of the friction force F_f is insensitive to the increase of ripple height.

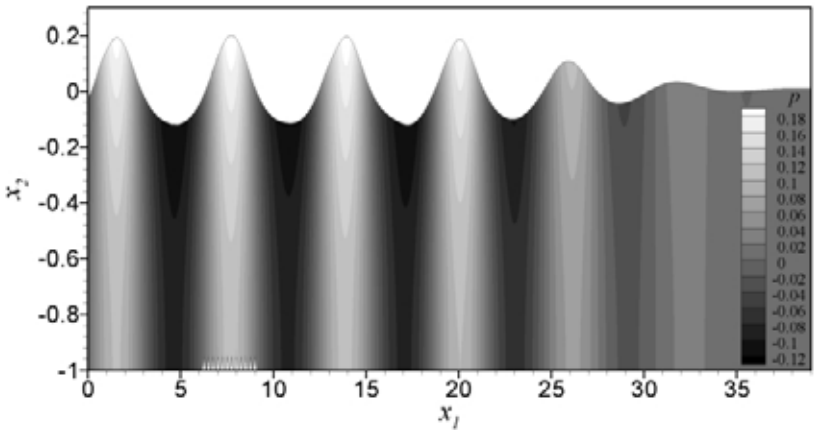

Figure 4. Dynamic pressure distribution, during wave propagation over ripples of height $h_r = 0.05$.

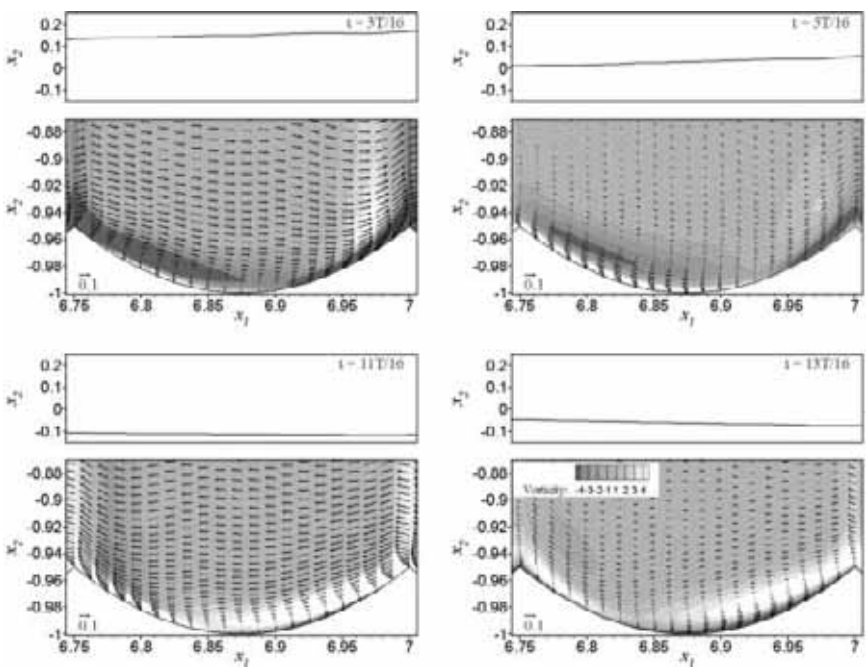

Figure 5. Velocity and vorticity field between successive ripple crests and free surface elevation, at time instants of a wave period, for ripples of height $h_r = 0.05$.

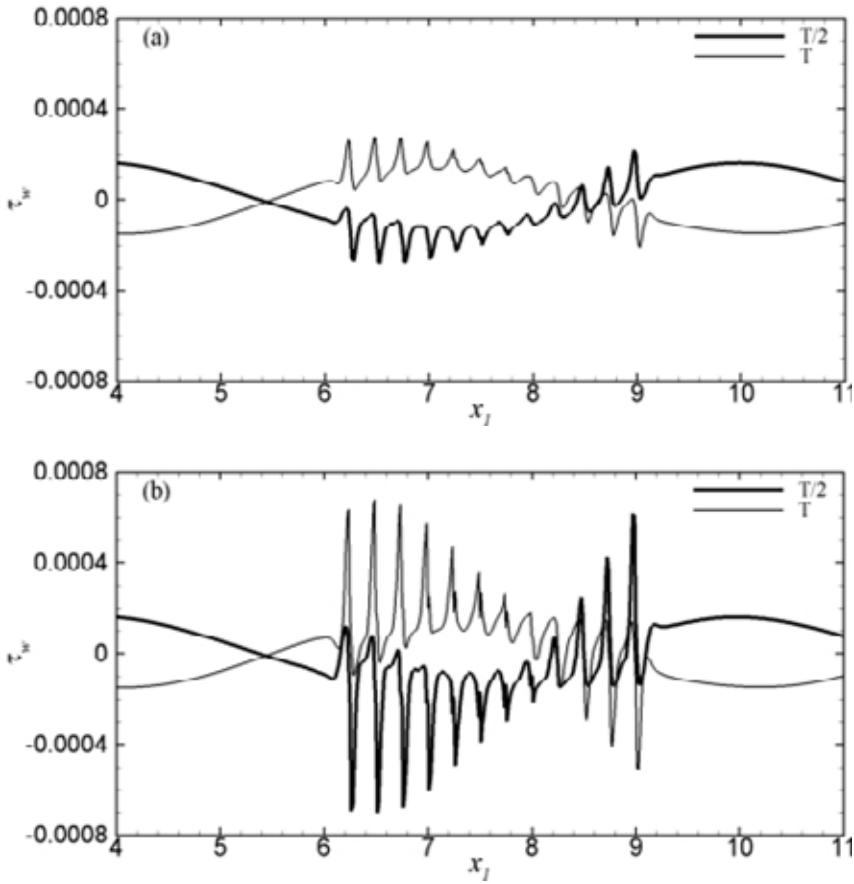

Figure 6. Wall stress distribution, at two time instants of a wave period, for ripples of height (a) $h_r = 0.02$ **and (b)** $h_r = 0.05$ **.**

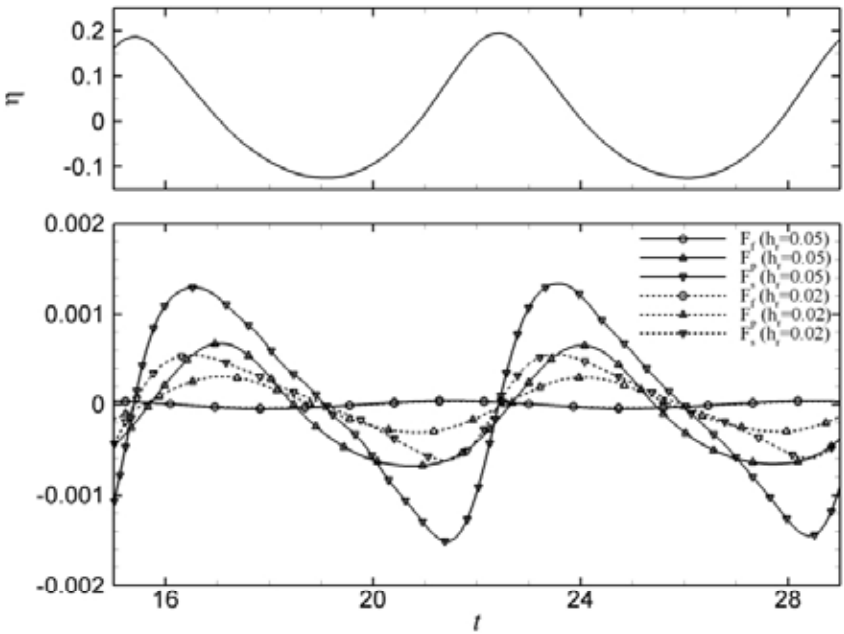

Figure 7. Time evolution of free surface elevation above a ripple trough and drag forces (friction drag force F_f, dynamic pressure drag force F_p and hydrostatic pressure drag force F_s) on the same ripple.

CONCLUSIONS

During wave propagation over a rippled bed, flow separation occurs at the ripple crests, which leads to the formation of clockwise and counterclockwise vortices at the downslope and the upslope side of a crest, respectively. The amplitude of the wall shear stress over the rippled region increases significantly with increasing ripple height and steepness, while the corresponding friction drag force seems to be insensitive to this increase. The amplitude of the pressure – dynamic and hydrostatic – drag forces both increase linearly with increasing ripple height. Therefore, the percentage of friction in the total drag force decreases with increasing ripple height.

ACKNOWLEDGMENTS

This paper is part of the 03ED617 research project, implemented within the framework of the "Reinforcement Programme of Human Research Manpower" (PENED) and co-financed by National and Community Funds (25% from the Greek Ministry of Development-General Secretariat of Research and

Technology and 75% from E.U.-European Social Fund). Funding by the Patras Port Authority is also greatly appreciated.

REFERENCES

Blondeaux, P., and G. Vittori. 1991. Vorticity dynamics in an oscillatory flow over a rippled bed, *Journal of Fluid Mechanics*, 226, 257-289.

Davies, A.G., and C. Villaret. 1999. Eulerian drift induced by progressive waves above rippled and very rough beds, *Journal of Geophysical Research*, 104 (C1), 1465-1488.

Dimakopoulos, A.S., and A.A. Dimas. 2006. Numerical simulation of nonlinear wave propagation and breaking over constant-slope bottom, *Proceedings of 25th International Conference on Offshore Mechanics and Arctic Engineering*, OMAE, 92163.

Fredsøe, J., K.H. Anderson, and B.M. Sumer. 1999. Wave plus current over a ripple-covered bed, *Coastal Engineering*, 38, 177-221.

Fredsøe, J., and R. Deigaard. 1992. *Mechanics of coastal sediment transport*, World Scientific, Singapore.

Huang, C.J., and C.M. Dong. 2002. Propagation of water waves over rigid rippled beds, *Journal of Waterway, Port, Coastal, and Ocean Engineering*, 128 (5), 190-201.

Longuet-Higgins, M.S. 1981. Oscillating flow over steep sand ripples, *Journal of Fluid Mechanics*, 107, 1-35.

LONGTERM STABILITY OF A HARBOUR PROTECTION MEASURE BY GEOTEXTILE SAND BAGS

Dr.-Ing. Daniel Schade[1]

The harbour List is a small harbour in the North Sea. In 1994 severe erosion problems were detected. The tidal inlet moved towards the harbour quay walls and the gradient of the seaward slope profile became steep. The final protection work was carried out with non woven geotextile sand bags with a volume of 1.0 m³. 23,000 sand bags were placed in water depth between MSL – 3.50 m and MSL – 20.00 m. During the last ten years as-laid-measurements were carried out. It could be seen, that the sand bag laying seems to be a method which could stabilize the erosion process and could be used for final design of harbour or coast protection measures.

INTRODUCTION AND PROBLEM

The harbour List is a small harbour for fishing and sailing vessels in the north east part of the island Sylt in the North Sea. The Harbour is connected to the North Sea by a tidal inlet called Lister Ley which has a water depth of more than 20 m (see fig. 1 and 2).

A severe erosion problem on the seaward side was detected during reconstruction works at the harbour quay walls in 1994. The gradient of the seaward profile rose up to 1 to 1.5 and even up to 1 to 1 in some areas. The stability of the harbour quay walls was not longer guaranteed.

In an immediate measure in 1994 8.000 sand bags with a volume of 1.0 m³ were placed on the seaward slope. Our consultant company was asked by the local coast conservation department to look for a final design of the protection work.

For that, the following parameters had to be taken into account:

- current velocity in the Lister Ley up to 1.5 m/s, on the sea bed up to 1.2 m/s
- movement of the sea bed of the tidal inlet towards the harbour in a magnitude of 140 to 180 m between 1977 and 1995
- due to the static equilibrium, the gradient of the seaward slope of the embankment should be less than 1 : 3 with a calculation level of the soil at -4.00 m

[1] Ingenieurbüro Mohn GmbH, Industriestr. 36, 25813 Husum, Germany

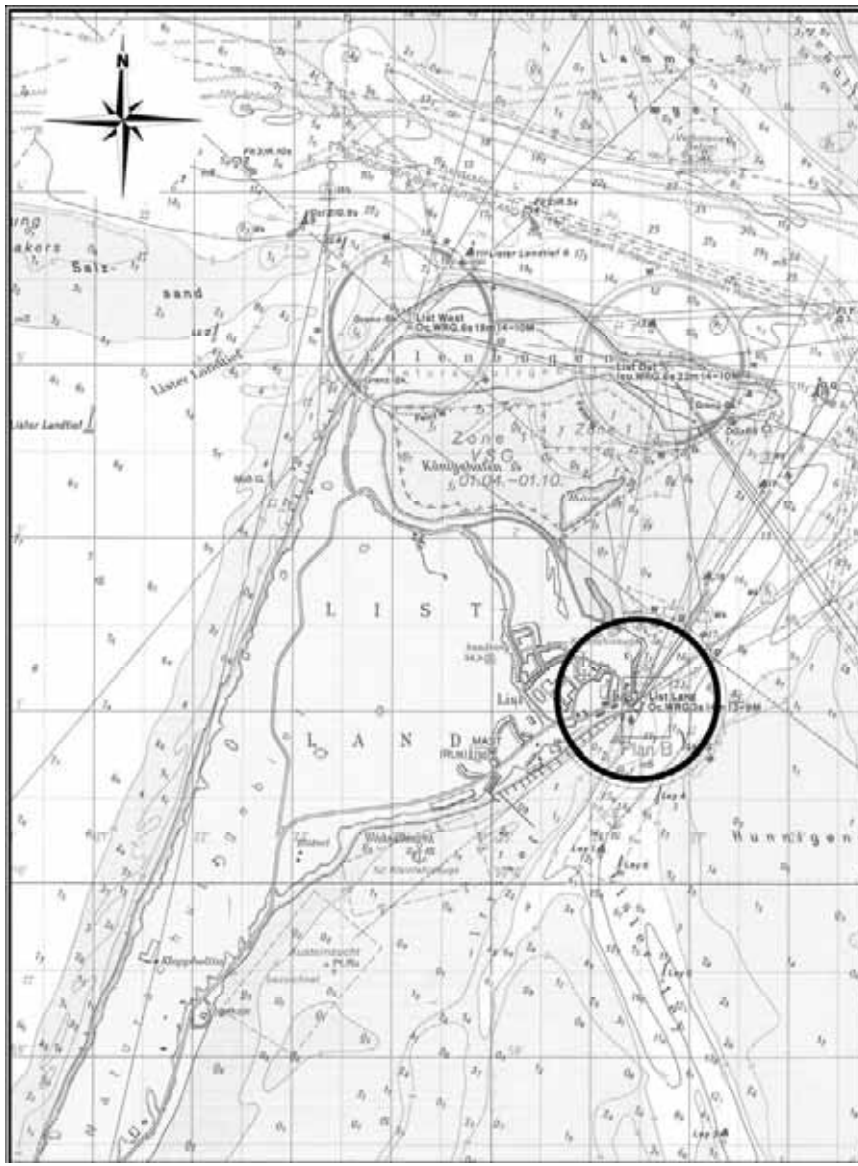

Figure 1. Sea chart, northern part of the island Sylt

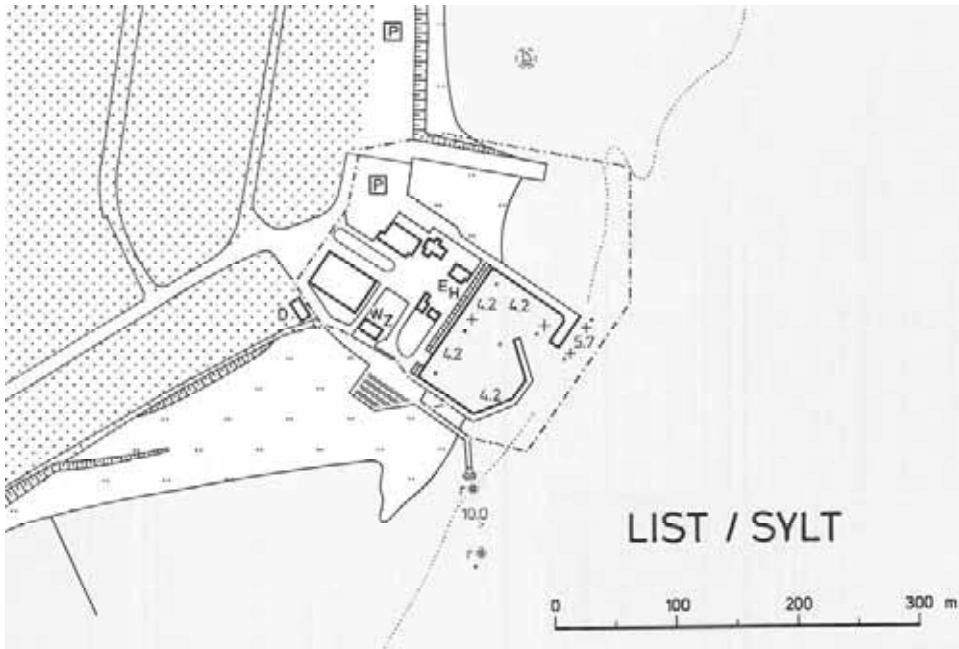

Figure 2. Harbour chart, List

SOIL

The soil in front of the harbour and even in the tidal inlet consists of sand layers with a light up to a medium storage density. The sand layer has no erosion stability not even on the sea bed of the tidal inlet.

SOLUTION

The sand bags which were placed in the immediate measure were located in a water depth between MSL-5.00 m and MSL-14.00 m. A first as laid measurement showed a continuing erosion process below the NN-14.00 m line. The original solution for the final protection measure was to establish a quarry stone revetment. There were several reasos to search for other solutions:

- The movement of the sea bed of the tidal inlet towards the harbour leads to a protection measure with a maximum of flexibility.
- The costs for a quarry stone revetment with a necessary depth of more than NN-20.00 m are extremely high.
- The accurate laying of filter was hardly possible because of the current velocity up to 1.2 m/s.

Due to these effects we decided to construct a protection measure with non woven geotextile sandbags. We used 1.0 m³ sandbags, dimensions roughly 2.80 * 1.10 * 0.35 m. The sand bags were filled up to 80 % to allow a maximum of flexibility of the laying of each sand bag. Due to the static equilibrium, the chosen profile had an upper berm with a slope of 1:3 and a starting level of -3.50 m. The embankment slope was 1:2 and the bottom slope 1:4. 15,000 sandbags were used for the final design. In fig. 3 a typical profile was presented.

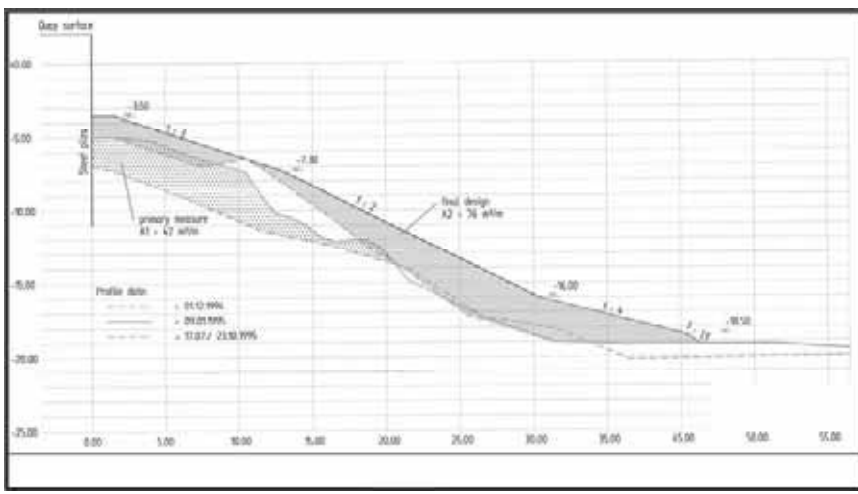

Figure 3. Typical profile List harbour

Most of the sandbags were produced in polypropylene (pp), the upper layer was produced in a combination of polypropylene and polyamide (pa); using the advantage of both, the pp-material as the good strength and the pa-material as the good resistance against rub-of. In addition, this different material offered the possibility to check the accuracy of the laying by a different colour of the upper layer. In fig. 4 is a chart of the laid sand bags included.

The protection measure was carried out during the winter 1996/97. The accuracy of the laying was controlled during the work by a diver company. To avoid the risk of erosion at the borders, the protection work was carried out on both sides in the adjoining shallow parts. In fig. 4, a chart of the sand bag laying plan is included.

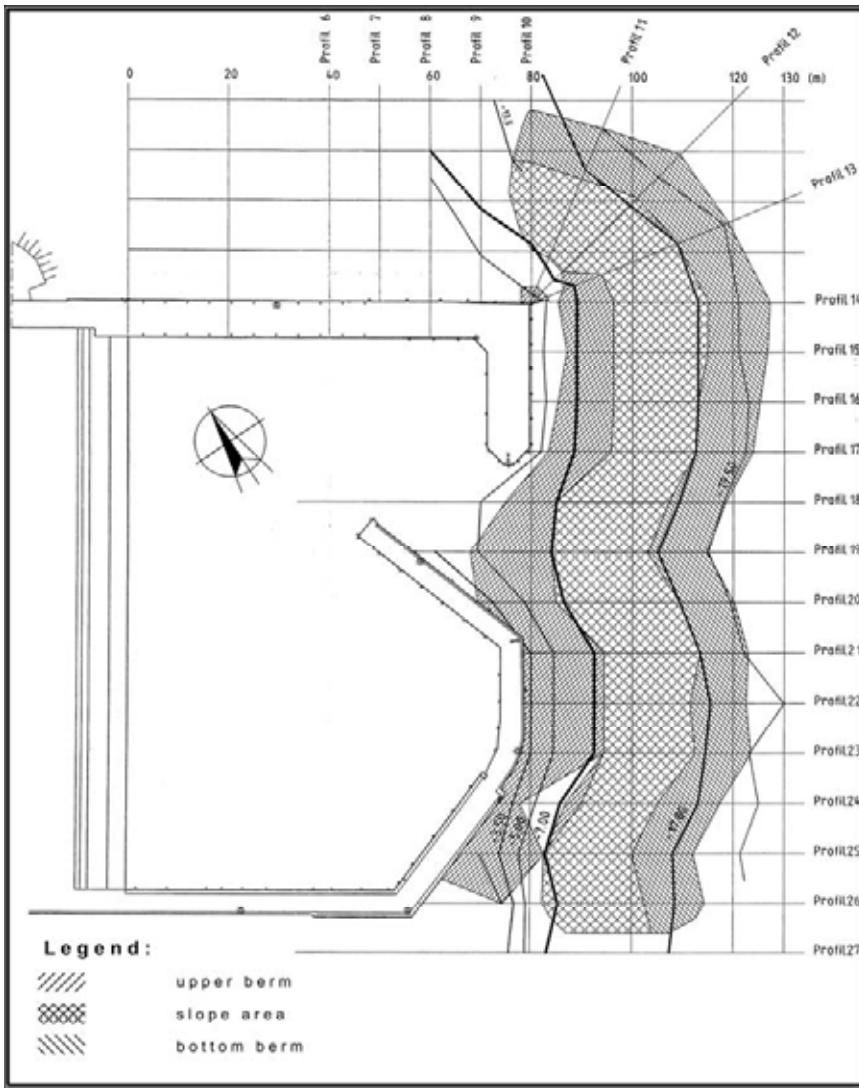

Figure 4. Plan of sand bag laying

SURVEILLANCE

As-laid-measurements were carried out each year from 1997 to 2000 and again in 2002; 2004 and 2005. In 1997 and 2000 a side scan sonar measurement was carried out, in 2000 together with video profiles. The check work in the near shore area was done with a hydrographical survey and a digitized field

model. The stability of the Lister Ley was checked by a surveillance of defined measuring profiles.

Near shore area

With the first measurements some local movements were detected. In the north-eastern part local erosion areas occurred with a maximum erosion of 1.0 m to 1.5 m (see fig. 5). Sedimentations were detected more to the south.

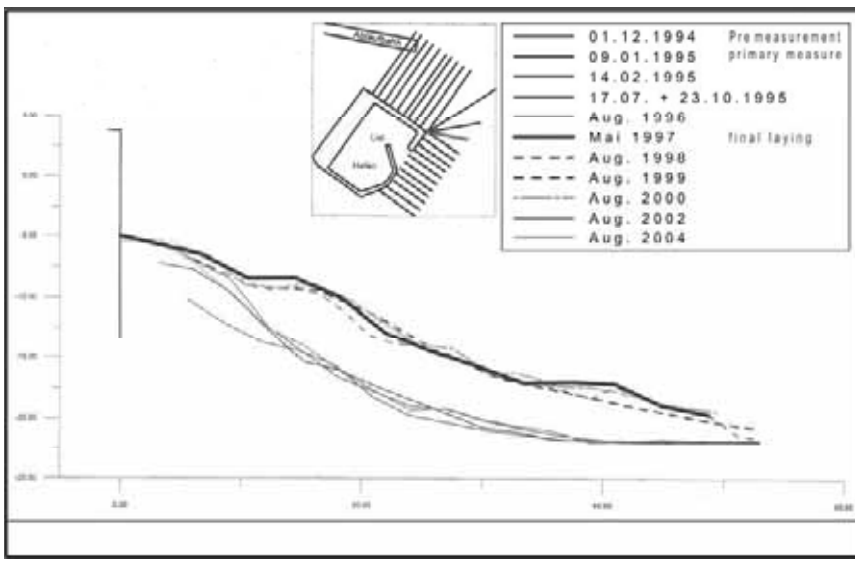

Figure 5. Profile with measurement results

A side-scan sonar surveillance, a video control and an all around surveillance took place in the year 2000. During the surveillance movements in the embankment area of the sandbags were detected. In the connection part to the harbour sheet piles were no measurable changes in length and height detected. The video profile control showed the geotextiles in the upper zones as well as the lower zones of the sandbags with biological settlements (see fig. 6). The settlement in the upper zones, the lighter zones, is stronger than in the lower parts. The north east corner with the strongest current velocity is the least settled. In the upper, shallower outline areas of the sheet piles are the sandbags mainly covered with sand. The spaces, which occurred due to a sandbag movement, are mainly filled with sand.

No additional changes were detected during the last measurements in 2004 and 2005.

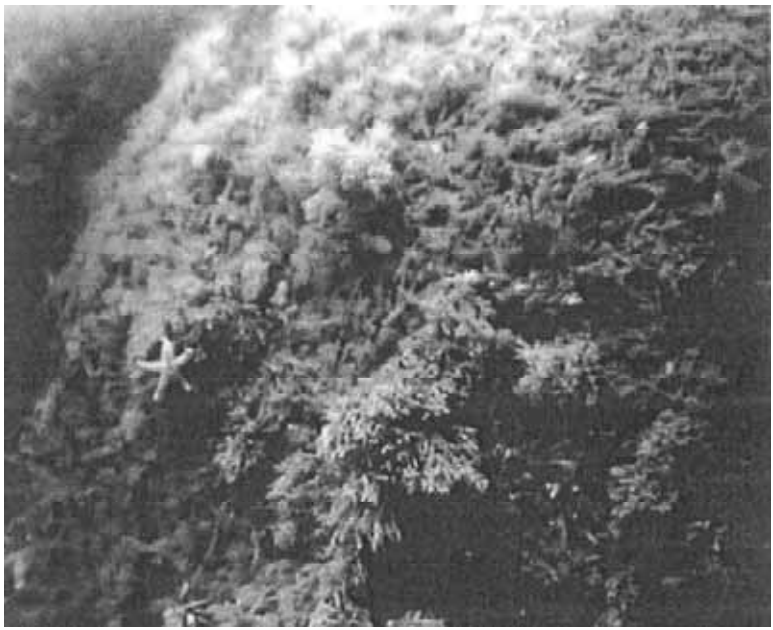

Figure 6. Sand bag surface with biological settlements

Stability of Lister Ley

The control measurements of the Lister Ley showed that the tendency of the west drift of the tidal inlet will be stopped.

The reason for the change of the process could not be solved during the investigation.

CONCLUSION

The paper shows that the static equilibrium of the harbour quay walls is still given after more than 10 years. The sandbags are in a stable position, so that no further erosion has taken place. The surface of the geotextile sandbags is still undamaged; partly the surface is covered with plants and mussels. Due to the coverage with mussels and plants, the sedimentation tendency will be supported and the stability of the construction will increase. In addition, the coverage with sand and organic material will minimize the risk of rub-of, so that there is no need to use the sandbags with the combined pp- and pa-material.

The method of using non woven geotextile sandbags to fill a local eroding area seems to be a method which could stabilize the eroding process and could be used for a final design of protection measures. In conclusion the method should be supported as well from the economic as from the technical point of view.

ACKNOWLEGMENTS

Harbour owner:	Local authority List
Support:	Land Schleswig-Holstein, LKN-SH, Agency for Coastal Defence, National Park and Marine Conservation
Executive firm:	Heinrich Hirdes GmbH, Colcrete von Essen GmbH
Supplier of geotextiles:	Naue GmbH & Co. KG
As laid survey and data delivery:	Land Schleswig-Holstein, LKN -SH, Agency for Coastal Defence, National Park and Marine Conservation
Side scan sonar:	Institut für Geowissenschaften, University Kiel

The author thanks the LKN-SH, the Agency for Coastal Defence, Schleswig-Holstein (former ALR Husum) for the delivery of the as laid measurement data

REFERENCES

ALR Husum:	Protection measures harbour List, Hydrological and Morphological Study, 1995, 1998 till 2005, unpublished
Schwarzer, K.	Video analysis, Report of the Institute of Geomorphologics, University Kiel 2000, unpublished
Schade, D.	Feasibility study for a soil bed protection measure, harbour List, Ingenieurbüro Mohn GmbH, 1996, unpublished

IKÜS – INTEGRATED COASTAL MONITORING SYSTEM

(german: Integriertes Küsten-ÜberwachungsSystem)

A Research Project funded by the German Federal Ministry of Education and Research (BMBF) and the German Coastal Engineering Research Council (GCERC)

Dr.-Ing. A. Sudau[1] and Dipl.-Ing. R. Weiß[1]

Knowledge of the earth surface, crustal movements, and long-term sea-level variations is essential for engineering applications and scientific purposes. Planning and design of coastal defence structures, waterways, new harbour terminals, as well as investigations of Global Change, long-term sea-level variations, but also risk analyses depend on exact GeoBase data. To derive longterm trends and to estimate influences one needs accurate and homogeneous height data and knowledge of their changes during a reference period. For statements about climatic sea-level variations and decision-making about response strategies, also non climatic changes, like vertical movements of the earth's crust, have to be considered.

The new concept and the goal of the research project IKÜS envisages the development of an integrated approach to the determination of heights and monitoring in coastal regions. Measurements made by different height sensors (levelling, gravity, GPS, and water-level) will be gathered and combined into one unified set of data of heights and their changes during a given reference period under consideration of sensor-specific characteristics. Historical and present-day data based on different reference systems and frames are transferred into one unified system. All data of the different height sensors are stored in a uniform IKÜS database. The study area is the German Bight (Figure 1).

[1] Departement Geodesy, Federal Institute of Hydrology, Am Mainzer Tor 1, 56068 Koblenz, Germany

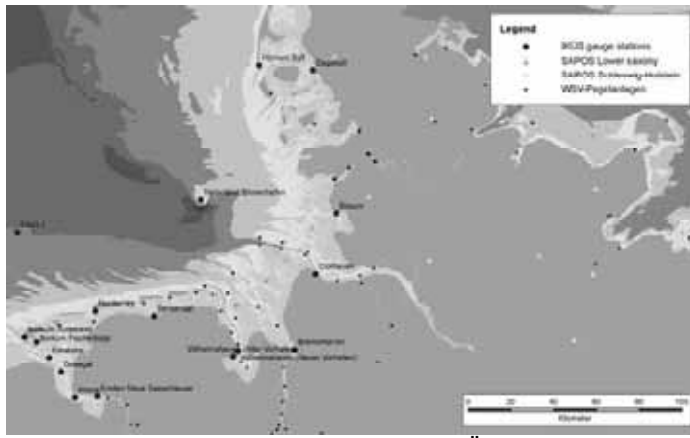

Figure 1. Study area German Bight with IKÜS gauge stations

IKÜS is a joint project of the:

- Geodetic Institute of the Dresden University of Technology (TUD)
- The Institute of Geodesy and Photogrammetry of the Technical University of Braunschweig (TUB)
- The State Survey + Geospatial Basic Information Lower Saxony (LGN)
- The Federal Institute of Hydrology (BfG)

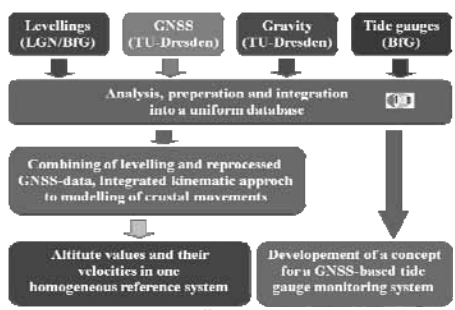

Figure 2. IKÜS Workflow

Because of different methods of GPS observations and evaluations, only heterogeneous GPS results are available today. Since heights are the most critical component of GPS results, the presently available data are not suitable for investigations of vertical recent movements. The part of the Dresden University of Technology in this project is the reprocessing of GPS-data from different national GPS reference sites and tide gauges in coastal regions of the German Bight by using the newest scientific methods with uniform parameters and software packages.

The State Survey + Geospatial Basic Information Lower Saxony will prepare and evaluate levelling measurements of the nation-wide ordnance datum

network of Lower Saxony. These levellings were accomplished during different periods (approximately 1912, 1935, 1955 and 1985). In addition to these data, the Federal Institute of Hydrology prepares and evaluates levellings along German federal waterways, measured by the Federal Waterway and Shipping Administration. Both kinds of levelling measurements from different agencies are prepared and evaluated by the same criteria and the resulting height differences and their accuracies, will be integrated into the IKÜS monitoring system.

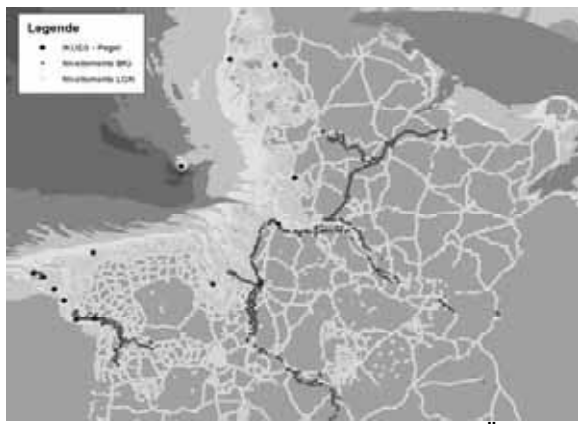

Figure 3. Levellings and gauge stations for IKÜS

In addition, the Federal Institute of Hydrology processes and evaluates water-level data from the Federal Waterways and Shipping Administration. The acceptance of long-term water-level time series as indicators of climatic changes implies that the elevation of gauges and their reference datums remain constant or are known over the entire observation period. According to the German Manual for Water Level Gauging and Discharge Measurements ('Gauging Manual', Pegelvorschrift), the decisive part of any conventional gauging station is the staff gauge consisting of the staff with the scale and at least three benchmark points (Pegelfestpunkte PFP). The origin (Nullpunkt) of the gauge staff scale is called the gauge datum (Pegelnullpunkt PNP). The benchmark points (PFPs) are used to monitor the height level of the gauge staff and serve to check the immediate surroundings of the gauge station for vertical land movements. In reality, PFPs are sometimes subject to vertical movements. Based on experience and with view to the local conditions, at least one of the PFPs has then to be defined as the representative one. The level differences between PFPs and the PNP that were registered when the gauge was established are called the level setpoint differences (Sollhöhenunterschied (Δhsoll)). Regular levellings between the benchmarks and the gauge-zero points ensure that the height of the gauge in relation to the benchmarks can find due consideration. Moreover, the benchmarks are related by levellings to the nation-

wide ordnance datum network of the German Federal States (especially Lower Saxony), thus allowing the comparison of water-level data from gauging sites at different locations. For this reason, the 'Gauging Manual' requires the level alignment of PFPs, and thus also of PNPs to the official height reference system. All official water-levels, provided by the Federal Waterways and Shipping Administration, are stored in the IKÜS database.

Tectonic and anthropogene influences (e.g. extraction of natural gas) may cause vertical movements of the earth's surface (recent crust movements), and the installed water-level sensors (gauges) follow these movements. Frequently, true variations of the water level and recent movements of the earth's crust superimpose. Unidentified or neglected vertical movements of the gauges can be mistaken for water-level variations, while those due to hydrological or climate-related causes cannot be identified.

For historical reasons, there are now in Germany several official height reference systems in existence that deviate by up to several centimetres and cannot be combined among each other. Because water-level gauges are referred to different respectively valid height reference systems, their elevation references differ. Currently, for the first time a revision of the German Main Level Network (Deutsches Haupthöhennetz) is being performed according to uniform criteria throughout the reunified Germany. As a consequence, updated elevation levels of all gauges will be available around 2011. Temporal and spatial comparisons or analyses of time series are possible only if all gauge levels can be referenced to one common datum. This is not the case for the time being. The correct evaluation of water-level series presupposes the transfer of historical and present-day reference levels into one system that is homogenous in space and time.

The 'Gauging Manual' stipulates that with the initial installation of a gauge in coastal waters the gauge datum (PNP) must be fixed at an elevation of NN – 5.00 m. Furthermore, the level setpoint differences and, consequently, the inner geometry of the gauges should be kept unchanged during the service-life of the gauge, if possible. However, when the heights of the benchmark points (PFPs) change, inevitably a contradiction arises that leads to different interpretations of the 'Gauging Manual' concerning the preservation of the PNP levels and the handling of transitions between height-reference systems. There are to-date two methods to respond to changes in gauge elevation: On the one hand, a mechanical shift of the gauge staff and respective corrections in the level setpoint differences (Sollhöhenunterschied - Δhsoll) are made. On the other hand, the height of the gauge datum (PNP) is changed, while the level setpoint differences (Sollhöhenunterschied (Δhsoll) are retained. In the course of time, both methods have been practised at one and the same gauge. Changes between height reference systems have not been taken into account often. The consequences are inhomogeneous data inventories. From a geodetical viewpoint, these data are inadequate to serve as a basis for the verification of climate-induced water-level changes.

Within the GCERC-project IKÜS, the effects of the above-mentioned practices have been studied at selected gauges. In the following, these effects will be presented exemplarily:

1. Recent crustal movements, the example of the island of Norderney

In the course of time, the tidal gauge of Norderney had two different locations and several benchmark points (PFPs) as reference (Figure 4). Some PFPs are in the immediate vincity of the gauge staff (e.g. PFP 55/56) while the PFP 1 is located in some distance and is pegged as a deep-foundation pipe benchmark. The latter has been chosen to be the representative benchmark for the gauging station.

Figure 4. Location of the PFPs for the gauge Norderney (Source: Luftbildnavigator Niedersachsen)

The official elevations of PFP 1 and of the gauge datum (PNP) of the gauge Norderney are compiled in Table 1. At this gauge, the gauge staff have been shifted and the height of the PNP have been changed.
The reason for the need to modify the fixing height of the staff may be changes in the elevation of the location of the gauge such as land subsidence. The shift of the gauge staff by the amount of this subsidence constitutes a 'mechanical compensation' of the discovered height changes (e.g. caused by a vertical crustal movements). Thus, these movements are not reflected in the measured water levels (Figure 5).

Table 1: Elevations and level setpoint differences Δh_{soll} of PFP 1 at the gauge Norderney					
Date	Location Staff gauge	PFP 1 (reference benchmark) H [m]	Δh_{soll} [m]	PNP (gauge datum) H [m]	Modification
01.11.1935	Harbour	5,014	10,014	-5,000	
16.12.1957	Harbour	4,999	10,014	-5,015	Change of PNP
16.12.1957	Riffgatt	4,999	9,999	-5,000	Shift of gauge staff / Δh_{soll}
25.04.1984	Riffgatt	4,968	9,968	-5,000	Shift of gauge staff / Δh_{soll}
30.11.1994	Riffgatt	4,981	9,968	-4,987	Change of PNP

At the gauge Norderney, the benchmark points PFPs 55/56 and 63/64 are more affected by subsidence than PFP 1. The increased subsidence of the land was positively verified by regular levellings between PFP 1 and the other PFPs.
From 1957 to 1984, PFP 1 experienced a vertical movement of 1.1 mm/a, while the PFPs 55/56 and 63/64 that are located directly at the gauge, subsided by 2.6 and 2.7 mm, respectively.
Relative to PFPs 55/56 and 63/64, the water levels increased faster due to the stronger land subsidence at their sites. Consequently, in addition to the changed water level with relation to PFP 1, this subsidence of the PFPs 55/56 and 63/64 should be accounted for when designing and dimensioning coastal structures.

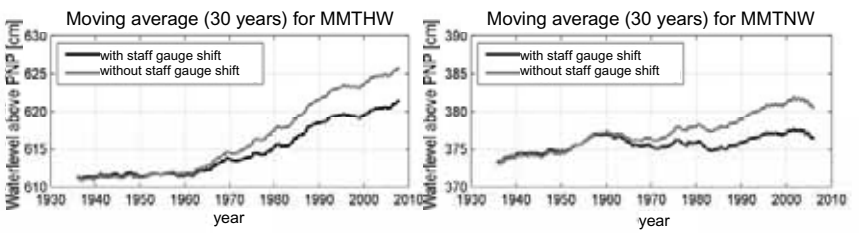

Figure 5. Water-levels and trends with and without staff gauge shifts at the gauge Norderney

2. Change of the height-reference system

Starting in 1912, the introduction of the height system DHHN12 (Deutsches Haupthöhennetz 1912) for the first time took the gravity field of the earth into account. This made it particularly suitable for applications in hydrology (NN - new system). The preceding system 'NN – old system', did not meet this requirement, and it is not compatible with DHHN12. The island of Norderney was aligned to the 'NN – old system' in 1907; the connection to 'NN – new system' followed in 1928. Due to the incompatibility of these two reference systems, their data cannot be combined, that means level data from the two systems cannot be used conjointly for water level trend analyses. Therefore, over the entire period between 1900 and 2005 water-level trend analyses are not acceptable with data from this gauge. A correct evaluation requires the transfer

of the data obtained before 1928 into the height reference system 'NN – new system'.

3. Change of reference system at the gauge Helgoland

Because of Helgoland's location in the open sea, it had not been possible until a few years ago to transfer the height reference system from the mainland to the island. Consequently, the so-called 'Helgoland ordinance datum' (Helgoländer Null – HN) had been introduced as a special solution, and the gauge datum PNP Helgoland was set at HN – 5.00 m. Some years ago, a satellite-based transfer of the official ordinance height system NN to Helgoland was accomplished, followed by the allocation of new NN heights to all benchmarks and PNPs of the island. The competent federal authority, the Waterways and Shipping Office (Wasser- und Schifffahrtsamt - WSA) Tönning, changed the height of the Helgoland gauge datum from HN – 5.00 m to NN – 5.00 m. The Helgoland reference height system HN is 0.27 m above the height reference system NN, what necessitated a downward shift of the gauge staff by 0.27 m. Water levels recorded at this tide gauge show a jump of 0.27 m since the date of this modification (Figure 6).

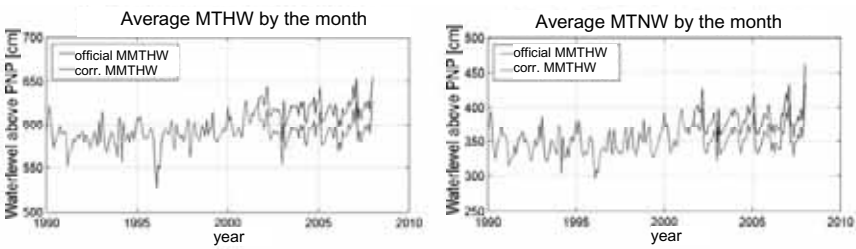

Figure 6. Effect of the system change from the Helgoland ordinance datum HN to NN on the water-level records

4. Recent crustal movements at Knock-Emden

The region Groningen (The Netherlands) is an example of vertical crustal movements induced by the extraction of natural gas that has been practiced there since 1957. The effects of these movements with a subsidence rate of more than 3 mm/a reach as far as the region between the island of Borkum and the town of Emden, where also the water-level gauges are affected (e.g. gauge Knock). At this gauge, the elevation was adjusted twice, in 1975 and in 1999, the height of the gauge datum (PNP) differs by 5.3 cm. The linear trends of the monthly averaged MTHW using the official PNP are 3mm/a and with a more realistic PNP, when the land subsidence was accounted for by interpolation, 0.6mm/a (Figure 7). The trends after 1999 were not derived, because no updates of the gauge-datum elevation since then are available. The apparent water-level rise is

obviously correlated with the subsidence rates. These phenomena can be found elsewhere in Germany too, also in inland regions.

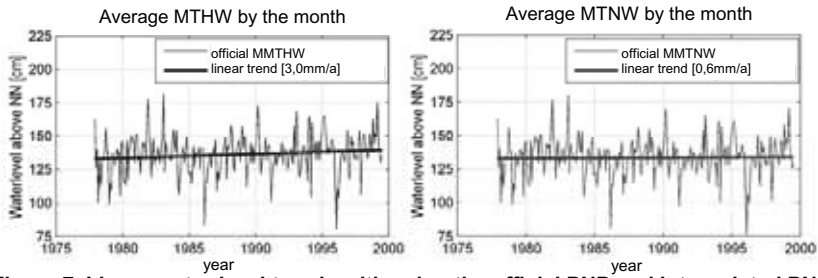

Figure 7. Linear water-level trends with using the official PNP and interpolated PNP at the gauge Knock

Recent tectonic crustal movements can be determined (and used for water-level analyses) only by evaluation of large-scale levellings beyond national borders or in the context of GNSS-supported height monitoring.induced water-level changes.

Analyses of long-periodicity water-level variations have to take the above-mentioned geodetic aspects into account. Moreover, the 'mechanical' shifting of gauge staffs resulting from a misinterpretation of the ‘Gauging Manual’ must be corrected. Only then, meaningful statements can be made about climate-induced water level changes. In order to avoid misinterpretations, it is necessary to transfer the existing gauge-datum points (PNPs) and benchmark points (PFPs) into one height reference system that is homogeneous in terms of space and time.

The Technical University of Braunschweig had combined the reprocessed GNSS-data, the prepared and evaluated nation-wide levellings and the gauge levellings into an integrated kinematic approach under consideration of the accuracies of different height sensors.

Height data are regarded as temporally varying values, and their changes due to seasonal and long-term effects or anthropogenic influences are parameterized. The parameterization is preformed by means of radial basic functions. Large coastal areas are linked together in one height system that is homogeneous in terms of time and space.

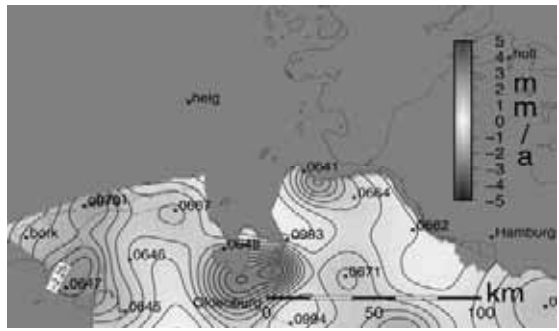

Figure 8. First results of the Technical University of Braunschweig: Isolines of velocities of vertical land movements [mm/a] in the southern German Bight

The overall result of this project will be a unified set of homogeneous heights that was developed in relation to a given epoch and a set of data on height changes of highest precision and universality. This will allow to recognise, qualify and quantify regional and/or local vertical crustal movements (Figure 8). These movements may caused by anthropogenic or natural effects. Examples of such causes are natural gas exploitation, glacial isostatic adjustments, or mining. The combination of these results with corrected water levels from the BfG allows to derivate long-term water-level trends (Figure 9).

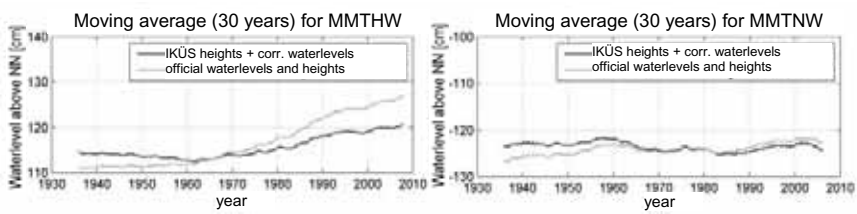

Figure 9. Water-level trends as a result of the Combination of the Results from the Technical University of Braunschweig with correctet water levels records

For several years now, the use of GNSS-methods has made it possible to monitor elevation changes and to feed the results into a global compatible reference system. Although this method needs further development, transboundary monitoring of long-periodicity water-level variations and combination with data from other sensor systems (e.g. satellite altimetry) have already become possible. Cooperation between administrational and scientific institutions can make the information about long-periodicity water-level variations so reliable that it may be used as an indicator of climatic changes.

The coupling of historical and present-day levellings from different authorities and water-level observations by the Federal Waterway and Shipping Administration with the results of the most advanced sensor technology, like satellite-based positioning, allows to distinguish between the signals of vertical

recent movements (caused by tectonic or anthropogenic influences) and long-term sea-level variations. With this knowledge it will become possible to improve climatic scenarios of Global Change and to develop response strategies.

REFERNCES

Augath, W., Broßmann, M., Schlüter, W., Sudau, A., Winter, R. 2000. NNSAT: Precise Height Supervision of Tide Gauges with GPS; *Wegener Meeting Cadiz, Sept. 2000*

Liebsch, G. 1997. Aufbereitung und Nutzung von Pegelmessungen für geodätische und geodynamische Zielstellungen, *Mitteilung Deutsche Geodätische Kommission DGK*, Heft 485,1997.

Augath, W., Niemeier W., Pelzer H. 1979. On the Signeficance of Measurded Height Differences in Nothern Germany. *AVN*, Nr, 86, S. 405-412

Landesarbeitsgemeinschaft Wasser (LAWA), Bundesministerium für Verkehr (BMV) Berlin und Bonn. 1997. Pegelvorschrift. *Berlin und Bonn*

Leonhard, T. 1987. Zur Berechnung von Höhenänderungen in Norddeutschland – Modelldiskussion, Lösbarkeitsanalyse und numerische Ergebnisse. *Dissertation Universität Hannover*

ESTIMATION OF EXTREME STORM SURGE AND ITS DURATION IN JAPANESE BAYS BY USING STOCHASTIC TYPHOON MODEL

Hiroyasu Kawai[1], Noriaki Hashimoto[2] and Kuniaki Matsuura[3]

In Japan long storm surge defense has been constructed for the design water level taking account of the storm surge by the standard typhoon based on Typhoon Vera in 1959. Yet storm water level may exceed the design one in small probability. This study, therefore, tried to estimate the extreme storm surge and storm water level with a return period of 10 to 1,000 years in Japanese major bays by using a stochastic typhoon and storm surge model. The result shows that the return period of the current design water level at three major locations, Tokyo, Nagoya, and Osaka, is a few hundred years or more in the current typhoon climatology. But the extreme storm surge may vary with the future change in typhoon climatology due to global warming.

INTRODUCTION

Severe tropical cyclones, such as Typhoon Maemi making landfall on Korea in 2003, Hurricane Katrina on the United States in 2005, Cyclone Sidr on Bangladesh in 2007, and Cyclone Nargis on Myanmar in 2008, frequently triggered terrible storm surge disaster in the latest decade. Typhoon Bart in 1999 brought significant storm surge into East Japan at the time of a spring high tide and that situation induced the most enormous damage in Japan since Typhoon Vera in 1959, named *Isewan Typhoon* in Japan (Kawai et al. 2007, Takahashi et al. 2002). Fig. 1 shows the water mark on the roof of one-story house on land below the high tide level. Fortunately no coastal dike was breached and the house had no severe damage, but twelve residents, mainly the aged, were drawn to death due to quick rise of flooding water level in the early morning. Fig. 2 shows that frequent wave overtopping covered the whole runway at a bayside airport and the impulsive wave pressure collapsed the seawall parapet. The crest height of wave-dissipating blocks was insufficient for the coincidence of the storm surge and high waves with the spring high tide. One of major causes for these failures is the water level that is higher than the design water level for defense facility.

A few ten typhoons appear each year mainly in the latitude of 10 to 20 degrees in the Northwest Pacific Ocean and take tracks to the west and/or north. Some of them affect Japan. Actually the frequency of landfall on Japanese main islands is 2.6 per year on the average. Unfortunately the islands have several

[1] Marine Environment and Engineering Department, Port and Airport Research Institute, 3-1-1 Nagase, Yokosuka, 239-0826, Japan
[2] Faculty of Engineering, Kyushu University, 744, Motooka, Nishi-ku, Fukuoka, 819-0395, Japan
[3] Metropolitan Regional Office, Japan Weather Association, 3-1-1, Higashi-Ikebukuro, Toshima-ku, Tokyo, 170-6055, Japan

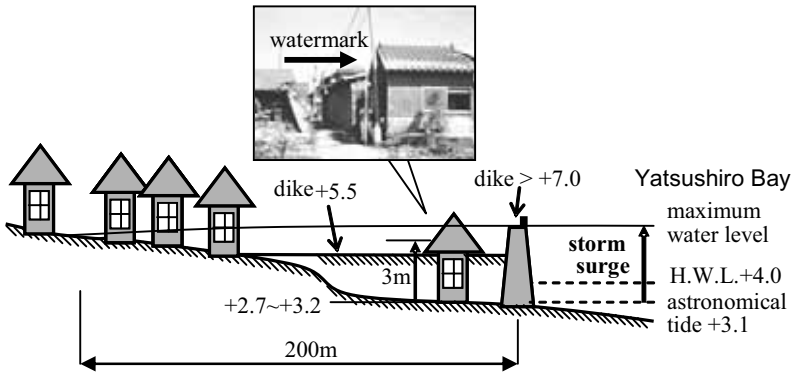

Fig.1. Storm surge flooding over a residential area below sea level, on the coast of Yatsushiro Bay, Japan, due to Typhoon Bart in 1999.

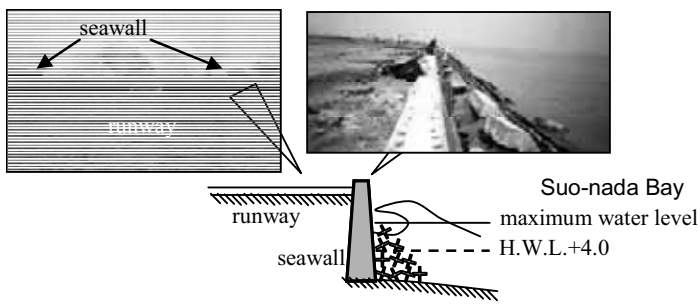

Fig.2. Inundation over a bayside airport due to wave-overtopping and collapse of seawall parapet due to impulsive wave pressure, on the coast of Suo-nada Bay, Japan, due to Typhoon Bart in 1999

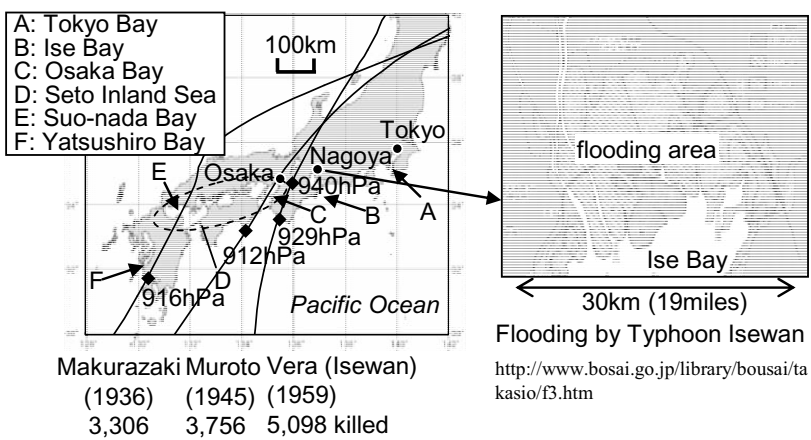

Fig.3. Three major disastrous typhoons before 1959 (left) and the storm surge flooding area by Typhoon Vera (right)

bays that are less than 30m in water depth and are several ten km in length in the parallel direction to typical typhoon tracks. Fig.3 shows that three major economical areas, including Tokyo, Nagoya and Osaka, lie on the coast of these bays and have wide low-lying land. That is a reason why Japan has a storm surge history with the loss of many lives and expensive properties.

Fig. 3 shows the track of three major disastrous typhoons between 1930 and 1959. Typhoon Vera generated a storm surge of 3.5 m on an astronomical tide level that was higher than the mean water level, at Nagoya on the coast of Ise Bay. Its storm surge flooding took approximately 5,000 lives away. The event was recorded as the worst storm surge disaster in Japanese history. It is very interesting from a meteorological viewpoint that the event occurred in the same decade as the Great Storm Surge Disaster in the Netherlands and Germany on the North Sea.

Following the disaster, the Japanese Government determined the standard typhoon with an intensity of Typhoon Vera, simulated the storm surge in major bays with numerical models, and then began the construction of concrete coastal defense for the possible worst storm water level. Japanese coastal engineers, therefore, imagine the rare encounter probability of such the design water level during their lifetime. On the other hand the discussion on the return period is still insufficient. If the mean sea level would rise and the tropical cyclone intensity would increase, the return period will become short.

By this reason the probabilistic meaning of the current design water level should be identified. That seems very important work to enhance the discussion how much risk should we accept by considering the balance of the initial cost of measures versus the expected amount of the loss in future disaster. This study, therefore, simulated a stochastic typhoon model and estimated the return period of the current design water level.

DESIGN WATER LEVEL FOR STORM SURGE DEFNSE

Current Design Water Level

In Japan the design water level for storm surge defense is determined by one of the following criteria in general;

(a) the sum of the mean spring high tide level and the maximum storm surge, recorded at a tide station or simulated for a standard typhoon,

(b) the highest water level recorded.

The criterion (a) is adopted for major bays with large population and expensive properties such as Tokyo Bay, Ise Bay, and Osaka Bay as mentioned before, while the criterion (b) is adopted for the other bays such as the central region of Seto Inland Sea. The return period of the design water level is not quantitatively evaluated in the current design system.

Difficulty in Estimation of Extreme Storm Water Level

The most reliable and direct method for the estimation of extreme storm water level is extreme-value analysis of water levels obtained at a tide station. But

the history of tide observation is still short in Japan except for a few tide stations. The number of tide stations is insufficient compared with the regionality in storm surge phenomena. Some measurements did not work in some disastrous storms.

On the other hand the Japan Meteorological Agency has been conducting relatively accurate typhoon observation and reanalysis since 1950's. The number of the typhoons with a disastrous storm surge is, however, limited within the latest half century. Actually no typhoon like a standard typhoon made landfall near the bays. The magnitude of storm surge varies with various typhoon parameters such as the track, the central pressure, the radius of maximum wind speed, and the forwarding speed. That makes it impossible to define the return period of the current standard typhoon based on Typhoon Vera. By these reasons, it is difficult to estimate the encounter probability of the standard typhoon as well as extreme storm water levels.

STOCHASTIC TYPHOON AND STORM SURGE MODEL

Concept of Stochastic Typhoon Model

Fig. 4 illustrates the concept of the stochastic typhoon model that simulates the track and parameters, such as the central pressure and radius of numerous typhoons, based on real typhoon statistics, with the Monte Carlo Method. The model is known as one of the tools to breakthrough the difficulty in the estimation of extreme storm water levels (Hashino and Kuwata 1987, Hatada and Yamaguchi 1996). For instance, Hashimoto et al. (2004) divided typhoons affecting Japan between 1951 and 1999 into five seasons (June and July, August, September, October, and other months), and estimated the value of the parameters and their variation with time in each rectangular cell with a width of 1.5 degrees in

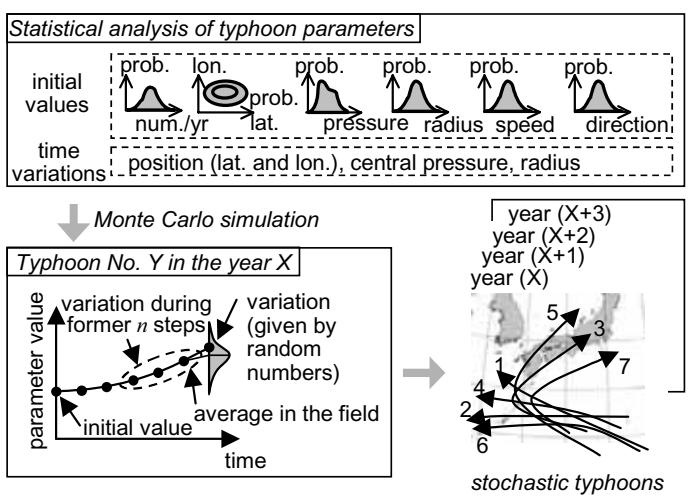

Figure 4: Concept of stochastic typhoon model, simulating numerous typhoon tracks and parameters.

longitude and a height of 1.5 degrees in latitude. Then they developed an auto-regression model to describe the track and the variation of each parameter with time, for each typhoon.

$$T_i = T_{i-1} + \Delta T_i \tag{1}$$

$$\Delta T_i = S(x_i, y_i) + \sum_{m=1}^{n} A_m Z_{i-m} + \nu_i \tag{2}$$

Hence, i is the time step with an interval of one hour in this paper, T_i is the typhoon parameter, ΔT_i is the variation with time, $S(x_i,y_i)$ is the mean variation at the longitude x_i and latitude y_i, A_m is the auto-regressional coefficient of which order is determined by Akaike's Information Criteria, Z_{i-m} is the deviation, and υ_i is the white noise.

Assumption of Future Typhoon Climatology in Stochastic Typhoon Model

According to recent meteorological research on the future climate in the northwest Pacific region, typhoon intensity may increase on the average while severe typhoon frequency may decrease (Oouchi et al. 2006). Typhoon climatology changes affect storm surges and wave heights and consequently increase the failure probability of coastal and port facilities.

The Meteorological Research Institute, Japan and the Japan Meteorological Agency predicted the global weather until the year 2100 for the medium SRES scenario A2 by using their climate model, CGCM. Then they simulated the regional weather around Japan in the current climate from 1981 to 2000 and the future climate from 2081 to 2100, by using their regional climate model with a spatial resolution of 20 km, RCM20. They provided the grid point values of the daily mean atmospheric pressure and wind speed and direction (Ishihara et al. 2004). This study followed a simple assumption that the filed $S(x_i,y_i)$ in Eq. (2) will move toward north by 1.5 degrees in longitude and that the probability distribution of the typhoon origin will not change (Kawai et al. 2006).

Selection of Stochastic Typhoons

This study chose the target area that includes Tokyo Bay, Ise Bay, Osaka Bay, and some other bays in west Japan, as shown in Fig. 5 and gave hourly latitude, longitude, central pressure, and radius of the maximum wind speed, of the stochastic typhoons during 500 years in the current and future climate respectively. Some stochastic typhoons may have small storm surges that will be omitted in the extreme-value analysis. That is a reason why this study selected the stochastic typhoons having a central pressure below 970 hPa within the semi-circle with a long radius of 800 km shown in the figure. The semi-circle is so wide that the stochastic typhoon similar to one of the historical disastrous typhoons (1) to (11) is selected. The number of the stochastic typhoons selected for the storm surge simulation is 1,301 and 1,399 for the current and future typhoon climatology respectively.

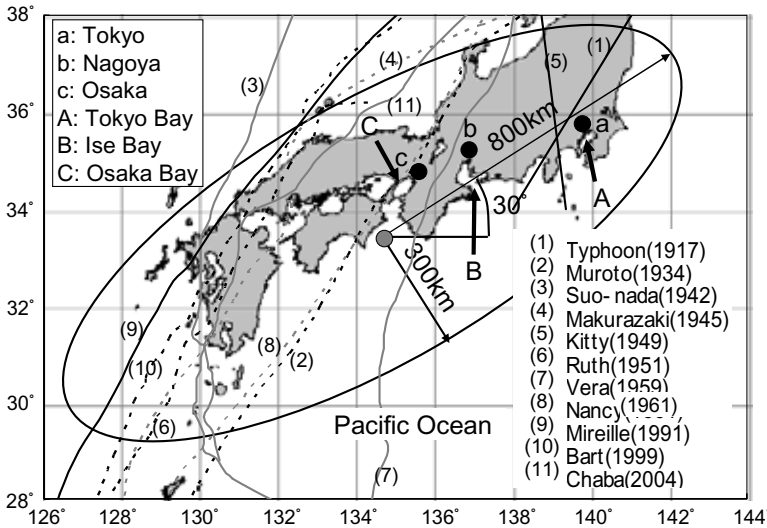

Figure 5: Area for the selection of stochastic typhoons and actual historical typhoons (1) to (11) affecting the area.

Marine Surface Pressure and Wind Model

The marine surface pressure field $p(r)$ of each stochastic typhoon was given with Myer's empirical model. The wind field was given considering the gradient wind $U_1(r)$ and the effect $U_2(r)$ of typhoon forwarding.

$$p(r) = p_c + \Delta p \exp(-r_0/r) \tag{3}$$

$$U_1(r) = C_1 U_{gr}(r) = C_1 \left\{ -\frac{rf}{2} + \sqrt{\left(\frac{rf}{2}\right)^2 + \frac{\Delta p}{\rho_a}\frac{r_0}{r}\exp\left(-\frac{r_0}{r}\right)} \right\} \tag{4}$$

$$U_2(r) = C_2 \frac{U_{gr}(r)}{U_{gr}(r_0)} V_T \tag{5}$$

Where r is the radial distance from the typhoon center, p_c is the central pressure, is the difference between the central and environmental pressures, r_0 is the radius of maximum wind speed, C_1 and C_2 are empirical parameters, to be assumed 0.65 in this study, ρ_a is the density of air, and V_T is the forwarding speed. That is the reason why this study used a conventional marine surface pressure, wind, and storm surge model.

Storm Surge Model

The storm surge of each stochastic typhoon was computed by a liner long wave model.

$$\frac{d\eta}{dt} + \frac{\partial M}{\partial x} + \frac{\partial N}{\partial y} = 0 \tag{6}$$

$$\frac{\partial M}{\partial t} = fN - gD\frac{\partial \eta}{\partial x} - \frac{D}{\rho_w}\frac{\partial p}{\partial x} + \frac{\tau_{sx} - \tau_{bx}}{\rho_w} + A_h\left(\frac{\partial^2 M}{\partial x^2} + \frac{\partial^2 M}{\partial y^2}\right) \quad (7)$$

$$\frac{\partial N}{\partial t} = -fM - gD\frac{\partial \eta}{\partial y} - \frac{D}{\rho_w}\frac{\partial p}{\partial y} + \frac{\tau_{sy} - \tau_{by}}{\rho_w} + A_h\left(\frac{\partial^2 N}{\partial x^2} + \frac{\partial^2 N}{\partial y^2}\right) \quad (8)$$

Where M and N is the flux flow at x and y component respectively, η is the water elevation, D is the total depth, A_h is the horizontal eddy diffusion, ρ_w is the density of sea water, τ_s is the sea surface stress with Mitsuyasu's drag coefficient, and τ_b is the sea bottom stress with Maning's roughness coefficient. This storm surge model does not include the term for wave setup in the governing equations. Fig. 6 shows the computational domain for the storm surge simulation. The minimum grid interval is 1.8 km. This storm surge model uses two-way nested grid system.

After the storm surge of each stochastic typhoon was computed, the best-fitting extreme-value function of the storm surges was selected from the Gumbel (FT-I) Distribution, FT-II Distribution (k=2.5, 3.33, 5, 10), and Weibull Distribution (k=0.75, 1, 1.4, 2) and the extreme-value with a return period of 10 to 1,000 years was estimated at each computational grid.

EXTREME STORM SURGE AND STORM WATER LEVEL

Extreme Storm Surge in Current Typhoon Climatology

Fig. 7 shows the plane distribution of the extreme storm surge in the current typhoon climatology. The Weibull Distribution (k=1.4 or 2.0) was selected at the majority of the grids. The 10-year-return storm surge is larger than 1 m at the innermost of several bays such as Tokyo Bay, Ise Bay, and Seto Inland Sea. The 100-year-return storm surge exceeds 1 m in the whole area of these bays and reaches 3 m at the innermost of Ise Bay, Osaka Bay, and Ariake Bay. The

1 0 0 0 -

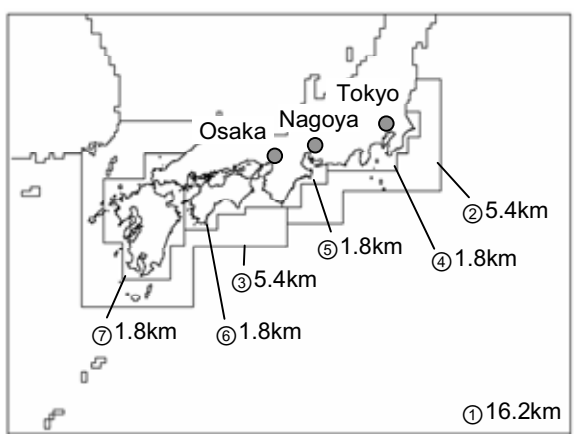

Figure 6: Computation area of storm surge simulation.

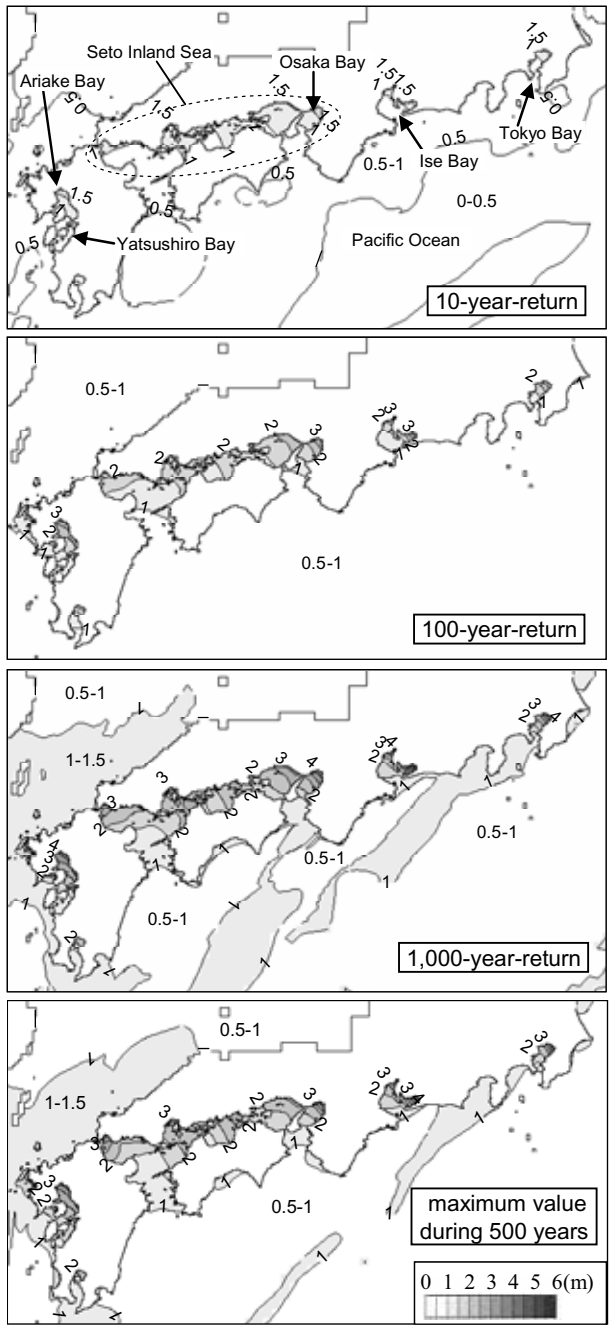

Figure 7. Distribution of 10 to 1000-year-retun and maximum storm surge.

year-return storm surge reaches 4 m in the innermost of these bays.

Fig. 8 shows the extreme-value function of the storm surges at three major locations. The current design water level for storm surge defense includes the storm surge of 3 m at Tokyo near the innermost of Tokyo Bay, 3.5 m at Nagoya at the innermost of Ise Bay, and 3 m at Osaka at the innermost of Osaka Bay. The storm surge of 3 m at Tokyo includes a margin above the storm surge simulated for the standard typhoon. The return period of the storm surge included in the current design water level is estimated near 100 years at Nagoya and Osaka and near 1,000 years at Tokyo.

Extreme Storm Water Level in Current Typhoon Climatology

The duration of severe storm surge at a location is normally less than half day because the typhoon crosses or passes by the region with a forwarding speed of several ten kilometers per hour. If the peak of the storm surge coincides with a

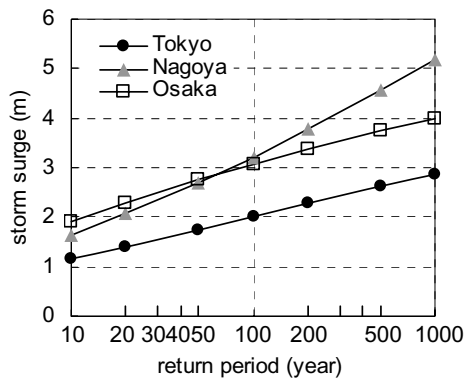

Figure 8. Storm surge with a return period of 10 to 1000 years at major locations.

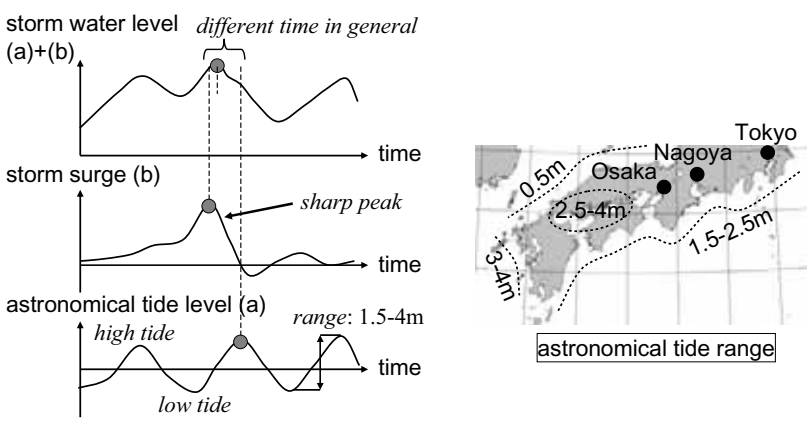

Figure 9. Calculation of storm water level.

low tide, then the total storm water level does not necessarily reach a disastrous one because the range of the spring tide is 1.5 to 2.4 m at Tokyo, Nagoya, and Osaka and reaches 4 m at some other locations. On the other hand, even if a small storm surge coincides a spring high tide, the total tide level sometimes becomes enough high to trigger the inundation over land areas. That is a reason why the time series of the storm water level was calculated as a linear summation of the time series of the astronomical tide level and the storm surge, as shown in Fig. 9. The astronomical tide level was calculated with 60 tidal constituents.

Fig. 10 shows the extreme-value function of the total tide levels at the major locations. The current design water level is 5.1 m, 5.9 m, 4.8 m above the lowest tidal level at Tokyo, Nagoya, and Osaka respectively. The simulation result shows that the return period of the water level is a few hundred years at Nagoya and Osaka and is much longer than 1,000 years at Tokyo, while it is known that the Primary Flood Defense in the Netherlands is designed for the extreme water level with a return period of 1,250 or 10,000 years. However, the slope of the extreme-value function in the figure is so mild that the return period varies sensitively with the water level. For instance, if we take uncertainty in the water level of 0.5 m due to estimation errors, the return period becomes half or less.

Storm Duration in Current Typhoon Climatology

The displacement of coastal defense facility and the amount of wave-overtopping, during a storm depend on not only the highest water level in the storm but also the duration of the water level near the highest. The storm duration, therefore, should be considered in the procedure of the performance evaluation of coastal defense. This study defined 'storm duration' as the duration of the water level within 0.5 m difference from the highest water level during the storm, as shown in Fig. 11. Fig. 12 shows the result for three major locations. The storm duration tends to be short if the highest water level is high. The average storm duration of ten high storms is longer at Tokyo than at Nagoya and Osaka.

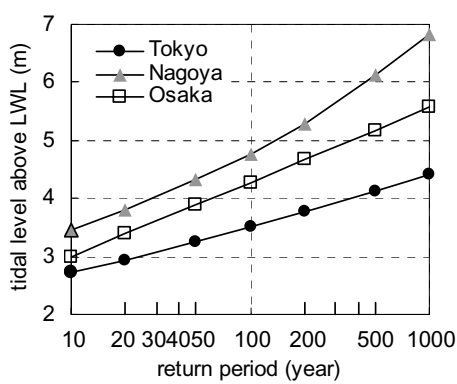

Figure 10. Extreme storm water level with a return period of 10 to 1000 years at major locations.

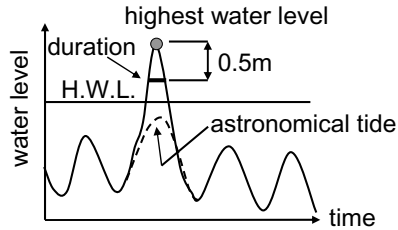

Figure 11. Definition of storm duration in this study.

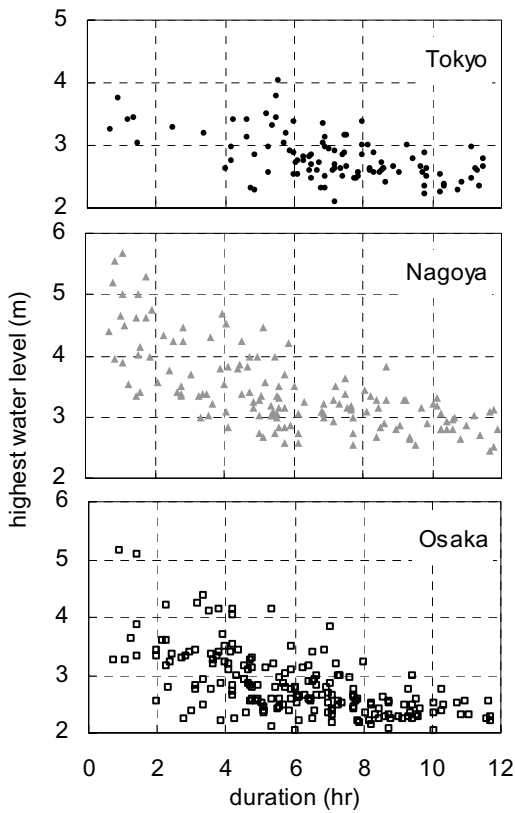

Figure 12: Relation between storm duration and highest water level.

Effect of Typhoon Climatology Change on Extreme Storm Surge

Fig. 13 shows the distribution of the 100-year-return storm surge under the future typhoon climate which was assumed before. Comparison with Fig. 7

introduces that the storm surge becomes large in the bays on the west side of Kyushu Island and in Seto Inland Sea and becomes small in some other regions.

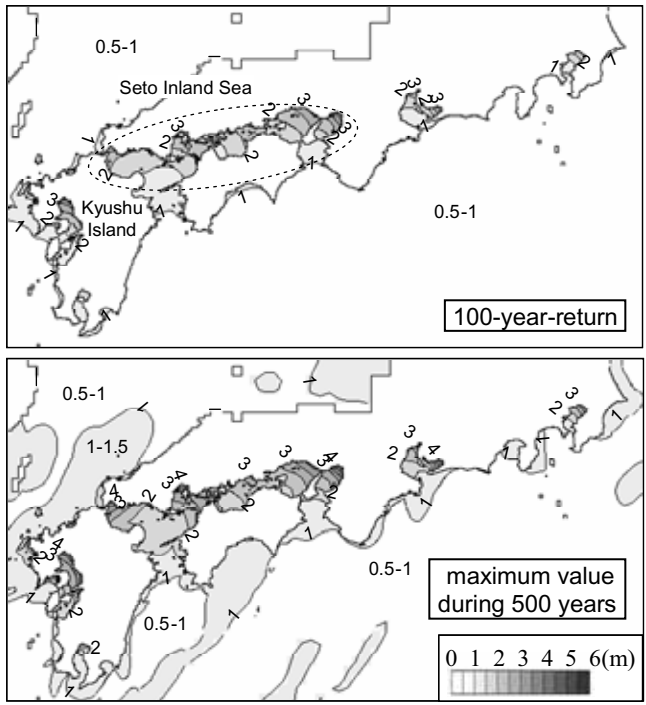

Figure 13: 100-year-return and maximum storm surge in future typhoon climatology.

Such the variation with the typhoon climate change may be significant at the innermost of bays.

CONCLUDING REMARKS FOR FUTURE RESEARCH

This study gave stochastic typhoons, calculated the marine surface pressure and wind field of each typhoon with an empirical model, computed the storm surge with a conventional storm surge model with a spatial grid resolution of 1.8 km, and then estimated the extreme storm surges and storm water levels in Japanese major bays. The result showed that the return period of the current design water level is a few hundred years at Nagoya and Osaka and is much longer than 1,000 years at Tokyo. However, we should take care of the uncertainty in the estimation and future mean sea level rise and typhoon intensification due to global warming. Moreover, we need to pay our attention on that there are wide areas below sea level on the inside of storm surge defense and some port facilities in the outside of the defense.

This study could show a part of the basic framework of the probabilistic assessment of external forces on coastal defense. Such the assessment may be

useful for the discussion on how high or low is the current safety degree and how much risk should we accept. In future research, we would like to introduce a more reliable global warming scenario, improve the stochastic typhoon model, conduct a more precise storm surge model, predict extreme water levels and wave heights, and then provide more useful information for the discussion on the long-term plan for storm surge disaster mitigation under global warming. Such the stochastic assessment is necessary for other places not only in Japan.

REFERNCES

Hashimoto, N., H. Kawai and K. Matsuura. 2004. Development of stochastic typhoon model for performance design of coastal structures, *Proceedings of 29th International Conference on Coastal Engineering*, ASCE, 3615-3627.

Hashino, M. and Y. Kuwata. 1987. Evaluation of concurrent characteristics of rainfall and storm surge by a stochastic typhoon model, *Journal of Natural Disaster Science*, 9, 1, 79-97.

Hatada, Y., and M. Yamaguchi. 1996. A stochastic typhoon model and its application to the estimation of storm surge and wave height, *Proceedings of 25th International Conference on Coastal Engineering*, ASCE, 1389-1402.

Ishihara, K., K. Kurihara, K. Wada, M. Murase, Y. Tomizawa. 2004. Reproducibility of rainfall characteristic by MRI-RCM20 for flood and drought risk assessment, *Proceeding of Annual Scientific Meeting*, Autumn 2004, Meteorological Society of Japan, B169, 145.

Kawai, H., N. Hashimoto, and K. Matsuura. 2006. Improvement of stochastic typhoon model for the purpose of simulating typhoons and storm surges under global warming, *Proceeding of the 30th International Conference on Coastal Engineering*, ASCE, 1838-1850.

Kawai, H., S. Takahashi, T. Hiraishi, N. Hashimoto, and K. Matsuura. 2007. Lessons learned from recent storm surge disasters and estimation of extreme tidal levels for coastal defense performance by using stochastic typhoon model, *Proceedings of 17th International Conference on Ocean and Polar Engineering*, 1792-1799.

Oouchi, K., J. Yoshimura, H. Yoshimura, R. Mizuta, S. Kusunoki, and A. Noda. 2006. Tropical cyclone climatology in a global-warming climate as simulated in a 20 km-mesh global atmospheric model: frequency and wind intensity analyses, *Journal of the Meteorological Society of Japan*, 84-2, 259-276.

Takahashi, S., H. Kawai, and T. Takayama. 2002. Storm surge disaster by typhoon No.9918 -performance design of coastal defense-, *Proceeding of the Solutions to Coastal Disasters Conference 2002*, ASCE, 735-749.

SPH AND SUBMARINE LANDSLIDES

Tatiana Capone[1], Andrea Panizzo[2] and Joe Monaghan[3]

In the present work SPH (Smoothed Particle Hydrodynamics) numerical simulation of submarine landslide generated waves is presented. The landslide is modeled as a Non-Newtonian fluid, through a bi-viscosity model, tested with a viscometer test case, and its interaction with the water is studied using the experimental results given by Rzadkiewicz et al. (1997).
SPH is a Lagrangian numerical method introduced to simulate free surface flows, in this approach a continuum is represented with a finite number of particles. Field variables are interpolated with a weight function (kernel) over the neighbor particles. Even though SPH was introduced in astrophysics (Gingold and Monaghan, 1977), it has been applied in hydraulics since the beginning of the 90s. It is particularly used in coastal engineering for its capability to represent free surface flows without any particular constraint.

INTRODUCTION

Water waves generated by submarine landslides occur quite frequently and often have devastating consequences. A recent example is the Sissano tsunamis on the north coast of New Guinea, that resulted in the death of approximately 2000 people. Subsequent sub-sea observations, together with numerical modelling (Tappin et al 2001) suggested that the tsunamis was due to an underwater landslide which was triggered by an earthquake.

Amongst all the scientific works carried out on the topic, that of Jiang & LeBlond in 1994 considered a three dimensional numerical model for tsunami generated by submarine landslides, simulated as a mudflow, showing the importance of three dimensional effects in the effectiveness of tsunamis generation and considering the landslide as a granular flow.

In the present work the numerical computations of such phenomena are carried out using a mesh-free numerical model, the Smoothed Particle Hydrodynamics (SPH), introduced by Gingold and Monaghan (1977) in astrophysics, and then applied to the simulation of free surface flows (Monaghan, 1994). SPH was already successfully used to simulate landslide generated waves (Panizzo & Dalrymple, 2004; Panizzo et al., 2006), because of its capability to represent generation, propagation and run up of tsunamis waves without any particular constraint on the shoreline or the free surface. In those works, the landslide movements were modelled as rigid bodies sliding down from a slope. It is clear that the assumption of a non deformable landslide could

[1] DITS, “Sapienza” University of Rome, Via Eudossiana 18, Rome, 00184, Italy
[2] DITS, “Sapienza” University of Rome, Via Eudossiana 18, Rome, 00184, Italy
[3] School of Mathematical Sciences, Monash University, Melbourne, 3800 Clayton, Australia

change significantly the generated water waves, if compared to real deformable landslides.

The present work deals with the simulation of the submarine landslide as a non-Newtonian fluid. The Bingham model seems to be one of the best to represent the viscoplastic behaviour (Masson et al., 2006) of these kind of fluids in which no deformation takes place until a certain stress is applied, as extensively reported in literature (Barnes et al., 1989). In the present work a particular kind of Bingham viscosity model is used.

The interaction of such a fluid with the water will be investigated, as well as the water waves generated in the (so called) near field. The work is being carried out in the framework of a wider research program on tsunamis waves generated by landslides, which has been funded by the Italian Ministry of Research (www.tsunamis.it).

RHEOLOGICAL MODEL

In order to model a Bingham fluid flow we have to refer to the constitutive equation of a generalized newtonian fluid, it differs from a newtonian one in the way that the shear stress t depends upon the shear rate tensor (i.e. the gradient of the velocity field) at a particular time:

$$\mathbf{D} = \frac{1}{2}\left(\nabla \mathbf{u} + \nabla^t \mathbf{u}\right) \tag{1}$$

Usually this tensor is used in the formulation of the viscosity field in the form of its second invariant:

$$\left|\mathbf{D}\right| = \sqrt{\mathbf{D} : \mathbf{D}} = \sqrt{D_{ij} D_{ij}} \tag{2}$$

The constitutive law for the generalized newtonian fluids is thus of the following form:

$$\tau = \mu\left(\left|\mathbf{D}\right|\right)\mathbf{D} \tag{3}$$

in which the relation between viscosity and the second invariant of the shear rate tensor is specified.

The Bingham plastic behavior is represented by the presence of a critical yield stress under which no deformation takes place. Above this level viscosity depends upon the second invariant of the shear rate tensor, as usual for the generalized newtonian fluids, and the yield stress.

In this work we propose a slightly different Bingham model that is present in literature with the name of ”bi-viscosity model” (Beverly and Tanner, 1992). The main difference between this kind of model and the classical Bingham one is that in the un-yielded region a greater viscosity is given to the fluid, instead of having no deformation at all. The constitutive equations are the following:

$$\left|\mathbf{D}\right| \le \frac{\tau_y}{2\alpha\mu} \Leftrightarrow \tau = 2\alpha\mu\mathbf{D} \tag{4}$$

$$\left|\mathbf{D}\right| > \frac{\tau_y}{2\alpha\mu} \Leftrightarrow \tau = \left(\frac{\tau_y}{\left|\mathbf{D}\right|} + 2\mu\right)\mathbf{D} \tag{5}$$

In our SPH code Bingham rheology is modeled in the way to have an effective viscosity in the momentum equation (see Monaghan 2005) function of D, using an average between the value of its second invariant for particle *a* and its neighbor *b*:

$$\mu_{eff} = F\left(\left|\overline{\mathbf{D}}_{ab}\right|\right) \tag{6}$$

Dividing by density the kinematic effective viscosity is calculated

$$\nu_{eff} = \frac{1}{\rho} F\left(\left|\overline{\mathbf{D}}_{ab}\right|\right) \tag{7}$$

and from this value it is possible to achieve the artificial viscosity term present in the momentum equation through the relation given by Monaghan, 2005.

$$\nu_{eff} = \frac{15}{112} K^{eff} v_{sig} h \tag{8}$$

$$\Pi_{ab}^{eff} = -\frac{K^{eff} v_{sig} \mathbf{v}_{ab} \cdot \mathbf{r}_{ab}}{\overline{\rho}_{ab}\left|\mathbf{r}_{ab}\right|} \tag{9}$$

$$\frac{d\mathbf{v}_a}{dt} = -\sum_b m_b \left(\frac{P_a}{\rho_a^2} + \frac{P_b}{\rho_b^2} + \Pi_{ab}^{eff}\right)\nabla_a W_{ab} \tag{10}$$

Annular Viscometer Test

The viscoplastic behavior of the non-newtonian viscosity was tested with an annular viscometer test. It consists in an axisymmetrical problem of a flow between two coaxial cylinder that can be treated as a fully bi-dimensional test. The outer cylinder is kept fixed while the inner one has an angular velocity $\omega=1$ *rad/s*.

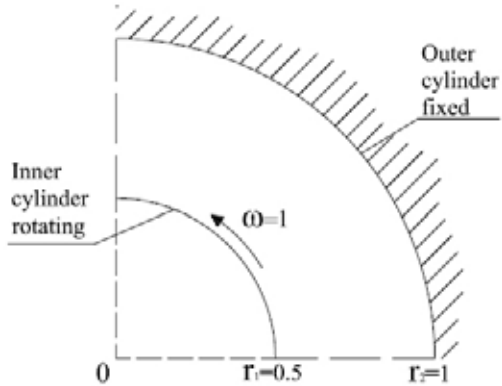

Figure 1. Geometrical domain for the annular viscometer test.

As shown in Fig. 1, the inner cylinder radius is equal to *0.5 m*, while the outer one is equal to *1.0 m*.

The steady state solution for the annular viscometer is expressed in term of tangential velocity and is calculated for our particular non-newtonian rheology, and shown below:

$$r < r_s \Leftrightarrow v_t = \omega r + \frac{\tau_y r}{\sqrt{2}\mu}\left\{\ln\left(\frac{r}{r_1}\right) + \left(\frac{r_s^2}{2}\right)\left(\frac{1}{r^2} - \frac{1}{r_1^2}\right)\left(1 + \frac{1}{\alpha}\right)\right\}$$
$$r > r_s \Leftrightarrow v_t = \frac{\tau_y r_s^2}{2\sqrt{2}\alpha\mu}\left(\frac{1}{r^2} - \frac{1}{r_2^2}\right)\left(1 + \frac{1}{\alpha}\right) \quad (11)$$

The simulations were conducted following the viscosity parameters given by Vola et al., 2004, τ_y*=10 N/m*^{2}, μ*=1 Pa·s* e ρ*=1000 kg/m*^{3}, with different values of α and with different initial particles spacing.

The best solution was achieved with a variable resolution between the region close to the rotating cylinder and the outer fixed, and with α*=50*. Below are shown the results in terms of particles positions, underlying the difference between the plug (with grey dots) and the shear zone (with black dots)

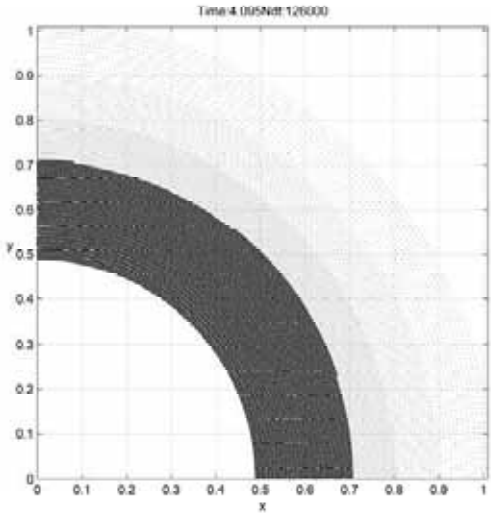

Figure 2. Particles positions after more than 4 seconds (unyielded and yielded region in grey and black dots respectively).

and tangential velocity compared with the calculated one:

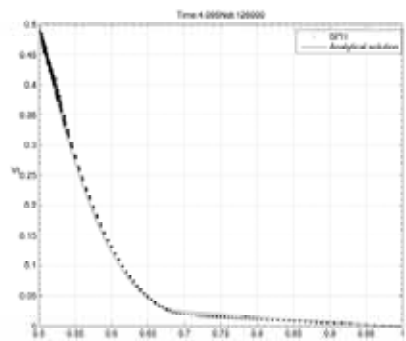

Figure 3. Tangential velocity after more than 4 seconds (dots for SPH solution and line for computed one).

The stationary solution is in perfect agreement with the calculated one, also the "switch radius", that represents the radius at which the behavior of the fluid change between unyielded and yielded one, is well represented.

NUMERICAL MODELING OF EXPERIMENT

In order to understand the capability of our SPH code to model submarine landslides, the experiments of Rzadkiewicz et al., 1997 were tested and performed, consisting in a mass of sand allowed to slide from a slope of 45°.

A sketch of the geometrical domain of the experiment is shown below.

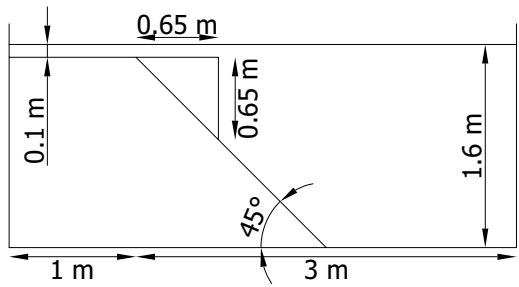

Figure 4. Geometrical Domain.

The simulations were performed with 16819 particles, corresponding to an initial spacing of 0.015 m. Ghost particles represent our boundaries, being a portion of fluid with mirrored characteristics on the opposite side of the boundary. Below particles positions at the beginning of the simulation is shown.

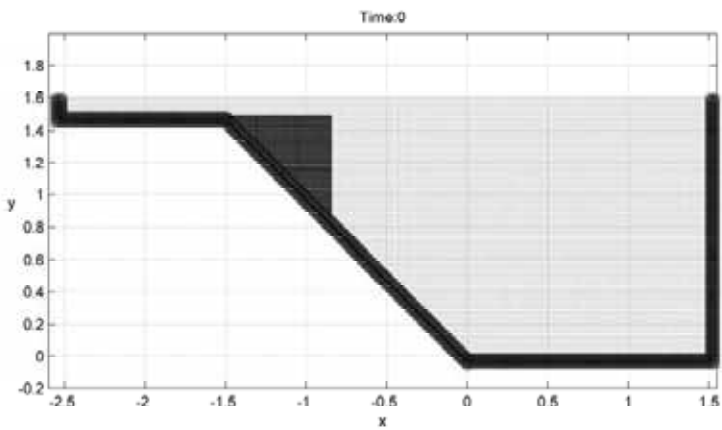

Figure 5. Particles Positions at the beginning of the simulation.

The fluid density is $\rho=1000\ kg/m^3$ and the viscosity is set as $\mu=0.001\ Pa{\cdot}s$.

The sand density is $\rho=1950\ kg/m^3$, this is the value defined in the experiments. The rheological parameters were not measured in the experiments but chosen by trials and errors by Rzadkiewicz et al., 1997 for the numerical simulations. Always with this approach we set this parameters as $\mu=1.0\ Pa{\cdot}s$ for the viscosity and $\tau=1000\ N/m^2$, they differ from the values used in the numerical simulations of the experiment by Rzadkiewicz et al., 1997 only for the viscosity and not for the yield stress that is the same. This is due to the necessity for our particular rheological model to give a non-zero value to the

viscosity, that is indeed the approach used by Rzadkiewicz to have an immediate liquefaction of the material.

RESULTS

Experimental results are given in terms of elevation of the free surface at *t=0.4 s* and *t=0.8 s*. Below at the same times, particles positions are plotted, it is possible to distinguish in the mass of sand with a darker grey the shear zone that is typical of a Bingham fluid flow.

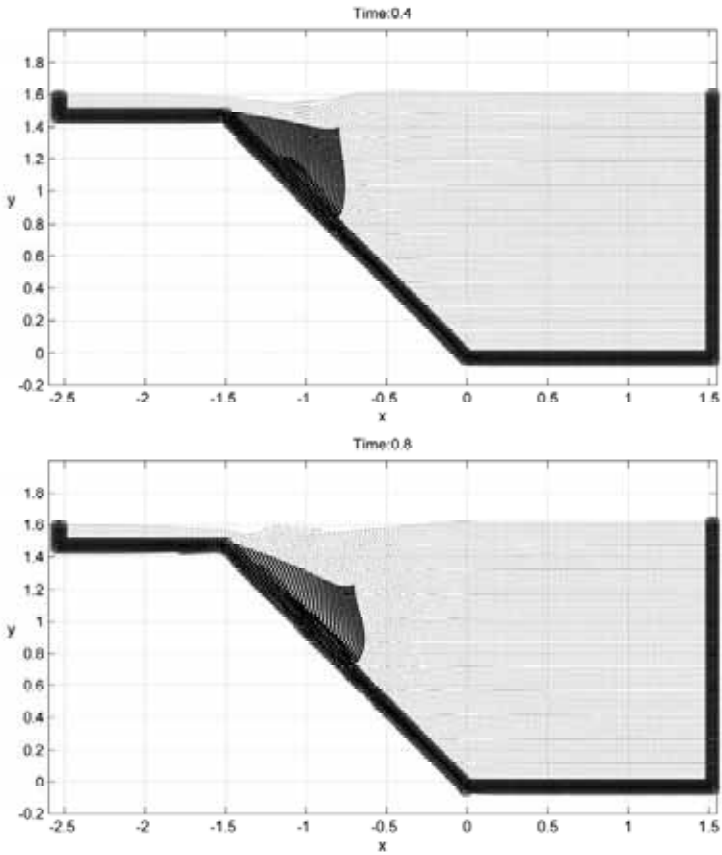

Figure 6. Particles Positions at times t=0.4 s and t=0.8 s.

Comparison between experimental and computed waves are shown in the following plots:

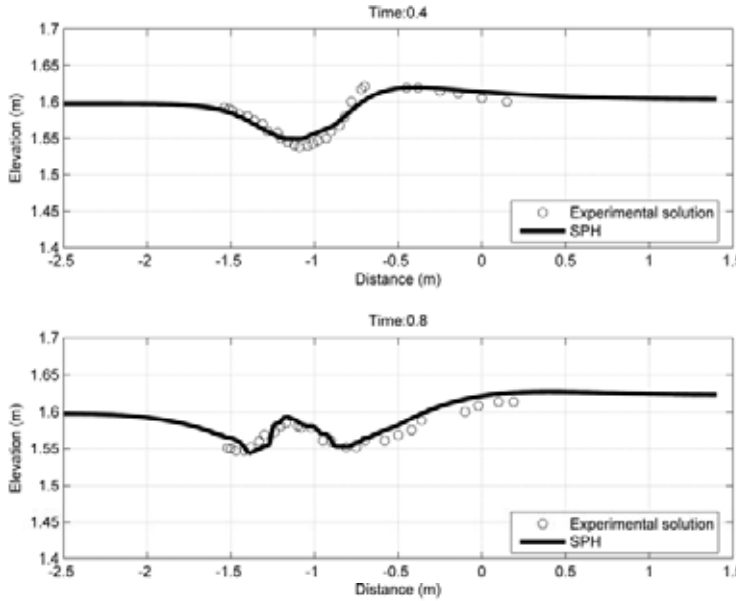

Figure 7. Elevations of the free surface at times t=0.4 s and t=0.8 s.

In conclusion it is possible to reproduce Bingham fluid with SPH, testing rheological parameters with simple two dimensional test. Moreover reproducing a mass of sand falling into the water it is possible to obtain excellent agreement with experimental results, in terms of interaction with the water and shape of the landslide, with only a slight underestimation of the wave amplitude especially at the beginning of the slide motion.

REFERENCES

Barnes, H.A., J.F. Hutton, and K. Walters. 1989. An introduction to rheology, *Elsevier, Amsterdam*.

Beverly, C.R., and R.I Tanner. 1992. Numerical analysis of three-dimensional Bingham plastic flow, *Journal of Non-Newtonian Fluid Mechanics*, vol.42.

Capone, T., and A. Panizzo. 2003. SPH simulation of non-newtonian mud flows, *3rd Spheric Workshop, Lausanne 3rd-6th June*.

Gingold, R.A., and J.J. Monaghan. 1977. Smoothed Particle Hydrodynamic: theory and application to non-spherical stars, *Monthly Notices of the Royal Astronomical Society*, 181, 375-389.

Masson, D.G., et al. 2006. Submarine landslides: processes, triggers and hazard prediction, *Phil. Trans. R. Soc. A*, 364, 375-389.

Monaghan, J.J. 1994. Simulating free surface flow with SPH. *Journal of Computational Physics,* 110, 399-406.

Monaghan, J.J. 2005. Smoothed Particle Hydrodynamics, Reports on Progress in Physics, 68.

Panizzo, A., and R.A. Dalrymple. 2004. SPH modeling of underwater landslide generated waves. *Proceedings ICCE 2004,* ASCE.

Panizzo, A., G. Cuomo, and R.A. Dalrymple. 2006. 3D-SPH simulation of landslide generated waves. *Proceedings ICCE 2004,* ASCE.

Rzadkiewicz, S.A., C. Mariotti, and P. Heinrich. 1997. Numerical simulation of submarine landslide and their hydraulic effects, *Journal of Waterway, Port, Coastal and Ocean Eng.*, 149-157.

Tappin, D.R., P. Watts, G.M. McMurtry, Y. Lafoy, and T. Matsumoto. 2001. The Sissano Papua New Guinea tsunami of July 1998- offshore evidence of the source mechanism.

Vola, D., F. Babik, and J.C. Latch. 2004. On a numerical strategy to compute gravity currents of non-newtonian fluids, *Journal of Computational Physics,* 201, 397-420.

ENHANCEMENT OF SUPRATIDAL FORMS ON TIDAL FLATS BY DREDGED MATERIAL

Hanz Dieter Niemeyer, Florian Ladage, Cornelius Meyer
& Hans-Joachim Stephan[1]

Supratidal areas exist on the tidal flats in the southern German Bight between the Elbe and Weser estuary since the 17th century, varying in appearance and extend. It can be shown that supratidal forms would (re-)develop on a morphological unit called Eversand when additional sediment is supplied and certain conditions are met. So, instead of depositing dredged material on defined dumping sites, the sediment could be used to enhance development of supratidal forms.

Introduction

Within the scope of extending the harbour of Bremerhaven the question arose, whether it is possible to dump dredged material on tidal flats in order to enhance the (re-)development of supratidal forms rather than bringing the material to defined dumping sites within the Weser estuary (fig.1). The following questions had to be answered:

- Did supratidal forms exist in the past in the western part of the tidal area called Wurster Watt?
- Why do they not exist anymore or are showing an erosional tendency?
- Where might supratidal forms remain if sediment is supplied artificially?

Morphological changes

On the basis of reconstructions of historical morphological states (Homeier 1962) and more recent topographical surveys, variations in spatial extension since 1650 have been reconstructed for the three main morphological units Tegeler Plate, Eversand and Knechtsand. Supratidal forms can be detected on Knechtsand since 1650, showing an erosional tendency. The existence of a small supratidal area is verified on Eversand during the 18th century as well. There might be two reasons for the disappearance of supratidal features during the last centuries: Either the erosional forces have increased significantly in these areas or the sediment balance has changed as sediment input varies.

There is no evidence that hydrodynamical forces have increased; neither the long-term development of tidal water levels or storm surges nor the frequency of storm surges. But it seems quite obvious that sediment balance and morphological development in the western part of the Wurster Watt depends very much on morphological changes within the outer Weser estuary. Especially the course of the main channels has shifted significantly thereby forcing a

[1] Coastal Research Station, Lower Saxony Water Management, Coastal Defence and Nature Conservation Agency, An der Mühle 5, 26548 Norderney, Germany

reshaping of the estuarine ebb delta (fig.2). Accordingly sediment passing the outer estuary via the ebb delta will now weld with the Wurster Watt at a quite different place supporting again the formation of supratidal features (Niemeyer et al. 2007).

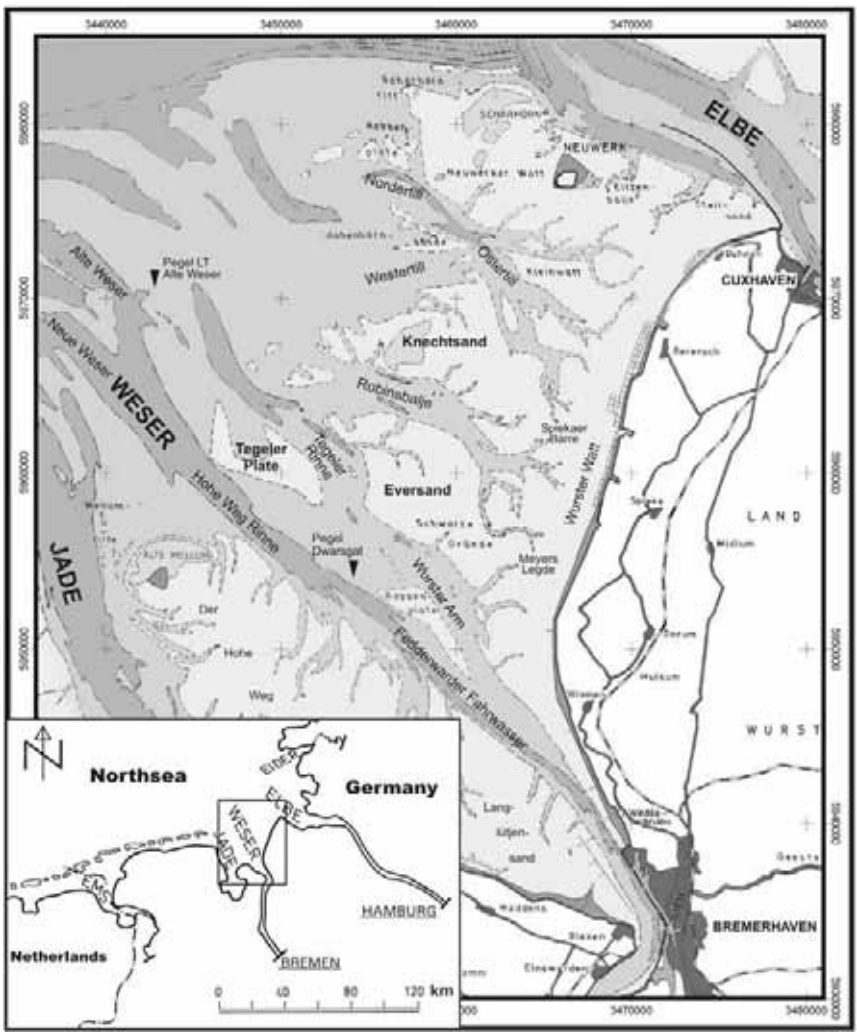

Figure 1. investigation area with morphological units

During the last centuries the NNE-migration of channels and morphological units in the western Wurster Watt slowed down. But it was not until 1920 when some stabilization of the morphological conditions could be achieved by a hydraulic construction built in the main channel of the Weser estuary fixing

channel geometry to a certain amount. Due to continuous sediment accretion in central parts of Eversand areas lying above MSL+1m are expanding.

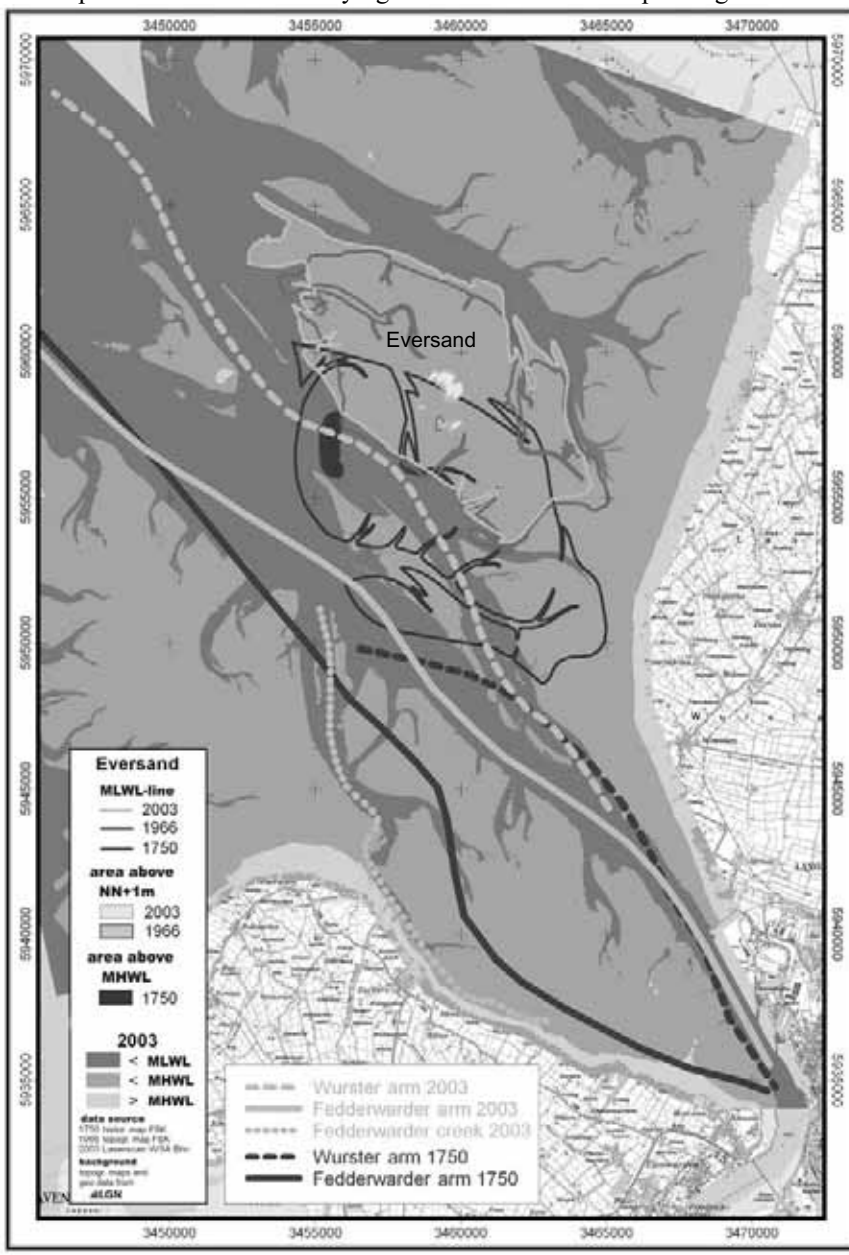

Figure 2. migration of channels and morphological units to NNE since 1750 within investigation area

Conclusions

An alternative to defined dumping sectors are areas at the basement of tidal flats where transportation factors exist which are similar to those at the foreshore of beaches. In order to select an appropriate area the following points must be considered: the slope angle has to enable a landward directed transportation of sediments. The wave-induced transportation of the dredged material should be directed towards accretion areas (fig. 3). With respect to channel systems that have not yet fully adjusted to changed conditions, the stabilization and accessibility of the tidal flat unit has to be taken into account. As for economic considerations the water depth should be sufficient for high-capacity dredging vessels. Against the background of these considerations a alternative dumping area is suggested that is situated in the foreshore on the western coast of Eversand.

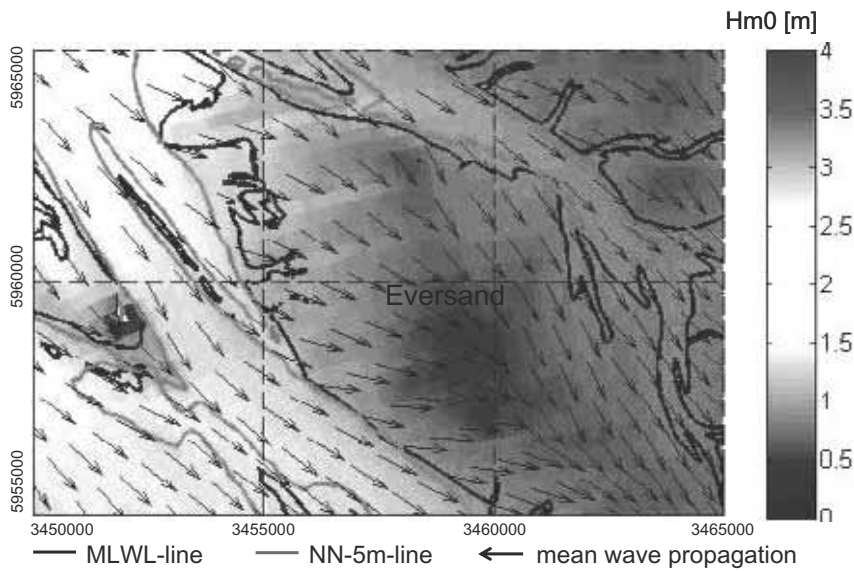

Figure 3. significant wave-height and wave propagation with expected sediment transport direction; wind: NW, u=15m/s; NN+2m

REFERENCES

Homeier, H. (1962): Historisches Kartenwerk 1:50000 der Niedersächsischen Küste. - Jber. Forschungsstelle für Insel- und Küstenschutz, Norderney, 1961, Bd. 13

Niemeyer, H. D., Ladage, F. and H.-J. Stephan (2007): Untersuchungen zur Bildung von Strandinseln und tidehochwasserfreien Platen im westlichen Wurster Watt im Hinblick auf das Einbringen von Baggergut. - Gutachten 02/07, NLWKN-FSK, Norderney

SEDIMENTATION OF THE SPANISH RESERVOIRS AS SAND SOURCE FOR BEACH NOURISHMENT

Virginia Sánchez[1]

The increasing difficulty to find and to exploit new marine or terrestrial deposits for the nourishment of beaches is a reason to look for other different possibilities. Besides, sediments constitute an essential, integral and dynamic part of the river basins, estuaries and coastal zones. Therefore they should be managed adequately as a resource in view of its ecological and socioeconomic value. The combination of two problems, the first the evident erosive tendency of the Spanish coast and the second the sedimentation in reservoirs, the Directorate General of Coasts of the State Secretary of Territory and Biodiversity of the Spanish Ministry of Environment commissioned CEDEX with the following study to verify the validity of the sedimentation of the Spanish reservoirs to be used as sand source for beach nourishment. This poster shows the results of the first stage of study, already concluded, where information about the current situation of sedimentation of the Spanish reservoirs near coastal zones is compiled. It is analysed the nature of the sediments and finally the necessary requirements for the dam and the material are marked in order to be considered to be valid for beach nourishment.

METHODOLOGY

The study has been divided in the following phases: (1) Knowledge of the present condition of sedimentation of the Spanish reservoirs;(2) Selection of viable reservoirs according to the proximity to the coast and the volume of sedimentation;(3) Determination of the requirements that give viability to a project of resource management of reservoir sedimentation.

SEDIMENTATION OF THE SPANISH RESERVOIRS

About the knowledge of the present condition of sedimentation in Spain, the volume of sedimentation is still unknown and therefore the total capacity of the Spanish reservoirs. There is a lack of information about sedimentation and the main data of this study coming from bathymetry studies made by the Centre for Hydraulic Studies from the CEDEX, in numerous dams of the Spanish geography, from 1967 up to now. Besides it was used the layer HIDRO (ArcGis) of the Directorate General of the Water of the Ministry of Environment.

The situation of the sedimentation in Spain according to the data provided by the Centre for Hydrographic Studies of the CEDEX (concerning 109 dams) is:

- The volume of storage is about 17,000 hm^3 and the volume of sedimentation is about 5,016 hm^3.

[1] Área de Estudios de Costas, Centro de Estudios de Puertos y Costas (CEDEX), c/ Antonio López 81, Madrid, 28026, España.

- About 58% of the 109 reservoirs has a volume of sedimentation lower than its storage capacity.
- About 33% of them has a volume of sediments from 10% to 50% of its storage capacity.
- Only the volume of sediments of 9% of them is higher than 50% of its storage capacity.

Figure 1: Valdeinfierno reservoir (Initial capacity: 25 hm^3; Volume of sediment acumulated: 14 hm^3)

The analysis of samples of sediments of 72 reservoirs presents as result the following average sediment size distribution: 23 % of sand, 58% of silt and 19% of clay. The average geochemical composition is: 80% silica and the rest, carbonates and volatile matter (including an average content of organic matter from 5% to 7%.

The spatial distribution of the sediment in the bottom usually has a decreasing size gradient from the end of the reservoir to the area near the dam when the water level of the reservoir has a little change and the bottom outlets are not frequently operated. However, it is possible to find reservoirs where this tendency does not appear, so it would be advisable to make drilling cores in order to know the stratigraphy of the reservoir.

SEDIMENT REMOVING SYSTEMS

There are three main strategies of managing sedimentation inside reservoirs:

- Minimising sediment loads entering
- Minimising deposition
- Removing accumulated sediments

In spite of the remedial measures that have been done to decrease the erosive process in the catchment area and the transport of solids through the river (soil and conservation measures, reforestation and improvement of permanent ground grass cover) it is obvious that a great amount of sediments still reach the reservoir. The knowledge of the potential use of this sedimentation is the objective of this study and therefore is necessary to know how to remove it from the basin of the reservoir.

The main techniques of sediment removal in a reservoir can be classified according to the type of sediments:

Table 1. Techniques of sedimentation removal according the type of sediments

Gravel/Sand		Silt/Clay	
Mechanical removal (empty reservoirs)	Dredging machine (full reservoir)	Flushing/density current	Dredging machine (suction pump)

The extraction methods used in empty reservoirs are the same used for the traditional excavation . Its application is limited to the delta or reservoir banks of granular or unconsolidated material.

The use of a dredging machine to lift the material located on the bottom and bring it to the land, by mean for example of belt conveyors, needs to create a storage area to allow the material to dry before transportation. This system is generally used when it is not advised to empty of the reservoir because it is essential to community life, water supply or irrigation in arid regions.

The flushing or emptying of the basin opening the bottom and half-bottom outlets, allows the natural flow to remove sediments which are located in the basin but bring them downstream. Generally this method is combined with another mechanical system, which increases its effectiveness and reduces considerably the amount of water consumed. A suction pump, located on a floated barge, lifts the material from the bottom and conveys it to a storage area. There are some suction pumps easily dismountable and transportable by highway or railway and they are able to work at 15-20 m dept.

In most of the cases it would be necessary a treatment area where separate the coarse material and reflow the silt and clay.

The managing strategies of the sedimentation in Spain up to now are: the building of debris dams, the reforestation of the soil, the removing of the material by flushing through bottom outlets with partial or total emptied of the reservoir and the dredging. These management methods are not adequate with the aim of the subsequent use of the sediments as nourishment material. There is also one of them, the dredging, that would be adequate but the volume of dredged material has not been enough to be interesting for nourishment (for example the Foix, Linsoles, Sarra and Gállego reservoir were dredging, but the volume of sediments was between 5,000 -15,000 m^3).

USE OF RESERVOIRS SEDIMENTS AS SAND SURCE FOR BEACHES

The principal requirements that it is necessary to know and that give viability to a project of resource management of reservoir sedimentation as sand source for beach nourishment are:

Regarding reservoirs

- Description of the reservoir (specially its distance to the coast)

The main characteristics of the reservoir, type, location, distance to the coast, storage capacity, maximum and minimum level height.

- Quantity of the sediments

Annual rate and total volume of sedimentation in the reservoir. It would be necessary periodic bathymetries.

- Stratigraphy of the sediments

Vertical and horizontal distribution of the sediments, thickness of the layers of different size materials (gravel, sand, silt, clay). It would be necessary to make deep and superficial drillings.

- Compatibility between the extraction and the ordinary exploitation

The objective of the reservoir as water supply, irrigation, hydroelectric power station or its recreational use by fisherman, sailor influences the selection of the extraction method and the right period of the year to carry the extraction out.

- Location in areas of special protection

The location of the reservoir in a natural reserve could not allow to carry out this kind of project or perhaps would force to establish corrective and preventive measures in an environmental oversight program.

- Available storage area to dry material

It could be necessary to have a storage area near the reservoir in order to dry the extracted material before its transportation or to treatment it.

- Original limnology (reservoir / river)

The original limnology of the reservoir and the river should be study in order to determine the differences between the situation before and after the extraction. This could help to regenerate the habitat if it would be necessary (checking by field-test in specific points).

Regarding sediments and water

- Physical and mineralogical analysis

The main data of the physical analysis are: the percentage of sands, D_{50} and the mineralogical composition (Illite, Calcite, Quartz, Dolomite…)

- Chemical analysis

The main data of the chemical analysis are the metal concentrations (Zn, Cu, Pb, Ni, Cr, Cd and Hg), contamination and content of organic matter. The values of these parameters would make necessary a decontamination pretreatment of the water before to return it to the basin.

- Biological analysis

It should be take samples of water, sediments, macrobenthos and fishes and analyze them in order to know if there is a background effect.

The following figure shows a scheme of the treatment of the extracted sediment:

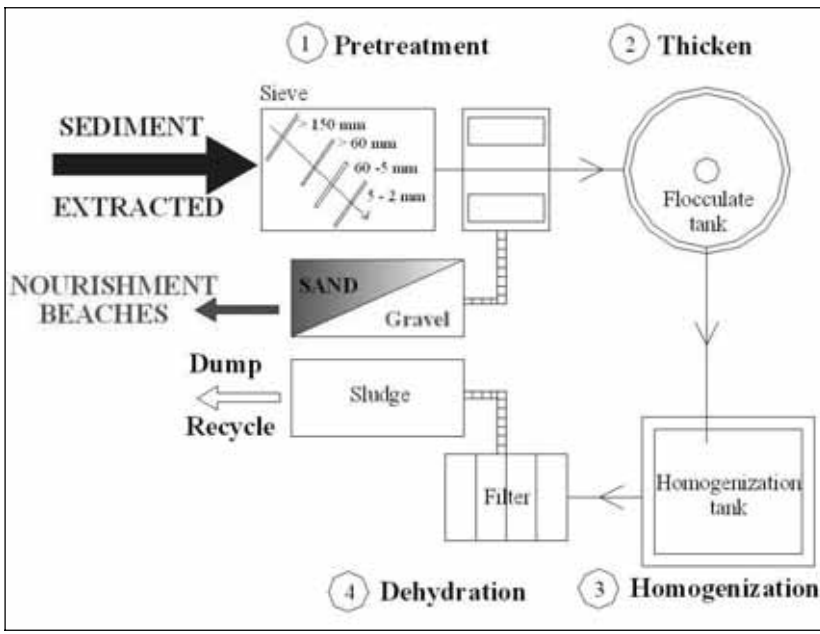

Figure 2: Scheme of the treatment of the extracted sediment.

POTENTIAL USE OF SPANISH RESERVOIRS SEDIMENTS

The volume of sediments in Spain is estimated from a small sample of 109 reservoirs about 5.000 hm^3, but there are about 1200 reservoirs in Spain, so the total quantity is expected to be higher. Nevertheless the main techniques of management carried out are: small dredging (5000 m^3), some isolated flushing and at times building a new dam recovering the capacity of storage.

It were selected the reservoirs located near the coast with data of its sedimentation and volume of sands. Later it were selected those which volume of sand was higher than 0.2 hm^3 and the maximum distance from the coast 50 km, and those which volume of sand was higher than 0.5 hm^3 and the distance from 50 km to 100 km.

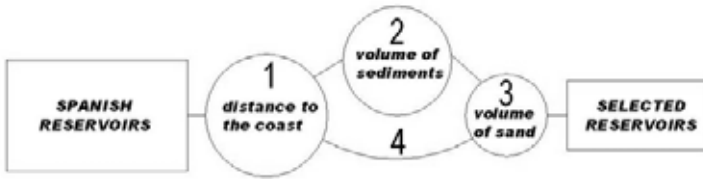

Figure 3: Scheme of the basic criteria to select available reservoirs.

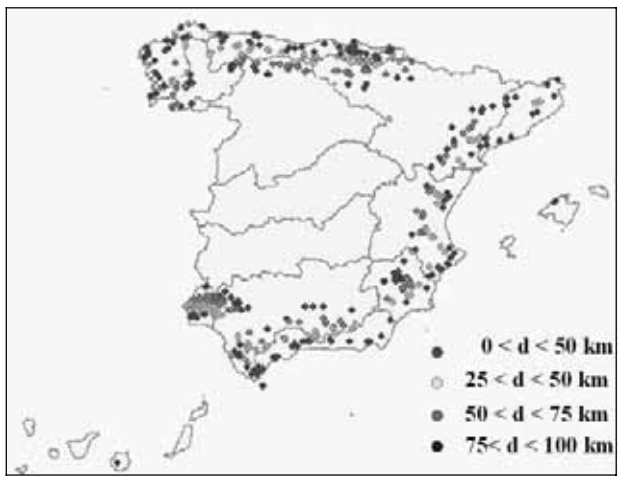

Figure 4: Distribution of the Spanish dams located maximum 100 km away from the coast.

Table 2. Result of the analysis of the Spanish sedimentation

• CRIT.1: 451 are located in a radius of 100 km from the coast
• CRIT.2: 51 with sedimentation data → Vol. storage: 6,036 hm³; Vol. sediments : 397 hm³
• CRIT.3: 35 with size distribution data → % sand : 14 %; Vol. sand : 28 hm³
• CRIT.4 → d < 50 km + Vol. sand > 0.2 hm³; d > 50 km + Vol. sand > 0.5 hm³
19 RESERVOIR SHORT-LISTED → Vol. Sand : 26 hm^3

Only 11 % of the reservoirs placed at a maximum of 100 km from the coast possess information about their sediments, the remaining percentage has no data. The analyzed information does not seem to be very promising, except the short-listed 19 reservoirs used for research and it is advisable to obtain more information from the rest using topographic and bathymetric surveys. Finally only 19 reservoirs have been selected, and they have 26 hm^3 of accumulated sand. It is very important to understand that the sediments in reservoirs could be

use as a resource and not as a residue. The sandy component could be use as sand for beaches while the rest could be use for the improvement of lands, the creation of vegetable land or building material.

Figure 5 - Sediment extracted near the Ribarroja's dam, currently being studied for use to reduce problems of subsidence in the Ebro Delta.

The following phase would be select a reservoir where carry out pilot actions to evacuate sediments and in view of the lack of information it is recommended to increase this with bathymetric surveys in the reservoirs near the coast and to implement a database to gather information about reservoirs sedimentation.

CONCLUSIONS

The volume of sedimentation is still unknown in Spain and therefore the total capacity of the Spanish reservoirs. There is a lack of information about sedimentation and a great scattering of that already existing. It is recommended to increase it with bathymetric surveys in the reservoirs near the coast and to implement a database to gather information about reservoirs.

The volume of sediments is estimated about 5,000 hm^3 from a small sample of 109 reservoirs, but there are about 1200 reservoirs in Spain, so the total quantity is expected to be higher. Nevertheless the main techniques of management carried out are: small dredging (≈ 5,000 m^3), some isolated flushing and at times building a new dam recovering the capacity of storage.

This study has pointed out the main requirements that give viability to a project for the use of the reservoir sediments as sand source for beach nourishment.

It has been selected 19 reservoirs according to the proximity to the coast and the volume of sand (26 hm^3). In order to select a reservoir where pilot actions to evacuate sediments could be carried out it will be necessary at least:

- Regarding reservoir: (1) little distance from coast; (2) good stratigraphy (not dispersed sands); (3) percentage of sand: as high as possible, to reduce the cost of extraction and treatment; (4) compatibility between extraction and exploitation; (5) preferably not located in areas of special protection;

(6) available storage area to dry material before transportation, and (7) knowledge of the limnology of the river and the reservoir.

- Regarding sediments: (1) size distribution and D50 compatible with the beach where it would be dump; (2) content of organic matter: as low as possible, to reduce the risk of eutrophitation and environmental impact; (3) low metal concentrations and contamination, because the need for treatment would increase significantly the cost of the management.
- Regarding environment: (1) to check the recommended limit of the concentration of suspended solids in the reservoir by field-test measuring: suspended solids, turbidity and fish fauna in the reservoir and the river; (2) to carry out more detailed studies concerning the effects of the release of metals in the water with toxicological essays.

This kind of project demands the coordination of the parts involved: water, coastal and environmental authorities and industrial promoters. It requires as well, transparency with the stakeholders: inhabitants, fishermen and land owners.

ACKNOWLEDGMENTS

The author gratefully acknowledge the information provided by Rafael Cobo Rayán of the Centre of Hydraulics Studies of the CEDEX.

REFERENCES

Buceta, J.L. 2004. "Guía metodológica para la elaboración de estudios de impacto ambiental de las extracciones de arenas para la regeneración de playas". Centro de Estudios de Puertos y Costas del CEDEX.

Borrachina. P., Palau. A., and Espinos, J. 2002. Protocolo para la minimización de efectos ambientales sobre la fauna ictícola en el vaciado de embalses. *VII Jornadas Españolas de Presas*. Comité Nacional Español de Grandes Presas. Vol. 3, 371-381.

Caroni, E. and V. Fiorotto. 2007. Integrated sediment management approach for a chain of reservoirs on the Cellina river. *Interreg IIIb. Alpine Space Program*. Project Alpreserv.

Cesare, G., and Pieer-Benoît R. 2007. Restoration and preservation of storage capacity in the small alpine reservoir Tourtemagne. *Interreg IIIb. Alpine Space Program*. Projetc Alpreserv.

Cobo, R. 2002. Modelos de sedimentación de embalses. *Jornadas Seprem. Sociedad Española de Presas y Embalses*., 88-101.

Cristóbal, F. 2005. Destino final de fangos de depuración. *XXIII Curso sobre tratamiento de aguas residuales y explotación de estaciones depuradoras.* Tomo II. CEDEX

European sediment research network. 2004. Contaminated sediments in European river basins.

Jacobsen, T. 1997. Removal of sediments from a reservoir with the saxophone sediment sluicer. *XIX International Congress on large dams. ICOLD* (q. 74, r. 26)

Jornadas Seprem. 2002. *Sociedad española de presas y embalses*.

Poulos, S.E., and M.B. Collins. 2002. Fluvial sediment fluxes to the Mediterranean Sea: A quantitative approach and the influence of dams. Sediment flux to basins: causes, controls and consequences. *Geological Society, London,* special publications, 191, 227-245

Sanctus, E. 1997. Sedimentation phenomena and evacuation methodologies or the Sabetta reservoir on the Sussento river in the Campania Appennine Chain (Southern Italy). *XIX International Congress on large dams*. ICOLD (q. 74, r. 69)

Serrano, M. 1997. Sediment removing systems. *XIX International Congress on large dams. ICOLD* (q. 74, r. 31)

Schneider, J., Knoblauch, H., and H. Badura. Sediment management techniques. *Interreg IIb. Alpine Space Program*. Projetc Alpreserv.

Universitat politécnica de Catalunya. 2008. *Incidencia de los embalses en la dinámica fluvial. Opciones para una gestión sostenible*. Flumen.

White, R. 2001. Evaluation of sediments from reservoirs. Thomas Telford. HR

Yoon, T.H., and M.K. Kim. 1997. Long-term estimation of spatial distribution of sediment deposition in a reservoir. *XIX International Congress on large dams. ICOLD* (q. 74, r. 19).

EROSIONAL IMPACT ON DANISH COASTS DUE TO CLIMATE CHANGE

Carlo Sørensen[1] and Thorsten Piontkowitz[2]

An atlas of Denmark showing additional coastal erosion by 2050 due to a climate change related sea level rise (IPCC A2) is produced by combining wind data, wave energy calculations, a coastal classification scheme and automated fetch calculation in a GIS environment. Further, detailed local impact assessments are carried out at four pilot sites facing different challenges and reflecting coastline variability. Results at the national and the local level point to the necessity of developing methods for predicting coastline evolution for different coastal types. Decisions regarding long-term adaptation measures should be made on the regional or local level to better account for variations in the coastal zone. The availability of data differs between locations. We recommend the planning and initiation of a national strategy to collect data on local level to allow for local impact assessments. This strategy should define the type and quality of the data as well as set the general framework for impact assessments to allow for the composition of neighbouring local impact assessments into one regional assessment.

INTRODUCTION

Denmark has a long and diverse coastline regarding its geological and geographical characteristics. Open coasts and tidal flat coasts facing the North Sea and sheltered coasts in fiords and bays with fetches that vary from a few hundred metres to several hundred kilometres add to the coastal complexity. The societal interest in realistic estimations of the consequences of climate change has grown greatly in recent years. Various interest groups such as property owners, municipalities, NGOs, the press and organisations with relation to the coastal zone are requesting reliable statements and scenarios concerning the consequences of climate change at different scales for the Danish coastline. The range of scale may go from statements concerning all 7,300 km coastline to an assessment for a particular groin field at a certain coastal location. Hence, impact assessments of the consequences of climate change on the Danish coastline can be complex and multisided depending on the scale of regard, which implicates the following questions:

- How may we proceed in assessing the potential consequences of climate change at different scales?
- At which quality and informative value can impact assessments be performed at different scales?
- What is needed to perform these impact assessments at different scales?

[1] Danish Coastal Authority, Højbovej 1, Lemvig, DK-7620, Denmark, cas@kyst.dk
[2] Danish Coastal Authority, Højbovej 1, Lemvig, DK-7620, Denmark, tpi@kyst.dk

In the Danish national strategy for adaptation to climate change (Danish Government, 2008) the coastal area is one of a total of 11 sectors where climate change may have a large impact and where *ad hoc* adaptation strategies are advocated. Tools for decision-making need to be further developed and answering the above questions may be one step in this direction; pointing to solutions as well as to areas where our current knowledge is still insufficient. Further, a strategy for communicating impact assessments may lead to more reliable and cost-efficient adaptation strategies being applied at all levels.

The main objectives are thus to analyze how approaches for impact assessments of the consequences of climate change can be realized at different scales for the complex Danish coastline. The study further aims at

- Highlighting basic principles needed to perform impact assessments at different scales, such as input data
- Improving the knowledge of the effects of climate change on coastal defence systems
- Enhancing the understanding of the interplay between the coastal defence system and the related socio-economic system under changing boundary conditions
- Improving the process of informing relevant parties (policy makers, public, media, etc.) about the consequences of climate change in the coastal zone in an appropriate way.

The present paper discusses results graphically presented at the poster session (ICCE ´08). Please refer to Piontkowitz and Sørensen (2008) or the poster, both available at the Danish Coastal Authority (DCA) homepage www.kyst.dk for colour presentations of mentioned themes/figures.

METHODS

The following scales and investigation methods are adopted as starting points: At national level analysis of potential additional coastal erosion due to sea level rise along the entire Danish coastline until year 2050 is undertaken and implemented by the production of a GIS-based coastal erosion atlas. At local level more detailed impact assessments of the consequences of climate change at four different coastal locations are performed, Fig 1. The pilot sites represent different types of coast, different types of coastal defence measures and different degrees of hinterland occupation.

For the projections of sea level rise the A2 scenario (IPCC, 2007) is used. Local level impact assessments are further made for a 6 mm/y sea level rise. Additionally, at the two pilot sites situated on the North Sea coast a modified A2 scenario is used that incorporates the 4 mm/y sea level rise experienced there since 1973 (Knudsen, Sørensen and Sørensen, 2008) which may affect the assessments of the future needs for sand nourishments on the North Sea coast .

Figure 1. Map of Denmark showing the locations of the four pilot sites.

At national level

Previously the only study to evaluate stretches of erosion and deposition along the entire Danish coastline was performed by Bird (1974). Numerous studies, however, have dealt with coastal development on local and regional scales. DCA has registered all coastal defence measures from aerial photographs and video and produced a map of inferred littoral transport directions based on e.g. accumulations behind groins and marine depositional landforms (see e.g. DCA, 1999). Furthermore, a registration of low-lying areas and reclaimed areas has previously been carried out. A compilation of these studies forms the background for evaluating the current state of the Danish coastline. Coastal erosion is by far more common than deposition.

A simplified coastal classification scheme divides the coastline into 5 categories: rocky coasts, soft cliff coasts, tidal flat/marsh coasts, and sandy/littoral dune coasts.

To get a measure of the wave energy levels along the coastlines, the SPM-formulas were applied to wind measurements and fetch calculations in an automated GIS environment. In order to be representative on a regional scale, 10 year data series of wind speed and wind direction from the Danish Meteorological Institute were obtained from 16 locations around Denmark and corrected to 10 m's height. Fetch calculations were based on and further developed from Ekebom, Laihonen, and Suominen (2003a,b). The alongshore resolution was for computational purposes set at 5 km, Fig 2. For each 5 km of coastline wind- and wave roses were then computed and simplified into 7 wave

energy classes as well as into inferred littoral transport directions (or no significant net transport).

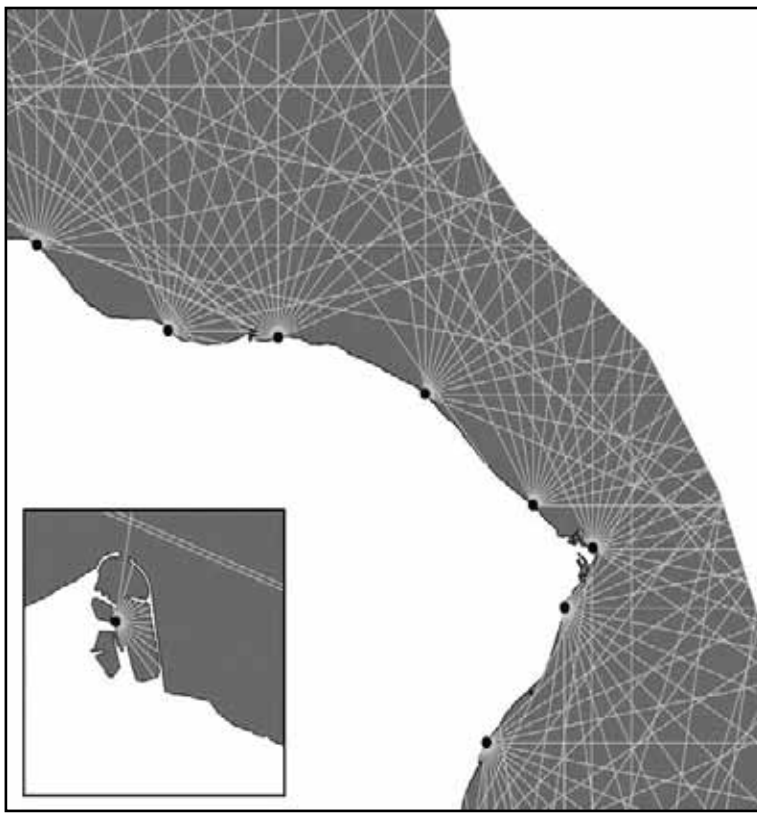

Figure 2. Example of fetch calculations made at 5 km intervals along the Danish coastline. Points that are not representative of a particular stretch of coast are omitted (inserted) in the erosion atlas.

In the vast literature on coastal profile development and coastal erosion in relation to sea level rise, still no one model seems to satisfactorily describe and predict coastal development. Used for decades in various forms, mainly due to its simplicity, is the Bruun rule and variations thereof. There are studies in favour (e.g. Zhang, Douglas and Leatherman, 2004) and against the use of the Bruun rule (e.g. Cooper and Pilkey, 2004). Still, the rule may only be valid for unconsolidated coasts. Suggestions have been forwarded that estimations based on the historical coastline evolution, on expert judgments, or, on probabilistic methods may in many cases be more valid alternatives. Of a particular interest to future studies of the Danish coastlines, however, is the recent work on soft cliff erosion (e.g. Dickson, Walkden and Hall, 2007; Walkden and Dickson, 2008). Jensen and Knudsen (2008) found that the increased coastal erosion due

to sea level rise and a climatic deterioration will be modest (1-2 m) by year 2050 and increase considerably in the second half of this century. They combined a Bruun rule approach of averaged profile steepness with wave exposure (exposed, moderately exposed, and protected coasts).

In this study a combination of a Bruun rule approach (on the sandy/littoral dune coasts), investigations of historical erosion rates from aerial photographs, previous studies and expert judgements from several colleagues with knowledge and experience in coastal evolution was used to assess the potential future additional erosion due to climate change in the matrix combining the coastal classes with the calculated energy levels energy. Existing coastal defence measures were ignored.

The four pilot sites

The four pilot sites (Fig. 1), selected to reflect the coastline variability and the different challenges facing the communities in the year 2050 due to coastal erosion, inundation and flooding, and, investigated into more detail, are:

- *Ballum-Koldby* on the Danish Wadden Sea coast is a low-lying agricultural area protected by a summer dike only.
- *Houvig* on the open North Sea coast of Jutland contains many holiday houses. The coast is sand nourished and managed dunes protect the hinterlands from flooding during storm surges.
- Løgstør is a small town in the Liim Fiord of which a large part is liable to flooding during storm surges. Coastal erosion is currently experienced adjacent to the town and harbour.
- Aabenraa is a town situated in a fiord in southern Jutland towards the Baltic Sea and is liable to flooding but is currently experiencing relatively little coastal erosion along the fiord.

No single model accommodates parameterizations for the different classes of coastline and, in general and at the pilot sites, data availability is scarce and varying. Different methods were thus applied at each of the four pilot sites. First, however, historic evolution at the sites was investigated from old charts, aerial photographs and from satellite photos. Together with investigations of the physical appearance of the coastline, morphological features, the degree of coastal protection and infrastructure, this forms the basis for the local assessments. Secondly, all available data on hydrodynamic forcing, depth measurements etc. were gathered and analysed in relation to current sediment budgets and the vulnerability to flooding, and a first approximation of the impact of climate change is assessed. As coastal erosion rates are not linear in time in an ever evolving coastal landscape with a large natural climatic variability, this is not an easy task. Where possible, the coastal erosion is looked into in morphological units that take into account the coastal areas of erosion, transitional areas and areas of deposition but, even so, this may not suffice. One example is the pilot site at Løgstør where the breach towards the North Sea of

the Liim Fiord barriers in 1825 had a large impact of storm surge water levels and coastal erosion rates, and another is Ballum-Koldby where the shifting of sand further out in the Wadden Sea may lead to a different hydrodynamic forcing in the future. The differentiation between the 'natural' coastal erosion and the additional erosion due to climate change is difficult, and has not been made for all pilot sites.

RESULTS

A coastal erosion atlas of Denmark

One outcome of the study at a national level is the production of a coastal erosion atlas of potential additional coastal erosion until year 2050 due to a climate change related sea level rise. The additional erosion amounts to between 0 m (rocky coasts) and 5-7 m on the exposed sandy/littoral dune coasts facing the North Sea. The less exposed coastlines face an additional erosion of 0.5-3 m. On the North Sea coast the additional erosion only constitutes a small fraction of the total erosion with current natural rates (with no sand nourishment) of 1-7 m/y. At some coasts currently experiencing no erosion the impact will become relatively larger. In relation to the coastal erosion atlas thematic maps of the coastal classification, of wind energies, wave energies and of littoral transport directions have been produced (see Piontkowitz and Sørensen, 2008). Together with previously produced maps of e.g. extreme water levels, these may be refined into valuable tools for impacts assessments and adaptation strategies when downscaled to accommodate local conditions.

One, of course, may argue both that the uncertainties are too large in assessing future coastal erosion and that it is impossible to differentiate between current and future erosion rates. Erosion also depends on the combination of a number of parameters (water level, wave-energy, wave refraction, sediment composition and abundance, shifting points of wave attack etc.). Still, the atlas may be used to get an overview.

The map does not tell, however, if this erosion actually will occur, as this locally will depend on the current and future states of the coast. Future additional erosion may be negligible, or, turn out to become considerably larger than assessed at the national level. It has to be investigated in more detail and to be divided into erosion, permanent inundation and the liability to flooding. It further has become increasingly apparent that in many cases the sea level rise itself is inferior to changes in the wind climate, and thus to the wave energies reaching the coast, in determining the future rate of change. Finally does the transitional zone between the North Sea and the Baltic Sea show a complex signature of water level variations with non-periodic extremes that are not always directly related to storm events in the Danish waters, as will the manifestation of a future global sea-level rise differ regionally due to variations in glacial isostatic adjustment (GIA).

The four pilot sites

The consequences of climate change for Ballum-Koldby will mainly result in the loss of land due to inundation and more frequent flooding of the polder area behind the summer dike. Based on the chosen scenarios (A2 and 6mm/yr) the land loss until 2050 along the 6 km of coastline totals 0.36 km^2 (59.5 m^2/m) and 0.41 km^2 (67.8 m2/m), respectively. It is, however, unclear to which degree erosion will occur as the geomorphologic processes at the foreland in front of the summer dike are at present dominated by net sedimentation due to a very flat foreshore combined with offshore areas of sedimentation. Inundation will cause a landward retreat of the salt marsh and allow erosion of the marsh soils. The most severe consequence of climate change, however, is an increased frequency of flooding from a return period of 1.2 y to 2-4 times per year in 2050. This will complicate agricultural use of the area and may cause destruction of existing building structures. Site-specific measures, such as minor ring dikes or movable flood protection barriers, at the five farms may be considered.

At Houvig the coastal stretch of interest totals 10 km and may be described as a highly exposed littoral dune coast. The hinterland is characterised by a variety of tourist activities and app. 2,000 holiday houses of which some are placed less than 150 m from the coastline. These are threatened in particular as local dunefoot retreat of up to 25 m has been recorded during individual storms in recent years. Land loss due to inundation by 2050 is 8.8 m^2/m (A2) and 10.7 m^2/m (6 mm/y), respectively. The autonomic coastal retreat rate, based on the average of 1.35 m/y from 1957 to 1996, will lead to a land loss of 730.000 m^2 in 2050 relative to 1996. Dune erosion may lead to safety criteria against flooding not being met at several locations. Even with an increase in the amount of sand being nourished, the site will be under pressure.

Aabenraa is currently experiencing a sea level rise and will under a climate change scenario be even more vulnerable to flooding of the lower-lying parts of the town. Regarding the coastal erosion, sediment transport rates have been small in the fiord over the last couple of centuries but may increase considerably at some locations in the future. The susceptibility to flooding, however, is the main issue here. As extreme water levels in Aabenraa are sometimes related to rarely occurring wave phenomena in the Baltic Sea – North Sea transition, a future climatic deterioration may bear larger implications on the surge levels and the associated consequences, than the sea level rise alone.

Finally, Løgstør is currently experiencing both flooding of the town and coastal erosion of the adjacent coastlines during storm surges. Even with the current rates of erosion, problems are foreseen in the near future as breaches at the coast toward a canal behind the coastline may lead to new points of attack from the waves and to diminishment of some of the current natural flood protection. Furthermore, the current and recently improved storm surge barriers at the town may prove insufficient even with a modest sea level rise. A water level of 1.92 m with a statistical return period of 100 y today is expected to occur every 7 (6 mm/y) to 30 years (A2) by 2050.

DISCUSSION AND CONCLUSIONS

Rates of impact of climate change on coastal erosion, inundation and flooding were found to vary greatly between the pilot sites relating to the varying coastline classifications, profile steepness, exposure and orientation of the coastline etc. as well as within different morphological units at the individual pilot sites. In general, from the pilot sites and elsewhere along the Danish coastline it therefore may be concluded that impact assessments even at a local level may be a difficult task. Attention must be given to the subject regarding both the methodology and the way it is incorporated in the coastal management at all levels. Progress has to be made from just assessing consequences of sea level rise from elevation maps by local authorities.

The approach used for producing the national erosion atlas compared to those used for the local assessments at the four pilot sites show that on the local level assessments are most adequate if credible results are available to allow for sustainable decisions. Reasons are:

- Impacts of climate change along the Danish coastline vary and have to be considered in decision making processes; also reflected in decisions made on a national level.
- Decisions regarding long-term adaptation measures should be made on the regional or local level, i.e. they should account for local variations in the coastal zone.
- In the process of communicating adaptation measures, public perception on climate change and on its consequences relate to local and thus well-known conditions and measures.
- The availability and quality of data is crucial in the impact assessment. On a local level data are easy to acquire or generate. The intention of a detailed impact assessment on national level to allow for sustainable decisions considering local variations is rather unpromising due to the tremendous workload. At a local level, the performance of impact assessments including the generation of necessary data is manageable.

Further work is needed on coastal change models that accommodate the coastal variability and incorporates climate change. Tools for the assessment of impacts of climate change are very much in demand by local authorities and the work carried out on the four pilot sites are currently in the progress of being transformed into guidelines and tasks for utilisation at a broader scale. This, hopefully, will yield a basic reference for the sharing of knowledge between local authorities and provide realistic scenarios of the future coastal change to be expected.

Based on the above observations, the idea to assist and work together with municipalities in initiating and formulating adaptation strategies to climate change for the coastal sector was developed. The form chosen is to visit relevant employees from the coastal municipalities (3-4 neighbouring municipalities at a

time) for a one day seminar to establish the dialogue and discuss issues relevant to the planning, the management and future challenges facing their coastlines in relation to climate change. So far seminars have either been planned or held by the Danish Coastal Authority for 67 of the 75 local Danish municipalities that have a coastline.

The seminars have been very rewarding to all but have also revealed that, whereas mitigation measures such as energy saving have some focus, tools for decision-making and the focus on adaption strategies are either absent or still in their infancy in most of the visited municipalities. Also, the communication across all levels from the citizens to the government and research institutions needs to be improved. From a scientific point of view it is, however, important to communicate coastal erosion (and deposition) and extreme water levels as continuous physical processes that have been experienced for millennia around Denmark. Extreme water levels occur and coastal erosion rates vary on a seasonal to decadal scale. Uncertainties are large in projections of sea level rise and in estimates of future coastal erosion rates. The consequences of climate change may become severe but only by communicating in an understandable and serious way can we develop sound adaptation strategies and combat beginning public 'climate nausea'.

The availability of data differs from location to location. However, adequate data are needed to perform impact assessments in the coastal zone to allow for sustainable decisions. We recommend the planning and initiation of a national strategy to collect data on local level to allow for local impact assessments. This strategy should define the type and quality of the data as well as set the general framework for impact assessments to allow for the composition of neighbouring local impact assessments into one regional assessment.

ACKNOWLEDGMENTS

The study has been carried out as a part of the SAFECOAST project, co-financed by the European Union in the framework of the INTERREG 3B North Sea program for transnational projects.

REFERENCES

Bird, E.C.F. 1974. Coastal changes in Denmark during the past two centuries. *Skrifter i Fysisk Geografi*, 8, 21pp.

Cooper, J.A.G. and Pilkey, O.H. 2004. Sea-level rise and shoreline retreat: time to abandon the Bruun Rule. *Global and Planetary Change*, 43, 157-171.

Danish Government. 2008. *Strategi for tilpasning til klimaændringer i Danmark*. Schultz, Copenhagen, www.ens.dk, 43pp.

DCA. 1999. *Danmarks Indre Kyster, Kortlægning af kystbeskyttelsen*. Danish Coastal Authority, Lemvig, Denmark, 43pp.

Dickson, M.E., Walkden, M.J., and Hall, J.W. 2007. Systemic impacts of climate change on an eroding coastal region over the twenty-first century. *Climatic Change*, 84(2), 141-166.

Ekebom. J., Laihonen, P. and Suominen, T. 2003a. Measuring Fetch and Estimating Wave Exposure in Coastal Areas. *Littoral 2002, The Changing Coast*. EUROCOAST / EUCC, Porto – Portugal, 155-160.

Ekebom, J., Laihonen, P. and Suominen, T. 2003b. A GIS-based step-wise procedure for assessing physical exposure in fragmented archipelagos, *Estuarine, Coastal, and Shelf Science*, 57(5-6), 887-898.

IPCC. 2007. *Climate Change 2007: The Physical Science Basis. Contribution of Working Group I to the Fourth Assessment Report of the Intergovernmental Panel on Climate Change*. Solomon, S., D. Qin, M. Manning, Z. Chen, M. Marquis, K.B. Averyt, M. Tignor and H.L. Miller (ed.). Cambridge University Press, Cambridge, United Kingdom and New York, NY, USA, 996 pp.

Jensen, J. and Knudsen, S.B. 2008. *Klimaændringers effekt på kysten*. Danish Coastal Authority, Lemvig, Denmark, 71pp.

Knudsen, S.B., Sørensen, C., and Sørensen, P. 2008. *Mean Sea Levels in the Danish Wadden Sea*. Danish Coastal Authority, Lemvig, Denmark, 38pp.

Piontkowitz, T., and Sørensen, C. 2008. *Consequences of Climate Change along the Danish Coasts*. Safecoast Action 5A. Danish Coastal Authority, Lemvig, Denmark.

Sørensen, C., and Ingvardsen, S.M. 2007. *Extreme sea level statistics for Denmark, 2007*. Danish Coastal Authority, Lemvig, Denmark, 245pp.

Walkden, M. and Dickson, M. 2008. Equilibrium erosion of soft rock shores with a shallow or absent beach under increased sea level rise. *Marine Geology*, 251, 75-84.

Zhang, K., Douglas, B.C., and Leatherman, S.P. 2004. Global warming and coastal erosion. *Climatic Change*, 64, 41-58.

AUTHOR INDEX

AUTHOR INDEX

SUBJECT INDEX

ISBN: 978-3-941277-05-2